AN INVESTIGATION INTO COLD DWELL FATIGUE BEHAVIOUR IN Ti6246 AND OTHER AEROSPACE ALLOYS

by

RICHARD JAMES WHITTAKER

A thesis submitted to

The University of Birmingham

for the degree of

DOCTOR OF ENGINEERING

Department of Materials and Metallurgy

The University of Birmingham

Edgbaston

Birmingham

B15 2TT

June 2011

Abstract

The susceptibility of Ti6246 to cold dwell fatigue behaviour has been assessed as part of a wider investigation into the relationship between optical microstructure, crystallographic texture, mechanical behaviour and material processing for various common titanium aerospace alloys.

Assessment of the full range of production microstructures for Ti6246 has shown acceptable maximum texture intensities and common crystallographic size variations. Debit on cold dwell fatigue life has only been observed at very high proportions of the ultimate tensile strength of the material. Heat treatment to eliminate potential 'good' factors in the dwell response of conventional microstructures was also noted not to produce a large cold dwell fatigue life debit. Similar microstructures in the conventionally cold dwell fatigue sensitive alloy Ti6242 also displayed no debit on fatigue life under equivalent loading conditions.

A difference in dwell fatigue behaviour between the two alloys was expected based on previous results. Whilst clear planar slip bands can form in both alloys, the absence of dwell effects may potentially be attributed to one or more factors. A volumetric effect may be responsible. Alternatively, the large colony microstructures may be susceptible to other failure modes to the extent that the mechanism of cold dwell fatigue facet formation is not activated before failure occurs via a different mechanism. Thirdly, whilst planar slip is observed, there may be an insufficient build-up of dislocation stresses at the boundaries of weakly orientated effective structural units. As a result the stress redistribution mechanism for cold dwell fatigue failure may be unable to occur.

Characterisation of optical microstructures and textures has revealed a range of textures associated with different alloys and product forms. It has been noted that common crystallographic features may be observed in very different microstructures in these alloys. It is postulated from this work that the optical microstructure should not be taken as an accurate indication of the effective structural unit size in titanium alloys.

Acknowledgements

The work undertaken in this thesis has been jointly funded by the Engineering and Physical Sciences Research Council (EPSRC) and Rolls-Royce plc. Acknowledgement is given for the financial support provided by both parties.

For day-to-day industrial supervision and input into the broader direction of work the contribution provided by Dr. Katharine Fox is gratefully acknowledged. Grateful acknowledgement is also given to Adrian Walker for his involvement in the wider supervision of the doctorate and his advice and ideas on the subject. Thanks are extended to Thomas Jackson and Nigel Martin for their assistance in areas of work contained within the thesis.

From the University of Birmingham Professor Paul Bowen is acknowledged for his academic supervision. Grateful thanks are also extended to Dave Price for assistance in the mechanical testing work undertaken during the doctorate. Acknowledgement is also given to Dr. Aijun Huang for the training and support provided relating to EBSD analysis techniques.

From Timet UK Paul Garratt is acknowledged for his assistance in vacuum heat treatment work. For a wider contribution to the direction of the thesis acknowledgement is given to Dr. Dave Rugg, Dr. Mark Dixon and Dr. Alex Davidson.

Glossary of Terms

AD	Axial Direction
BCC	Body Centered Cubic
BSE	Back Scattered Electron
°C	Degrees Celsius
CDF	Cold Dwell Fatigue
COM	Crystal Orientation Map
CPFE	Crystal Plasticity Finite Element
CRSS	Critical Resolved Shear Stress
DDW	Dense Dislocation Wall
DLCF	Dwell Low Cycle Fatigue
DSCL	Declared Safe Cyclic Life
EBSD	Electron Back Scattered Diffraction
ESU	Effective Structural Unit
FEG	Field Emission Gun
FCG	Fatigue Crack Growth
FCP	Fatigue Crack Propagation
HCF	High Cycle Fatigue
HCP	Hexagonal Close Packed

HP	High Pressure
HPC	High Pressure Compressor
IP	Intermediate Pressure
IPC	Intermediate Pressure Compressor
IPF	Inverse Pole Figure
K	Kelvin
LCF	Low Cycle Fatigue
LCDF	Low Cycle Dwell Fatigue
MLI	Mean Linear Intercept
MSRR	Rolls-Royce Material Specification
NDE	Non Destructive Evaluation
NTSB	National Transportation Safety Board
OEM	Original Equipment Manufacturer
OIM	Orientation Imaging Map
OPS	Oxide Polish Suspension
OR	Orientation Relationship
PSCL	Predicted Safe Cyclic Life
PWHT	Post Weld Heat Treatment
RD	Radial Direction
R-R	Rolls-Royce

SEI	Secondary Electron Imaging
SEM	Scanning Electron Microscope
SHT	Solution Heat Treatment
SRAS	Spatially Resolved Acoustic Spectroscopy
TD	Tangential Direction
TEC	Thermal Expansion Coefficient
TEM	Transmission Electron Microscopy
Ti6242	Ti-6Al-2Sn-4Zr-2Mo (% by weight)
Ti6246	Ti-6Al-2Sn-4Zr-6Mo (% by weight)
Ti6/4	Ti-6Al-4V (% by weight)
Ti685	Ti-6Al-5Zr-0.5Mo-0.25Si (% by weight)
Ti829	Ti-5.5Al-3.5Sn-3Zr-1Nb-0.25Mo-0.3Si (% by weight)
Ti834	Ti-5.8Al-4Sn-3.5Zr-0.7Nb-0.5Mo-0.35Si-0.06C (% by weight)
TRE	Red Top Investigation
TVAR	Triple Vacuum Arc Remelt
UD	Unidirectional Rolled
UTS	Ultimate Tensile Strength
VAR	Vacuum Arc Remelt
XR	Cross Rolled

Table of Contents

1 Introduction 1-2
1B Volume B - Figures and tables…..... 1-5

2 Literature review – Cold dwell sensitive fatigue in titanium alloys 2-2
2.1 Compressor disc design and requirements 2-2
2.2 Titanium applications in aero gas turbine engines 2-5
2.3 Titanium and its alloys 2-7
2.3.1 Properties of titanium 2-7
2.3.2 Classification of alloys 2-8
2.3.2.1 Near alpha alloys 2-8
2.3.2.2 Alpha + beta alloys 2-10
2.3.2.3 Beta alloys 2-11
2.4 Compressor disc processing 2-12
2.4.1 Ingot production and conversion to billet 2-12
2.4.2 Forging and heat treatment of compressor disc material 2-14
2.4.3 Machining operations 2-16
2.4.4 Forging and heat treatment of Ti6246 compressor discs 2-17
2.4.5 Other titanium alloys with compressor disc applications 2-21
2.4.5.1 Ti685 2-21
2.4.5.2 Ti834 2-21
2.4.5.3 Ti6/4 2-22
2.4.5.4 Ti6242 2-22
2.4.5.5 Ti829 2-23
2.4.6 Microstructural terminology 2-23
2.4.6.1 Beta processed alloys 2-23
2.4.6.2 (Alpha + beta) processed alloys 2-24
2.5 Texture 2-25
2.5.1 Mechanical property effects and processing influences 2-25
2.5.2 Electron back scatter diffraction (EBSD) analysis 2-26
2.5.3 Texture representation using pole figures 2-28
2.6 Plastic deformation and fatigue 2-31
2.6.1 Plastic deformation in titanium 2-31
2.6.2 Fatigue 2-34
2.6.3 Crack lifing methods 2-37
2.6.4 Low cycle fatigue behaviour in Ti6246 2-38
2.7 Cold dwell fatigue behaviour 2-42
2.7.1 Overview 2-42
2.7.2 Historical background – In-service experience 2-43
2.7.3 Cold dwell fatigue mechanisms 2-46
2.7.3.1 Hydrogen effects 2-46
2.7.3.2 Microstructure/micro-texture influences 2-50
2.7.3.3 Time dependent strain accumulation/Combined hydrogen effects 2-56
2.7.3.4 Stress redistribution/Off-loading theories 2-61
2.7.3.5 Macrozone and Effective Structural Unit Size Concepts 2-72
2.7.3.6 Crystal Plasticity Finite Element Modelling 2-78
2B Volume B - Figures and tables 2-82

2.8 Compressor disc design and requirements 2-82
2.9 Titanium applications in aero gas turbine engines 2-84
2.10 Titanium and its alloys 2-85
2.11 Microstructural terminology 2-88
2.12 Texture in metals 2-93
2.13 Plastic deformation and fatigue 2-96
2.14 Cold dwell fatigue behaviour 2-100

3 Experimental procedures 3-2
3.1 Sample preparation 3-2
3.2 Optical microscopy 3-2
3.3 Scanning Electron Microscopy 3-3
3.4 Electron Back Scatter Diffraction 3-3
3.5 Mechanical testing 3-5
3.5.1 Tensile testing 3-5
3.5.2 Fatigue testing 3-5
3B Volume B - Figures and tables 3-7
3.6 Electron Back Scatter Diffraction 3-7
3.7 Mechanical testing 3-9

4 Cold dwell fatigue behaviour in Ti6246 alloy 4-2
4.1 Introduction 4-2
4.2 Experimental method 4-4
4.2.1 Assessment of optical microstructures 4-4
4.2.2 Assessment of crystallographic textures 4-8
4.2.3 Cold dwell fatigue testing of production disc material 4-8
4.2.4 Cold dwell fatigue testing of non-standard Ti6246 microstructures 4-11
4.3 Results 4-14
4.3.1 Assessment of optical microstructures 4-14
4.3.2 Assessment of textures 4-15
4.3.3 Cold dwell fatigue testing of production material 4-15
4.3.4 Cold dwell fatigue testing of non-standard Ti6246 microstructures 4-16
4.4 Discussion 4-18
4.4.1 Assessment of optical microstructures 4-18
4.4.2 Assessment of crystallographic textures 4-24
4.4.3 Cold dwell fatigue testing of production material 4-25
4.4.4 Cold dwell fatigue testing of non-standard Ti6246 microstructures 4-27
4.5 Conclusions 4-32
4B Volume B - Figures and tables 4-35
4.6 Introduction and experimental method 4-35
4.7 Results 4-42
4.7.1 Assessment of optical microstructures 4-42
4.7.2 Assessment of textures 4-49
4.7.3 Cold dwell fatigue testing of production material 4-55
4.7.4 Cold dwell fatigue testing of non-standard Ti6246 microstructures 4-62

5 Cold dwell fatigue performance of beta processed titanium alloys 5-3
5.1 Introduction 5-3
5.2 Experimental method 5-6
5.2.1 Characterisation of source material 5-6
5.2.1.1 Ti6246 effective strain distribution modelling 5-6
5.2.2 Blanks sectioning 5-7
5.2.2.1 Ti6246 pancake forgings 5-7
5.2.2.2 Ti6242 discs 5-7
5.2.3 Heat treatment 5-7
5.1.1.1 Ti6246 heat treatment 5-7
5.1.1.2 Ti6242 heat treatment 5-9
5.2.3.1 Friction welding of Ti6242 specimens 5-11
5.2.4 Mechanical testing 5-13
5.2.4.1 Tensile testing 5-13
5.2.4.2 Fatigue testing 5-13
5.3 Results 5-15
5.3.1 Material characterisation 5-15
5.3.1.1 As-received Ti6246 optical microstructures 5-15
5.3.1.2 As received Ti6246 crystallographic textures 5-15
5.3.1.3 As received Ti6242 optical microstructures 5-16
5.3.1.4 As received Ti6242 crystallographic textures 5-16
5.3.1.5 Ti6246 microstructures following beta heat treatment 5-16
5.3.1.6 Ti6246 textures following beta heat treatment 5-18
5.3.1.7 Ti6242 microstructures following beta heat treatment 5-19
5.3.1.8 Ti6242 textures following beta heat treatment 5-20
5.3.2 Mechanical testing 5-20
5.3.2.1 Ti6246 tensile testing 5-20
5.3.2.2 Ti6246 fatigue testing 5-21
5.3.2.3 Ti6242 tensile testing 5-21
5.3.2.4 Ti6242 fatigue testing 5-21
5.3.3 Specimen fractography 5-22
5.3.3.1 Ti6246 tensile tests 5-22
5.3.3.2 Ti6246 fatigue tests 5-22
5.3.3.3 Ti6242 tensile tests 5-22
5.3.3.4 Ti6242 fatigue tests 5-22
5.3.4 Fatigue test strain accumulation behaviour 5-23
5.4 Discussion 5-24
5.4.1 Beta heat treatments 5-24
5.4.2 Ti6246 cold dwell fatigue testing 5-25
5.4.3 Ti6242 cold dwell fatigue testing 5-27
5.5 Conclusions 5-30
5B Volume B - Figures and tables 5-33
5.6 Experimental method 5-33
5.6.1 Ti6246 strain profile modelling 5-33
5.6.2 Ti6246 cut-up diagrams 5-34
5.6.3 Ti6242 cut-up diagrams 5-35
5.6.4 Heat treatment 5-36
5.6.5 Specimen rotary friction welding 5-37

5.7 Results 5-40
5.7.1 Ti6246 As-received microstructure 5-40
5.7.2 Ti6246 As-received texture 5-41
5.7.3 Ti6242 As-received microstructure 5-44
5.7.4 Ti6242 As-received texture 5-45
5.7.5 Ti6246 heat treated microstructures 5-48
5.7.6 Ti6246 heat treated textures 5-51
5.7.7 Ti6242 heat treated microstructures 5-52
5.7.8 Ti6242 heat treated textures 5-58
5.7.9 Tensile testing 5-60
5.7.10 Fatigue testing 5-61
5.7.11 Specimen fractography and microstructures 5-66
5.7.11.1 Ti6246 tensile specimens 5-66
5.7.11.2 Ti6246 LCF specimens 5-68
5.7.11.3 Ti6246 dwell LCF specimens 5-69
5.7.11.4 Ti6242 tensile specimens 5-70
5.7.11.5 Ti6242 LCF specimens 5-72
5.7.11.6 Ti6242 dwell LCF specimens 5-74
5.7.12 Strain accumulation data 5-76
5.8 TWI report on rotary friction welding of Ti64/Ti6242 Cylinders 5-77

6 Characterisation of macrozone and effective structural unit sizes in Ti alloys 6-2
6.1 Introduction 6-2
6.2 Experimental procedure 6-4
6.3 Results and discussion 6-5
6.3.1 Ti685 disc material 6-5
6.3.1.1 Ti685 cold dwell fatigue test specimens 6-11
6.3.2 Ti-6Al-4V fan disc material 6-14
6.3.2.1 Ti6/4 cold dwell fatigue test specimen 6-14
6.3.3 Ti834 disc material 6-20
6.3.4 Ti6242 material 6-23
6.3.4.1 Ti6242 billet 6-24
6.3.4.2 Ti6242 disc 6-27
6.3.5 Ti6246 disc material 6-30
6.3.5.1 Beta forged Ti6246 disc material 6-30
6.3.5.2 Alpha-beta solution heat treated Ti6246 6-37
6.3.5.3 Beta annealed Ti6246 6-39
6.3.6 Ti829 cold dwell fatigue test specimens 6-42
6.4 Conclusions 6-47
6B Volume B - Figures and tables 6-51
6.5 Introduction 6-51
6.6 Experimental procedure 6-52
6.7 Results 6-53
6.7.1 Ti685 disc material and test specimens 6-53
6.7.2 Ti-6Al-4V DLCF test specimen 6-63
6.7.3 Ti834 disc 6-70
6.7.4 Ti6242 billet 6-74

6.7.5 Ti6242 disc 6-81
6.7.6 Ti6246 disc material 6-84
6.7.7 Ti829 disc and test specimens 6-99
6.7.8 Conclusions 6-108

7 Processing effects on texture in Ti6246 forgings 7-1
7.1 Introduction 7-1
7.2 Experimental method 7-2
7.3 Results 7-5
7.3.1 Grain flow 7-5
7.3.2 Microstructure and texture assessments 7-5
7.3.2.1 As-forged condition 7-5
7.3.2.1.1 Isothermal pancake forging 7-6
7.3.2.1.2 Hot die pancake forging 7-8
7.3.2.1.3 Hammer pancake forging 7-11
7.3.2.2 Solution heat treated condition 7-13
7.3.2.2.1 Isothermal pancake forging 7-13
7.3.2.2.2 Hot die pancake forging 7-16
7.3.2.2.3 Hammer pancake forging 7-19
7.3.2.3 Age heat treated condition 7-21
7.3.2.3.1 Isothermal pancake forging 7-22
7.3.2.3.2 Hot die pancake forging 7-23
7.3.2.3.3 Hammer pancake forging 7-23
7.3.2.4 Production disc forgings 7-23
7.4 Discussion 7-25
7.4.1 Effect of forging method on grain flow and optical microstructure 7-25
7.4.1.1 Isothermal forging 7-26
7.4.1.2 Hot die forging 7-30
7.4.1.3 Hammer forging 7-32
7.4.2 Effect of forging method on crystallographic texture 7-37
7.4.2.1 Isothermal forging 7-37
7.4.2.2 Hot die forging 7-41
7.4.2.3 Hammer forging 7-42
7.4.3 Cold dwell fatigue behaviour/Effective structural unit size effects 7-44
7.5 Conclusions 7-47
7.5.1 Isothermal forging 7-47
7.5.2 Hot die forging 7-48
7.5.3 Hammer forging 7-49
7B Volume B - Figures and tables…. 7-51
7.6 Experimental details 7-51
7.7 Results 7-53
7.7.1 Grain flow profiles 7-53
7.7.2 Microstructure and texture assessment 7-55
7.7.2.1 Isothermal pancake – As-forged condition 7-55
7.7.2.2 Hot die pancake – As-forged condition 7-64
7.7.2.3 Hammer pancake – As-forged condition 7-68
7.7.2.4 Isothermal pancake – Solution heat treated condition 7-75
7.7.2.5 Hot die pancake – Solution heat treated condition 7-83

7.7.2.6 Hammer pancake – Solution heat treated condition.....7-93
7.7.2.7 Isothermal pancake – Age heat treated condition 7-100
7.7.2.8 Hot die pancake – Age heat treated condition.....7-102
7.7.2.9 Hammer pancake – Age heat treated condition 7-103
7.7.2.10 Production disc forgings.....7-105
7.8 Discussion.....7-108

8 Conclusions and Further Work..... 8-2
8.1 Summary of conclusions..... 8-2
8.2 Further work..... 8-5

9 References.....9-1

1 Introduction 1-2

1B Volume B - Figures and tables…….....1-5

1 Introduction

The work contained within this thesis covers the key findings of a study of the optical microstructures, crystallography and mechanical behaviour of the Ti6246 alloy and various other titanium aerospace alloys. The alloys that have been studied are listed in Table 1-1, which also gives the various forms and conditions in which each alloy has been assessed. The major focus of the investigation was the susceptibility of Ti6246 to a failure mode referred to as cold-dwell fatigue (CDF) behaviour.

CDF behaviour is a well-documented problem affecting several common titanium aerospace alloys. For sustained sub-yield stresses at ambient temperatures a failure mode can occur as a result of stress redistribution from weakly orientated onto strongly orientated regions of microstructure. This is related to the anisotropy in material properties associated with the crystal structure of titanium at low temperatures. The result of stress redistribution is the formation of quasi-cleavage facets on a plane normal to the direction of applied stress. CDF is primarily a crack initiation problem. Early crack initiation can allow fatigue crack growth at lower cyclic lives and may lead to potentially catastrophic failure of compressor disc components during predicted safe disc operating lifetimes. Occurrences of CDF failure in compressor disc components have been reported from several original equipment manufacturers.

Since the CDF mechanism was first recognised in 1973 a considerable amount of time and effort has been devoted to the characterisation of the mechanism and the reduction or elimination of this sensitivity. The majority of the published work is studied under a literature review that forms the second chapter of this thesis.

The first chapter of results (chapter four) discusses the investigation of CDF behaviour in Ti6246. The need for an assessment of behaviour under dwell loading arose after large optical structural units were observed on the diaphragm sections of a batch of Trent engine Intermediate Pressure compressor discs. Assessment using electron back-scatter diffraction (EBSD) also indicated the existence of large regions of common crystallographic texture. Based on these observations a comprehensive assessment of variations in optical microstructures and textures was undertaken as part of an investigation into Ti6246 dwell fatigue behaviour. Also included in this chapter are the results of mechanical testing of Ti6246 in standard and modified microstructural conditions.

Chapter five follows on from the mechanical testing work discussed in chapter four. This work is concerned with the development of a Ti6246 microstructure more likely to show susceptibility to CDF loading. There is a comparison of the mechanical behaviour of this material both to that of previous results and to behaviour in a conventionally dwell sensitive alloy subject to heat treatment processing to generate a similar microstructure.

Chapter six investigates the relationship between optical microstructures and crystallography for a number of common titanium aerospace alloys. EBSD assessment has been used both to characterise the strength of textures in different alloys and product forms and to establish differences in optical and crystallographic microstructures. Further work studies the crystallography of laboratory test specimens to infer effective structural unit sizes.

Chapter seven discusses the variations in optical microstructures and textures observed in a batch of pancake forgings produced using different forging methods

and post-forge processing routes. This work also considers the development of the optical microstructure and texture with the typical forging, solution heat treatment and ageing operations associated with the conventional processing of Ti6246.

The thesis is concluded with a discussion of the findings of doctorate and the major conclusions of the work. Recommendations are also made for further work. This forms chapter eight.

1B Introduction – Figures and tables

Table 1-1 – Relevant Titanium alloys and processing history [1-7]

Alloy	Composition (wt.%)	Beta Transus /°C	Form	Processing History
Ti6246	Ti-6Al-2Sn-4Zr-6Mo	945	Disc forging	Beta forged, (Alpha + Beta) SHT'd, Aged(*)
				As for (*) then Beta annealed
				As for (*) then (Alpha + Beta) SHT'd
			Pancake forging	Beta forged, (Alpha + Beta) SHT'd, Aged
Ti834	Ti-5.8Al-4Sn-3.5Zr-0.7Nb-0.5Mo-0.35Si-0.06C	1045	Disc forging	(Alpha + Beta) forged, (Alpha + Beta) SHT'd, Aged
Ti685	Ti-6Al-5Zr-0.5Mo-0.25Si	1020	Disc forging	(Alpha + Beta) forged, Beta SHT'd, Aged
			Specimens from disc	
Ti829 (Ti5331s)	Ti-5.5Al-3.5Sn-3Zr-1Nb-0.25Mo-0.3Si	1015	Specimens from disc	(Alpha + Beta) forged, Beta SHT'd, Aged
Ti6/4	Ti-6Al-4V	990	Disc	(Alpha + Beta) forged, (Alpha + Beta) SHT'd, Aged
Ti6242	Ti-6Al-2Sn-4Zr-2Mo	995	6" Ø billet	(Alpha + Beta) conversion from 34" Ø ingot
			Disc forging	(Alpha + Beta) forged, (Alpha + Beta) SHT'd, Aged (#)
				As for (#) then Beta annealed

2 Literature review – Cold dwell sensitive fatigue in titanium alloys 2-2
2.1 Compressor disc design and requirements 2-2
2.2 Titanium applications in aero gas turbine engines 2-5
2.3 Titanium and its alloys 2-7
2.3.1 Properties of titanium 2-7
2.3.2 Classification of alloys 2-8
2.3.2.1 Near alpha alloys 2-8
2.3.2.2 Alpha + beta alloys 2-10
2.3.2.3 Beta alloys 2-11
2.4 Compressor disc processing 2-12
2.4.1 Ingot production and conversion to billet 2-12
2.4.2 Forging and heat treatment of compressor disc material 2-14
2.4.3 Machining operations 2-16
2.4.4 Forging and heat treatment of Ti6246 compressor discs 2-17
2.4.5 Other titanium alloys with compressor disc applications 2-21
2.4.5.1 Ti685 2-21
2.4.5.2 Ti834 2-21
2.4.5.3 Ti6/4 2-22
2.4.5.4 Ti6242 2-22
2.4.5.5 Ti829 2-23
2.4.6 Microstructural terminology 2-23
2.4.6.1 Beta processed alloys 2-23
2.4.6.2 (Alpha + beta) processed alloys 2-24
2.5 Texture 2-25
2.5.1 Mechanical property effects and processing influences 2-25
2.5.2 Electron back scatter diffraction (EBSD) analysis 2-26
2.5.3 Texture representation using pole figures 2-28
2.6 Plastic deformation and fatigue 2-31
2.6.1 Plastic deformation in titanium 2-31
2.6.2 Fatigue 2-34
2.6.3 Crack lifing methods 2-37
2.6.4 Low cycle fatigue behaviour in Ti6246 2-38
2.7 Cold dwell fatigue behaviour 2-42
2.7.1 Overview 2-42
2.7.2 Historical background – In-service experience 2-43
2.7.3 Cold dwell fatigue mechanisms 2-46
2.7.3.1 Hydrogen effects 2-46
2.7.3.2 Microstructure/micro-texture influences 2-50
2.7.3.3 Time dependent strain accumulation/Combined hydrogen effects 2-56
2.7.3.4 Stress redistribution/Off-loading theories 2-61
2.7.3.5 Macrozone and Effective Structural Unit Size Concepts 2-72
2.7.3.6 Crystal Plasticity Finite Element Modelling 2-78

2B Volume B - Figures and tables 2-82
2.8 Compressor disc design and requirements 2-82
2.9 Titanium applications in aero gas turbine engines 2-84
2.10 Titanium and its alloys 2-85
2.11 Microstructural terminology 2-88
2.12 Texture in metals 2-93
2.13 Plastic deformation and fatigue 2-96
2.14 Cold dwell fatigue behaviour 2-100

2 Literature review – Cold dwell sensitive fatigue in titanium alloys

2.1 Compressor disc design and requirements

In a gas turbine engine air is compressed, mixed with fuel, ignited in a combustor and expanded through a turbine. Combustion gas expulsion provides thrust. The compressor, combustor and turbine form the central part of a gas turbine, commonly referred to as the engine 'core' [8].

In civil aero-engines there are typically two or three rotating spools of multi-stage compressor assemblies, driven by one or more turbine stages via connecting shafts. A large fan is often present at the front of the engine, in a design known as a turbofan. A diagram showing the cross-section of a typical two-spool turbofan civil aero-engine is displayed in Figure 2-1.

Compressor assemblies consist of several stages. An intermediate pressure (IP) drum compressor assembly taken from a Rolls-Royce Trent engine is displayed in Figure 2-2. This assembly contains eight compressor disc stages.

The geometry of an individual compressor disc is illustrated in Figure 2-3. The rim is located at the outer circumference with the bore forming the inner circumference. The diaphragm extends between the bore and rim. Fixtures for attaching compressor blades are typically dovetail or circumferential slots located on the outer circumference of the rim.

In a compressor assembly as air passes through each stage the pressure is progressively increased. With increasing pressure there is an associated temperature increase through adiabatic heating. Static air enters the inlet at ambient temperature, dependent on flight

altitude and weather conditions. A typical civil aero-engine compression ratio of 25:1 leads to temperatures in excess of 600°C in the high-pressure stages of compression [9].

Compressor disc rotational speeds typically vary between 3,000 and 15,000 rpm depending on engine type and the location of a disc within the compressor [10]. Under these operating conditions the mechanical design of discs in the rear stages of the core compressor is very challenging. There are three major factors to be considered:

- High rim speed
- High temperatures
- Additional loads from the drive arm connecting the shaft to the turbine

Under these operating conditions compressor discs experience high stresses. The disc bore operates at high stress and temperature whilst the rim is subject to lower stresses but higher temperatures. The temperature and stress gradients that exist within a disc and the cyclic variation of these thermal and centrifugal stresses give rise to low cycle fatigue (LCF) behaviour. In the simplest case this major stress variation occurs once per flight cycle. This is the current design limitation for aero-engine discs [11].

For optimised performance a compressor disc should have low values of coefficient of thermal expansion and elastic modulus as well as a high value of LCF strength. The ratio of *(modulus*expansion coefficient)/LCF strength* should be minimised [12].

Because of their design and the conditions they operate under, compressor discs are classified within Rolls-Royce as "Critical Group A" components. Critical Group A parts are often rotating parts that are subject to significant LCF during service and therefore have a finite safe operating life. Figure 2-4 displays Critical Group A parts in a Rolls-Royce Trent

800 engine. The failure of a Critical Group A component in flight is likely to represent a serious hazard to the continued operation of an aircraft [13]. For discs the weight and rotational speed during operation make containment upon failure extremely difficult. It is therefore very important to ensure factors such as alloy selection, processing and machining are all carefully controlled to minimise the risk of defects that could lead to in-service failure.

2.2 Titanium applications in aero gas turbine engines

Prior to the development of titanium alloys, engines designs used steels extensively. Titanium alloys were first introduced as compressor blades and discs in the Pratt and Whitney J57 engine in 1952. This immediately achieved weight savings of approximately 200kg [12].

Despite significant weight savings, in the late 1950s there was a marked decrease of interest in titanium alloys partly due to their relatively poor creep properties. Since then titanium alloy selection has emphasised cost-effectiveness and high specific strength properties relative to nickel alloys, steels and other light alloys [12]. A comparative figure illustrating the specific strength capability of the different aerospace alloys is shown in Figure 2-5.

Aerospace industry applications currently account for approximately 80% of titanium production [12]. Titanium alloys have been used extensively in the aerospace industry primarily as they offer a lower density alternative to other suitable materials. With operating temperature capabilities close to 600°C they were initially identified as potential alloys for critical rotating components in the various compressor stages.

Continuous development of low-density titanium alloys has allowed for a substantial reduction in the weight of aero-engines. This has led to greater thrust-to-weight ratios, lower fuel consumption and greater payloads, allowing improved performance and lower ownership costs [11]. Application in compressor discs and blades was particularly advantageous. In addition to the significant weight saving due to improved specific strength relative to steel or nickel alloys, the weight saving on blades reduced rim stresses sufficiently that the disc itself could be reduced in weight. In the context of the Rolls-Royce RB211-535 E4 engine, the use of titanium blades and discs in the HP compressor gave a weight saving of 40% per compressor stage when compared to the alternative nickel alloy design [14].

The strength of titanium alloys is comparable to that of steels, although they have approximately half the density. They possess good corrosion resistance and have low values of thermal expansion coefficient (TEC). On the basis of their desirable material properties, titanium alloys have been used increasingly extensively in aero-engines over the last fifty years. They now constitute over a quarter of the weight of a typical large fan blade engine. Titanium alloy usage in a typical modern jet engine is illustrated in Figure 2-6.

Alloy development was originally driven by the need for increased power to weight ratios. In modern engine design environmental performance is also a key consideration [15]. Although significant funding has been invested in the development of alternative materials in response to continually increasing thermal and mechanical demands, the application of titanium alloys in aero-engines is guaranteed for the foreseeable future. This is primarily due to design conservatism and financial considerations. Alternatives are expensive to develop, difficult to manufacture on industrial scales and as yet unproven under service conditions [16].

2.3 Titanium and its alloys

2.3.1 Properties of titanium

At ambient temperature (and pressure) elemental titanium exists in a hexagonal close packed (HCP) crystal structure (alpha phase) which is stable to ~882°C. At this temperature titanium undergoes an allotropic transformation to a body centred cubic (BCC) structure (beta phase). This temperature is known as the beta transus (β_T). The BCC structure is stable from the beta transus up to the melting temperature of ~1678°C. The crystal structures of the alpha and beta phases are displayed in Figure 2-7 [17].

Titanium may be alloyed with other elements to achieve a wide range of material properties. The addition of alloying elements modifies the beta transus, with elements classified according to their effect on the stability of the alpha and beta phases. Aluminium, oxygen and nitrogen dissolve preferentially in and stabilise the alpha phase whilst molybdenum and vanadium are common beta stabilisers [18]. Elements that show no significant effect on the transus temperature are classified as neutral elements and include zirconium, tin and silicon.

Simplified diagrams showing the effect of alloying additions on the beta transus are displayed in Figure 2-8 [18]. These phase diagrams display the Ti-rich regions of the three recognised pseudo-binary titanium alloy systems. The alpha stabilising element phase diagram is displayed in Figure 2-8a. The level of alpha stabilisation can be described by Equation 2-1 [12]. Aluminium equivalent is usually kept below 9wt% as precipitation reactions can occur at higher values and have a detrimental effect on material properties.

Beta stabilisers are used as they provide advantages in terms of forging and heat treatment. They can be divided into two distinct categories, beta isomorphous elements (shown in Figure 2-8b) such as Mo and V, and beta stabilisers that promote eutectoid formation (Figure

2-8c). Beta eutectoid elements favour compound formation and include Cu, Ni and Fe. Beta stabilisation is described by the molybdenum equivalent (Equation 2-2). A molybdenum equivalent in excess of 10 allows the retention of beta phase on cooling to room temperature.

The chemistry of the near alpha alloy Ti6242s (Ti-6wt%Al-2wt%Sn-4wt%Zr-2wt%Mo-0.1%Si) illustrates the importance of composition in alloy design. Tin and zirconium additions provide solid solution hardening of the alpha phase. Beta stabilising molybdenum is added to improve forgeability and the response to heat treatment. There is a small silicon addition that increases strength and creep resistance [12].

2.3.2 Classification of alloys

Alloys of titanium are classified into three main groups designated alpha (α), alpha + beta ($\alpha+\beta$) and beta (β). Property requirements can be achieved in a given alloy through a balance of the alpha and beta phases in the microstructure. Microstructures are controlled and developed through a combination of alloy chemistry, mechanical work and heat treatment [12, 19, 20].

Alpha alloys are divided into sub-groups of single-phase alpha, near-alpha alloys and conventionally age-hardened alloys such as Ti-Cu compositions. Single-phase alpha alloys are Ti-O alloys that are effectively grades of commercially pure titanium.

2.3.2.1 Near alpha alloys

Near-alpha alloys contain less than 2wt% composition of beta-stabilising elements. They were developed to meet demands for higher operating temperatures in engine compressors. They exhibit the greatest creep resistance of all titanium alloys at ~400°C [12]. This has

been attributed to the decrease in stacking fault energy with increasing aluminium addition [21]. Near-alpha alloys are typically forged in the (alpha + beta) phase field to retain primary alpha grain structures. Forging above the beta transus allows deformation to occur more easily although the practice is generally avoided due to the potential for grain growth and the associated adverse effects on ductility.

Heat-treatment of near-alpha alloys may be in the (alpha + beta) phase field or above the beta transus. Recommended heat treatment in the (alpha + beta) phase involves solution treatment of an alloy at a temperature providing approximately equal proportions of alpha and beta phase. Air-cooling forms a microstructure of Widmanstätten alpha platelets interspersed amongst equiaxed grains of primary alpha (definitions of microstructural terminology are provided in section 2.4.6). The Widmanstätten phase nucleates and grows from the beta phase on cooling from the solution temperature. Near-alpha alloy microstructures are stabilised using heat treatment at temperatures of 500-590°C. The microstructural condition is designed to maximise creep strength [12].

Heat treatment in the beta phase field varies according to the alloy. Examples of beta heat treated near alpha alloys are Ti685 and Ti829. Ti685 is heat treated by quenching from 30°C above the beta transus temperature. This produces laths of martensitic α' separated by thin films of retained beta. An ageing step at 500-550°C transforms α' to α, relieving quenching stresses and strengthening the alloy [12]. Ti834 is heat treated at the beta transus to retain small amounts (~5% volume) of alpha phase. This approach minimises the problem of beta grain growth by pinning grain boundaries [12].

2.3.2.2 Alpha + beta alloys

(Alpha + beta) alloys were developed as an alternative to alpha alloys which have strength limitations due to ordering reactions at higher solute contents. They have higher tensile strengths and improved formability although their creep performance above 400°C is worse. They usually contain some additions to stabilise the alpha phase along with 4-6wt% of beta stabilisers. This allows retention of significant levels of beta phase on quenching from beta or (alpha + beta) phase fields [12].

Heat treatment of (alpha + beta) alloys may involve annealing, quenching or full heat treatment. Annealing can be used in beta-isomorphous alloy systems to provide uniform properties in thick sections. This may be from above transus (beta-annealed condition) or from the (alpha + beta) phase field (mill-annealed condition) [12].

Whilst (alpha + beta) alloys with relatively low beta stabilisation form martensitic alpha phases on quenching, metastable beta structures can be achieved on quenching in sufficiently beta-stabilised compositions [22]. Ageing at elevated temperatures may be used to decompose the quenched structures to achieve a range of properties. Full heat treatment of these alloys involves solutioning in the (alpha + beta) phase field and quenching then ageing to transform retained beta. For example the Ti-6Al-4V alloy follows these stages of heat treatment to give a microstructure of equiaxed primary alpha grains in a fully transformed beta matrix.

High strength titanium alloys for mechanical and structural applications are generally two-phase (alpha + beta) alloys. These alloys are typically used in forged components such as fan blades. They now represent the most commercially important class of titanium alloys. Ti-6Al-4V alone accounts for over 50% of alloy sales in Europe and the USA [12].

2.3.2.3 Beta alloys

Beta alloys have less widespread applications than other titanium alloy types due to problems with intermetallic phase formation. They have compositions with sufficient beta stabilisation to retain a fully beta structure at room temperature. They initially attracted interest as they offer improved forming characteristics over other alloys. These alloys also have the advantage of increased hardenability resulting from the presence of high levels of solute elements. These advantages are likely to result in greater use of beta alloys in future applications [12].

2.4 Compressor disc processing

A schematic diagram illustrating the manufacture of compressor discs from ingot through to finish geometry is displayed in Figure 2-9. Each stage of the manufacturing route is discussed in greater detail in the following sections.

2.4.1 Ingot production and conversion to billet

Titanium metal is typically extracted from its commonly occurring oxide (TiO_2) using the Kroll process. Chlorination of the ore produces $TiCl_4$ which is then reduced to pure titanium through reaction with magnesium. Following extraction the titanium is a porous metallic sponge. A formulation stage following extraction adds 'master-alloys' (such as Al and V) to the sponge according to requirements. This mix is blended to a composition and compacted into D-shaped briquettes. Briquettes are plasma welded together to form a consumable electrode. Weld inspections are conducted to ensure the electrode is of acceptable quality [12, 23].

Following compaction to primary melt electrode the metal undergoes further refinement to remove impurities and macro-segregation effects. This refinement is necessary for material used in aerospace and other high integrity applications where cleanliness, homogeneity and improved fatigue and fracture toughness of the final product are essential requirements. Typically the refinement process for critical application alloys is Triple Vacuum Arc Remelting (TVAR). Initially the primary melt electrode is electrically vacuum arc melted and resolidified to form ingot. The TVAR process involves the vacuum melting and solidification of the ingot a further two times.

All three VAR melts involve the continuous melting of the electrode by means of an arc under vacuum. A temperature in the range of 1600-1650°C is sufficient to melt most

titanium alloys. DC power is applied to strike an arc between the electrode and the base-plate of a copper mould contained in a water-cooling jacket. The intense heat generated by the arc melts the tip of the electrode and a new ingot is progressively formed in the cooled mould. The electrode is negatively charged and the melt pool is positively charged. A high vacuum is maintained throughout the remelting process as it is essential to avoid contact between hot titanium and the atmosphere. This is due to the tendency to form brittle refractory oxides and nitrides which are difficult to dissolve in subsequent melts [24].

Modern VAR processes use computer technologies to continuously monitor the consumable electrode weight and other process parameters including remelting rate and arc gap. These variables can then be adjusted using closed loop control systems. Melting parameters are controlled via standard programs for given compositions, ingot sizes and material grades. The introduction of such technology has resulted in improved reproducibility in terms of metallurgical properties.

Primary benefits of the VAR process include minimal gas content (hydrogen and nitrogen), a high level of cleanliness, the reduction of unwanted trace elements with high vapour pressures and the removal of salt (a by-product of the Kroll process). Reversing the direction of solidification of an ingot between melting stages also minimises segregation, which may appear as tree-ring patterns [24]. Tree-ring patterns are typical titanium ingot defects. They usually represent negative crystal segregation. These patterns appear to have little effect on material properties [24].

Following the VAR process the ingot is typically 30-36 inches in diameter, 6-7 feet in length and weighs approximately seven tonnes. Ingots are inspected and machined prior to subsequent processing. Barrel analyses are performed to check ingot chemistry [25].

An ingot microstructure consists of a very coarse grain size with a fully transformed sub-structure. This ingot is conversion forged to billet with a typical diameter between 8 and 14 inches. Techniques used for the conversion process include drop hammers, mechanical presses and hydraulic presses. Initial working typically involves hot press forging due to the sensitivity of the as-cast structure of arc-melted ingots to cracking.

The main aims of the conversion forging process are to refine the beta grain size of the coarse as-cast structure and to develop primary alpha grains. Generally a higher level of alpha content is found in billet than in disc forgings, with directionality commonly observed in the alpha grains [25].

The billet may be sectioned into smaller lengths during the conversion process to allow easier handling. Following forging the oxidised ends of the billets are cut off and discarded, as is the material that formed the top cavity of the ingot, which often has aluminium segregation. Turning operations are undertaken on the outside diameter and slices of billet are removed for microstructural analysis and mechanical property tests. Billet is subject to an ultrasonic inspection, then cut to 'use' or 'mult' sections. These are short lengths of billet, the size of which depends on the volume of the die for a specific component forging.

2.4.2 Forging and heat treatment of compressor disc material

A 'mult' (sectioned from billet) is forged to disc geometry using shaped dies. Mults are preheated to the forging temperature in a clean furnace atmosphere (in order to prevent excess hydrogen absorption). Electric preheating furnaces are preferred to oil or gas furnaces for this reason. Alloys may be forged in the (alpha + beta) phase field or above beta transus depending on the material property requirements.

Forging often involves multiple stages, particularly if it is not possible to reduce the forging to the finish geometry in one operation. A two-stage forging process involves mult deformation to a preform shape. The preform is allowed to cool before reheating and finish forging. The as-forged shape is referred to as a 'black' forging. A flash line is normally present on the black forging at the point of contact between the upper and lower dies. This 'overflow' of excess material indicates that the forging material has fully filled the die space. Flash material is removed after forging.

Die temperature, mult temperature and forging strain rate are controlled based on the requirements of the disc in terms of geometry, size reduction, strain levels etc. Die temperature is an important consideration as the low thermal conductivity of titanium can lead to localised chilling in thin forging sections where temperature effects are more pronounced. This can result in uneven metal flow and/or cracking. Rapid closed die forging operations involving hammer or mechanical presses normally use dies preheated to 150-250°C. Slower operations using hydraulic presses typically have die temperatures of 400-600°C. Isothermal forging uses dies at a similar temperature to the preheated mult [25].

Die material is a major consideration with a choice of either cast ceramic or metallic dies. Cast ceramic dies have some applications in isothermal forging operations. Metallic dies are more expensive as die faces are nickel or cobalt alloys in order to have adequate hardness and oxidation resistance at high operating temperatures. Forging of titanium at high temperature often uses molybdenum dies [12].

Heat treatment typically follows the finish forging operation. Treatments vary depending on the alloy used and the material property end requirements. Increased cooling rates can be achieved following forging using fan air-cooling, oil quenching or water quenching. Some of

the typical heat treatments possible for the different classes of titanium alloys were discussed under section 2.3.2.

2.4.3 Machining operations

The stage that normally follows heat treatment is machining. In machining of compressor discs, the finish forging is roughly machined to a rectilinear shape as specified in a condition of supply drawing. Typically the 'rectilinear' is ultrasonically inspected, etched for surface condition and dye penetrant inspected. In addition to NDE inspections a test ring is removed to allow checks of microstructure and mechanical properties. Standard tests determine tensile and creep strengths. Test-rings not analysed are stored for the operational lifetime of the material. Following inspection of the rectilinear, finish machining operations are undertaken to produce the component to final engineering drawing requirements. Axi-symmetric features are generally produced by turning, with a combination of milling and broaching used to produce blade slots. Drilling and reaming operations are used to produce holes [13].

Issues concerned with machining arise from the low thermal conductivity of titanium alloys. The small area of contact between a cutting tool and a part can result in high cutting temperatures during machining operations. Lower cutting speeds are required relative to other alloys such as steels (six times greater thermal conductivity). There is also a tendency with titanium alloys for machined chips to stick to the cutting edge of the tool (known as galling). For these reasons titanium alloys must be machined at relatively low speeds using temperature resistant cutting tools [12].

Finish-machined discs are etch and penetrant inspected then assembled into compressor disc assemblies. Fabrication of drum assemblies may involve joining using mechanical fasteners (i.e. nuts and bolts) or electron beam welding (EBW) techniques.

2.4.4 Forging and heat treatment of Ti6246 compressor discs

The alloy Ti-6Al-2Sn-4Zr-6Mo (wt%) is a solid solution strengthened (alpha + beta) titanium alloy used in elevated temperature applications including aero-engine compressor discs at temperatures up to 480°C [26, 27]. It offers an attractive combination of high strength, fracture toughness, creep resistance and LCF properties. These advantages have led to an increasing replacement of alloys such as Ti5331s, Ti6242 and Ti6/4 with Ti6246 [27]. Ti6246 also offers a cost reduction compared to the near alpha alloy Ti834, being a more widely available non-proprietary material composition.

Ti6246 was developed by Pratt & Whitney in the mid 1960s [28]. Further work was undertaken over the following decades to investigate various thermomechanical process routes and the combinations of mechanical properties that could be achieved. The balance between LCF life and fracture toughness was the main obstacle in the development of the alloy due to an inverse relationship between these properties.

Work by Chakrabarti et al. studying process routes found that (alpha + beta) processed Ti6246 displays improved LCF properties whilst beta processed Ti6246 displays better fracture toughness, crack growth resistance and creep resistance properties [29]. It was concluded that two process routes showed optimum property combinations [30]:

- (Alpha + beta) preform, (alpha + beta) finish forge, SHT/Air cool, Age/Air cool
- (Alpha + beta) preform, beta finish forge, SHT/Air Cool, Age/Air Cool

For compressor disc applications a standard Ti6246 beta-processing route is as follows:

The forging is produced and machined as outlined in the preceding sections. Hot working of the alloy may be above the beta transus or high within the (alpha + beta) phase field. The latter method prevents excessive beta grain growth as grain boundaries are pinned by alpha phase.

Final hot working operations are performed in the beta phase field. This is because of the combination of material properties that can be achieved. Forging deformation is designed to finish at temperatures slightly in excess of the beta transus. Fast cooling (water quenching) is applied immediately after deformation to avoid recrystallisation of the deformed beta grain structure.

On water quenching there is a partial transformation of beta to a martensitic orthorhombic alpha (α") phase. This phase transformation has been characterised by various studies [22, 31-34]. Orthorhombic α" phase can be distinguished from HCP α' and α structures using X-ray diffraction. Diffraction profiles show five peaks characteristic of α" in comparison to three peaks associated with HCP alpha phases [32, 35-37].

Following beta processing and fast cooling, moderate to heavily strained microstructure are characterised by elongated beta grain structures with dynamic recrystallisation along grain boundaries. In part due to the high levels of deformation on forging, beta grains exhibit discontinuous grain boundaries. If the post-forge cooling rate is sufficiently low (i.e. in large cross-sections) alpha layers can nucleate and grow along these boundaries [22].

Alpha and retained beta phases display crystallographic relationships described by the Burgers orientation relationship (Equation 2-3) [22]. Alpha phase precipitates preferentially at beta grain boundaries due to the incoherent nature of the (alpha + beta) interface. After saturation of grain boundary nucleation sites growth of the alpha phase will then occur

perpendicular to grain boundaries in the form of 'colonies' of parallel platelets known as "side-plates" (example microstructures are given in section 2.4.5) [22]. The extent of side-plate formation is dependent on cooling rate and beta stabilisation level. Faster cooling rates and increasing beta stabilisation suppress the formation of side-plates instead favouring the precipitation and growth of Widmanstätten alpha structures [22, 38].

An important consideration in the processing of Ti6246 is the input of sufficient hot work to deform prior beta grain boundaries. This is necessary to prevent formation of continuous alpha layers along prior beta grain boundaries. Continuous alpha boundary layers have a deleterious effect on mechanical properties including tensile ductility, high cycle fatigue strength and fracture toughness. It is important that their presence is minimised [27, 38].

It is also important to have a high enough cooling rate to minimise the formation of side-plates as Ti6246 is capable of extensive side-plate formation when subject to slow cooling rates following forging. As with continuous grain boundaries, side-plates are to be avoided as they also provide large effective slip lengths, leading to reductions in resistance to crack nucleation and fatigue strength [27].

Following finish forging an appropriate heat treatment is used. For Ti6246 a two-step solution heat treatment (SHT) and age is applied. Heat treatments are based on the decomposition of retained metastable beta to form alpha phase. The SHT is high in the (alpha + beta) phase field. Martensitic orthorhombic alpha formed by water quenching from above beta transus undergoes phase decomposition during SHT. Various studies have reported the instability of the α" phase with prolonged exposure to elevated temperatures [32, 35, 39]. The SHT temperature and time allow the precipitation and growth of HCP alpha platelets throughout the prior beta grain structure [26].

Ageing heat treatment is at lower temperature and precipitates a high volume fraction of very fine secondary alpha platelets between the coarse alpha plates. These are statistically arranged in all 12 variants of the Burgers relationship (Equation 2-3). The volume fraction of alpha phase available for precipitation during ageing is determined by the difference between the solution treatment temperature and the ageing temperature. The low temperature age is particularly important as the volume fraction of these precipitates influences the yield stress that can be obtained. Increasing the volume fraction leads to a closer alpha platelet spacing that hinders dislocation movement according to the Orowan relationship. Another important consideration is to ensure the age is at a temperature well above the brittle intermetallic precipitation temperature (typically approximately 400°C) [38].

The heat treatment schedule for Ti6246 disc forgings is displayed schematically in Figure 2-10. The beta transus temperature for Ti6246 is approximately 945°C. Typical processing involves forging at (β_T+30°C) and water quenching. SHT is at (β_T-30°C) for 1-2 hours before fan air-cooling to room temperature. Ageing is at 595°C for eight hours before air-cooling to room temperature. The microstructure that is produced by this combination of hot working and heat treatment is a mixture of a retained beta matrix, coarse primary alpha platelets and fine secondary alpha platelets. The typical microstructure of Ti6246 is displayed in Figure 2-11. This microstructure is defined more clearly in section 2.4.6.

In processing beta-forged Ti6246 the objective is to achieve a microstructure consisting of high aspect ratio Widmanstätten primary alpha platelets evenly interspersed within a deformed, coarse-grained transformed beta matrix containing a fine scale distribution of secondary alpha platelets [40]. This provides the optimum balance of mechanical properties in the finished product. In practice there is significant variation in the optical microstructure of Ti6246 disc material due to variations in forging strains and cooling rates. In the described

condition Ti6246 has a relative density of 4.68Mg/m^3, typical 0.2% proof stress of 1170MPa and tensile strength of 1270MPa [40].

2.4.5 Other titanium alloys with compressor disc applications

2.4.5.1 Ti685

Ti685 is a high temperature, medium strength, creep resistant alloy that has applications in intermediate to high-pressure compressor disc forgings [41]. It has a near alpha alloy composition and is typically forged in the (alpha + beta) phase field. It is SHT'd above the beta transus (1050°C for 30 minutes) and oil quenched, aged for a period of 24 hours at 550°C then air cooled [4]. For large components the SHT oil quench gives a cooling rate that produces an optimal combination of alpha platelet and retained beta film thicknesses. This gives a lamellar alpha colony structure designed for maximum creep and FCG resistance. The lower temperature age releases residual stresses introduced during phase transformation. It also breaks up beta films into semi-continuous layers that are very effective at blunting crack growth but which do not provide a high diffusivity path for detrimental high temperature creep effects [42]. Silicon additions enhance creep resistance.

2.4.5.2 Ti834

Ti834 is the highest temperature capability titanium alloy available for aerospace applications. It has applications in intermediate and high-pressure compressor discs. It is a near alpha alloy with high tensile strength and creep resistance at temperatures up to 600°C. It has good forgeability and weldability. The properties result from solid solution strengthening and (alpha + beta) heat treatment at temperatures close to beta transus [3]. The composition is designed to provide small changes in alpha phase fraction at temperatures close to the beta transus. The low gradient beta transus approach curve allows the retention of primary alpha

grains at temperatures very close to beta transus. This widens the allowable processing range for which wrought product retains the small grain size required for good creep performance [12].

2.4.5.3 Ti6/4

Ti-6Al-4V (Ti6/4) is the most commonly used (alpha + beta) alloy. It is a high strength alloy with a maximum operating temperature of 300-350°C and good creep resistance properties below this temperature. It is used for fan blade and disc applications [6].

Processing usually begins with TVAR ingots. Press or hammer forgings are used at sub-transus temperatures. Heat treatment involves solutioning at a temperature marginally below beta transus. A one-hour hold at a temperature between 945-985°C is used to vary the primary alpha phase fraction as required. Water quenching after SHT forces beta phase transformation to Widmanstätten alpha. The microstructure then consists of 15-45% equiaxed primary alpha, varying depending on the intended application. To relieve residual stresses a two-hour anneal at 700°C is applied followed by air cooling to room temperature [43].

2.4.5.4 Ti6242

Ti6242 is a medium strength and intermediate temperature alloy capable of long term application at temperatures up to 540°C. It has an excellent combination of tensile strength, creep strength and toughness [7]. Typical applications include discs, blades and impellers. It is an (alpha + beta) processed alloy with a bimodal microstructure that is optically similar to Ti6/4.

2.4.5.5 Ti829

Ti829 (Ti5331s) is a near alpha alloy that offers weldability, high strength, and high temperature creep resistance [5]. It is a derivative of the IMI685 alloy containing niobium and tin additions, designed for improved creep performance at 500-600°C [44].

Processing using alternate beta and (alpha + beta) working operations is often undertaken to avoid excessive prior beta grain growth. Final forging operations are undertaken in the (alpha + beta) phase field. Forged components are solution heat treated at temperatures marginally above the beta transus for a short period of time (30 minutes) and air-cooled or oil quenched (depending on section size). Ageing is undertaken at ~625°C for two hours followed by air-cooling [5]. The solution and ageing heat treatments serve similar purposes to those of Ti685 material (outlined in section 2.4.5.1).

2.4.6 Microstructural terminology

The microstructures produced in titanium alloys vary according to factors including alloy composition and processing route. In this thesis the microstructures of a number of alloys have been characterised. This work requires the use of specific terminologies to refer to microstructural features. Common terms can be used interchangeably to refer to different features in different microstructures. To clearly define optical features in the various microstructures, schematics, optical micrographs and SEM images have been labelled accordingly in the following sections. The terminology defined in this section is applied throughout the thesis.

2.4.6.1 Beta processed alloys

This refers to alloys that have been forged and/or SHT'd above their beta transus temperature. Ti6246 is forged above beta transus and SHT'd in the (alpha + beta) phase

field. It is aged at lower temperature. Ti685 is (alpha + beta) forged, SHT'd above beta transus and aged at lower temperature.

The microstructure in beta processed Ti6246 is highly variable depending on the forging conditions. Typical microstructural features in the fully heat-treated alloy are labelled in Figure 2-12 to Figure 2-15. Alpha features with a less acicular (i.e. more rounded/equiaxed) morphology are often referred to as 'blocky alpha' features. Typical blocky alpha features are displayed in Figure 2-16. These features are attributed to sample sectioning effects.

Recrystallisation is often observed at prior beta grain boundaries. The example in Figure 2-17 shows equiaxed recrystallised grains in a heavily deformed microstructure. The recrystallised grains are more easily identified in the as-forged condition (as in Figure 2-18), prior to SHT, when the microstructure contains relatively limited alpha precipitation.

Beta grains often contain sub-structures, including subgrains or cell wall boundaries [45, 46]. These features are highlighted in the microstructure displayed in Figure 2-19.

2.4.6.2 (Alpha + beta) processed alloys

Alloys forged and heat treated in the (alpha + beta) phase field include Ti6/4, Ti6242 and Ti834. Typical microstructures consist of equiaxed primary alpha grains (retained through forging deformation) and a lamellar structure of alpha platelets referred to as either transformed beta or secondary alpha phase. There are also small levels of retained beta phase present as layers between the secondary alpha lamellae [47]. Because of the processing route it is not possible to identify the outline of prior beta grains in optical microstructures. However, beta grain flow can be identified by macro-etching. Typical microstructural features are labelled in Figure 2-20 and Figure 2-21.

2.5 Texture

2.5.1 Mechanical property effects and processing influences

Texture is the distribution of crystallographic orientations in a material. If orientations are fully random the material is described as having no texture. If material displays preferred orientations the texture intensity is dependent on the percentage of crystals that have the preferred orientations. A material with no texture, i.e. completely random crystal orientations, will show isotropic properties at length scales sufficiently larger than crystal size. A perfect single crystal is the other extreme, with anisotropic properties according to crystal geometry. This is illustrated by Figure 2-22 where the elastic modulus of alpha titanium can be seen to vary with crystal orientation w.r.t. loading axis. The anisotropy arises due to the number of slip systems operating in the HCP structure. The highest modulus is achieved when the stress axis is parallel to the c-axis as this gives the lowest number of operational slip systems. Conversely when the stress axis is perpendicular to the c-axis a greater number of slip systems can operate and modulus is lower as a consequence.

Because of potentially unfavourable material anisotropy the development of strong textures is avoided where possible or minimised in order to achieve isotropic properties in components. Conversely, the anisotropic properties of strongly textured materials are now being utilised in some applications where it is possible to align loading direction with the direction of best material properties. Where desired, changes in texture may be achieved through the processing route. For example, unidirectionally rolled Ti6/4 plate is known to exhibit a strong texture where the basal planes of the alpha crystal structure lie normal to the rolling direction. This texture is illustrated in Figure 2-23.

2.5.2 Electron back scatter diffraction (EBSD) analysis

Texture can be determined by various quantitative and qualitative methods. The most common quantitative methods are X-ray diffraction and electron back-scattered diffraction (EBSD) analysis.

EBSD is a microstructural technique used to obtain information related to the crystallographic texture of any crystalline material. EBSD can be used to identify and index the seven crystal systems[1]. Its applications include crystal orientation mapping, defect studies, phase identification and regional heterogeneity investigations. Traditionally these types of studies have been carried out using other methods including x-ray diffraction (XRD) and neutron diffraction [48].

EBSD uses a scanning electron microscope (SEM) equipped with a backscatter diffraction camera. The diffraction camera consists of a charge coupled device (CCD) video camera linked to a phosphor screen. The screen is inserted into the specimen chamber of the SEM at an angle greater than or equal to 90° to the electron beam. A polished specimen is loaded into the specimen chamber and tilted at a high angle (~70° from horizontal) towards the diffraction camera [48].

A stationary electron beam strikes the tilted sample, and electrons impinging on the specimen interact with the atomic lattice planes of the crystal structures. The atoms in the sample inelastically scatter a fraction of these electrons. Close to the sample surface inelastically scattered electrons form a divergent source. Electrons may be incident on crystal/atomic planes at angles satisfying the Bragg equation (see Equation 2-4).

[1] Cubic, Tetragonal, Rhombohedral, Hexagonal, Orthorhombic, Monoclinic, Triclinic

Many of the electron interactions satisfy Bragg conditions and undergo backscatter diffraction. Due to the angle of the specimen these diffracted electrons are directed towards and impinge upon the phosphor screen of the diffraction camera causing it to fluoresce. Fluorescent light is detected by the CCD and an image termed a diffraction pattern is formed on the camera. Electrons are diffracted to form a set of pairs of large angle cones that correspond to each diffracting plane. Regions of enhanced electron intensity are formed between the cones on the phosphor screen. These increased electron intensity regions are observed on the diffraction pattern as lines known as Kikuchi bands [48].

Diffraction patterns are unique to the microstructural-crystallographic properties of a material. Each diffraction pattern shows several intersecting Kikuchi bands, with the centre line of a Kikuchi band corresponding to the projection of a diffracting crystal plane on the phosphor screen. Kikuchi bands can therefore be indexed individually by the Miller indices of the diffracting plane forming them [48].

As crystal orientation changes the resulting diffraction pattern also changes. Kikuchi band positions can therefore be used to calculate crystal orientations and grain boundary misorientations. Through the diffraction pattern EBSD mapping is used to determine texture over a specified area of a sample. This may be a specific feature such as a grain boundary or an area representative of the overall microstructure. The area of interest is divided into a grid of pixels, with data collected for each individual pixel in the map. The electron beam is focused on a small area within each pixel and the diffraction pattern for that location is assessed to determine crystallography. The small interaction volume of the EBSD technique allows for the measurement of individual crystallites rather than a volume of material.

The quality of the acquired data can be adjusted depending on time constraints. Factors to consider include the size of the area to be mapped, the step size (i.e. the map resolution/number of pixels), accelerating beam voltage, background diffraction and sample preparation. The condition of the sample surface is extremely important in obtaining high quality results using EBSD as diffraction only occurs within ~10-50nm of the sample surface [49]. It is important that no plastic deformation or scratching is present in the specimen surface as this lowers pattern quality. Samples are unetched to retain a smooth surface for uniform EBSD pattern intensities.

Once data has been collected a crystal orientation map (COM) can be plotted, displaying crystal orientations over the selected area. This can be useful in determining misorientations between phases, crystallographic size of optical features, and in analysis of grain boundaries and hence grain size distributions.

2.5.3 Texture representation using pole figures

In some cases it is useful to know how strongly textured a material is without further details of the texture. A value known as the "texture index" (the mean square value of the orientation distribution) is commonly used. Randomly orientated material has a texture index equal to unity. The square root of the texture index, the "texture strength", is also used to describe texture. The advantage of this term is that it uses the same units as texture measurements [50].

Where further information is required an EBSD scan of a representative area of a larger sample can provide information on the overall texture of the material. This information may be displayed as a pole figure. A pole figure displays the distribution of grain orientations using a stereographic plot to describe the spatial distribution of the poles of a specific

crystallographic plane. A stereographic projection is constructed by placing a crystal unit at the centre of a sphere. For a given crystal unit orientation, the normal vectors of a specified set of crystallographic planes can be drawn to intersect the surface of the sphere at different locations. Considering only vectors that intersect points in the upper half of the sphere, lines are constructed between these intersection points and the base of the sphere. Taking a 2D section through the sphere at the centre line (i.e. equatorial plane), the points at which the constructed lines intersect this plane are recorded. A pole figure is a plot of the equatorial plane showing the positions at which lines intersect this plane.

The stereographic projection of a BCC structure with normal directions of the {100} planes aligned with sample axes is displayed in Figure 2-24. This figure illustrates the points at which (100) crystal plane normal vectors intersect the surface of the sphere and the constructed lines from these surface points to the base of the sphere. It also displays the locations at which the constructed lines from points in the upper hemisphere intersect the equatorial plane. For the crystal orientation displayed in Figure 2-24 the (100) pole figure is displayed in Figure 2-25.

A pole figure is specific to a set of crystallographic planes, i.e. only points generated from a specific set of crystal planes are included in a pole figure. Each individual crystal orientation may display several points on a pole figure.

EBSD allows the capture of information on crystal orientations over large areas. When the data collected in an EBSD map is presented in a pole figure it may elicit information on the overall texture of the selected region. This information may then be considered to be representative of a wider processing texture, depending on the map size and quality.

For a random texture an even distribution of intensities should be observed over the pole figure. However, microstructures are often not randomly oriented, tending towards particular textures depending on alloy composition and processing history. This leads to what is referred to as a "preferred" orientation, or crystallographic texture of the alloy. Where this is the case intensities will be concentrated within certain areas of the pole figure. Random and preferred texture pole figures are displayed in Figure 2-26.

In HCP structures such as alpha titanium the texture is most conveniently represented by a pole figure that shows the distribution of the poles of the {0001} basal plane. To allow a complete description of the texture a second pole figure is required due to the rotational symmetry of the basal plane. In titanium alloys the prism $\{10\bar{1}0\}$ pole is generally used because it is orthogonal to {0001} and it is an active slip plane.

The example of unidirectionally rolled Ti6/4 plate illustrates preferred texture. The {0001} pole figure highlights the tendency for basal planes to align with c-axes normal to the rolling direction in the plane of the plate. This texture was displayed in Figure 2-23. The $\{10\bar{1}0\}$ pole figure shows prism plane alignment with the rolling direction.

Pole figures define crystallographic orientation distributions with reference to sample axes. Alternatively, inverse pole figures (IPFs) display orientation distributions (w.r.t. crystallographic planes of a crystal structure) for a specific sample axis. For example the HCP cell structure has the IPF displayed in Figure 2-27. This defines the distribution of colours on a COM. The IPF has this shape as a result of the HCP crystal geometry. There is a 90° rotation between {0001} and either $\{10\bar{1}0\}$ or $\{11\bar{2}0\}$ planes and a 30° rotation to translate between $\{10\bar{1}0\}$ and $\{11\bar{2}0\}$ planes. Higher angle rotations are accounted for by the rotational symmetry of the crystal.

2.6 Plastic deformation and fatigue

2.6.1 Plastic deformation in titanium

When a material is placed under a stress it experiences a strain. The simplest example of this is a uniaxial tensile test, where strain increases proportionally with stress up to a limit. Under these conditions the material deforms elastically, i.e. the deformation is reversible on unloading. Beyond this point deformation changes from elastic to plastic behaviour and deformation is irreversible. The stress at which deformation is observed to change from elastic to plastic is referred to as the yield point. In a uniaxial tensile test conducted under steadily increasing strain, plastic deformation will continue up to a point defined as the ultimate tensile strength (UTS). At this point plastic deformation becomes unstable and the cross-section of the specimen reduces significantly at a single position along the gauge length. This is known as 'necking'. From the UTS, as the material continues to accumulate strain the nominal stress decreases rapidly, up to the point at which fracture occurs. A typical stress-strain curve for a uniaxial tensile test is shown in Figure 2-28.

Plastic deformation involves two different mechanisms: twinning and crystallographic slip. Twinning occurs when two regions of material have a symmetry relation across a common plane. This requires a displacement of a fraction of an interatomic spacing in the material. Twins may form either to minimise strain energy where dislocation motion is not possible (deformation twins) or to reduce interfacial energy (annealing twins).

Crystallographic slip involves the displacement of crystal planes by whole atomic spacings. It is a shear deformation process. Different slip systems operate in crystal structures, with each system defined by slip direction and slip plane. The applied stresses required for slip vary depending on the plane and orientation w.r.t. the applied stress. The lowest shear

stresses are observed on the most closely packed crystallographic planes along the most densely packed directions.

Slip requires very high stresses if crystal planes are displaced rigidly. However, if slip occurs by a process known as dislocation motion then only low stresses are required to give gradual displacement of crystal planes. Dislocations are crystallographic defects of which there are two main types, edge and screw dislocations. Edge dislocations are present when an extra plane is introduced between two crystal planes causing lattice distortion. Screw dislocations occur when a plane of atoms is split such that part of the plane is raised by a single lattice displacement over the rest of the plane. The point at which the plane changes is the screw dislocation. Schematic diagrams of edge and screw dislocations are displayed in Figure 2-29.

Dislocations are described by the 'line direction' and the 'Burgers vector'. The line direction refers to a vector along the core of the dislocation where distortion of the lattice is greatest. The Burgers vector is an expression of the magnitude and direction of the atomic displacement occurring when a dislocation moves [51]. For the edge dislocation in Figure 2-29 the Burgers vector is identified by the letter 'b' and the black line. The blue line represents the dislocation line direction.

When slip occurs the dislocation moves perpendicular to the line direction whilst individual atoms move parallel to the Burgers vector. The differences in terms of edge and screw dislocations are displayed in Figure 2-30.

In practice dislocations are commonly observed to have both screw and edge type properties. These are referred to as mixed dislocations, which have a dislocation motion direction somewhere between parallel and normal to the applied stress direction.

Plastic deformation depends on the ability of dislocations to move. Material strength can therefore be increased by impeding dislocation movement. Deformation increases the number of dislocations present (dislocation density) leading to an overlapping of the strain fields that surround adjacent dislocations. When this occurs the resistance to further dislocation motion is increased also increasing the strength of the material. This process is referred to as strain hardening. Alternative strengthening mechanisms include solid solution hardening, grain size reduction and precipitation hardening.

As well as material strengthening resulting from dislocation interactions, it is also possible for dislocations of opposite signs to annihilate each other. This is dynamic recovery, which causes a decrease in the strain hardening rate.

As described earlier, the propensity for slip to occur depends on the crystal structure, plane and direction of slip as well as the dislocation density. At lower stresses slip occurs more favourably on close packed planes due to the smaller displacements required for slip. In close packed cubic structures such as BCC material the number of close packed slip planes is high and high ductility results. For BCC crystal structures there are two close packed directions for each (110) plane as illustrated in Figure 2-31. As there are five other planes in the {110} set of planes, each also containing two <111> slip directions, there are a total of twelve slip systems of the <111>{110} type [51].

In the HCP unit cell there are fewer close packed directions. Slip occurs in <100> directions on {0001} planes. For a single {0001} plane there are three close packed <100> directions. These are the [100], [010] and [110] directions. These three slip systems are indicated by the arrows in Figure 2-32. There are two independent close packed slip systems in HCP

structures as slip along the [110] direction in the (0001) plane is a combination of slip on [100](0001) and [010](0001) [51].

In addition to the close packed basal plane directions, slip can also occur on prismatic and pyramidal planes. Figure 2-33 shows the different slip systems in operation in the HCP crystal structure. These are basal (B), prismatic (P) and first-order pyramidal (π_1) slip planes containing the Burger's vector $\underline{a}$, and first and second-order (π_2) pyramidal slip planes containing the Burger's vector ($\underline{c}$ + $\underline{a}$). As described earlier these systems are activated under different applied stresses.

Where crystal structures are uniformly arranged over an area of microstructure it is possible for slip to occur in bands over the extent of these regions. Slip bands are recognised as regions of parallel slip planes. It is generally observed that slip bands are limited in length by features such as grain boundaries or crystal misorientations.

2.6.2 Fatigue

Fatigue is one of four principal mechanisms of fracture in metals; the other mechanisms are dimple rupture, cleavage and decohesion. Fatigue is the most common failure mode in aero-engines; in a wider context it has been estimated that fatigue is responsible for around 90% of all in-service mechanical failures [52]. It may be defined as the failure of a material through the repeated application of a stress. Fatigue failure is the result of progressive, localised and permanent structural damage. The applied stress may be much lower than the material UTS, i.e. the stress required to produce fracture under a single load application [53].

Fatigue testing may be used to establish the relationship between the level of applied stress (S) and the number of cycles to cause failure (N), with results plotted in the form of an S-N curve. Typical S-N curves are displayed in Figure 2-34. In certain materials such as steels

there is a threshold stress below which failure by fatigue will not occur and infinite life is observed. This is the endurance limit. This material behaviour is displayed as curve A in Figure 2-34. Titanium in benign environmental conditions displays such behaviour.

Most non-ferrous materials do not show a fatigue limit. A continuously decreasing stress with increasing cycles is observed similar to curve B. Materials displaying such a fatigue response usually have a stress for failure specified for a given number of cycles, typically 1×10^7 cycles.

The process of fatigue consists of three stages:

- Stage I – Crack initiation
- Stage II – Progressive crack growth/propagation
- Stage III - Final catastrophic failure regime

Stage I (initiation) is the stress cycles spent accumulating damage before crack formation. It is the consequence of repeated forward and reverse slip along suitable crystallographic slip planes. Crack growth over a short distance along the slip plane produces a faceted surface. This first stage of fatigue is most likely to be observed in fractures resulting from low stress and a high number of cycles. Metal fatigue cracks initiate and propagate in regions where the strain is most severe [53].

Stage II consists of the majority of crack growth. It generally involves a trans-granular mechanism. Ductile striation features indicate this region of the crack (for sufficiently high stress intensities), marking the position of the crack front after each stress reversal. The spacing of these striations can be useful in prediction of the crack propagation rate. The second stage of crack growth may be described by a linear relationship known as the Paris

law. This states that crack growth rate is related to stress intensity range in the form of Equation 2-5.

Stage III describes the sudden failure of the material. This results from the reduction of cross-section under load due to the increasing crack size. This increases the stress intensity, with catastrophic failure when the plain strain fracture toughness (K_{IC}) of the material is reached.

Low Cycle Fatigue (LCF) and High Cycle Fatigue (HCF) are terms used to describe fatigue fracture characteristics. From a metallurgical perspective they simply represent fatigue failures at different positions on the S-N curve. A HCF failure is usually defined as such if a total of 10,000 cycles or more is achieved.

In the aerospace industry slightly different interpretations can be applied to the terms LCF and HCF. A typical flight cycle develops maximum stresses in discs under take-off conditions. If the stresses causing crack initiation and propagation are experienced on a once per flight basis, then cracking behaviour may be described as LCF controlled. In this definition a failure would be regarded as LCF even if the disc achieves in excess of 10,000 flight cycles. A HCF failure would result from a vibratory condition where numerous stress reversals occur on each flight cycle.

In fatigue failures the ratio between initiation cycles and propagation cycles can vary considerably. Plain LCF failures may typically have initiation cycles accounting for 40-60% of total life. If defects are present in the material, cracks may initiate more easily at these locations and initiation may account for a much lower proportion of life. At the other extreme, initiation cycles may account for up to 99% of life in HCF failures. In terms of failure origins LCF loading is more likely to provide several initiation sites due to the high

loading stresses. HCF is more likely to show a single initiation site due to the much lower stresses placed on the component [53].

2.6.3 Crack lifing methods

The (initiation and) growth of fatigue cracks may be predicted using fracture mechanics methods. It involves application of the theories of elasticity and plasticity to microscopic crystallographic defects to predict macroscopic mechanical failure of components.

Early lifing methods for gas turbine discs adopted conservative approaches with designs intended for a fixed operating lifetime following which the component was to be retired and replaced. This was referred to as "safe-life" design practice or the fatigue lifetime concept. S-N and ε-N curve data was utilised in setting safe operating conditions for service life. Fixed scatter was assumed for all cast and wrought forgings, with limited cyclic fatigue and overspeed testing used to determine safe operating life [54].

The detection of a fatigue crack during the specified safe life would see a component "retired for cause". This was due to the inability to determine crack growth rates or the point at which fast fracture (Stage III growth) would occur.

The "safe-life" approach was inefficient as it ignored potential remaining component life during which any existing cracks would continue to grow at sub-critical rates. This led to the development of linear elastic fracture mechanics (LEFM). This method was introduced into aerospace applications from around 1970 onwards. Using this method it became possible to correlate multiple component and specimen tests. This allowed for a more consistent definition of the margin to a failure event [54].

The "damage tolerant" LEFM lifing methodology requires periodic inspection of components. This is undertaken using non-destructive evaluation (NDE) technologies. An accurate

prediction of crack propagation characteristics is also required and is established from specimen testing. The assumption is made that a pre-existing crack of the maximum size not detectable using NDE techniques will grow from the first loading cycle.

The development of a 'holistic' approach to crack lifing, accounting for the different stages of fatigue cracking, is a more suitable method for accurate prediction of component lifetimes. This is particularly the case for compressor discs as they spend a high proportion of their operating lifetime in the initiation and early crack growth stages. The high disc operating stresses require that only a small LEFM critical flaw size be present for crack propagation.

Further improvements in lifing philosophies may be achieved through advances in the NDE techniques currently in use; ultrasonic, X-ray, eddy current and dye penetrant inspections. Improvements in the resolution of crack/defect size detection using these methods and the development of alternative NDE techniques will allow for improvements in future lifing assessments.

2.6.4 Low cycle fatigue behaviour in Ti6246

Various researchers have investigated the fatigue crack initiation and propagation behaviour of Ti6246 in both bimodal and beta processed microstructural conditions [38, 55-62]. The relevant literature is discussed in this section.

In 1997 Hall reviewed fatigue crack initiation in (alpha + beta) titanium alloys [55]. It was stated that total fatigue life is dominated by crack nucleation and short crack growth events. Short crack growth is considered to be of a length scale that is small compared to relevant microstructural dimensions and/or local plasticity length scales [56].

In titanium alloys the microstructure and crystallographic texture are considered to dominate the early fatigue behaviour [55, 63]. For example, in the work of Birosca et al.

various experimental techniques were used to characterise the propagation of fatigue cracks in beta processed Ti6246 [57, 58]. This work has shown lamellar type colony microstructures have relatively smooth short crack paths whilst Widmanstätten microstructures force the crack tip to divert according to alpha platelet morphological orientations [57, 58]. Other researchers have published similar findings [59].

In terms of crack initiation behaviour, various researchers have published different findings. Demulsant and Mendez investigated lamellar Ti6246 microstructures and stated that crack initiation in air occurs mostly at alpha/beta interfaces regardless of the applied stress. They noted multiple cracks at parallel interfaces. As for other researchers, they observed growth of short cracks at rates highly dependent on microstructure [55, 59]. In their work they cited other studies suggesting the accumulation of damage at alpha/beta phase interfaces in Widmanstätten microstructures. An illustration of the coalescence of individual phase interface short cracks is displayed in Figure 2-35 [59]. In their work they suggested two competing fracture mechanisms; one along alpha/beta phase interfaces and the other along alpha phase slip planes [59]. It has been reported that crack initiation occurs at phase interfaces under low strains and along slip bands at higher strains [1].

In further work, Mendez et al. asserted that beta processed Ti6246 microstructures showed a transition from surface to sub-surface initiation sites at values of (maximum applied stress/yield stress) less than 0.72 [62]. Surface cracks were observed at alpha lamellae/beta matrix interfaces as reported previously. It was suggested that the mechanism may be heavily influenced by the test environment, due to the absorption and/or diffusion of active species (i.e. hydrogen and oxygen). These processes would be favoured by local stress gradients resulting from deformation incompatibilities between the phases [62]. This was supported by further work published by Mendez in 2002 [63]. In this work it was noted that a cleavage-

like process occurring under vacuum conditions across individual alpha platelets in Widmanstätten microstructures would not be possible in air due to the level of damage resulting from phase interface cracking [63].

Another mechanism of interface fatigue cracking would be that of crack nucleation along alpha layers at beta grain boundaries [27]. This behaviour has been reported in both beta annealed lamellar and beta processed Widmanstätten microstructures [64]. It is widely acknowledged that in titanium alloys the grain boundaries have a strong influence on crack nucleation and propagation [27]. High angle boundaries are known to be favourable sites for crack nucleation [57].

The presence of continuous undeformed alpha layers at beta grain boundaries is a problem affecting not only fatigue performance but also other mechanical properties such as tensile strength and fracture toughness [27, 38]. It is widely recognised that the presence of such structures should be avoided in beta processed titanium alloys. The theory proposed by Sauer and Luetjering is that crack nucleation resistance is strongly dependent on the effective slip length parallel to the grain boundary alpha layers [38, 60]. Continuous alpha layers lead to significantly softer zones in the regions adjacent to beta grain boundaries as compared to the aged beta matrix [27, 38]. Because of the influence of the grain boundaries there is a mechanical anisotropy in elongated beta grain microstructures, where fatigue properties are at a minimum at 45°. This is explained by a shear stress controlled dislocation pile-up model (as displayed in Figure 2-36) where the effective slip length when stressed in directions 'L' or 'ST' is identified as 'D_2' but when stressed at a 45° orientation is the much larger 'D_1' dimension [38, 60]. In their experimental work, Sauer and Luetjering noted that crack nucleation sites show a faceted area angled at ~45° to the stress axis. This was

concluded to indicate that cracks nucleate along a favourably oriented grain boundary alpha layer or zone [60].

In some microstructural conditions internal fatigue origins may result as the consequence of slip band separation due to accumulated fatigue damage [55]. This would be more likely to occur in primary alpha grains in bimodal microstructures but may also occur in suitably oriented colonies in beta processed microstructures [55, 65]. Hall recognised that near alpha alloys microstructures may contain large domains of crystallographically aligned alpha phase acting as the controlling feature in initiation behaviour. However, in microstructures containing large planar interfaces (i.e. primary alpha platelets) and a high retained beta fraction the initiation behaviour would be controlled by separation at these alpha/beta interfaces (as in Figure 2-35).

Summarising the experimental evidence, Hall stated that the desired microstructure for resistance to nucleation and early crack growth would consist of small grains with short interfaces and no macro or micro-scale textures [55]. Fatigue crack nucleation could be inhibited by reducing slip distances and eliminating large planar interfaces [55, 61]. Critical microstructural features have been identified as individual primary alpha grains, prior beta grains, alpha colonies and/or regions of common alpha orientation [61].

2.7 Cold dwell fatigue behaviour

2.7.1 Overview

Development of alloys such as Ti6246 has been driven by the need for improved temperature capability and competitive fatigue strengths at lower temperatures. However, despite improved creep resistance, titanium alloys have been widely reported to be susceptible to extended periods under stress at low temperatures (<200˚C). The phenomenon is referred to as 'cold dwell fatigue' sensitive behaviour [66]. Dwell sensitivity is a problem concerning compressor discs where failure occurs at significantly lower stresses than predicted using laboratory specimen testing. This has been shown to potentially reduce cycles to failure (dwell loading cf. cyclic loading) by up to an order of magnitude in laboratory tests.

Cold dwell fatigue (CDF) failures are characterised by sub-surface nucleation of fatigue cracks. Cracks initially form as "quasi-cleavage" facets on or near to the {0001} basal plane of alpha titanium normal to the hoop (principal) disc stress [67].

It has been established that a contributing factor to the initiation of CDF cracks is the presence of large areas of common crystallographic alignment of alpha phase. Where a common alpha crystallographic orientation exists across neighbouring grains (under a favourably orientated stress) a facet may traverse the grain boundary along the common basal plane. This may occur even where the optical microstructure shows changes in appearance. This makes it difficult to characterise initial facet size according to grain size. This causes difficulties in lifing calculations as the initial facet size can have a strong influence on the crack growth life of a disc.

As outlined previously, containment of compressor discs on failure is difficult due to their weight and rotational speeds [13]. Disc spin rig testing has established a very flat stress to life relationship for CDF failures. The implication is that for stresses exceeding the threshold level only a low value of predicted safe cyclic life (PSCL) can be declared. Furthermore, the sub-surface nature of cracking makes detection inherently more difficult than for equivalent surface cracks. In practice if there is a risk of CDF failure this results in more frequent NDE inspections and greater expenditure on service management.

2.7.2 Historical background – In-service experience

Prior to 1973 there was no recognised experience of the CDF phenomenon. However, the requirement for increasing temperatures in high-pressure compressors meant the material capabilities of the Ti6/4 alloy were exceeded. There was a requirement for more advanced high temperature resistant alloys that led to the introduction of creep resistant near alpha alloys such as IMI829[2] and IMI685. The use of these alloys in compressor disc applications resulted in some premature test rig and in-service failures [16].

Rolls-Royce first recognised ambient temperature dwell sensitivity in 1973 following the uncontained failure of two IMI685 fan discs in RB-211 engines. Failures occurred after 335 and 279 flight cycles although earlier rig testing had shown no failures below 9,500 cycles [68]. Failures were attributed to dwell sensitivity in propagation from pre-existing cracks. As a result IMI685 fan discs were replaced with Ti6/4 discs as this alloy had already accumulated significant service experience. Later work demonstrated that crack initiation could be sensitive to dwell periods in other titanium alloys including Ti6/4, Ti65s, Ti829 and Ti834,

[2] IMI refers to IMI Titanium Limited. Following takeover by Timet, alloy names now have the prefix Ti. For example IMI685 is now referred to as Ti685. The terminology used in the literature review is as for the terminology in the source references.

although in standard microstructural forms these alloys showed little or no crack propagation dwell sensitivity.

In 1982 rig testing of IMI829 (Ti5331s) discs established the effect of cold dwell on crack initiation. This was followed with a series of rig test programmes on both IMI685 and IMI829 alloys, which concluded that cold dwell was a contributing factor in the burst of IMI685 HPC discs in two RB-211 engines in the 1980s. This work concluded that the primary cause was modest melt anomalies.

The alloy IMI834 was developed as a successor to the IMI829 alloy. The cold dwell performance of the alloy was a key concern during its development. High priority was given to ensuring the problems experienced in IMI829 were avoided in IMI834. Despite these efforts a rig test programme in 1992-3 established a cold dwell effect on initiation behaviour in the alloy. Similar behaviour to IMI685 and IMI829 was noted and it was concluded that finish forgings retained texture from billet material leading to adverse dwell behaviour.

Ti6246 was introduced into Rolls-Royce compressor disc applications in the mid 1990s. Work on the alloy at that time showed no limitations due to cold dwell sensitivity at the anticipated operating stresses. However, in 2002 concerns were raised following the observation of large-scale beta grain 'clusters' of common optical appearance. These clusters were observed on the diaphragm of compressor discs in an etched condition. The concern was that the clusters of common optical appearance might have indicated common crystallographic alignment. Further work confirmed the presence of large crystallographic units and additionally indicated that areas of optically varied microstructure could potentially display common texture. A large-scale programme of work was undertaken to characterise Ti6246 microstructures and crystallography - see chapter four [69].

Aside from Rolls-Royce other aero-engine OEMs are known to have in-service experience of CDF failure. Literature is available relating to failures in General Electric Aircraft Engines (GEAE) compressor discs. There have been three documented burst failures in the HPC3-9 stages of the GE CF6 engine from 1985 onwards. These discs are wrought from Ti6242 billet as a single forging/spool. Some failures have been attributed to melt anomalies such as hard alpha inclusions although other failures indicate CDF behaviour [70]. Frequent service inspections have also led to the discovery of cracking in operational engine compressor discs [71]. A document issued by the National Transportation Safety Board in August 1995 highlighted three known failures in CF6 engines as a result of dwell fatigue. The first of these (1985) involved the rupture of a stage 9 disc after ~4,000 flight cycles during take-off. The second incident occurred in May 1991 on a disc subject to ~10,500 flight cycles. The third incident occurred in May 1995 with the separation of a stage 8 disc after ~8,500 cycles, again during take-off. The failures were attributed to "dwell time fatigue" on the basis of fractographic assessment of recovered disc debris [70].

In the ensuing failure investigations GE attributed low-life dwell fatigue failures to excessive alpha grain growth [70]. This resulted from a slow cooling of the HPC3-9 spool during processing. Originally the spool was forged and machined from a 16" diameter billet. Following hard alpha inclusion disc failures this was modified to a 13" billet to improve inspectability. The design was later changed to produce two-piece spools from 12" and 13" billet, joining the two sections using inertia welding. A post-weld heat treatment and slow cool was then required to relieve welding residual stresses. It was the slow cooling stage of the heat treatment that GE determined as the major cause of dwell sensitive behaviour in the spool. To overcome the problem GE replaced the PWHT and slow cool with a stress

relief operation. The diameter of billet material was also changed such that all spools were manufactured from 8" billet [70].

As well as GEAE, in the late 1990s Honeywell are known to have recorded the in-service burst failure of a Ti6242 impeller. Pratt and Whitney recorded the failure of an IMI834 alloy impeller on testing early in the 2000's [71]. Other CDF failures may have occurred in-service although they are unknown to the author.

2.7.3 Cold dwell fatigue mechanisms

Research has attributed dwell sensitivity to a number of potential factors. These include temperature effects, time-dependent strain accumulation, stress ratio effects, internal hydrogen embrittlement, microstructural and micro-texture influences, synergistic fatigue-creep interactions and Stroh type dislocation reactions [72, 73]. Other research has argued that load level, section size and stress biaxiality all influence behaviour [74]. The various proposed mechanisms relating to CDF behaviour are discussed under the following sub-sections in a largely chronological appraisal of the available literature.

2.7.3.1 Hydrogen effects

Prior to the in-service failures of IMI685 fan discs in the early 1970s work had been undertaken relating to the effects of sustained loading on crack initiation and growth. It had been established that crack growth under sustained loading could occur at stress intensities significantly below the intensity for crack instability. Where observed, sub-critical crack growth had been attributed to stress corrosion, creep and/or the embrittlement effects of internal hydrogen [75].

Embrittlement of titanium alloys under sustained load had been related to residual hydrogen content in the late 1950s. Two theories concerning hydride growth at room temperature

were suggested. The first related to alpha stabilised alloys with hydrogen present in a metastable solid solution with hydride precipitation under stress. The second explanation suggested alloys with significant quantities of beta phase (higher hydrogen solubility than alpha phase) become super-saturated with hydrogen, with hydride precipitation in alpha or at alpha/beta phase boundaries [76].

Meyn cited previous research which suggested that embrittlement under sustained loading was related to residual hydrogen content. These works proposed that crack nucleation occurs either from hydrides precipitated under strain at alpha/beta interfaces or from regions of high strain where concentrated hydrogen remains in solution. Hydrogen in interstitial solution was thought to inhibit slip through the formation of atmospheres on dislocations, resulting in micro-cracking under deformation [77].

Despite previous research, studies in the early 1970s remained unclear whether sub-critical crack growth under sustained loading was the normal response of material in the vicinity of a sharp crack or the result of a secondary factor such as hydrogen embrittlement. Williams discounted the effects of internal hydrogen on sustained load cracking (SLC) behaviour for an alloy with 10ppm hydrogen content on the basis that this concentration was insufficient to significantly contribute to crack growth. Effects were instead attributed to creep behaviour [75]. This concurred with the research of Beachem which suggested that hydrogen contributes to SLC through a concentration of local plastic deformation. It was suggested that the presence of a sufficient hydrogen concentration dissolved in the lattice ahead of the crack tip aids whatever deformation processes the microstructure allows [78].

Based on fractographic observations, hydride formation was deemed to be influential in rather than causative of SLC behaviour. Interstitial hydrogen was known to partition strongly

to beta phase and concentrate at alpha/beta interfaces. Consequently tensile stresses in alpha phase were observed to lead to preferential initiation near phase interfaces [77].

Further work began to consider the influence of microstructure in the behaviour of material under sustained loading. Much of this work did not discount the influence of hydrogen, but instead developed theories relating hydrogen effects, microstructures and dwell behaviour as for the work of Eylon and Hall [79].

Work by Evans on the effects of hydrogen on dwell sensitive behaviour suggested that an increase in hydrogen content actually improved cyclic performance in IMI685 [66]. Despite this work, research published in 1988 again suggested hydride precipitation mechanisms in the cracking failure of the alloy Ti-4wt%Al [80]. Two mechanisms were suggested; fracture by localised plastic deformation and fracture of stress-induced titanium hydride precipitates.

Up to the late 1980s research had observed a dwell effect over the temperature range ~20°C to 200°C. Many authors had attributed this reduction in life to the effects of internal hydrogen embrittlement although a time dependent strain accumulation model was increasingly being cited as an explanation. From ~200°C up to ~400°C, dwell effects were observed to diminish to insignificant levels. Hydrogen embrittlement theories attributed this to the increased mobility of hydrogen atoms. Neal investigated the dwell susceptibility of six alloys (Ti6/4, Ti679, Ti6242s, Ti685, Ti829 and Ti550) and found no dwell effects in any alloy above 150°C, with the most detrimental CDF effects observed at 80°C [81].

The work undertaken by Neal also included a survey of the effects of hydrogen on dwell fatigue, with findings not dissimilar to those published by Evans, i.e. hydrogen content giving no detrimental effect on dwell cyclic life. It was concluded that near identical dwell debits

were observed at all hydrogen contents whilst LCF performance was seen to increase with hydrogen concentration [81]. For Ti685 these results are shown in Figure 2-37.

Although Evans previously dismissed the influence of hydrogen in CDF behaviour as a secondary factor, research in the early 1990s led to the conclusion that "*hydrogen plays a significant role in the deformation and failure mechanisms in IMI685*" [82]. IMI685 material was tested in various conditions. These included basketweave and aligned microstructures, and low to high hydrogen contents. They found a reduction from 60 to 20ppm hydrogen had little effect on cycles to failure in basketweave material, although an increase to greater than 100ppm hydrogen resulted in a significant decrease in the cycles to failure. In aligned colony material they found a reduction in life at low hydrogen content under cyclic and dwell tension. Life reductions were observed under different loading modes for high hydrogen contents [82].

Fractographic examination led to the suggestion that at high hydrogen contents failure may be through brittle hydride formation at alpha/beta interfaces similar to theories proposed by Pao and O'Neal [83]. There was a distinct step/plateau fracture surface appearance [82]. In low hydrogen materials at lower stresses basal plane facets could be observed as described in earlier research. For these failures the mechanism was considered to be time dependent strain accumulation and stress redistribution, according to a model developed by Bache and Evans in the early nineties and covered under section 2.7.3.4 [84].

The same researchers continued investigating behaviour under load in IMI685 [67]. Many of the earlier observations were reinforced, such as similar fatigue performance at a given percentage UTS for low (20ppm) and intermediate (60ppm) hydrogen contents, increased

strain accumulation rates in low hydrogen material and distinct basal facets in 20-60ppm hydrogen material at low stresses.

A description was given of two-stage fatigue behaviour in material with low and intermediate levels of hydrogen with a transition described at ~7,000 cycles. There was also a marked decrease in the proportion of the material UTS for failure at a given number of cycles in material with high hydrogen contents. These observations are displayed in Figure 2-38 and Figure 2-39 respectively.

Specimens with high hydrogen contents were tested in solid bar and tubular forms to demonstrate the repeatability of the results. Based on the experimental evidence it was stated that "*hydrogen atoms modify dislocation behaviour particularly at the lower concentrations but above a critical level they induce additional failure events*". It was also noted that these results were contradictory to those of Shih et al, cited earlier, which suggested that gaseous hydrogen environments increase dislocation mobility [67]. The work of Ulmer and Altstetter was cited as a suitable mechanism to explain behaviour. This associated slip localisation with hydrogen induced blocking of cross slip at dislocation pile-ups, providing an explanation for quasi-cleavage facet formation along intense slip bands due to the stresses generated by dislocation pile-ups [67].

In more recent work the influence of hydrogen content has received less attention. Material anisotropy and stress redistribution effects are the focus of more recent investigations into CDF behaviour.

2.7.3.2 Microstructure/micro-texture influences

Early observations of sustained load tests related sub-critical crack growth to the presence of cleavage-like facets in the slow crack growth region of the fracture surface. The number

of facets on the fracture surface reduced as initial stress intensity levels increased. Study of fracture surfaces showed a tendency for sub-critical cracking to progress through beta phase or along alpha-beta interfaces. This contrasted to other studies where sub-critical cracking predominately progressed through alpha phase. It was concluded that cleavage like facets aligned in bands parallel to the direction of crack growth and appeared to relate to microstructure. It was suggested that facets represent separation along alpha-beta interfaces and cleavage fracture of suitably orientated alpha particles [75].

Work in the late 1960s studied the nature of crack propagation in Ti-8Al-1Mo-1V and determined the cleavage plane characteristic in sustained load cracking fracture surfaces to be approximately 15° from the basal plane. The plane was *"tentatively identified as* $\{10\bar{1}7\}$ *or* $\{10\bar{1}8\}$*"* [85]. Further work observed cleavage facets orientated 12-15° from the basal plane, again potentially on $\{10\bar{1}7\}$ or $\{10\bar{1}8\}$ planes. Meyn discounted the influence of hydride precipitates in their formation, stating *"known habits of hydride precipitation in titanium alloys cannot conceivably lead directly or indirectly to cleavage 12-15° from* $\{0001\}_\alpha$*; and in every case where hydrogen or hydrides were observed to be the direct cause of cracking, the microstructural mode of cracking was intergranular, transgranular or interfacial cleavage near prismatic plane* $\{10\bar{1}0\}_\alpha$*, or along observed hydride-matrix interfaces*" [77]. Known habits of hydride precipitation in titanium alloys had previously been described as $\{10\bar{1}0\}$ and {1011} planes by Cotterill and others in a review of hydrogen embrittlement theory [85, 86].

Neal and Blenkinsop assessed internal fatigue origins in HCF specimens in (alpha + beta) titanium alloys and found no evidence of defects or pores. They suggested cleavage of alpha grains could be accounted for by internal fatigue origins. The mechanism they proposed was related to the restriction of operative slip systems with the addition of aluminium and the

associated alpha phase stabilisation. Restriction of dislocation movement to planar slip would lead to dislocation pile-ups at grain boundaries. This would result in stresses high enough to produce cleavage on the $\{10\bar{1}7\}$ plane before critical resolved shear stresses for slip could be attained on $\{10\bar{1}1\}$ and {0001} planes [87].

Stroh predicted cleavage crack formation to occur on a maximum normal stress plane at an angle of 70.5° to the slip plane containing a dislocation pile-up. With the dominant slip mode at ambient temperature being prismatic, the angle between the $\{10\bar{1}0\}$ prism plane and the $\{10\bar{1}7\}$ cleavage plane was estimated at approximately 75°. The $\{10\bar{1}7\}$ cleavage plane would therefore be close to the plane of maximum normal stress. This theory is illustrated in the schematic diagram in Figure 2-40.

In the 1970s several researchers investigated CDF behaviour in IMI685 following the in-service failures of fan discs. Eylon and Hall investigated the LCF behaviour of IMI685 in a beta processed and annealed condition [79]. Research had suggested that the microstructural feature controlling FCP was the presence of similar orientations of acicular alpha platelets termed 'colonies' [79]. The size and crystallographic alignment of colonies had been shown to influence crack path in Ti-11 and IMI685 alloys. A high incidence of crack growth normal to the long axis of alpha platelets had been observed in colony microstructures. This could be related to *"intense slip traces extending across colonies, seemingly unhindered by alpha/beta interfaces"* [88]. As for sustained loading tests, cleavage-like facets were observed in colony microstructures. Straight crack paths could be seen to follow intense shear bands that developed ahead of the propagating crack [88].

The level of scatter displayed in FCP results prompted work undertaken by Eylon and Hall on beta-processed IMI685. Data scatter restricted the operating capability of the alloy and in

turn limited the FCP advantages conferred by the beta-processed microstructure. Their study examined large forgings with significant microstructural variation through the cross-section, resulting from a range of cooling rates and beta strains [79]. Testing IMI685 under different microstructural conditions, Eylon and Hall observed significant differences in the LCF behaviour of the alloy. The results obtained are displayed in Figure 2-41 [79]. With the imposition of a dwell period a significant life debit was observed although no change in FCP rate was observed. Crack initiation behaviour was therefore considered to be relevant for further investigation. The life reduction observed with dwell loading was consistent with other research that attributed dwell behaviour to hydrogen effects [79]. On this basis a mechanism of hydrogen accumulation on or near to damage planes created by intense shear bands was suggested. A further suggestion was the possibility of meta-stable hydride precipitation as outlined by Hammond [89].

In their work on beta processed IMI685 Eylon and Hall noted that all specimens tested under CDF had sub-surface initiation sites. A cleavage-like fracture appearance was present with shear traces parallel to the plane of cleavage initiation. As in previous work a tendency for crack growth through colonies near perpendicular to the long axis of alpha platelets was noted. Crack initiation was thought to relate to the incidence of heterogeneous planar plastic deformation across a colony [79].

Eylon and Hall concluded that sub-surface initiation sites could be characterised by a very smooth oval-shaped region with a small pore at its centre. They termed these features "cleavage rosettes". Characterisation of these features showed the long axis boundaries of the inner cleavage area coincide with inter-alpha platelet boundaries. Beyond these boundaries the cleavage fracture continued on approximately the same plane to the colony boundary [79]. Further study of cleavage rosette regions showed that initiation cracks

propagated perpendicular to alpha platelets. Smaller cracks running parallel to the fatigue crack were explained by the presence of intense slip bands. Slip bands ended when encountering differently orientated colonies. Colonies of alpha platelets were hence considered to be similar to single crystals in terms of their slip behaviour [79].

With increasing understanding, the significant scatter observed in fatigue data for material with colony microstructures was attributed to the statistical probability of having a large colony at a critical location, suitably oriented with respect to the applied stresses, in order to form an intense shear band leading to Stage I crack growth [79].

It was suggested that pores at the centre of cleavage rosettes were associated with incompletely healed solidification porosity inherited from ingot. In normal material this porosity would have been removed during ingot breakdown processes. The theory of ingot porosity was supported by the fact that areas of the forging containing rosettes only received low levels of deformation [79].

In the late 1970s Evans and Gostelow continued research into the fatigue behaviour of IMI685 with a colonised microstructure [90]. Their work again confirmed a dwell fatigue debit with a life reduction in excess of an order of magnitude. Sub-surface crack initiation was observed with facets present at the crack origins. They were described as "cleavage" or "quasi-cleavage" facets. As with the SLC observations of Williams, CDF tests initiated cracks at multiple sites. The number of facets decreased with increasing stress. Observations were made supporting those of Eylon and Hall in regard to "cleavage rosettes" extending to colony boundaries. Studies also showed facet diameters corresponding to average alpha colony sizes [90].

Work by Davidson and Eylon on IMI685 and Ti-11 alloys characterised a number of fatigue facets to show orientations within 35° of the basal pole. However, it was also noted that IMI685 non-dwell specimens displayed pure basal facets unlike dwell tested specimens of the same alloy [91]. A plot of the different orientations and their proximity to the basal plane is given in Figure 2-42.

Work by Neal (1988) investigated both hydrogen and microstructure effects [81]. After discounting the effects of hydrogen (see previous section), the roles of both microstructure and alloy composition in dwell behaviour were questioned. Neal referred to previous research by Hack and Leverant suggesting that Ti6242S was not dwell sensitive even when beta heat-treated. In his work Neal recorded cyclic life debits in excess of 60% for Ti6242 in the (alpha + beta) microstructural condition. Based on the hypothesis that microstructure was not a major factor in CDF behaviour but composition was significant, a highly alpha stabilised experimental alloy was tested for comparison to standard alloys. Dwell cyclic life debit, aluminium equivalent and molybdenum equivalent were compared for different alloys and are reproduced in Table 2-1.

Neal concluded that heat treatment to change the microstructure (as for Ti6/4, Ti829 and Ti550) displayed no significant effect on dwell debit. It was noted however, that increasing levels of alpha stabilisation led to increasingly poor dwell performance. Neal suggested that highly alpha stabilised alloys were susceptible to planar slip in the alpha phase on or near to the basal plane when subject to sustained periods under stress. By contrast IMI550 was believed to have sufficient beta stabilisation that deformation under load would occur in the beta phase rather than as planar slip in the alpha phase [81].

2.7.3.3 Time dependent strain accumulation/Combined hydrogen effects

In work published by Evans and Gostelow CDF testing showed significant strain accumulation relative to cyclic testing [90]. Furthermore, strain-time records for dwell tests exhibited primary, secondary and tertiary stages characteristic of creep deformation and a close correlation could be observed between creep and dwell specimen lives. Fractographic comparisons showed similar facet formation behaviour. Based on these observations the formation of facets and the behaviour under CDF loading was attributed to "*accumulation of creep strain at peak stress*" [90].

Prior to research on CDF it had been postulated that dwell periods would only have an effect at elevated temperatures where creep could contribute to deformation behaviour. Researchers noted the disappearance of dwell effects at temperatures between ~80-150°C. On this basis the possibility of a creep interaction accounting for reduced life under dwell was considered to be unlikely. Instead research attributed the effect to strain induced hydrogen embrittlement as described under section 2.7.3.1. The decreasing CDF effect with increasing temperature was explained in terms of a reduced ability for interstitial atoms to act as locking agents [90]. The conclusion of Evans and Gostelow that dwell behaviour resulted from creep strain accumulation directly contradicted much of the previous work.

Despite the conclusions relating to strain accumulation, at higher stresses the extent of faceting on fracture surfaces decreased although there was still significant strain accumulation. It was therefore acknowledged that strain accumulation alone was unlikely to be responsible for facet formation. Although recognising an incomplete understanding of the mechanism of facet formation, Evans and Gostelow questioned the involvement of hydrogen embrittlement. They cited work by Bania and Eylon and also noted that work demonstrating

hydrogen embrittlement had used alloys with hydrogen contents in excess of several hundred parts per million [92]. The research of Hall and Hammond showing hydride formation under stress in conventional IMI685 was also questioned and attributed to the possibility of specimen contamination. It was suggested that facet formation through hydrogen or hydride effects alone in cyclic loading was unlikely as any stress assisted migration during loading would be reversed during the unloading phase of the cycle [90].

Instead of hydrogen embrittlement, a creep/hydrogen locking mechanism was described with high dislocation mobility and strain rate under initial load application. With continuing creep under load the strain rate decreases due to strain hardening, then becoming possible for hydrogen atoms to interact with dislocations to enhance hardening and promote conditions favourable for quasi-cleavage failure modes [90].

At the start of the 1980s Hack and Leverant continued to develop a model of combined hydrogen/creep deformation effects to explain decreases in fatigue life under dwell conditions. A comparison of previous research showed identical strains to failure, times to failure and fracture surface appearances for static loading and five minute dwell tests. These results are displayed in Figure 2-43 [93]. From comparison of creep and dwell data it was concluded that fatigue cracking under peak stress was not an important factor in the failure process [94].

Examination of cleavage facets indicated no defects were present at initiation sites. This contrasts with the results of Eylon and Hall for which 'pores' present at the centre of cleavage sites were attributed to ingot porosity [79]. As for the work of Davidson and Eylon, facets were usually found to correspond to a basal or near basal plane [94]. Hack and Leverant postulated that as slip is often active on the basal plane in titanium alloys with

higher aluminium content (increased alpha stabilisation), the formation of facets suggests the involvement of hydrogen in the fracture process [94]. This followed work by Hall and Hammond where hydride formation had been observed at crack tip locations in IMI685 [93].

A combined creep/hydrogen model was suggested to allow for the concentration of hydrogen at the initiation site coincident with or near active slip planes. This model involved creep deformation leading to the generation of slip bands. Blocking of a slip band at a colony or grain boundary produces a dislocation pile-up in turn creating a hydrostatic stress field. The stress field would then attract and concentrate hydrogen through diffusion. An example of colonised Ti685 microstructures was considered, with a shear band traversing a sub-surface colony but blocked at its boundaries. This was equated to a stressed, double-ended dislocation pile-up, illustrated in Figure 2-44 [93]. A value for hydrostatic stress could then be calculated based on the assumption of a shear band consisting of a single planar array of edge dislocations, equivalent to a Mode II crack. If this stress were to exceed that of an equivalent crack tip then a blocked shear band could induce a high enough stress to locally concentrate sufficient hydrogen to promote either crack initiation or hydride formation followed by cracking of the hydride [94].

This hypothesis was tested by conducting five minute dwell tests at temperatures of -73°C and 200°C. Testing at -73°C was intended to limit creep effects whilst still allowing significant hydrogen diffusion. At a temperature of 200°C hydrides would not form due to thermodynamic instability. Results at -73°C showed no creep deformation after an order of magnitude increase in the time on load compared to the time to failure for an identical test at room temperature. At 200°C an order of magnitude increase in time under load was also achieved relative to the time to failure for a room temperature test. This life increase was attributed to the absence of hydride formation [95]. From these results it was concluded

that time dependent deformation and internal hydrogen effects were acting in combination to induce the embrittlement required for failure [83].

Hack and Leverant noted the presence of secondary cracking parallel to facets. Such cracking had been described in earlier work by Eylon and Hall [79]. Secondary cracks were observed to partially traverse colony structures, suggesting that failure under dwell cycles was a progressive crack nucleation and growth process rather than a catastrophic failure from a single micro-crack [95].

Little research on CDF behaviour is available from the mid 1980s, however, interest in the subject resumed towards the end of the decade. In 1987 Evans published work on the IMI685 alloy. This work argued, contrary to the combined hydrogen/shear band model of Hack and Leverant, that increasing the hydrogen content of the alloy actually extended life under both cyclic and dwell conditions. The experimental work used a beta heat-treated and slow-cooled colony microstructure (previously shown to be highly susceptible to CDF [90]) with two different hydrogen concentrations. Fatigue behaviour is displayed in Figure 2-45. Under both dwell and cyclic test conditions an increase in life s observed when hydrogen content was increased from 10ppm to 50ppm. Examination of the fracture surfaces did not distinguish a change in the crack initiation mechanism. All fractures initiated at sub-surface locations with quasi-cleavage facets at crack origins. The similarity between the fracture surface features near the initiation site led Evans to suggest that initiation mechanisms were likely to be the same, probably involving time dependent strain accumulation [66]. This was similar to earlier work in which a mechanism of creep strain accumulation under loading was proposed [90].

Further work undertaken at 150°C was used to calculate activation energies for the diffusion of hydrogen in the alpha and beta phases. Evans suggested that calculated and known values of activation energy were similar enough in magnitude to support the theory of hydrogen movement associated with plastic flow at near ambient temperatures [66].

Another paper published by Evans at a similar time also studied the behaviour of IMI685 in a colony microstructure and made comparisons to conventional basketweave material [84]. It was found that for constant load creep tests and dwell tests (displaying near identical times to failure for a given stress) there were two distinct failure regimes. These were described as 'strain-dominated' and 'facet-dominated' failures. Strain dominated failures were noted at high stresses for aligned colony structures, characterised by higher rates of strain accumulation and higher fracture strains. Facets were present on these fracture surfaces although they were typically oriented at ~45° to the stress axis. At lower stresses the mechanism changed to facet dominated failures perpendicular to the stress axis. By contrast, in the basketweave microstructural condition only strain dominated failures were observed [84].

A paper by Thomsen and Hoeppner published in 1998 provided a concise summary of the research into CDF behaviour up to that point. They summarised that there were two major causes to which CDF behaviour was attributed; hydrogen related damage and strain accumulation [96]. In reviewing the case for the hydrogen explanation, they noted that the solid solubility of hydrogen is much lower in the alpha phase in comparison to beta phase. This would favour titanium hydride formation in the alpha phase (hence greater susceptibility in near alpha alloys), with an associated 15% volume change. This would lead to volumetric strains, stress concentrations and cracking. It was also noted that interstitial diffusion rates had previously been noted to be highest along the basal plane of HCP crystals [96].

The strain accumulation/cold creep explanation was based on work by Evans. In summary, hydrogen was acknowledged as a factor, although the major cause was given as strain accumulation and the influence on microstructural 'weak links' through stress redistribution processes [96]. The original model of Hack and Leverant was also cited, noting that strain accumulation was a necessary precursor to hydrogen diffusion to allow the formation of slip bands and hydrostatic stress concentrations [96].

2.7.3.4 Stress redistribution/Off-loading theories

Following on from observations of strain-dominated and facet-dominated failure types it was suggested that the Hack and Leverant shear band model of strain accumulation on inclined planes was unsuitable as it did not explain the development of facets with load normal orientation. In an alternative explanation Evans referenced a previous model attributing creep deformation to a microscopic redistribution of stresses [97]. Assuming the application of a uniform stress to a region of material, a distribution of deformation rates occurs in proportion to relative strengths. Primary creep results from the equalisation of individual creep rates through the redistribution of stresses from weak to strong regions [84]. This qualitative idea was the basis for a model that Evans and Bache would refine and develop further.

Evans recognised that whilst this model was developed for high temperature creep it could also be applied to IMI685 because of its large grain size and anisotropic crystallography. Based on the model outlined, loading would lead to increased stresses on basal planes orientated perpendicular to the applied stress (i.e. strong regions). Where stress redistribution is such that it exceeds a critical value on these planes it would then be possible to nucleate quasi-cleavage facets [84].

The stress redistribution model could be used to account for the development of load normal basal facets. However, as Evans had previously also observed facets inclined at ~45° it was necessary to also account for their formation. As these facet types occur at higher stresses it was suggested that strain accumulation in weak regions would occur at a rate fast enough not to allow stress redistribution to strong regions. This would prevent the formation of facets on planes normal to the applied stress [84].

No attempt was made to incorporate the interaction of hydrogen atoms under time dependent deformation into the model because of the uncertainty surrounding the effects of hydrogen on CDF behaviour [84]. For example, in work published at a similar time Evans stated that hydrogen "*at low concentrations tends to increase both dwell and cyclic lives whilst the reverse is true at high concentrations*" [98].

Much of the work up to this point had been concerned with facet formation as a failure mechanism associated with dwell sensitive materials, typically near-alpha titanium alloys. Evans recognised that facet formation may also occur under other loading modes as a result of time dependent strain accumulation. Facets observed at notches in Ti6/4 under cyclic fatigue and stress relaxation were also attributed to stress redistribution following time dependent strain accumulation. Because no facets were observed on the fracture surfaces of monotonic specimens it was postulated that facet formation was dependent on the accumulation of critical levels of strain [99].

Other work by Evans studied Ti6/4 to show that CDF behaviour was not limited to fully transformed microstructures. Material in both annealed and beta transformed conditions was shown to exhibit dwell sensitivity of a similar magnitude to near alpha alloys. Life reductions for the annealed microstructural condition (~750°C for two hours) of equiaxed

alpha and retained beta are displayed in Figure 2-46. As noted previously, Evans confirmed that the time to failure in creep tests was similar to time on load to failure for dwell fatigue tests. Both tests were noted to display initiation site facets.

In the mid 1990s the Ti6246 alloy was introduced as engine operating conditions became increasingly demanding and the requirement for higher strength titanium alloys arose. Ti6246 underwent a mechanical test programme prior to entry into service to determine the dwell response of the alloy [100]. In an attempt to ensure testing representative of in-service compressor discs, test-pieces were machined from a disc subject to conventional forging and heat treatment procedures. The overall conclusion of the work was that the dwell susceptibility of Ti6246 was low in comparison to near alpha alloys. There was no evident change in failure mechanism between cyclic and dwell LCF fatigue. The major conclusions from the programme of work were as follows; a two minute dwell on load has only a small effect on life to failure, temperature has no effect between 20-150°C and dwell loading shows little effect on crack propagation rate [100]. A cyclic life reduction by a factor of 1.5-2.2x under dwell loading at high stresses at a temperature of 80°C was observed. This life debit was found to converge at lower stresses. When stress was normalised against material UTS at different temperatures a plot against cycles to failure displayed little difference between the lives achieved at the different temperatures. As for testing at 80°C the reduction in cyclic life with the imposition of dwell periods was also minimal with temperature variations [100]. These results are displayed in Figure 2-47.

Fractographic examination showed no clear differences between cyclic and dwell specimens. This further supported the evidence that time on load had little effect on the behaviour of Ti6246 relative to other alloys. Crack initiation was predominately noted at specimen surfaces. Reports described "*featureless quasi-cleavage facets mostly restricted to small crack*

lengths or near surface regions" which were most evident in highly stressed LCF tests. This contradicted the previously published literature, which had always concluded that increasing numbers of facets could be observed on fracture surfaces at lower stresses. Facets were suggested to be the result of cracking between optically aligned alpha platelets [100].

Further work included in the Ti6246 test programme included tests on Ti834 alloy. For this alloy a life reduction in excess of an order of magnitude could be observed under dwell fatigue. The significant difference in results obtained from bar and forged disc was also noted. A plot of the CDF performance of the two conditions is given in Figure 2-48.

In 1997 Bache, Evans and Davies used the EBSD technique to assess the crystallography of IMI685 and IMI834 test specimens. For IMI685 with 60ppm hydrogen concentrations load normal facets were sectioned and confirmed to be along the basal plane by examination of the underlying microstructure of aligned alpha platelets. Neighbouring grains/colonies were also noted to have aligned platelet colonies although at optically different orientations [101]. As had been suggested in previous publications, increasing the hydrogen content of IMI685 to 200ppm resulted in a distinctly different fracture surface, with cracking thought to follow alpha/beta interfaces or prior beta grain boundaries [101].

For Ti834 numerous small facets (~20µm diameter) were observed for single test specimens. Due to the relatively small size of the facets it was possible to use EBSD to examine the facet fracture surface. An IPF showing the crystallographic orientations of the facets is displayed in Figure 2-49. Results showed very clearly that load normal facets formed along the basal plane [101, 102].

Based on their EBSD results Evans and Bache suggested that because of the unfavourable orientations of basal planes for slip, stress redistribution processes allow slip bands in

adjacent grains to induce stresses sufficient for facet formation in unfavourably oriented grains. They incorporated work suggesting that a critical combination of shear stress and tensile stress is required for faceting into the model of stress redistribution from neighbouring grains [65, 84, 103].

Work by Bache et al. continued with investigations of FCP in Ti685 in a slow cooled aligned colony microstructural form [104]. This work established the orientation of the colony in which a crack initiates as the most significant factor in the overall fatigue life of the material [104]. Whilst local differences in crystallography would appear to lead to stress redistribution and facet formation under dwell in most titanium alloys, highly textured materials would then be increasingly susceptible to fast crack propagation to failure.

The models proposed by Hack & Leverant and later by Evans had suggested intense planar shear along slip bands leading to dislocation pile-ups at colony boundaries was a key feature in CDF crack initiation. The most susceptible materials appeared to consist of aligned colony microstructures where slip could proceed easily across alpha/beta interfaces. Individual colonies allowed slip transmission because of the Burgers orientation relationship between alpha and beta phases. Basketweave structures were thought to be less susceptible because this microstructure reduced effective slip lengths.

In 1999 Suri et al. published research investigating the deformation behaviour of single colony crystals of near-alpha alloy Ti-5%Al-2.5%Sn-0.5%Fe. Crystals were oriented for slip on different prismatic planes and a pronounced anisotropy in deformation behaviour was observed. A colony orientated for maximum resolved shear stress on the $\left[2\bar{1}\bar{1}0\right]\left(0\bar{1}10\right)$ (a_1) slip system had shown no edge dislocation pile-ups, suggesting alpha/beta interfaces provided little resistance. By comparison, a colony orientated for maximum resolved shear

stress on the $[\bar{1}2\bar{1}0](10\bar{1}0)$ (a_2) slip system had shown dislocation pile-ups, which suggested a higher resistance to slip transfer [105].

Previous work on single-phase alpha alloys had shown no difference in creep behaviour with orientation. This had led to the assumption that alpha/beta interfaces were responsible for anisotropic behaviour. However, in the work of Suri et al. the anisotropy was attributed to the relative misalignment of slip systems between alpha and beta phases. This is shown schematically in Figure 2-50. TEM studies showed a_1 and b_1 slip directions are misoriented by 0.56° whilst the a_2 and b_2 slip directions are misoriented by 11.5° about $[0001]_\alpha//[101]_\beta$.

Misalignment of slip systems was proposed to lead to the formation of residual dislocations within the matrix during slip transmission as a result of decomposition of dislocations present at interfaces. The extent of interface dislocation decomposition was stated to be dependent on the orientation of the colony. This would explain differences in the levels of dislocation pile-ups observed for different colony orientations [105]. From this work it could then be hypothesised that only certain slip systems in favourable orientations allow for the accumulation of sufficient dislocation pile-ups at interfaces to allow for stress redistribution and facet formation processes.

It was suggested that for smaller misalignments between a_1 and b_1 slip systems each slip transmission event required a smaller magnitude of dislocation relative to higher slip system misalignments. A dislocation annihilation process was also observed after the passage of every 25 a_1 dislocations, preventing rapid dislocation pile-ups under strain. In contrast, slip systems with high misalignments showed rapid dislocation accumulation at interfaces under strain due to the higher magnitude of each dislocation required for a slip event and because dislocation annihilation was not possible [105].

In summary of their work Suri et al. stated that alpha and beta phases are oriented such that of the three prismatic slip systems in the alpha phase only a_1 type slip can easily transmit across alpha/beta interfaces. Greater interface resistance to slip transmission is noted for the other two slip vectors [105]. For significant dwell behaviour it can be assumed that not only must particular orientation relationships exist to allow redistribution of stresses, but also that dislocation pile-up stresses can build up due to the ability of the material to transmit planar slip easily across phase interfaces.

In further work Viswanathan published a schematic diagram displaying alpha $1/3<11\bar{2}0>$ vectors relative to the face of beta laths, displayed in Figure 2-51. In this work it was noted that a higher temperature allowed the activation of numerous slip systems to limit the observations of planar slip effects [106]. Further work from OSU showed small strain hardening exponents in titanium alloys due to the planar slip characteristics of the material. Grain boundaries and interface effects are then noted to be particularly important, with loading resulting in the progression of slip bands across favourably orientated grains and the development of local stress concentrations in neighbouring grains with orientations unsuitable for <a> type slip [107, 108].

General Electric had experienced dwell fatigue failures in Ti6242 compressor discs as far back as the mid 1980s, as referred to in a NTSB report in 1995 [70]. In 1999 Kassner et al. investigated the effect of primary alpha volume fraction variations on the cyclic and dwell fatigue performance of Ti6242. Different solution annealing temperatures were used to vary primary alpha content between ~5vol.% and ~60vol.%. Microstructures showed the conventional life debit under CDF at high stresses. As for other materials the debit factor was seen to diminish at lower stresses. A decrease in CDF life was observed with increasing primary alpha fraction although there appeared to be little effect on LCF life. Fractographic

analysis of dwell specimens led to the conclusion that primary alpha grains were the preferred crack nucleation site. This offered a potential explanation for increasing dwell debits with higher primary alpha contents. However, it was noted that conventional LCF testing also nucleated cracks preferentially in primary alpha grains, for which no change in cyclic life was observed with primary alpha content [109].

With regard to titanium anisotropy and facet formation under loading, Bache published results concerned with alloy processing and the subsequent effect on fatigue performance [110]. Based on theory to this point it was recognised that grain size and crystal anisotropy should control facet development. It was noted that material with a small grain size and a homogeneous structure should reduce the magnitude of shear and tensile stresses in 'strong' regions, also reducing the probability of facet formation.

To illustrate the importance of processing upon dwell fatigue behaviour the example of Ti834 in bar and disc conditions was illustrated. Bar material under test has shown a relatively limited life debit under dwell conditions whilst disc material was highly susceptible to dwell loading. This was illustrated previously in Figure 2-48 [100]. Both bar and disc were subject to the same SHT to give ~15% primary alpha in a transformed beta matrix, with similar grain sizes of 20-30µm. EBSD analysis determined that bar material contained an even distribution of equiaxed primary alpha grains whilst elongated and aggregated primary alpha was often observed in Ti834 disc, with regions of common crystallography significantly larger than individual primary alpha grains. Basal orientations in primary alpha grains also extended into the surrounding transformed beta microstructure. Bache suggested that whilst the rolling operation for bar material was sufficient to break down the prior beta grain structure the disc forging operation did not involve sufficient work "*to complete this process*" [110]. As

a consequence Ti834 (designed with a small grain size to minimise dwell sensitivity) was found to behave in a similar manner to the large colony Ti685 and Ti829 alloys.

The behaviour of Ti834 contrasted with the dwell performance of Ti6246, which was suggested to be superior because of a) processing above the beta transus to generate randomly orientated fine scale microstructural units and b) a fully transformed microstructure without an equiaxed primary alpha phase. Careful process control was recommended for optimisation of alloy performance, as in the case of unidirectionally rolled Ti6/4 plate [110].

Papers published by Bache in 2003 provided a review of the history of CDF [15, 16]. These discussed the contributing factors and the working mechanisms that had been proposed since the discovery of the dwell phenomenon. Much of the content of these papers was covered in earlier work and has been discussed. However, there are some additional points which illustrate the level of understanding at this time. For example, constraint and plane strain was originally considered to be a key factor in CDF behaviour because early failures occurred in large section fan discs. However, later testing demonstrated dwell effects in small laboratory specimens. Further work concerning the effects of section size led to the conclusion that bulk constraint is not a pre-requisite for CDF behaviour [16].

It was also stated that the effects of interstitial hydrogen in CDF remain unclear, in part because detection of precipitating hydrides is difficult. Detrimental performance had been noted for higher hydrogen contents although these tests displayed a different failure mode from conventional ‘quasi-cleavage’ facet initiation sites. Bache concluded that there was significant evidence against a hydride induced dwell failure mechanism although there may be a secondary role in plastic deformation and dislocation motion behaviour [16].

The alternative explanation of time-dependent strain accumulation resulting from planar slip effects has gained widespread acceptance. Initially however, there were two problems with this theory, one being sub-surface failure locations, the other the load-normal orientation of the facet plane. Evans and Bache developed the planar slip band model of Stroh to describe the 'stress redistribution' process between strong and weak grains. *"Slip within a favourably orientated grain with its basal plane inclined to the applied tensile axis induces a pile up at the boundary with a neighbouring grain. This in turn induces a shear stress in the "strong" grain and instigates the formation of a slip band which, under the combination of the applied cyclic tensile loading σ_1 and the supplementary tensile stress σ, progressively opens up to form the nucleus of a fatigue crack"* [16]. Forging and heat treatment residual stresses present in compressor discs also contribute significantly in extending operating stresses beyond the capability of the alloy to the point where stress redistribution occurs [16].

A second explanation of the stress redistribution process was also discussed in the review paper. This was a 'two element' model, consisting of neighbouring weak and strong grains subject to an applied stress. Based on the variation in elastic modulus according to basal plane orientation it follows that under stress the two grains attempt to deform to different strain levels. Microstructural constraints lead to an average strain across the two grains, such that different stress levels are imposed on each grain. This redistribution model again leads to the weakly orientated grain redistributing stress onto the strong grain to the point at which it is the strongly orientated grain that fails [16]. A schematic description of the two-grain model is shown in Figure 2-52.

The apparent CDF insensitivity of Ti6246 was attributed to an increased beta phase volume fraction, with the higher number of active slip systems in beta phase allowing more

heterogeneous slip deformation than in alpha phase. Heterogeneous slip behaviour would reduce local anisotropy between grains and hence lower grain-to-grain stress gradients [16].

The literature review to this point covers most of the available subject matter up to and including the publications of Bache in 2003 [15, 16]. Further research typically concerns the effects of texture and variant selection, the size of regions of common crystallography and deformation length scales, and finite element modelling of crystal behaviour under loading. These topics are discussed in the following two sections. Further work concerning mechanical behaviour is briefly discussed below.

In 2004 Sinha et al. studied the contribution of static and cyclic loading modes on CDF in bimodal Ti6242 [111]. Results showed a reduction in dwell life debit and lower plastic strains at failure for lower test stresses. Static loading tests using the same applied stress showed a rate of strain accumulation that was faster than cyclic fatigue but slower than dwell fatigue. The differences in the available literature were noted, with some publications supporting this result and other work contradicting it. Explanations of dwell period, alloy composition and microstructure were offered. It was also noted that as the maximum applied stress was increased the time to failure for static and CDF tests converged, highlighting the increased contribution of static loading rather than cyclic fatigue in the overall behaviour. Conversely, at lower stresses the cyclic nature of dwell loading dominated behaviour [111]. Although plausible explanations were offered for this behaviour, it is noted that only two CDF, two cyclic and two static load tests were undertaken. Verification of the behaviour would require further testing.

Bridier et al. have published work analysing active slip systems in bimodal Ti6/4 [112, 113]. They found that prismatic and basal slip systems were the dominant deformation types in

primary alpha grains. In nearly all cases the activated slip system was observed to be that with the highest Schmid factor (typically ≥0.3). Analysis of crystallographic orientations showed clear distinctions in the activated slip system according to the orientation in relation to the stress axis (see Figure 2-53a) [112]. However, for orientations with the basal plane very closely aligned to the stress axis no slip traces were noted.

To assess the dependence of slip system on Schmid factor and crystallography, IPFs displaying different slip trace types and Schmid factor iso-contours were plotted. They are displayed in Figure 2-53b-d [112]. It was noted that basal and prismatic slip events at Schmid factors of 0.35-0.40 have similar crystallographic orientations. The prismatic slip system is then preferred due to a lower CRSS [112, 113].

Study of deformed microstructures showed basal slip traces were finer and more homogeneously distributed than prismatic slip traces [112]. Savage et al. made similar observations in earlier work on Ti6242, in which prismatic slip events displayed large shear offsets whilst basal slip was observed as very fine homogeneously distributed traces with no shearing of beta laths [114]. In the work of Bridier it was also noted that closely oriented neighbouring grains could display continuous slip traces through grain boundaries, both across primary alpha-primary alpha and primary alpha-secondary alpha boundaries [112].

2.7.3.5 Macrozone and Effective Structural Unit Size Concepts

With increasing use of EBSD to assess crystallography it has become clear that grain size does not provide an accurate indication of the crystallographic nature of titanium alloys. An early example was provided in work by Bhattacharyya et al. in 2003 studying the crystallography of beta processed Ti6246 [115]. They noted that optical colonies growing from a shared grain boundary with significantly different growth directions actually show

parallel basal planes and a 10-11° rotation of the c-axis. This was related to the Burgers orientation relationship for which two alpha variants can form on a single {110} beta plane in alignment with two different <111> directions. A ~70° misorientation exists between these respective <111> directions but the misalignment between $\{11\bar{2}0\}$ poles is 60° leading to the crystallographic difference between "twin variants". Alpha platelet growth directions are <335> invariant lines which have a misorientation of ~80°. This is the optical misorientation between platelet growth directions when viewing parallel to {110} planes, although there is angular variation according to the plane of sectioning [115]. This leads to significant differences in optical microstructure for similar crystallographies. This has implications in terms of assessing the size of regions of common texture based on optical microstructures. Previous research correlated the CDF facet size to the optical microstructure [65, 84]. As optical microstructure does not provide an accurate indication of crystallography, facet sizes may exceed expected values.

Further work by Bhattacharyya et al. on the same subject noted that alpha platelets growing into two adjacent beta grains from a common boundary may have the same crystallography and large (~89°) or small (~29°) optical misorientations according to the orientations of parent beta grains [116]. Also considered was the case of adjacent beta grains with a common {110} pole, in which case interfacial energy is minimised when grain boundary alpha forms with the basal plane parallel to the shared {110} beta plane. In other work this preferential variant selection behaviour was reported to occur up to a critical angle of ~10° [116, 117]. In closely oriented adjacent beta grains this raises the possibility of the formation of several alpha variants across a beta grain boundary [117]. Again these findings increase the likelihood of textural units larger than expected from optical microstructure assessments.

In other work the crystallography of bimodal alloys has been studied in detail to understand variant selection and texture retention mechanisms. Previous work by Woodfield et al. demonstrated the presence of large crystallographic units in (alpha + beta) processed Ti6242, arising from inadequate billet deformation [118]. Some studies related the size of regions of common alpha texture in bimodal alloys to alpha colony structures in pre-deformation microstructures whilst other studies suggested the prior beta grain size as an important factor. A technique was developed to back-calculate the parent beta phase orientation based on alpha textures and the Burgers OR. A previous technique was proposed based on the selection of three alpha colonies assumed to originate within the same prior beta grain, with Euler angles input into a series of equations allowing the derivation of the prior beta orientation [119, 120]. However, whilst very high theoretical resolved percentages were estimated based on three known alpha textures, in practice this fraction was much lower. This was attributed to the selection of alpha colonies from different parent beta grains. In a later publication the method had been refined to give a probability greater than 72% that a parent beta orientation could be determined from two alpha variant orientations, rising to >98% with knowledge of a third alpha variant [121].

Glavicic et al. developed a similar method of texture back-calculation capable of accommodating alpha variants from different beta grains [122]. The technique was developed using beta processed Ti6/4 and validated in further work on beta annealed Ti6/4 using X-ray diffraction results for comparison. Also noted was the non-uniform distribution of alpha variants for the beta texture, i.e. variant selection on phase transformation [123].

Different studies developed methods to separate the textures of primary and secondary alpha phases in bimodal alloys. Germain et al. attempted to separate these texture components through morphology and EBSD pattern quality, although neither method

proved accurate separation of the two components. A third method was based on chemical composition and the resulting contrast differences in BSE imaging. Image processing software was used to overlay BSE images and EBSD maps, allowing separation of the primary and secondary alpha textures on the basis of BSE image contrast [124]. The method was used to assess texture heterogeneities in Ti834 billet and the respective contributions of primary and secondary alpha phases.

An alternative technique involved the correlation of EBSD maps with optical microscopy images obtained following etching to achieve sufficient levels of phase contrast. The exact location of the COM is an artefact of the EBSD technique as carbon contamination prevents the etching of the site of interest (provided a sufficiently small step size is used). Once this site of interest is identified, a light polish is sufficient to remove contamination from the surface and etching then displays the optical microstructure. Again this technique was used to assess primary and secondary alpha textures in Ti834 billet. It was also noted that a close approximation of the results could be achieved with significant time savings using an automated texture separation based on size distribution (primary alpha grains are significantly larger) [125].

Because of the inability to use optical microstructure as a reliable indicator of crystallography and hence mechanical performance, the concepts of macrozone size and effective structural unit size have arisen. Macrozone size is defined as the size of a region of common texture. Germain et al. used the term 'macrozone' to define large regions of alpha phase with strong local textures [126]. It was noted that macrozones were not limited to individual prior beta grains as suggested previously [127]. Primary alpha grains displayed significant differences in local textures between macrozones. The major secondary alpha component in a macrozone was found to correspond to the macrozone primary alpha

texture. The sharp local texture of a macrozone was therefore concluded to be a combination of primary alpha texture and the major secondary alpha texture component [126]. Differences in the evolution of primary and secondary textures in bimodal alloys were recognised, with primary alpha textures resulting from deformation and spherodisation of coarse alpha lamellae, whilst secondary alpha textures result on phase transformation with the preferential formation of variants sharing c-axis alignment with primary alpha grains [126]. Glavicic et al. reported the same mechanisms as responsible for the overall alpha texture of (alpha + beta) processed Ti6/4. A method to analyse primary and secondary alpha textures was proposed using a SHT to resolution secondary alpha, followed by slow cooling to promote epitaxial growth of primary alpha. Comparison of bimodal and annealed condition textures allows the determination of the primary and secondary texture components [128].

Experimental work investigating sub-transus processing effects in Ti834 billet recognised that whilst the macrozone size may extend beyond beta grains, the colony size influences the macrozone size. This is due to the similar deformation behaviour of alpha lamellae in a colony structure. Macrozones may then extend beyond this length if deformation rotates multiple alpha colonies towards a particular texture component [129].

In recent work, Wynne discussed the definition of a macrozone on an EBSD map based on a grid of 5x5 points, defining a macrozone criterion as eight or more points in the grid with a misorientation of less than 20° from the centre point. This considered macrozones in (alpha + beta) processed Ti834 billet, for which eight of 25 points would represent approximately 50% of the primary alpha grains. If a macrozone was identified, its size could be assessed by grid expansion until the criteria were no longer satisfied [130].

Whilst the definition of macrozone size became more specific through such work, there was still no clear definition linking macrozones to mechanical behaviour. A paper by Rugg et al. in 2007 introduced the effective structural unit (ESU) size concept, with the definition "*the length scale over which deformation processes do not recognise boundaries*" [131]. This definition clearly noted the influence of the loading regime on the ESU size, as whilst high angle boundaries may prevent slip transfer under low stress loads, higher stresses may overcome such boundaries, hence increasing ESU size. The importance of the ESU size concept to CDF behaviour was highlighted [131]. In other work Germain observed the ESU controlling fatigue behaviour in cross-rolled Ti6/4 plate to be influenced by the scale of texture banding rather than individual grain orientations, noting that processing routes creating extensive regions of common crystallography should be avoided [132].

In recent work, Sinha et al. studied life debits in bimodal Ti6242 CDF specimens [133-135]. A dwell specimen with a significantly lower life than the equivalent cyclic specimen was assessed. This specimen showed a large (>1mm cross-section) faceted area. The fracture surface was polished away in five increments of ~40µm (serial sectioning on a plane normal to loading axis) and EBSD mapped at each increment. Analysis showed the presence of a large region of ~500-750µm cross-section over which the crystallography was consistent with c-axes ~15-30° from the loading direction. This zone was identified as the initiation site. The remainder of the facet showed larger misorientations of the c-axis from the loading direction. Separate work examined a specimen tested under the same conditions and found the presence of secondary cracks. Whilst multiple crack initiation sites may therefore be present, the dominant crack was considered to be that with micro-texture most suitable for short crack growth following initiation. Following the growth of the short crack to the boundaries of the region of favourable texture (i.e. macrozone), it was then possible for near

planar crack propagation to occur over crystallographically varied neighbouring units, leading to the observed large scale load normal facet [134, 135]. This work showed differences between macrozone size and CDF facet size. The ESU size may be considered as the size of the facet forming over the micro-textured region or as the size of the facet, depending on the time/cycles that elapse between the two.

Analysis of Schmid factors showed that the micro-textured initiating region had a very low Schmid factor for basal slip, with surrounding regions oriented for prismatic and basal slip. From the Bache and Evans stress redistribution model it was assumed that dislocation pile-ups at the boundary of the basal load normal region would lead to off-loading behaviour. However, analysis showed a significant difference between the crack/slip plane angle of 70.5° according to the model, and the observed angle. Explanations for this difference included the non-basal orientation of the facet initiating section, the invalidity of the Stroh assumption of isotropic behaviour and the Stroh assumption of purely edge dislocation pile-ups [135].

2.7.3.6 Crystal Plasticity Finite Element Modelling

Whilst discussing the ESU concept, Rugg et al. considered its applicability to CDF behaviour. They also noted the use of CPFE modelling techniques in such a situation, for which a microstructural scale mechanical model accounting for time effects is required. The need to explain why a load controlled dwell cycle is much more likely than equivalent strain control conditions to result in facet formation was identified. Their work studied a combination of three adjacent grains with specific crystallographic orientations (potentially susceptible to facet formation) referred to as a 'rogue grain' combination [131, 136].

The rogue grain combination consists of a primary (P) grain with c-axis near parallel to loading direction, a secondary (S) grain with c-axis near perpendicular to loading direction

and a prismatic slip plane at 70° to the primary grain basal plane, and a tertiary (T) grain with similar crystallography to the primary grain. The schematic of this grain combination is displayed in Figure 2-54 [131].

Modelling of a polycrystal structure under uniaxial strain loading conditions showed an elastic-plastic response followed by stress relaxation during strain hold. For uniaxial stress loading the elastic-plastic response was followed by creep behaviour. Selection of a stress controlled loading condition equivalent to that attained under strain loading after a time of one second allowed the comparison of microscopic behaviour under the two forms of dwell loading. Analysis of stresses across the rogue grain combination showed lower values in the secondary and tertiary grains. Significantly higher stresses were observed at both grain boundaries. Strain controlled loading gave similar stresses both before and after a dwell period. However, stress controlled loading resulted in significant increases in stress at the grain boundaries, following creep in the secondary and tertiary grains leading to stress relaxation. Macroscopic stress is therefore accommodated through greater stresses on the primary grain [131].

In a separate publication discussing the same CPFE modelling work, the influence of orientations in the rogue grain combination was considered. For example, the prismatic slip plane angle relative to the load normal direction was considered. Results show that changes in the secondary grain orientation affected stresses within the secondary grain and less than half of the primary grain. There was no effect on the tertiary grain. Rotations of the primary grain showed the highest stresses when the c-axis was aligned parallel to the loading direction. A 22% reduction in stresses at the P-T boundary was calculated for a 90° rotation of the primary grain c-axis from load direction parallel. A ~16% reduction was observed at the P-S boundary with this primary grain rotation. It was concluded that whilst these were

not insignificant changes in stress levels, with the reasonable probability of such crystallographic combinations existing in real components, CDF facet formation could not be explained solely based on crystallography [137, 138].

The effect of the P-S grain boundary orientation was also considered over a range of angles, including a grain boundary angle coincident with the orientation of the secondary grain prismatic slip plane. At this boundary angle (60°) there is a maximal peak in the accumulated slip level. It was suggested that a crystallographic – morphological interaction exists when slip plane and grain boundary orientations coincide. Whilst the modelling work showed bad combinations of stress and slip over quite broad crystallographic orientations, the additional influence of boundary morphology (over a comparatively small range of angles) make CDF facet formation a strongly volume dependent behaviour [137].

Similar CPFE modelling work studied load shedding behaviour in bimodal Ti6242 alloy [139, 140]. C-axis mismatch, misorientation, Schmid factor mismatch and grain size influences on the hard-soft grain interaction were investigated. It was concluded that load shedding is high in regions of hard orientation grains surrounded by large soft grains with high basal or prismatic Schmid factor values. Whilst c-axis orientation mismatch and the misorientation were concluded not to dominate load shedding behaviour, their indirect influence on the Schmid factor was noted. Also noted was the strong dependence of load shedding on the size of the soft grain, but very weak effect of the size of the hard grain [139]. In another publication the same authors stated that "*load shedding is dictated by the evolution of plastic strain in the soft grain and any change in its size significantly changes the peak stress in the hard grain*" [141].

With further developments in the techniques of CPFE modelling, research investigating the CDF behaviour of titanium alloys is expected to continue for the foreseeable future. This work will be complemented by EBSD studies of crystallography and deformation behaviour and improved characterisation of macrozones and ESU sizes.

2B Literature review – Cold dwell sensitive fatigue in titanium alloys – Figures and tables

2.8 Compressor disc design and requirements

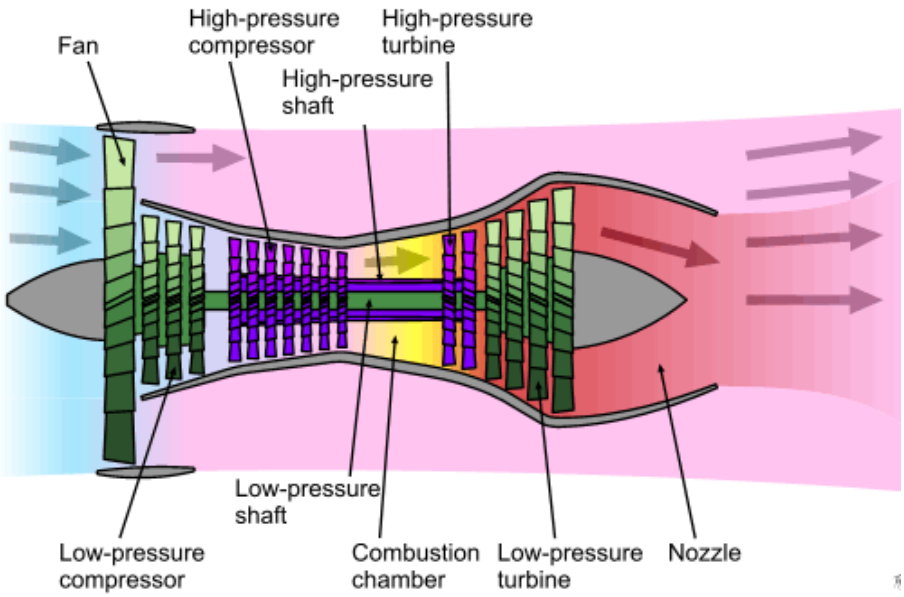

Figure 2-1 – Cross-section of a two spool low bypass turbofan aero-engine [142]

Figure 2-2 – Rolls-Royce Trent Engine Intermediate Pressure (IP) Compressor Drum Assembly Stages 1-8 [13]

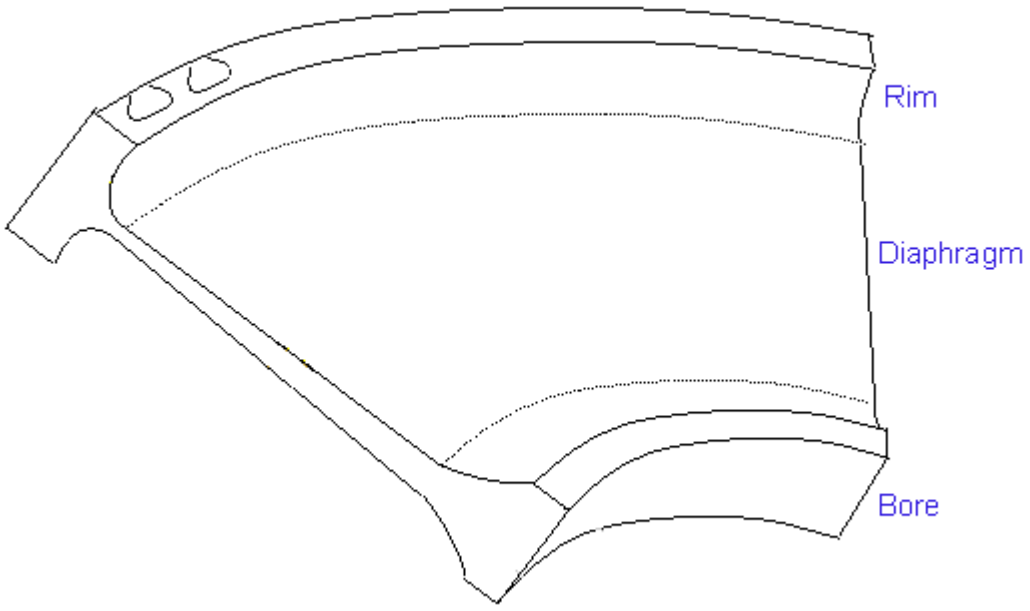

Figure 2-3 – Cross-section of typical compressor disc geometry [71]

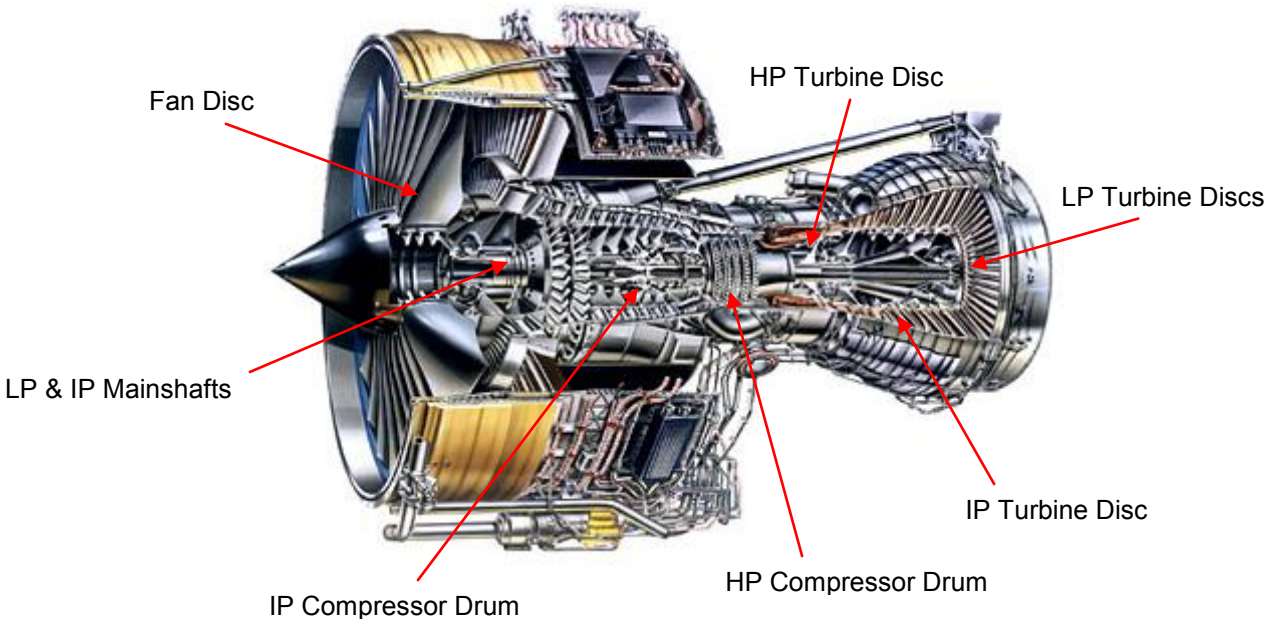

Figure 2-4 – Cross-section highlighting Critical Group A components on a Rolls-Royce Trent 800 engine [13]

2.9 Titanium applications in aero gas turbine engines

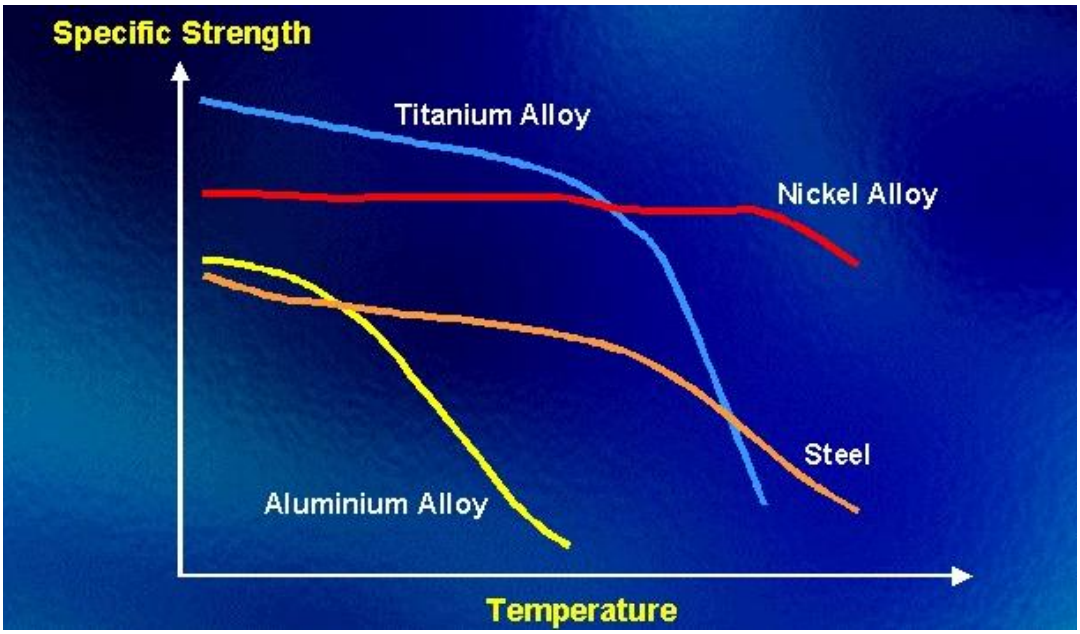

Figure 2-5 – Specific strength performance of aerospace alloys with temperature [143]

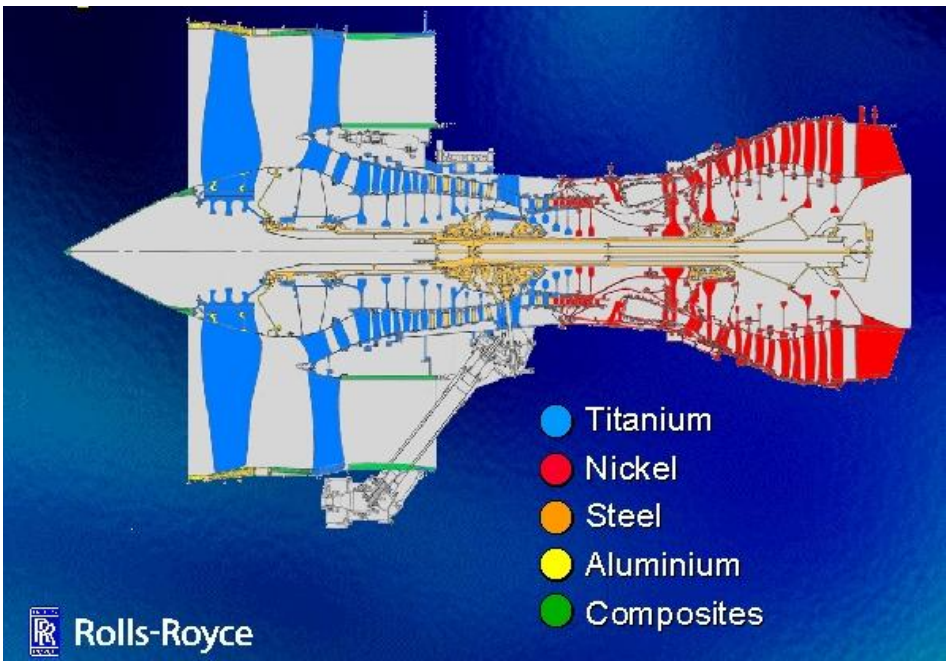

Figure 2-6 – Titanium alloy usage in a typical aero-engine [143]

2.10 Titanium and its alloys

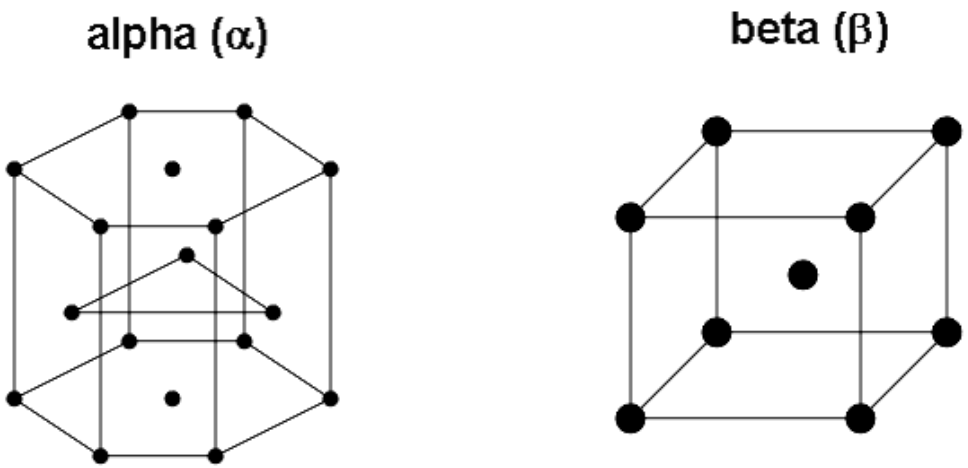

Figure 2-7 – Crystal structures of HCP alpha (α) and BCC beta (β) titanium [17]

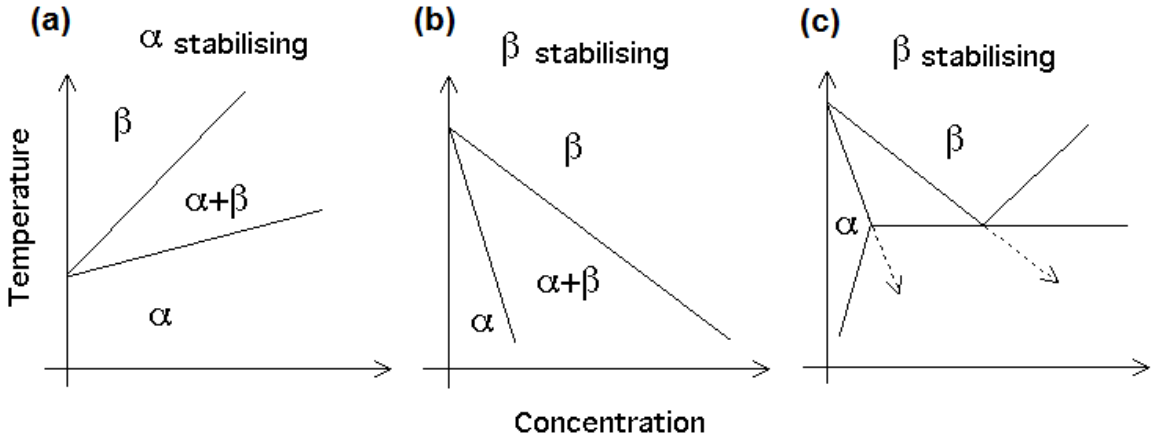

Figure 2-8 – Effect of additions of alpha stabilising and beta stabilising alloying elements on the beta transus temperature [18]

Equation 2-1 $$Alu\min ium\ Equivalent = Al + \frac{1}{3}Sn + \frac{1}{6}Zr + 10(O + C + 2N)$$

Equation 2-2 $$Molybdeum\ Equivalent = Mo + \frac{2}{3}V + \frac{1}{3}Nb + 3(Fe + Cr)$$

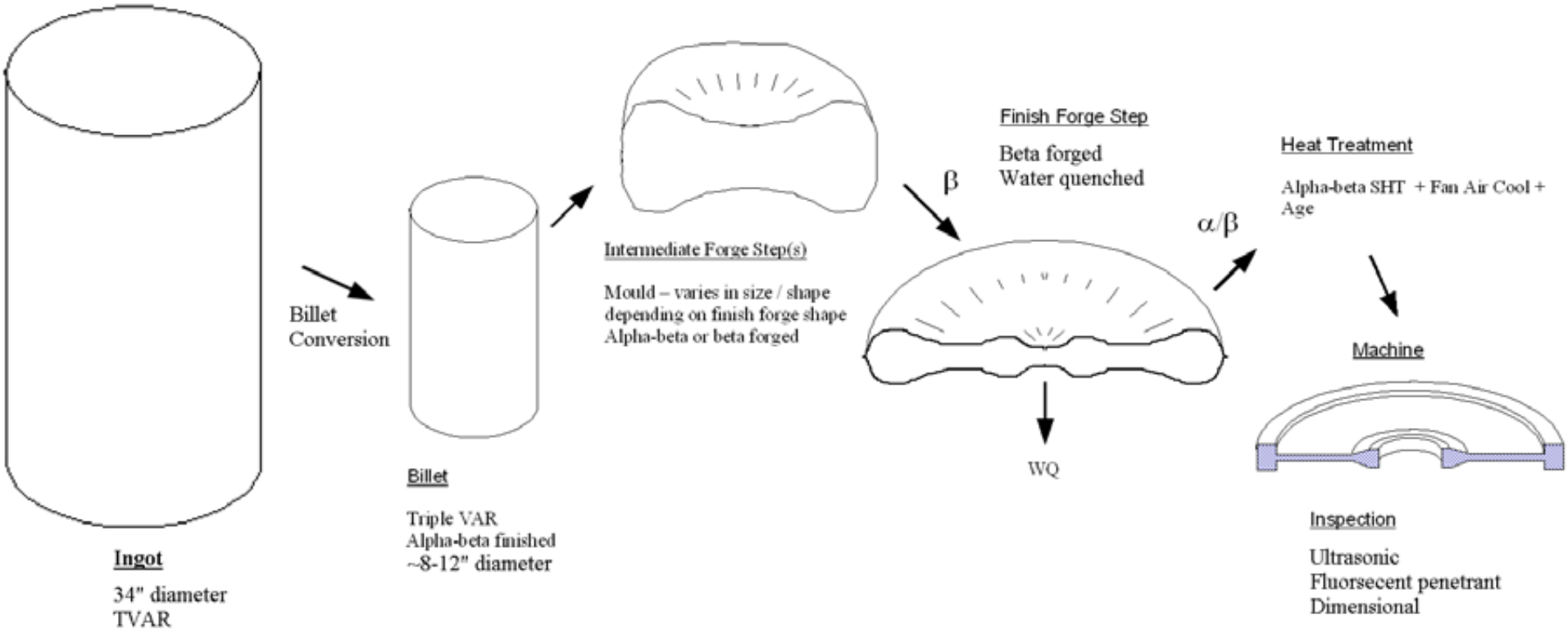

Figure 2-9 – Schematic illustration of compressor disc manufacturing route [71]

Equation 2-3 $(110)_\beta \,//\, (0001)_\alpha \,;\, [111]_\beta \,//\, [11\bar{2}0]_\alpha$

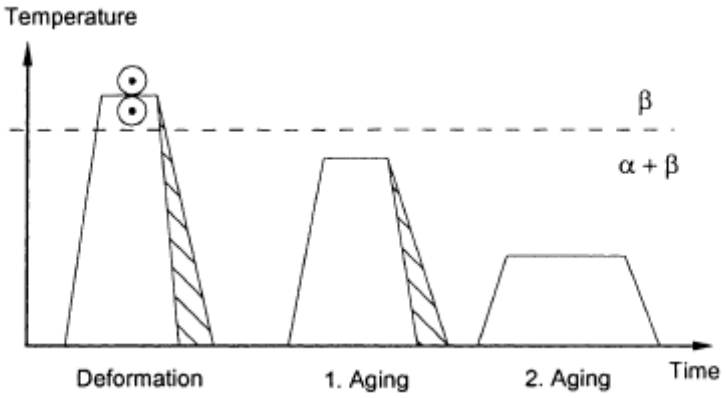

Figure 2-10 – Schematic beta processing of Ti6246. First aging is usually referred to as solution heat treatment [38]

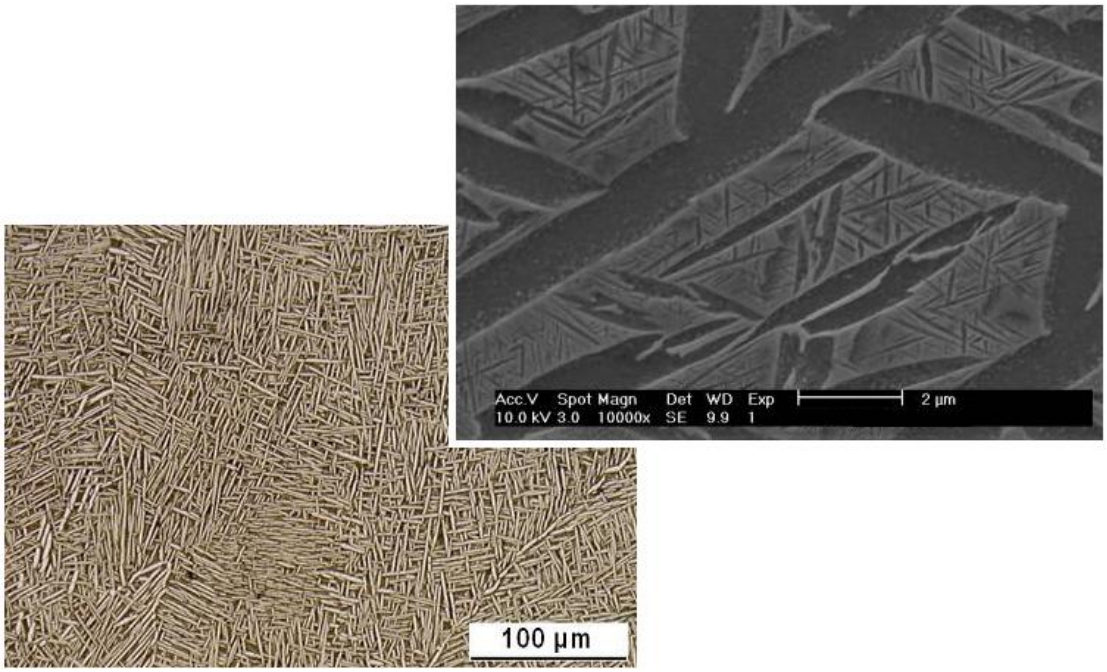

Figure 2-11 – Typical beta processed Ti6246 microstructure (Widmanstätten primary alpha platelets in retained beta matrix, fine secondary alpha platelets)

2.11 Microstructural terminology

Figure 2-12 – Typical optical microstructure of beta processed Ti6246

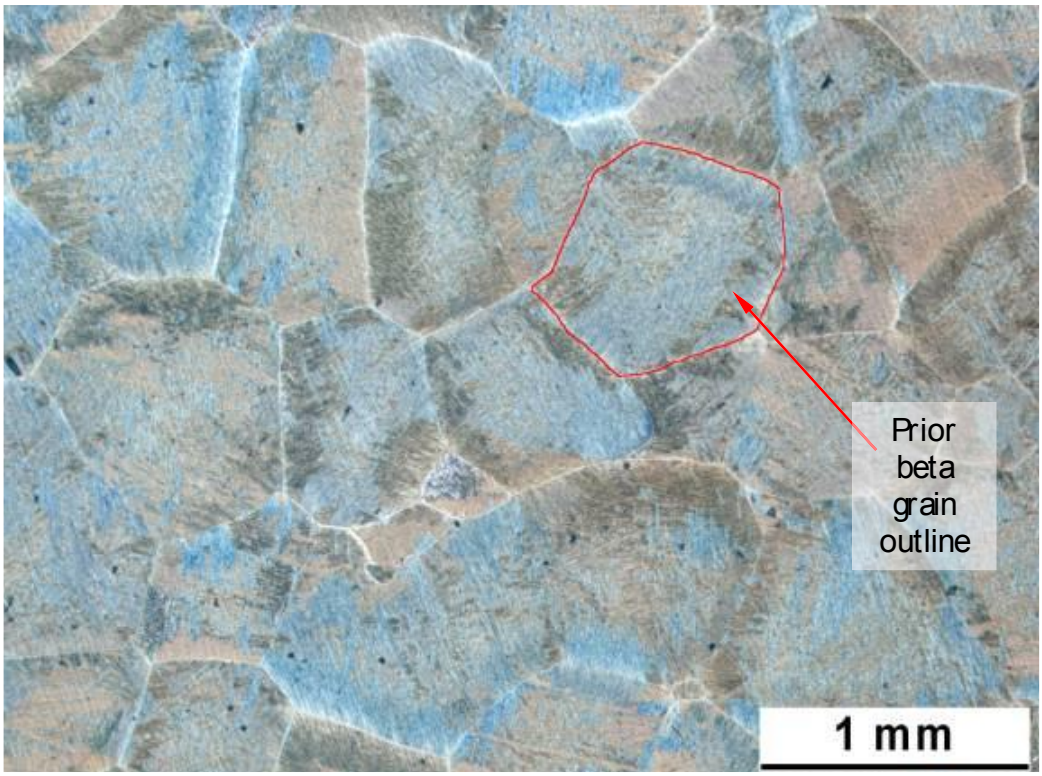

Figure 2-13 – Equiaxed prior beta grain outlines in beta annealed Ti6246

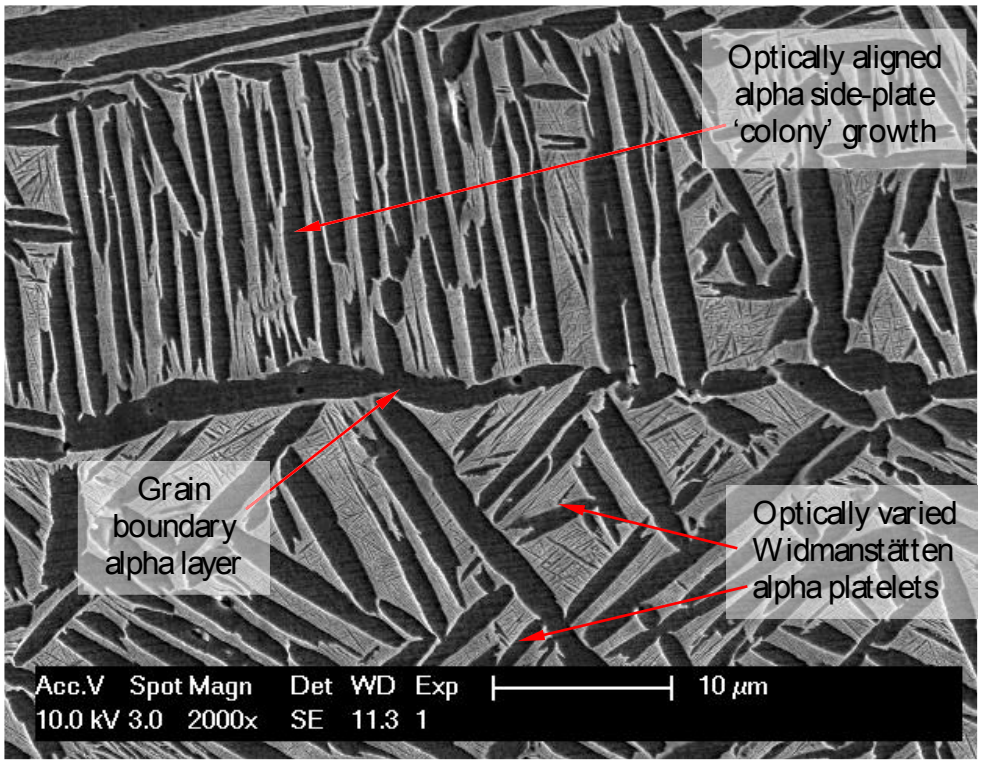

Figure 2-14 – Microstructure of beta processed Ti6246

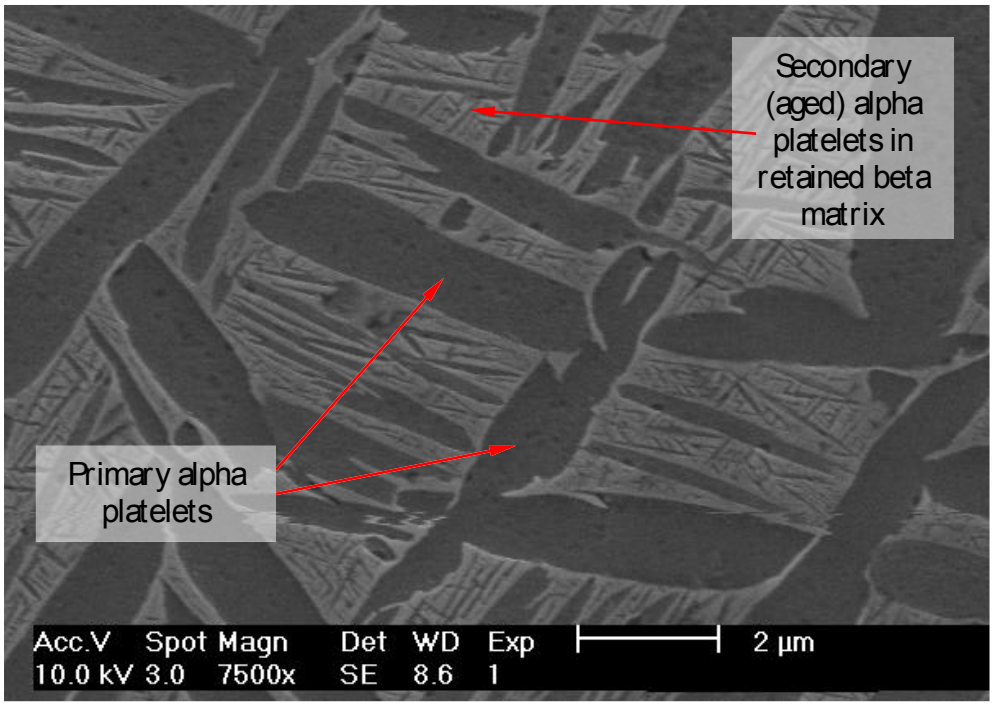

Figure 2-15 – Microstructure of beta processed Ti6246

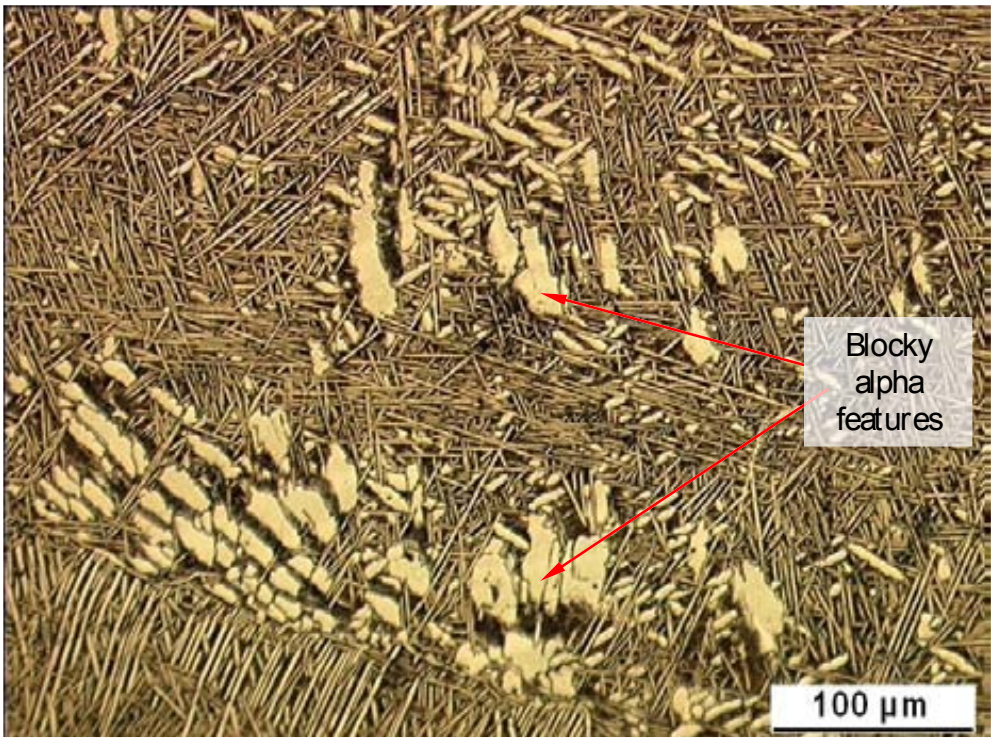

Figure 2-16 – Blocky alpha features in beta processed Ti6246

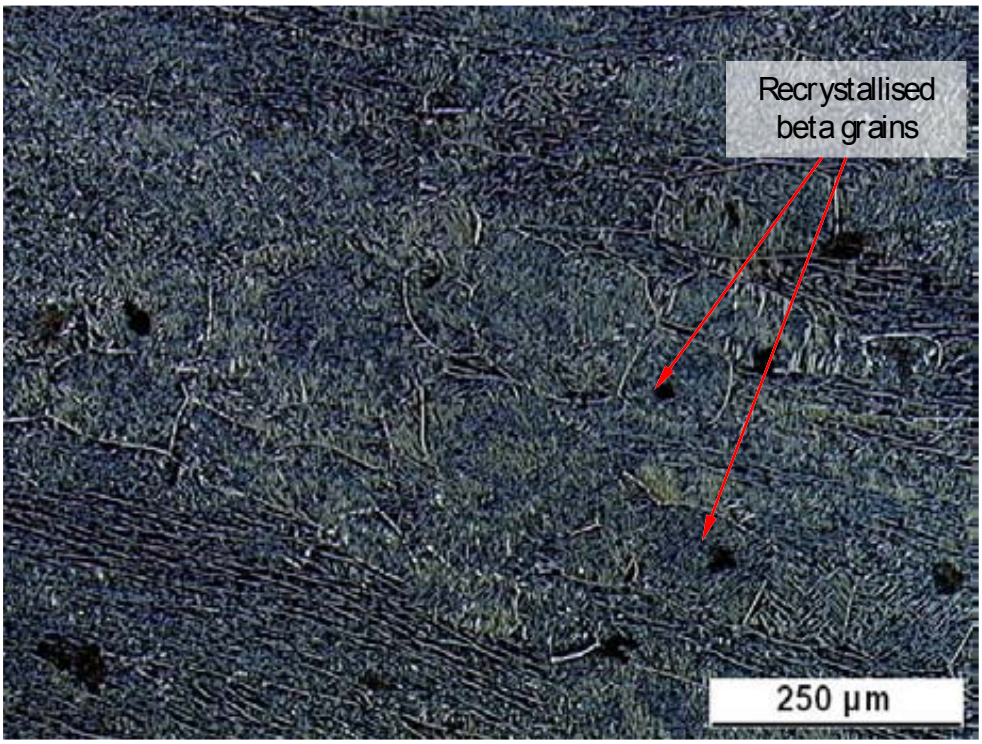

Figure 2-17 – Microstructure of beta processed Ti6246

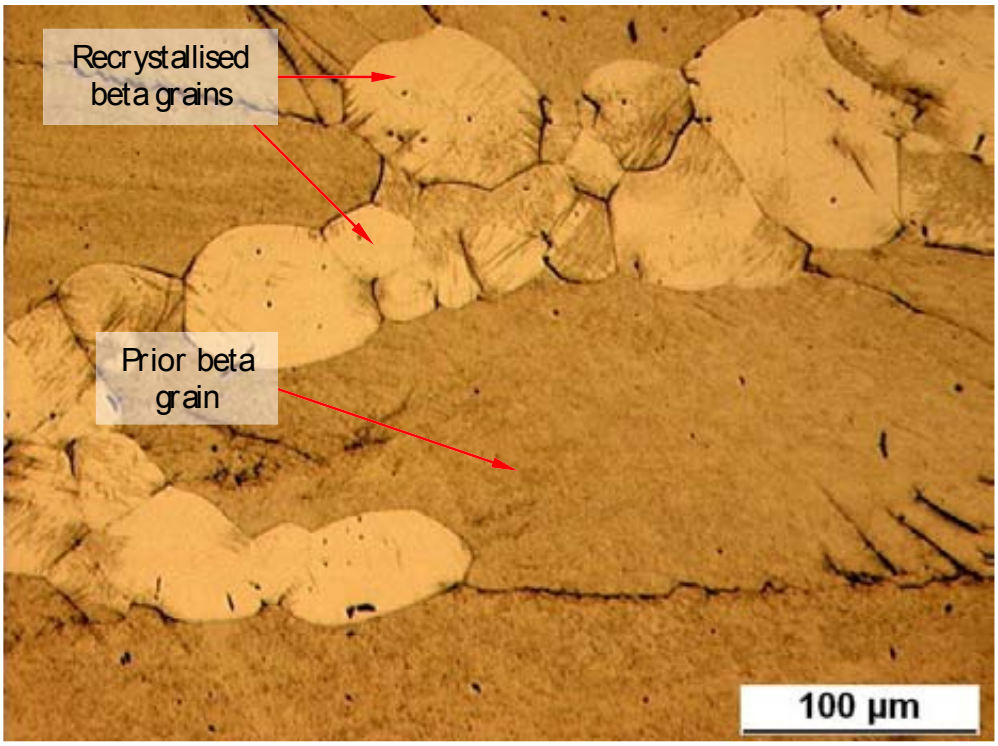

Figure 2-18 – Partial recrystallisation in beta forged water quenched Ti6246

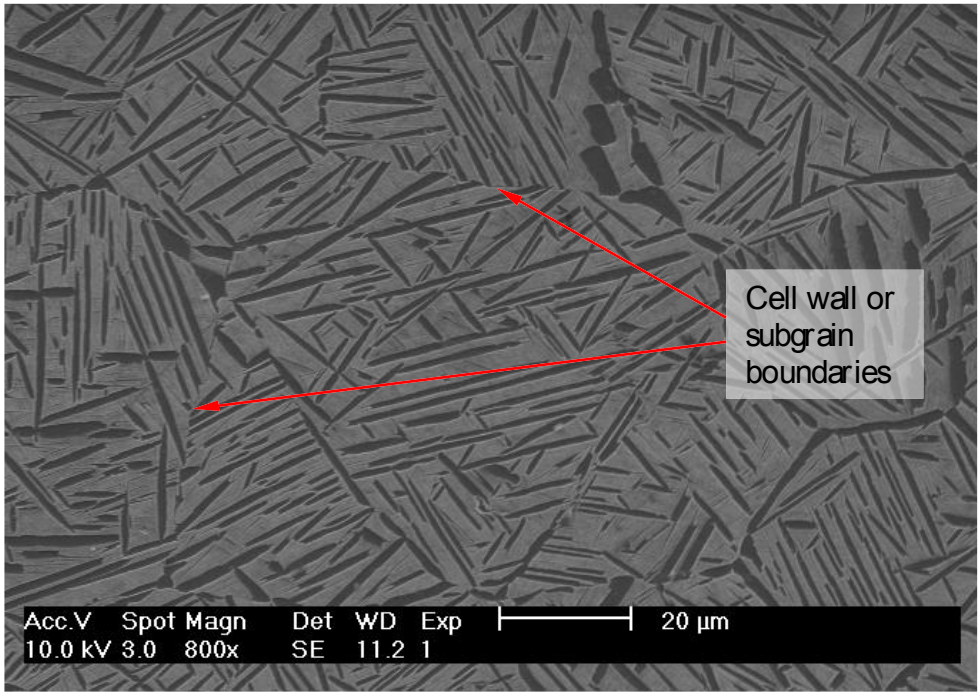

Figure 2-19 – Cell wall or subgrain boundaries in beta processed Ti6246

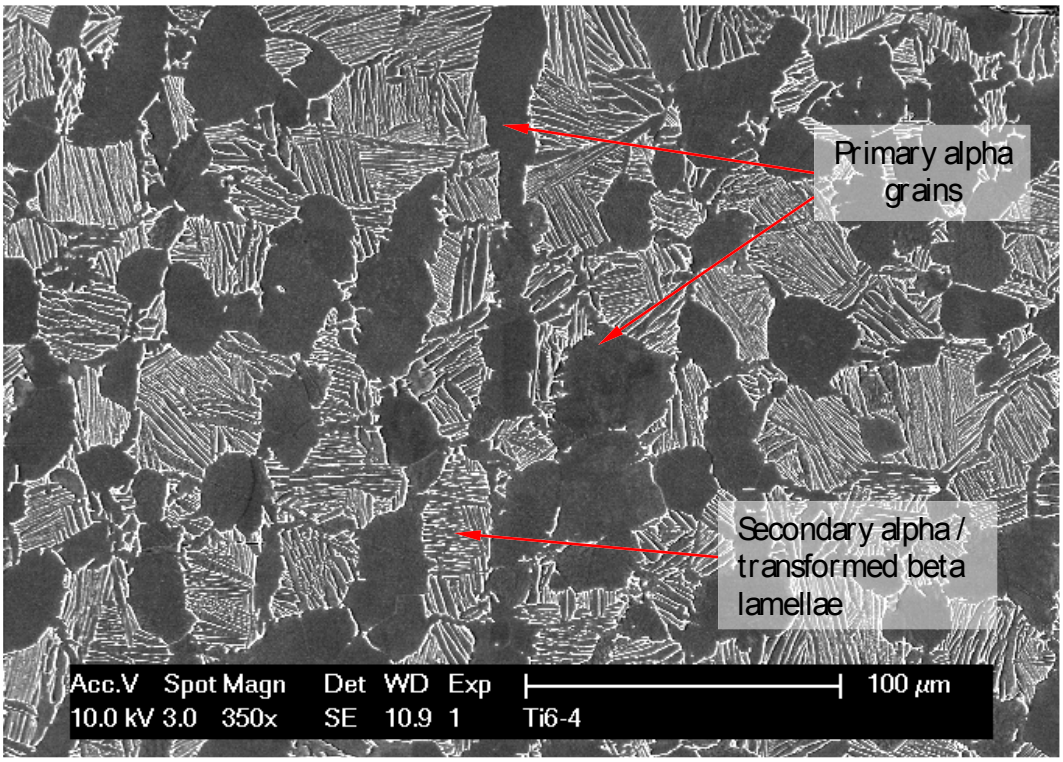

Figure 2-20 – Typical optical microstructure of (alpha + beta) processed Ti-6Al-4V

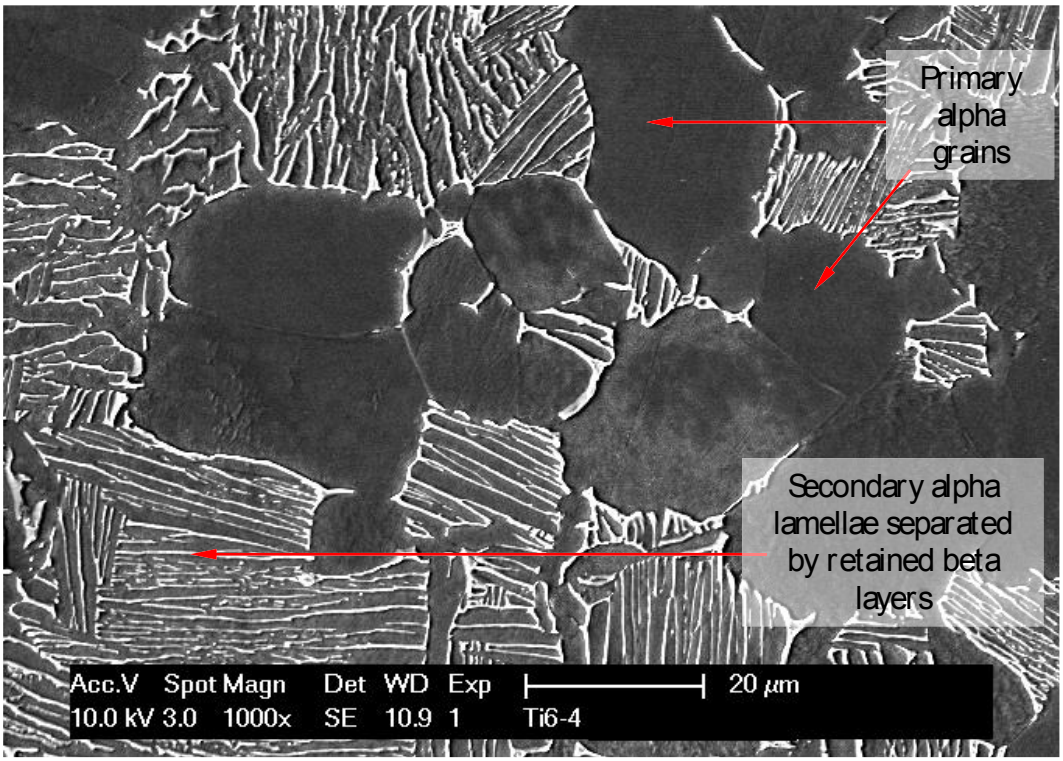

Figure 2-21 – Typical optical microstructure of (alpha + beta) processed Ti-6Al-4V

2.12 Texture in metals

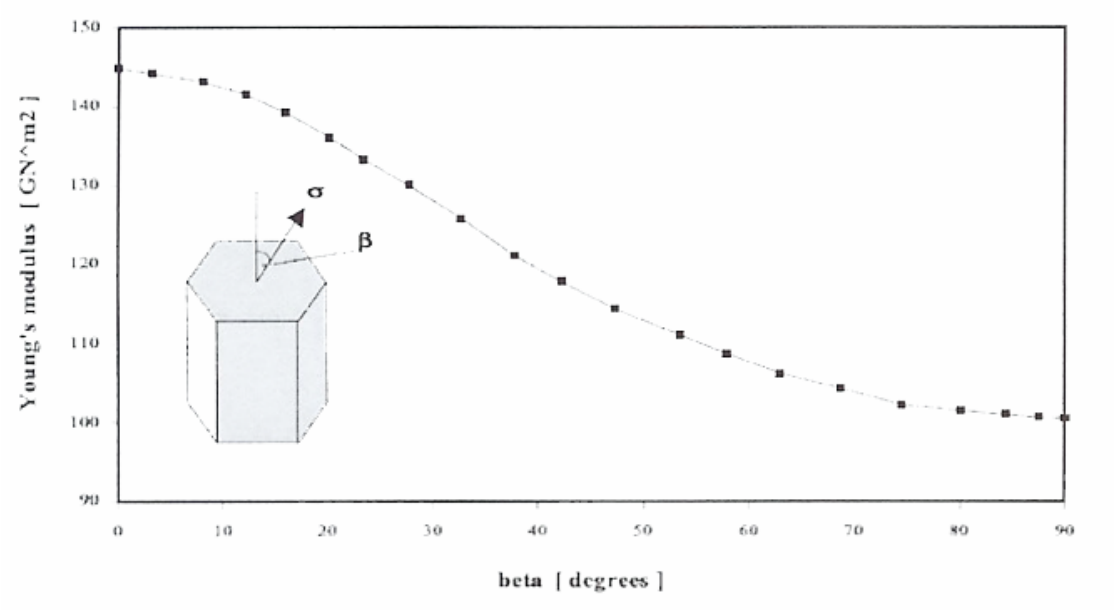

Figure 2-22 – Variation in elastic modulus with orientation of titanium crystal structure [52]

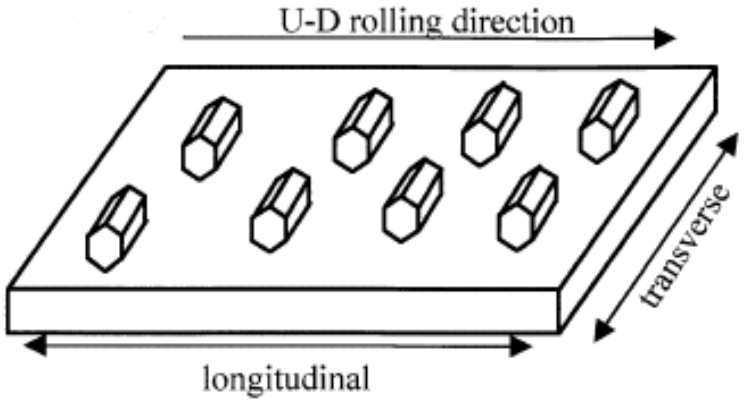

Figure 2-23 – Preferred orientation of alpha phase units in unidirectionally rolled Ti6/4 plate [144]

Equation 2-4 $$n\lambda = 2d\sin\theta$$

Where n is an integer, λ is the wavelength of electrons, d is the inter-atomic spacing of the diffracting plane and θ is the angle of incidence of the electrons on the diffracting plane.

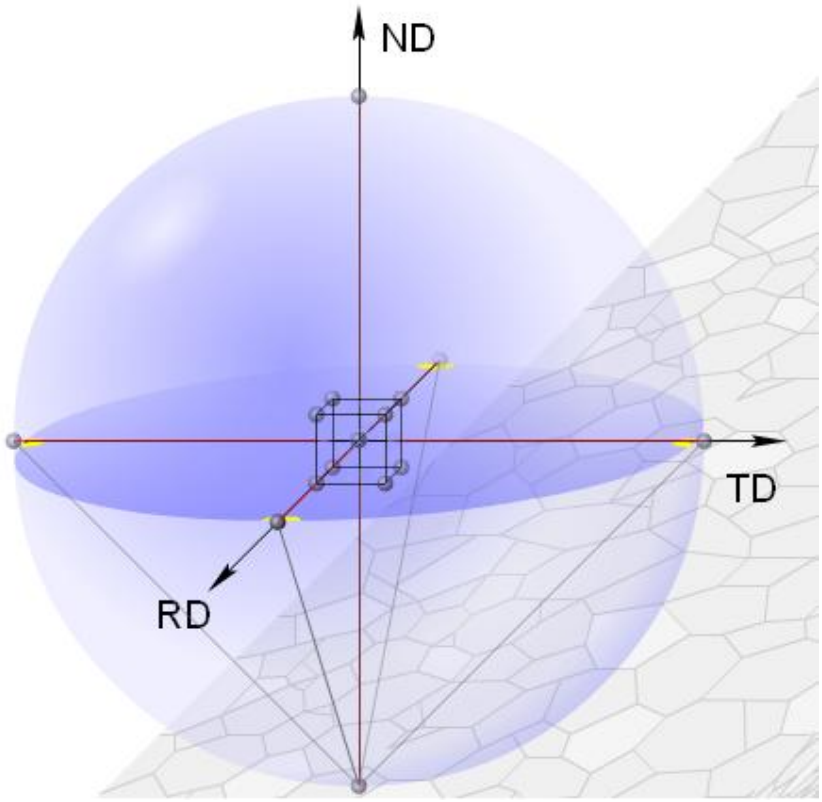

Figure 2-24 – {100} plane stereographic projection [Adapted from 145]

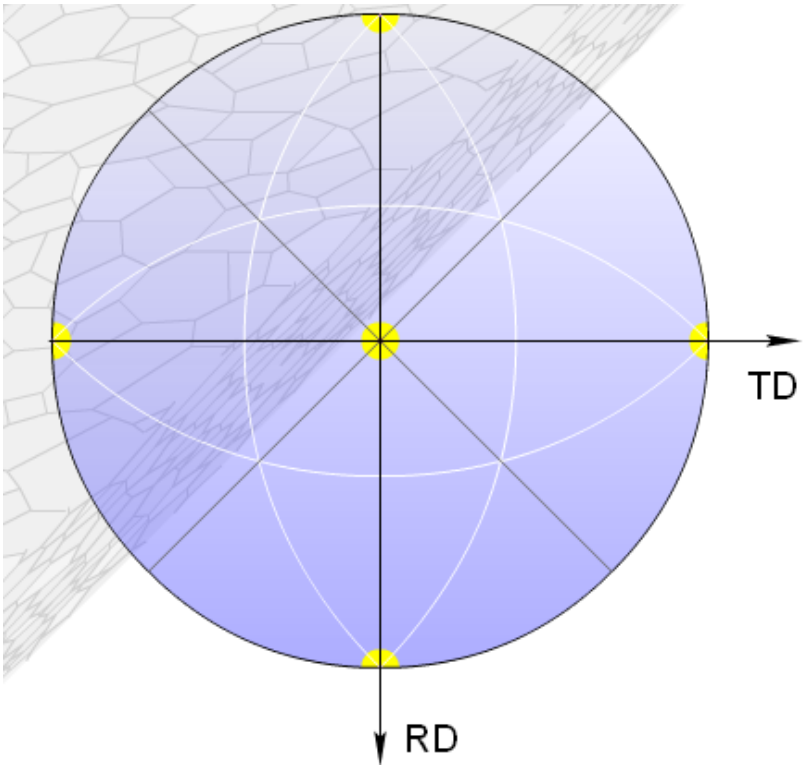

Figure 2-25 – {100} pole figure for the stereographic projection in Figure 2-24 [145]

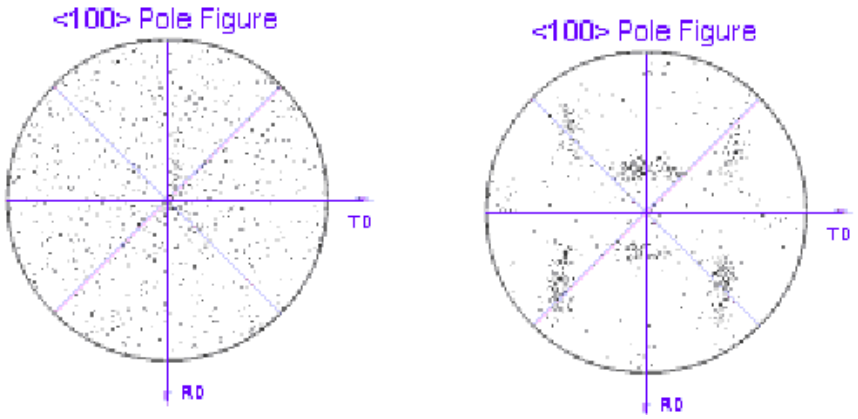

Figure 2-26 – <100> pole figures showing (a) random and (b) preferred texture orientations [145]

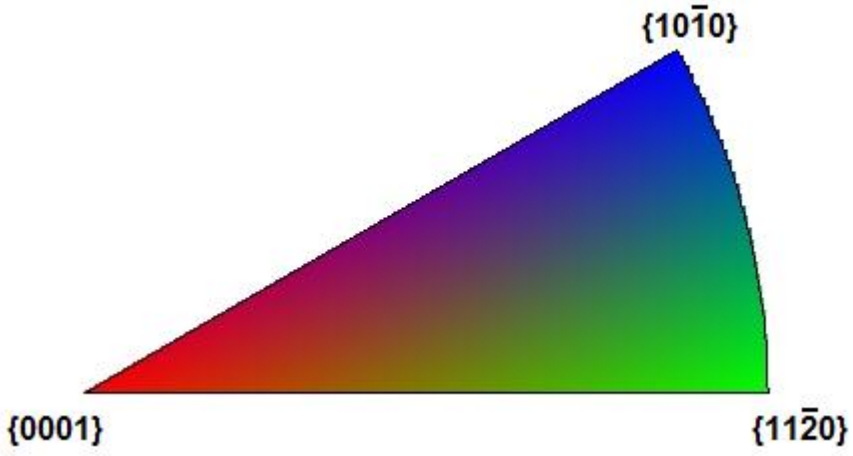

Figure 2-27 – Inverse pole figure for hexagonal close packed crystal structures [146]

2.13 Plastic deformation and fatigue

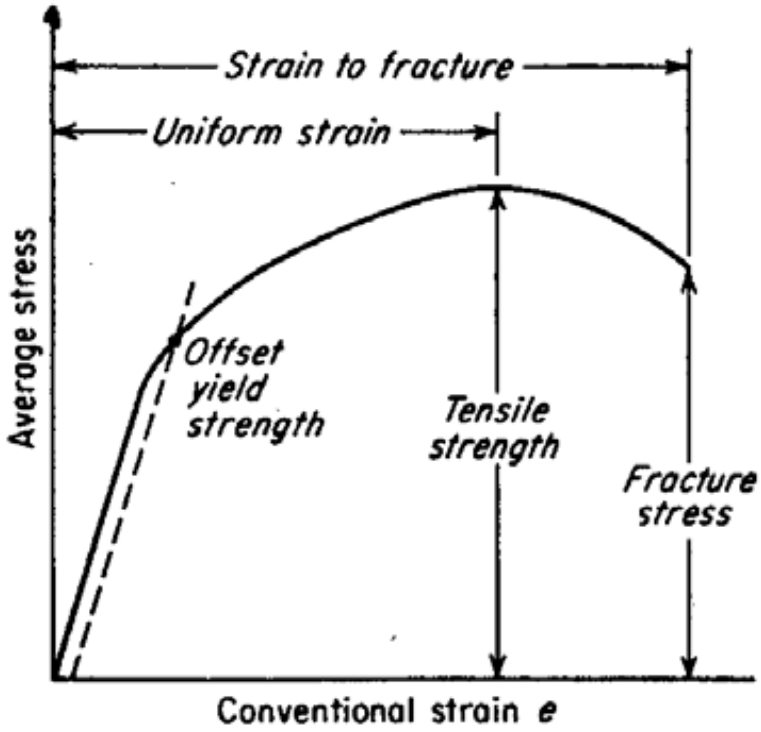

Figure 2-28 – Stress-strain plot for a uniaxial tensile test [147]

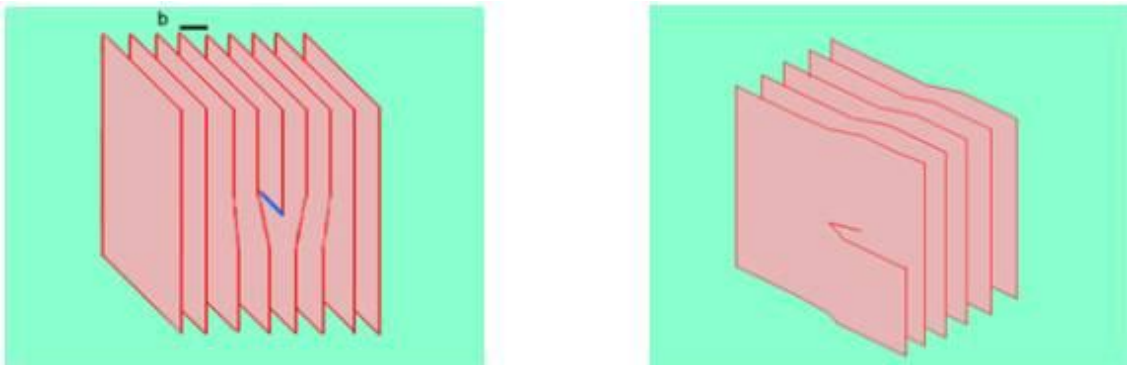

Figure 2-29 – Illustrations of edge and screw dislocation geometries [148]

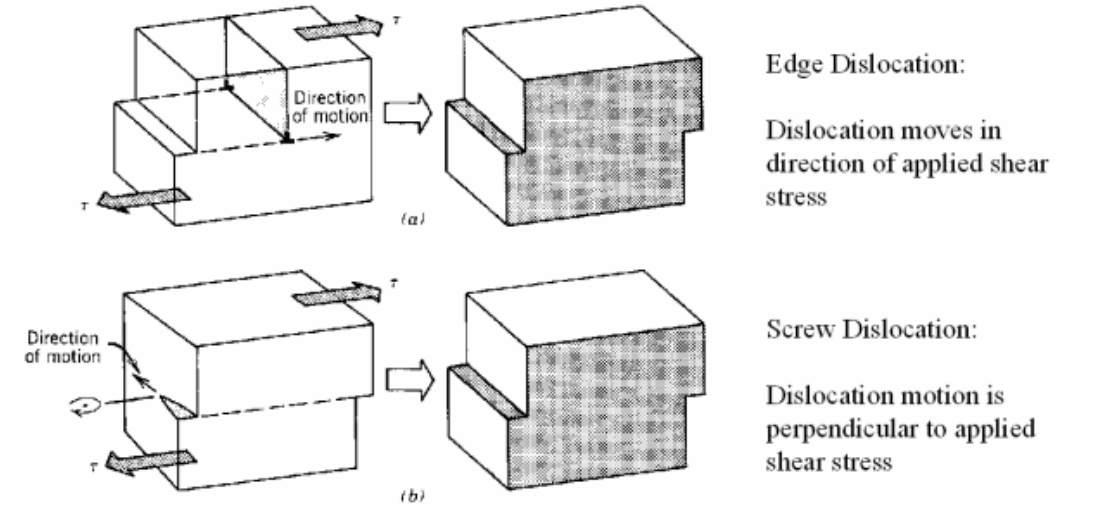

Figure 2-30 – Dislocation motion in edge and screw dislocations [149]

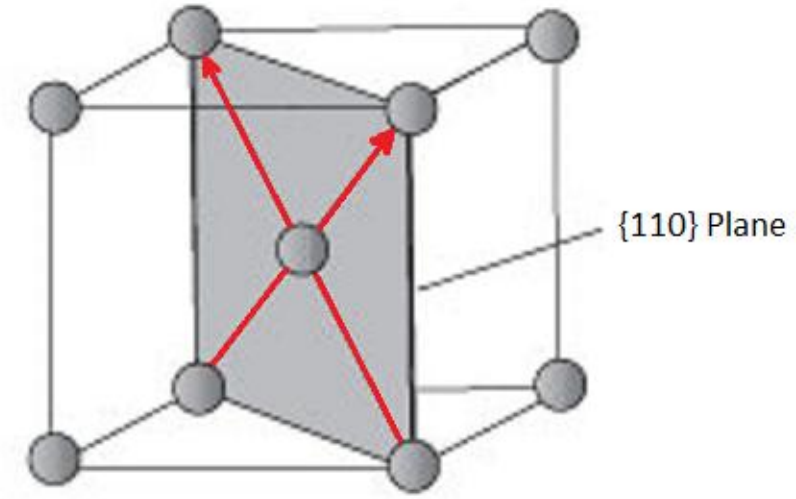

Figure 2-31 – Close packed <111> slip directions in the {110} plane of the body centered cubic (BCC) unit cell [Adapted from 150]

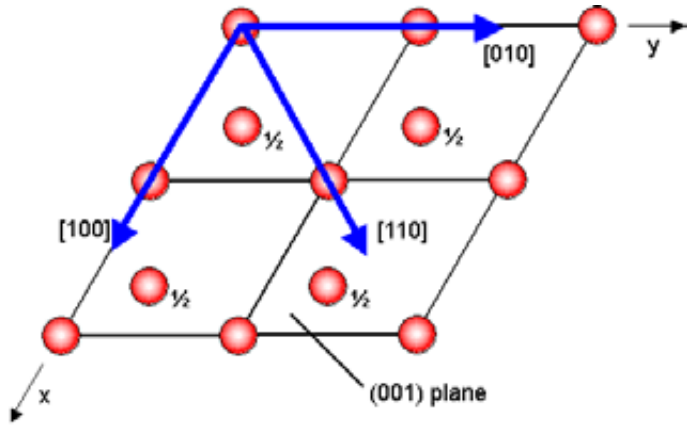

Figure 2-32 – Close packed slip systems in basal plane of HCP structures [51]

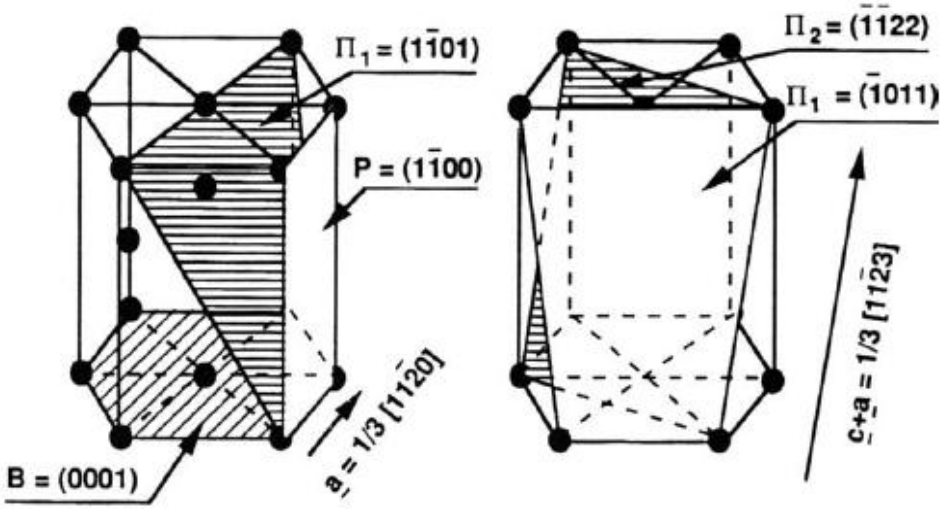

Figure 2-33 – Active slip systems in HCP metals [112]

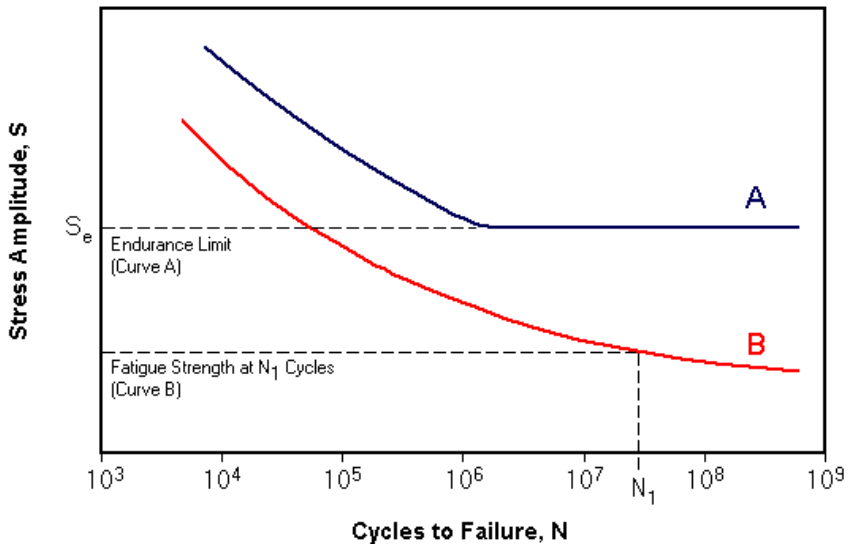

Figure 2-34 – Typical S-N curves [151]

Equation 2-5 $$da/dN = C(\Delta K)^m$$

Where a = crack length, N = number of cycles, ΔK = stress intensity range and C and m are empirical constants.

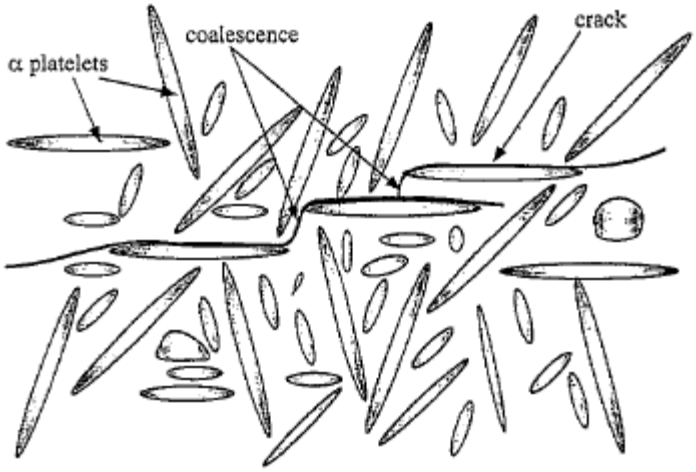

Figure 2-35 – Coalescence of alpha/beta interface cracks along primary alpha platelet boundaries with fatigue loading in air [59]

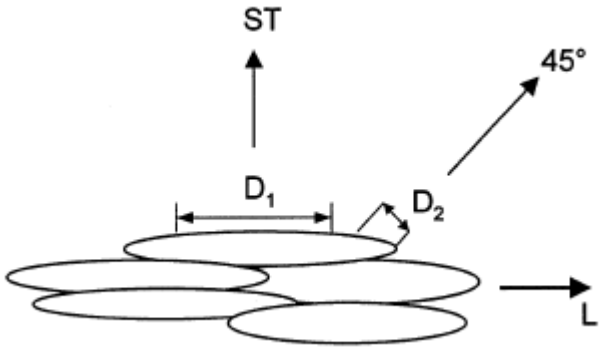

Figure 2-36 – Shear stress controlled dislocation pile up model taking "soft grain boundary area" length as the effective slip length controlling fatigue crack nucleation behaviour [60]

2.14 Cold dwell fatigue behaviour

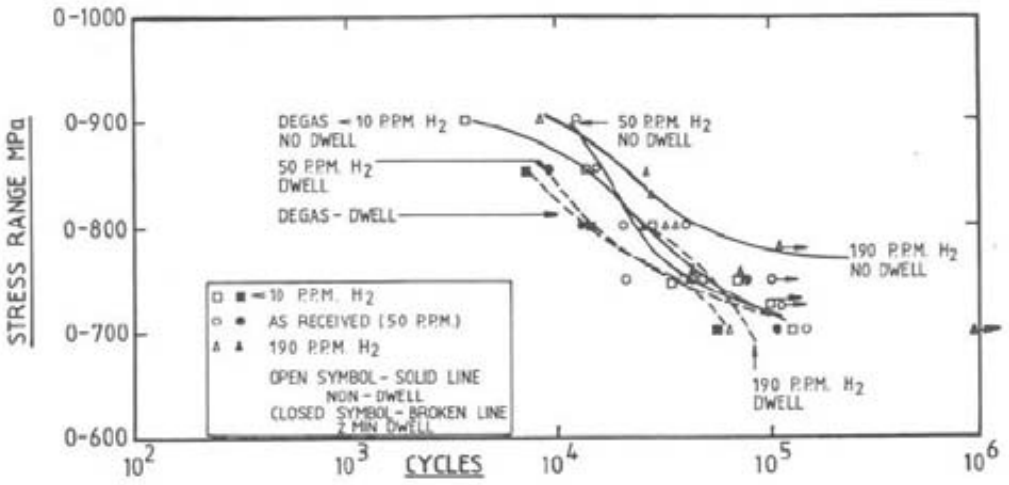

Figure 2-37 – Effect of hydrogen content on cyclic fatigue behaviour of IMI685 bar material [81]

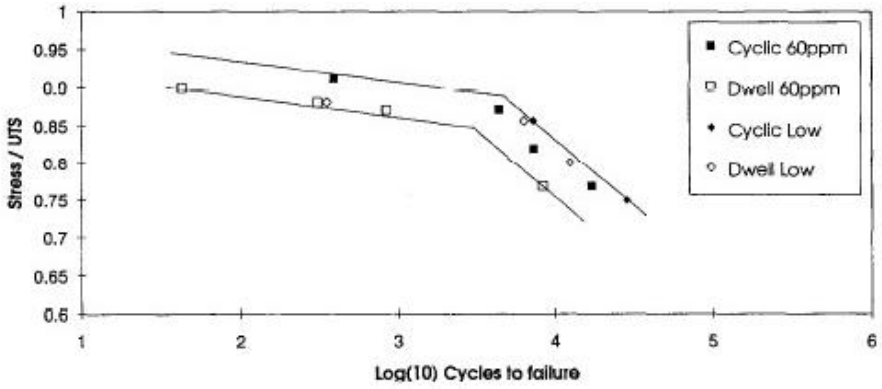

Figure 2-38 – Cyclic and dwell fatigue behaviour in low (20ppm) and intermediate (60ppm) hydrogen content material [67]

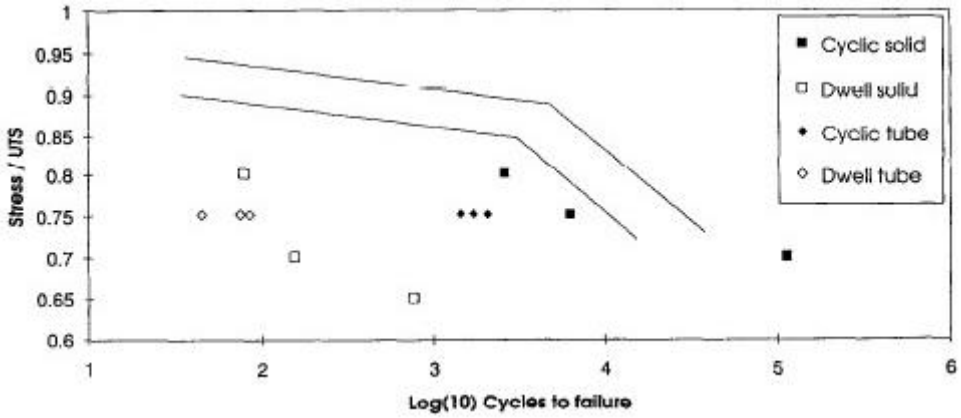

Figure 2-39 – Cyclic and dwell fatigue behaviour in high hydrogen content material (>100ppm) tested in solid and tubular specimens [67]

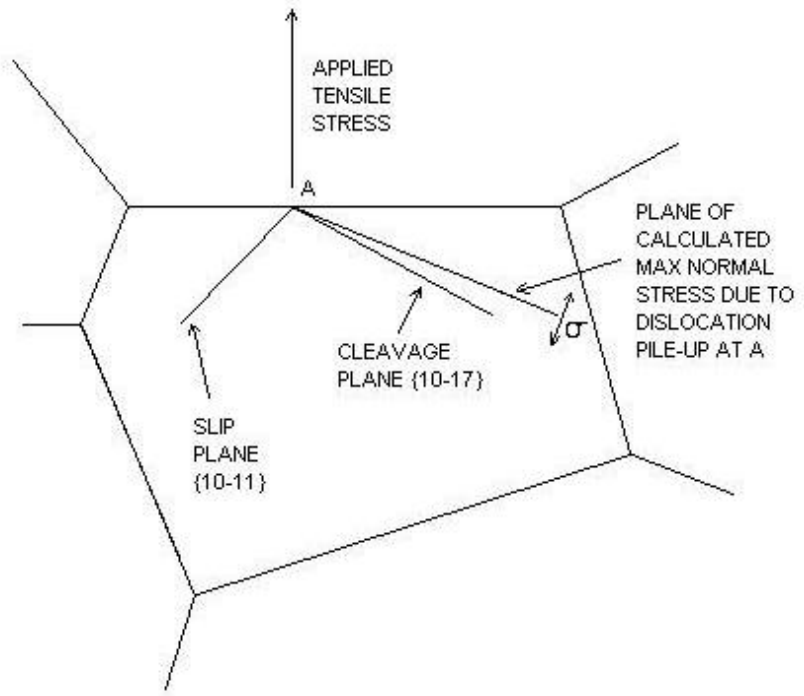

Figure 2-40 – The relationship between slip plane, cleavage plane and the plane of calculated maximum normal stress due to dislocation pile up [Adapted from 87]

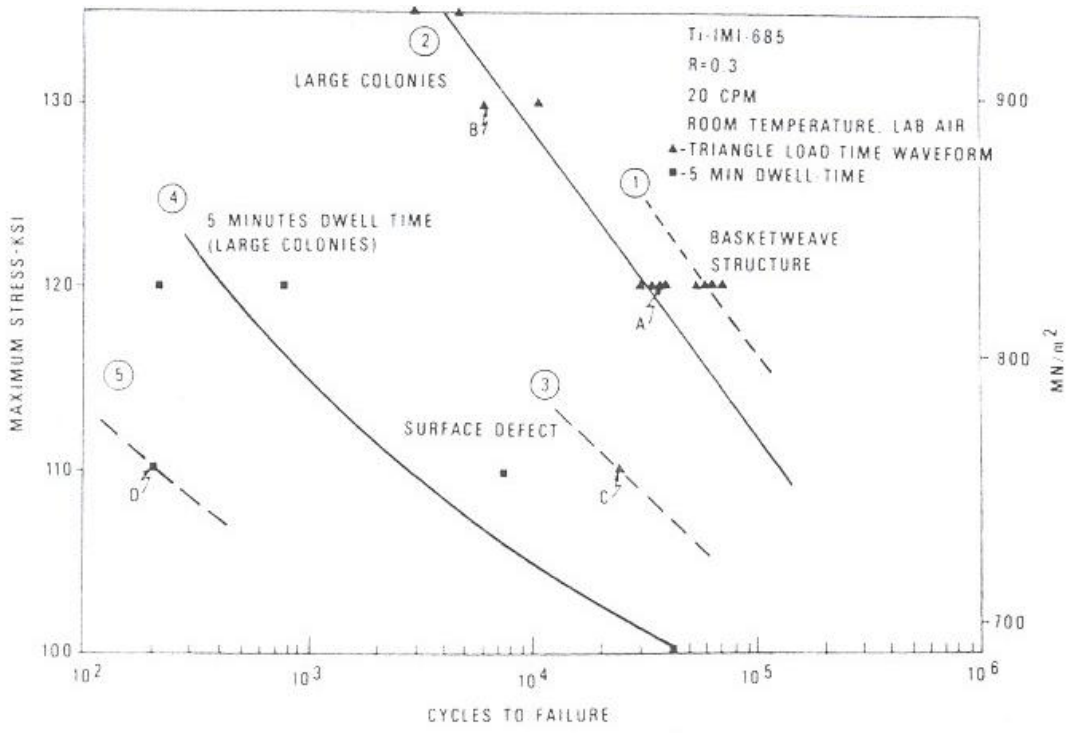

Figure 2-41 – Maximum stress vs. cycles to failure for different Ti685 microstructures and loading conditions. Curve 5 is a life prediction based on combined results of large colony structure, 5 minute dwell periods and internal defects [79]

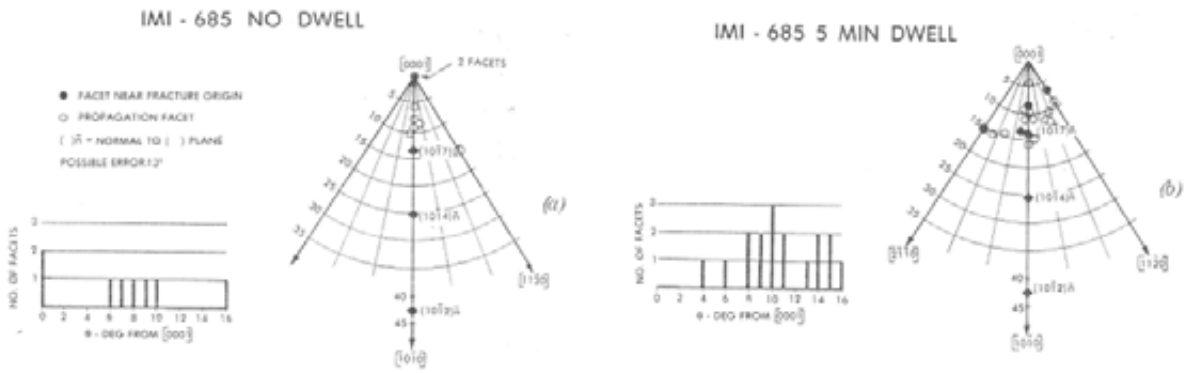

Figure 2-42 – Measured facet orientations for IMI685 under cyclic and 5 minute dwell conditions [91]

Table 2-1 – Comparison of alpha stabilisation and dwell sensitivity in titanium alloys [81]

Alloy	Heat Treatment	Al Equivalent %	Mo Equivalent %	% Dwell Cyclic Life Reduction*
Highly alpha stabilised alloy	(Alpha + Beta)	9.17	0.85	70
Ti6242S	(Alpha + Beta)	8.66	2.00	65
IMI829	(Alpha + Beta)	8.37	0.75	53
IMI829	Beta	8.37	0.75	43
IMI685	Beta	8.27	0.50	43
IMI679	(Alpha + Beta)	8.23	1.00	37
IMI318 (Ti6/4)	(Alpha + Beta)	8.30	3.00	16
IMI318 (Ti6/4)	Beta	8.30	3.00	20**
IMI550	(Alpha + Beta)	6.42	4.00	0
IMI550	Beta	6.42	4.00	20**

* Dwell cyclic life reduction is at 20°C and relative to cyclic life of ~15000 cycles

**Based on three test results displaying considerable scatter

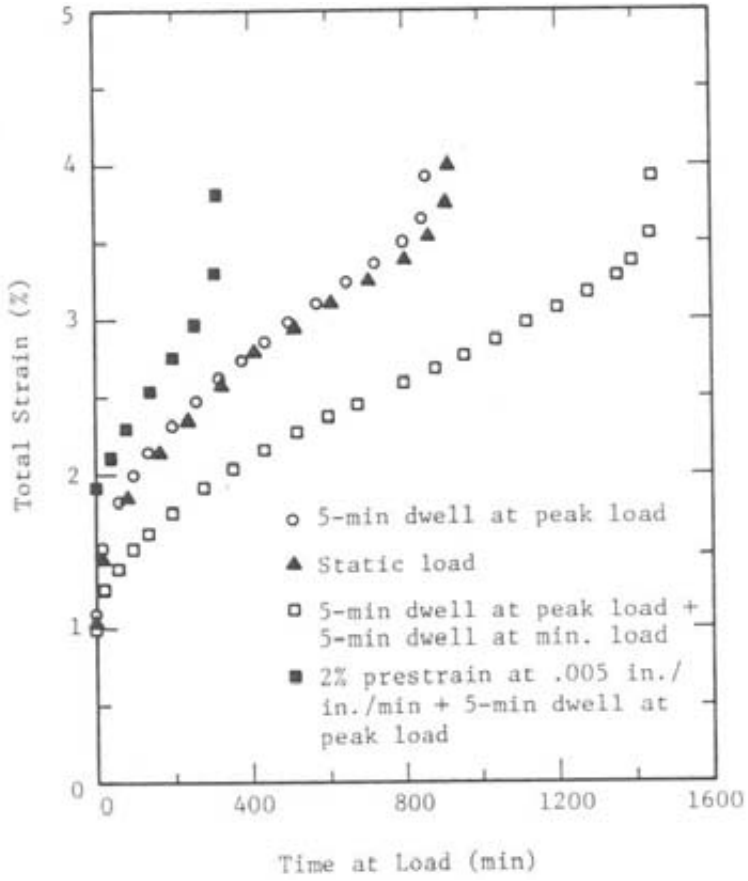

Figure 2-43 – Strain accumulation with time on load for IMI685 under load controlled test conditions at room temperature [93]

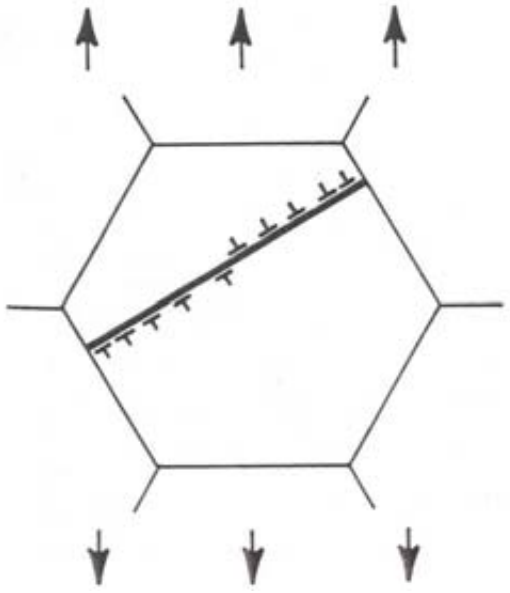

Figure 2-44 – Double-ended dislocation pile up blocked by colony boundaries [93]

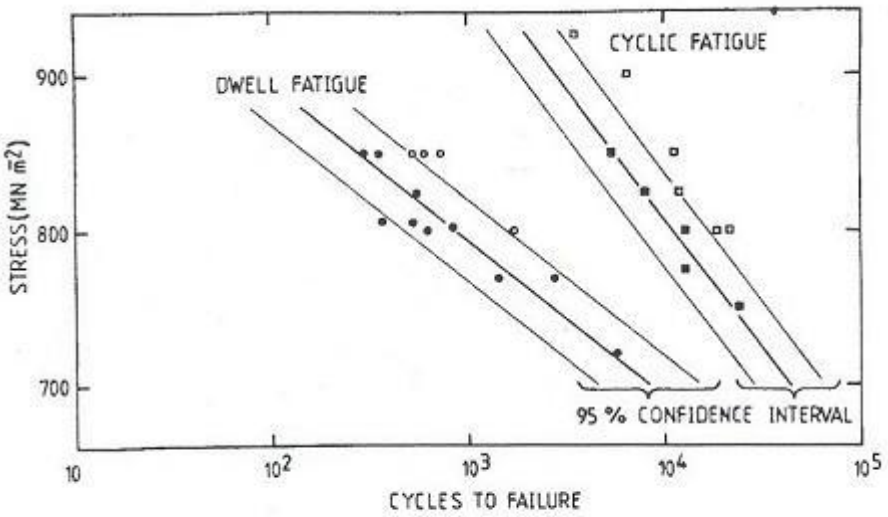

The effect of hydrogen and 300 sec dwell periods on the fatigue behaviour of IMI685. (●) Dwell, (■) cyclic, for hydrogen < 10 p.p.m. (○) Dwell, (□) cyclic for hydrogen ≃ 50 p.p.m.

Figure 2-45 – Effect of hydrogen content on the cyclic and the dwell fatigue behaviour of beta heat-treated colony IMI685 at ambient temperature [66]

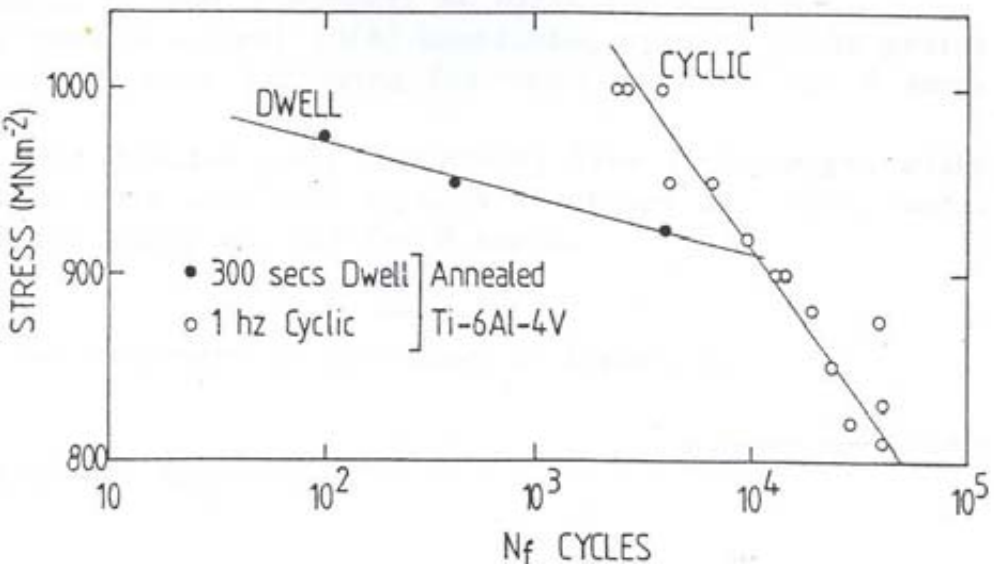

Figure 2-46 – Cyclic and dwell fatigue behaviour in annealed Ti6/4 [98]

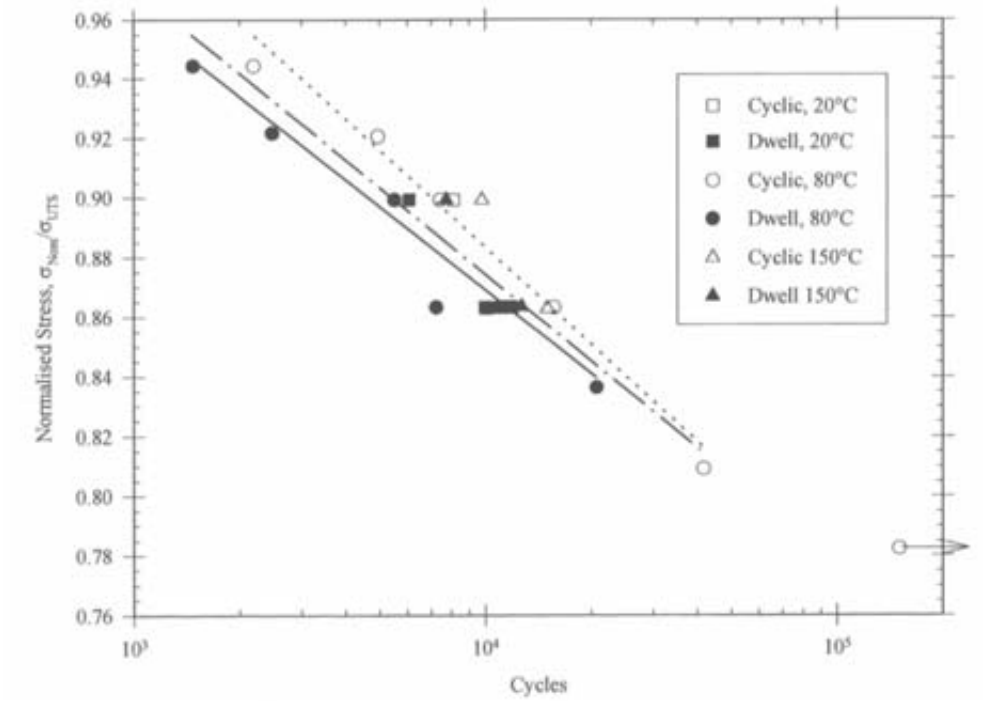

Figure 2-47 – Effect of temperature on cycles to failure for dwell (2 minute hold) and cyclic (15cpm) loading in Ti6246 [100]

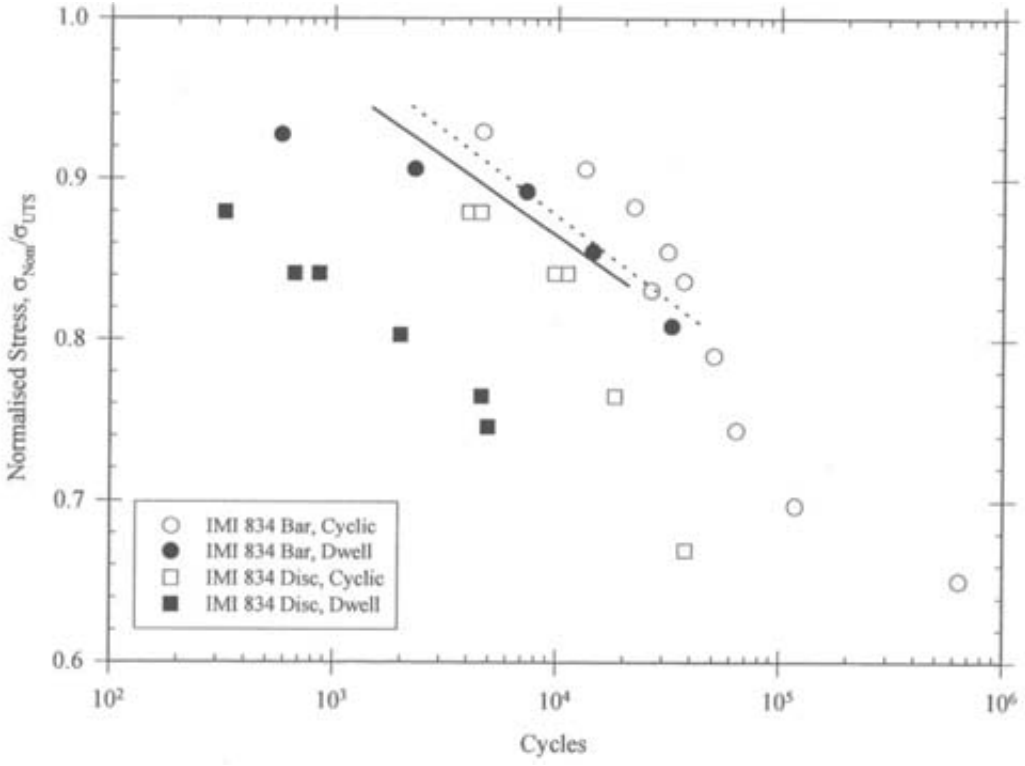

Figure 2-48 – Cycles to failure for Ti834 bar and disc material at 20°C. Dotted and solid lines represent cyclic and dwell performance of Ti6246 at 80°C respectively [100]

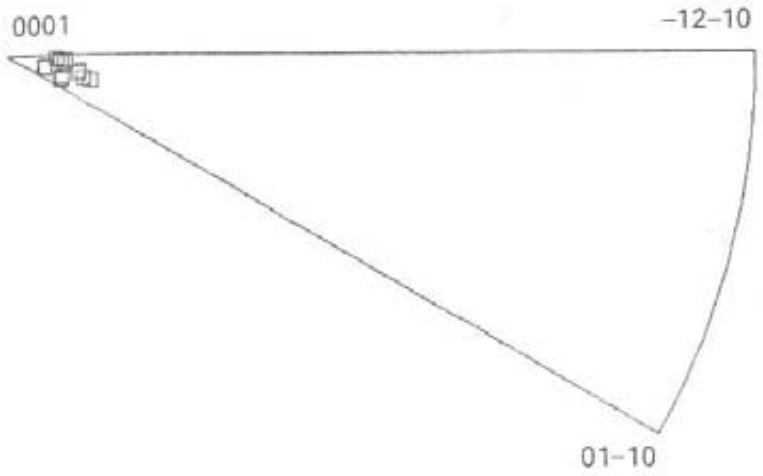

Figure 2-49 – Inverse pole figure displaying facet orientations in IMI834 [101]

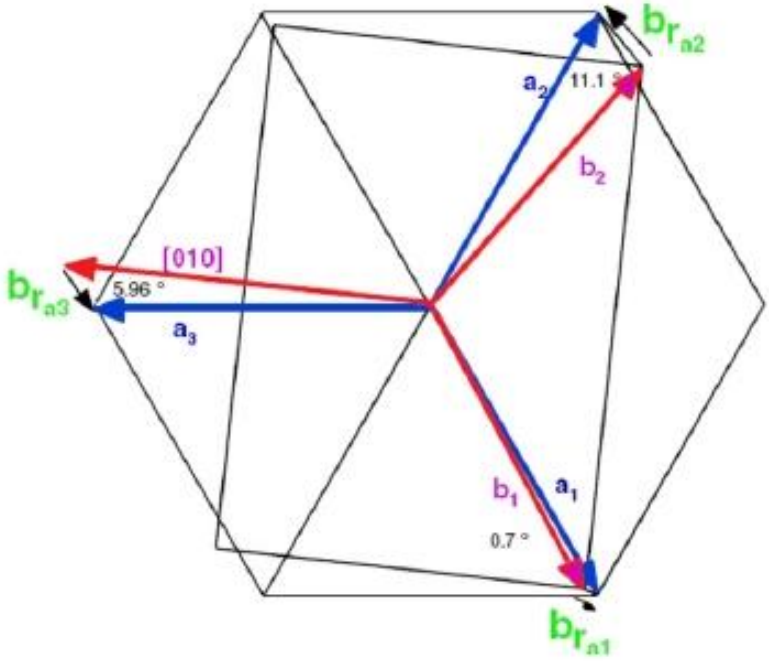

Figure 2-50 – Misorientations between alpha and beta slip directions for the {110} // {0001} plane according to the Burgers orientation relationship [139]

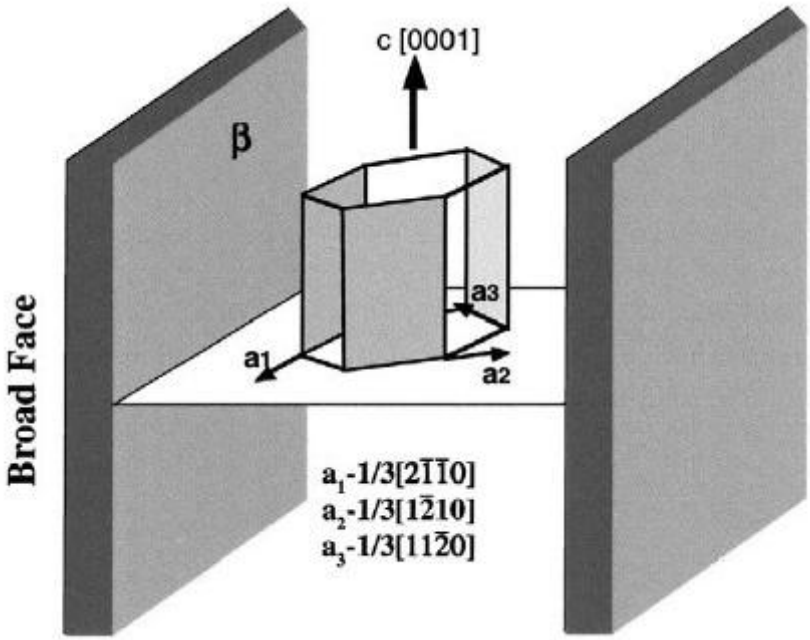

Figure 2-51 – Direction of $a_n\langle 11\bar{2}0\rangle$ type slip systems active in alpha-phase relative to beta lath orientations [106]

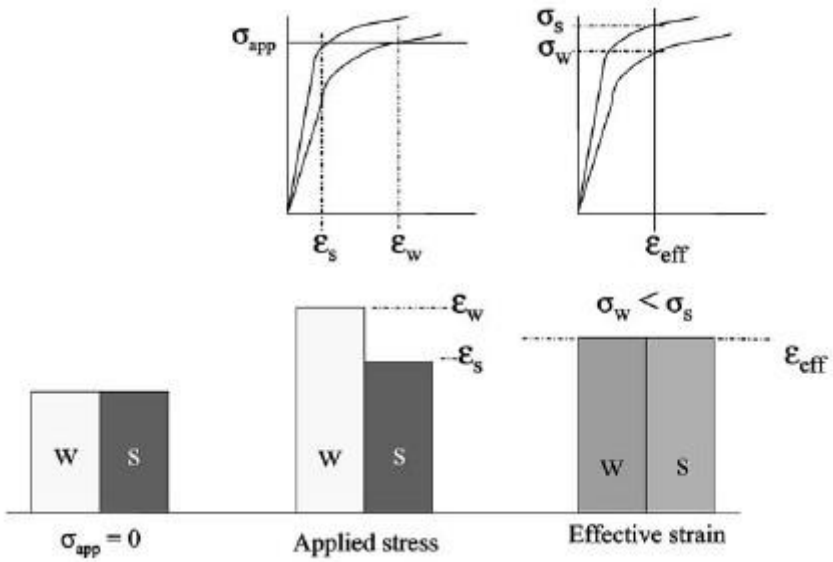

Figure 2-52 – Schematic of the two-grain stress redistribution model [16]

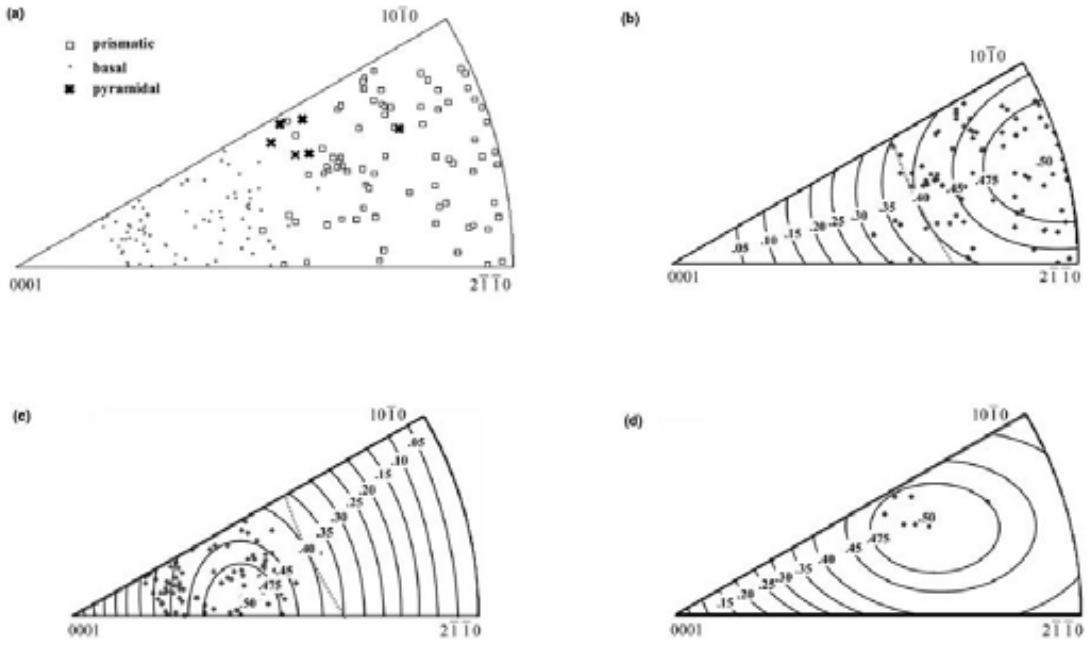

Figure 2-53 – Inverse pole figures showing (a) orientations of primary alpha grain displaying slip traces and (b) prismatic, (c) basal and (d) pyramidal slip system distributions with corresponding Schmid factor contour lines [111]

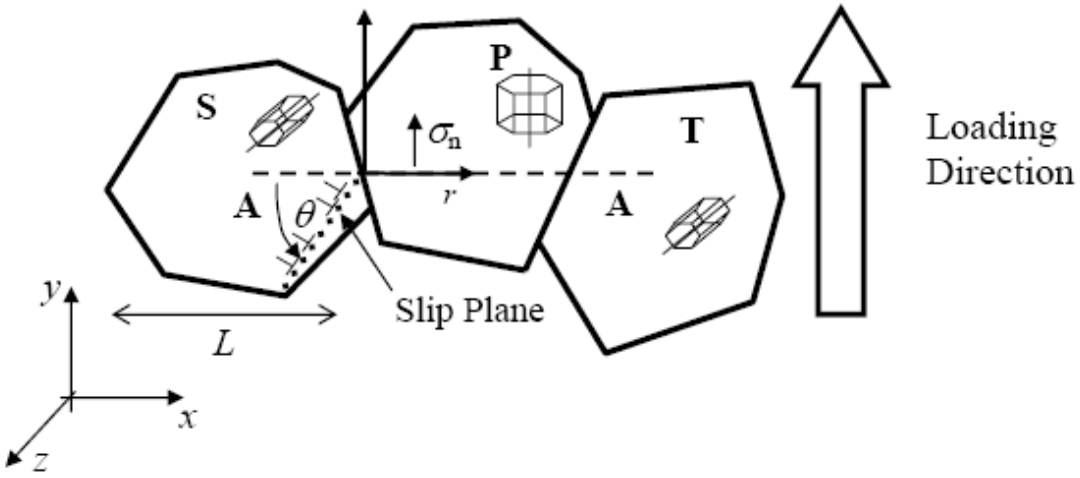

Figure 2-54 – Schematic of 'rogue grain' combination [131]

3 Experimental procedures 3-2
3.1 Sample preparation 3-2
3.2 Optical microscopy 3-2
3.3 Scanning Electron Microscopy 3-3
3.4 Electron Back Scatter Diffraction 3-3
3.5 Mechanical testing 3-5
3.5.1 Tensile testing 3-5
3.5.2 Fatigue testing 3-5

3B Volume B - Figures and tables 3-7
3.6 Electron Back Scatter Diffraction 3-7
3.7 Mechanical testing 3-9

3 Experimental procedures

Experimental techniques that are referred to frequently throughout the thesis are summarised in the following sections.

3.1 Sample preparation

Samples were sectioned from larger volumes using automated cutting machines with Silicon Carbide wheels under running coolant flow. Final cutting operations of the relevant surface were typically performed at a speed of ≤1.0mm/min. Samples of disc/pancake forgings have been taken on the axial/radial plane unless otherwise specified.

Samples were mounted in bakelite and prepared using standard metallographic techniques [12, 28]. This involved grinding to a suitable condition using progressively finer silicon carbide grit papers (typically to 2400 grit paper). This was followed by a polishing operation using a hydrogen peroxide activated colloidal silica oxide polish suspension (OPS) on a Chemcloth® polishing wheel for times varying between 15 and 60 minutes. After cleaning under running water samples were immersed in isopropanol or acetone and placed under a hot air current. This prevented water staining marks on the sample surface. If necessary, samples were etched using 2% HF – 10% HNO_3 solution (Kroll's reagent).

3.2 Optical microscopy

Assessment of optical microstructures used an Olympus Provis AX70 optical microscope. Magnifications varied between 50-500x. Micrographs were in the axial/radial plane (where axial direction represents forging compression axis, billet

axis, or specimen loading axis) unless otherwise specified. The axial direction is parallel to the vertical direction of each micrograph unless otherwise specified.

Analysis of optical micrographs used the Image Access Premium 5 software package. Where grain size has been characterised, the Heyn mean linear intercept (MLI) method has been used in accordance with the American Society for Testing and Materials (ASTM) E112 standard. Average aspect ratio was calculated by taking the MLI grain size in the direction of grain flow and dividing by the MLI grain size normal to grain flow.

3.3 Scanning Electron Microscopy

Higher magnification analysis used a Philips XL30 field emission gun (FEG) - scanning electron microscope (SEM). Magnifications typically varied between 100-10,000x. Operating conditions typically used working distances between 8-20mm and accelerating voltages of 10-20kV.

Micrographs were in the axial/radial plane (where axial direction represents forging compression axis, billet axis, or specimen loading axis) unless otherwise specified. The axial direction is parallel to the vertical direction of each micrograph unless stated otherwise.

3.4 Electron Back Scatter Diffraction

EBSD mapping used a JEOL7000 FEG-SEM unless otherwise specified. Samples were angled at 70º to the electron beam. Typical microscope settings used an accelerating voltage of 20kV and a working distance of ~10-15mm. Probe current and spot size values varied according to the settings that produced the best map indexing. Results were acquired and processed using Oxford Instruments INCA

version 17a software [146]. Standard EBSD settings used a minimum solution error of 2.5º and a minimum number of four indexed Kikuchi bands.

The size and resolution of crystal orientation maps (COMs) was varied depending on the alloy being mapped, time constraints on the microscope, and the feature of interest, e.g. macro-texture characterisation or local variant selection behaviour.

Pole figures are displayed as stereographic projections. Colour contour pole figures use a logarithmic scale to assess texture intensities (unless otherwise stated). Point intensity pole figures are typically used to compare local textures, e.g. between different alpha variants.

Samples were aligned with axial direction (i.e. forging compression axis, billet axis, or specimen loading axis) parallel to the map vertical direction unless otherwise specified. All crystal orientation maps (COMs) are displayed with reference to the relevant alpha or beta phase inverse pole figure colour keys. These IPF colour keys are displayed in Figure 3-1 and Figure 3-2 respectively.

Each crystal orientation map identifies the direction which the crystal orientations are displayed in relation to. Where COMs have been used to illustrate textures in disc or pancake forgings, textures are displayed with respect to orthogonal axes parallel to the axial, radial and tangential directions. These are denoted AD, RD and TD respectively. A schematic of the AD and RD axis notations is displayed in Figure 3-3. For example, an AD COM of material from a disc forging displays textures as viewed from the axial direction of the disc.

Where COMs have been used to assess textures in laboratory fatigue specimens, textures are defined w.r.t. the loading axis (AD) as in Figure 3-4, and arbitrary load

normal directions (RD and TD). Billet material COMs also display textures w.r.t. the axial direction (AD) and arbitrary directions normal to the billet axis (RD and TD).

3.5 Mechanical testing

3.5.1 Tensile testing

Tensile testing used standard Rolls-Royce tensile specimen geometries manufactured by approved suppliers. The standard tensile test specimen geometry is displayed in Figure 3-5.

All tensile tests were undertaken at the University of Birmingham using a Zwick 1484 closed-loop servo-hydraulic test frame. Testing was performed in a laboratory air environment at room temperature. Tests were conducted under displacement control using a fixed displacement rate of 0.5mm/min to failure. A strain extensometer was attached to the gauge length at positions 18mm apart (close to the gauge length ends). This displacement rate corresponds to a strain rate of approximately 4.63×10^{-4} s^{-1} (0.0278 min^{-1}). Tests began from a pre-load force of 100N.

3.5.2 Fatigue testing

Fatigue testing used standard Rolls-Royce low cycle fatigue specimen geometries manufactured by approved suppliers. Typically a large gauge diameter specimen (R-R specimen reference RLH10369) was used to maximise the volume of material on test. This LCF test specimen geometry is displayed in Figure 3-6. Some fatigue testing was also performed using specimens with a smaller gauge diameter (reference RLH8001).

All fatigue tests have been performed in laboratory air environments at ambient temperature (~298K) under load control using closed loop servo-hydraulic test

machines. Baseline tests were conventional 15 cycles per minute (cpm) LCF tests with a 1-1-1-1 trapezoidal loading waveform. The dwell fatigue tests were held on load for 120 seconds (i.e. a 1-120-1-1 load form). LCF specimens were tested to a run-out life of 1e5 cycles. Dwell LCF specimens were tested to run-out at 3e4 cycles.

Specimens were tested using an R=0.3 stress ratio in order to produce higher mean tensile stresses for a given stress range than R=0. This increase in stress ratio was selected because it was considered to promote the cold dwell fatigue mechanism. Testing was performed under load-control rather than strain control, again because this promotes CDF [152].

Testing relevant to this thesis was undertaken at three test houses; the University of Birmingham, the University of Swansea and the Rolls-Royce Materials Test laboratories. The relevant test house is specified as appropriate in the thesis.

Strain accumulation monitoring was performed for some fatigue testing undertaken at the University of Birmingham. Strain accumulation was monitored using an Epsilon Technical Corp. extensometer (model 3542-015M-020-ST). The extensometer gauge length was 15mm, with travel of +3mm/-3mm. Strain accumulation was monitored electronically using the National Instruments package Labview 7.1. Data was automatically recorded in Labview file formats. These results were analysed using Microsoft Office Excel 2007.

3B Experimental procedures – Figures and tables

3.6 Electron Back Scatter Diffraction

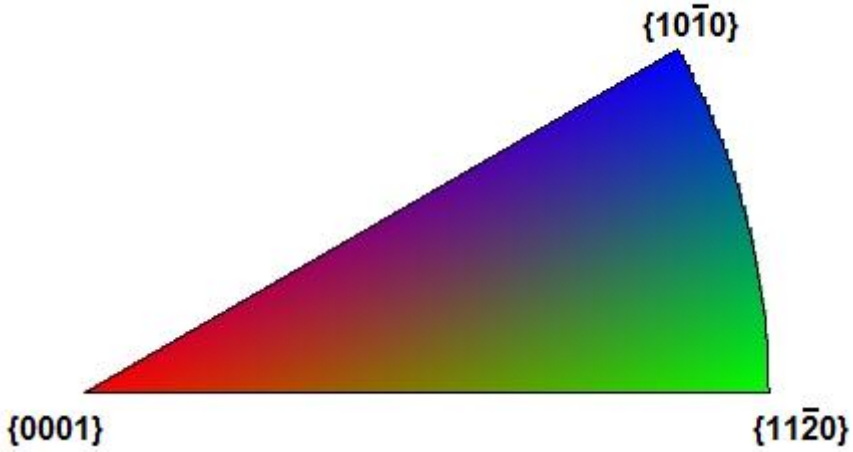

Figure 3-1 – Alpha phase inverse pole figure colour key [146]

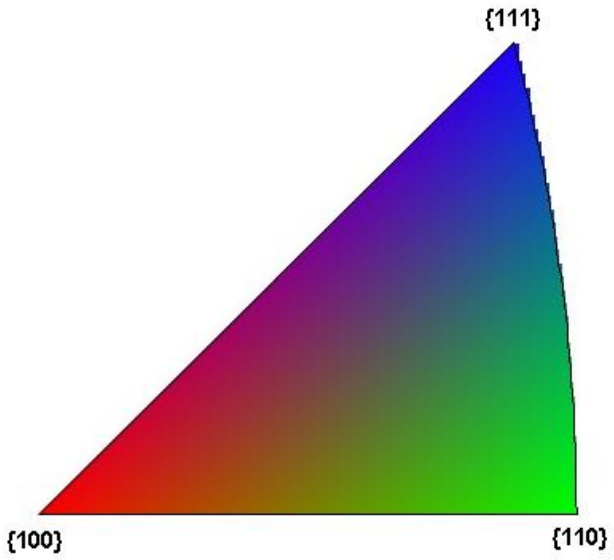

Figure 3-2 – Beta phase inverse pole figure colour key [146]

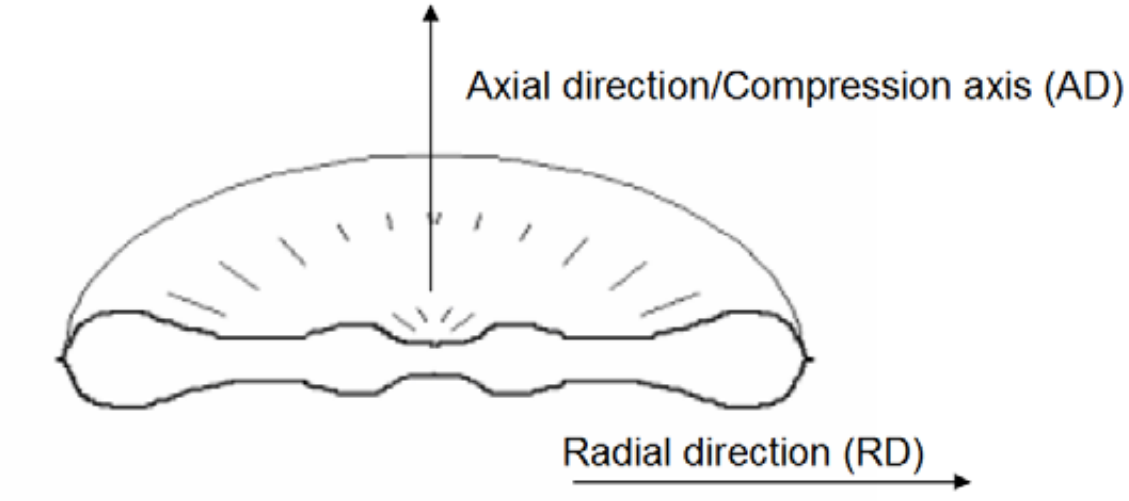

Figure 3-3 – Inverse pole figure map axis notations for disc and pancake forgings

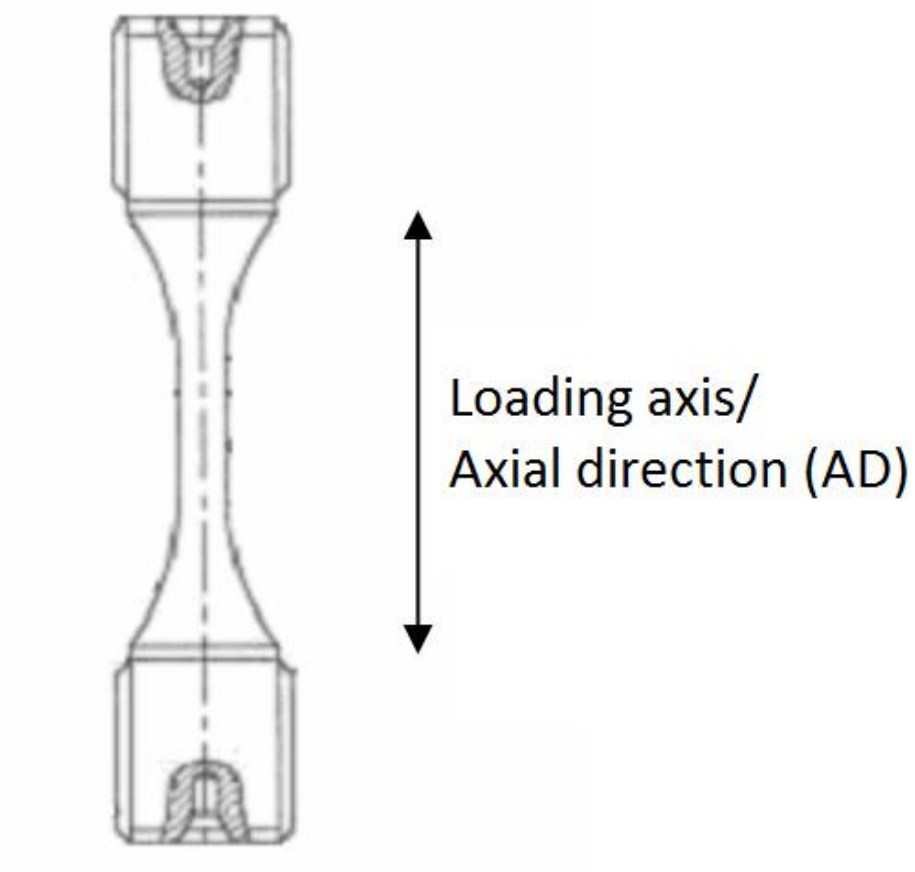

Figure 3-4 – Inverse pole figure axis notations for laboratory fatigue test specimens [153]

3.7 Mechanical testing

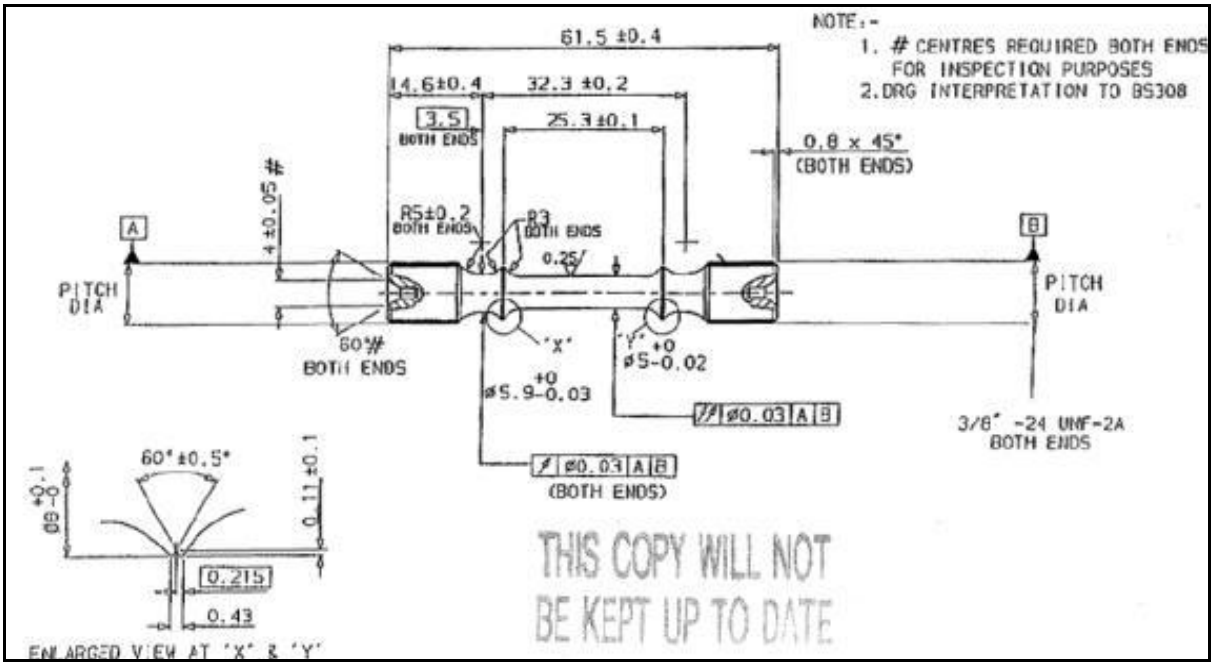

Figure 3-5 – RLH10004 Tensile test-piece geometry [153]
(Dimensions in mm except where stated)

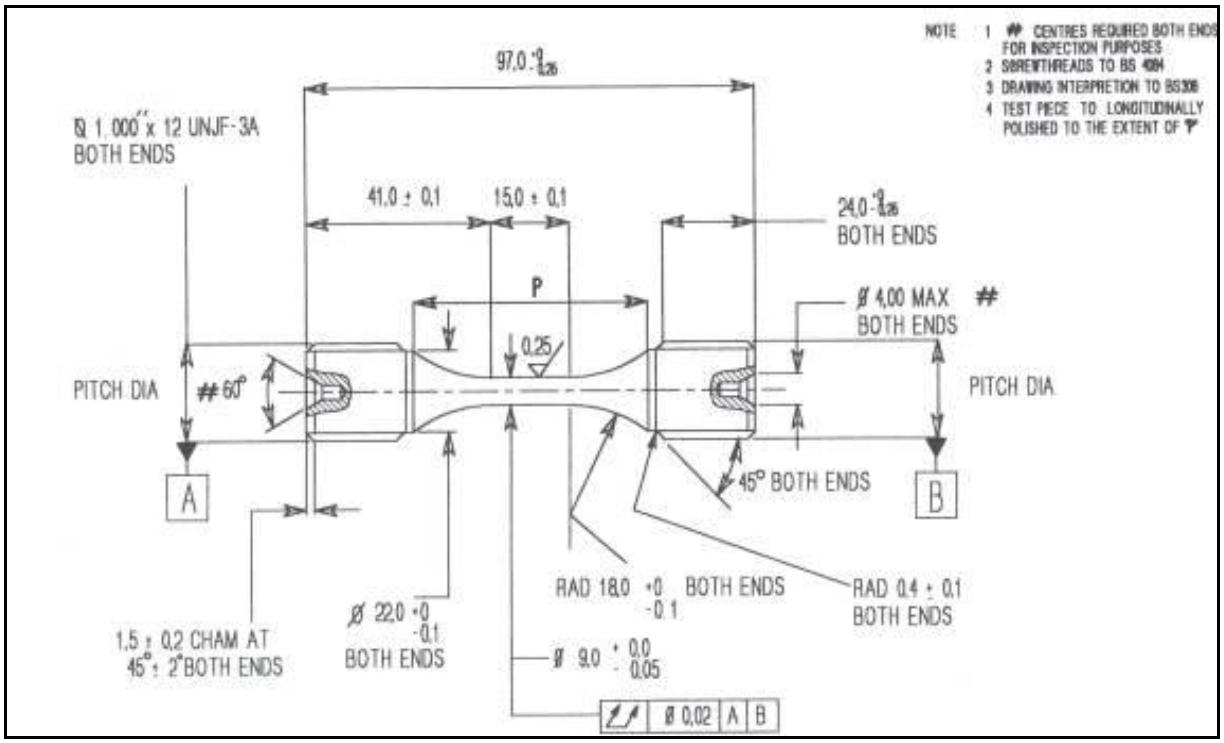

Figure 3-6 – RLH10369 Low Cycle Fatigue test-piece geometry [153]
(Dimensions in mm except where stated)

4 Cold dwell fatigue behaviour in Ti6246 alloy 4-2
4.1 Introduction 4-2
4.2 Experimental method 4-4
4.2.1 Assessment of optical microstructures 4-4
4.2.2 Assessment of crystallographic textures 4-8
4.2.3 Cold dwell fatigue testing of production disc material 4-8
4.2.4 Cold dwell fatigue testing of non-standard Ti6246 microstructures 4-11
4.3 Results 4-14
4.3.1 Assessment of optical microstructures 4-14
4.3.2 Assessment of textures 4-15
4.3.3 Cold dwell fatigue testing of production material 4-15
4.3.4 Cold dwell fatigue testing of non-standard Ti6246 microstructures 4-16
4.4 Discussion 4-18
4.4.1 Assessment of optical microstructures 4-18
4.4.2 Assessment of crystallographic textures 4-24
4.4.3 Cold dwell fatigue testing of production material 4-25
4.4.4 Cold dwell fatigue testing of non-standard Ti6246 microstructures 4-27
4.5 Conclusions 4-32

4B Volume B - Figures and tables 4-35
4.6 Introduction and experimental method 4-35
4.7 Results 4-42
4.7.1 Assessment of optical microstructures 4-42
4.7.2 Assessment of textures 4-49
4.7.3 Cold dwell fatigue testing of production material 4-55
4.7.4 Cold dwell fatigue testing of non-standard Ti6246 microstructures 4-62

4 Cold dwell fatigue behaviour in Ti6246 alloy

4.1 Introduction

In the early to mid 1990s Rolls-Royce developed Ti-6Al-2Sn-4Zr-6Mo for use in large civil engines, with introduction into service in 1997. To achieve the optimum combination of mechanical properties it was beta finish forged, (alpha + beta) solution heat-treated and aged. The demand for the alloy could be related to the need for improved temperature capabilities allied to higher tensile strength than Ti6/4 and competitive fatigue strength levels at lower temperatures.

The alloy was characterised for behaviour under cold dwell fatigue (CDF) conditions at the University of Wales, Swansea. No significant debit on cyclic life was observed for time on load in laboratory specimens during this investigation. In addition there was no evidence of load normal basal facet formation on laboratory specimens [100].

The need for further investigation into the CDF behaviour of the alloy arose in 2002 when large optical features (referred to as 'clusters') were detected on the diaphragm surfaces of a batch of compressor disc components in an etched rectilinear condition. These large optical features are displayed in Figure 4-1 and Figure 4-2. They are regions of multiple, distinct beta grains with uniform reflectivity.

It was suspected that these areas of common etch appearance on the diaphragm of discs corresponded to regions of common crystallographic alignment. Further work using electron backscatter diffraction (EBSD) analysis provided confirmation that large areas of common texture were present in these cluster locations, whereas previous work had shown Ti6246 to have a random alpha texture [154]. EBSD also indicated that areas of different optical microstructures might still display the same crystallographic textures. The possibility of large

textured regions within production disc material (and the large CDF facet sizes associated with these textural units) led to the conclusion that CDF behaviour may be a significant risk in Ti6246 compressor disc forgings. Mechanical testing was performed to assess the CDF behaviour of material in discs taken from the affected batch. These results were acceptable with the exception of two instances of early stress relaxation in strain controlled low cycle fatigue (LCF) specimens [155].

On this basis an investigation to study the variations in texture in production Ti6246 disc forgings and relate results to variations in optical microstructure was undertaken. A range of production Ti6246 disc forgings were selected for evaluation. The matrix was selected to cover the full range of conditions including different engines, disc stages, material suppliers and forging operations. Material was also taken from different locations within each forging. In selecting the material for assessment a wide range of forging strains, strain rates and cooling rates was covered.

Characterisation results were used in the selection of disc material with strong textures and large regions with similarities in optical microstructure (i.e. material more likely to display CDF susceptibility) for CDF testing. In addition to mechanical testing of production material representative of extremes of optical microstructure and texture, further work attempted to remove 'beneficial' features of the microstructure through heat treatment. Selected non-standard microstructures were then tested to further assess the CDF susceptibility of the alloy [69].

4.2 Experimental method

4.2.1 Assessment of optical microstructures

Samples were taken from the bore, diaphragm and rim sections of each disc forging selected for assessment. Three samples were taken from each location in order to view microstructures in axial-radial, axial-tangential and radial-tangential disc planes. A cut-away section of the geometry of a typical compressor disc and the location of metallographic samples within the disc are illustrated in Figure 4-3.

The list of samples included in the initial assessment of optical microstructures is given in Table 4-1. The assessment was primarily focused on the microstructures in disc bore locations due to the fact that this is the region most susceptible to dwell fatigue. This is due to a combination of high rotational plus residual stresses and the prolonged times at low temperature in the disc bore at the start of a flight cycle (i.e. during take-off). The extended time at low temperature occurs due to the large volume of material present in the disc bore, the large air-flows within the engine and the consequent thermal gradients, and the low thermal conductivity of titanium.

The forging methods may be characterised as follows:

- Isothermal – Die temperature equal to forging temperatures, i.e. above the beta transus, e.g. ~980ºC. Forging uses low strain rates.
- Hammer – Die temperatures ~150-250ºC, very high strain rates on forging.
- Press – Hot die press with die temperature ~500-600ºC. Strain rates intermediate between isothermal and hammer forging methods.
- Weber – Hot die press forging with similar operating conditions to the Press.

Following on from the conclusions of the initial assessment of optical microstructures a second survey was undertaken. This work concentrated mainly on diaphragm and rim microstructures in discs that had displayed unusual optical microstructures in bore locations. Some other samples were included in the assessment to broaden the range of production conditions. The list of samples is given in Table 4-2.

The assessment of optical microstructure covered various features including the prior beta grain size and aspect ratio, grain boundary alpha morphology, degree of alignment of alpha platelets in the microstructure, blocky alpha structures, primary alpha area fraction, beta fleck effects and the nature of secondary alpha precipitates in the microstructure.

Quantitative assessment of the maximum permissible values of features present in the optical microstructure (based on the Rolls-Royce material specification for Ti6246) led to the defined acceptable limits listed in Table 4-3. For the assessment of these features the method of characterisation is described below.

Grain boundary alpha has been assessed based on figures provided in the Rolls-Royce material specification for Ti6246. A grading between 1 and 10 was allocated to each sample based on the extent of continuity and the level of deformation of grain boundary alpha in the microstructure. A grading of 1 represents a fully deformed and discontinuous grain boundary alpha morphology throughout the sample. A grading of 10 represents continuous and straight (i.e. undeformed) grain boundary alpha that represents the worst observed case. Gradings of 8 and above lie outside the limits of the current material specification and Company Materials Engineering (CME) brochure. The criteria for the assessment of grain boundary alpha structures are displayed in Table 4-4. Figure 4-4 and Figure 4-5 show the

ideal grain boundary microstructure and the material specification limit of grain boundary alpha respectively.

The variations in the level of alignment of primary alpha platelets have been qualitatively interpreted using a scale of 1-10 in a similar manner to that for classification of grain boundary alpha. A grading of 1 indicates a random (or close to) microstructure in terms of the orientation of primary alpha platelets. Figure 4-6 illustrates the material specification standard for random primary alpha platelet alignment. This is purely based on optical appearance and no account is made of the texture of the primary alpha platelets.

A grading of 9 or 10 would indicate very high levels of alignment throughout the sample. This could be a tendency for the majority of platelets to align optically in a certain direction. It could also be the alignment of the majority of platelets but in multiple "colonies" with various optical orientations. As before a grading of 8 or above would exceed the limits of the material specification. The material specification states that optical colony size should not exceed $0.5mm^2$. Therefore where colonies of area equal to or greater than $0.5mm^2$ are observed a grading of 8 or above has been applied.

As for grain boundary alpha and platelet alignment, the level of blocky alpha within the microstructure was assessed qualitatively using a scale of 1 to 10. A sample grading of 1 corresponds to very little or no blocky alpha being observed throughout the sample cross-section. A grading of 10 would correspond to areas of blocky alpha significantly in excess of material specification limits. From the material specification the maximum area of blocky alpha permissible is considered to be $0.125mm^2$. A sample with a cluster of blocky alpha greater than this would be given a grading of 8 or above. The material specification gives an example of typical blocky alpha structures as displayed in Figure 4-7.

Primary alpha area fractions were measured using Image Access Premium 5 image analysis software to analyse SEM images. For each sample a minimum of five images over areas of ~150µm x ~100µm have been analysed to determine an average value for the primary alpha content. Images have been captured in areas where no significant blocky alpha or other potential sectioning effects are observed. Sectioning effects are avoided as they may distort measurements.

Image analysis gave values of primary alpha fraction and (retained beta + secondary alpha) content. Secondary alpha area fractions were not determined as this phase is irresolvable at the selected optical magnification (800x). Measurements taken from images were compared to values obtained from the MSRR specification. Using the same image analysis software the primary alpha content for the recommended microstructural objective is measured at 37%. Minimum and maximum primary alpha content levels are estimated at 28% and 55% respectively.

Samples have been examined using SEM to study secondary alpha structures for any evidence of secondary alpha alignment in production microstructures. A qualitative assessment is made regarding the level of secondary alpha platelet alignment in the sample. As with the volume fraction of primary alpha, quantitative analysis was undertaken in an attempt to determine variations in the proportion of secondary alpha relative to the retained beta matrix. However, due to the microscope resolution limitations it was not possible to accurately analyse these variations.

Beta fleck has been analysed by taking measurements of the area denuded of alpha laths. The material specification states a maximum area for a beta fleck affected region of 1.25mm^2. Samples are assessed against this specification requirement.

4.2.2 Assessment of crystallographic textures

For the assessment of texture, for each disc an additional sample was sectioned from the same location as the samples taken for optical assessment. A total of forty-four Ti6246 production disc forgings and four non-production pancake forgings were assessed using EBSD as part of the investigation of texture and cold dwell behaviour in Ti6246.

Sample preparation was performed at the University of Manchester. Each EBSD sample was mounted in the axial-radial plane and prepared using standard metallographic techniques. A final polishing step used a colloidal silica oxide polish suspension for three hours.

EBSD data acquisition was performed using a CamScan Maxim 2500-SEM at the University of Manchester equipped with the HKL system and Channel 5 software. A total area of 7mm^2 was mapped for each sample to provide a large-scale representation of texture in each disc. The map step size was 40µm, with an accelerating voltage of 20kV, a working distance of 15mm and a spot size of 4. EBSD mapping and analysis was undertaken by Dr. Laura Pocock and Dr. Michael Preuss. EBSD data was provided in the form of stereographic pole figure projections. Data was also provided on the maximum textures observed in the alpha and beta phases [156].

4.2.3 Cold dwell fatigue testing of production disc material

Ti6246 specimens for mechanical testing were obtained from four sources. These were Trent engine intermediate pressure (IP) stage 5, stage 7 and stage 3 discs and an engine clutch shaft. These are referred to as the IP5 disc, IP7 disc, IP3 disc and clutch shaft respectively.

The IP5 disc was selected for testing as it displayed visible clusters on the disc diaphragm. It was obtained from the original batch of twelve discs with visible clusters that were rejected

due to the possibility of large regions of common texture. The disc was forged on a hot die press. The diaphragm region of the disc was selected for dwell testing for two reasons; (a) the worst visible clusters were present on the diaphragm and (b) the strongest textures were present in the diaphragm. Fatigue specimens were machined from the section of the diaphragm showing the worst evidence of cluster grains. Axial fatigue specimens were machined in tangential, radial and 45° orientations to account for the possibility that macro-colony orientations may lead to stronger dwell effects in different directions [60].

As cold dwell behaviour is affected by a volumetric effect (greater volumes increase the probability of suitably orientated neighbouring regions of microstructure under constraint) test specimens were selected to maximise the volume of material tested. Large fatigue specimens with a 9mm gauge length diameter were selected rather than standard fatigue specimens with a gauge length diameter of 4.5mm. The IP5 disc diaphragm was not thick enough to machine specimens from so it was necessary to machine gauge lengths from the disc then attach Ti6/4 bar ends (for specimen threads) using an inertia welding technique. Welding was undertaken at the University of Manchester. Trials were performed to establish suitable welding parameters. Once optimum parameters had been established further specimen manufacture was undertaken at a pressure of 1800KPa and speed of 2200rpm [152].

After inertia welding specimens were subject to a post-weld heat treatment of two hours at 640°C followed by air-cooling. The PWHT was used to relieve residual stresses in the weld. PWHT was also necessary to produce a microstructural condition representative of in-service material [152]. After PWHT the dumbbells were machined to specimen geometry.

The clutch shaft drive arm was an isothermal forging. Specimens from the clutch shaft were tested to provide a baseline comparison of dwell performance in Ti6246 material with a random crystallographic texture. This selection was made based on EBSD results from a test ring sample taken from the forging. It was later established that the material had a non-random crystallographic texture following further EBSD assessment [152]. Specimen blanks were machined in an orientation with the loading axis parallel to the shaft axis. Blanks were subject to the standard PWHT. This was to provide consistency in the comparison to the cluster disc material [152]. Following PWHT the blanks were machined to specimen geometry.

The IP7 disc was included in the test programme as EBSD assessment of production forgings showed the strongest beta textures occurred in this disc. The disc was an isothermal forging. The strongest texture was present in the diaphragm although specimens were machined from a section close to the disc bore. This was necessary because the thickness of the diaphragm was less than the diameter of the specimen gauge length. Specimens were machined in radial and tangential orientations. As for cluster disc specimens it was necessary to inertia weld Ti6/4 bar ends to the specimens. The standard PWHT operation was applied following welding. Ten gauge length cylinders were manufactured.

The IP3 disc was selected for test as it was similar in both geometry and forging route to the production disc with the highest measured alpha texture (an IP7 disc). Insufficient material was available to test this disc. The hammer forged IP3 disc was available in the form of a heat-treated black forging. Ten specimen blanks were machined in radial and tangential directions, PWHT'd and machined to test specimens.

In total there were eight baseline and 18 dwell tests on IP5 disc diaphragm material. There were six baseline and six dwell fatigue tests on the clutch shaft specimens. Both the IP7 disc (maximum observed beta texture) and the IP3 disc (high predicted alpha texture) had five baseline and five dwell fatigue tests.

Specimens were fatigue tested at three Rolls-Royce approved mechanical test-houses as listed in chapter three section 3.5.2. This was necessary given the timescales associated with the work. Fatigue testing procedures were outlined in section 3.5.2. Fractographic assessment used standard optical and SEM techniques.

4.2.4 Cold dwell fatigue testing of non-standard Ti6246 microstructures

Testing of non-standard Ti6246 microstructures was undertaken to attempt to obtain a greater response to CDF loading than observed in conventional material. Microstructural variations were designed to minimise or remove features potentially limiting dwell susceptibility. The aim in doing so was to test dwell fatigue sensitivity in severe microstructural conditions.

Ti6246 material for heat treatment experiments was obtained from the clutch shaft drive arm forging that was used in the initial cold dwell testing programme on the basis that it was believed to have a near-random texture. A series of heat treatments were attempted to produce microstructural variations suitable for mechanical testing. Heat treatment experiments were conducted using a Lenton Thermal Designs furnace. Samples were prepared and assessed as described under section 4.2.1.

A number of heat treatments variations were trialled [157]. For mechanical testing two heat treatments were selected to produce distinct microstructures. The first heat treatment was a hold in the (alpha + beta) phase field at 910˚C (~30˚C below beta transus) for a time of

two hours prior to a 2˚Cmin^{-1} programmed furnace cool to 820˚C. At 820˚C material was removed from the furnace and a water quench was applied. The second heat treatment involved a two-hour hold at 970˚C (β phase field) followed by a slow cool at 2˚Cmin^{-1} to 840˚C then a furnace cool. Details of the heat treatment experiments are given in Table 4-5.

Once the optical microstructure of the heat-treated samples had been characterised the heat treatments were applied to specimen blanks prior to machining to test-piece geometries.

Ti6246 material was obtained from the bore of two Trent IP1 discs and from the diaphragm of a Trent IP5 disc. Ten specimen blanks were machined from IP1 disc bores in the tangential direction. These blanks were subject to the beta heat-treatment listed in Table 4-5.

Six cylinders were machined from the diaphragm of the IP5 disc. Three cylinders were orientated in the tangential direction and three cylinders were orientated in the radial direction. These cylinders were subject to the (alpha + beta) heat treatment listed in Table 4-5. Ti6/4 bar ends were inertia welded to these cylinders at the University of Manchester. A pressure of 1800KPa and speed of 2200rpm were used. Following inertia welding there was no PWHT to allow relief of welding residual stresses. This was necessary to prevent the precipitation of a secondary alpha phase in the microstructure. Beta heat-treated blanks and (alpha + beta) heat-treated dumbbells were machined to test-piece geometries.

In addition to the large gauge diameter test specimens there were seven (alpha + beta) heat-treated small gauge specimens. These specimens remained from a previous investigation into the possible use of stress-relaxation followed by HCF loading as a potential ‘fast’ test for dwell sensitivity (i.e. load normal facet formation). These specimens were machined from the same disc as the large section specimens and subject to the same heat treatment.

Fatigue tests were performed under the same conditions as for production microstructure tests. For the beta heat treatment five tests were performed at baseline and five tests were performed under CDF. For the (alpha + beta) heat-treated small gauge specimens there were four baseline and three CDF tests. For the large gauge (alpha + beta) specimens three baseline and three CDF tests were conducted.

Fatigue testing was undertaken at three test houses as for the specimens from production disc material. Fractographic assessment of test specimens used optical microscopy and SEM techniques.

4.3 Results

4.3.1 Assessment of optical microstructures

Results tables for the optical assessment of grain size, grain boundary alpha, primary alpha area fraction, primary alpha platelet alignment and blocky alpha structures for both the initial and secondary assessment of optical microstructures are included in the chapter appendix.

An assessment of the variation in MLI grain size measurements for the different forging methods is displayed in Figure 4-8 and Figure 4-9. This covers samples listed in Table 4-1 and Table 4-2.

Table 4-6 details the gradings of microstructural features for each of the samples included in the first phase of the microstructural characterisation study. Gradings were defined for each parameter using a scale of 1-10 comparable to that given in Table 4-4. Table 4-6 also includes a value for the primary alpha area fraction.

The variation in the grading of grain boundary alpha structures for the different forging methods is displayed in Figure 4-10. This assessment is for samples listed in Table 4-1. Variation in the extent of alignment of primary alpha laths within the microstructure is displayed in Figure 4-11. Typical optical colony structures where primary alpha platelets align normal or parallel to beta grain flow are displayed in Figure 4-12 and Figure 4-13 respectively. Figure 4-14 displays the variation in the extent of blocky alpha features in disc optical microstructures according to the plane of sectioning.

The typical microstructures of secondary alpha platelet morphologies in Widmanstätten primary alpha platelets, aligned primary alpha side-plate colonies and aligned colonies in hammer forgings are displayed in Figure 4-15, Figure 4-16 and Figure 4-17 respectively.

A plot of all the measurements of maximum $\{100\}_\beta$ and $\{0002\}_\alpha$ textures against qualitatively increasing prior beta grain elongation is displayed in Figure 4-18. It must be taken into account that this plot provides no quantitative assessment of the beta grain aspect ratio. The figure only shows the changes in texture measurements for apparent increase in the aspect ratio of optical prior beta grains.

4.3.2 Assessment of textures

Table 4-7 displays a list of maximum alpha and beta textures for the range of Ti6246 discs that have been assessed. Figure 4-19 and Figure 4-20 display the variations in the maximum texture intensities of the beta phase and the alpha phase with the method of disc forging for those production discs that have been EBSD assessed for texture. Similarly, Figure 4-21 and Figure 4-22 display back-to-back variations in maximum textures within individual discs according to the position of samples within the forging.

Changes in texture between the bore, diaphragm and rim of a disc can be compared using EBSD results from a Trent engine IPC7 forging. Figure 4-23 shows beta textures in the bore, diaphragm and rim of the disc. Figure 4-24 shows the corresponding measured alpha pole figures. Note that pole figures use a linear scale.

4.3.3 Cold dwell fatigue testing of production material

The typical optical microstructures of the CDF tested production variants are displayed in Figure 4-25 to Figure 4-28. All these microstructures are acceptable by the current material specification requirements. Figure 4-25 and Figure 4-26 show elongated prior beta grain structures with colonies of aligned primary alpha platelets and no recrystallisation. Figure 4-27 shows large relatively equiaxed beta grains with limited grain boundary recrystallisation and a distribution of fine Widmanstätten primary alpha platelets. Figure 4-28 shows a mixed

microstructure of unrecrystallised and recrystallised beta grains with fine Widmanstätten primary alpha platelets.

Mechanical test results for the "grain cluster" IP5 disc specimens are given in Table 4-8. Test results for the "randomly textured" clutch shaft forging material are given in Table 4-9. The majority of both the IP5 test specimens and the clutch shaft specimens failed at surface origins. Some sub-surface failures were observed for each material. A typical sub-surface fracture is displayed in Figure 4-29.

An S-N plot of cyclic vs. dwell fatigue results for the grain clustered IP5 disc is given in Figure 4-30. The S-N curve for the clutch shaft material is given in Figure 4-31. It is noted that some test specimens have significantly different grain flow directions according to the position in the forging from which they were sectioned.

CDF test results for the maximum beta texture and the high predicted alpha texture production disc material are listed in Table 4-10. These results are plotted in the S-N curve in Figure 4-32.

As for previous dwell testing the majority of specimens failed at surface origins. No faceted origins were observed on the IP7 specimen fracture surfaces. Two IP3 specimens were observed to initiate from sub-surface facets although these were angled at ~45° to the loading direction [27, 60]. No evidence of load-normal facets was observed. Typical specimen fracture surfaces are displayed in Figure 4-33 and Figure 4-34.

4.3.4 Cold dwell fatigue testing of non-standard Ti6246 microstructures

The heat treatment experiments outlined in Table 4-5 produced the optical microstructures displayed in Figure 4-35 and Figure 4-36. For the beta heat treatment the colony size was determined using the Heyn mean linear intercept technique (ASTM E112). A total of over

200 measurements of colony dimensions were made. Comparison to a typical Ti685 optical microstructure (taken from the bore of a HPC disc) shows that even in an extreme microstructural condition the colony size in Ti6246 was still considerably smaller than that in production Ti685 disc material. The comparison of optical colony size in the two alloys is displayed in Figure 4-37. Textures of these microstructures have not been characterised.

Testing of the small gauge (alpha + beta) heat-treated specimens gave the results in Table 4-11. The large gauge (alpha + beta) and beta heat-treated specimens gave the results listed in Table 4-12. The S-N curve for the results in Table 4-11 and Table 4-12 is displayed in Figure 4-38.

Following dwell and standard cyclic fatigue testing selected specimens were sectioned and examined for evidence of slip bands and sub-surface cracking. Slip bands were clearly observed in the microstructure of the beta heat-treated test variant. These were usually present across individual optical colonies of alpha platelets. Sub-surface cracking was also noted. Examples are given in Figure 4-39 and Figure 4-40. Slip bands were much harder to observe in the other test variants.

4.4 Discussion

4.4.1 Assessment of optical microstructures

Assessment of production Ti6246 discs has revealed significant variability in optical microstructures. However, for the features that have been assessed there is limited evidence of structures outside of the limits of the relevant Rolls-Royce material specification (both by quantitative and qualitative assessment, although it is noted that the specification is largely photographic rather than numeric).

Primary alpha platelet content is generally found to lie within the limits of the material specification. For the initial assessment of production material the minimum and maximum primary alpha contents were measured at 35.8% and 57.8% respectively. The minimum alpha level is above the specification minimum. The maximum observed is marginally greater than the specification maximum although by visual inspection the microstructure does not appear to be beyond the limits of the specification photographic standard. By comparison, Attallah et al. used low magnification SEM to characterise Ti6246 in the same microstructural condition and estimated a primary alpha content of ~47.5% ±1.7%. Their work using high magnification SEM was successful in resolving the ($\beta+\alpha_s$) microstructure and estimated a secondary alpha fraction within the beta matrix of 53%, leaving ~25% retained beta phase in the microstructure [158]. Whilst there are limitations associated with phase fraction assessment by SEM image analysis, there is consistency in the assessment technique and broad agreement with other published findings [158].

Systematic differences between the forging methods can be noted from the figures contained under the results section. Isothermally forged discs are generally observed to show higher aspect ratio prior beta grains whilst hot die forged discs show elongated grains although not

to the extent of isothermal forgings. Hammer forged discs show the most equiaxed grain shapes. This suggests either lower overall forging strains (dependent on the finish forging geometry) or greater levels of recrystallisation [159].

For microstructures of equiaxed grain shapes the maximum MLI dimension of beta grains is observed to conform to the maximum grain size based on analysis of the material specification. The highest aspect ratio beta grains are estimated to have length to width ratios of ~6:1 although there is no criterion for a maximum grain aspect ratio in the material specification. This is due to the impracticality of such quantification, as beta forging is deliberate and the sectioning plane of disc surfaces varies with respect to grain flow.

In terms of grain boundary alpha layers and alignment of primary alpha platelets in the optical microstructure, results show that the hammer forging method often produces more marginal structures. Some hammer forged microstructures have been observed which have grain boundary alpha structures and/or colony sizes on the limits of the material specification. The isothermal forging route tends to produce the most deformed grain boundary structures whilst the two hot die press forging methods produce microstructures that are similar in terms of the degree of alignment in the microstructure and the grain boundary alpha structures.

The isothermal forging method is believed to produce the most deformed grain boundary alpha structures because of the continuous application of a low strain rate at a near-constant temperature. This is thought to allow the introduction of forging strain into the microstructure (including the prior beta grain boundaries) without inducing extensive recrystallisation [46, 159]. On cooling following forging in the beta phase field, alpha layers are then able to precipitate on heavily deformed prior beta grain boundaries [22, 158].

By comparison, hammer forging at low strain rates in high cooling rate locations (i.e. near surfaces) allows relatively equiaxed large scale prior beta grains to develop undeformed grain boundary alpha layers. It is unclear as to why the grain boundary alpha layers in hammer forgings appear more continuous than those forming in hot die press and isothermal forgings when subject to similar effective strain levels. Potential explanations may involve the differences in forging temperatures and cooling rates experienced by different forging methods and the effect on transformation kinetics, i.e. when alpha layers form on the beta grain boundaries [22].

Although optical assessment shows low strain hammer forged microstructures do not usually grow large (i.e. high aspect ratio alpha platelet) "side-plate" colonies there is evidence of optical alignment of short aspect ratio alpha platelets that extend over large proportions of individual grains with a growth axis approximately parallel to the grain flow direction. This is considered to represent a potentially more dwell sensitive microstructure as large regions of common texture may exist in grains for which neighbouring colonies/grains with a favourable orientation relationship to allow off-loading of stresses and basal plane facet formation [84, 90]. Examples of hammer-forged microstructures have been noted with colony areas in excess of the material specification recommended maximum size.

No clear relationship can be observed between the prior beta grain aspect ratio and the gradings of grain boundary alpha structures. This is an unexpected result as a higher prior beta grain aspect ratio is an indication of a greater level of work in the material (disregarding the possibility of recrystallisation to form equiaxed grain morphologies with undeformed boundaries) and an expected consequence would be the formation of more heavily deformed grain boundary alpha structures [38]. Similar observations are made for

assessment of primary alpha platelet alignment, i.e. no correlation is clearly observed when related to beta grain aspect ratio.

Plots of other variables, for example gradings of alpha platelet alignment against blocky alpha, show no clear correlations exist for the microstructures of production disc Ti6246. Whilst trends can be identified relating to the different forging routes, no clear connections can be established between the different microstructural variables.

Hot die and isothermal forgings were noted to show an increased tendency to form side-plate colonies. These aligned alpha platelets grow from prior beta grain boundaries at angles approximately 70-90˚ to the boundary length. For elongated prior beta grains this is observed as alignment of platelet long axes near parallel to the forging compression axis. A typical example of side-plates growing from a grain boundary was given in Figure 4-16. Hammer forgings do not appear to show extensive side-plate formation as regularly as the hot die and isothermal forgings. This is potentially because recrystallisation occurs more readily in hammer forgings, the consequence being that the long prior beta grain boundaries of heavily deformed grains allowing the formation of large side-plate colony structures are less frequently observed. The reason for the lack of formation of side-plates in low strain equiaxed regions of hammer forgings is unclear. It is assumed to relate to high temperature losses on forging leading to temperatures low enough to favour precipitation of alpha structures within the prior beta grain rather than precipitation and growth from the grain boundaries [22].

Unrecrystallised high strain regions of hammer forgings were noted for a tendency to form aligned primary alpha platelets significantly different to conventional side-plate structures. There is no similar example in the reviewed literature. Often, contained within a single prior

beta grain are coarse alpha platelet features aligned with the direction of grain flow. Surrounding these coarse platelets a distribution of finer alpha platelets lying in parallel can sometimes be observed. In these structures the primary alpha platelet long axes therefore lie normal to the forging compression axis. The coarse platelets have been noted to show evidence of exposure to deformation. This suggests that they may have formed during the forging operation. An example is displayed in both Figure 4-13 and Figure 4-17. If this is the case, the potential sequence of events for the formation of these colonies may be as follows; coarse primary alpha platelet features form during beta finish forging, fine primary alpha platelets (common optical alignment) precipitate during SHT, secondary alpha platelets precipitate during ageing.

A comparison of the different forging routes and the extent of blocky alpha in the resulting disc microstructures shows no clear differences. A comparison of gradings of blocky alpha features according to the plane of sectioning highlighted that blocky alpha effects are most pronounced in the radial/tangential plane. This effect is most pronounced for microstructures in the diaphragm region of discs. This is presumably because the high forging strain (and hence high grain flow) favours the formation of alpha platelets that lie in the plane the diaphragm. It is therefore concluded that blocky alpha structures are the result of a sectioning effect through alpha platelets at a shallow angle.

Optical examination revealed no beta fleck effects in the range of production microstructures included in the assessment. Based on this observation it is inferred that chemical segregation of beta stabilisers is not a problem affecting Ti6246 disc forgings.

Secondary alpha platelets can be observed in all production microstructures as a basketweave (Widmanstätten) distribution in the retained beta matrix. Precipitation

behaviour appears unaffected by the nature of the surrounding primary alpha platelets, e.g. aligned platelets growing from a prior beta grain boundary, Widmanstätten platelets forming within a beta grain, or aligned platelets forming within a beta grain. In hammer forgings where coarse and fine primary alpha platelets are observed to align with the grain flow, high magnification analysis of the microstructure reveals the presence of basketweave secondary alpha platelets. The microstructures in these different cases are displayed in Figure 4-15, Figure 4-16 and Figure 4-17.

The plot in Figure 4-18 shows how with increasing elongation of the prior beta grains there is little change in the alpha and beta texture measurements. Between estimated aspect ratios of 1:1 and 4:1 the majority of texture intensities (for both phases) are between 4-7x random. Only at high aspect ratios (> 5:1) is the beta texture observed to increase significantly. As these high texture measurements form only a small proportion of the full assessment they do not provide definitive evidence that high aspect ratio beta grains equate to high beta textures. Furthermore, there are some microstructures with highly elongated beta grains that show relatively weak beta (and alpha) textures. This is likely to be related to recrystallisation leading to significant reductions in texture [159].

In summary some optical features have been observed that lie outside the specification limits. The most notable exceptions are colony features and grain boundary structures in large equiaxed grain (i.e. low forging strain) bore regions of hammer forgings. These are infrequent occurrences and the majority of the microstructures examined as part of the optical assessment are within the bounds of the material specification.

4.4.2 Assessment of crystallographic textures

As discussed under the previous section there appears to be little or no correlation between prior beta grain elongation and maximum beta and alpha texture intensities. There is also limited evidence of increased texture intensities correlating to increasing levels of optical alignment of primary alpha platelets in microstructures.

From results (see Figure 4-19) the hammer forging technique appears to generate the lowest beta texture intensities. This general trend is presumed to relate to the observation of higher levels of beta grain recrystallisation in hammer forgings [159].

Hot die forgings show increased variability of beta texture with some maximum intensities of 2-3x random and other measurements up to ~15x random. Most of these differences in beta texture are observed to relate to the location within a disc (see Figure 4-21). Hot die forged discs that show low (3-4x random) beta texture in the bore and/or rim also show high (>10x random) textures in diaphragm sections. Similar observations of high beta textures in diaphragm (and rim) sections of isothermal forgings were also made. Figure 4-21 confirms that in general disc bore locations show the lowest beta texture intensities.

Alpha texture intensities generally appear to be more consistent at moderate values (5-10x random). Those discs with very high beta texture intensities were not observed to show similarly high alpha textures, i.e. strong variant selection does not occur in these forgings. Figure 4-20 shows little relation between the forging method and alpha texture. Figure 4-22 shows similar results in terms of a lack of correlations between disc region and maximum alpha texture.

The strongest alpha textures are observed in hammer and isothermal forgings. Results show that stronger alpha textures in isothermal forgings appear to translate from strong beta

texture intensities. By contrast, where strong alpha textures are present in hammer forgings they seem to have resulted from variant selection occurring during the phase transformation from relatively low/moderate beta texture intensities.

It is noted that the percentage of EBSD maps indexed as beta phase (see Table 4-7) is low (typically less than 15% area or 750 data points) and as such the reliability of the data in comparison to alpha phase measurements (typically in excess of 60% area or 2950 data points) is low. Results are therefore assessed with caution based on the available data. Further support for the trends highlighted in this discussion could be obtained with the use of the X-ray diffraction technique [160, 161]. SRAS would also provide an indication of the size of regions of common texture (macrozones) [162].

4.4.3 Cold dwell fatigue testing of production material

Fatigue testing of conventional production disc forging microstructures has not provided evidence of sensitivity to CDF behaviour. This conclusion is based on both the absence of load normal fatigue facets on specimen fracture surfaces and the relatively low reduction in cyclic life (only at high stresses).

The production material testing covered a range of forging conditions and resulting microstructures and textures. The micrographs in Figure 4-25 to Figure 4-28 indicate that a range of microstructures have been tested. Both the Trent IP5 disc and the clutch shaft forging microstructures show evidence of the existence of alpha colonies (potentially acting as individual ESUs) in their optical microstructures. In comparison the IP3 and IP7 disc microstructures show Widmanstätten alpha platelet arrangements. Both microstructures show evidence of recrystallisation. In the IP3 hammer forging equiaxed prior beta grains can be distinguished with some recrystallisation on grain boundaries. Again, partial

recrystallisation has occurred in the IP7 disc although the fact that there is a strong beta texture indicates that heavily deformed unrecrystallised grains remain in the microstructure (these grains are difficult to distinguish based on the micrograph in Figure 4-28).

The dwell testing results for the IP5 disc show a limited life debit at lower stresses (see Figure 4-30). As the test stresses were increased some of the CDF tests have displayed low lives to failure. These failures are believed to be the result of general yielding of the specimens rather than dwell fatigue. Specimen fracture surfaces show no evidence of load normal facets to suggest dwell fatigue sensitivity. In addition, the testing of specimens in radial, tangential and 45° orientations provided no evidence of a change in fatigue behaviour according to test direction [152].

Testing of the clutch shaft forging showed some low cyclic lives both in LCF and dwell tests. Examination of the fracture surfaces revealed these specimens failed through general yielding behaviour rather than facet formation. A grain flow of ~45° was noted for those specimens with low cyclic lives. This was attributed to sectioning of specimens from a location in the forging where grain flow was at 45° to the radial direction. The result of this sectioning effect was a lower yield strength which was believed to have allowed the early cyclic failures [152]. Published work suggests an increase in effective slip length for grain boundary orientations at 45° to applied stress as in figure 2-36 [27, 38, 60]. Aside from these premature failures, the clutch shaft material was concluded not to be cold dwell sensitive as some dwell specimens had shown cyclic lives close to those of standard LCF tests and there was no evidence of load normal facet formation [16].

Testing of the maximum production alpha and beta disc textures gave the cyclic life distribution displayed in Figure 4-32. The IP3 disc showed a low debit on cyclic life under

CDF at stresses up to a high percentage of the UTS. IP7 disc (maximum beta texture) results at lower stresses showed a low reduction in cyclic life with dwell loading. Higher test stresses led to some much larger debits on life. The two low cycle to failure results were attributed to the exhaustion of ductility at test stresses close to the UTS. A ductile micro-void coalescence fracture surface failure was observed in both cases again providing evidence that the alloy is not dwell sensitive [152].

4.4.4 Cold dwell fatigue testing of non-standard Ti6246 microstructures

Dwell fatigue testing of conventional beta finish forged, alpha-beta solution heat-treated and aged microstructures showed no significant CDF effect. There was no significant reduction in cyclic life even at very high percentages of UTS. In addition the fractographic examination of fatigue specimens revealed no load normal facets.

Potential mitigating factors producing non-dwell sensitive behaviour in Ti6246 were thought to include the influence of secondary alpha platelets and the level of retained beta content in the final microstructure. Secondary alpha platelets may prevent the formation of long planar slip bands and reduce the effective slip length of Ti6246 in its conventional microstructural form. A high retained beta content may be beneficial as there are a greater number of operative slip systems (relative to alpha phase) to accommodate plastic deformation [28, 69]. Accommodation of slip in the beta phase prevents or reduces the formation of planar slip bands and dislocation pile-up stresses at slip band boundaries. A third potential factor is incoherency at alpha/beta interfaces preventing easy slip transmission [116, 139, 141]. Again this would reduce dislocation pile-up stresses at slip band boundaries. A list of factors affecting slip transmission behaviour is given in Figure 4-41 [131].

Heat treatment trials were undertaken in an attempt to generate a Ti6246 microstructure with increased susceptibility to cold dwell behaviour. Heat treatments were chosen to either reduce or eliminate the effects of beneficial features on mechanical behaviour. Optical assessment was used to select two suitable heat treatments. From the series of experimental heat treatments two selections were made which represented extreme microstructural conditions.

For the (alpha + beta) heat treatment (see Figure 4-35) a temperature close to beta transus was used to re-solutionise aged alpha platelets. A two hour hold was applied to allow time for some of the retained beta matrix to transform to primary alpha platelets, i.e. to reduce the beta matrix content both through the coarsening of existing primary alpha platelets and through the precipitation and growth of new alpha platelets.

As stated earlier, secondary alpha platelets contribute significantly to the mechanical properties of the material because they reduce the effective slip length during deformation. Without their presence, potentially larger slip bands can form, dislocation pile-up stresses increase and CDF behaviour becomes more likely to occur [16, 69]. Decreasing the beta phase fraction would promote deformation in limited alpha slip systems and aid the formation of planar slip bands on single slip systems as associated with CDF behaviour [69].

The second heat treatment, a hold in the beta phase field followed by slow controlled cooling through the transus temperature, was selected to allow the growth of large colonies of aligned primary alpha platelets within the microstructure (see Figure 4-36). The hold above the transus temperature led to the rapid growth of beta grains and a morphological change to equiaxed structures. The colony structures were associated with precipitation and growth of alpha platelets from prior beta grain boundaries. Because of the large grain size

and the slow cooling rate it was possible to grow large regions of aligned platelet structures. These structures should display a consistent Burgers OR between alpha and retained beta phase over large areas. Such a microstructure should provide easy dislocation paths for the formation of planar slip bands under certain applied load orientations [114, 139].

As for testing of production disc microstructures, large gauge fatigue specimens were used (for most tests) in order to increase the volume of material on test. This was to increase the probability of neighbouring 'units' with crystal orientations suitable for CDF behaviour, i.e. stress redistribution. Fractographic examination indicated that no load normal facets were present on the fracture surfaces of any specimens. Angled facets could often be observed on the fracture surface of beta heat-treated specimens, under both dwell and cyclic loading [84]. By comparison the fracture surfaces of (alpha + beta) heat-treated specimens showed no clear facets. For most specimens the fracture origin was unclear although in some cases it was possible to distinguish surface or sub-surface initiation sites. These could not be clearly related to the form of test (i.e. dwell/cyclic) or the microstructure.

From the plot of S-N behaviour in Figure 4-38 it can be seen that there was no large reduction in cyclic life under CDF loading for either beta heat-treated specimens or (alpha + beta) heat-treated small gauge specimens. As the test stress was increased to a higher proportion of the material UTS a larger CDF debit was noted for the beta heat-treated specimens. This was attributed to cold creep behaviour rather than dwell fatigue sensitivity [163, 164]. This conclusion was supported both by the absence of load normal facets on specimen fracture surfaces and by strain accumulation monitoring showing greater disparities between 15cpm and two minute dwell strain accumulation levels with increasing test stresses.

In the case of the large gauge (alpha + beta) heat-treated specimens, weld-line failures occurred for one cyclic test and one dwell test. Because only six tests were performed in total this left only two cyclic and two dwell tests from which to assess behaviour. A significant debit on life was observed under CDF loading. However, because of the limited data and the non-dwell sensitive behaviour of the small gauge specimens it was suggested that the life debit for the large gauge specimens could be attributed to data scatter. Further evidence supporting this included fractographic work indicating that dwell fatigue specimens displayed purely ductile failures (micro-void coalescence) [163].

It was concluded from fatigue test results that Ti6246 in the various microstructural conditions does not show a significant CDF debit until subject to stresses in excess of 90% of UTS [163]. This compares favourably with data relating to alloys such as Ti685, Ti834 and Ti829 for which notable life reductions are observed at much lower UTS fractions [16, 81, 102, 164].

Following on from testing, examination of (alpha + beta) heat-treated test specimens did not identify clear slip traces in the microstructure. It is unlikely that slip traces would extend over significant length-scales given the Widmanstätten nature of alpha platelets and the relatively high retained beta content in the microstructure [69].

By comparison beta heat-treated microstructures clearly showed planar slip traces extending across individual alpha platelet colonies. In most cases it was possible to observe multiple slip traces running in parallel across single colonies. These slip traces were observed at angles between ~40-50° from the loading axis. Some evidence of sub-surface cracking along these slip bands was noted (see Figure 4-40). No observations were made of slip traces traversing multiple optical colonies within a single prior beta grain. Similarly there was no evidence of

slip transmission between alpha colonies in neighbouring prior beta grains. Based on these observations and the lack of load normal facets on the fracture surfaces of dwell tested specimens it is concluded that no significant stress off-loading occurs between weak and strong crystal orientations. This is despite a microstructure similar to that of the known dwell sensitive alloy Ti685 [16, 81]. The major difference between the alloys is the greater beta stabilisation of Ti6246. This chemistry difference results in thicker beta films in a Ti6246 colony microstructure. Whilst fatigue loading still allows the formation of planar slip bands the lack of off-loading behaviour suggests that stress concentrations at the slip band boundaries are insufficient to cause failure. The alternative explanation suggests a lack of sufficient material on test to achieve a combination of crystal orientations suitably orientated to cause dwell off-loading [16].

4.5 Conclusions

Assessment of optical microstructures has indicated that Ti6246 in production disc forgings usually conforms to the requirements of the material specification. Some microstructures have been observed that may lie outside the acceptable standards of the specification. One example non-conformance is alpha platelet colonies of a single orientation over areas exceeding that of the maximum stated colony size. Another example is continuous grain boundary alpha layers present in some low strain microstructures.

From the optical assessment there is also evidence of systematic differences between the microstructures produced using different forging methods. Hammer forgings have indicated a greater propensity for recrystallisation than hot die and isothermal forgings.

There is also evidence to suggest that hammer forgings are more likely to form networks of continuous and undeformed grain boundary alpha layers and large colonies of aligned alpha platelets. Both these observations are associated with detrimental mechanical performance.

Assessment of the texture in Ti6246 discs has shown that texture intensities are usually limited to maximum values of 3-8x random. This observation is made for both beta and alpha textures. In general there is little evidence of a strong variant selection mechanism in Ti6246 production disc material. Stronger beta textures are usually present in the diaphragm of disc forgings. Bore locations usually show lower textures. This is assumed to result from the geometry of the forging and the levels of forging strain that the respective regions of the forging receive. In addition it is noted that the weakest beta textures usually occur in hammer forgings. This observation may be attributed to an increased tendency for recrystallisation in hammer forgings.

When strong beta textures are present in disc material it is usually observed that a (relatively) strong alpha texture forms. There are some instances where strong alpha textures have resulted from weaker beta textures, i.e. variant selection has occurred on phase transformation during post-forge cooling. Hammer forgings are noted to show the greatest evidence of variant selection leading to stronger alpha textures.

The dwell fatigue testing of the IP5 disc and the reference clutch shaft material has provided no indication of a susceptibility to dwell sensitive behaviour in beta forged, (alpha + beta) solution heat-treated and aged Ti6246. In the majority of tests a surface origin can be observed on the fracture surface. Where sub-surface failures have occurred the origins have been noted to form at angles approximately 45° to the loading direction. There are also some specimens that have failed at very low cyclic lives. These are accounted for by the fact that testing used stresses at very high proportions of the material UTS. Cold creep mechanisms are suggested, leading to an exhaustion of ductility and consequent failure through micro-void coalescence.

Mechanical testing of the extremes of production Ti6246 microstructures (high predicted alpha texture, maximum measured beta texture) showed no evidence of dwell fatigue sensitivity. Some sub-surface specimen failures were noted although fractographic analysis identified no load normal faceting. Additionally dwell tests were performed up to very high proportions of UTS for which no significant reduction in cyclic life was recorded.

Ti6246 also does not show CDF sensitive behaviour in non-standard microstructural conditions. Neither of the tested heat treatments provided evidence of load normal facets or a debit in cyclic fatigue life.

For beta heat-treated specimens planar slip bands have been observed in optical microstructures extending across alpha colonies. There was no evidence of transmission of slip traces across the boundaries of optical colonies, either within prior beta grains or across the boundaries between different prior beta grains. Slip bands form at angles to the loading direction (~45°) and it is presumed that angled facets on specimen fracture surfaces correspond to cracks that have initiated on such slip bands. Some sub-surface cracking has been observed on slip bands in support of this assumption.

(Alpha + beta) heat-treated specimens (with no secondary alpha precipitates) display no clear evidence of slip bands. Based on the dwell testing behaviour it can be concluded that secondary alpha platelets alone are not the mitigating factor preventing CDF sensitive behaviour in Ti6246 (assuming that planar slip band formation is a pre-requisite for CDF). Based on the microstructures that have been tested (and the behaviour of other alloys) it is postulated that a key factor in preventing CDF behaviour in Ti6246 is the high retained beta fraction that results from the 6wt.% molybdenum content.

NB:- This is the most detailed survey thus far undertaken of microstructural features in Ti6246 to the R-R material specification for the alloy. Whilst some features were identified as marginal to the current specification requirements, these requirements were defined based on more limited work undertaken during material development.

4B Cold dwell fatigue behaviour in Ti6246 alloy – Figures and tables

4.6 Introduction and experimental method

Figure 4-1 – Grain clusters observed on the diaphragm of a compressor disc rectilinear in an etched condition

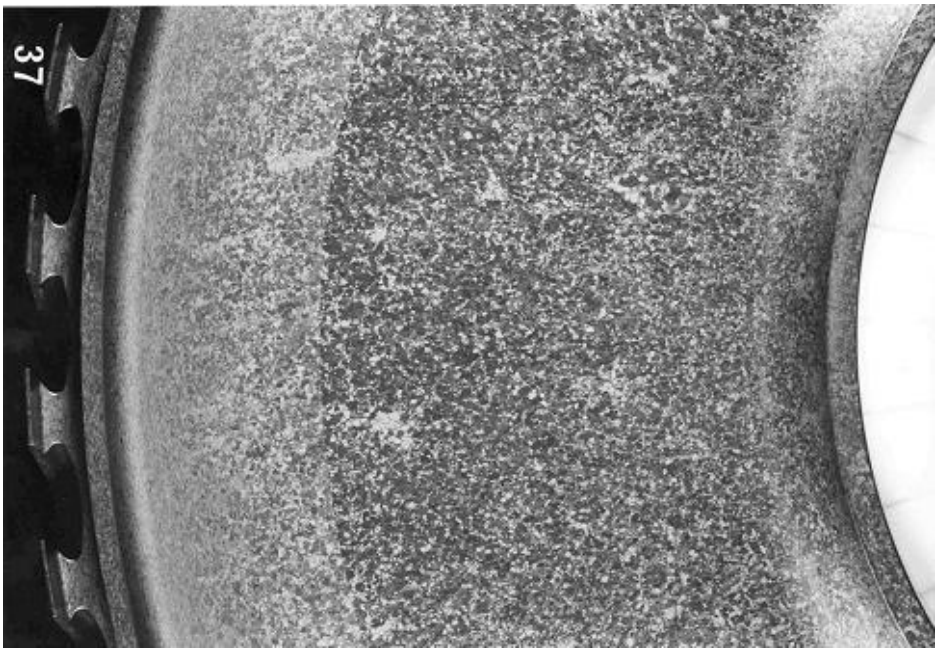

Figure 4-2 – Grain clusters observed on the diaphragm of a machined compressor disc

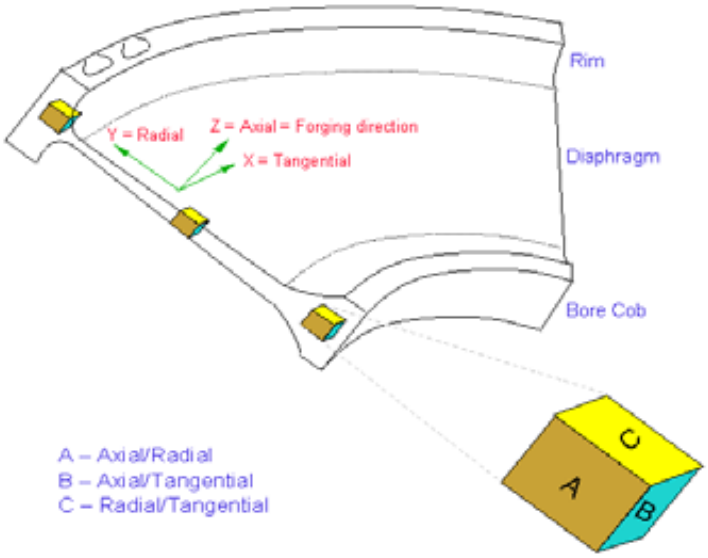

Figure 4-3 – Disc geometry and location of metallurgical samples [71]

Table 4-1 – Details of samples included in initial Ti6246 optical microstructure assessment survey

Sample	Sample Location	Forger	Method	Disc
3	Bore	Ladish	Isothermal	T800 IP6
6	Bore	Ladish	Weber Hot Die	T800 IP5
T9	Bore	Wyman Gordon	Press	T800 IP6
V9	Bore	Wyman Gordon	Press	T800 IP6
12	Bore	Ladish	Isothermal	T500 HP1
13	Rim	Wyman Gordon	Hammer	T500 HP1
14	Diaphragm	Wyman Gordon	Hammer	T500 HP1
15	Bore	Wyman Gordon	Hammer	T500 HP1
18	Bore	Ladish	Weber Hot Die	T500 IP1
21	Bore	Wyman Gordon	Hammer	T500 IP1
22	Bore	Wyman Gordon	Hammer	T500 IP7
22Z	Bore	Wyman Gordon	Hammer	T500 IP7
23	Bore	Wyman Gordon	Hammer	T500 IP7
30	Bore	Wyman Gordon	Hammer	V2500 HP7
33	Bore	Wyman Gordon	Hammer	BR715 HP5
36	Bore	Ladish	Isothermal	T800 IP7
42	Bore	Wyman Gordon	Press	T800 IP7
47	Bore (Above Beta Transus)	Wyman Gordon	Press	T800 IP1
51	Bore	Wyman Gordon	Press	T800 IP5

where e.g. T800 IP6 indicates the sample is taken from the Trent 800 Intermediate Pressure Compressor Stage 6 Disc.

Table 4-2a – Samples included in second phase of Ti6246 optical microstructure assessment survey

Sample	Location	Forger	Method	Disc	Relevance
1	Rim	Ladish	Isothermal	T800 IP6	EBSD results show high variant selection
2	Diaphragm	Ladish	Isothermal	T800 IP6	Rim sample shows high variant selection
28	Rim	Wyman Gordon	Hammer	V2500 HP7	Bore samples show aligned large and fine scale alpha platelets
29	Diaphragm	Wyman Gordon	Hammer	V2500 HP7	Bore samples show aligned large and fine scale alpha platelets
34	Rim	Ladish	Isothermal	T800 IP7	Diaphragm shows highest beta texture
35	Diaphragm	Ladish	Isothermal	T800 IP7	Highest beta texture in EBSD assessment
49	Rim	Wyman Gordon	Press	T800 IP5	Bore shows high level of primary alpha platelet alignment
50	Diaphragm	Wyman Gordon	Press	T800 IP5	Bore shows high level of primary alpha platelet alignment
Ladish 5A	Near Axial Centre	Ladish	Hammer	Non-production pancake forging	Assess for grain boundary structures and alpha platelet alignment in hammer forgings
Ladish 11A	Near Axial Centre	Ladish	Hammer	Non-production pancake forging	Assess for grain boundary structures and alpha platelet alignment in hammer forgings
Ladish 12A	Near Axial Centre	Ladish	Hammer	Non-production pancake forging	Assess for grain boundary structures and alpha platelet alignment in hammer forgings
SIP slice D4 S1	Mid-radius	KHI	Hammer	Non-production pancake forging	Assess for grain boundary structures and platelet alignment in hammer forgings

Table 4-2b – Samples included in second optical microstructure assessment

Sample	Location	Forger	Method	Disc	Relevance
22Z Macro-slice	Diaphragm	Wyman Gordon	Hammer	T500 IP7	Bore shows continuous grain boundary structures and alpha platelet alignment
22Z Macro-slice	Rim	Wyman Gordon	Hammer	T500 IP7	Bore shows continuous grain boundary structures and alpha platelet alignment
IP3 Black Forging	Bore	Wyman Gordon	Hammer	T500 IP3	Material selected for mechanical testing
IP3 Black Forging	Diaphragm	Wyman Gordon	Hammer	T500 IP3	Material selected for mechanical testing
IP3 Black Forging	Rim	Wyman Gordon	Hammer	T500 IP3	Material selected for mechanical testing
Clutch Shaft	Clutch Shaft	Ladish	Isothermal	Drive arm	Blocky alpha structures noted in material previously dwell tested
Clutch Shaft	Clutch Shaft	Ladish	Isothermal	Drive arm	Blocky alpha structures noted in material previously dwell tested
MRA90970	Bore	Ladish	Isothermal	T800 IP6	Previously dwell tested disc material
MRA41742	Bore	Ladish	Hot Die	T800 IP5	Previously dwell tested disc material
Industrial Trent IP5	Bore	Wyman Gordon	Hot Die	T800 IP5	Examined for evidence of in-service plastic deformation
Industrial Trent IP7	Bore	-	-	T800 IP7	Examined for evidence of in-service plastic deformation

Table 4-3 – Ti6246 optical microstructure acceptability limits (Criteria based on assessment of R-R Ti6246 material specification)

Criterion	Value
Maximum equiaxed prior beta MLI grain size	500µm
Maximum area of common optical alignment of alpha platelets	0.5mm^2
Maximum area of blocky alpha features	0.2mm^2
Maximum dimension of blocky alpha features	750µm
Maximum primary alpha platelet content	55%
Minimum primary alpha platelet content	28%
Maximum beta fleck affected area	1.25mm^2

Table 4-4 – Grading criteria for assessment of grain boundary (GB) alpha layers in beta forged, (alpha + beta) SHT'd and aged Ti6246

Grading	Criteria
1-2	Little/no GB alpha observed. Well deformed and discontinuous
3-4	GB alpha layers form reasonably frequently. No evidence of boundaries outside of specification limits
5-6	Frequent GB alpha, typically within specification requirements. Some very localised regions of non-conformance may be observed
7-8	Limits of specification acceptability. Some non-conformances may be observed
9-10	Undeformed and continuous GB alpha throughout the sample. Examples can be observed which are outside specification limits.

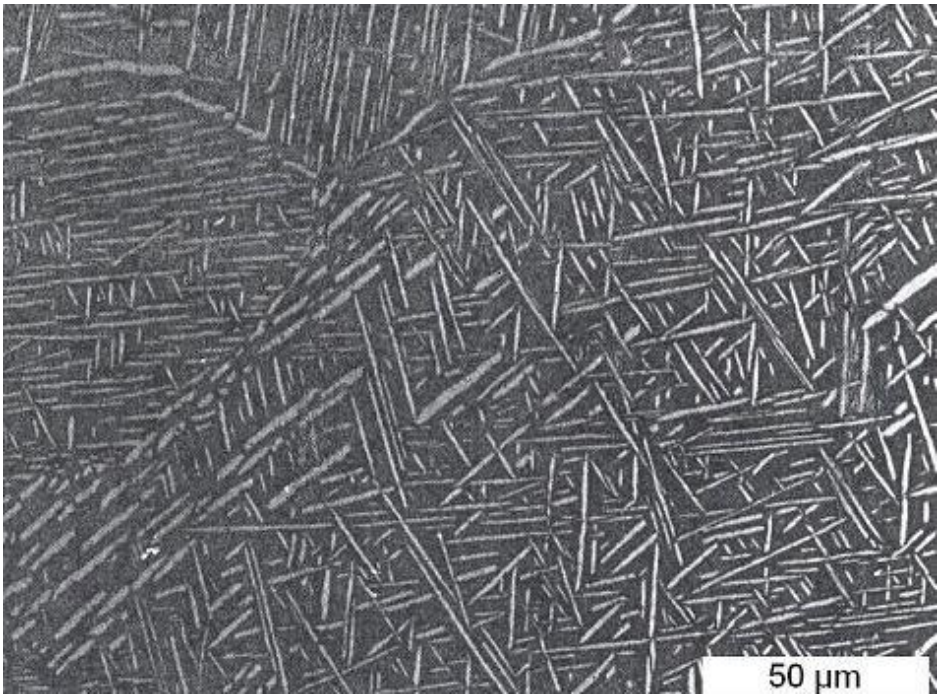

Figure 4-4 – Ideal grain boundary alpha morphology
(Taken from R-R CME brochure for Ti6246)

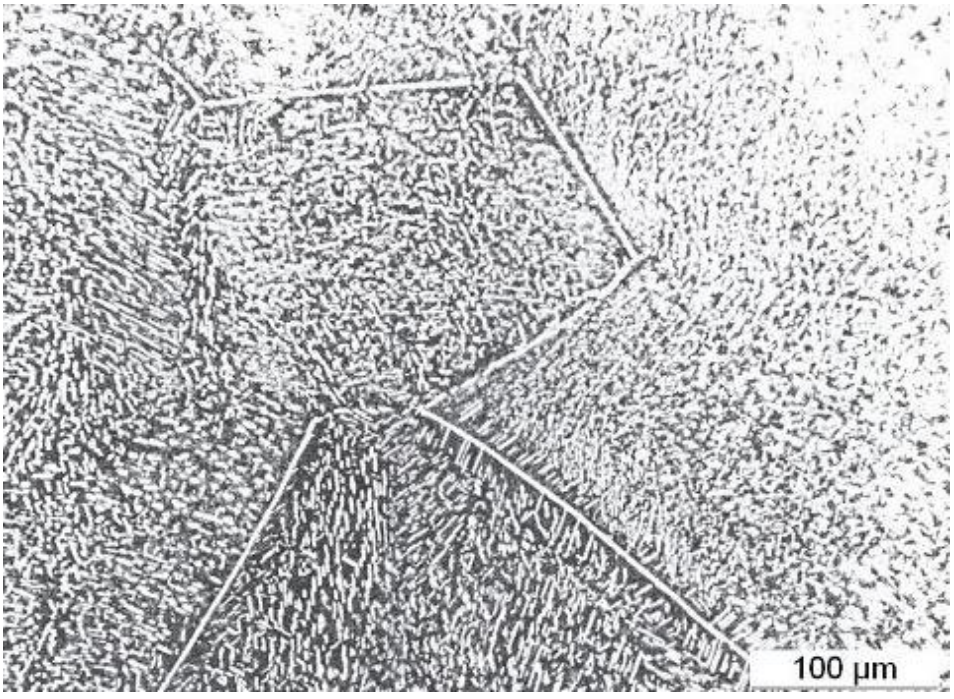

Figure 4-5 - Continuous grain boundary alpha
(Taken from R-R CME brochure for Ti6246)

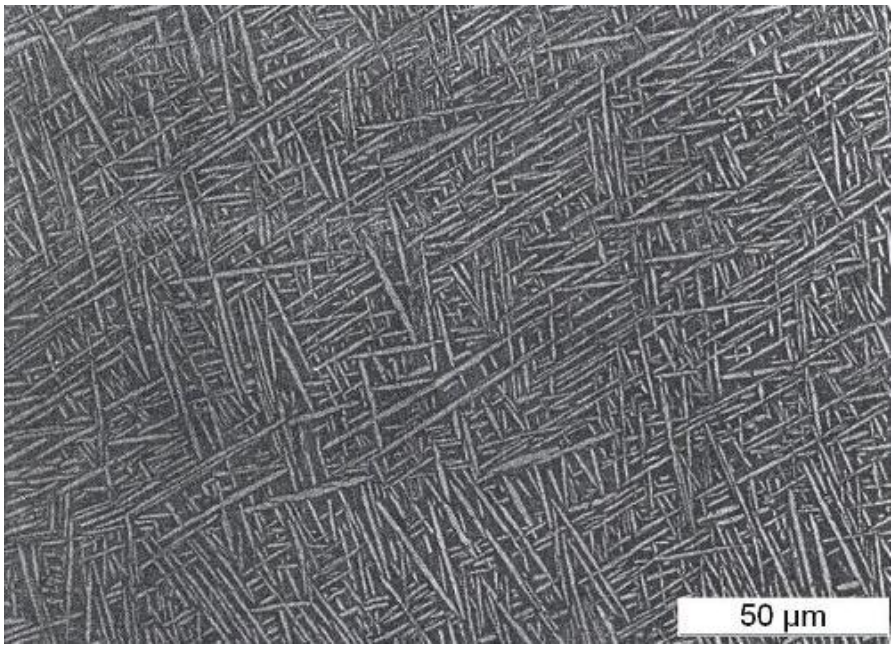

Figure 4-6 – Random alignment primary alpha platelet microstructure (Taken from R-R CME brochure for Ti6246)

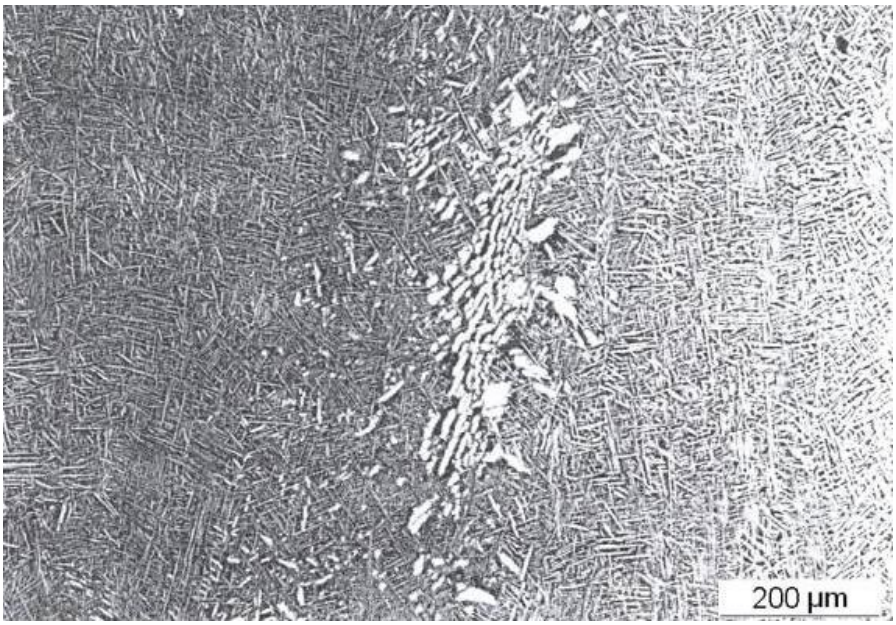

Figure 4-7 – Blocky alpha feature (Taken from R-R CME brochure for Ti6246)

Table 4-5 – Ti6246 heat treatment conditions

Heat treatment	Furnace Temp /ºC	Hold time /hrs	Cooling rate /˚Cmin^{-1}	Finish Temp /˚C	Cooling rate
α/β	910	2	2	820	Water Quench
β	970	2	2	840	Furnace Cool

4.7 Results

4.7.1 Assessment of optical microstructures

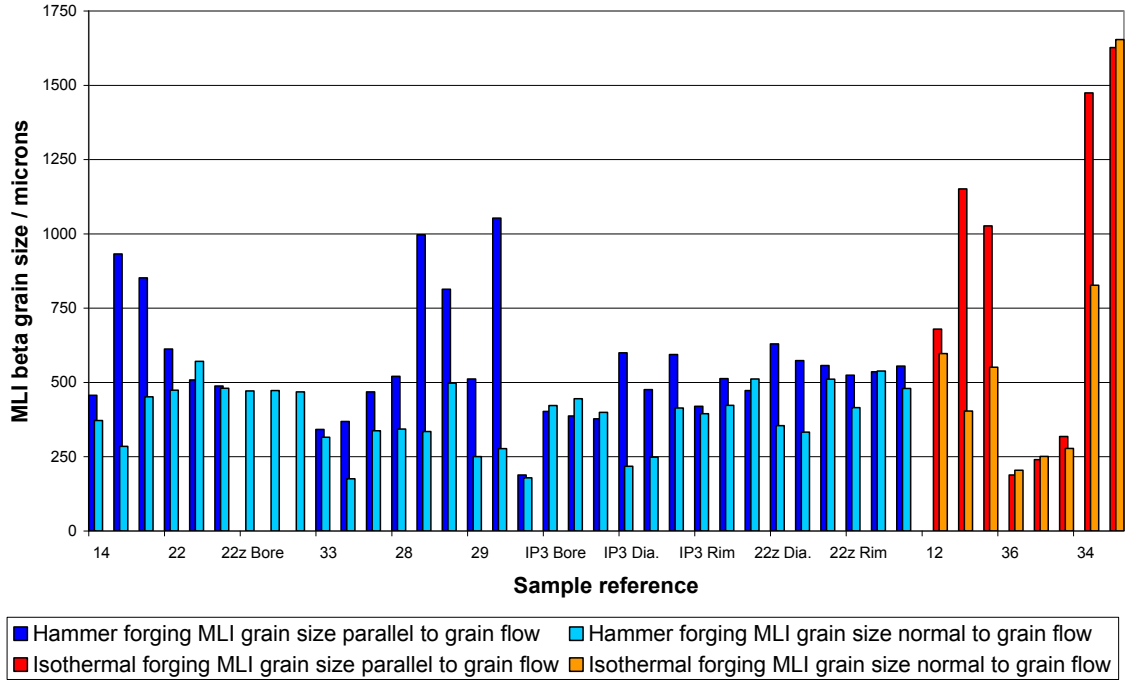

Figure 4-8 – Variation in MLI prior beta grain size for hammer and isothermal forgings (Measurements in directions parallel and normal to grain flow)

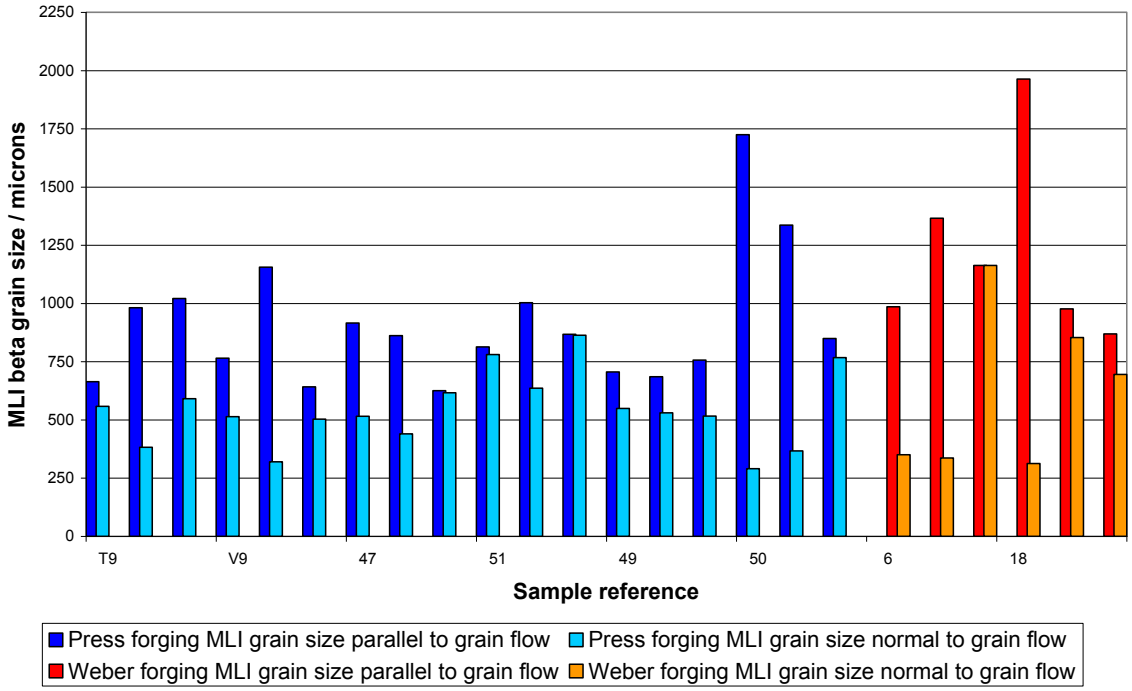

Figure 4-9 – Variation in MLI prior beta grain size for Press and W eber forgings (Measurements in directions parallel and normal to grain flow)

Table 4-6a – Microstructural assessment results (First phase)

Sample	Plane	Grain boundary alpha grading	Primary alpha platelet alignment	Blocky alpha grading	Primary alpha area fraction
3	Ax-Rad	1	2	1	42.8
3	Ax-Tan	1	2	1	42.3
3	Rad-Tan	1	4	2	41.3
6	Ax-Rad	2	4	1	44.9
6	Ax-Tan	3	5	2	44.6
6	Rad-Tan	3	3	7	49.1
T9	Ax-Rad	2	2	2	54.5
T9	Ax-Tan	2	2	4	57.6
T9	Rad-Tan	1	3	5	57.8
V9	Ax-Rad	2	1	1	54.4
V9	Ax-Tan	1	1	2	52.1
V9	Rad-Tan	2	1	4	52.1
12	Ax-Rad	1	1	1	46.8
12	Ax-Tan	1	1	2	48.4
12	Rad-Tan	1	2	1	48.3
13	Ax-Rad	2	3	1	52.8
13	Ax-Tan	7	7	4	40.1
13	Rad-Tan	4	6	3	55.3
14	Ax-Rad	2	4	1	52.8
14	Ax-Tan	2	4	1	48.7
14	Rad-Tan	2	5	2	51.2
15	Ax-Rad	1	2	1	52.0
15	Ax-Tan	1	3	1	46.9
15	Rad-Tan	2	4	2	51.8
18	Ax-Rad	1	1	1	42.7
18	Ax-Tan	3	2	2	41.0
18	Rad-Tan	2	2	2	35.8
21	Ax-Rad	1	2	2	55.1
21	Ax-Tan	3	3	3	50.2
21	Rad-Tan	1	2	2	54.6
22	Ax-Rad	3	1	1	52.9
22	Ax-Tan	4	2	1	51.7
22	Rad-Tan	6	2	1	56.0
22z	Ax-Rad	4	7	1	40.9
22z	Ax-Tan	4	5	2	46.0
22z	Rad-Tan	6	6	1	45.1
23	Ax-Rad	3	2	1	48.8
23	Ax-Tan	3	2	1	47.5
23	Rad-Tan	3	2	2	49.3
30	Ax-Rad	2	4	1	44.2

Table 4-6b – Microstructural assessment results (First phase)

Sample	Plane	Grain boundary alpha grading	Primary alpha platelet alignment	Blocky alpha grading	Primary alpha area fraction
30	Ax-Tan	2	6	1	42.9
30	Rad-Tan	4	5	4	49.5
33	Ax-Rad	1	4	1	51.9
33	Ax-Tan	2	4	1	51.9
33	Rad-Tan	3	5	2	53.7
36	Ax-Rad	2	1	4	44.5
36	Ax-Tan	1	4	5	45.1
36	Rad-Tan	1	1	3	45.1
42	Ax-Rad	1	3	1	47.3
42	Ax-Tan	2	4	1	49.9
42	Rad-Tan	2	3	3	48.0
47	Ax-Rad	2	4	2	57.7
47	Ax-Tan	2	3	3	55.2
47	Rad-Tan	2	4	6	53.7
51	Ax-Rad	1	5	1	38.3
51	Ax-Tan	2	5	2	37.7
51	Rad-Tan	1	5	3	38.7

NB – Sample IDs are given in Table 4-1

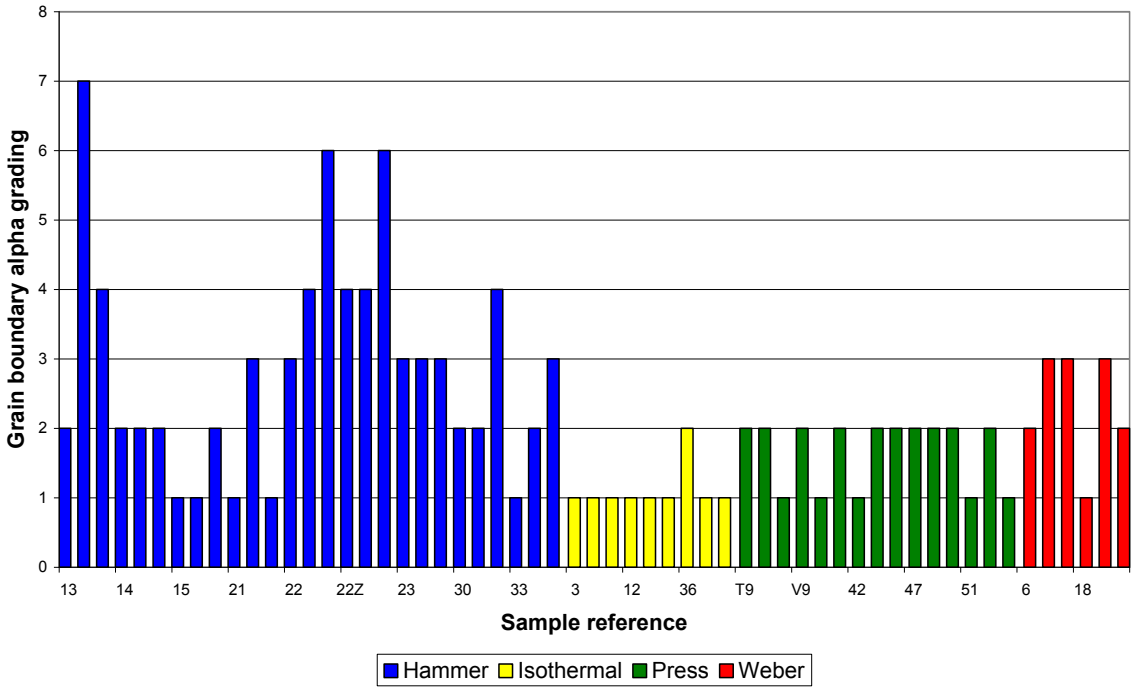

Figure 4-10 – Variation in the grading of grain boundary alpha features in bore of disc forgings for the different forging methods

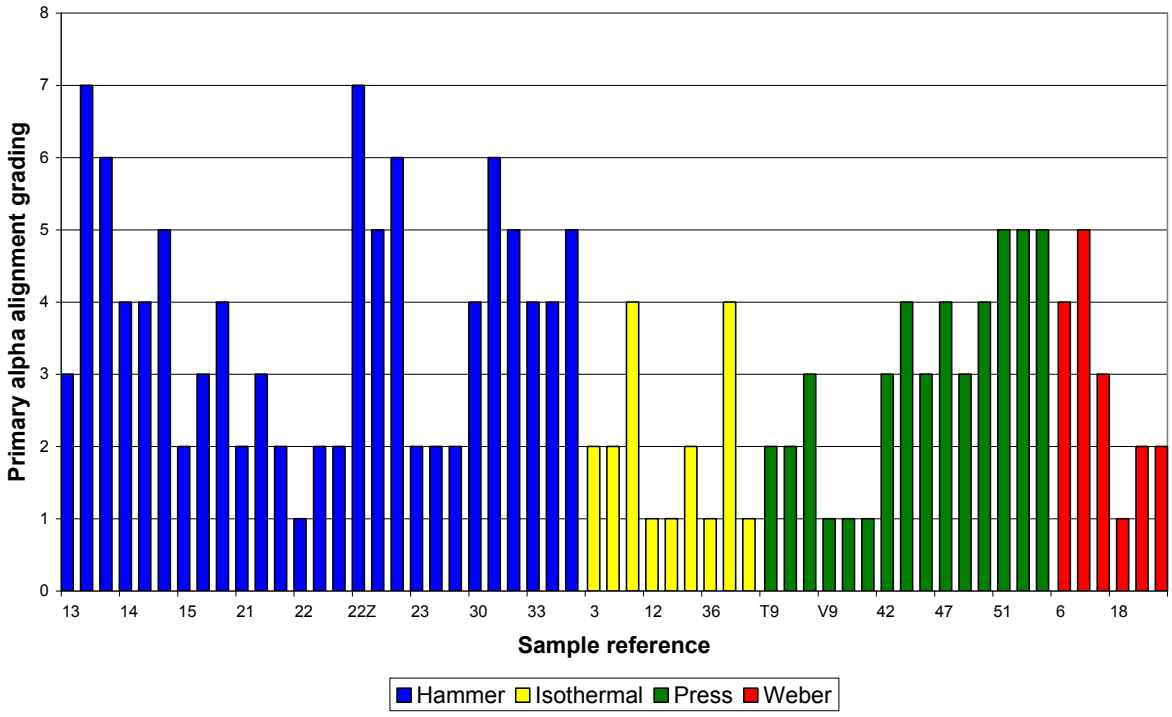

Figure 4-11 – Variation in the grading of primary alpha platelet alignment in bore of disc forgings for the different forging methods

Figure 4-12 – Optical colony in isothermal forged production disc material (Clutch shaft forging)

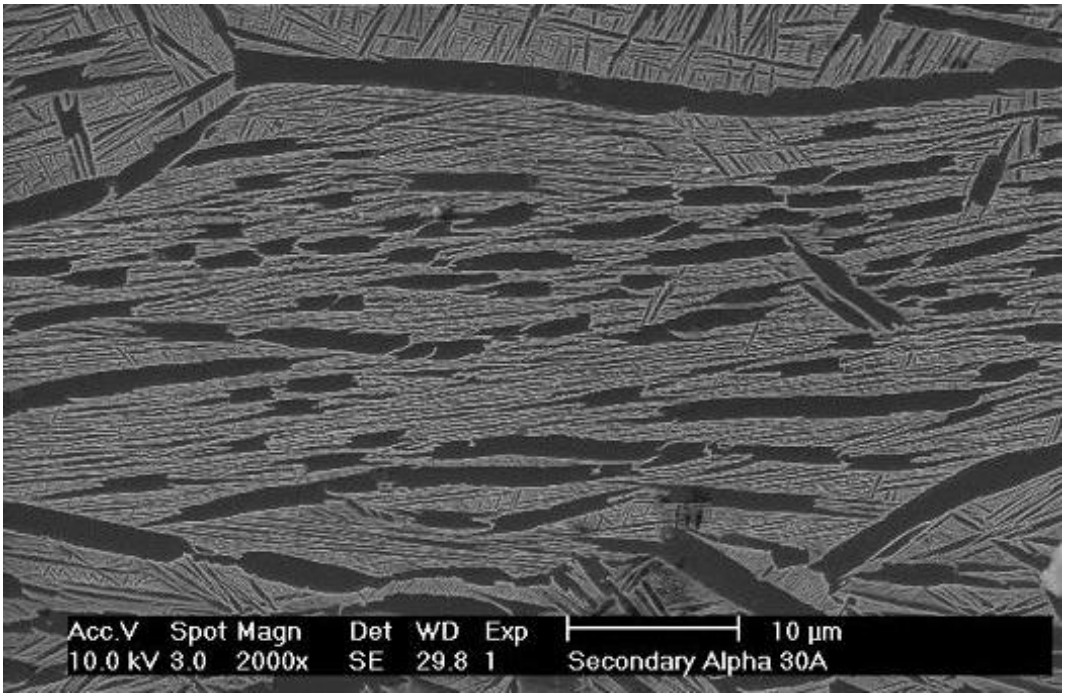

Figure 4-13 – Optical colony in hammer forged production disc material (V2500 HP7 Disc Bore)

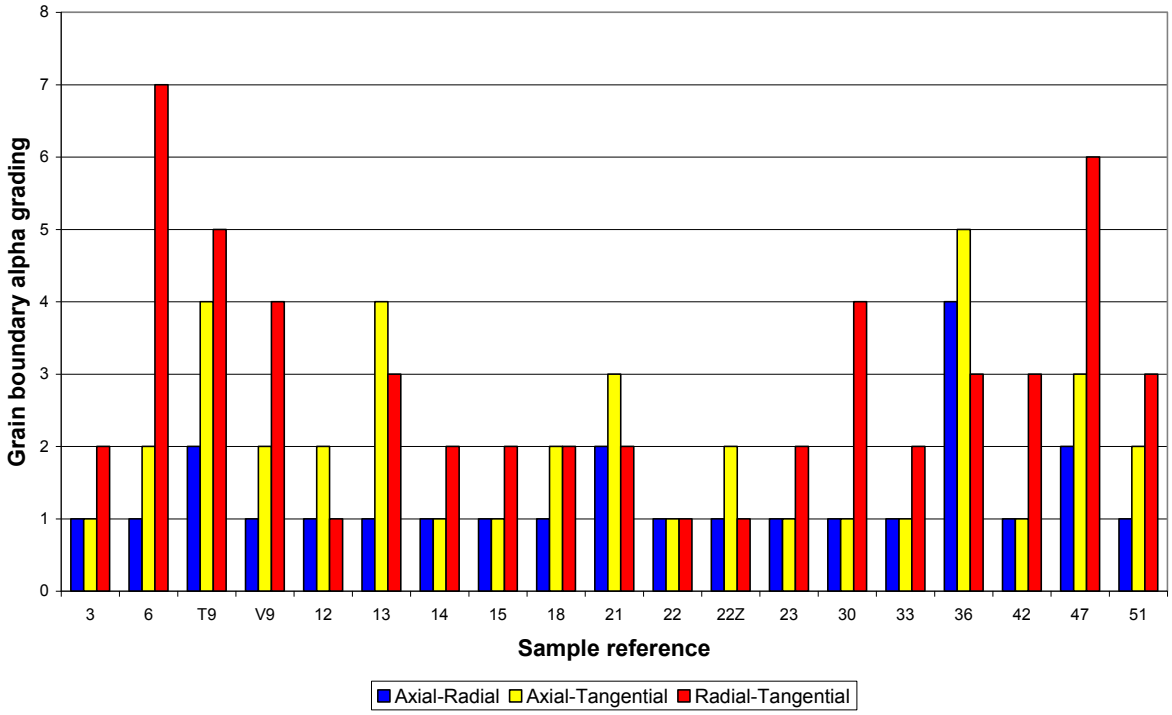

Figure 4-14 – Variation of blocky alpha grading with sectioning plane for samples from the bore location of disc forgings

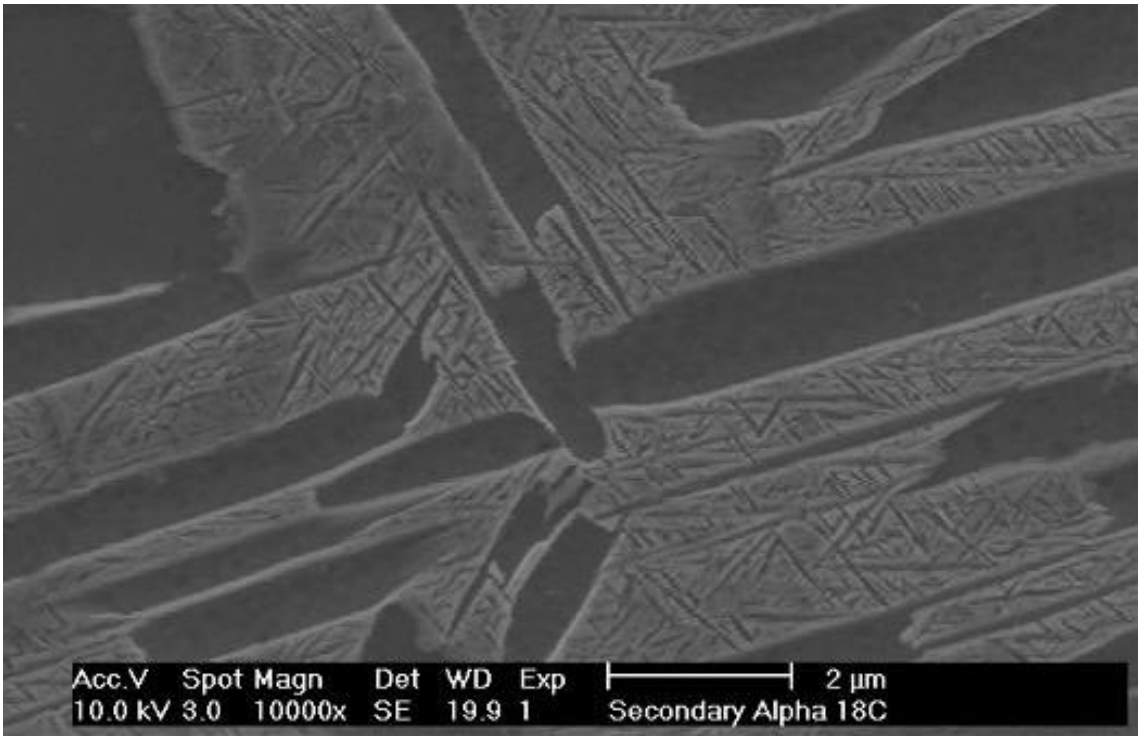

Figure 4-15 – Secondary alpha platelets in W idmanstätten primary alpha platelets (T500 IP1 Disc Bore)

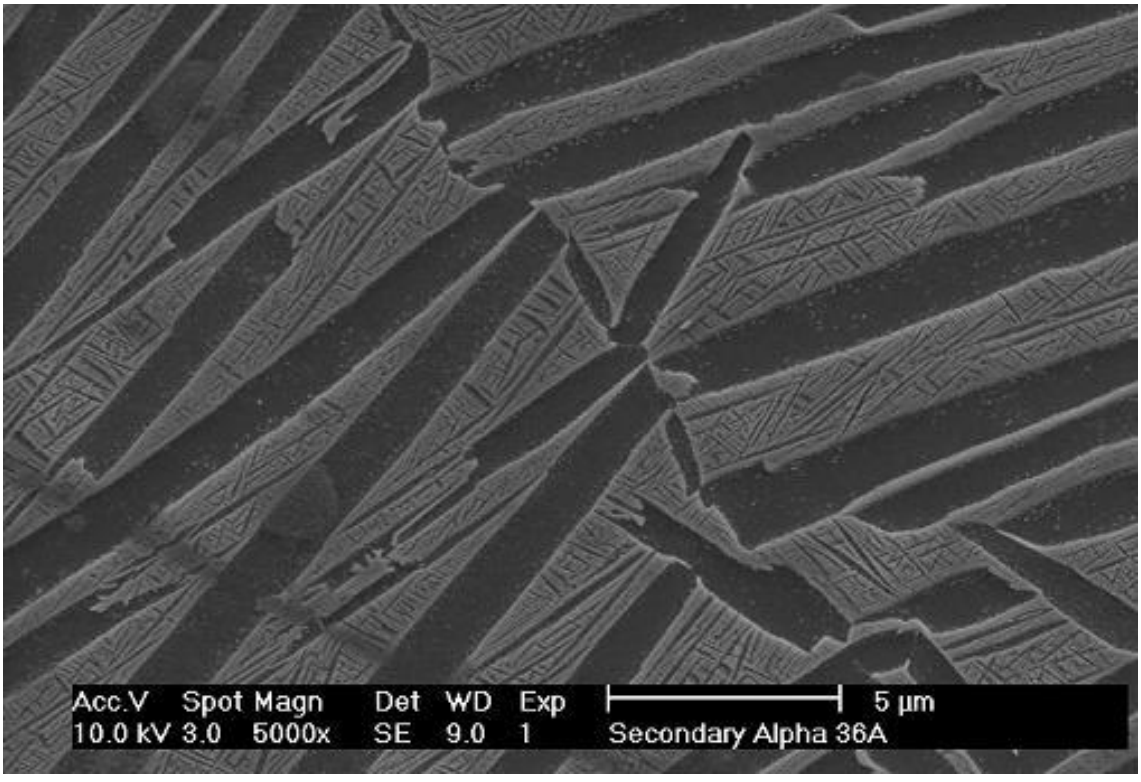

Figure 4-16 – Secondary alpha platelets in aligned primary alpha side-plate colony (T800 IP7 Disc Bore)

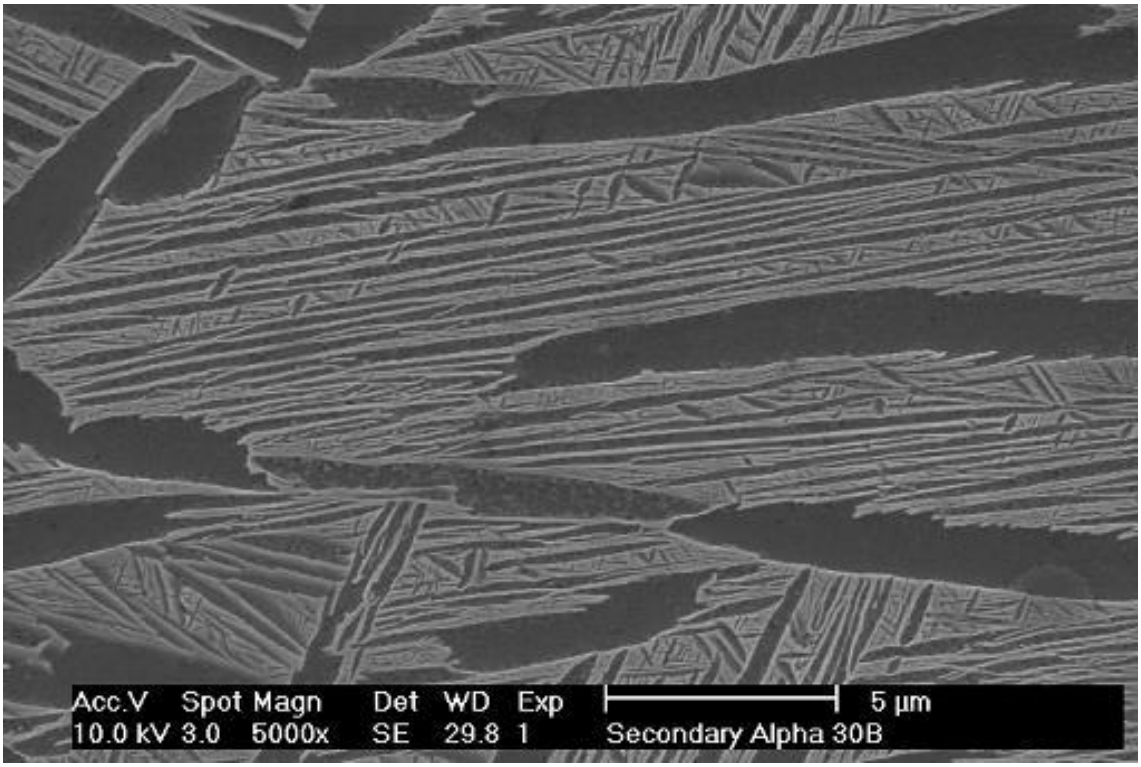

Figure 4-17 – Secondary alpha platelets in aligned colony in hammer forging (V2500 HP7 Disc Bore)

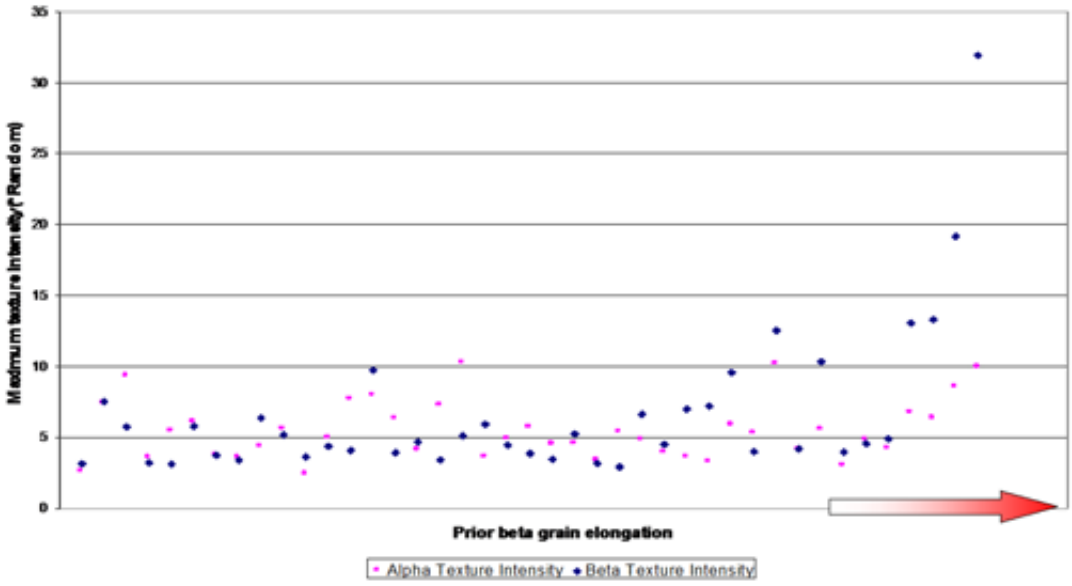

Figure 4-18 – Variation of maximum {0002} alpha and {100} beta phase texture intensities with qualitatively increasing prior beta grain aspect ratio (based on assessment of grain structures on an axial/radial plane)

4.7.2 Assessment of textures

Table 4-7a – Texture assessment results

Disc	Forging	Supplier	Location	Beta %	β max {100}	Alpha %	α max {0002}
T800 IP6	Isothermal	Ladish	Rim	20.8	12.53	72.3	10.15
			Diaphragm	5.3	4.90	39.0	4.20
			Bore	13.4	5.78	52.3	6.07
T800 IP5	Hot Die	Ladish Weber	Rim	18.6	3.91	69.4	6.29
			Diaphragm	4.7	16.14	23.3	5.94
			Bore	15.9	9.58	59.3	5.86
T800 IP6[a]	Hot Die	Wyman Gordon (Livingston)	Rim	-	-	-	-
			Diaphragm	11.2	6.99	66.4	3.59
			Bore	12.0	4.69	58.9	4.11
T800 IP6[b]	Hot Die	Wyman Gordon (Livingston)	Rim	-	-	-	-
			Diaphragm	12.3	7.21	70.6	3.25
			Bore	9.0	9.74	54.4	7.96
T500 HP1	Isothermal	Ladish	Rim	17.0	3.46	66.7	4.50
			Diaphragm	17.9	4.19	70.1	4.11
			Bore	6.5	3.97	48.4	3.01
T500 HP1	Hammer	Wyman Gordon (Lincoln)	Rim	-	-	-	-
			Diaphragm	-	-	-	-
			Bore	12.6	3.17	69.2	3.37
T500 IP1	Hot Die	Ladish	Rim	23.8	3.87	67.2	5.70
			Diaphragm	21.5	13.05	70.8	6.73
			Bore	15.1	2.92	57.2	5.39
T500 IP1	Hammer	Wyman Gordon (Lincoln)	Rim	-	-	-	-
			Diaphragm	-	-	-	-
			Bore	5.6	3.74	53.5	3.74
T500 IP7	Hammer	Wyman Gordon (Lincoln)	Rim	15.0	3.62	62.1	2.40
			Diaphragm	11.0	6.37	70.7	4.33
			Bore	6.8	5.11	65.7	10.25
T900 IP1	Hot Die	Wyman Gordon (Livingston)	Bore (centre)	4.0	3.41	51.1	3.29
			Bore (front)	21.4	3.22	67.1	3.55
			Bore (rear)	15.8	4.00	78.1	5.26
V2500 HP7	Hammer	Wyman Gordon (Lincoln)	Rim	-	-	-	-
			Diaphragm	-	-	-	-
			Bore	4.4	4.56	51.1	4.82
BR715 HP5	Hammer	Wyman Gordon (Lincoln)	Rim	-	-	-	-
			Diaphragm	-	-	-	-
			Bore	10.8	5.92	66.4	3.61
T800 IP7	Isothermal	Ladish	Rim	20.2	19.16	73.6	8.52
			Diaphragm	6.0	31.92	23.8	9.93
			Bore	8.5	6.63	40.2	4.83

Table 4-7b – Texture assessment results

Disc	Forging	Supplier	Location	Beta %	β max {100}	Alpha %	α max {0002}
T800 IP7	Hot Die	Wyman Gordon (Livingston)	Rim	17.0	5.25	72.7	4.55
			Diaphragm	5.7	10.34	39.2	5.54
			Bore	17.1	3.39	64.6	3.56
T800 IP1	Hot Die (Above β_T)	Wyman Gordon (Livingston)	Rim	-	-	-	-
			Diaphragm	-	-	-	-
			Bore	7.4	4.46	51.1	4.86
T800 IP5	Hot Die	Wyman Gordon (Livingston)	Rim	15.8	3.12	62.4	5.44
			Diaphragm	6.1	13.30	29.7	6.33
			Bore	5.8	4.38	61.4	4.94
T500 IP3	Hammer	Wyman Gordon (Lincoln)	Rim	12.8	5.75	64.0	9.31
			Diaphragm	14.7	5.18	66.8	5.56
			Bore	11.0	7.53	65.4	7.39
T800 IP6	Isothermal	Ladish	Bore	12.0	3.41	68.8	7.23
T800 IP5	Hot Die	Ladish	Bore	13.8	4.50	56.0	3.91
Clutch Shaft	Isothermal	Ladish	Shaft	-	5.72	-	9.35
			Shaft	-	4.94	-	5.35

a – VSMPO billet material

b – Timet billet material

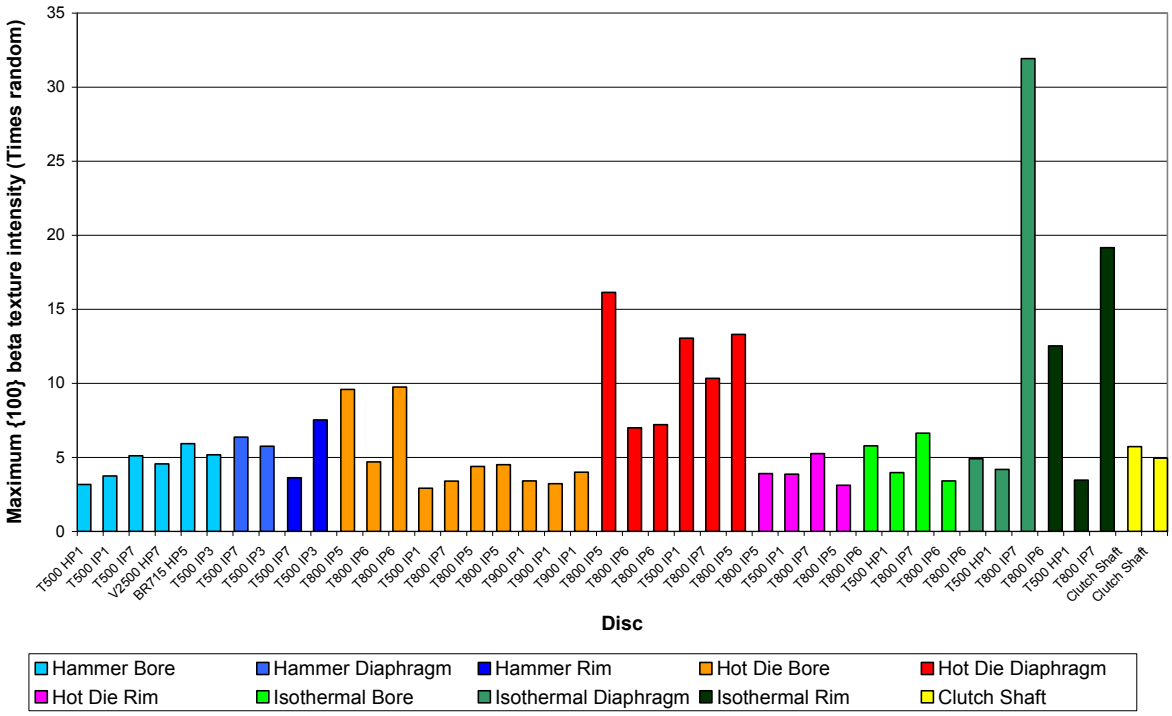

Figure 4-19 – Variation of maximum {100} beta texture intensity with forging method and the position of the sample within the forging

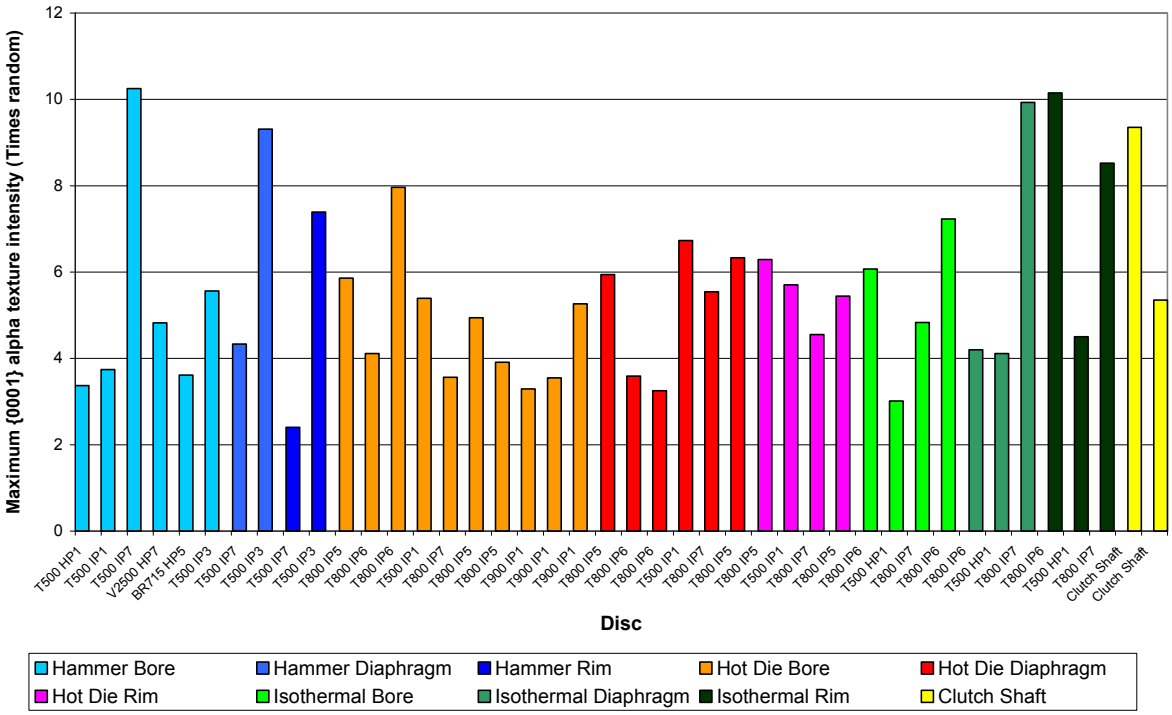

Figure 4-20 – Variation of maximum {0001} alpha texture intensity with forging method and the position of the sample within the forging

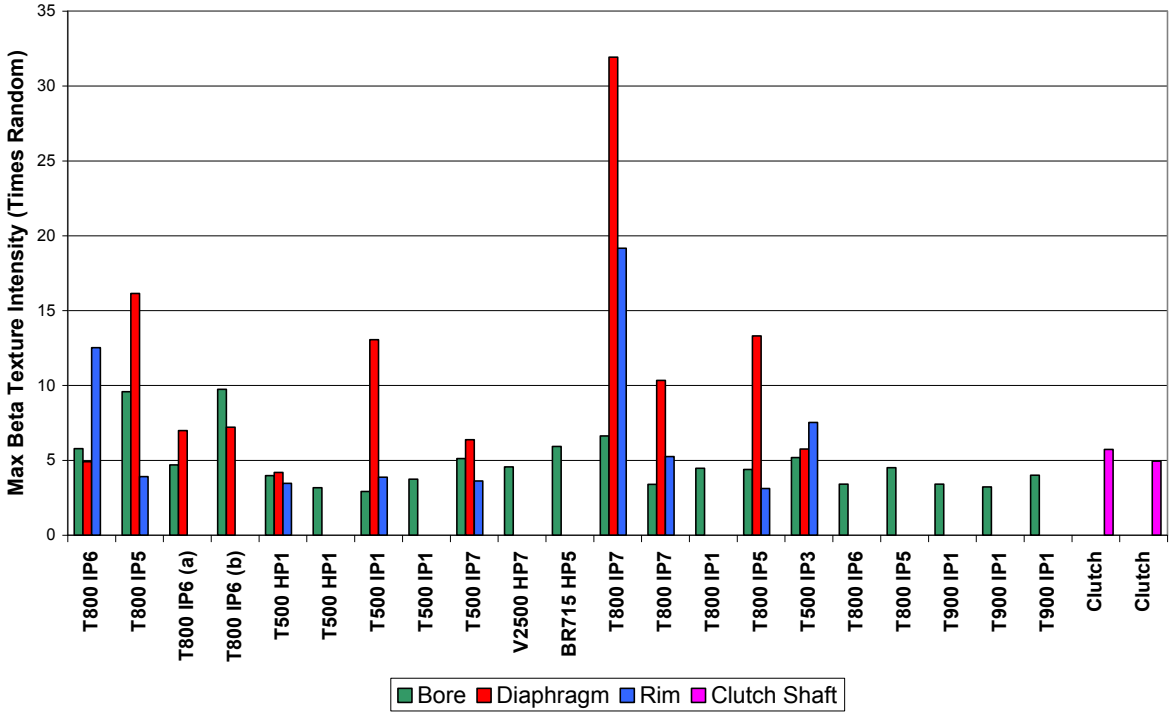

Figure 4-21 – Variation of maximum {100} beta texture intensity with sample location within the forging

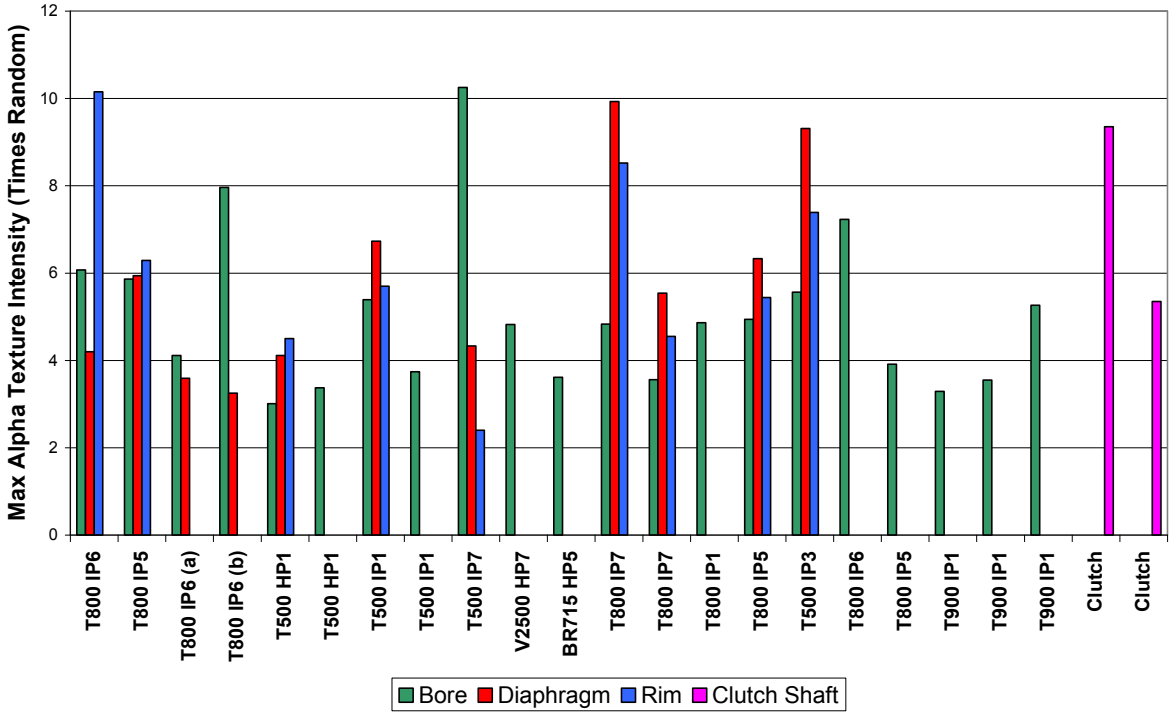

Figure 4-22 – Variation of maximum {0001} alpha texture intensity with sample location within the forging

Rim position:

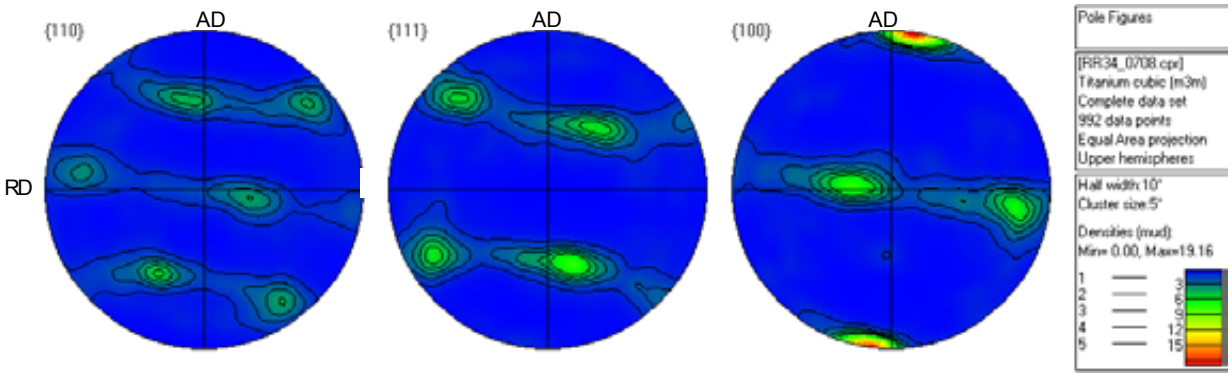

Diaphragm position:

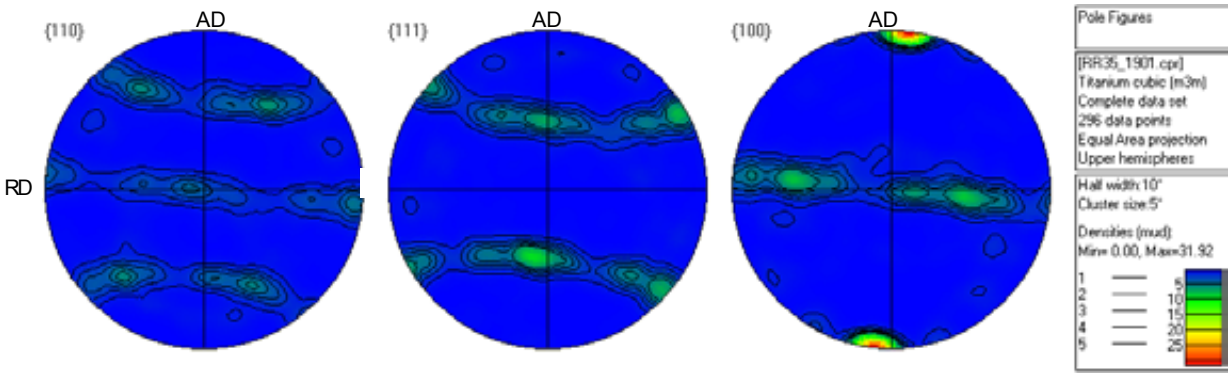

Bore position:

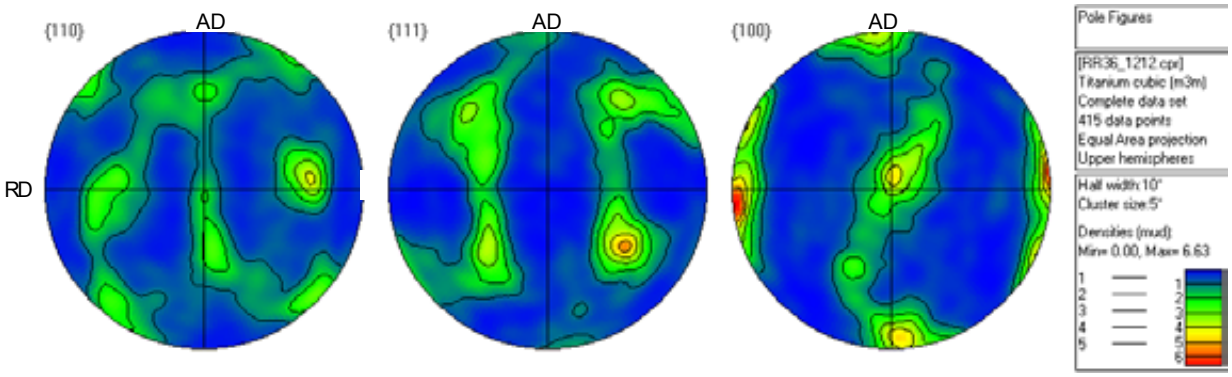

Figure 4-23 – Variations in beta texture with location of sample within a Trent engine IPC stage 7 compressor disc. (Texture intensities displayed using a linear scale) [156]

Rim position:

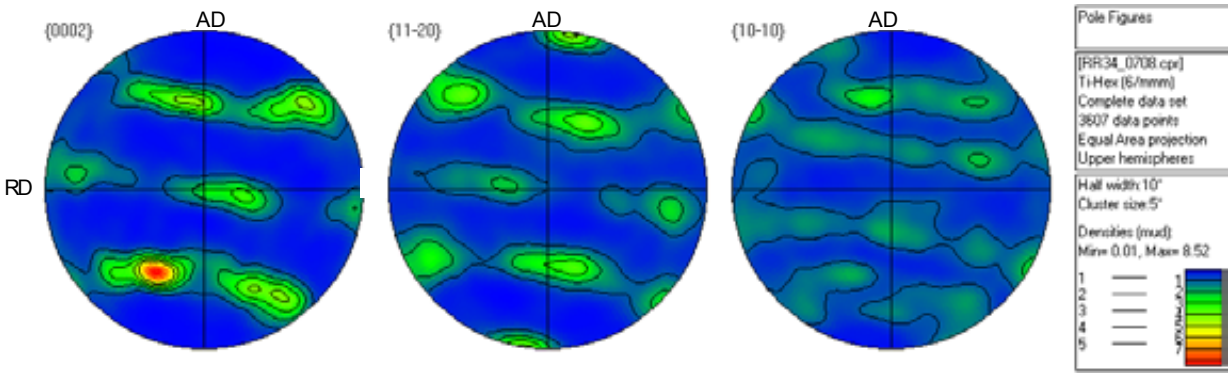

Diaphragm position:

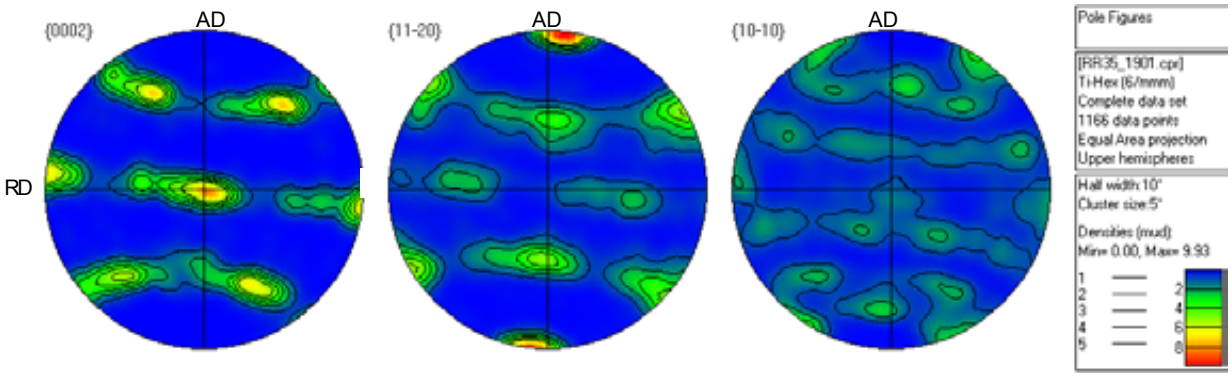

Bore position:

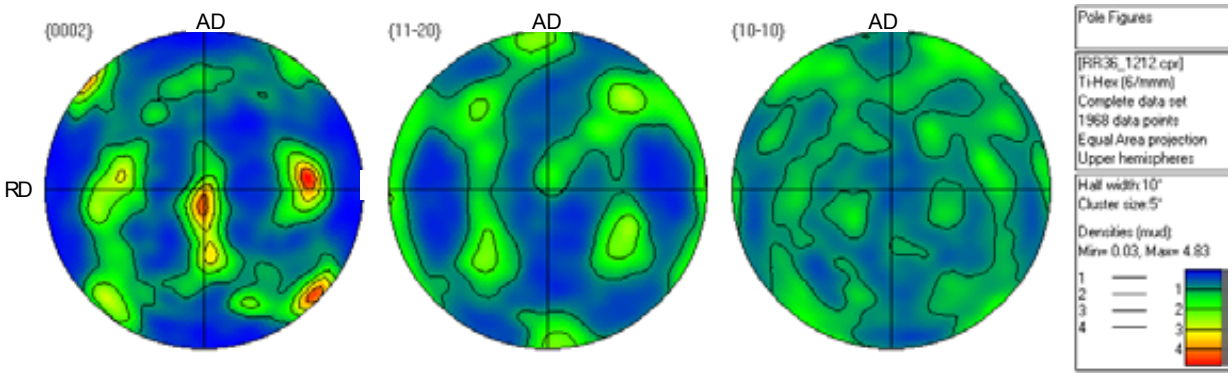

Figure 4-24 – Variations in alpha texture with location of sample within a Trent engine IPC stage 7 compressor disc. (Texture intensities displayed using a linear scale) [156]

4.7.3 Cold dwell fatigue testing of production material

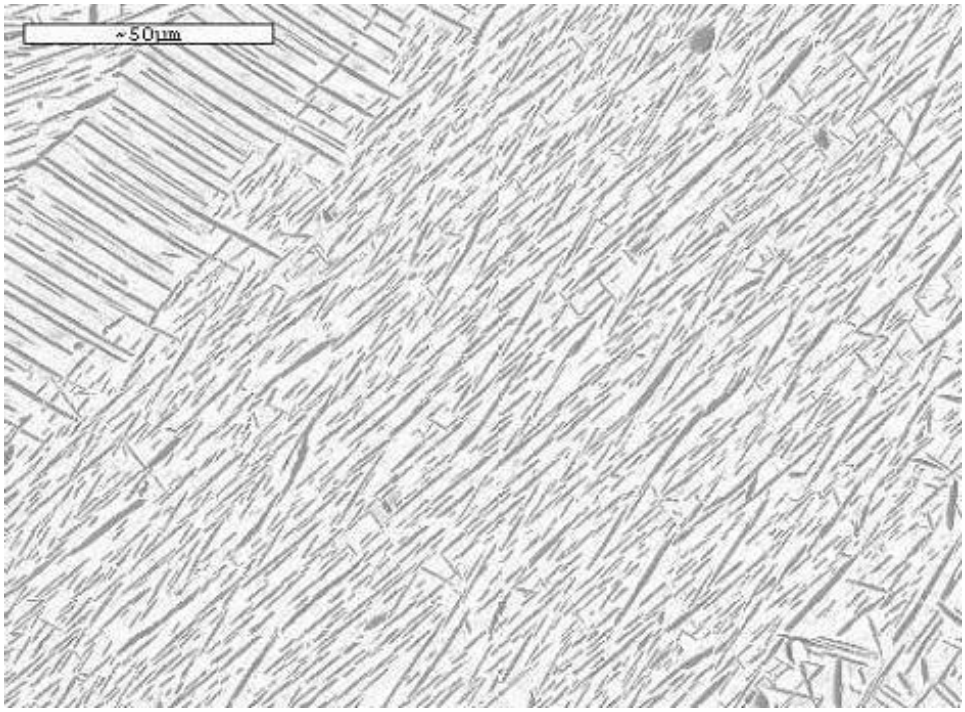

Figure 4-25 – Typical microstructure of IPC stage 5 disc test specimen

Figure 4-26 – Typical microstructure of clutch shaft forging test specimen

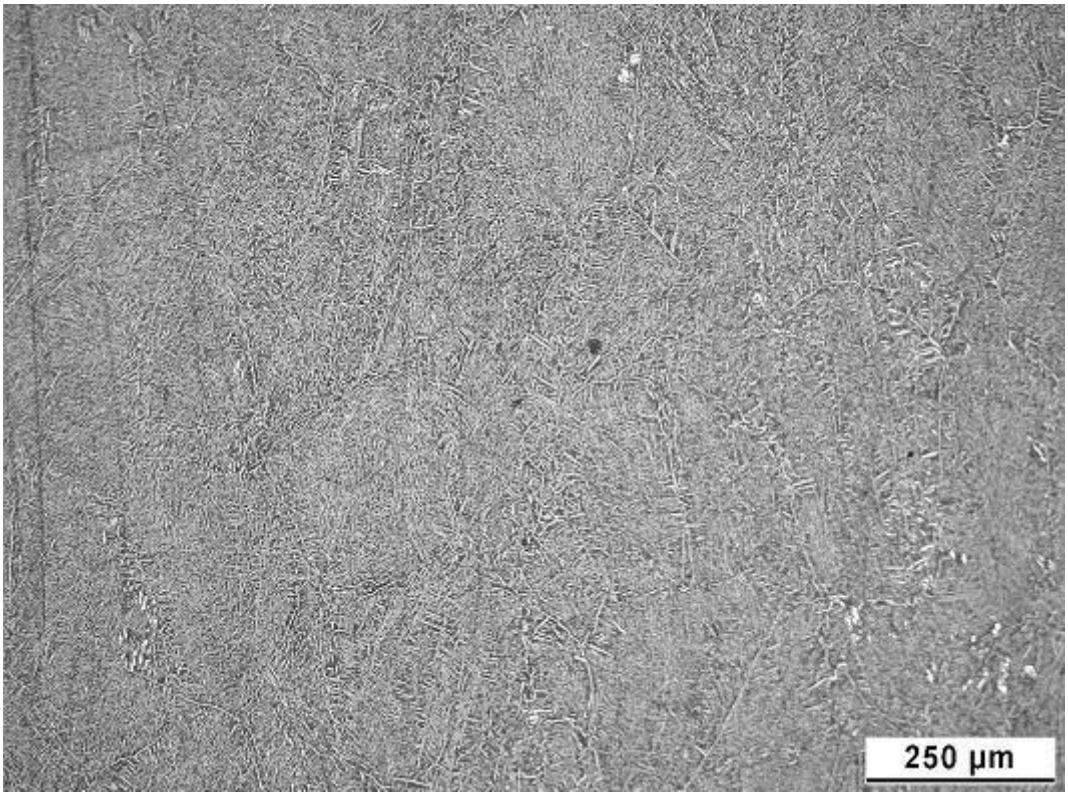

Figure 4-27 – Typical microstructure of IPC stage 3 disc test specimen

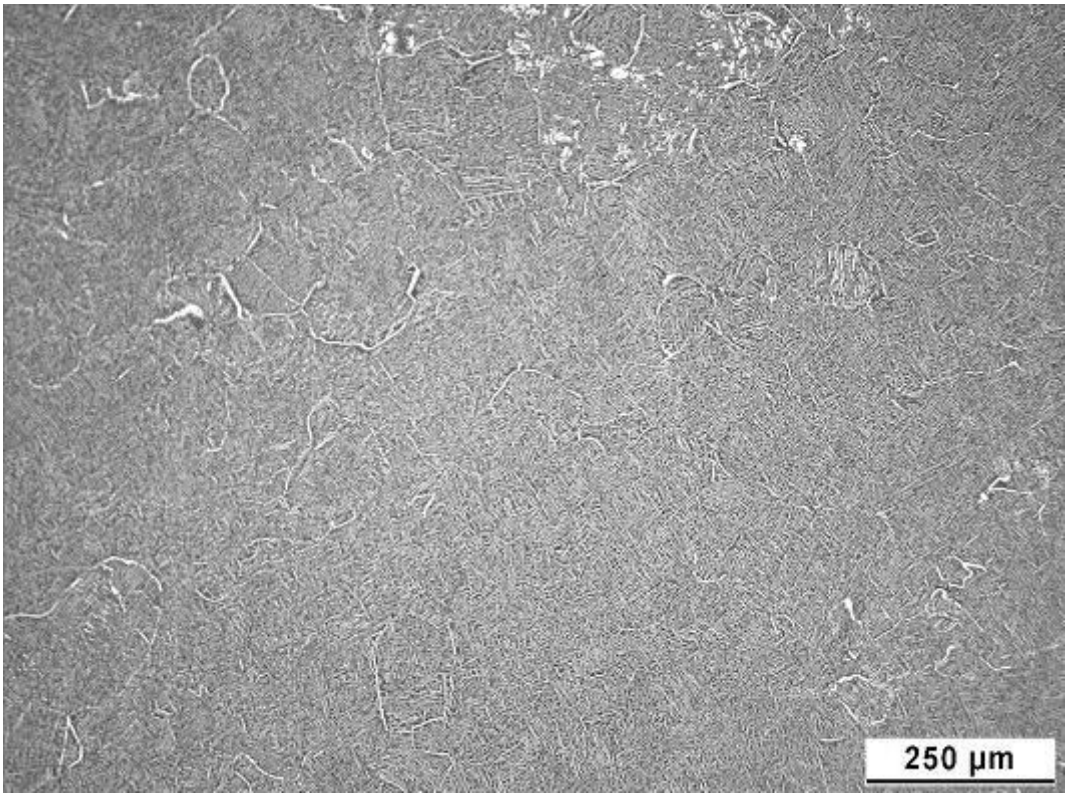

Figure 4-28 – Typical microstructure of IPC stage 7 disc test specimen

Table 4-8 – Cold dwell fatigue test results for IPC stage 5 cluster disc [152]

Specimen orientation	Test	Max stress /MPa	Cyclic life	Test house
Radial	15cpm	1080	22199	Swansea
Radial	15cpm	1140	18629	Elton Rd
Tangential	15cpm	1200	7644	Elton Rd
Tangential	15cpm	1000	110,309*	Elton Rd
Tangential	15cpm	1080	32393	Elton Rd
Tangential	15cpm	1140	18049	Elton Rd
45°	15cpm	1140	5935	Elton Rd
45°	15cpm	1200	2948	Birmingham
Radial	2 minute dwell	1200	92	Elton Rd
Radial	2 minute dwell	1140	14867	Swansea
Radial	2 minute dwell	1140	5455	Elton Rd
Radial	2 minute dwell	1140	13248	Elton Rd
Radial	2 minute dwell	1080	25528	Birmingham
Tangential	2 minute dwell	1140	11843	Swansea
Tangential	2 minute dwell	1170	2783	Swansea
Tangential	2 minute dwell	1080	17631	Elton Rd
Tangential	2 minute dwell	1170	8103	Swansea
Tangential	2 minute dwell	1200	375	Swansea
Tangential	2 minute dwell	1140	9877	Elton Rd
Tangential	2 minute dwell	1080	30656*	Elton Rd
Tangential	2 minute dwell	1200	941	Elton Rd
45°	2 minute dwell	1140	14537	Elton Rd
45°	2 minute dwell	1170	6446	Birmingham
45°	2 minute dwell	1080	30037*	Elton Rd
45°	2 minute dwell	1200	3022	Elton Rd
45°	2 minute dwell	1080	28518	Elton Rd

* indicates test run-out i.e. specimens remaining unbroken at the recorded number of loading cycles

Table 4-9 – Cold dwell fatigue test results for clutch shaft forging [152]

Specimen orientation	Test	Max stress /MPa	Cyclic life	Test house
Axial	15cpm	1140	9708	Elton Rd
Axial	15cpm	1200	4#	Elton Rd
Axial	15cpm	1080	23051	Elton Rd
Axial	15cpm	1040	69111	Elton Rd
Axial	15cpm	1170	3249	Elton Rd
Axial	15cpm	1060	33548	Elton Rd
Axial	2 minute dwell	1080	14393	Swansea
Axial	2 minute dwell	1140	152	Swansea
Axial	2 minute dwell	1060	11389	Birmingham
Axial	2 minute dwell	1140	1#	Birmingham
Axial	2 minute dwell	1080	20180	Elton Rd
Axial	2 minute dwell	1170	1#	Birmingham

# indicates failure through yielding

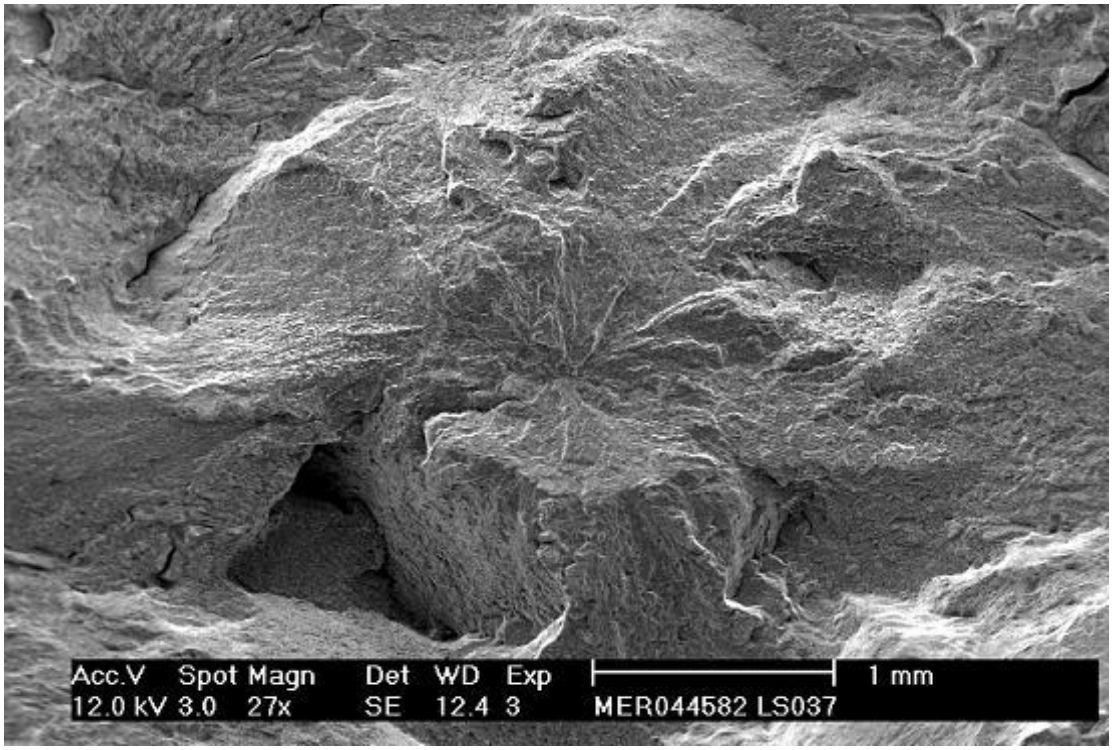

Figure 4-29 – Sub-surface failure origin in cold dwell fatigue tested IPC5 disc test specimen [152]

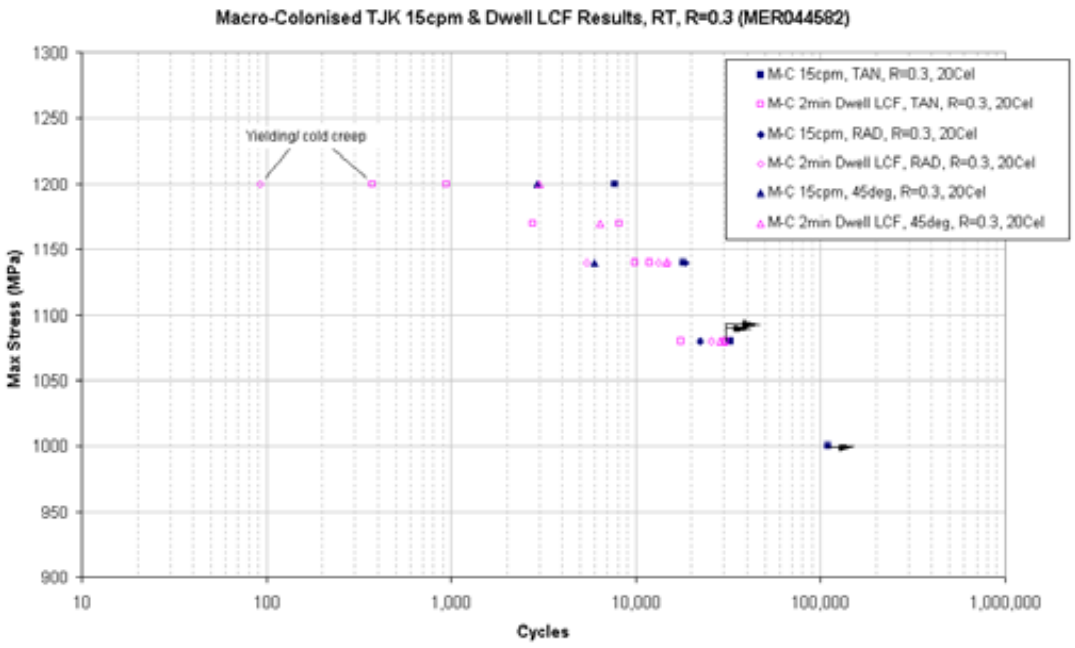

Figure 4-30 – Cyclic vs. cold dwell fatigue behaviour for "clustered" IPC stage 5 disc [152]

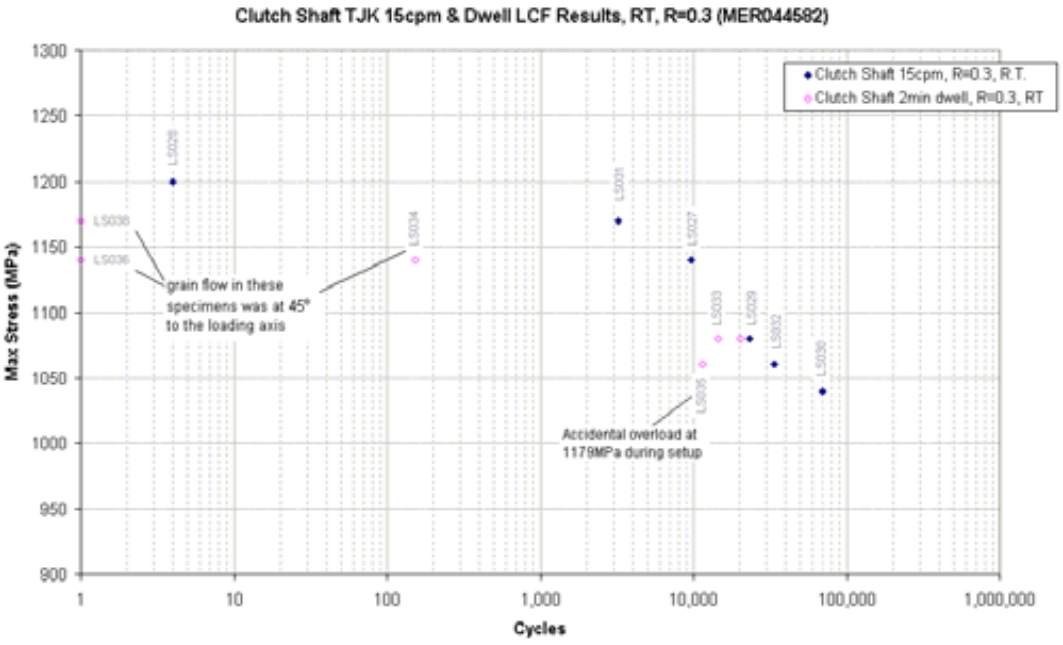

Figure 4-31 – Cyclic vs. cold dwell fatigue behaviour for "randomly textured" clutch shaft forging [152]

Table 4-10 – Cold dwell fatigue test results for "worst-case" production Ti6246 disc forgings [152]

Disc	Specimen orientation	Test	Max stress /MPa	Cyclic life	Test house
Trent IPC7	Tangential	15cpm	1040	21640	Elton Rd
Trent IPC7	Tangential	15cpm	1080	15483	Elton Rd
Trent IPC7	Tangential	15cpm	1140	7607	Elton Rd
Trent IPC7	Radial	15cpm	1050	10152	Elton Rd
Trent IPC7	Radial	15cpm	1110	4892	Birmingham
Trent IPC7	Tangential	2 minute dwell	1040	17867	Birmingham
Trent IPC7	Tangential	2 minute dwell	1080	18743	Birmingham
Trent IPC7	Tangential	2 minute dwell	1140	15	Birmingham
Trent IPC7	Radial	2 minute dwell	1050	1#	Birmingham
Trent IPC7	Radial	2 minute dwell	1100	285	Elton Rd
Trent IPC3	Tangential	15cpm	1080	34592	Elton Rd
Trent IPC3	Tangential	15cpm	1140	9788	Elton Rd
Trent IPC3	Tangential	15cpm	1170	2192	Elton Rd
Trent IPC3	Radial	15cpm	1103	13822	Elton Rd
Trent IPC3	Radial	15cpm	1140	10115	Birmingham
Trent IPC3	Tangential	2 minute dwell	1090	6006	Elton Rd
Trent IPC3	Tangential	2 minute dwell	1120	8468	Birmingham
Trent IPC3	Tangential	2 minute dwell	1140	3340	Birmingham
Trent IPC3	Radial	2 minute dwell	1100	7949	Elton Rd
Trent IPC3	Radial	2 minute dwell	1140	1603	Birmingham

# indicates weld-line failure

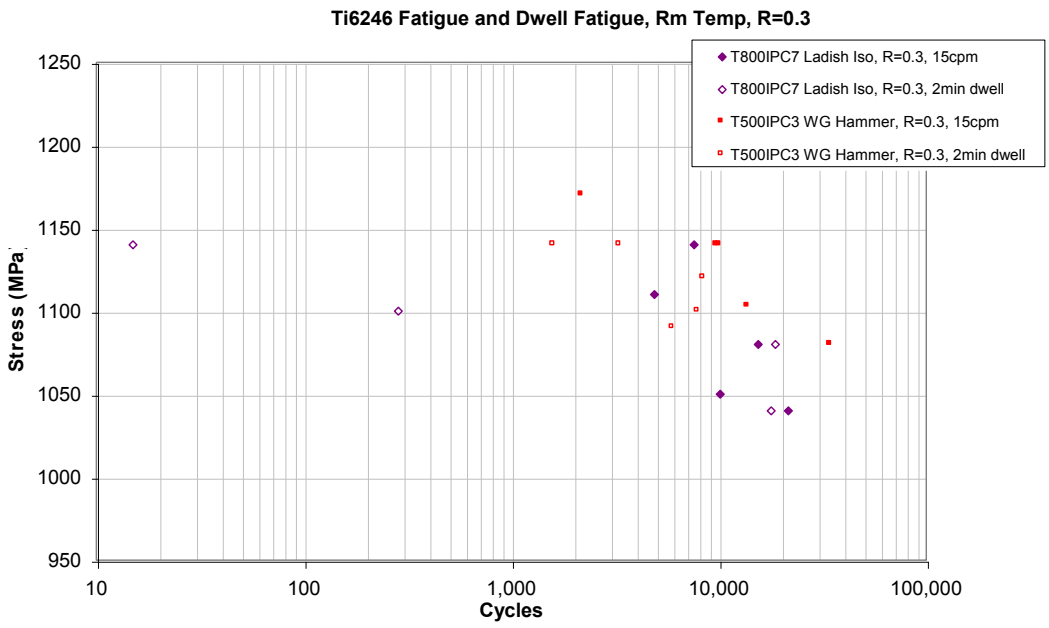

Figure 4-32 – Cyclic vs. cold dwell fatigue behaviour for high alpha texture IPC stage 3 and maximum measured beta texture IPC stage 7 discs [152]

Figure 4-33 – Typical fracture surface of IPC stage 3 disc dwell test specimen showing no faceting and no clear origin [152]

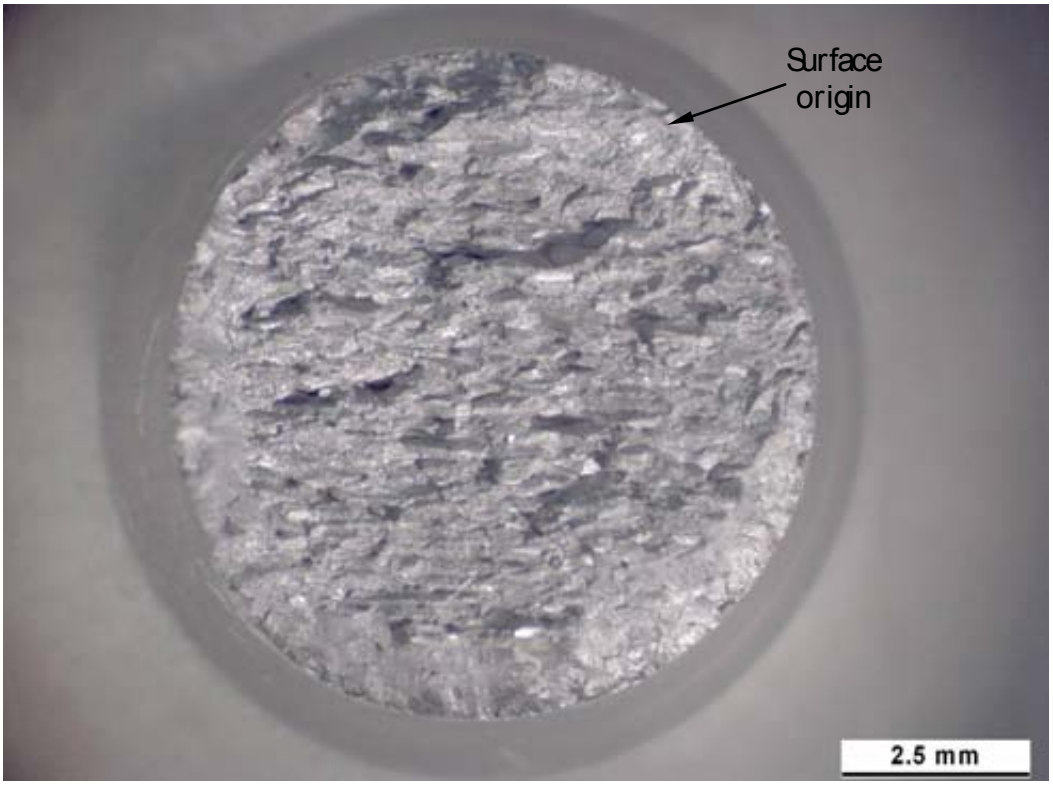

Figure 4-34 – Typical fracture surface of IPC stage 7 disc dwell test specimen showing surface origin and ductile failure [152]

4.7.4 Cold dwell fatigue testing of non-standard Ti6246 microstructures

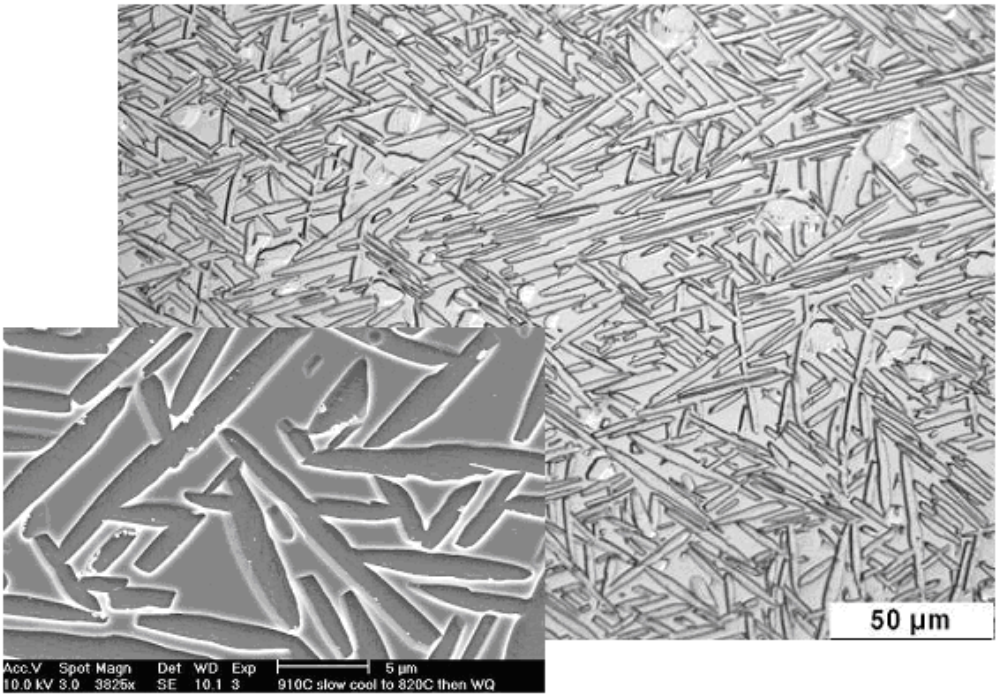

Figure 4-35 – (Alpha + beta) heat-treated Ti6246 microstructure [157]

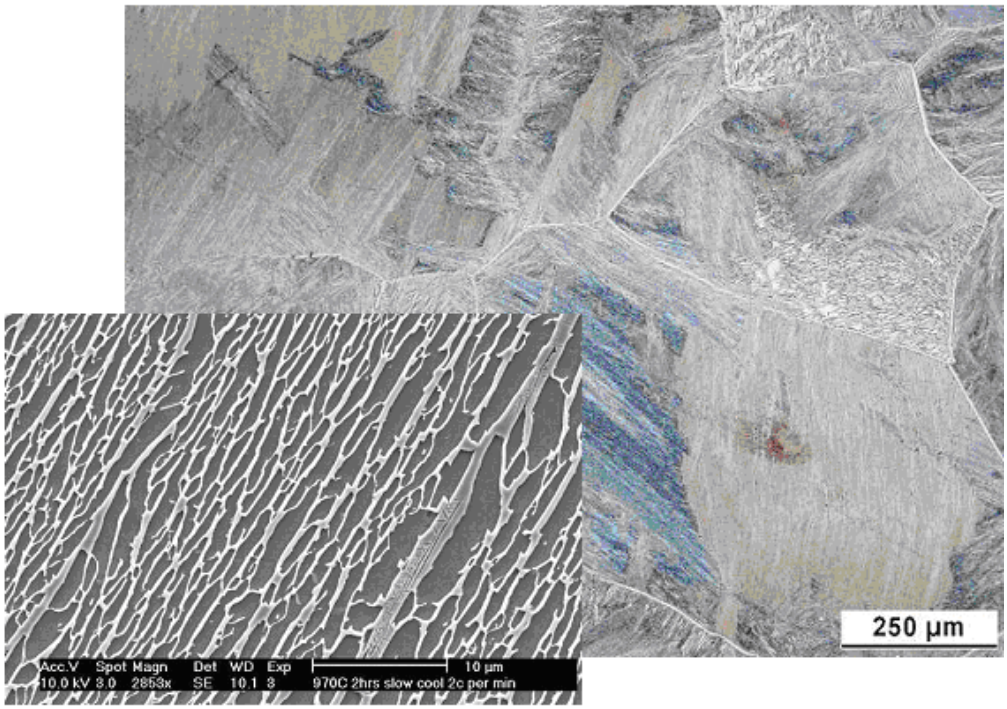

Figure 4-36 – Beta heat-treated Ti6246 microstructure [157]

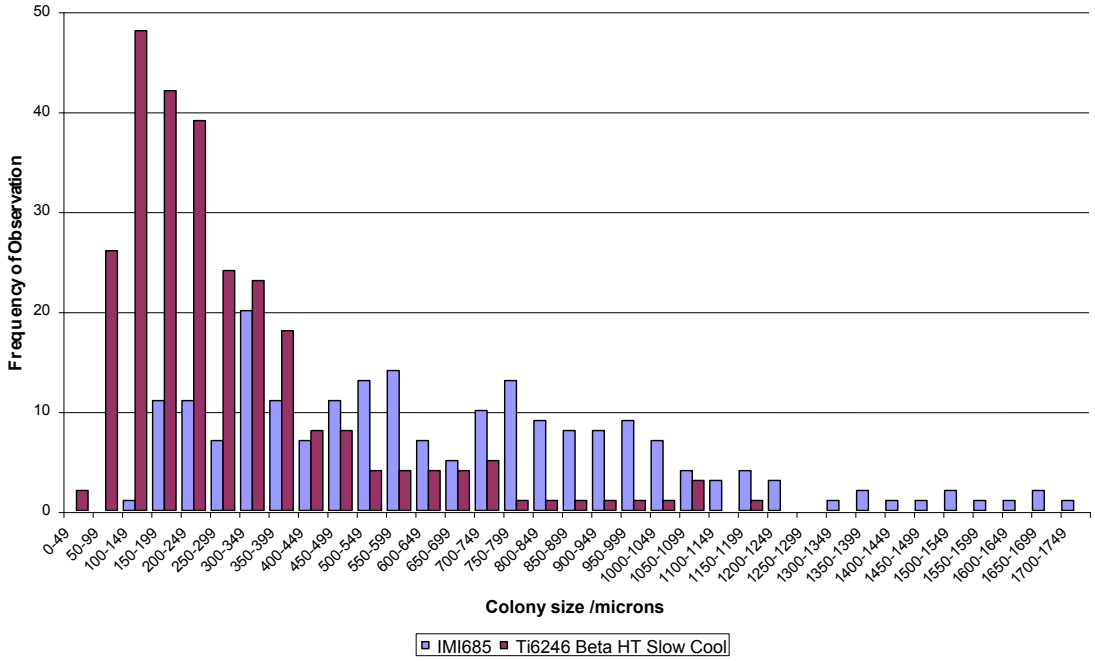

Figure 4-37 – Optical colony size comparison for (beta annealed + slow cooled) Ti6246 and beta processed Ti685 production disc material

Table 4-11 – Cold dwell fatigue test results for small gauge test specimens [163]

Heat treatment	Specimen orientation	Test	Max stress /MPa	Cyclic life	Test house
α/β	Tangential	15cpm	790	14308	Swansea
α/β	Tangential	15cpm	940	3126	Swansea
α/β	Radial	15cpm	725	39868	Swansea
α/β	Radial	15cpm	890	4351	Swansea
α/β	Tangential	2 minute dwell	790	12680	Swansea
α/β	Radial	2 minute dwell	790	13901	Swansea
α/β	Radial	2 minute dwell	890	4604	Swansea

Table 4-12 – Cold dwell fatigue test results for large gauge test specimens [163]

Heat treatment	Specimen orientation	Test	Max stress /MPa	Cyclic life	Test house
α/β	Tangential	15cpm	790	9019#	Birmingham
α/β	Tangential	15cpm	790	23912	Birmingham
α/β	Radial	15cpm	890	7811	Birmingham
α/β	Radial	2 minute dwell	790	17012	Swansea
α/β	Radial	2 minute dwell	890	4286#	Elton Rd
α/β	Tangential	2 minute dwell	890	3934	Birmingham
Beta	Radial	15cpm	800	77642	Birmingham
Beta	Radial	15cpm	850	43864	Elton Rd
Beta	Radial	15cpm	900	21976	Birmingham
Beta	Radial	15cpm	925	11563	Birmingham
Beta	Radial	15cpm	950	5784	Elton Rd
Beta	Radial	2 minute dwell	880	18765	Elton Rd
Beta	Radial	2 minute dwell	900	9891	Birmingham
Beta	Radial	2 minute dwell	925	5212	Elton Rd
Beta	Radial	2 minute dwell	925	3906	Elton Rd
Beta	Radial	2 minute dwell	950	2066	Elton Rd

# indicates weld-line failure

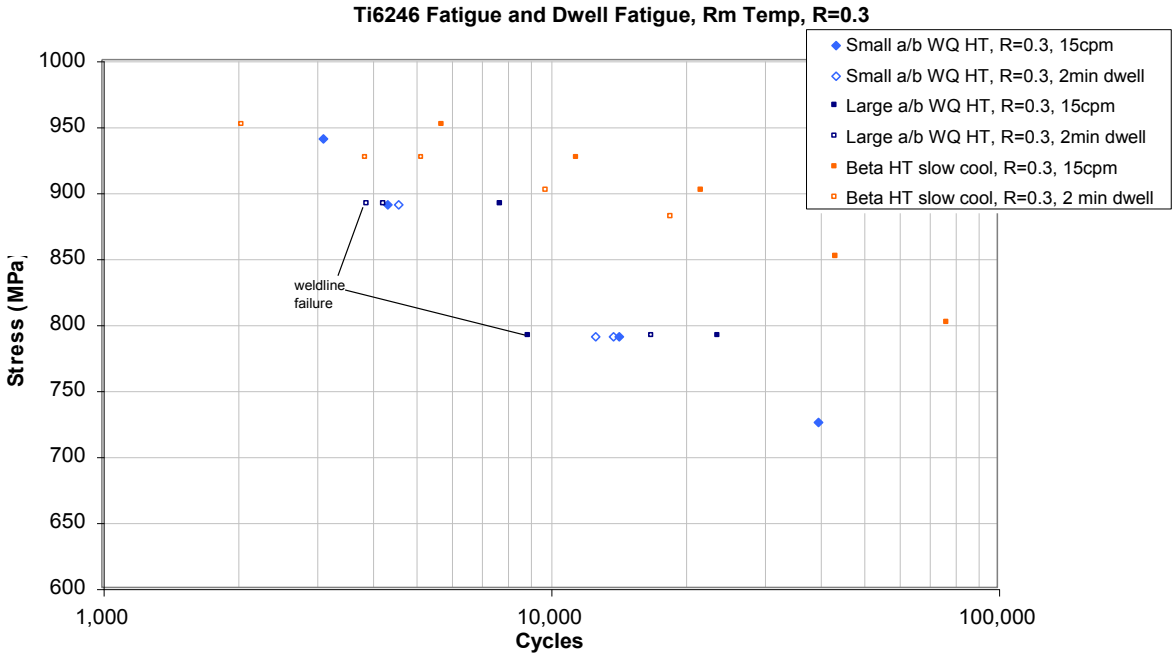

Figure 4-38 – Cold dwell fatigue test results for (alpha + beta) and beta heat-treated Ti6246 variants [163]

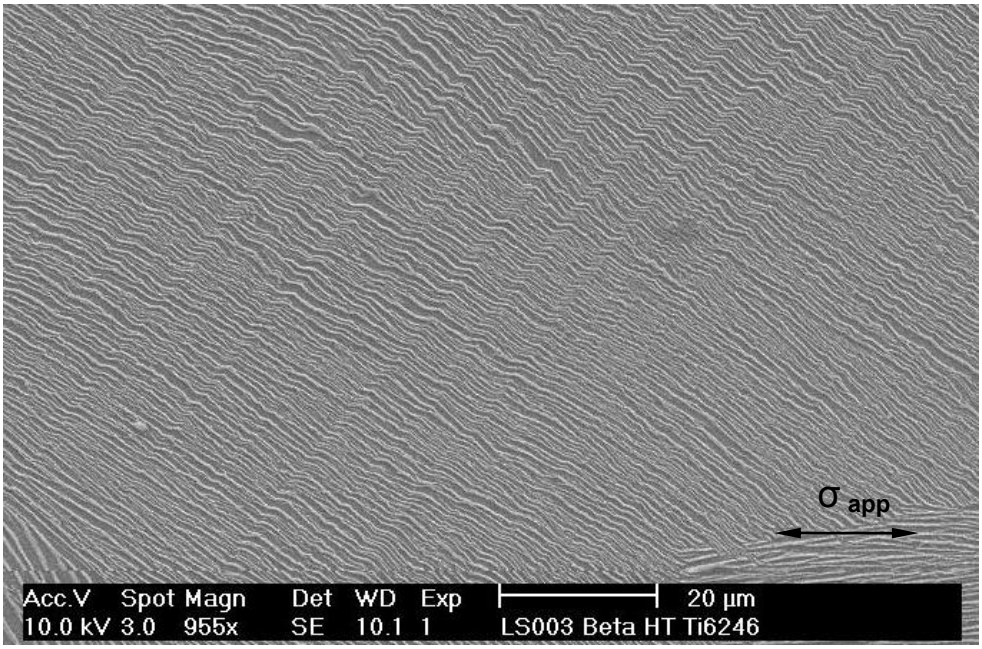

Figure 4-39 – Angled slip traces in a beta heat-treated Ti6246 cold dwell fatigue test specimen [163]

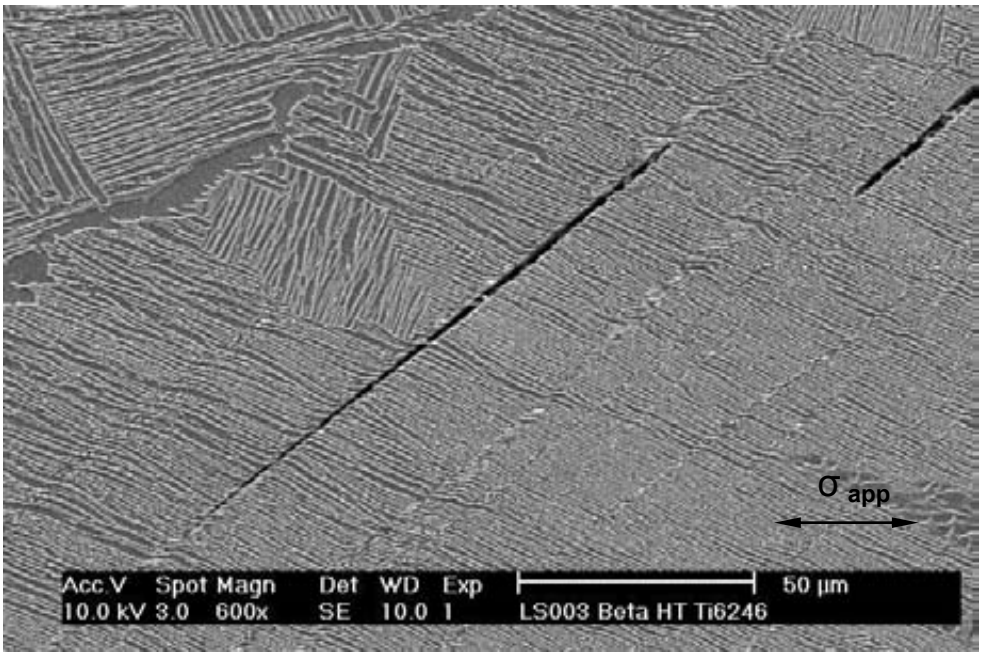

Figure 4-40 – Angled sub-surface cracking in a beta heat-treated Ti6246 cold dwell fatigue test specimen [163]

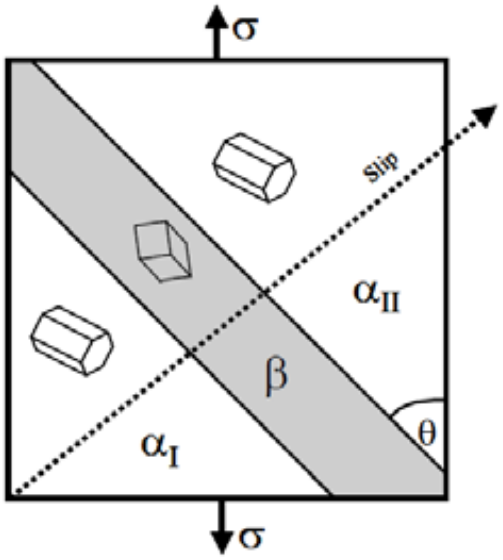

Slip transmission function of:

(i) Relative orientation of α_I and β and β to α_{II} giving favourable or unfavourable alignment of preferred slip systems.

(ii) Orientation angle, θ

(iii) Stress, either macro applied or local due to crystal plasticity.

(iv) Length scale and slip planarity

(v) Loading rate

(vi) Local chemistry, driven by alloy partitioning, changing CRSS for individual slip systems

Figure 4-41 – Factors affecting slip transmission across alpha/beta phase interfaces [131]

5 Cold dwell fatigue performance of beta processed titanium alloys 5-3
5.1 Introduction 5-3
5.2 Experimental method 5-6
5.2.1 Characterisation of source material 5-6
5.2.1.1 Ti6246 effective strain distribution modelling 5-6
5.2.2 Blanks sectioning 5-7
5.2.2.1 Ti6246 pancake forgings 5-7
5.2.2.2 Ti6242 discs 5-7
5.2.3 Heat treatment 5-7
5.1.1.1 Ti6246 heat treatment 5-7
5.1.1.2 Ti6242 heat treatment 5-9
5.2.3.1 Friction welding of Ti6242 specimens 5-11
5.2.4 Mechanical testing 5-13
5.2.4.1 Tensile testing 5-13
5.2.4.2 Fatigue testing 5-13
5.3 Results 5-15
5.3.1 Material characterisation 5-15
5.3.1.1 As-received Ti6246 optical microstructures 5-15
5.3.1.2 As received Ti6246 crystallographic textures 5-15
5.3.1.3 As received Ti6242 optical microstructures 5-16
5.3.1.4 As received Ti6242 crystallographic textures 5-16
5.3.1.5 Ti6246 microstructures following beta heat treatment 5-16
5.3.1.6 Ti6246 textures following beta heat treatment 5-18
5.3.1.7 Ti6242 microstructures following beta heat treatment 5-19
5.3.1.8 Ti6242 textures following beta heat treatment 5-20
5.3.2 Mechanical testing 5-20
5.3.2.1 Ti6246 tensile testing 5-20
5.3.2.2 Ti6246 fatigue testing 5-21
5.3.2.3 Ti6242 tensile testing 5-21
5.3.2.4 Ti6242 fatigue testing 5-21
5.3.3 Specimen fractography 5-22
5.3.3.1 Ti6246 tensile tests 5-22
5.3.3.2 Ti6246 fatigue tests 5-22
5.3.3.3 Ti6242 tensile tests 5-22
5.3.3.4 Ti6242 fatigue tests 5-22
5.3.4 Fatigue test strain accumulation behaviour 5-23
5.4 Discussion 5-24
5.4.1 Beta heat treatments 5-24
5.4.2 Ti6246 cold dwell fatigue testing 5-25
5.4.3 Ti6242 cold dwell fatigue testing 5-27
5.5 Conclusions 5-30

5B Volume B - Figures and tables 5-33
5.6 Experimental method 5-33
5.6.1 Ti6246 strain profile modelling 5-33
5.6.2 Ti6246 cut-up diagrams 5-34
5.6.3 Ti6242 cut-up diagrams 5-35
5.6.4 Heat treatment 5-36

5.6.5 Specimen rotary friction welding....5-37
5.7 Results....5-40
5.7.1 Ti6246 As-received microstructure....5-40
5.7.2 Ti6246 As-received texture....5-41
5.7.3 Ti6242 As-received microstructure....5-44
5.7.4 Ti6242 As-received texture....5-45
5.7.5 Ti6246 heat treated microstructures....5-48
5.7.6 Ti6246 heat treated textures....5-51
5.7.7 Ti6242 heat treated microstructures....5-52
5.7.8 Ti6242 heat treated textures....5-58
5.7.9 Tensile testing....5-60
5.7.10 Fatigue testing....5-61
5.7.11 Specimen fractography and microstructures....5-66
5.7.11.1 Ti6246 tensile specimens....5-66
5.7.11.2 Ti6246 LCF specimens....5-68
5.7.11.3 Ti6246 dwell LCF specimens....5-69
5.7.11.4 Ti6242 tensile specimens....5-70
5.7.11.5 Ti6242 LCF specimens....5-72
5.7.11.6 Ti6242 dwell LCF specimens....5-74
5.7.12 Strain accumulation data....5-76
5.8 TWI report on rotary friction welding of Ti64/Ti6242 Cylinders....5-77

5 Cold dwell fatigue performance of beta processed titanium alloys

5.1 Introduction

The investigation into cold dwell fatigue (CDF) behaviour in Ti6246 discussed in chapter four provided evidence that Ti6246 in a beta processed, (alpha + beta) solution heat treated and aged microstructural condition does not show susceptibility to sustained periods of CDF loading. Further work involving testing of Ti6246 in what were believed to be two 'susceptible' microstructural conditions[1] also failed to produce CDF behaviour [69].

Further work was undertaken in an attempt to produce a beta processed and slow-cooled microstructure more dwell-sensitive than the previously tested variant. It was suggested that increased susceptibility could be achieved by manipulating the microstructure in one or more of the following ways:

- Increasing the dimensions of alpha platelet colonies (potentially through increasing the prior beta grain size)
- Increasing alpha platelet width (and/or alpha phase fraction)
- Reducing the thickness of retained beta layers (and/or beta phase fraction)

The rationale behind increased dwell susceptibility with a larger colony size was based on the observation of planar slip across individual alpha colonies in microstructures subject to CDF [163, 165]. An increase in the planar slip length should allow the accumulation of greater dislocation pile-up stresses at colony boundaries. In this situation the probability of stress redistribution between neighbouring weak and strong colony orientations should

[1] 'Susceptible' microstructures display large cyclic life reductions and the formation of load normal 'quasi-cleavage' facet features under peak loading for sustained periods at low (<200°C) temperatures.

increase as the interfacial stresses increase [16, 136]. Increasing the prior beta grain size through heat treatment, an increase in alpha colony sizes should be achievable provided that a sufficiently slow cooling rate is applied in order to avoid Widmanstätten alpha precipitation [22, 157].

An increase in alpha platelet width is thought to be favourable for inducing CDF behaviour based on a reduction in the number of alpha/beta interfaces over a given slip band length. Fewer phase interfaces over a slip length should allow dislocation transmission to the boundaries of ESUs to occur under lower applied stresses and again allow the accumulation of greater pile-up stresses [108, 139]. Reduced beta layer thicknesses are favoured for CDF testing because of the greater number of active slip systems in beta phase in comparison to alpha phase [28]. Thick retained beta layers in a colony microstructure may prevent planar slip band formation because heterogeneous slip behaviour is more likely to occur through the beta phase. If planar slip bands cannot form because retained beta layers prevent dislocation movement the pile-up stresses forming at the boundaries of weakly orientated colonies would be lower. In this situation it is unlikely that there would be sufficient local stress disparity to allow load shedding to occur between weak and strong alpha colony orientations [136, 140].

Based on the above theories, further heat treatments of Ti6246 material were attempted to study the extremes of microstructure that can be produced. A suitably 'susceptible' microstructure was then selected for CDF testing.

For comparison to dwell LCF testing of Ti6246, work has been undertaken to test the dwell susceptibility of Ti6242. Ti6242 is commonly used in an (alpha + beta) processed microstructural condition. Previous in-service incidents and academic research suggest that

the alloy can display CDF susceptibility in its bimodal condition [118, 140, 165]. The alloy provides a good comparison to Ti6246 because of the 4wt% molybdenum chemistry difference. The alloy is less heavily beta stabilised than Ti6246 and a lower beta fraction should be retained for an equivalent processing route. Similar beta processing heat treatments have been undertaken for Ti6242 material to attempt to produce a colonised microstructure.

Prior to testing it was postulated that Ti6242 should show a greater CDF life debit than Ti6246 because of the increased alpha stabilisation of the alloy [81]. The presence of greater levels of retained beta in Ti6246 is believed to inhibit CDF behaviour [69]. Testing beta processed Ti6242 and Ti6246 microstructures under similar conditions (as a proportion of material UTS), it should be possible to determine the magnitude of the effect of the retained beta content on the CDF response of these alloys.

Following CDF testing, this chapter discusses fractography and strain accumulation behaviour for both cyclic and dwell fatigue tests.

5.2 Experimental method

5.2.1 Characterisation of source material

Ti6246 material for beta heat treatment experiments was obtained from two pancake forgings used in a previous investigation into the formation of strain induced porosity in disc forgings [166]. Ti6242 material was obtained from the bore section of three compressor discs (AE3007 Stage 10 discs) supplied by Rolls-Royce Corporation. Both materials were received in their standard microstructural forms. The optical microstructures and textures of source materials were characterised using standard experimental techniques and procedures.

5.2.1.1 Ti6246 effective strain distribution modelling

The two Ti6246 pancakes supplied from a previous material investigation were designated A1 and B2. Both pancakes were forged from VSMPO billet material. Pancake A1 was forged from billet of 200mm diameter and 105mm height. Upsetting was from 105mm to a finish height of 40mm. Material was heated to 40ºC above beta transus and forged (using dies at a temperature of 150ºC) with an upset rate of 20mm/second. Effective strain profile modelling was performed using DEFORM. Ti6/4 data was used in the modelling work [166]. The final strain profile is displayed in Figure 5-1.

Pancake B2 was forged from billet stock of 300mm x 300mm. Upsetting was from 150mm to 60mm. Again a work-piece temperature of (β_T + 40ºC), die temperature of 150ºC, and upset rate of 20mm/second were used. DEFORM software again used Ti6/4 modelling data [166]. The predicted strain profile of the pancake forging is displayed in Figure 5-2.

5.2.2 Blanks sectioning

5.2.2.1 Ti6246 pancake forgings

A total of 15 blanks for LCF specimens and 5 blanks for tensile specimens were machined from the Ti6246 pancakes. Diagrams illustrating cut up to specimen blank geometries are given in Figure 5-3 and Figure 5-4.

5.2.2.2 Ti6242 discs

Ti6242 discs were sectioned to obtain 22 LCF gauge length specimen blanks and 5 tensile specimen blanks. Two discs (designated A and B) were machined as illustrated in the diagram in Figure 5-5, whilst the third disc (disc C) was machined according to the diagram in Figure 5-6.

Specimen blanks were labelled A1-A9, B1-B9 or C1-C9 according to the disc from which they were machined. Tensile specimen blanks (A1, A6, B1, B6 and C1) were blanks of 64mm length x 12mm width x disc axial depth (~15mm). LCF gauge length blanks were 36mm length x 15mm width x disc axial depth (~15mm).

5.2.3 Heat treatment

5.1.1.1 Ti6246 heat treatment

Initial Ti6246 heat treatment work attempted to achieve significant beta grain growth through exposure to temperatures in excess of beta transus for prolonged periods (>5 hours) using an air furnace. This approach was considered unsuitable for a heat treatment for CDF testing because of (a) the extreme oxidation of specimens leading to large scale spallation, (b) variation in microstructure through representative cross-sections, potentially due to oxygen pick-up and the consequent alpha stabilisation effects and (c) the lack of clarity regarding the effects of oxygen and hydrogen content on the CDF behaviour.

Because of the issues surrounding the use of an air furnace a two-stage heat treatment was devised to avoid these problems. For the first stage the blanks were heat-treated to achieve grain growth in a vacuum furnace. Heat treatment involved a twenty-hour hold at a temperature of 1100˚C. This was followed by cooling at ~6˚Cmin^{-1} to a temperature of ~750˚C at which point a helium quench was applied. Such a relatively fast cooling rate was not suitable to achieve the very coarse alpha colony microstructure desired for mechanical testing. The cooling rate was selected because it was not practical to use an extremely slow cooling rate in the vacuum furnace (due to time and cost constraints).

The second stage of the heat treatment was therefore intended to achieve the coarse colonised microstructure. This involved re-solutioning the blanks above the beta transus for a relatively short period of time before using a very slow cooling rate to promote the growth of coarse alpha colonies. An air furnace was used for the second stage of the heat treatment. Samples were held at a furnace temperature of 970ºC for one hour. In order to establish a suitable microstructure for testing, a series of different cooling rates were trialled. Blanks A1-2 and B2-13 were used for these heat treatment experiments. Experimental variations are listed in Table 5-1.

Following assessment of the optical microstructures of trial samples a heat treatment was selected and applied to blanks to be machined to mechanical test specimens. The selected heat treatment route is outlined below:

- Vacuum heat treatment for 20 hours @ 1100ºC
- Furnace cool at 6ºCmin^{-1} to 800ºC
- Helium quench to room temperature
- Heat treatment for 1 hour @ 970ºC

- Furnace cool at 0.1ºCmin^{-1} to 750ºC
- Water quench to room temperature

Ti6246 specimen blanks were vacuum heat treated in three batches due to furnace size restrictions. The batches are listed below:

Batch A: A1-1, A1-4, A1-B, B2-7, B2-11, B2-15, B2-D

Batch B: A1-3, A1-A, B2-8, B2-10, B2-14, B2-E

Batch C: A1-5, B2-6, B2-9, B2-12, B2-C

Following vacuum heat treatment all Ti6246 blanks were heat treated in the air furnace as a single batch. After heat treatments the blanks were machined to specimens.

5.1.1.2 Ti6242 heat treatment

Similar work was undertaken on Ti6242 disc material. Having already established the effect of cross-section size on the microstructure of Ti6246, heat treatment work on Ti6242 only assessed the microstructures in samples of a representative size (i.e. cross-sections similar to specimen blank sizes).

From the 22 LCF blanks, four blanks were subject to heat treatment to select a suitable microstructure for dwell testing. Some material was sectioned from these specimens to assess the microstructure and texture in the as-received condition in the three discs. The remaining material was used in heat treatment experiments.

As the effects of prolonged exposure to atmospheric conditions at temperatures in excess of beta transus were severe for Ti6246, heat treatments to achieve grain growth in Ti6242 used a vacuum furnace. No heat treatments to achieve grain growth under atmospheric conditions were attempted.

Vacuum heat treatment was as per Ti6246 blanks, i.e. 20 hours at 1100°C, cooling at 10°Cmin^{-1} to a temperature of 800°C then helium quenching. Following this heat treatment, in comparison to the grain sizes observed in Ti6246 the grain size in Ti6242 was significantly smaller (~4-5 times smaller in terms of MLI size). Two blanks were retained in the condition obtained following the first heat treatment. The other two blanks were subject to a repeat heat treatment (20 hours @ 1100ºC) to coarsen the prior beta grains. The temperature of the furnace was not increased for the second heat treatment (to increase grain growth kinetics) because of the limitations of the furnace. Two cycles of the heat treatment gave grains estimated to be no smaller than half the size of the Ti6246 vacuum heat-treated blanks. Given the established CDF sensitivity of Ti6242 in a bimodal microstructural form this was considered an adequately large prior beta grain size from which to determine dwell sensitivity in a beta processed condition [81, 118].

Of the four Ti6242 blanks used to select a suitable microstructure, small sections were taken from blanks subject to one and two heat treatment cycles. Grain size and microstructure were assessed in each case. Remaining material was subject to air furnace heat treatments intended to coarsen the primary alpha platelet structures and reduce the number of alpha/beta phase interfaces over alpha colony dimensions. Two heat treatments were attempted. Both of these involved briefly solutioning the material at temperatures above beta transus before cooling at rates of 5ºCmin^{-1} and 1ºCmin^{-1} respectively to a temperature of 800ºC and water quenching. Details of the heat treatment are given in Table 5-2.

The most suitable microstructure for testing was selected as the material subject to two vacuum heat treatment cycles then cooled at 10ºCmin^{-1} in the vacuum furnace. Although it was possible to coarsen the primary alpha platelet structures and hence reduce the number

of alpha/beta interfaces (and potentially increase sensitivity to dwell effects) with the application of a slower cooling rate it was decided that this was unnecessary. This decision was made for two reasons, outlined in the next paragraph.

Firstly, given previous investigations of CDF in Ti6242 and its likely susceptibility in beta processed colonised form it was thought to be unnecessary to coarsen the microstructure in order to observe dwell fatigue effects [118]. Secondly, the application of an air furnace heat treatment with a very slow cooling rate would allow alpha case formation on the specimen blank surface and the pickup of oxygen and other interstitial elements. This was a concern because of the small size of the blanks and the need to maintain as large a section size as possible prior to an operation involving inertia welding blanks to dumbbell ends. Reducing the blank section size by alpha case removal before inertia welding (due to potentially detrimental effects on weld integrity) would result in weld-lines located at gauge radius positions closer to the gauge length. This would increase susceptibility to failure at inertia welds rather than in the specimen gauge length.

5.2.3.1 Friction welding of Ti6242 specimens

Friction welding was performed at The Welding Institute (TWI) using a FW11 continuous drive rotary friction welding machine. Blanks previously heat treated to form suitable microstructures were machined to cylinders of 34mm length x 13mm diameter. Cylindrical gauge lengths were used for inertia welding to prevent the ingestion of hot flash and oxygen into the weld zone potentially creating hard alpha defects in the weld. Specimen bar ends were sectioned from aerospace grade 32mm diameter Ti6/4 bar in 40mm lengths. A total of 18 gauge length cylinders and 36 bar ends were supplied to TWI. Friction welded dumbbells had the geometry displayed in Figure 5-7.

The work used a total of four gauge lengths in trial welds to determine friction welding parameters; three tensile specimens and one dumbbell for sectioning and metallographic assessment. The three tensile specimens were loaded to failure. In each case failure occurred in the gauge length away from the weld-affected region of the dumbbell. UTS values of 892MPa, 935MPa and 952MPa were recorded.

Following trial welds the parameters used for manufacture of 14 dumbbell specimens were as follows:

- Rotational speed 3000rpm
- Frictional force 6kN (46Nmm^{-2})
- Forge force 8kN (62Nmm^{-2})
- Burn off 3mm

The typical shape of the friction-welded dumbbells is shown in Figure 5-8. Further details of the friction welding work are provided in a summary report, provided by TWI on completion of the work package – see volume B section 5.8.

In addition to the work conducted by TWI, a tensile specimen was sectioned and examined following tensile testing. No weld defects, porosity or cracking were observed within the weld. The weld was characterised by a transition from the respective microstructures of the Ti6242 gauge and the Ti6/4 bar to a martensitic microstructure with a very fine beta grain size. This was attributed to a rapid post-weld cooling rate. The heat-affected zone of the weld was estimated to be 2.5-3.0mm in width. The microstructures in the friction weld are shown in Figure 5-9 to Figure 5-12.

As was the case with previous inertia welding work, PWHT for stress relief was not applied to these test specimens. This was because the heat treatment was designed to avoid the precipitation of fine secondary alpha platelets [157]. A prolonged exposure to the conventional PWHT temperature of 640ºC may allow the precipitation of secondary platelets, potentially reducing dwell susceptibility through a reduction of effective slip length and/or the reduction/prevention of planar slip band formation.

5.2.4 Mechanical testing

After heat treatment, Ti6246 blanks were machined to test-piece geometries. Two LCF specimen blanks were sectioned to check optical microstructure following heat treatment, leaving a total of five tensile and 13 LCF specimens. Fatigue testing used test-piece geometry RLH10369, previously used for the investigation of CDF sensitivity in Ti6246 production disc material (see chapter four).

From the three Ti6242 discs supplied by RRC there were a total of five tensile specimen blanks and 14 fatigue specimen dumbbells that were machined to test-pieces.

5.2.4.1 Tensile testing

Five tensile tests each were performed on Ti6246 and Ti6242 specimens using the equipment and method described in chapter three.

5.2.4.2 Fatigue testing

Fatigue testing was performed at the University of Birmingham. Procedures are described in chapter three. Maximum test stresses were initially selected based on tensile test results. In the testing of both Ti6246 and Ti6242 the first LCF test was selected at ~95% of estimated

UTS. Test stresses were then selected accordingly to establish fatigue behaviour over a suitable cyclic range.

A total of five baseline LCF tests and six cold dwell LCF tests were conducted on Ti6246 specimens. Initial LCF test peak stress was 760MPa (95% of estimated UTS of ~800MPa). From this result further test stresses were selected. The dwell LCF test settings were then selected for comparison of fatigue behaviour at the high end of this stress range.

A total of seven baseline LCF tests and six cold dwell LCF tests were conducted on Ti6242 specimens. The initial LCF test peak stress was 800MPa (~95% of estimated UTS of ~850-860MPa). Further test stresses were selected from this result.

5.3 Results

5.3.1 Material characterisation

5.3.1.1 As-received Ti6246 optical microstructures

Significant variations in optical microstructures were observed in both pancake forgings A1 and B2. Microstructures changed according to forging strains and post forge cooling rates. In more heavily worked sections of the pancake high aspect ratio beta grains were observed, whilst lower deformation strains led to equiaxed grains in other areas. Grain flow aligned coarse primary alpha platelets are present in high strain microstructures. In low strain regions there was evidence of optical alignment of primary alpha platelets. Typical microstructures from higher strain locations within each pancake are displayed in Figure 5-13 and Figure 5-14.

5.3.1.2 As received Ti6246 crystallographic textures

As for the significant variability of the optical microstructure of the pancake forgings, significant variations in texture also occur. This is demonstrated from two sets of EBSD results, the first taken from a low forging strain location in pancake A1, the second from a high strain location in pancake B2. These results are given in Figure 5-15 to Figure 5-21.

Both pancakes show varied beta textures and the presence of large colonies of alpha platelets. The alpha colonies in pancake B2 that have been mapped are more elongated in comparison to the EBSD results of pancake A1, consistent with the higher aspect ratio of prior beta grains.

5.3.1.3 As received Ti6242 optical microstructures

Optical assessment showed similar grain flow patterns and microstructures in the bore of each of the three compressor disc forgings. Typical optical microstructures in these discs are displayed in Figure 5-22, Figure 5-23 and Figure 5-24.

5.3.1.4 As received Ti6242 crystallographic textures

EBSD work characterised the texture variations in the disc bore. Based on the similarity in microstructures across the three available discs, only disc B was selected for texture assessment. Two extreme positions were selected, one in a region of high grain flow, the other in a region of low grain flow.

EBSD maps were obtained at low, intermediate and high magnifications (relative to the scale of the microstructure). Because of the alpha stabilisation of the alloy and the EBSD acquisition settings used, only very low levels of beta phase were detected. Therefore only alpha phase crystal orientation maps were acquired. These maps and the associated analyses are displayed in Figure 5-25 to Figure 5-30.

5.3.1.5 Ti6246 microstructures following beta heat treatment

Various beta heat treatments experiments were conducted in attempts to create a more CDF susceptible microstructure. For brevity only those experiments on representative size specimens are included in these results (refer to Table 5-1).

The prior beta grain size following a twenty-hour vacuum hold at 1100ºC can be observed from the surface condition of specimen blanks (see Figure 5-31). Despite variations in beta grain size and shape in the source material, the beta heat treatment led to a homogeneous

microstructure and grain size distribution. The starting microstructure/grain size does not show an influence on the microstructure achieved following beta heat treatments.

Following vacuum heat treatment, 10ºCmin^{-1} cooling to 800ºC then helium quenching to low temperature, the microstructure formed at the centre of an LCF specimen blank is displayed in Figure 5-32. This is the microstructure corresponding to sample 1A from Table 5-1. Similar microstructures were observed in blanks from both pancake A1 and pancake B2 following the vacuum heat treatment.

Samples 1B, 1C, 1D and 1E were re-solutioned and subject to a very slow cooling rate through the beta transus to a temperature at which complete beta to alpha phase transformation had occurred. At this temperature the blank was water quenched to avoid precipitation of secondary alpha phase. The microstructure at the centre of sample 1B is displayed in Figure 5-33. The microstructures of sample 1C, 1D and 1E are displayed in Figure 5-34, Figure 5-35 and Figure 5-36 respectively.

In the material selected for CDF testing (Table 5-1, Sample 1B) the MLI prior beta grain size and colony size measurements were taken. Ten measurements of MLI prior beta grain size (covering a total of 75 prior beta grain boundaries) were taken. The average prior beta grain boundary spacing was calculated at ~3850µm. Assuming a relatively uniform distribution of equiaxed prior beta grain morphologies (as observed on sectioning) the average beta grain volume was calculated at ~56.8mm^3.

A similar set of ten measurements of alpha colony MLI size (covering a total of 429 alpha colony boundaries) gave a calculated alpha colony cross-section size of ~610µm. The average alpha colony volume was therefore calculated as 0.23mm^3.

For a LCF test specimen with a 9mm gauge diameter and a 15mm gauge length the volume of material under test is ~950mm^3. Therefore for the Ti6246 microstructure examined the typical number of prior beta grains under test would be 17. The average number of colonies under test in the gauge length is calculated at ~4,200.

5.3.1.6 Ti6246 textures following beta heat treatment

Corresponding EBSD assessment was undertaken to confirm that the large optical units in the microstructures assessed in section 5.3.1.5 contained single crystallographic orientations. An optical site of interest in sample 1B was selected in which five distinct prior beta grains could be identified (shown in Figure 5-37).

Despite the relatively low retained beta content of the microstructure, from EBSD maps it is possible to identify the different beta textures present in these five grains. Beta COMs are displayed in Figure 5-38.

Each prior beta grain shows a distinct orientation. Any preferred deformation texture that may have existed in the billet material prior to heat treatment appears to have been removed. The corresponding alpha phase COMs (enhanced using a nearest neighbour fit for unindexed and beta phase points) show the presence of large alpha colonies in the microstructure. These are displayed in Figure 5-39.

The extremely low cooling rate allowed diffusional transformation and the growth of alpha colonies from the prior beta grain boundaries [22, 157]. Large colonies extend over distances of several millimetres. No Widmanstätten alpha platelets are present in the optical microstructure following beta heat treatment.

5.3.1.7 Ti6242 microstructures following beta heat treatment

As for Ti6246, full-size Ti6242 blanks were used in heat treatment trials to avoid variations in microstructure with section size. The experimental variations listed in Table 5-2 are displayed in Figure 5-40 to Figure 5-48. Samples subject to two beta heat treatment cycles rather than one displayed a similar microstructure although the prior beta grain size and colony size had increased as a result of the additional time above the beta transus temperature.

Material used for mechanical testing was subject to a forty hour hold above the beta transus (at 1050ºC) under vacuum conditions followed by a 5ºCmin^{-1} controlled furnace cool to 800ºC and helium quench to low temperature. The large prior beta grain size can be observed from the surface condition of specimens following vacuum heat treatment. This is shown in Figure 5-49. The microstructure of the specimens is shown in Figure 5-50 and Figure 5-51.

As for Ti6246 test material the MLI prior beta grain size and colony size measurements were taken. Ten measurements of MLI prior beta grain size (covering a total of 51 prior beta grain boundaries) were taken. The average prior beta grain size was calculated as ~2650µm. Assuming equiaxed prior beta grain shape (as observed on sectioning) the average beta grain volume was calculated at ~19.0mm^3.

A similar set of twelve measurements of alpha colony MLI size (covering a total of 247 alpha colony boundaries) gave a calculated alpha colony size of ~740µm. The average alpha colony volume was therefore calculated as ~0.40mm^3.

For a LCF test specimen with a 9mm gauge diameter and a 15mm gauge length the volume of material under test is ~950mm^3. Therefore for the Ti6242 microstructure examined the

average number of prior beta grains under test in the gauge length would be 50. The average number of colonies in the gauge length is calculated at ~2,400.

5.3.1.8 Ti6242 textures following beta heat treatment

Because of the relatively low beta content of the alloy it is difficult to resolve beta grain textures at the magnifications and step sizes used. However, the beta heat treatment is believed to result in a weakening of the beta macro-texture, and a range of alpha colony orientations are observed in the material. Alpha COMs are given under section 5.7.8. The corresponding microstructure for these texture assessments is displayed in Figure 5-54. EBSD assessment showed the presence of large colonies of common alpha orientations, with crystallographies corresponding to optical colony sizes.

5.3.2 Mechanical testing

5.3.2.1 Ti6246 tensile testing

Tensile tests were performed to determine an approximate material UTS in order to select suitable stresses for fatigue testing. A total of five tensile tests were conducted on Ti6246 specimens. Details of heat treatment, specimen geometry and test conditions are listed under the experimental method (section 5.2). The stress-strain curve for the test data is plotted in Figure 5-55.

Results show an average UTS of 783MPa with a standard deviation of 52MPa. Discounting the low result obtained from HT002 (possibly due to a volume of weak colony orientations in a specific section of the specimen gauge length) the average UTS of the four remaining tensile specimens was 814MPa with a standard deviation of 26MPa. As an approximation the UTS was estimated at 800-810MPa.

5.3.2.2 Ti6246 fatigue testing

The results of the Ti6246 fatigue test programme are listed in Table 5-3 (see section 5.7.10). A plot of these results in comparison is given in Figure 5-57. This compares the dwell fatigue performance of this material to the results from previous CDF testing of beta heat treated Ti6246. The graph in Figure 5-58 compares the two data sets when normalised against assumed UTS values.

5.3.2.3 Ti6242 tensile testing

A total of five tensile tests were conducted on Ti6242 specimens under the same test conditions as for Ti6246 specimens. The stress-strain plot for the five specimens is displayed in Figure 5-56. Results show an average UTS of 848MPa with a standard deviation of 24.5MPa.

5.3.2.4 Ti6242 fatigue testing

The results of the Ti6242 fatigue test programme are given in Table 5-4 (section 5.7.10). A plot of these results in comparison to the results of the large grain Ti6246 microstructure is given in Figure 5-59. The graph in Figure 5-60 displays these results when the test stresses are normalised against the assumed UTS values.

A second comparison between the results of the Ti6242 testing and the results of the original beta heat treatment Ti6246 test programme (see chapter four) is given in Figure 5-61 (normalised against material UTS).

Fractographic assessment of LCF specimens is provided in appendix 5.7.11.5. DLCF specimens are assessed under section 5.7.11.6.

Strain accumulation was monitored for three LCF tests and for all dwell LCF tests. Strain accumulation results are provided in section 5.7.12.

5.3.3 Specimen fractography

5.3.3.1 Ti6246 tensile tests

Ti6246 tensile specimens showed shear type failures with angled fracture surfaces rather than cup-and-cone type features. This was attributed to the size of the alpha colonies in the microstructure in relation to the specimen gauge width. There was limited planar slip in the specimens. Typical specimen fracture surfaces and underlying microstructures are displayed in the figures in section 5.7.11.1.

5.3.3.2 Ti6246 fatigue tests

Fractographic assessment of LCF specimens is provided in appendix 5.7.11.2. DLCF specimens are assessed under section 5.7.11.3.

5.3.3.3 Ti6242 tensile tests

Tensile failures in beta heat-treated Ti6242 specimens showed similar behaviour to that of Ti6246 specimens. Angled fracture surfaces were observed with the microstructure resulting in tortuous crack growth paths. The figures in section 5.7.11.4 display fractography and microstructure.

5.3.3.4 Ti6242 fatigue tests

Fractographic assessment of LCF specimens is provided in appendix 5.7.11.5. DLCF specimens are assessed under section 5.7.11.6.

5.3.4 Fatigue test strain accumulation behaviour

The following Ti6246 test specimens were monitored for strain accumulation behaviour during fatigue testing:

LCF specimens: - LF009 (800MPa), LF014 (780MPa)

DLCF specimens: - LF004 (800MPa), LF008 (780MPa), LF010 (770MPa), LF012 (750MPa), LF015 (790MPa)

Results show highly varied strain accumulation behaviour in both LCF and DLCF tests. Faster strain accumulation rates (per load cycle) and greater total strain accumulation levels were observed in dwell specimens. The graph in Figure 5-83 compares the strain accumulation behaviour of two DLCF tests and an LCF test. Note that the DLCF test LF008 actually failed after 8,112 cycles although strain data was only recorded to ~4,700 cycles. The strain at failure is unknown.

The following Ti6242 test specimens were monitored for strain accumulation behaviour during fatigue testing:

LCF specimens: - A9 (800MPa), C5 (750MPa), C8 (725MPa)

DLCF specimens: - C4 (825MPa), A8 (800MPa), B8 (800MPa), B5 (750MPa), C7 (725MPa), C9 (750MPa)

As for beta heat treated Ti6246, test results show highly varied strain accumulation behaviour. Faster strain accumulation rates (per load cycle) and greater total strain accumulation levels were observed in specimens with a two-minute dwell at peak stress although there was significant variation in the strain accumulation behaviour of DLCF tests. Results are plotted in Figure 5-84.

5.4 Discussion

5.4.1 Beta heat treatments

Beta annealing heat treatments were able to successfully create an alpha colony microstructure in both Ti6246 and the Ti6242 alloys. Because previous work (chapter four) had already investigated this microstructure for Ti6246 alloy, further modifications were necessary to produce a microstructure with potentially higher susceptibility to CDF. This was achieved through increasing the beta grain size and the alpha colony size [157]. Initial heat treatments under atmospheric conditions above the beta transus temperature noted significant increases in grain size for low (<2hr) hold times, with a gradual reduction in the grain growth rate at increasing times. This was attributed to a reduction in driving forces for grain growth, e.g. effective strain levels in the material [167]. Also noted was the development of large layers of alpha case on the surfaces of specimen blanks. To prevent spallation a hold time and temperature was selected and applied under vacuum conditions. A moderate cooling rate was used due to time constraints on usage of the vacuum furnace. This produced a microstructure of Widmanstätten alpha platelets. A second heat treatment briefly re-solutioned above transus before applying a very slow cooling rate to develop coarse alpha colony structures. This was intended to reduce the number of potential barriers to dislocation movement through a reduction in alpha/beta interfaces. Because of the alloy chemistry it was not possible to further reduce the beta phase fraction using these slow cooling rates. The extremely slow cooling rate led to the coarsening of both alpha and beta phases [117]. However, the presence of coarse beta layers in the heat treated material and their influence on CDF behaviour was disregarded due to the very large alpha colony size and the very coarse nature of alpha platelets.

Ti6242 heat treatments did not produce the same level of beta grain growth for similar beta phase hold times and temperatures (relative to respective beta transus temperatures). As such, to achieve a similar coarse beta grain microstructure in Ti6242 specimen blanks it was necessary to apply two beta heat treatments. Again a moderate through transus cooling rate was applied to the specimen blanks. However, because of the reduced beta stabilisation of the alloy the cooling rate was adequate to produce a microstructure of colonised alpha platelet growth [168, 169]. The alpha and beta phase were relatively fine in comparison to the Ti6246 microstructure, with more similarity to the Ti6246 microstructure produced for CDF testing in chapter four. The finer nature of the platelets and the consequent higher number of alpha/beta interfaces over colony cross-sections was not considered to be a drawback due to the known increased CDF susceptibility of Ti6242 [81].

The various as-received and heat treated microstructures were assessed using microscopy and EBSD techniques. X-ray diffraction would also have provided an assessment of macro-textures in the various conditions [158]. Polarised light and SRAS assessments could also have been used to characterise macrozone sizes in the different materials [28, 162, 170].

5.4.2 Ti6246 cold dwell fatigue testing

Ti6246 in a beta colony microstructural form with an extremely coarse grain and colony structure showed no substantial CDF effect. There was a small dwell debit on cyclic life at high test stresses (~92-96% UTS) and a noted life debit at higher stresses (~97-98% UTS). The dwell debit at higher stress levels could be attributed to cold creep effects [165, 168, 171]. Further evidence that Ti6246 is not a CDF sensitive material is provided in the absence of any 'quasi-cleavage' load normal initiation facet features at sub-surface locations on DLCF specimen fracture surfaces [16].

There is no evident difference in the fractography of LCF and DLCF specimens, with a mixture of surface and sub-surface initiation failures. In some LCF tests it is possible to observe fatigue controlled growth away from an origin (see Figure 5-66), whilst in other cases it is not possible to identify an origin (Figure 5-67). Similar examples for DLCF tests are given in Figure 5-68, Figure 5-69 and Figure 5-70. Because of the microstructure the crack growth path is highly tortuous and there are typically numerous angled facets across the fracture surface [90, 164]. Angled facets are assumed to result from crack propagation.

Sectioning of several test specimens revealed a widespread absence of planar slip bands (observed as shear offsets at alpha/beta interfaces) both near to the fracture surface and throughout the gauge length. This is in contrast with the Ti6246 colony microstructure tested in chapter four, in which extensive planar slip bands could be observed. As the development of planar slip bands is considered as a pre-cursor to stress redistribution at colony/grain boundaries and the formation of CDF cracks, their absence in the microstructure provides an explanation for the lack of a CDF effect in the alloy [16]. Because planar slip effects could be observed across alpha colonies in the previously tested colony microstructure, it is clear that the alpha stabilisation of the alloy is sufficient to allow such deformation behaviour to occur.

The absence of planar slip deformation is attributed to excessive coarsening of the beta phase. Increases in the prior beta grain size and alpha colony size lead to a reduction in the UTS of the material, although the test stresses used were maintained at a similar proportion of UTS to those in previous work. An increased alpha colony size was considered to be detrimental to CDF performance (provided that volume effects do not dominate test specimen behaviour) because of increased effective slip lengths and dislocation pile-up stresses. However, in achieving this highly coarse alpha colony microstructure both alpha

platelets and retained beta layers have coarsened. This has reduced the number of phase interfaces over individual colony cross-sections, which may be considered as a factor in promoting dislocation movement and increasing boundary pile-up stresses [106]. The absence of planar slip is therefore considered to result from the increased coarseness of the retained beta layers. Whilst planar dislocation movement may occur across individual alpha platelets, it is likely that the increased number of active slip systems in the beta phase prevent any colony size planar slip bands from forming [69].

Behaviour under LCF and dwell fatigue loading appears to be controlled by fatigue mechanisms based on fractographic analysis. In some cases fatigue crack growth can be observed from surface origins. However, in many cases a clear initiation site cannot be identified. Fracture surfaces are highly non-planar due to the microstructure and its influence on the crack growth path [57-59, 64, 90]. In all specimens the majority of the fracture surface consists of ductile failure through micro-void coalescence. Only small areas of some specimens can be identified as progressive fatigue crack growth [59, 60].

5.4.3 Ti6242 cold dwell fatigue testing

Testing of Ti6242 in the microstructural form described in section 5.3.1.7 for susceptibility to CDF has shown no clear effect on cyclic life. The results presented in Figure 5-59 to Figure 5-61 show highly variable behaviour in both LCF and DLCF results although there is no clear trend of a significant cyclic life reduction with the imposition of dwell loading periods.

As for fracture surfaces of beta colonised Ti6246 fatigue specimens, Ti6242 specimens were observed to display highly varied fractographic profiles, but no evidence of load normal quasi-cleavage initiation facets. Sample B8 showed failure during the second loading cycle.

This was attributed to a static overload failure resulting from an unfavourable combination of alpha colony orientations in the specimen gauge length. Other premature failures could similarly be attributed to variations in macroscopic specimen strength.

Sectioning and optical analysis of specimen microstructures revealed widespread planar slip deformation throughout the gauge length of both LCF and dwell specimens. Therefore, unlike in the case of the Ti6246 test programme discussed in the previous section, the beta layers in the colony Ti6242 microstructure do not provide sufficient resistance to the formation of trans-colony planar slip bands. Slip bands extend across alpha colonies and there are usually multiple parallel slip bands present in individual colonies [165]. Examples are given in the figures in sections 5.7.11.5 and 5.7.11.6. There appears to be a greater concentration of planar slip bands in dwell fatigue specimens although there does not appear to be an increase in shear offsets with the increased time on load. In contrast to beta heat treated Ti6246 specimens, planar slip dislocation movement in Ti6242 dwell fatigue specimens can continue across the boundaries of alpha colonies as displayed Figure 5-82.

The absence of a true CDF effect in Ti6242 is unexpected, given previous work displaying significant cyclic life reductions in bimodal, beta forged and (alpha + beta) solution heat treated, and beta annealed microstructures [81, 118, 165]. Given the microstructure and test stresses a large life reduction resulting from stress redistribution effects was expected. Its absence may be explained by volume effects (i.e. insufficient appropriately oriented colonies in specimen gauge lengths) [16]. However, this is unlikely given the estimated number of alpha colonies in a gauge length and the probability that there were one or more suitable combinations of neighbouring colonies in one or more of the dwell fatigue specimens [136, 140].

An alternative explanation is that failure occurs through micro-void coalescence or cleavage cracking rather than fatigue mechanisms. This hypothesis is supported by the absence of clear fatigue crack origins in the specimen fracture surfaces [53]. In some cases, featureless planar cracks (assumed to be cleavage cracks) show transformation to a ductile failure mode with progressive crack growth. In other cases, as for Ti6246 fracture surfaces, it is not possible to identify crack origins. Larger angled facets are often identified as the probable initiation site, although these facets display no evidence of cleavage or fatigue crack growth. Instead, cracking may occur through micro-void coalescence and 100% ductile failure. This may be explained given the planar nature of slip deformation and the large shear offsets that may form at phase interfaces [165]. Other researchers have reported that void formation will occur at alpha/beta interfaces (in similar Ti6242 colony microstructures) at certain levels of plastic strain [165]. Increasing deformation leads to void coalescence and the development of angled facet-like features through a ductile failure mechanism [109, 135, 172].

Given the significant size of alpha colonies in the microstructure under current investigation, the probability of micro-void formation under high applied stresses and large plastic strains (in all fatigue specimens) is high. This is based on the theory that larger colonies present greater effective slip lengths, allowing greater dislocation activity and consequent increases in the shear offsets observed at alpha/beta interfaces. However, although the theory supports a micro-void coalescence failure mechanism, there is no evidence of voiding in the microstructure of sectioned specimens and no conclusive proof of this mechanism.

In summary, whilst Ti6242 is conventionally susceptible to CDF in more than one microstructural condition, a coarse colony microstructure does not show such behaviour. No evidence of fatigue dominated cracking behaviour has been observed, with cleavage and micro-void coalescence mechanisms instead suggested to control cyclic life.

5.5 Conclusions

The following conclusions have been drawn from the work investigating beta heat treatments and cold dwell fatigue behaviour of Ti6246 and Ti6242 alloys:

- Beta heat treatment of Ti6246 with a heterogenous optical microstructure leads to the development of a relatively homogeneous microstructure of equiaxed beta grains.
- Longer exposure to supra-transus temperatures allows the development of very large Ti6246 beta grain structures. The initial period (~1-2hrs) of beta heat treatment leads to considerable beta grain growth, beyond which the rate of growth is substantially lower.
- Given a very large Ti6246 prior beta grain size a very low cooling rate is required to ensure the complete transformation to an alpha colony microstructure. The cooling rate required leads to the significant coarsening of both beta and alpha phases.
- Ti6242 shows different grain growth characteristics from Ti6246 despite a similar heat treatment temperature in respect of the beta transus temperature for each alloy. This difference in growth behaviour may result from compositional differences (due to a slower rate of molybdenum diffusion in Ti6246).
- Ti6242 shows an ability to form colony microstructures at much higher through-transus cooling rates than Ti6246 for similar large beta grain microstructures. This behaviour is attributed to the lower beta stabilisation of the Ti6242 alloy.
- Tensile testing of Ti6246 confirmed the significant strength reduction of the heat treated variant (cf. production disc forgings) associated with the large increase in beta grain size.

- Cold dwell fatigue testing of Ti6246 in the large beta grain/alpha colony microstructural condition showed low cyclic life debits for high applied stresses (>90% UTS) at room temperature. Only at very high stresses (>95% UTS) was a significant life debit observed. Some specimens showed surface initiation and fatigue crack growth, although in many cases the initiation site could not be identified.
- Sectioning of several Ti6246 specimens was unable to identify planar slip features (pre-requisite for cold dwell fatigue behaviour) in gauge length sections. This absence of planar slip deformation could not be attributed to the alloy composition, as previous work noted widespread planar slip in the alloy under both LCF and DLCF loading. The absence of planar slip is instead explained by the excessive coarsening of the beta phase, which contains a higher number of active slip systems than alpha phase and is therefore more able to dissipate planar dislocation pile-ups.
- As for Ti6246, tensile testing of Ti6242 following beta heat treatment shows a substantially lower UTS than for the typical production disc forging microstructure. Again this is attributed to the large beta grain size.
- Cold dwell fatigue testing of beta colonised Ti6242 showed no clear indication of susceptibility, both in terms of specimen cyclic lives and fracture surface characteristics. Whilst planar slip behaviour was able to occur across alpha colonies the cold dwell fatigue mechanism does not appear to have activated.
- The absence of cold dwell fatigue in the Ti6242 microstructure is unexpected given the literature available on the subject. Fractographic analysis instead suggests that failures are dominated by cleavage cracking (along favourably oriented crystallographic planes) or micro-void coalescence and ductile failure as a result of

void formation on planar slip bands at alpha/beta interfaces due to the size of alpha colonies and the resulting shear offsets.

- Both Ti6242 and Ti6246 test results show greater levels of total strain accumulation in DLCF specimens, highlighting the contribution of static loading and cold creep effects to the total plastic strain at failure.

5B Cold dwell fatigue performance of beta processed titanium alloys – Figures and tables

5.6 Experimental method

5.6.1 Ti6246 strain profile modelling

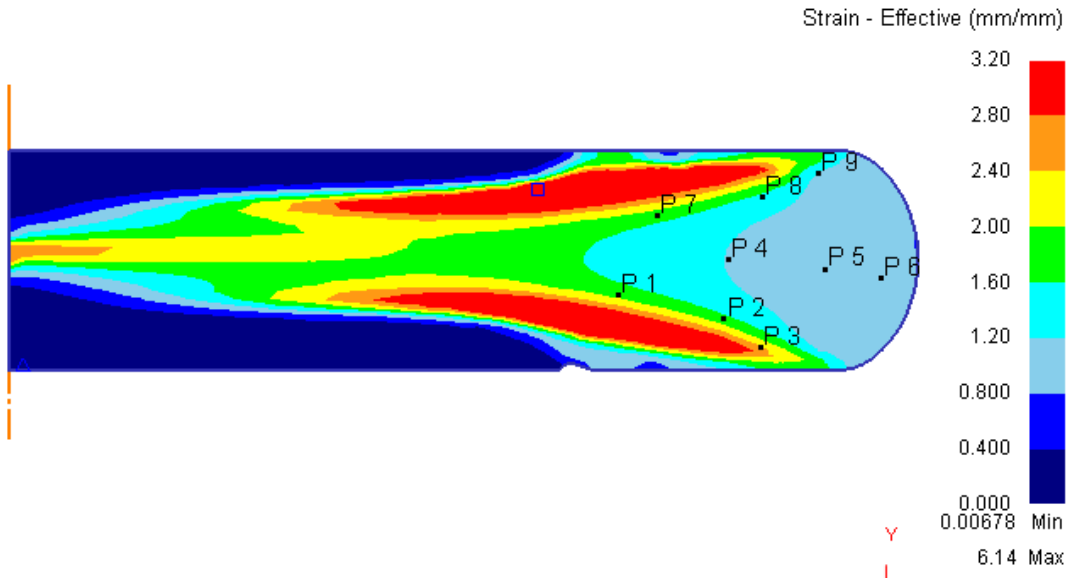

Figure 5-1 – Effective strain profile in pancake A1 following upset forging of billet material [166]

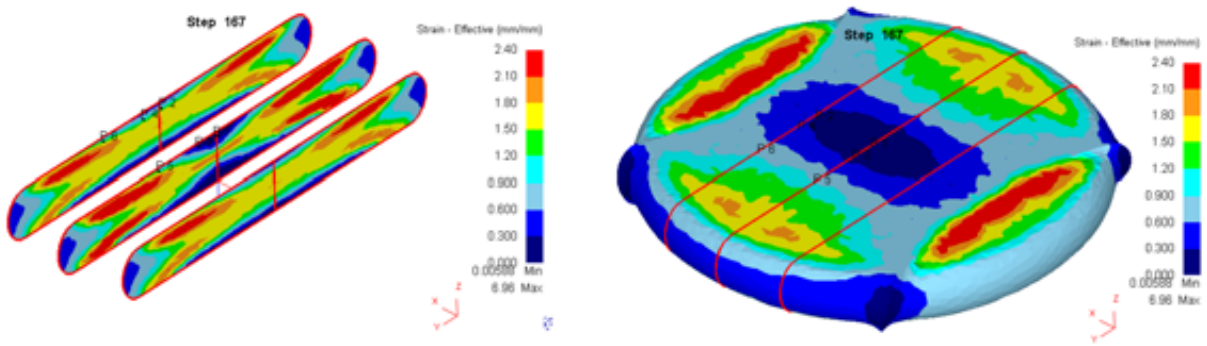

Figure 5-2 – Effective strain profile in pancake B2 following upset forging of billet material [166]

5.6.2 Ti6246 cut-up diagrams

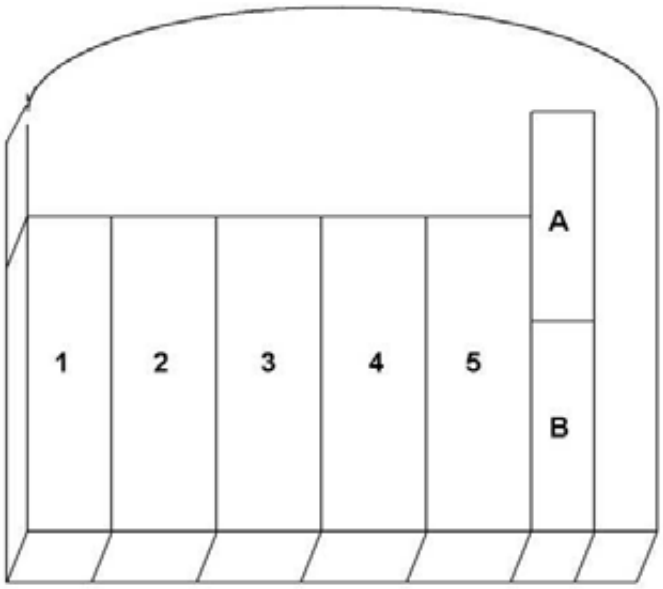

Figure 5-3 – Sectioning of pancake A1 (Billet axis and pancake forging compression axis both normal to this face)

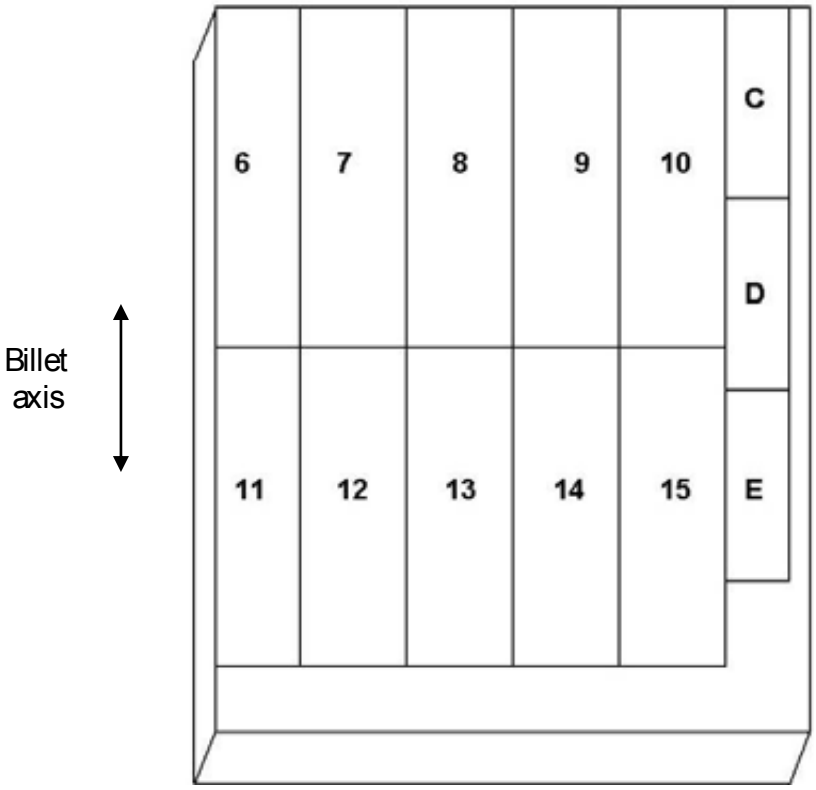

Figure 5-4 – Sectioning of pancake B2 (Pancake forging compression axis normal to this face)

5.6.3 Ti6242 cut-up diagrams

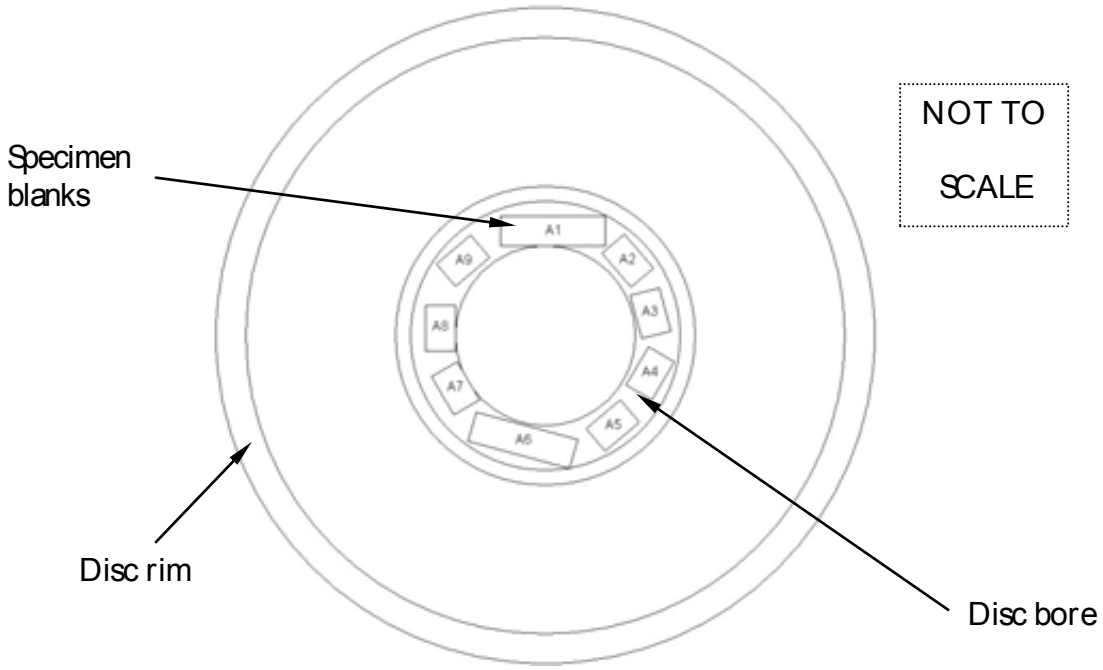

Figure 5-5 – Sectioning of Ti6242 specimen blanks from compressor disc bores (Plan view schematic of disc front face)

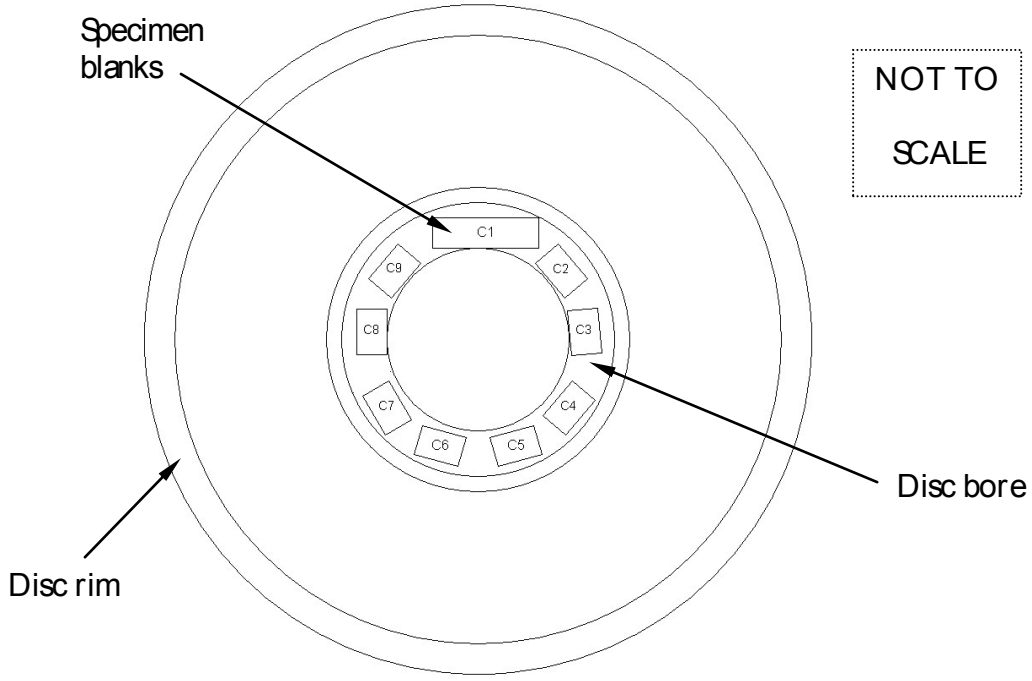

Figure 5-6 – Sectioning of Ti6242 specimen blanks from compressor disc C bore (Plan view schematic of disc front face)

5.6.4 Heat treatment

Table 5-1 – Ti6246 heat treatment experimental variations*

Sample	Supra-transus hold details	Cooling rate /ºCmin^{-1}	Sub-transus hold details	Quench details
1A	N/A	N/A	N/A	N/A
1B	970ºC / 1 hour	0.1	N/A	WQ @ 750ºC
1C	970ºC / 1 hour	0.1	900ºC / 10 hours	WQ @ 750ºC
1D	970ºC / 1 hour	0.1	900ºC, 850ºC, 800ºC (All 20 hr holds)	WQ @ 750ºC
1E	970ºC / 1 hour	0.2	900ºC, 850ºC, 800ºC (2 hr holds)	WQ @ 750ºC

* All specimen blanks initially subject to a 20-hour hold at 1100ºC under vacuum conditions with 6ºCmin^{-1} cooling rate to 800ºC, helium quench to room temperature

Table 5-2 – Ti6242 heat treatment experimental variations**

Sample	Vacuum heat treatment cycles	Further heat treatment details		
		Supra-transus hold details	Cooling rate /˚Cmin^{-1}	Quench details
2A	1	N/A	N/A	N/A
2B	1	1050ºC/20 minutes	5.0	WQ @ 800ºC
2C	1	1050ºC/ 0 minutes	1.0	WQ @ 800ºC
2D	2	N/A	N/A	N/A
2E	2	1050ºC/20 minutes	5.0	WQ @ 800ºC
2F	2	1050ºC/0 minutes	1.0	WQ @ 800ºC

** All specimen blanks initially subject to one or two cycles of 20-hour hold at 1100ºC under vacuum conditions with 10ºCmin^{-1} cooling rate to 800ºC, helium quench to room temperature

5.6.5 Specimen rotary friction welding

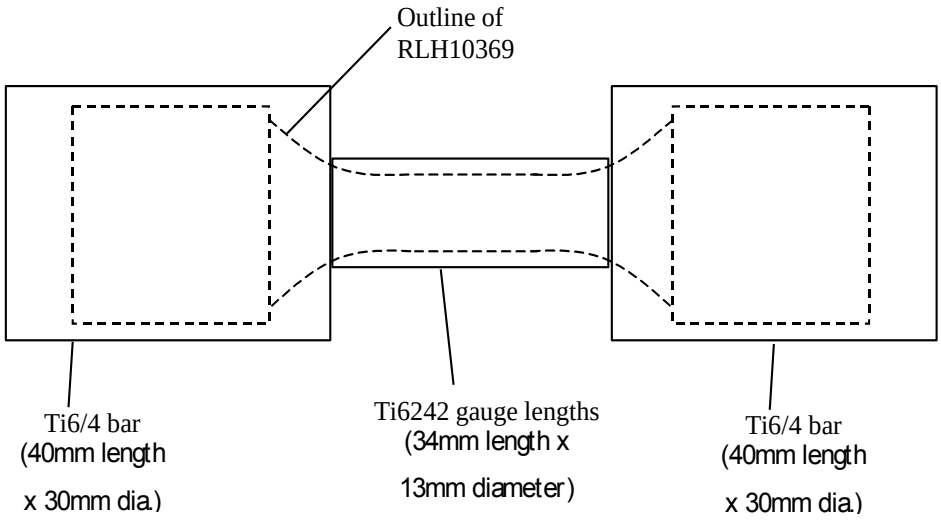

Figure 5-7 – Friction welded test-piece schematic diagram

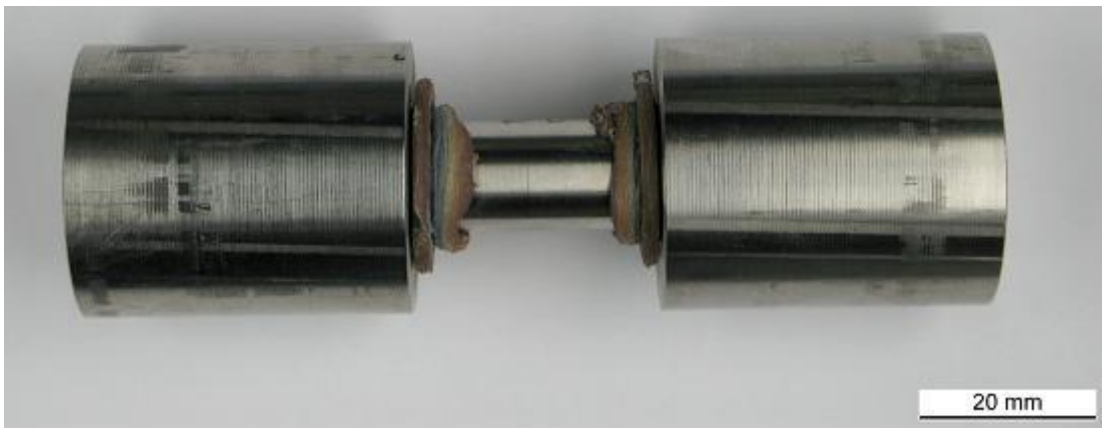

Figure 5-8 – Friction welded dumbbell specimen A8

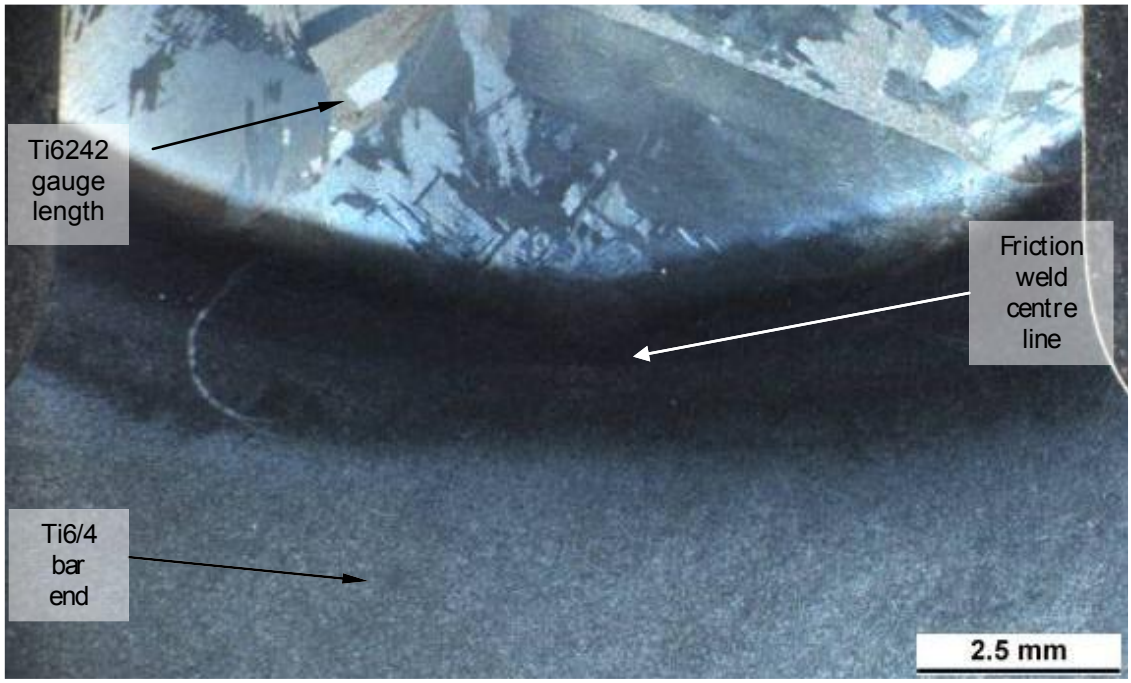

Figure 5-9 – Cross-section profile of typical friction weld specimen

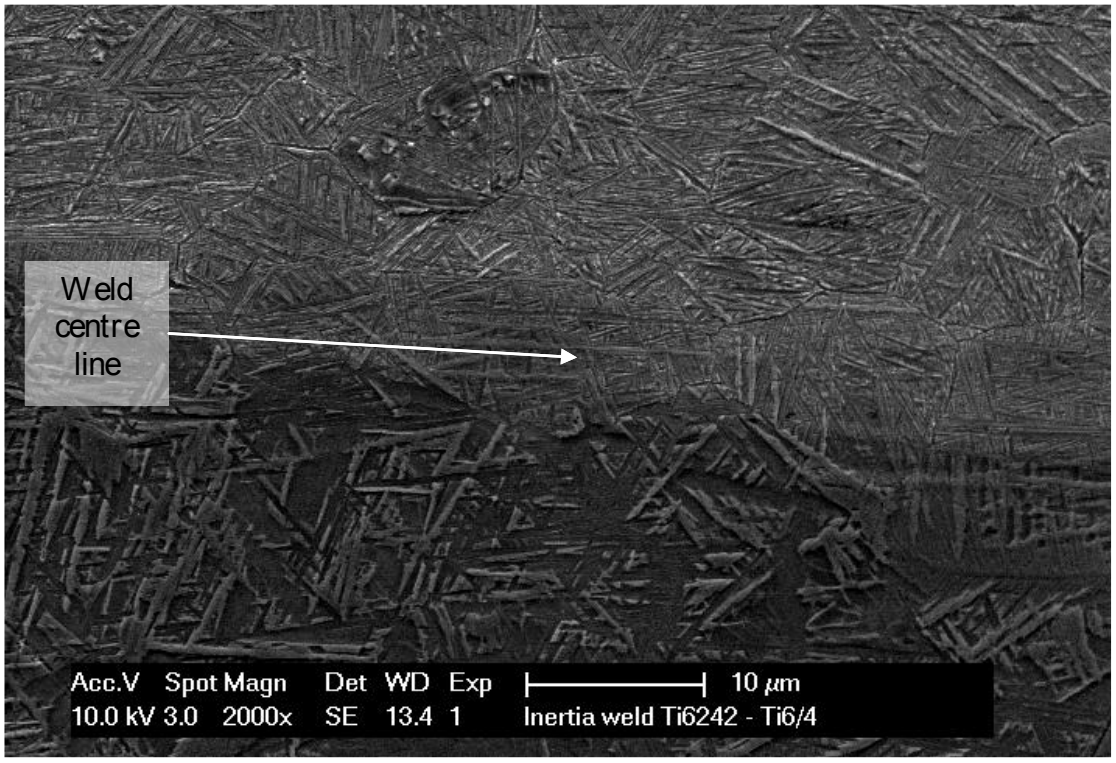

Figure 5-10 – Friction weld microstructure (At weld centre line)

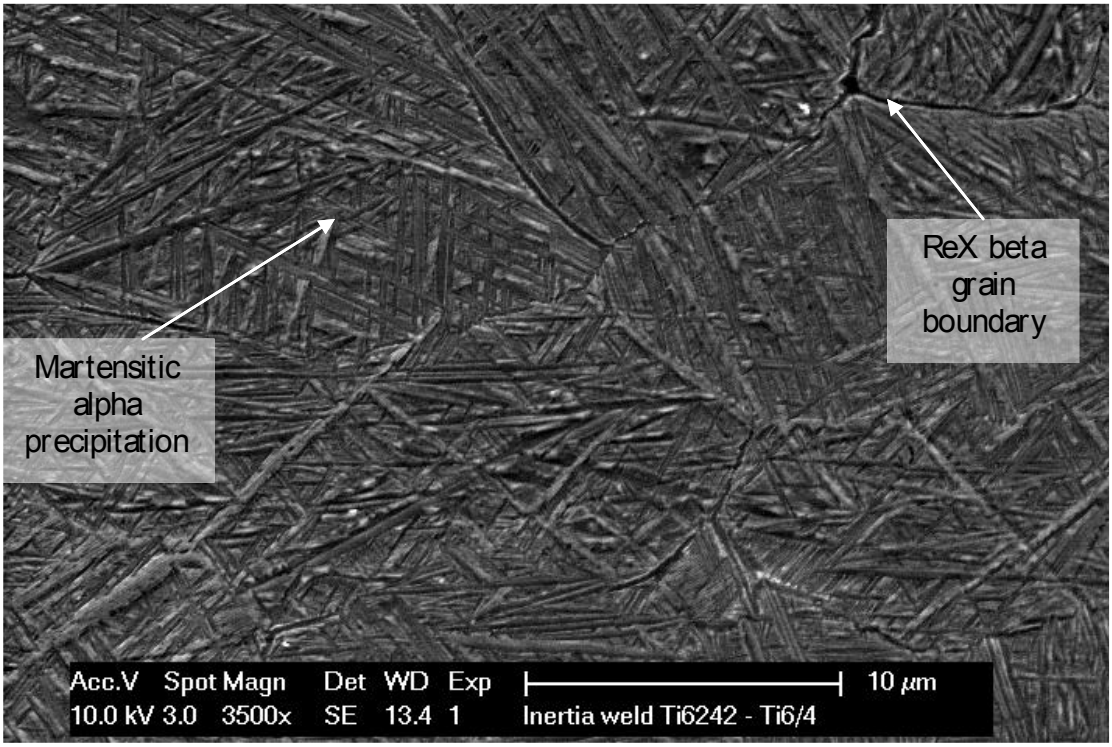

Figure 5-11 – Friction weld microstructure (Towards Ti6242 gauge length)

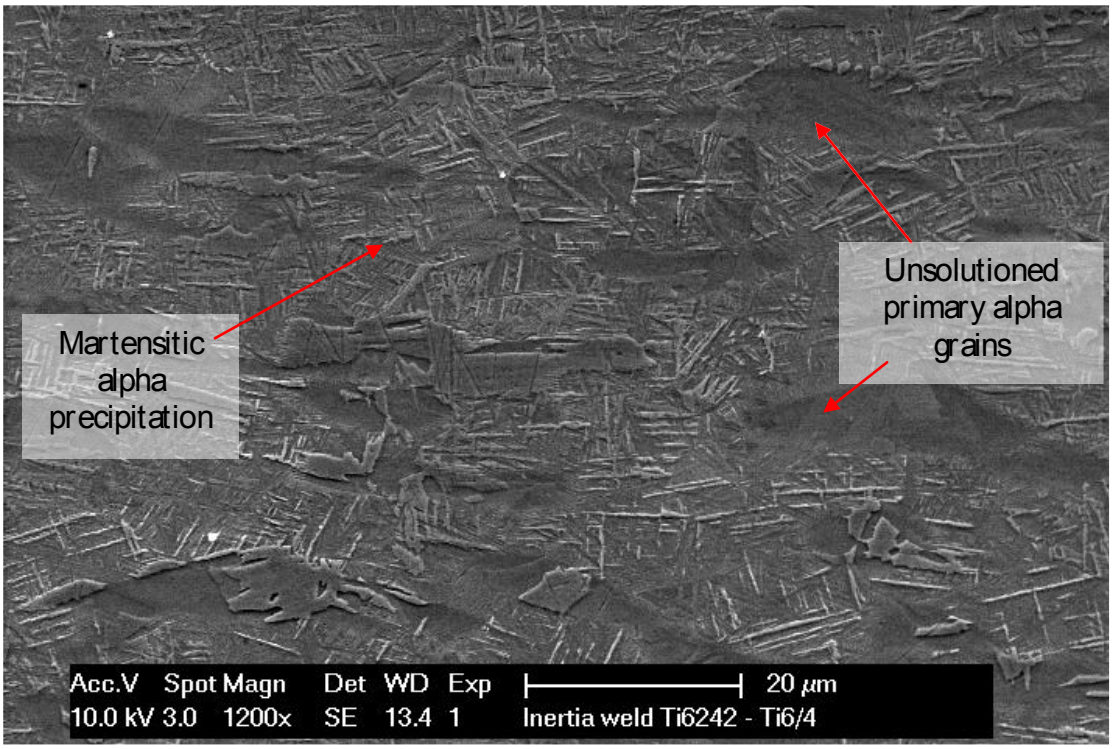

Figure 5-12 – Friction weld microstructure (Towards Ti6/4 bar end)

5.7 Results

5.7.1 Ti6246 As-received microstructure

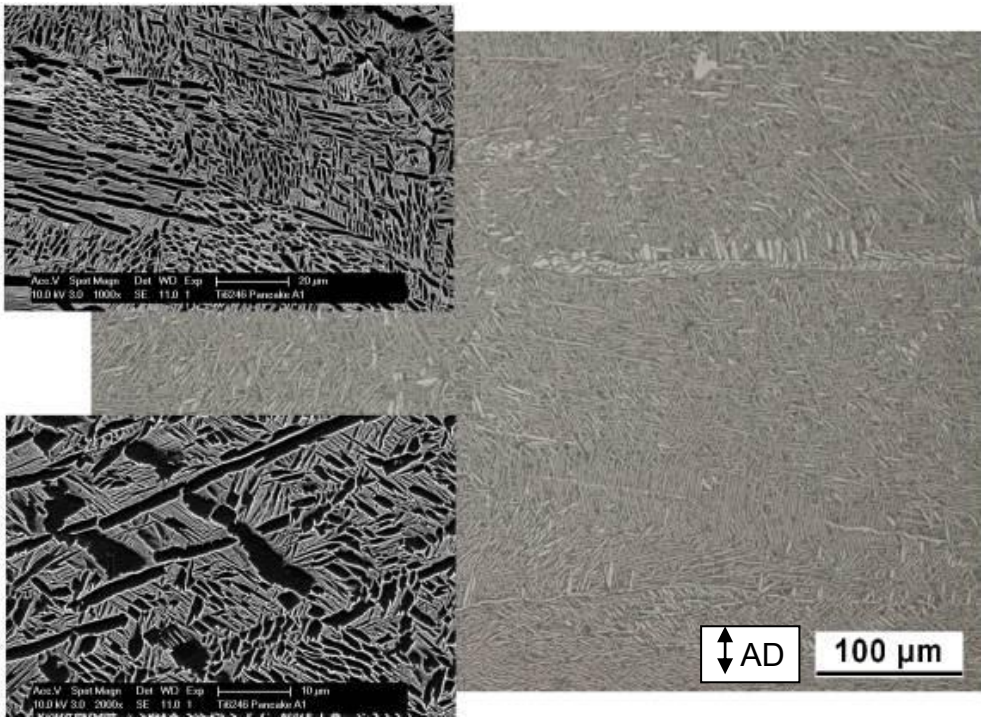

Figure 5-13 – As-received microstructural condition of pancake forging A1

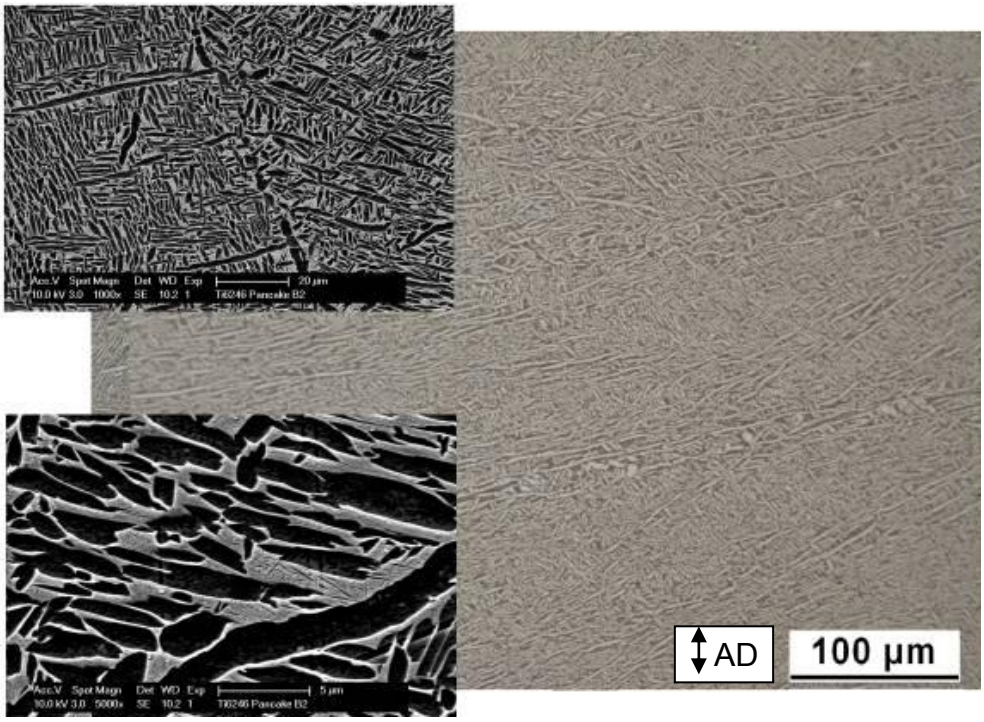

Figure 5-14 – As-received microstructural condition of pancake forging B2

5.7.2 Ti6246 As-received texture

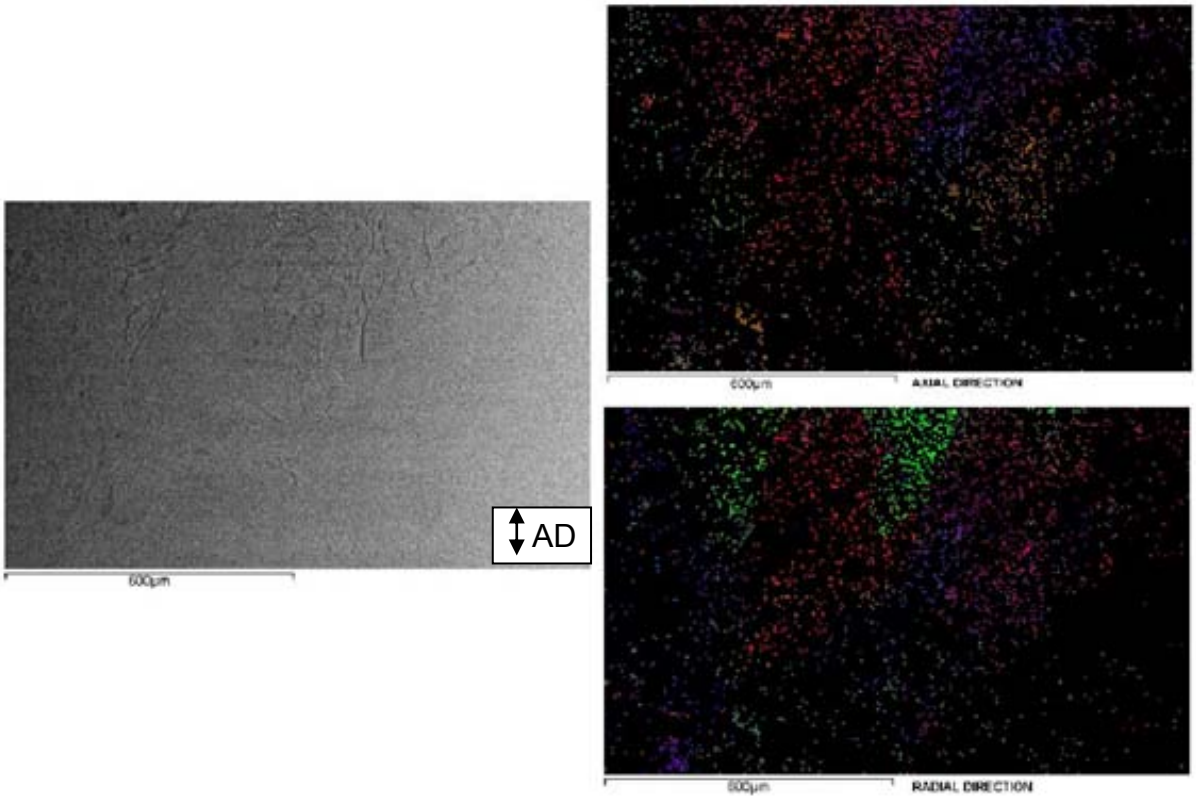

Figure 5-15 – SEM image of low strain region of pancake A1 microstructure. Corresponding COMs displaying beta textures w.r.t. axial (AD) and radial (RD) pancake directions

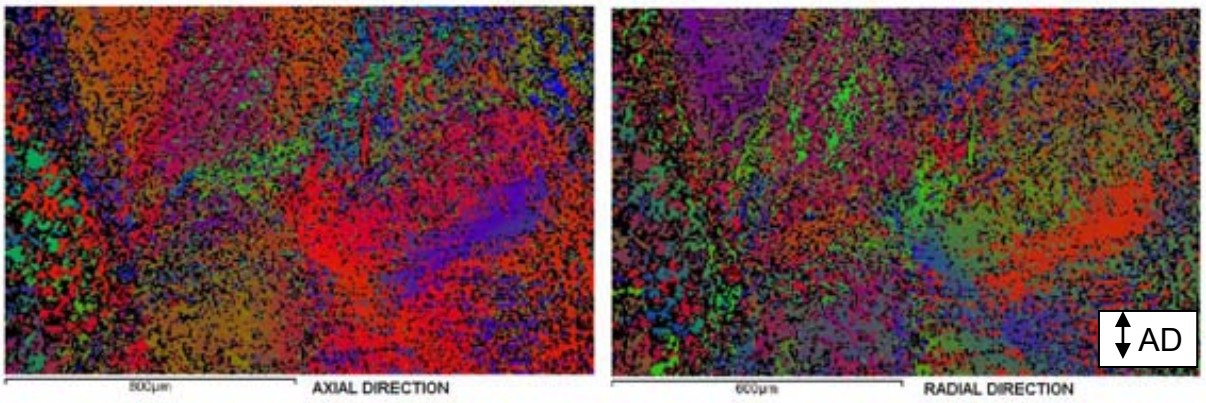

Figure 5-16 – COMs displaying alpha textures w.r.t. axial and radial directions for pancake A1, corresponding to area displayed in Figure 5-15

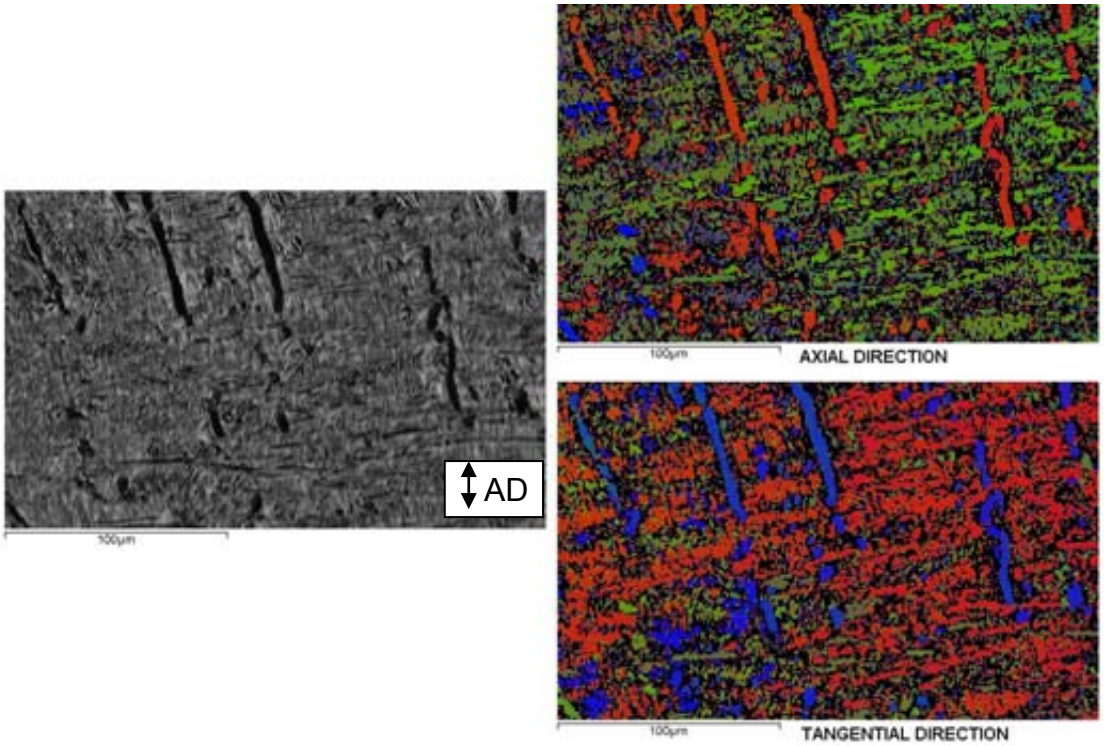

Figure 5-17 – SEM image of microstructures in pancake A1. Corresponding COMs displaying alpha textures w.r.t. axial and tangential pancake directions

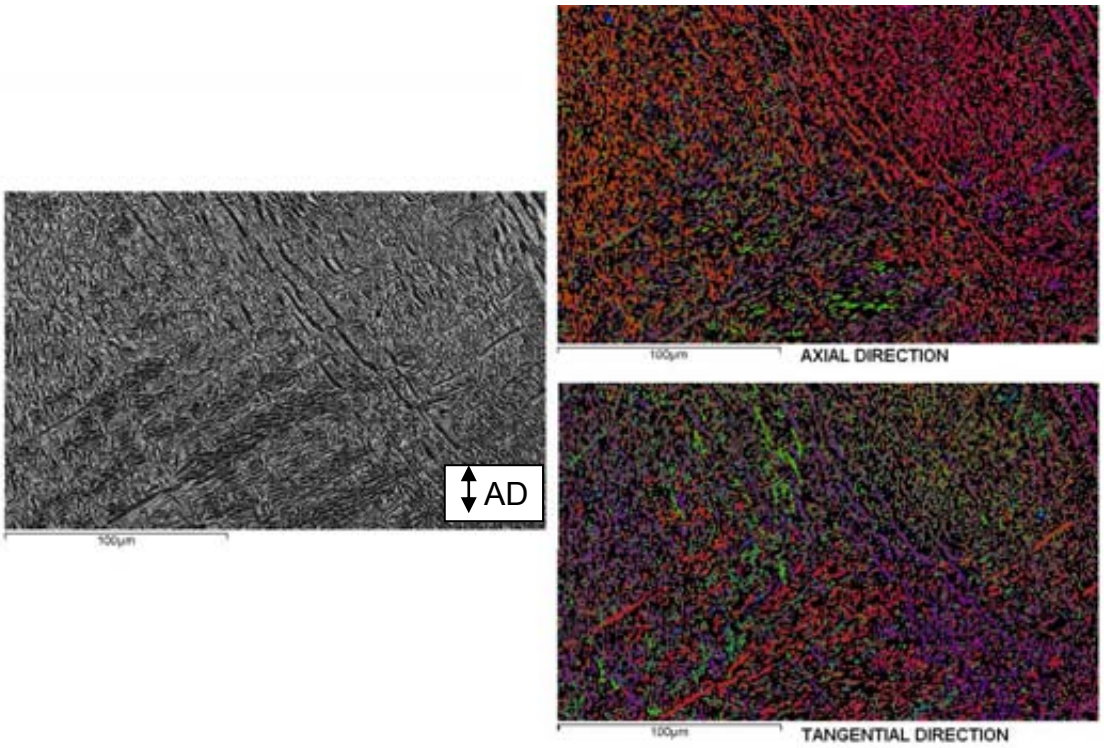

Figure 5-18 – SEM image of alpha platelet colony microstructure in pancake A1. Corresponding COMs displaying alpha textures w.r.t axial and tangential pancake directions

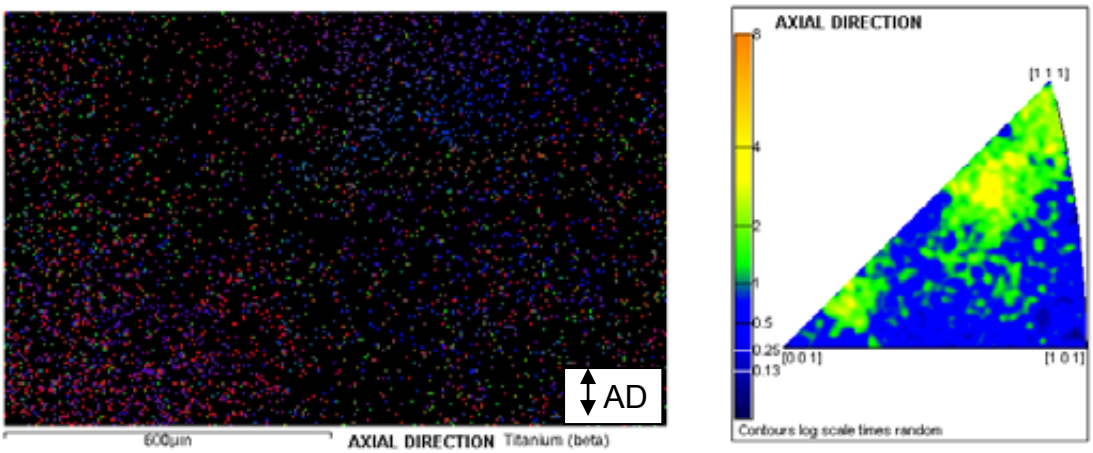

Figure 5-19 – Beta phase COM displaying textures w.r.t. AD pancake direction for high strain region of pancake B2. Corresponding axial direction inverse pole figure

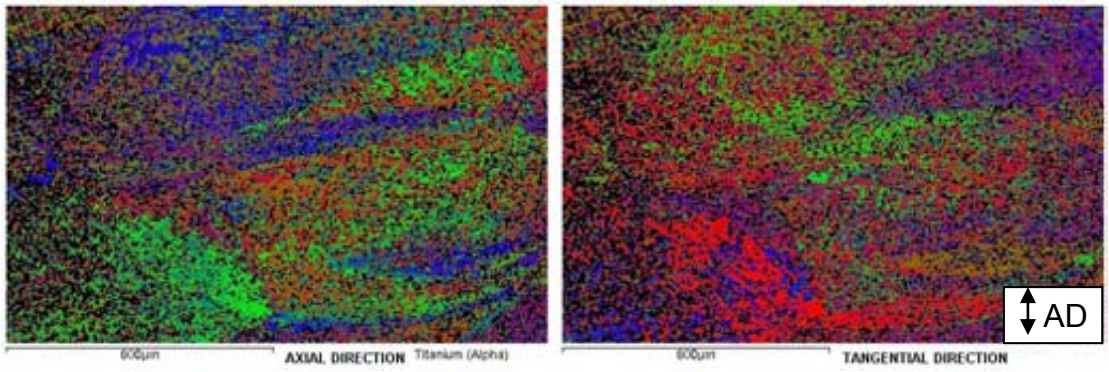

Figure 5-20 – Alpha phase COMs displaying textures w.r.t. axial and tangential pancake directions for high strain region of pancake B2

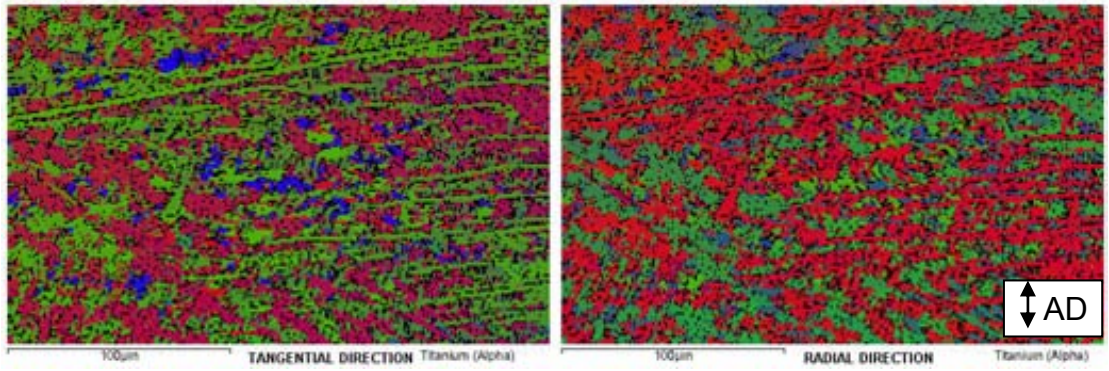

Figure 5-21 – Alpha phase COM displaying textures w.r.t tangential and radial pancake directions for high strain region of pancake B2

5.7.3 Ti6242 As-received microstructure

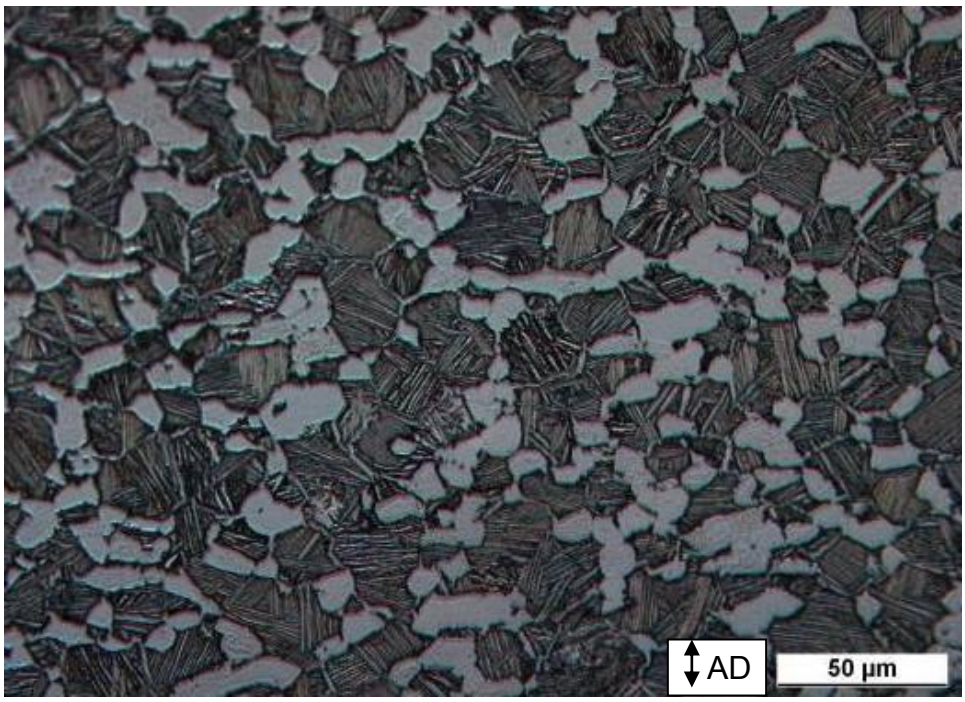

Figure 5-22 – Microstructure of Ti6242 compressor disc (A7) bore centre

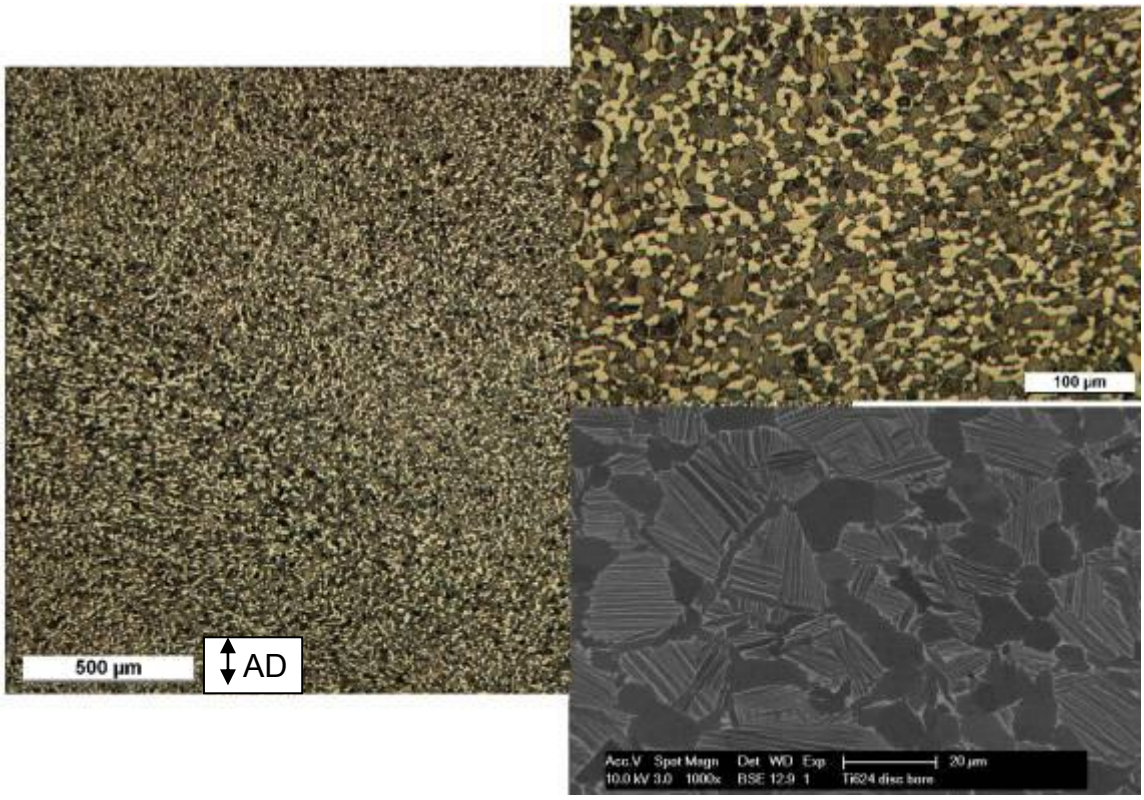

Figure 5-23 – Microstructure of Ti6242 disc (A7) bore edge (High macro beta grain flow)

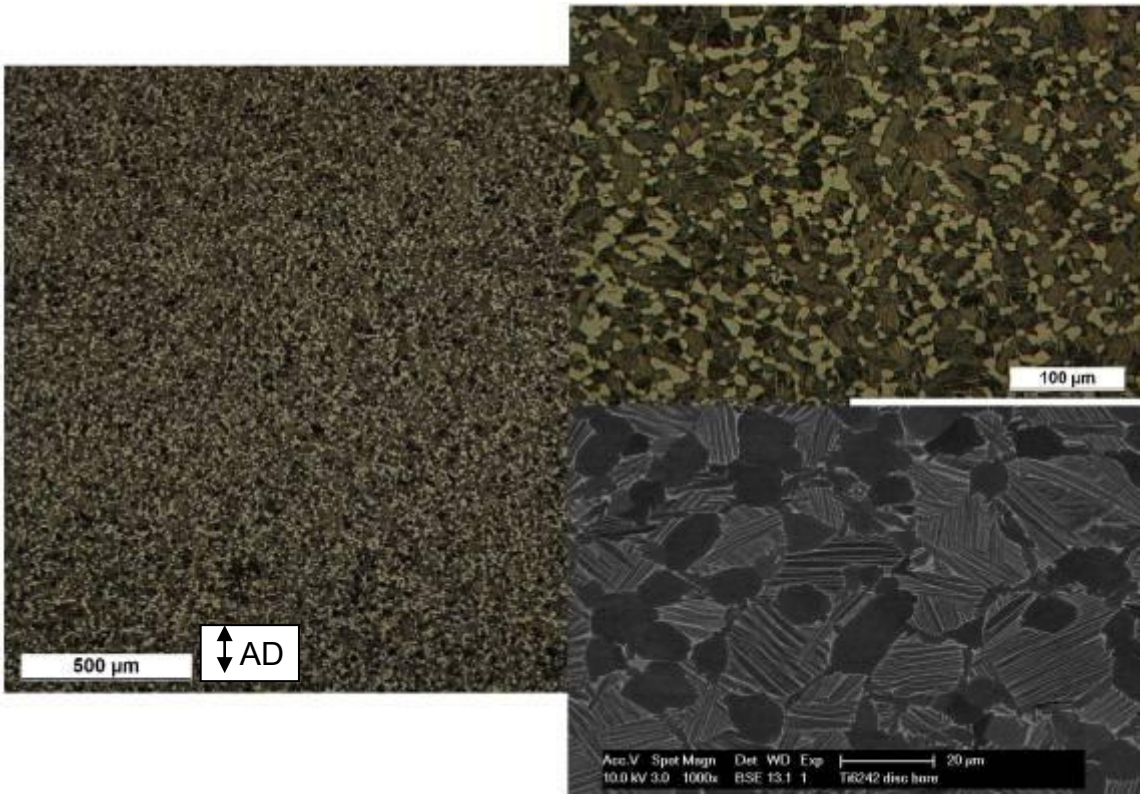

Figure 5-24 – Microstructure of Ti6242 disc (A7) bore edge (Low macro beta grain flow)

5.7.4 Ti6242 As-received texture

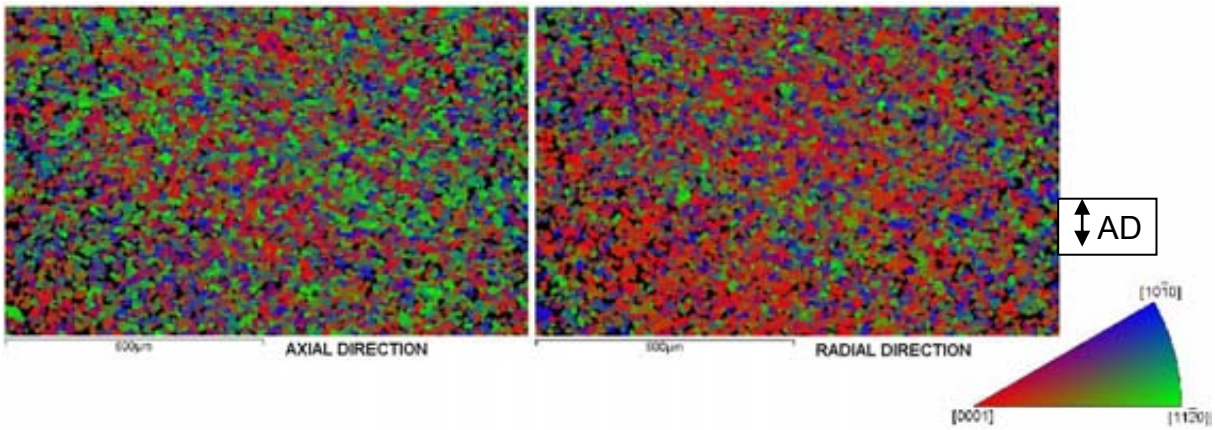

Figure 5-25 – Alpha macro-texture in Ti6242 compressor disc B in region of low aspect ratio beta grains. Textures displayed w.r.t. axial and radial disc directions

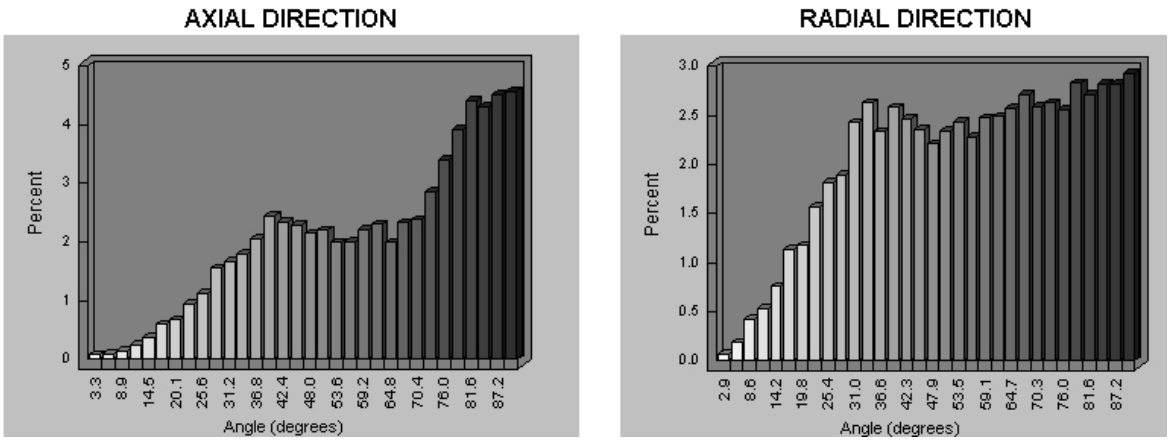

Figure 5-26 – Distribution of {0001} basal plane orientations w.r.t. axial and radial disc directions for crystal orientation maps in Figure 5-25

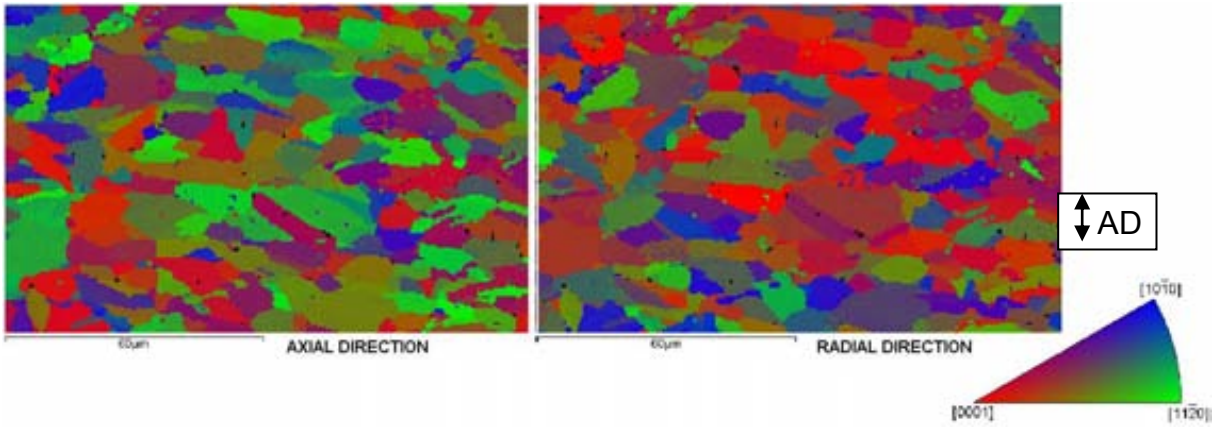

Figure 5-27 – Alpha micro-texture in Ti6242 compressor disc B in region of low aspect ratio beta grains. Textures displayed w.r.t. axial and radial disc directions

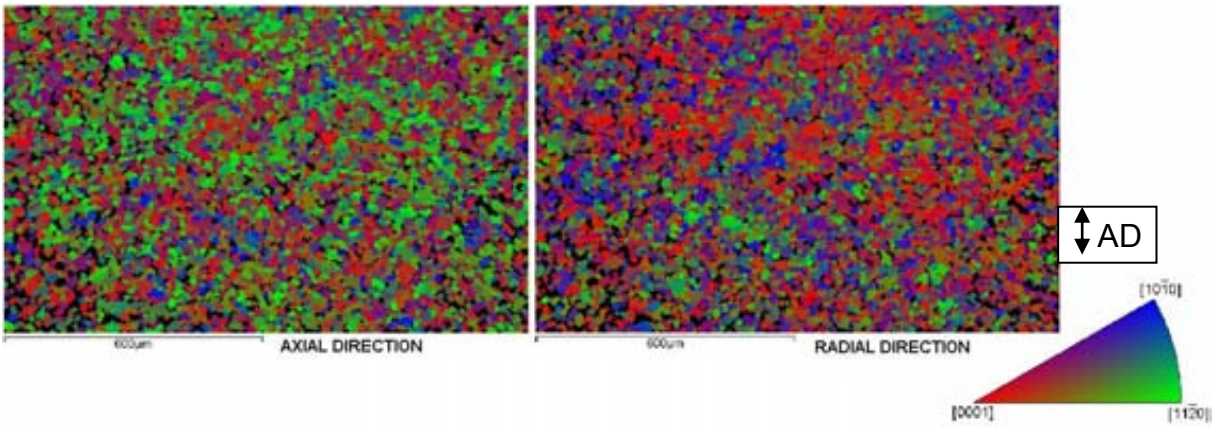

Figure 5-28 – Alpha macro-texture in Ti6242 compressor disc B in region of high aspect ratio beta grains. Textures displayed w.r.t. axial and radial disc directions

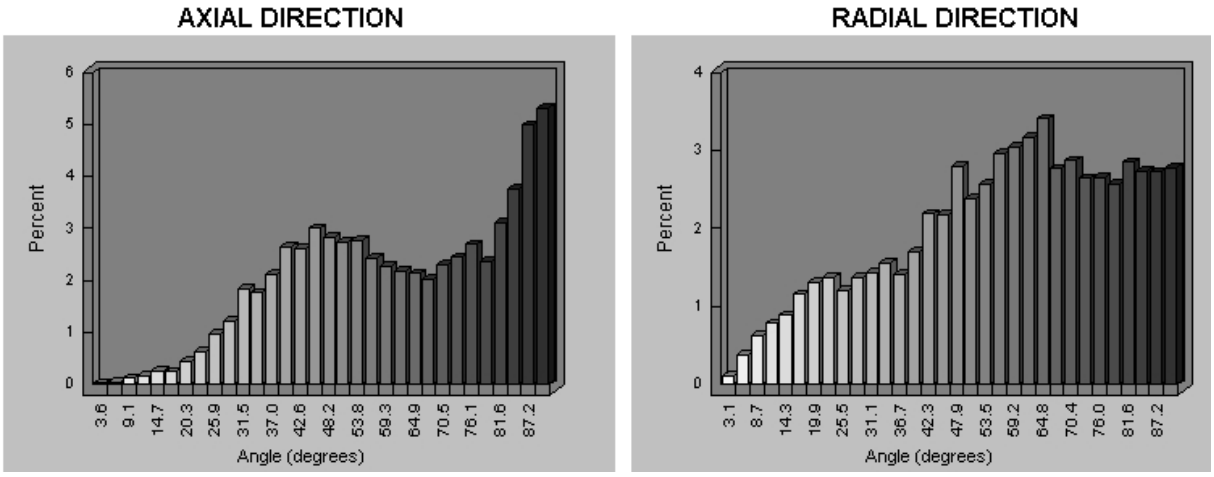

Figure 5-29 – Distribution of {0001} basal plane orientations w.r.t. axial and radial disc directions for crystal orientation maps in Figure 5-28

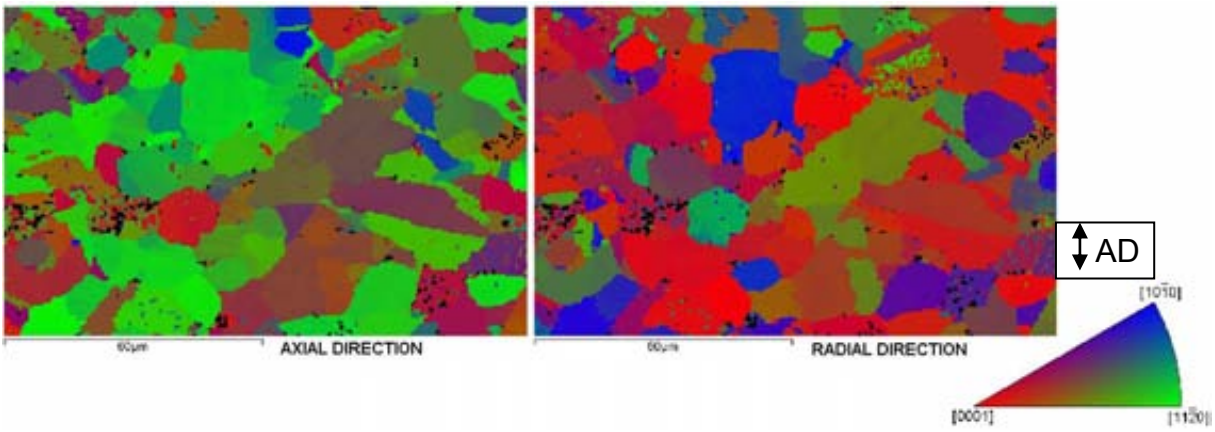

Figure 5-30 – Alpha micro-texture in Ti6242 compressor disc B in region of high aspect ratio beta grains. Textures displayed w.r.t. axial and radial disc directions

5.7.5 Ti6246 heat treated microstructures

Figure 5-31 – Prior beta grain size following beta phase field vacuum heat treatment (Specimen blanks A1-2 and B2-13)

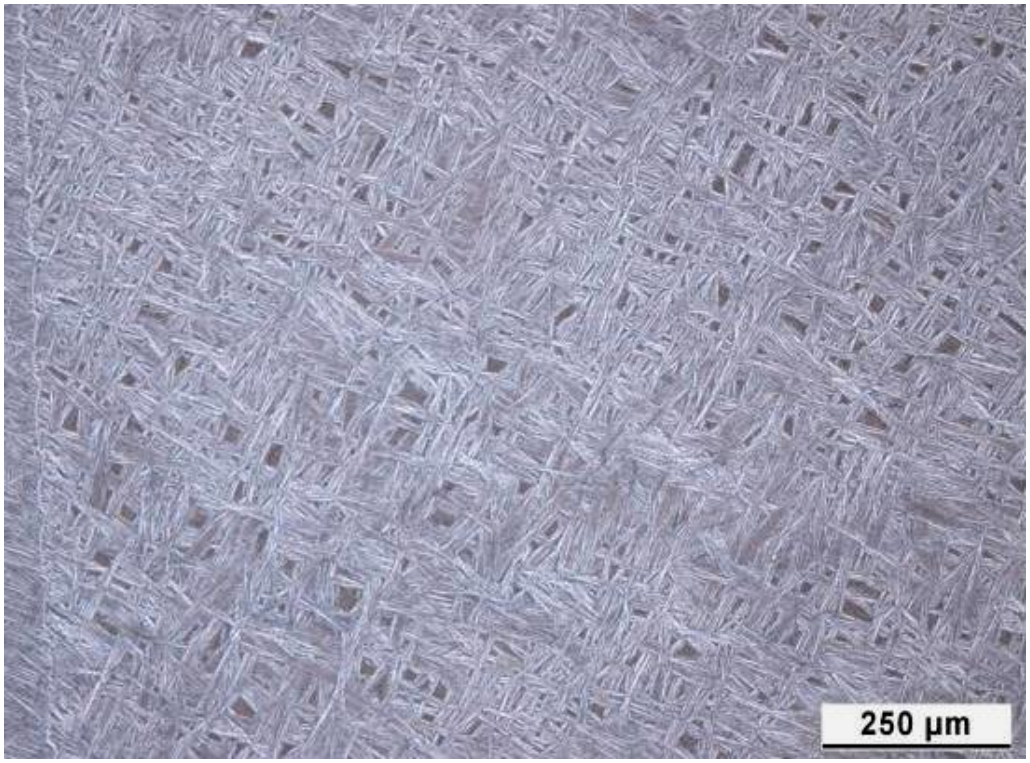

Figure 5-32 – Microstructure in blank A1-2 following vacuum heat treatment 1A (see Table 5-1)

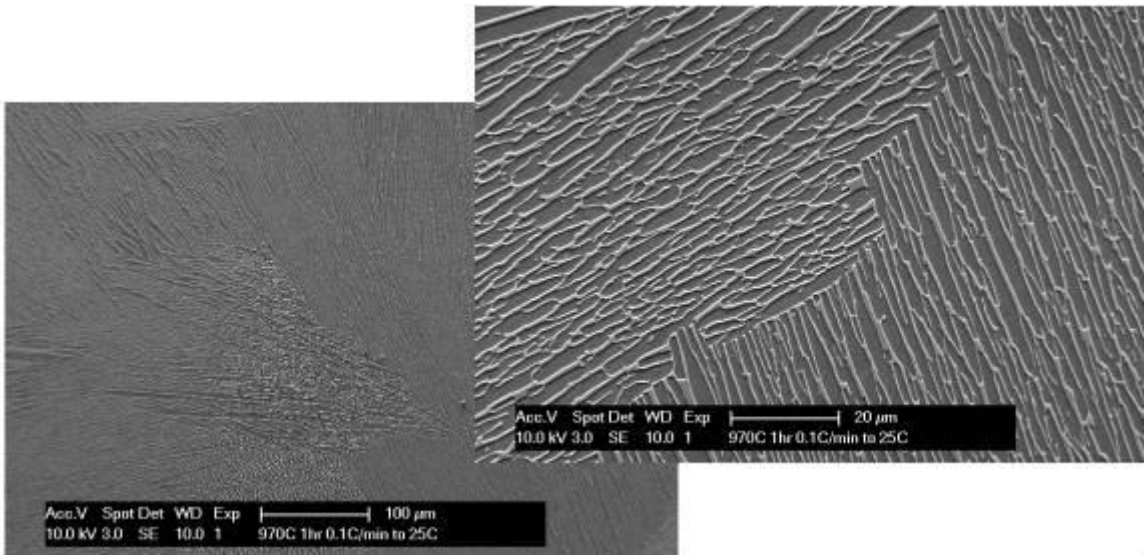

Figure 5-33 – Microstructure of sample 1B (see Table 5-1)

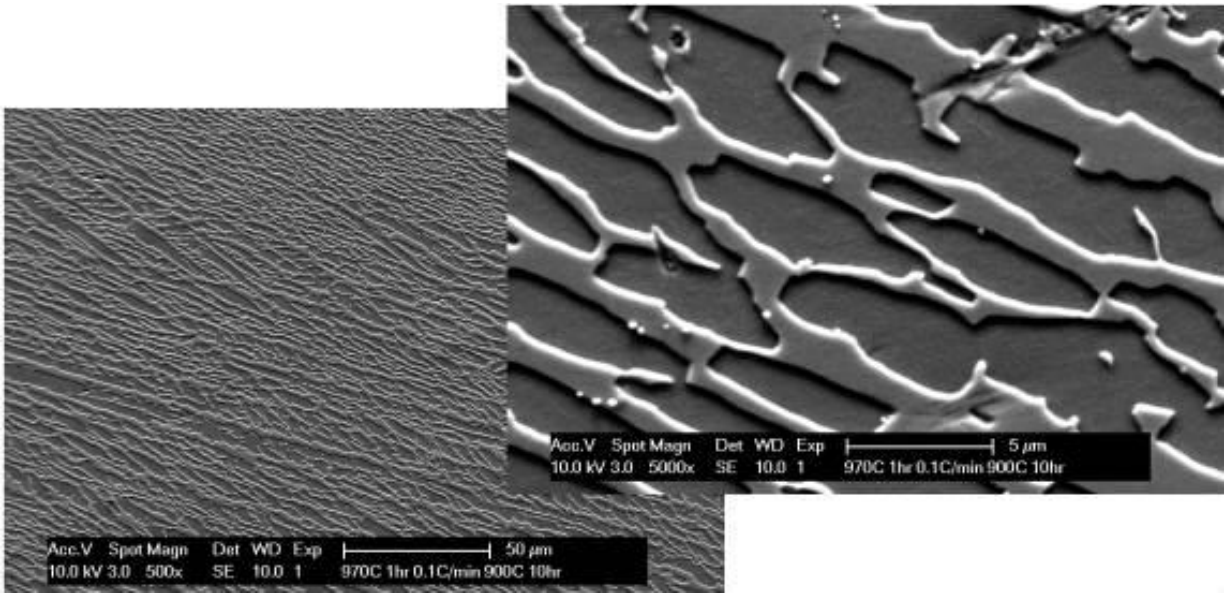

Figure 5-34 – Microstructure of sample 1C (see Table 5-1)

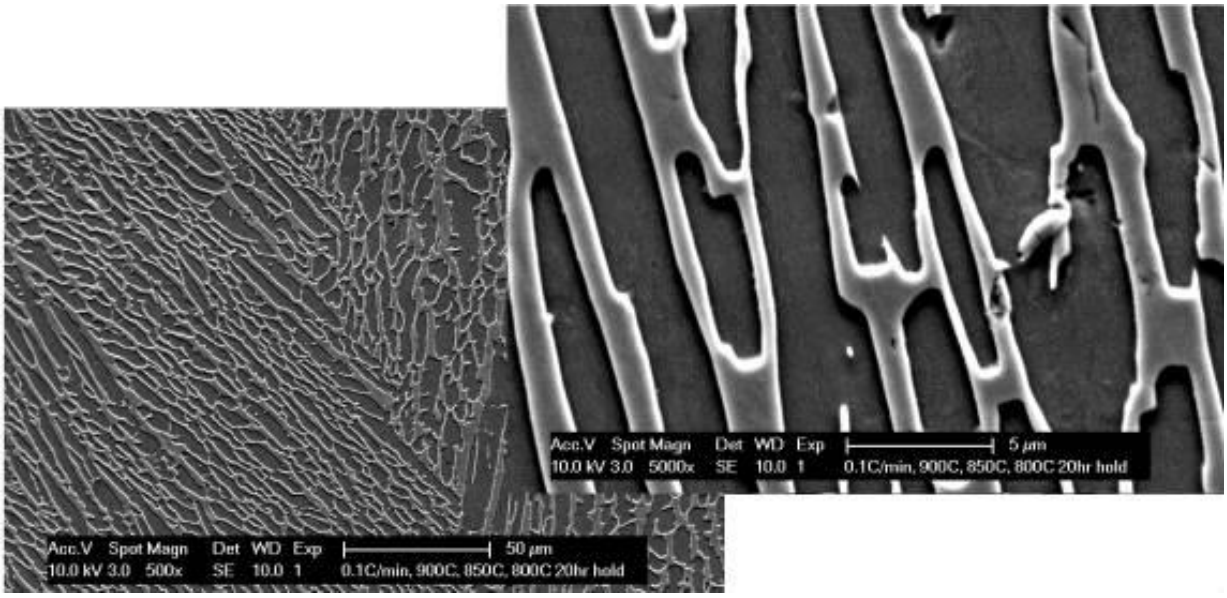

Figure 5-35 – Microstructure of sample 1D (see Table 5-1)

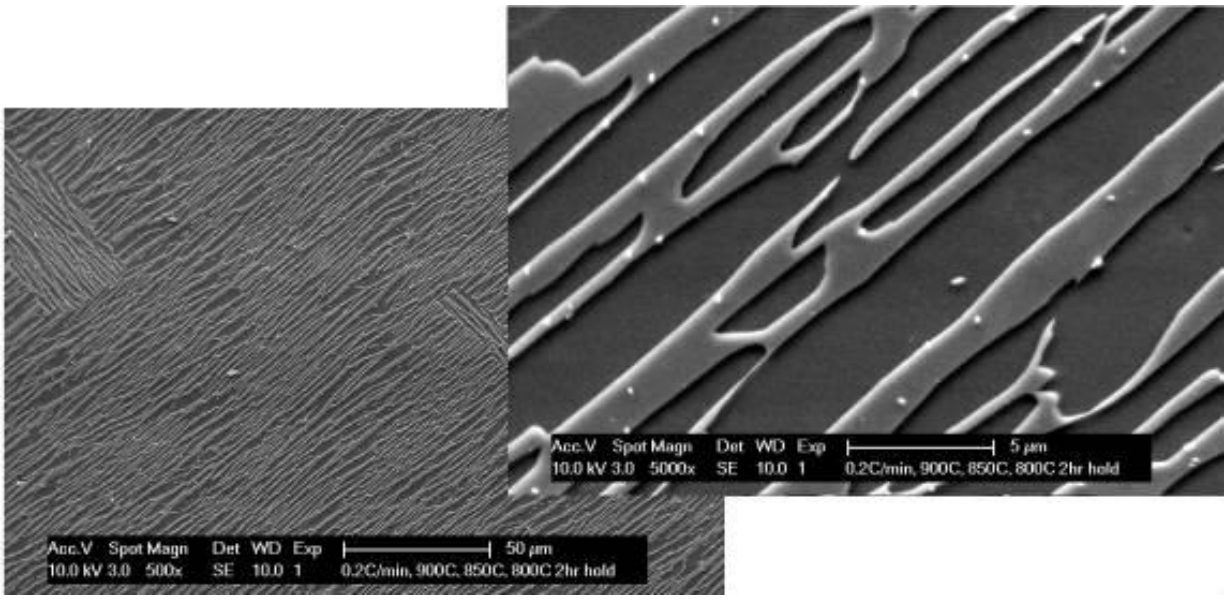

Figure 5-36 – Microstructure of sample 1E (see Table 5-1)

5.7.6 Ti6246 heat treated textures

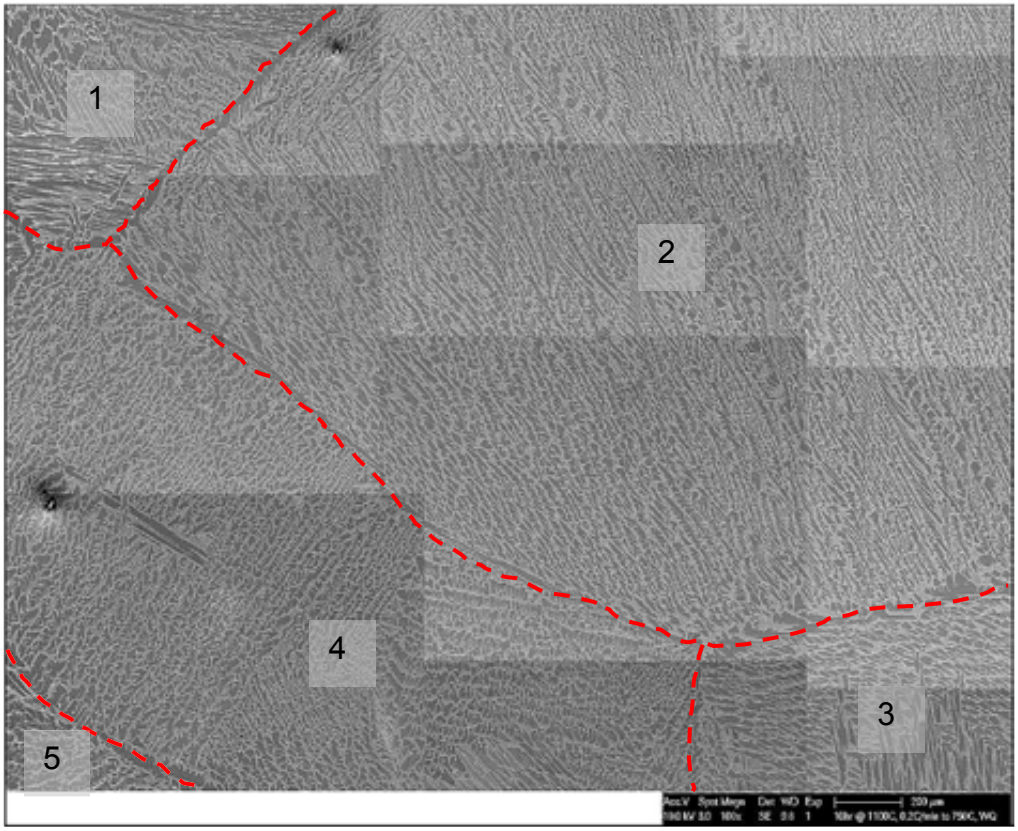

Figure 5-37 – Secondary electron image of beta HT'd Ti6246 (Sample 1B) EBSD map site of interest (Prior beta grain boundaries outlined)

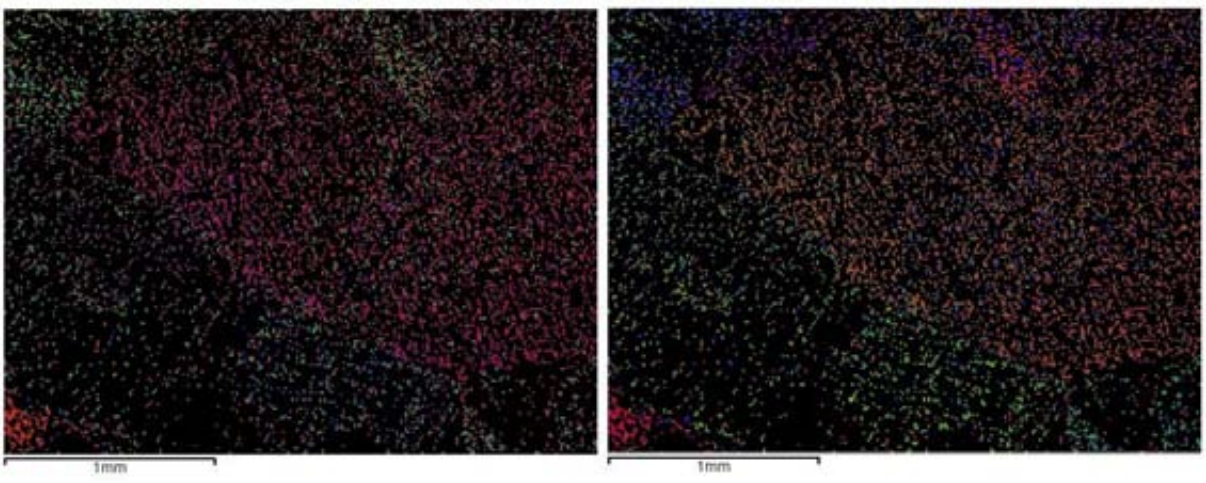

Figure 5-38 – Ti6246 sample 1B beta phase COMs (Orientated w.r.t. arbitrary axis directions)

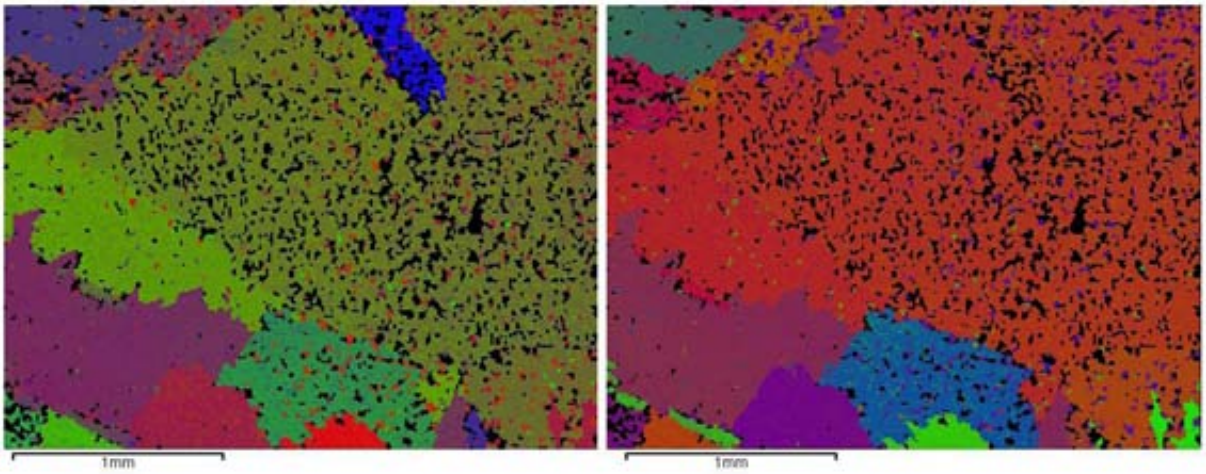

Figure 5-39 – Ti6246 sample 1B alpha phase COMs (Orientated w.r.t. arbitrary axis directions)

5.7.7 Ti6242 heat treated microstructures

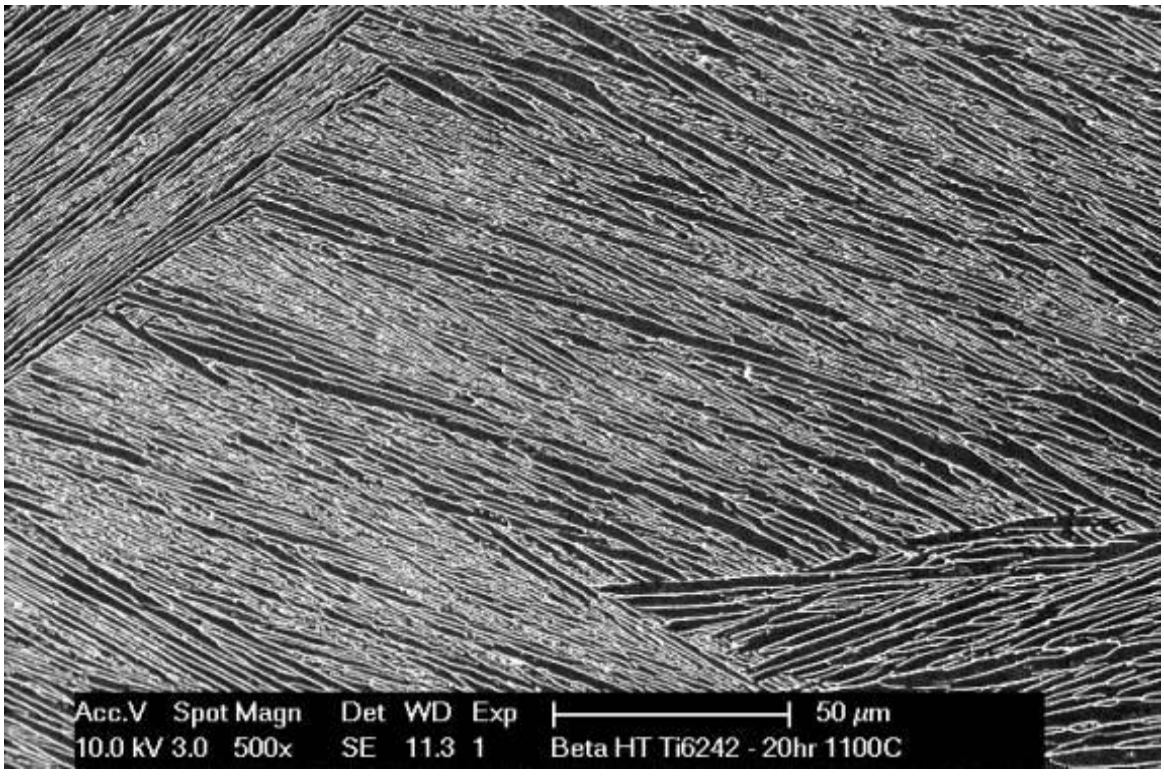

Figure 5-40 – Microstructure of sample 2A (see Table 5-2)

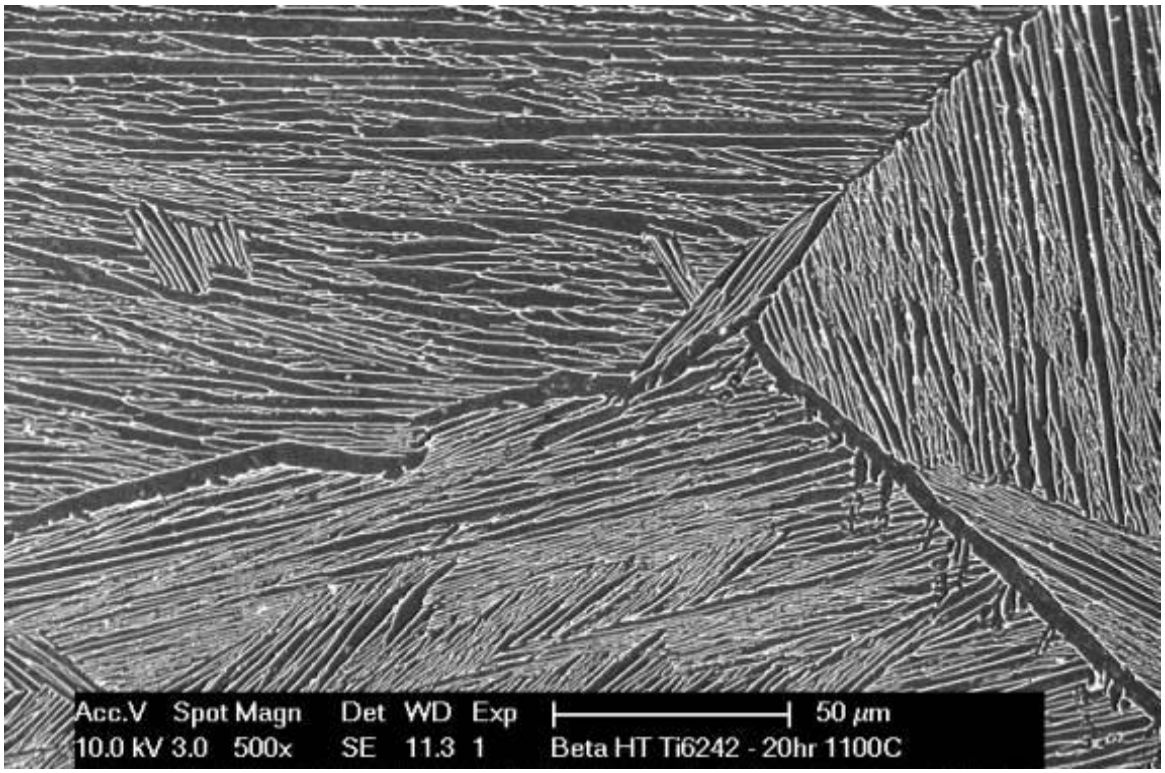

Figure 5-41 – Microstructure of sample 2A (see Table 5-2)

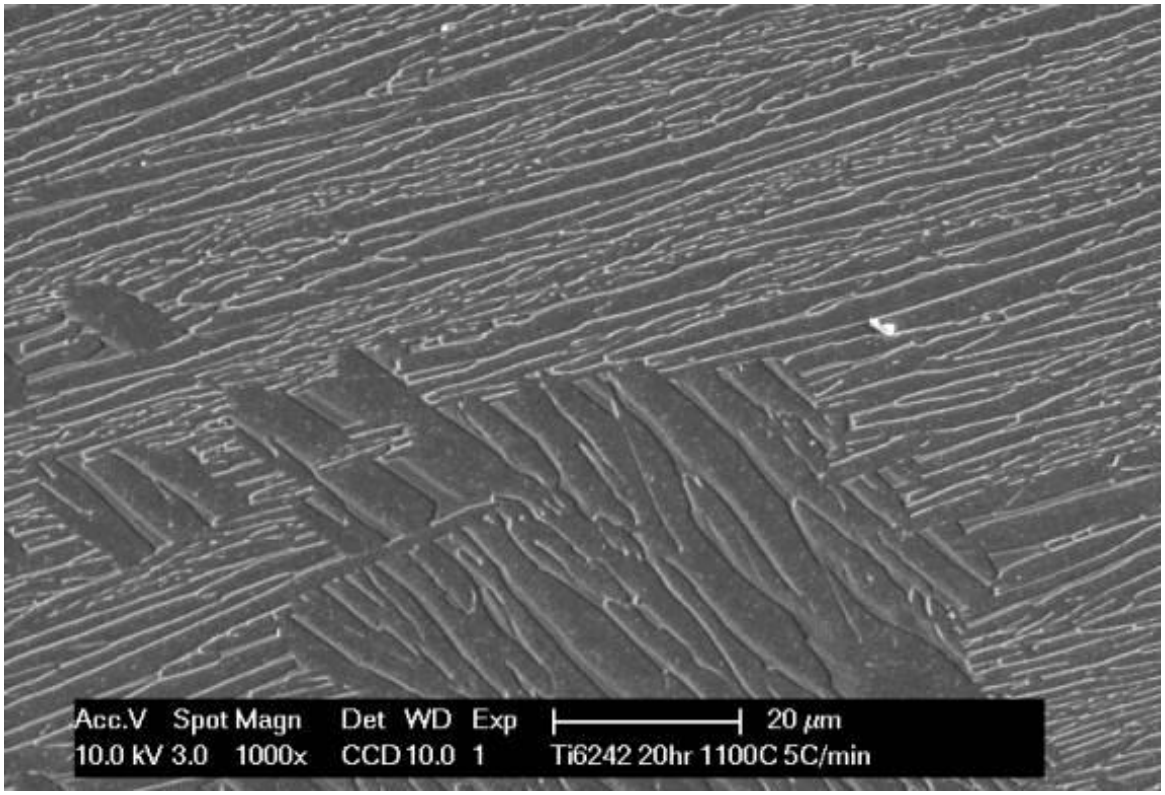

Figure 5-42 – Microstructure of sample 2B (see Table 5-2)

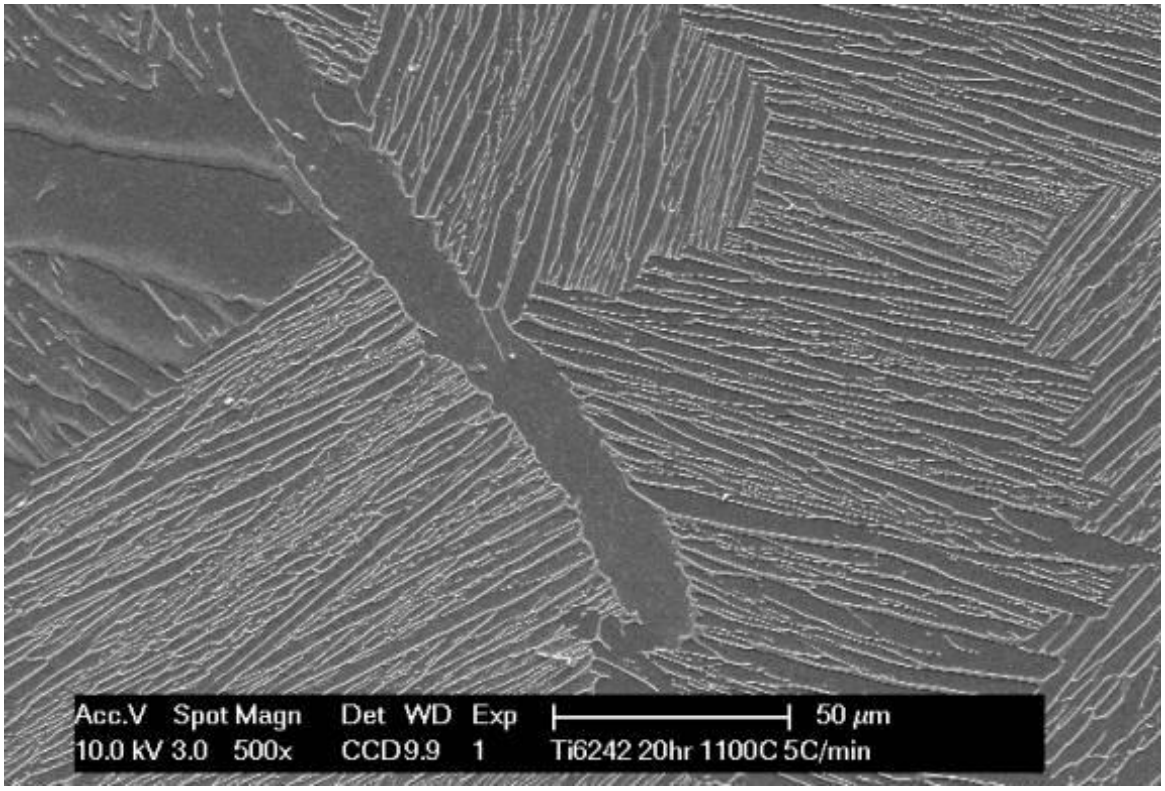

Figure 5-43 – Microstructure of sample 2B (see Table 5-2)

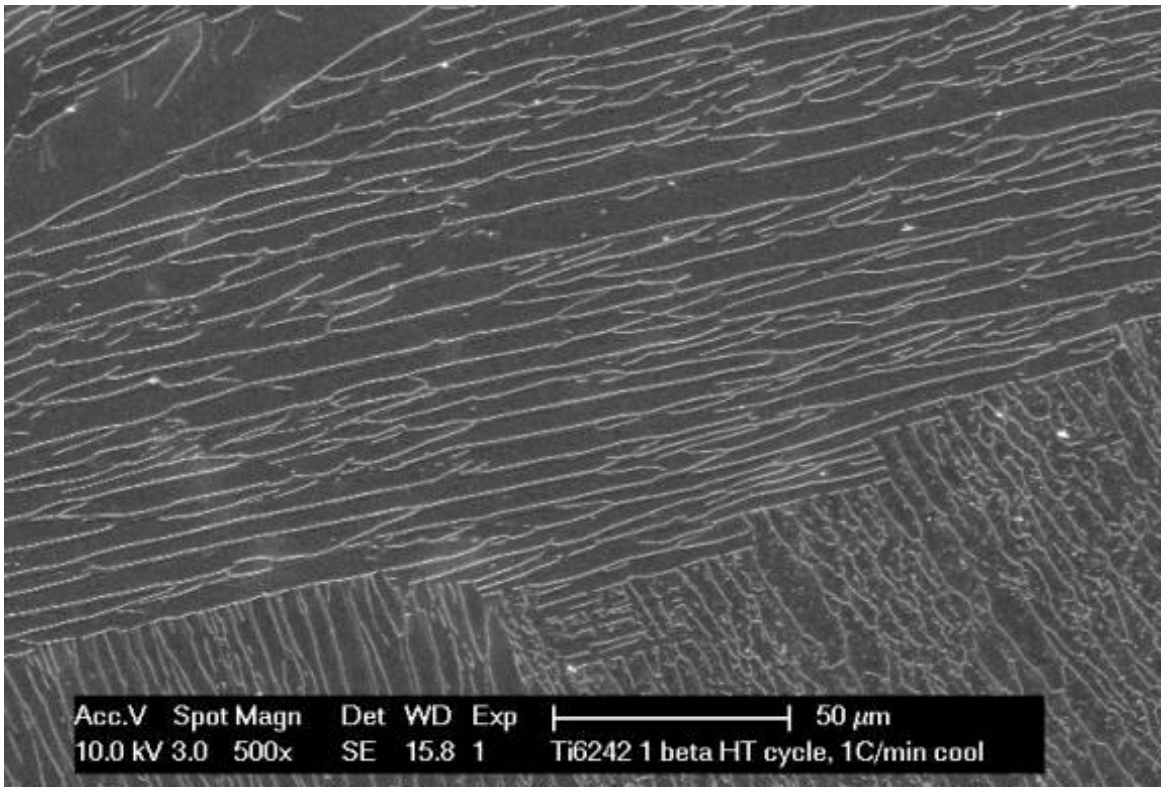

Figure 5-44 – Microstructure of sample 2C (see Table 5-2)

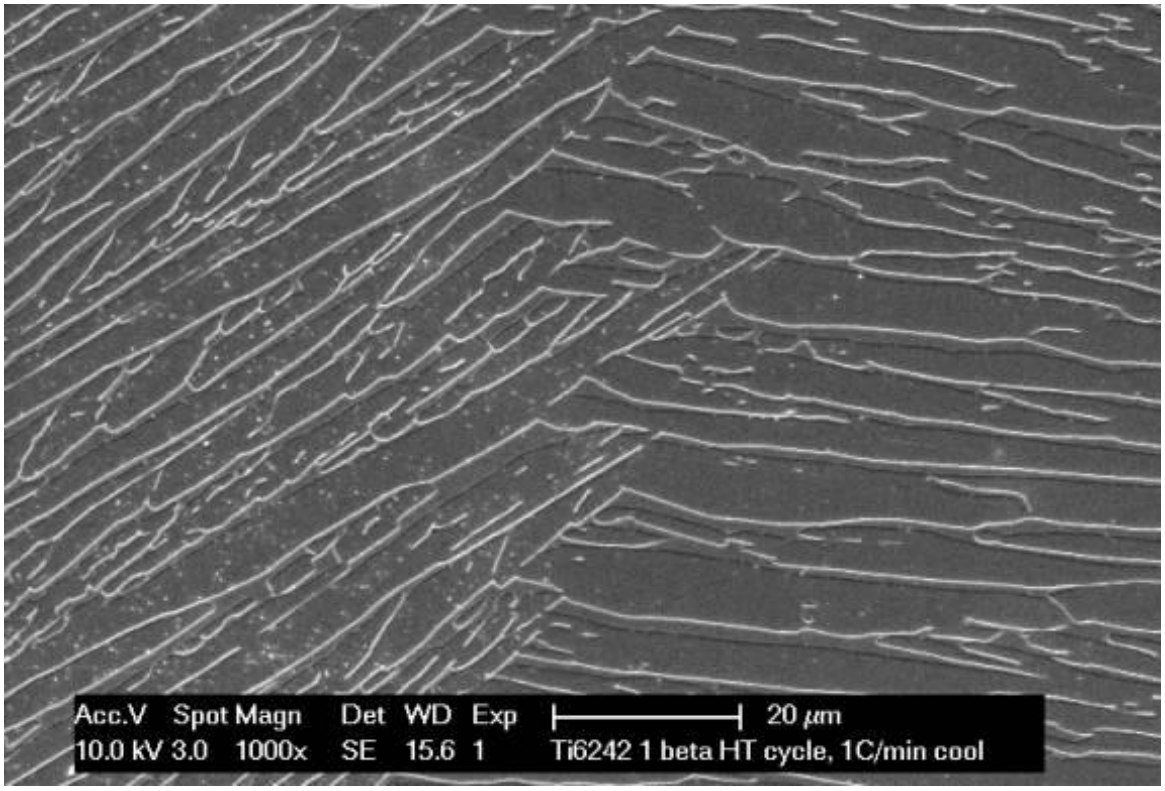

Figure 5-45 – Microstructure of sample 2C (see Table 5-2)

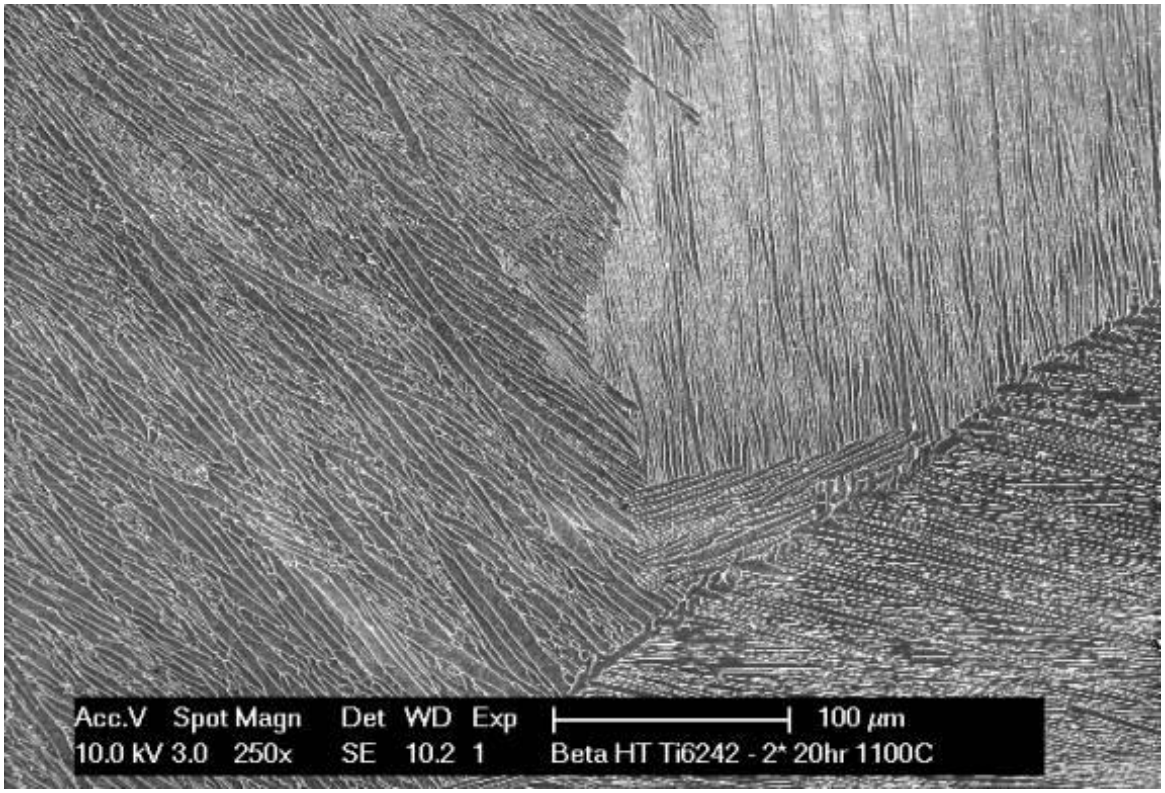

Figure 5-46 – Microstructure of sample 2D (see Table 5-2)

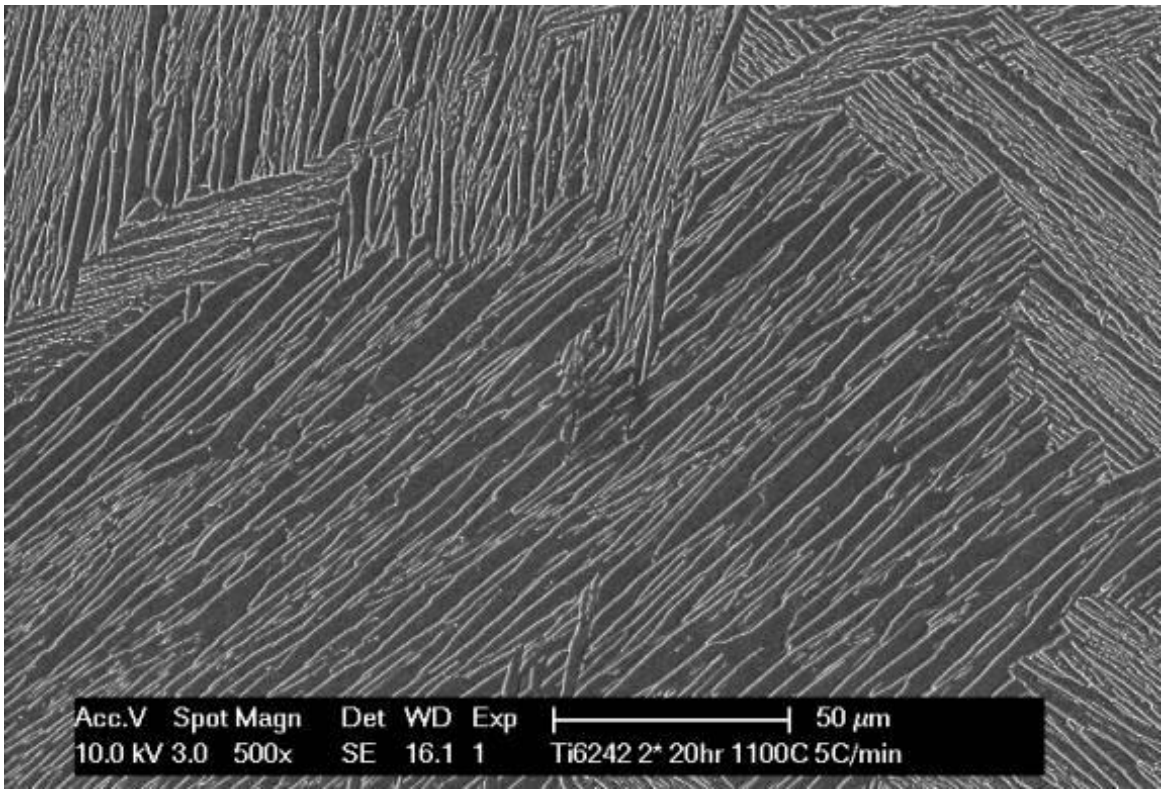

Figure 5-47 – Microstructure of sample 2E (see Table 5-2)

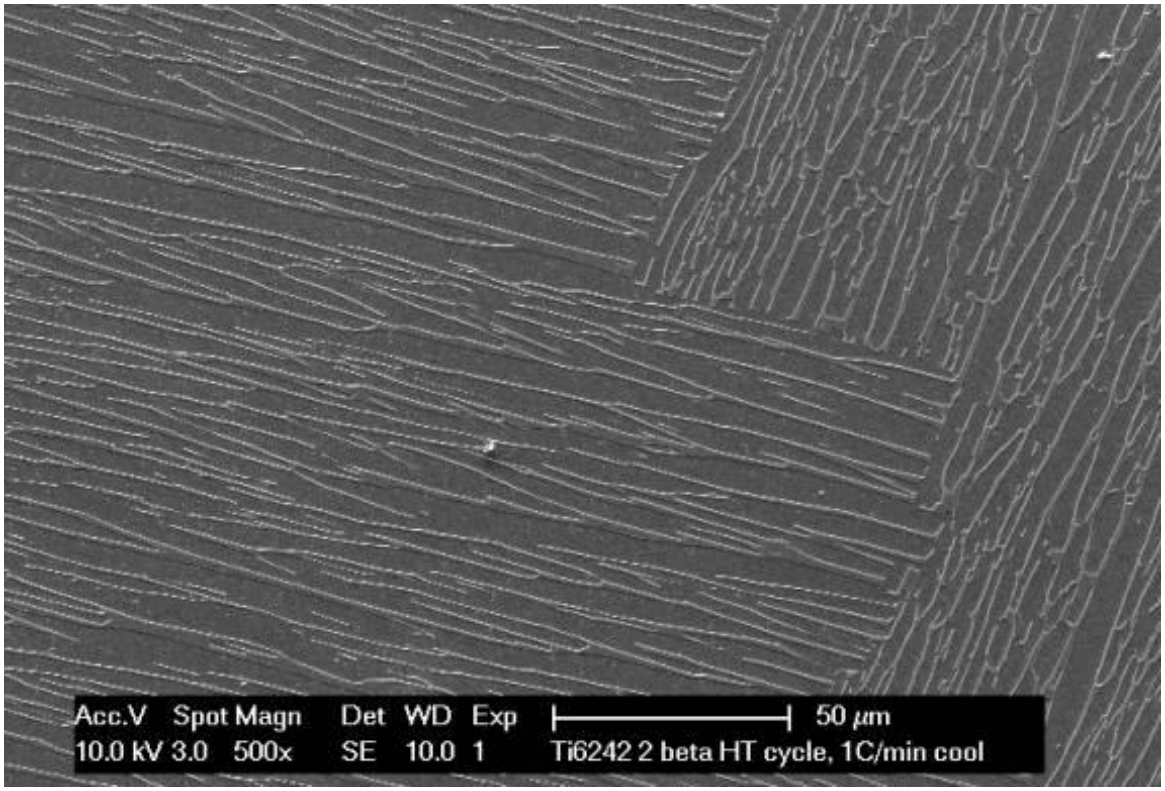

Figure 5-48 – Microstructure of sample 2F (see Table 5-2)

Figure 5-49 – Surface condition of vacuum heat-treated Ti6242 (Specimen blank C1)

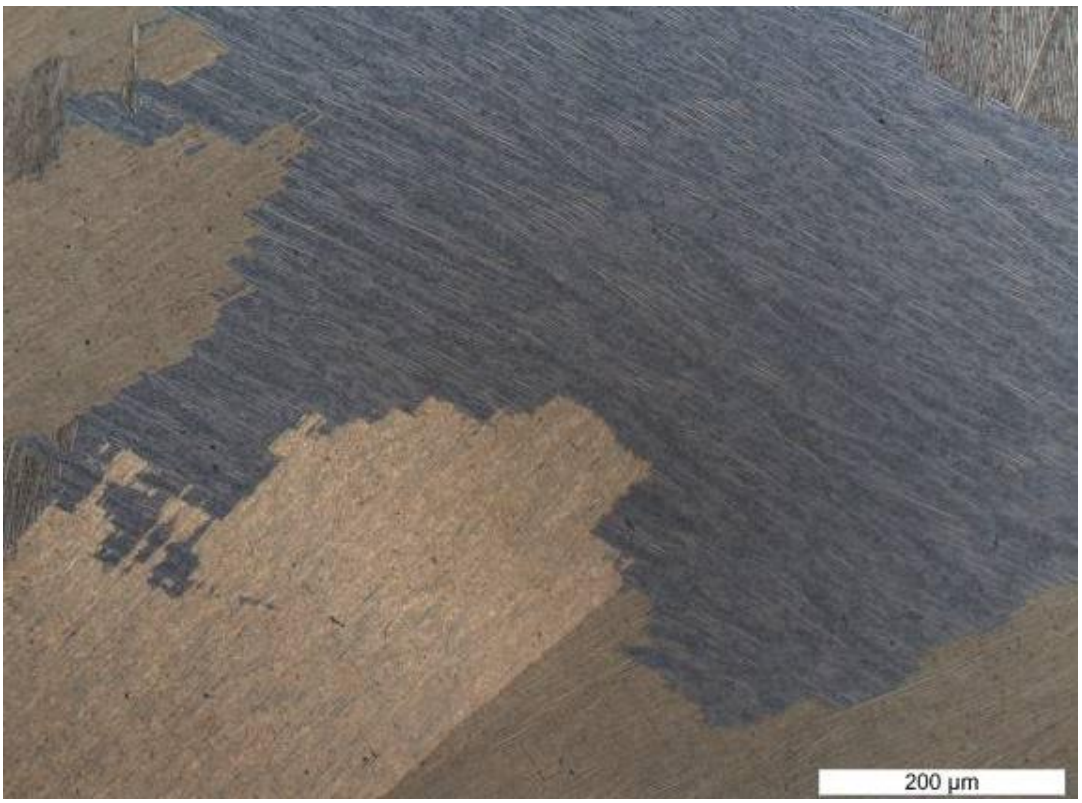

Figure 5-50 – Microstructure of Ti6242 test material (Specimen blank A1)

Figure 5-51 – Microstructure of Ti6242 test material (Specimen blank A1)

5.7.8 Ti6242 heat treated textures

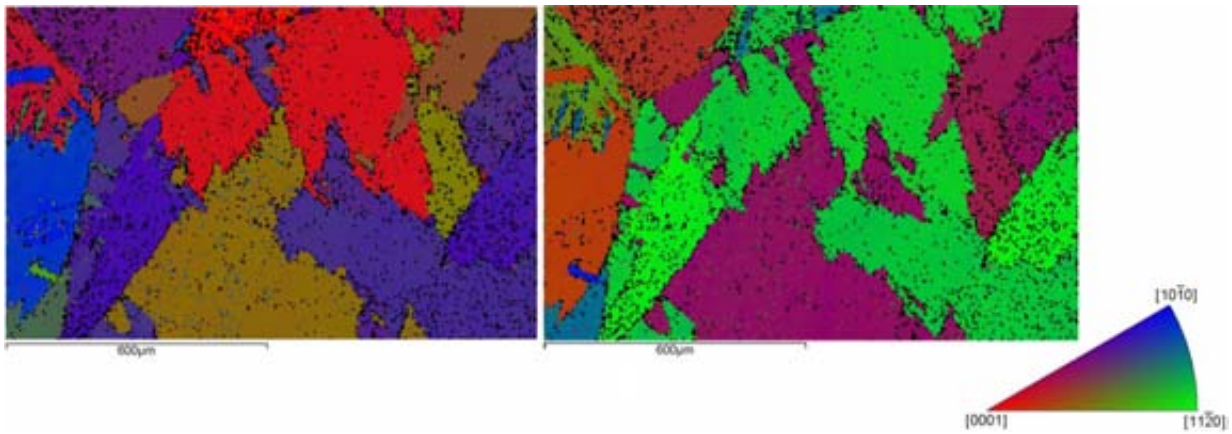

Figure 5-52 – Alpha textures in Ti6242 blank sample 2D following beta heat treatment. Orientated w.r.t. arbitrary axis directions

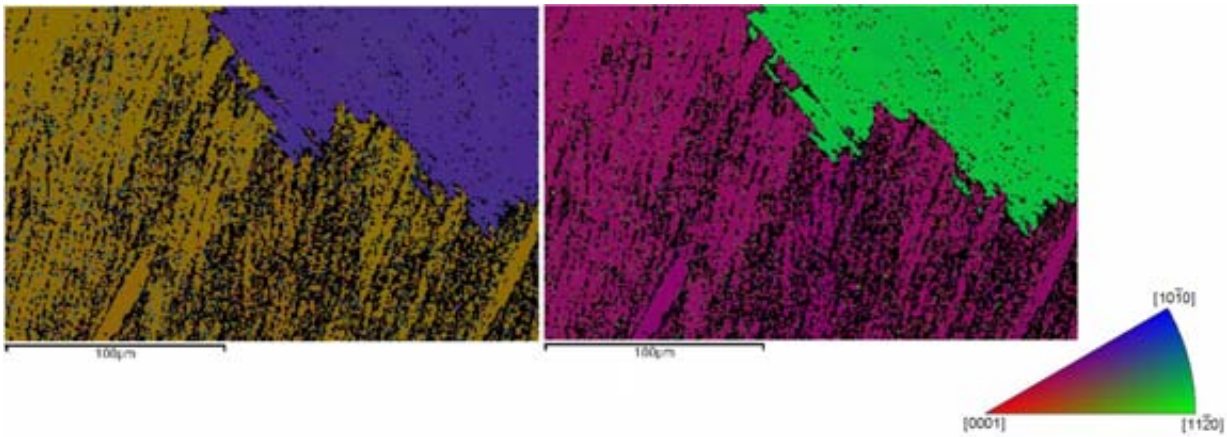

Figure 5-53 – Alpha textures in Ti6242 blank sample 2D following beta heat treatment. Orientated w.r.t. arbitrary axis directions

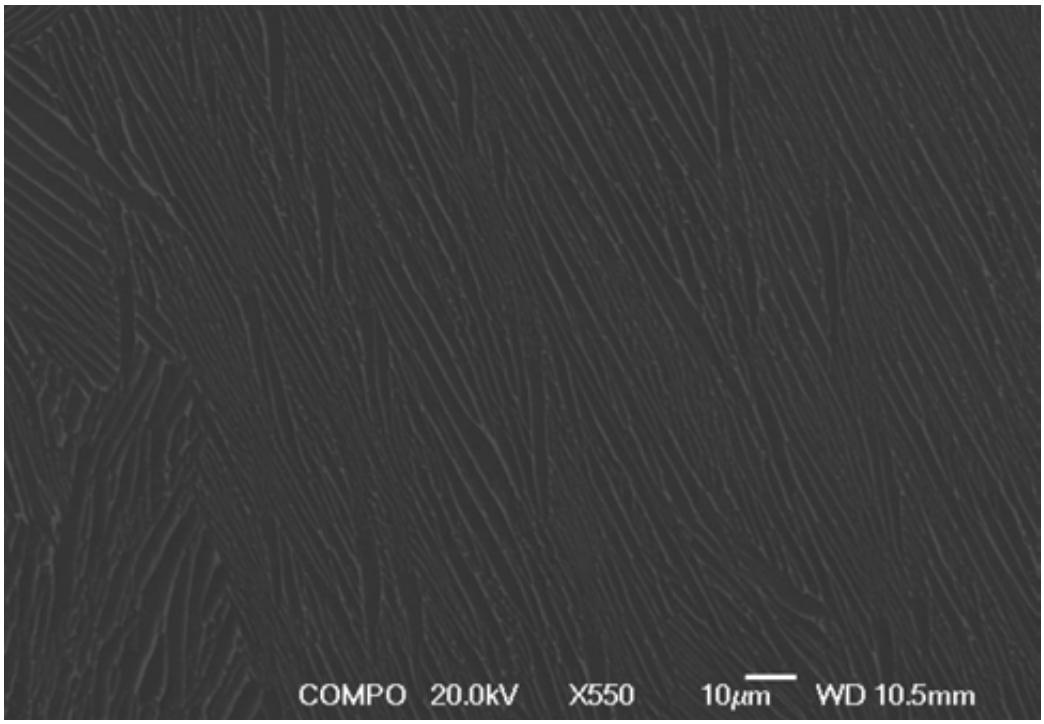

Figure 5-54 – Back scatter electron imaging microstructure of Ti6242 following beta heat treatment 2D (see Table 5-2)

5.7.9 Tensile testing

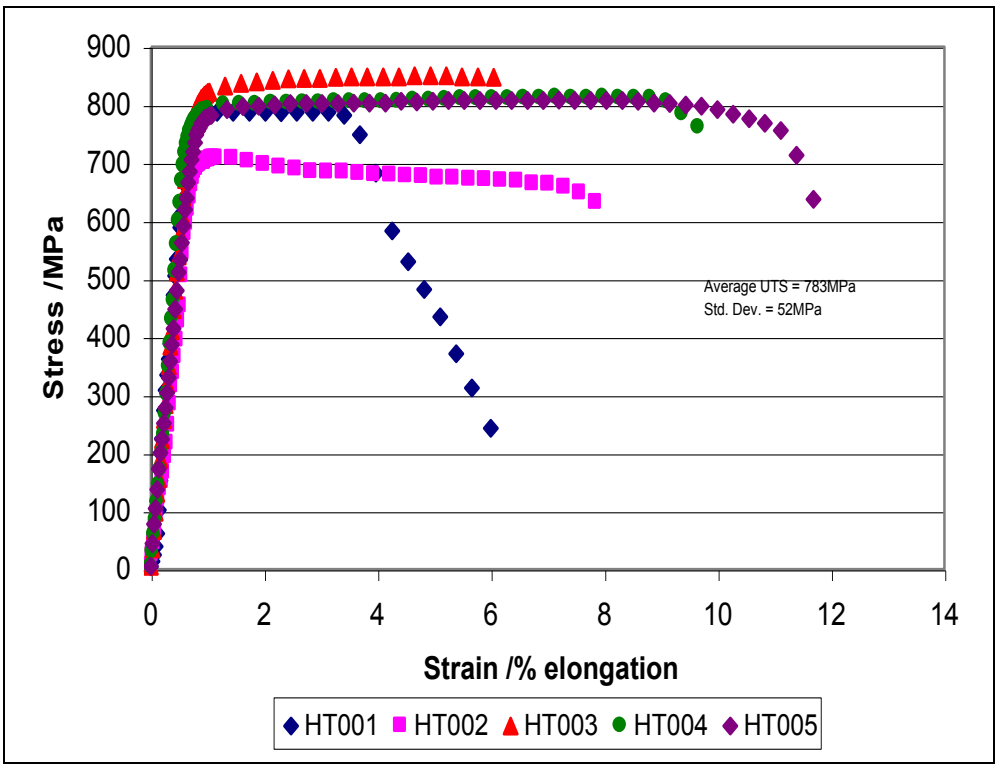

Figure 5-55 – Stress-strain curves for Ti6246 tensile test data

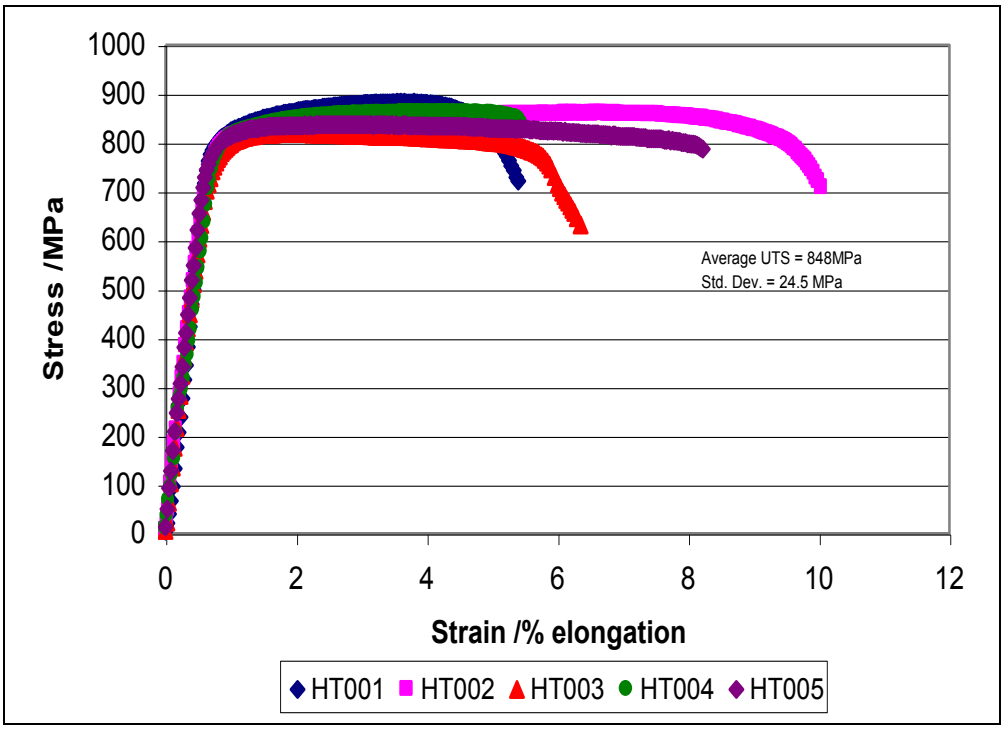

Figure 5-56 – Stress-strain curves for Ti6242 tensile test data

5.7.10 Fatigue testing

Table 5-3 – Fatigue test results for beta heat-treated Ti6246 specimens

Specimen	Test	Max stress /MPa	Cycles to failure	Fracture surface
LF001	15cpm	940 (Over-stress)	58	Overload. Gross plastic deformation
LF003	15cpm	720	62389	Surface initiation. Flow lines on fracture
LF004	2 min dwell	800	355	Surface initiation
LF005	15cpm	767	13223	Sub-surface initiation
LF006	2 min dwell	760	5589	Sub-surface initiation (from grain boundary?)
LF007	15cpm	745	15315	Surface initiation, cleavage crack
LF008	2 min dwell	780	8112	Surface initiating fatigue crack
LF009	15cpm	800	10387	Sub-surface initiation, unclear origin
LF010	2 min dwell	770	10956	Surface initiation, fatigue crack growth
LF011	Untested	-	-	-
LF012	2 min dwell	750	9200	Sub-surface fatigue crack growth
LF014	15cpm	780	13527	Surface initiation
LF015	2 min dwell	792	800	Sub-surface, cleavage cracking

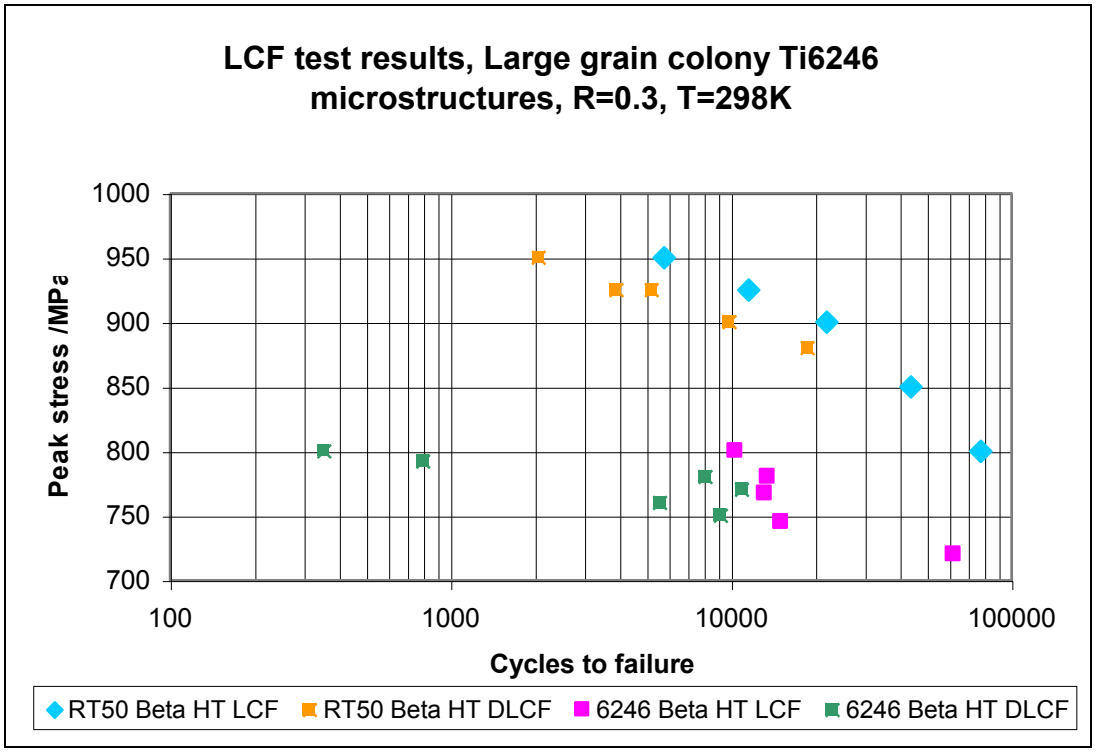

Figure 5-57 – Fatigue test results for beta heat treated Ti6246

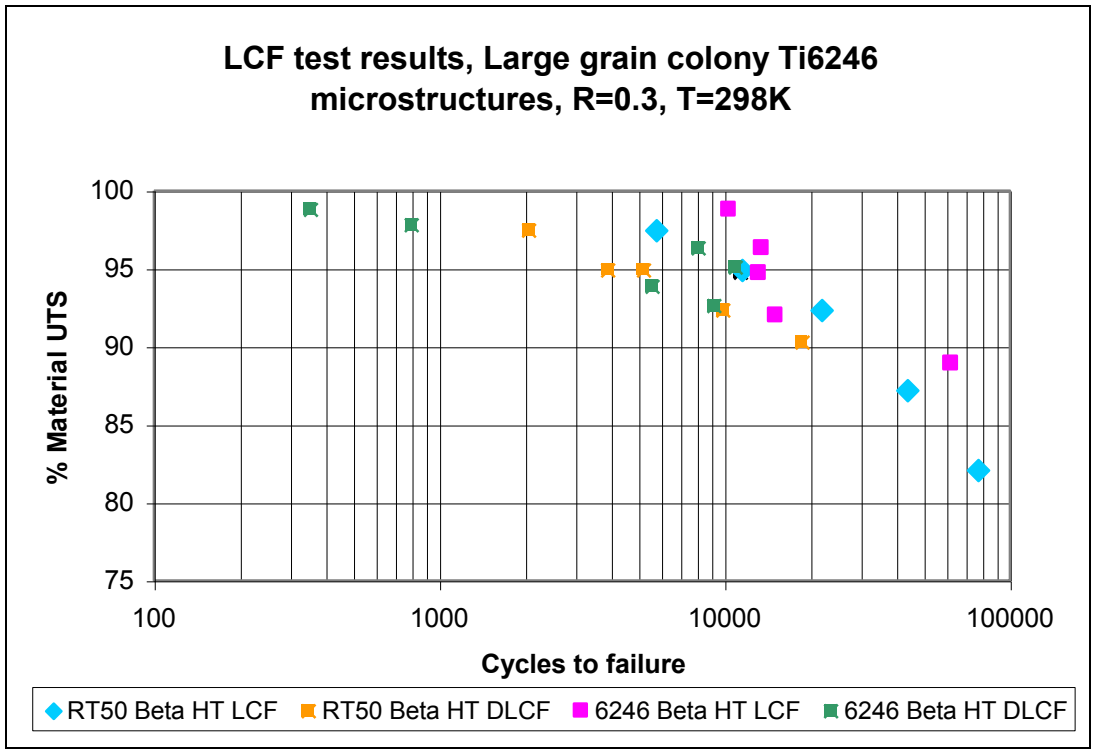

Figure 5-58 – UTS normalised DLCF test results for beta heat treated Ti6246

Table 5-4 – Fatigue test results for beta heat-treated Ti6242 specimens

Specimen	Test	Max stress /MPa	Cycles to failure	Fracture surface features
A5	15cpm	825	3920	Sub-surface initiation
A9	15cpm	800	34893	Surface initiation, angled facet feature
B7	15cpm	800	22061	Surface initiation
B9	15cpm	775	31849	Probable surface initiation. No clear origin
C3	15cpm	850	470	Sub-surface initiation
C5	15cpm	750	26117	Surface initiation
C8	15cpm	725	62282	Probable surface initiation, sub-surface load normal features
A8	2 min dwell	800	15371	Sub-surface initiation, angled facet feature
B5	2 min dwell	750	812	Sub-surface initiation at grain boundary?
B8	2 min dwell	800	2	Surface initiation, very large angled facet
C4	2 min dwell	825	2901	Sub-surface initiation, angled facet feature
C7	2 min dwell	725	591	Sub-surface angled facet feature
C9	2 min dwell	750	5836	Sub-surface initiation. No clear origin
C2	Compressive overload failure on machine setup			

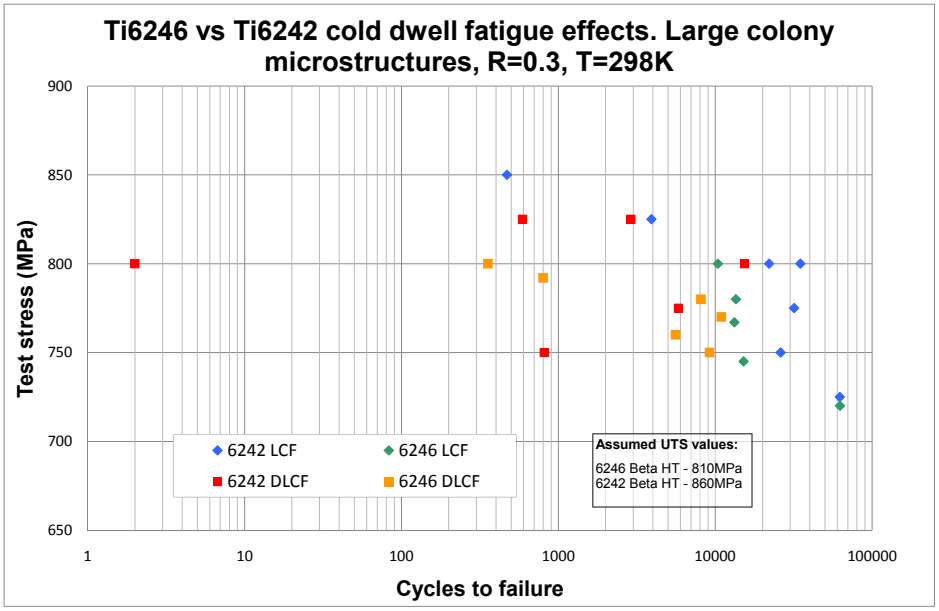

Figure 5-59 – Fatigue test results for beta heat treated Ti6242 (with comparison to results of Ti6246 test programme in Table 5-3)

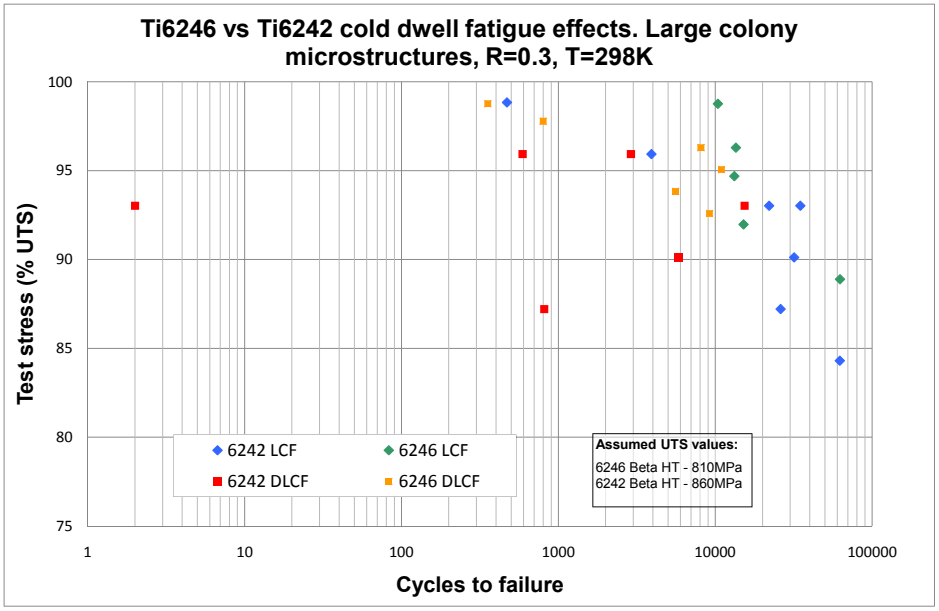

Figure 5-60 – UTS normalised fatigue test results from Figure 5-59

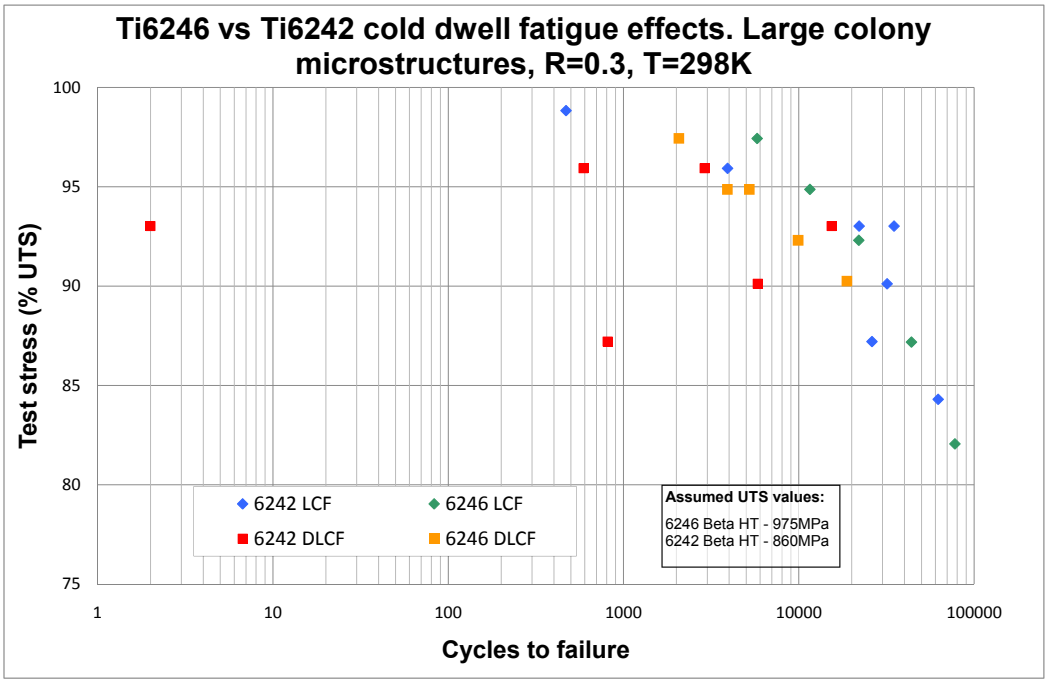

Figure 5-61 – UTS normalised fatigue test results for beta heat treated Ti6242 (With comparison to Chapter 4 dwell fatigue test results of beta heat treated Ti6246 material)

5.7.11 Specimen fractography and microstructures

5.7.11.1 Ti6246 tensile specimens

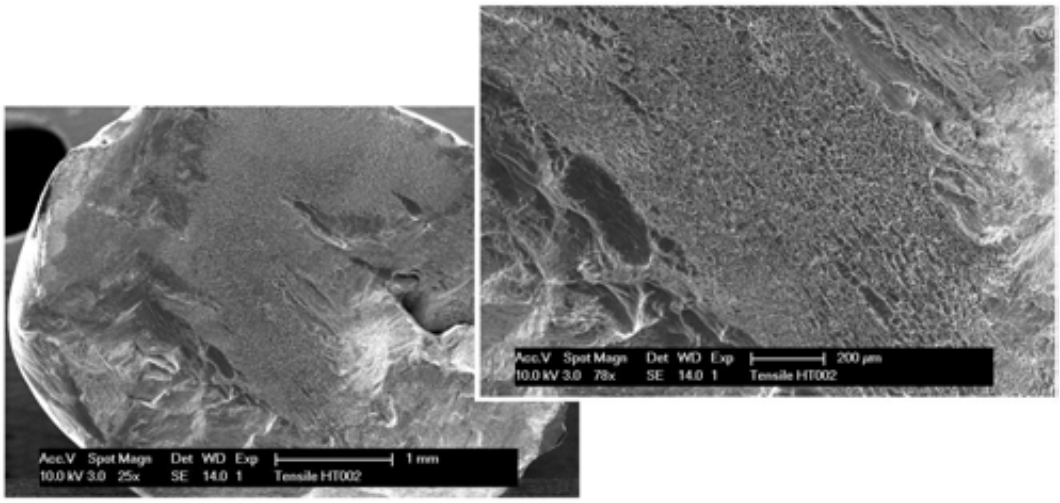

Figure 5-62 – Ti6246 tensile specimen HT002 fracture surface

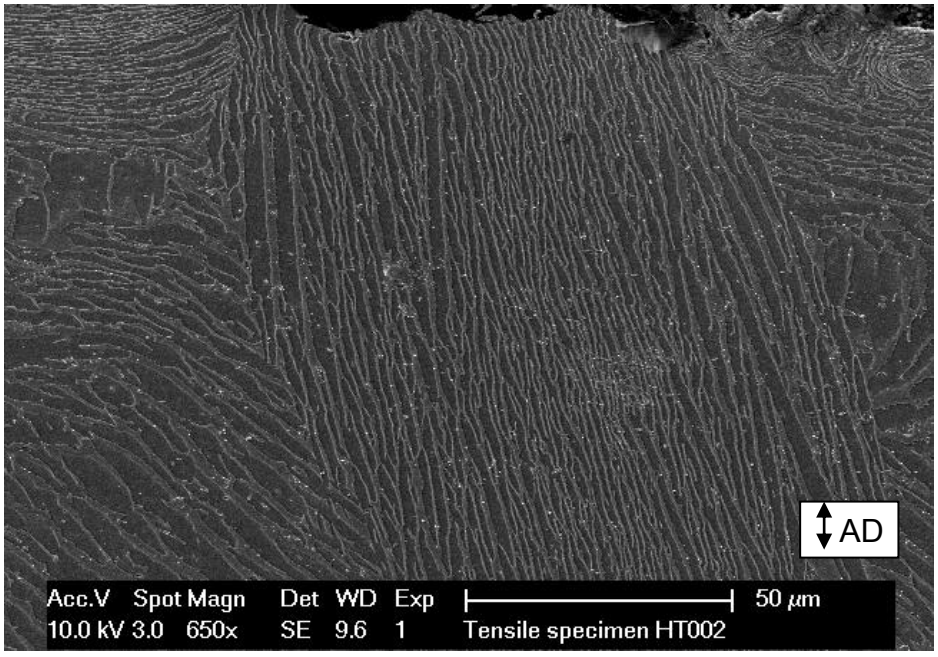

Figure 5-63 – Specimen HT002 typical sub-surface microstructure (AD is the axial direction, i.e. specimen loading axis)

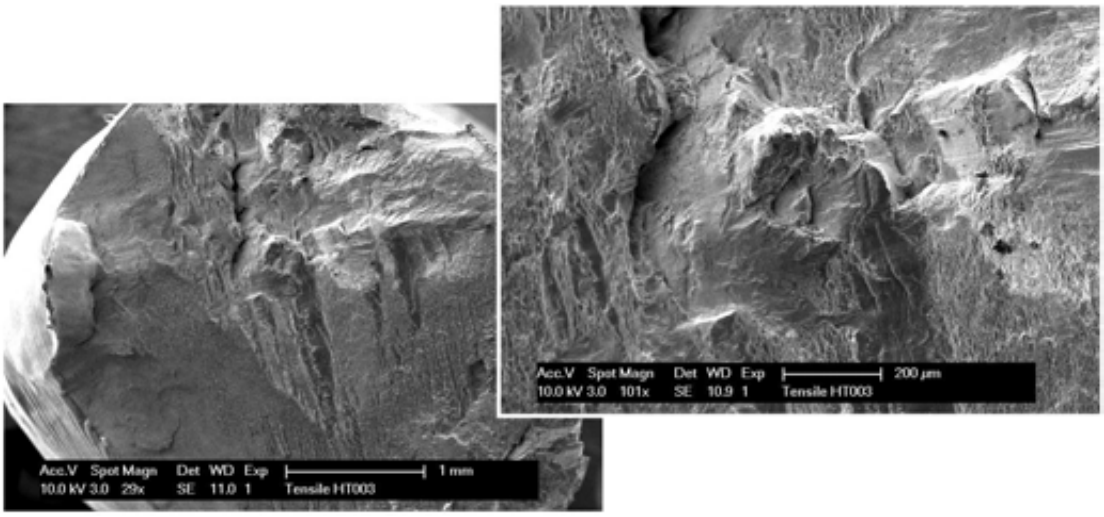

Figure 5-64 – Ti6246 tensile specimen HT003 fracture surface

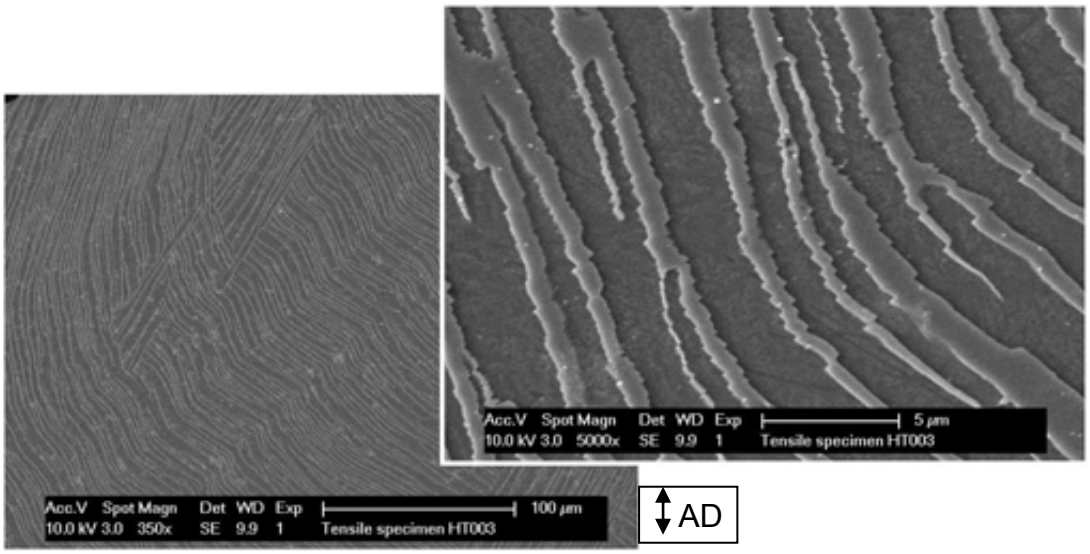

Figure 5-65 – Specimen HT003 sub-surface microstructure showing planar slip band formation at ~45° to loading axis

5.7.11.2 Ti6246 LCF specimens

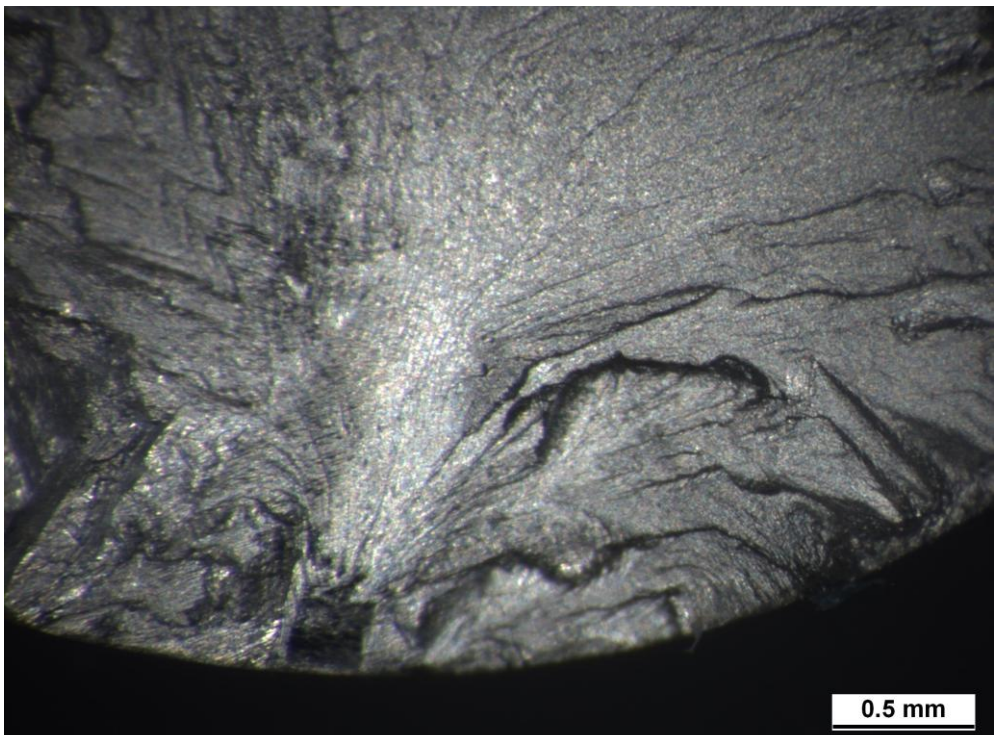

Figure 5-66 – LCF test specimen LF003, 720MPa, 62,389 cycles to failure. Flow lines away from surface initiation site

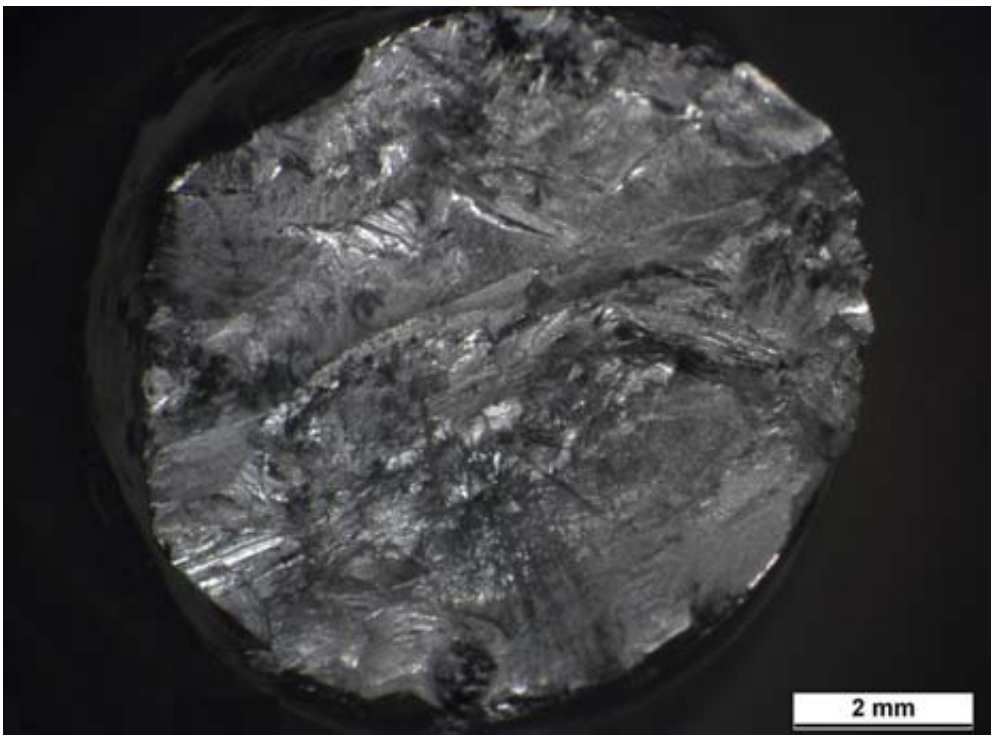

Figure 5-67 – LCF test specimen LF005, 767MPa, 13,223 cycles to failure. Sub-surface initiation, unclear origin

5.7.11.3 Ti6246 dwell LCF specimens

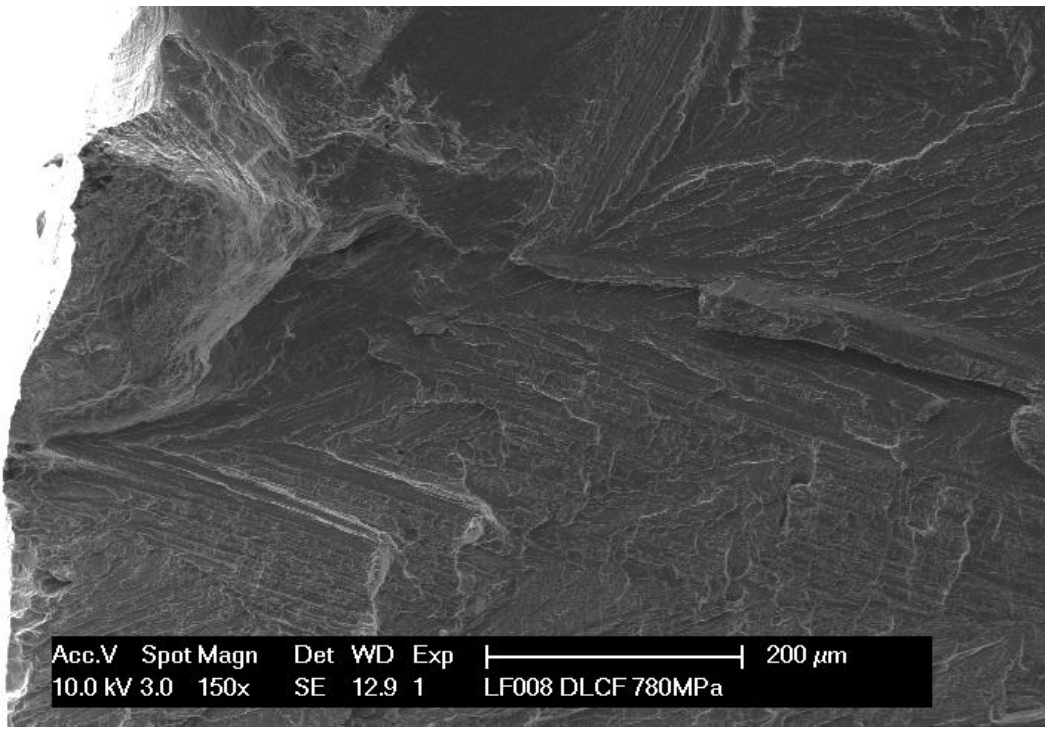

Figure 5-68 – DLCF test specimen LF008, 780MPa, 8,112 cycles to failure. Surface initiation, fatigue crack growth

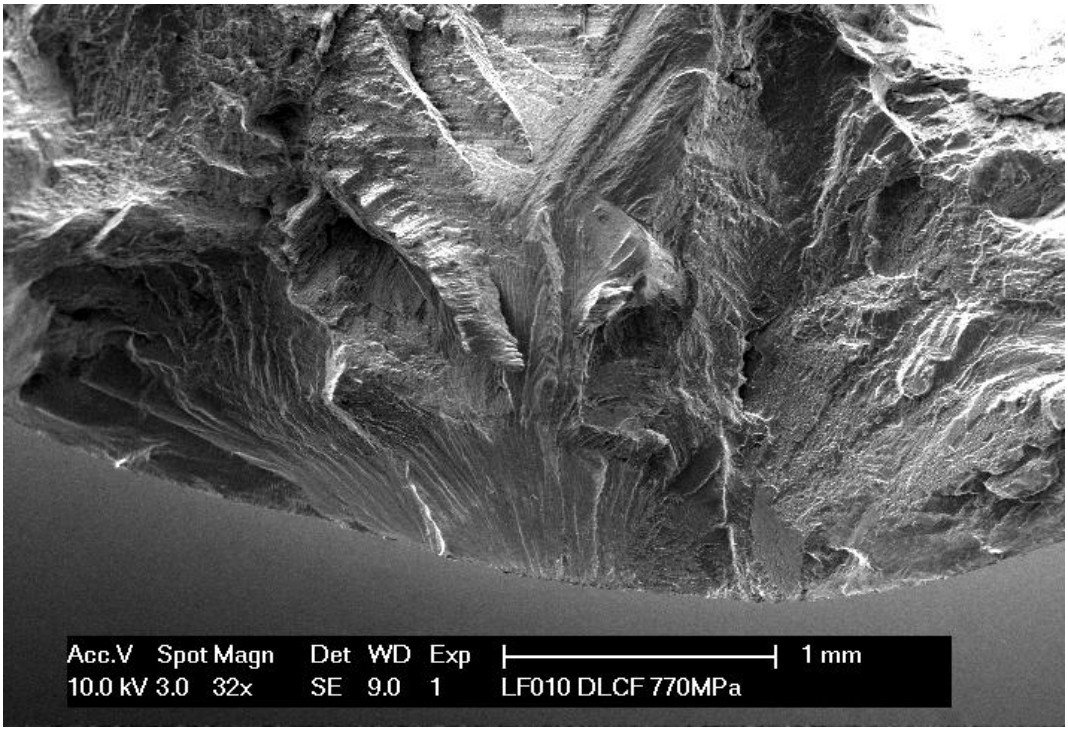

Figure 5-69 – DLCF test specimen LF010, 770MPa, 10,956 cycles to failure. Surface initiation, fatigue crack growth

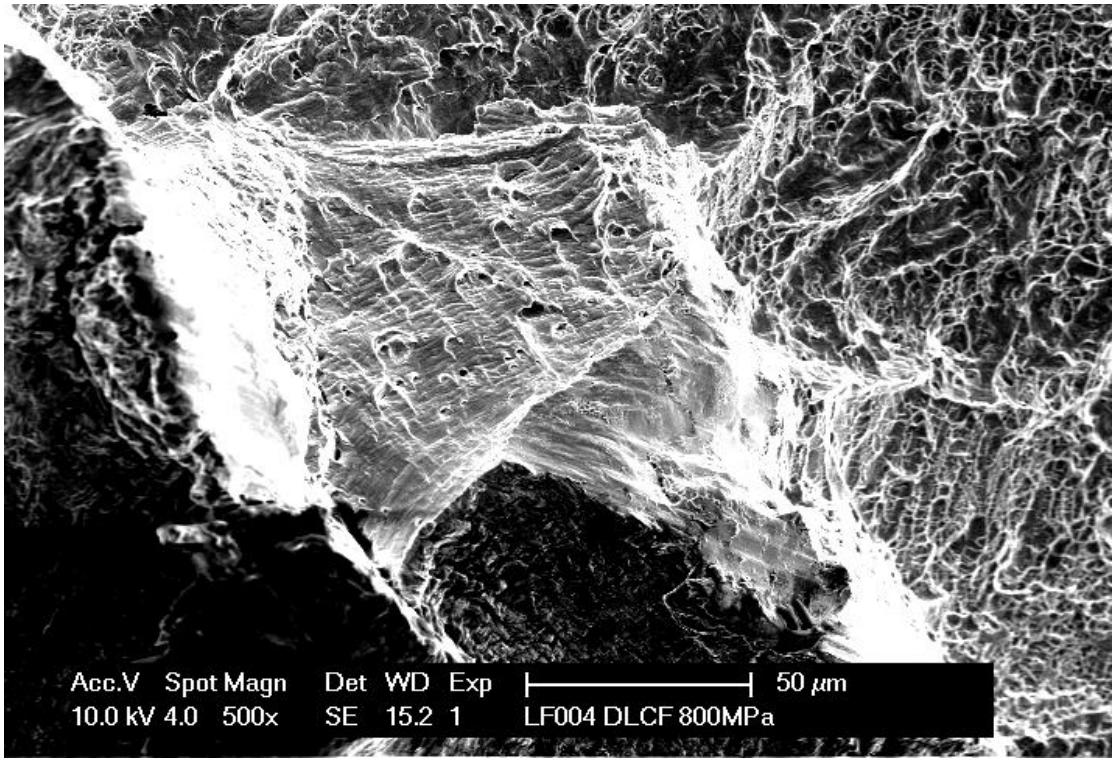

Figure 5-70 – DLCF test specimen LF004, 800MPa, 355 cycles to failure. Surface initiated fatigue crack growth with transition to ductile failure

5.7.11.4 Ti6242 tensile specimens

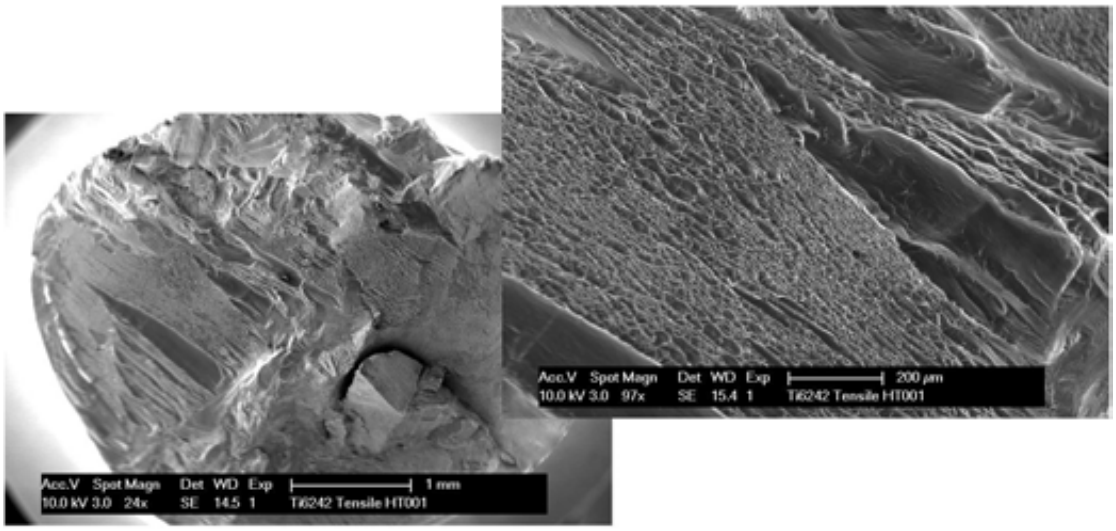

Figure 5-71 – Ti6242 tensile specimen HT001 fracture surface

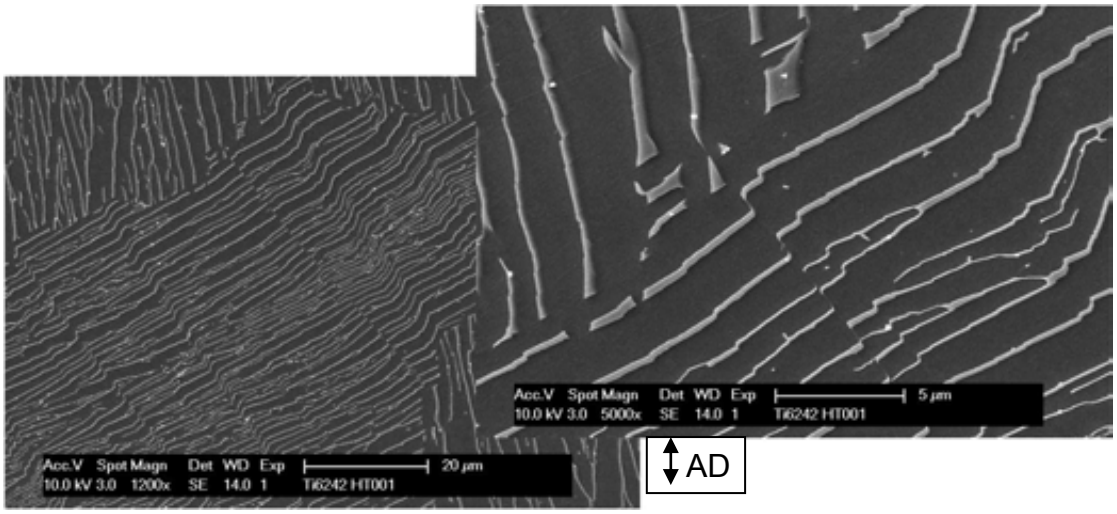

Figure 5-72 – Specimen HT001 sub-surface microstructure showing planar slip bands

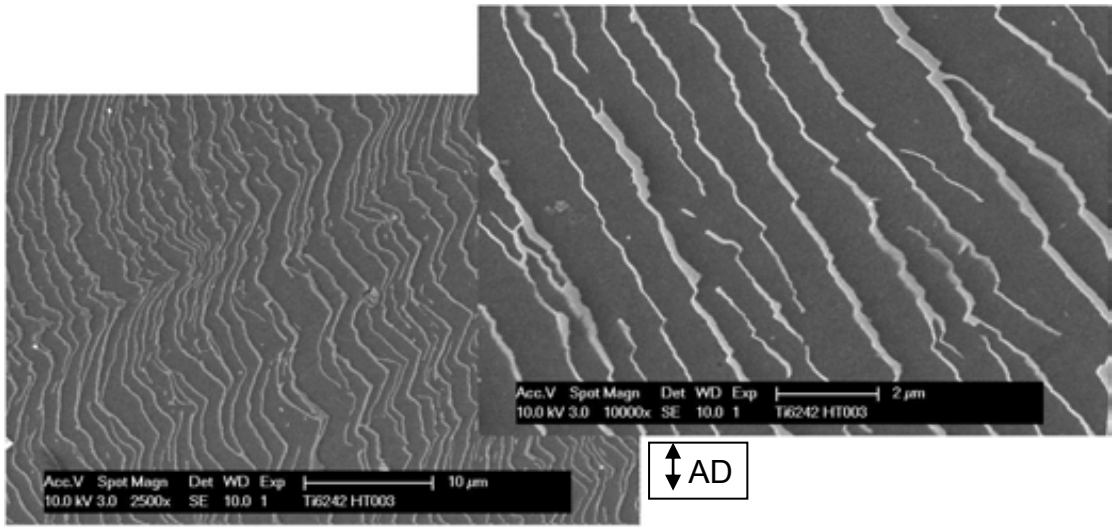

Figure 5-73 – Specimen HT003 sub-surface microstructure showing planar slip bands

5.7.11.5 Ti6242 LCF specimens

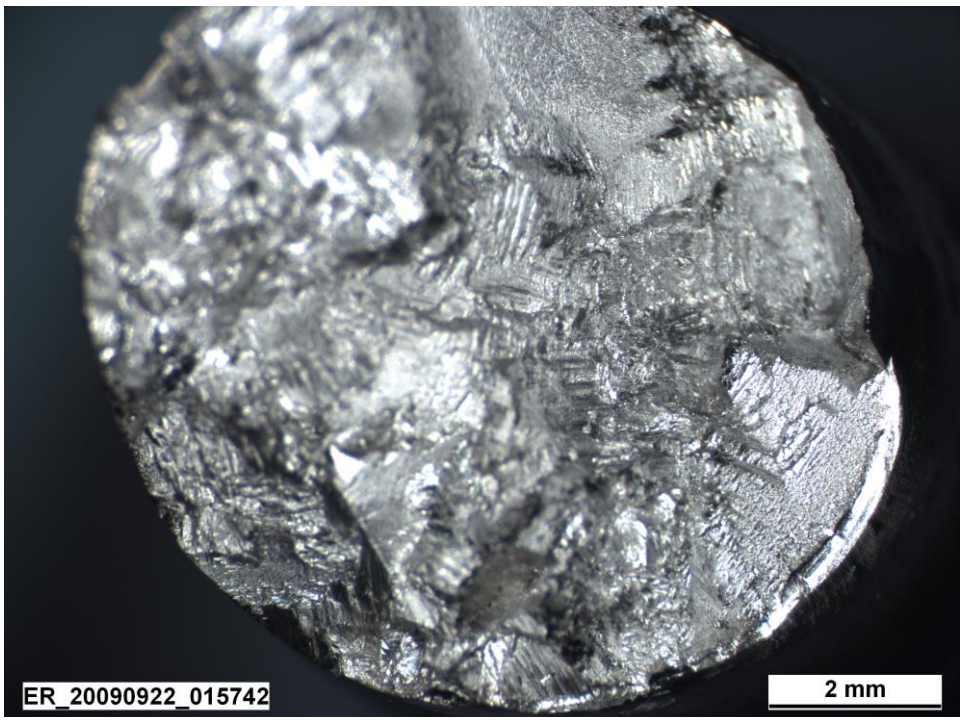

Figure 5-74 – LCF test specimen B7, 800MPa, 22,061 cycles to failure. Surface initiation, no clear fatigue crack growth

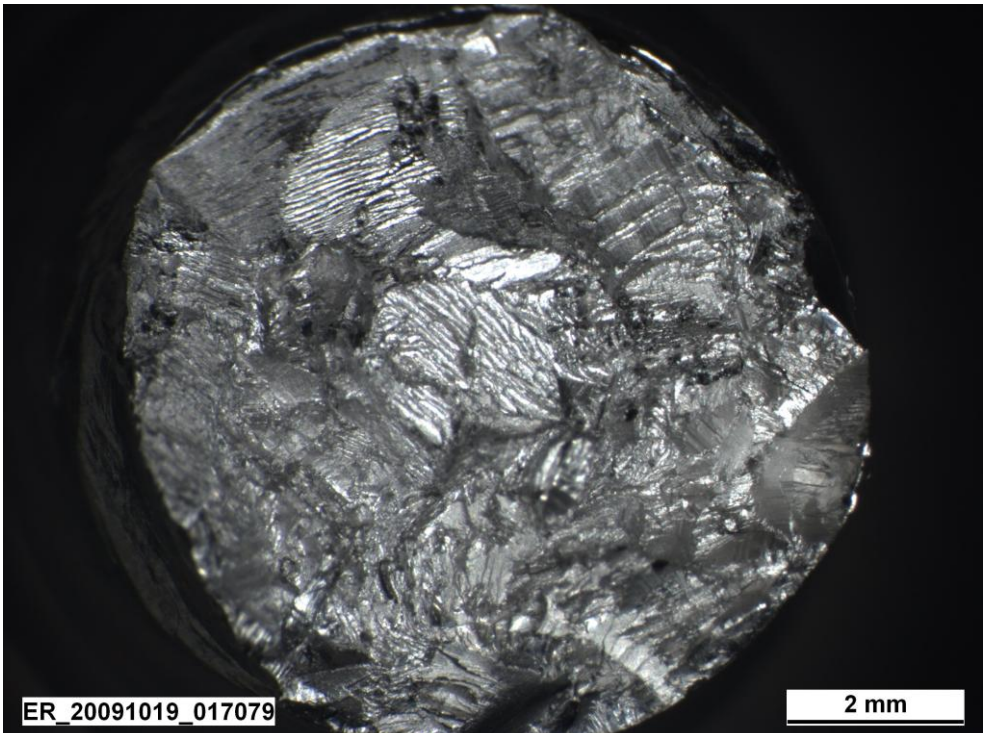

Figure 5-75 – LCF test specimen C8, 725MPa, 62,282 cycles to failure. Surface initiation, largely ductile failure

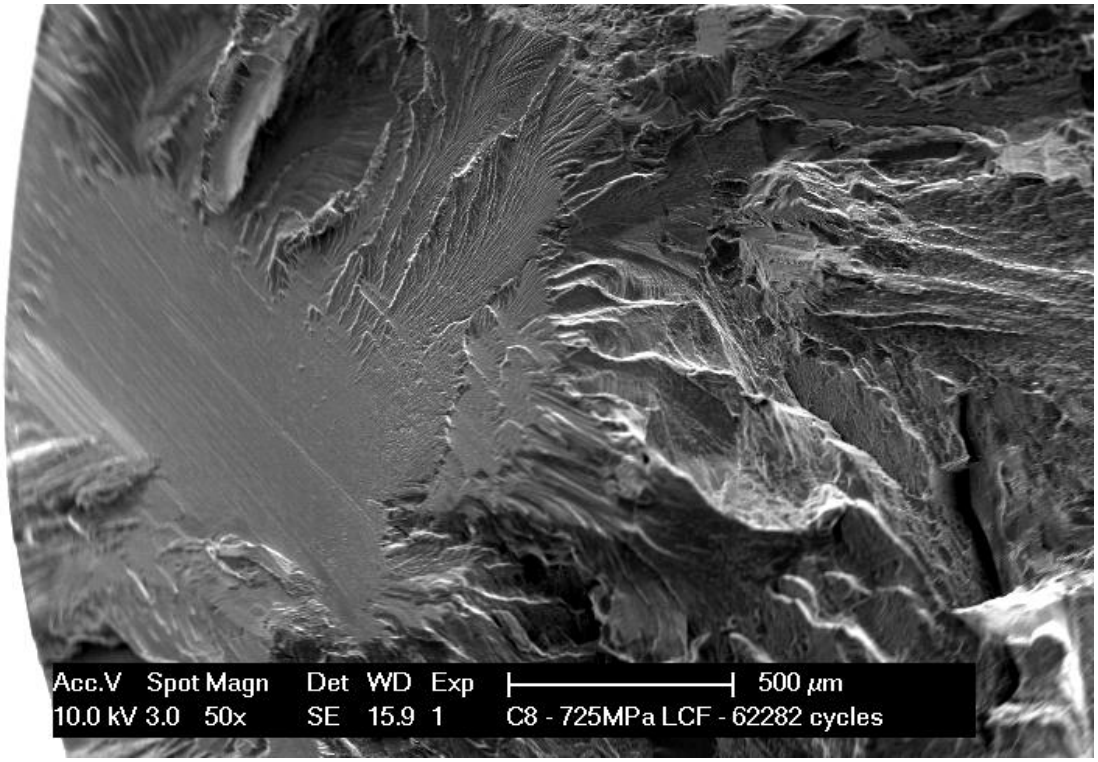

Figure 5-76 – LCF test specimen C8, 725MPa, 62,282 cycles to failure. Possible cleavage (featureless) cracking, transition into ductile failure

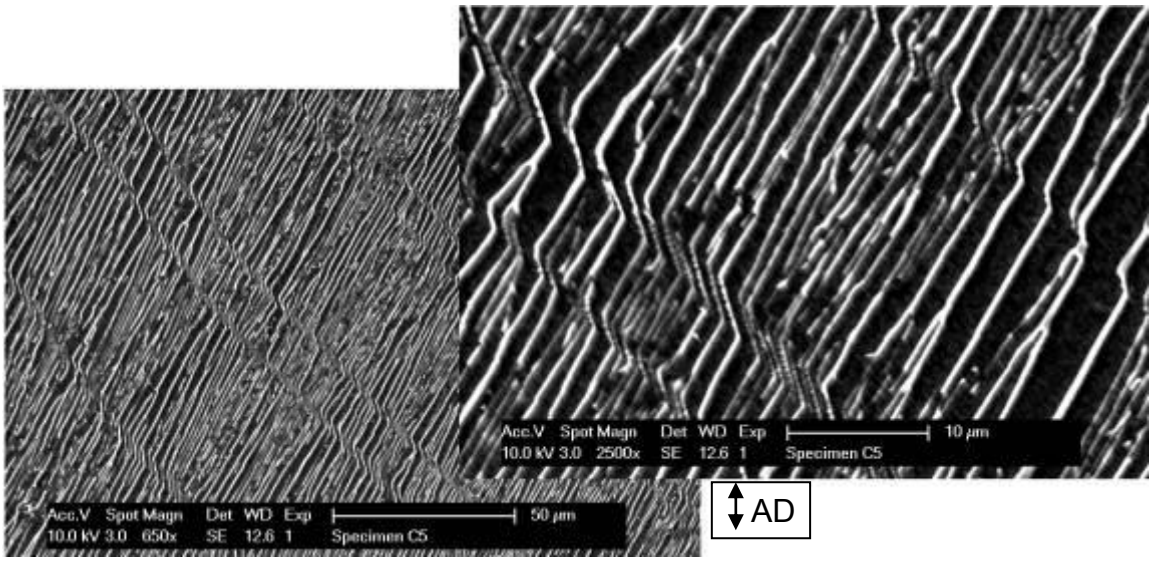

Figure 5-77 – Trans colony slip band features in LCF test specimen C5

5.7.11.6 Ti6242 dwell LCF specimens

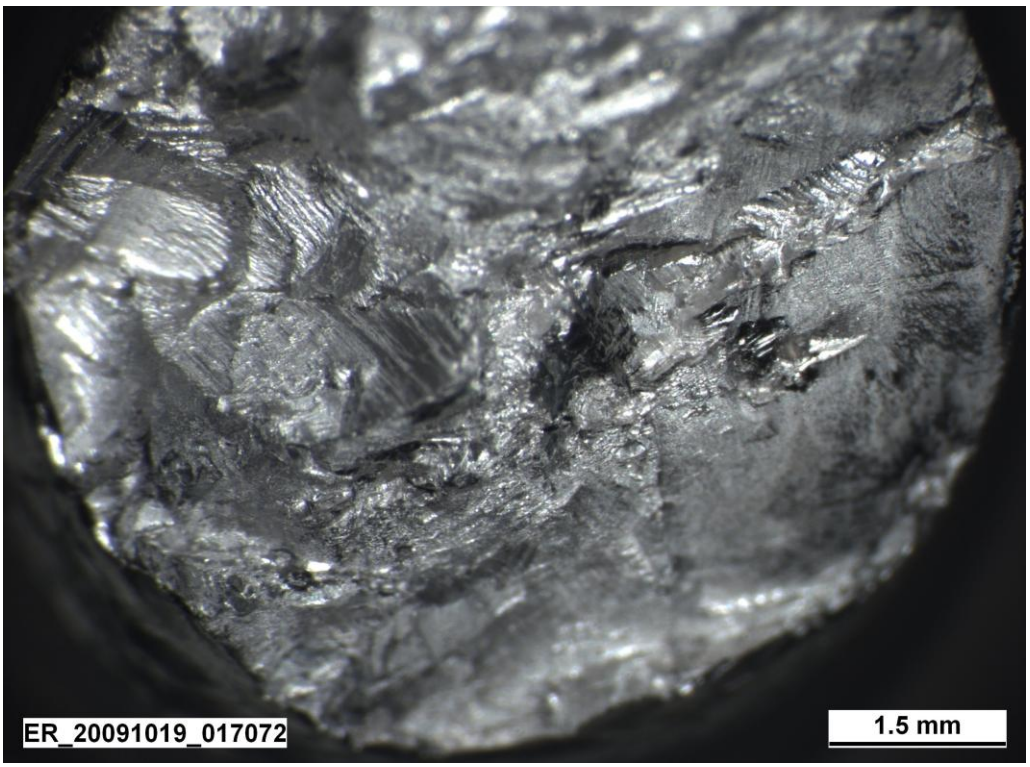

Figure 5-78 – DLCF test specimen C4, 825MPa, 2,901 cycles to failure.

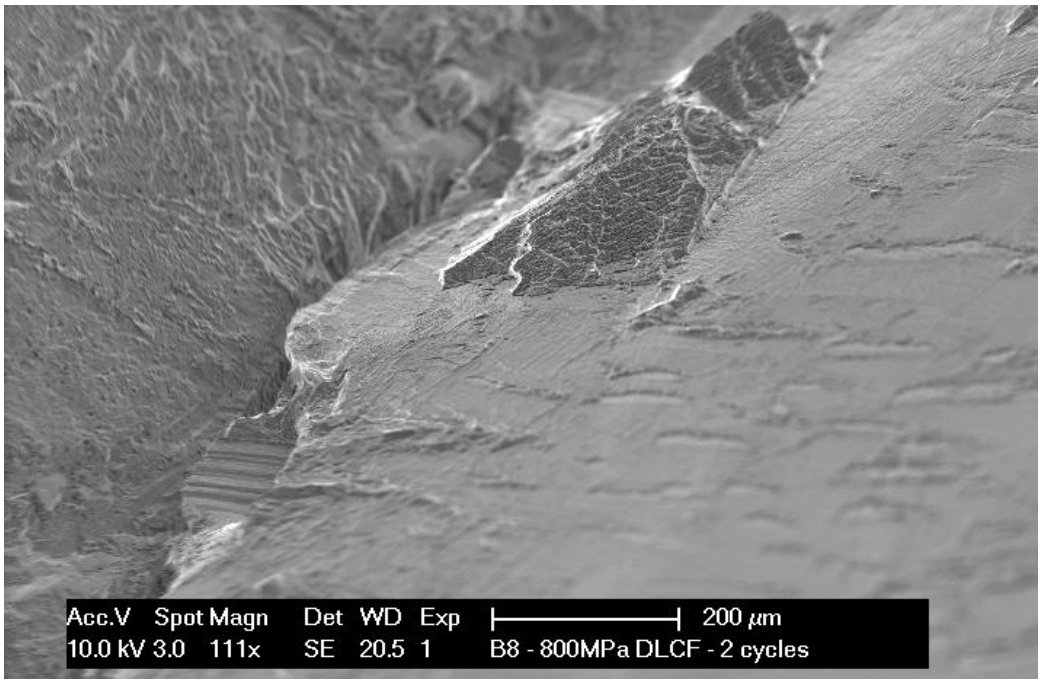

Figure 5-79 – DLCF test specimen B8, 800MPa, 2 cycles to failure. Large angled facet, cleavage cracking

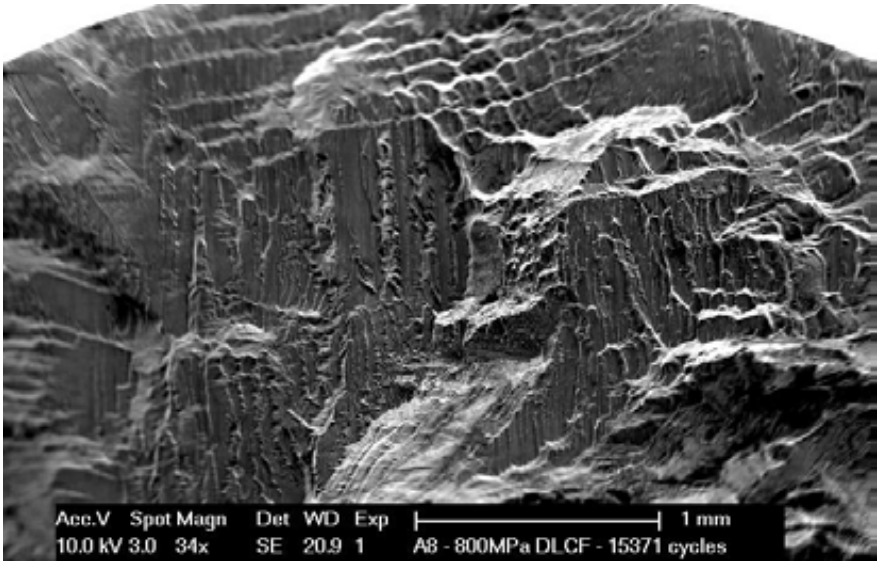

Figure 5-80 – DLCF test specimen A8, 800MPa, 15,371 cycles to failure. Large angled facet, micro-void coalescence

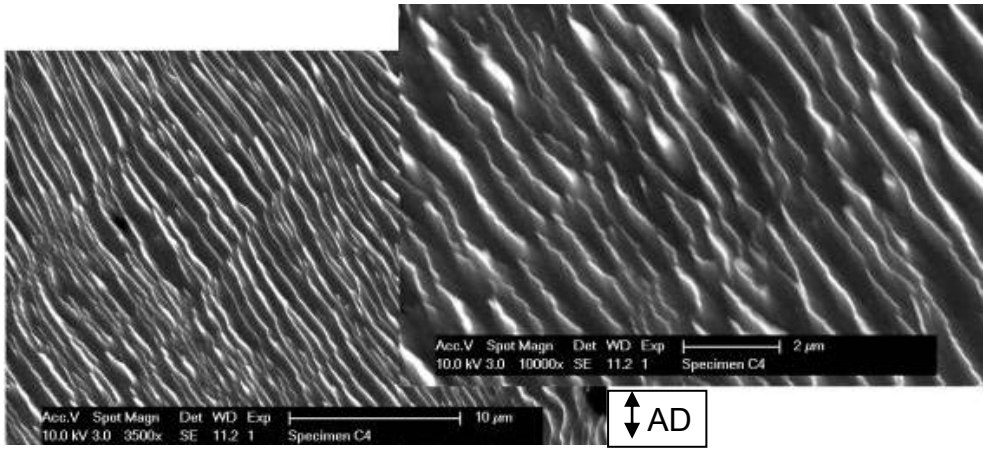

Figure 5-81 – Trans colony slip band features in DLCF test specimen C4 (At fracture surface)

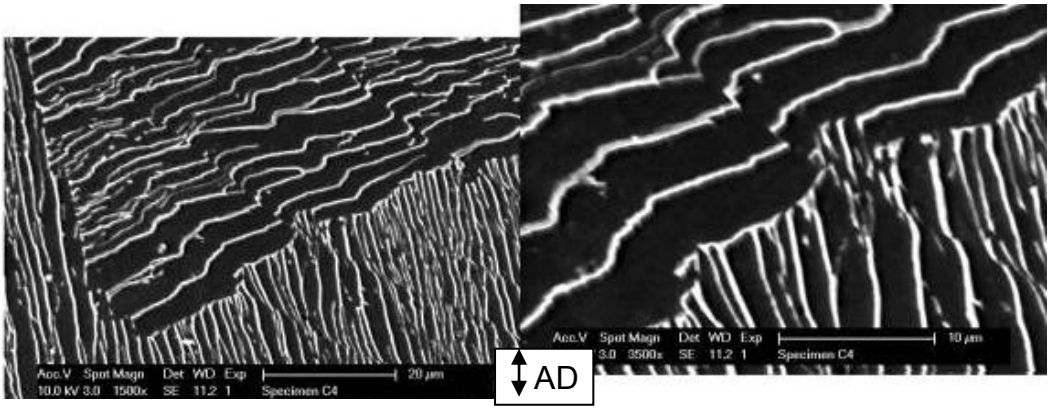

Figure 5-82 – Trans colony slip band features in DLCF test specimen C4 (Sub-surface location). Slip transmission extends across colony boundary

5.7.12 Strain accumulation data

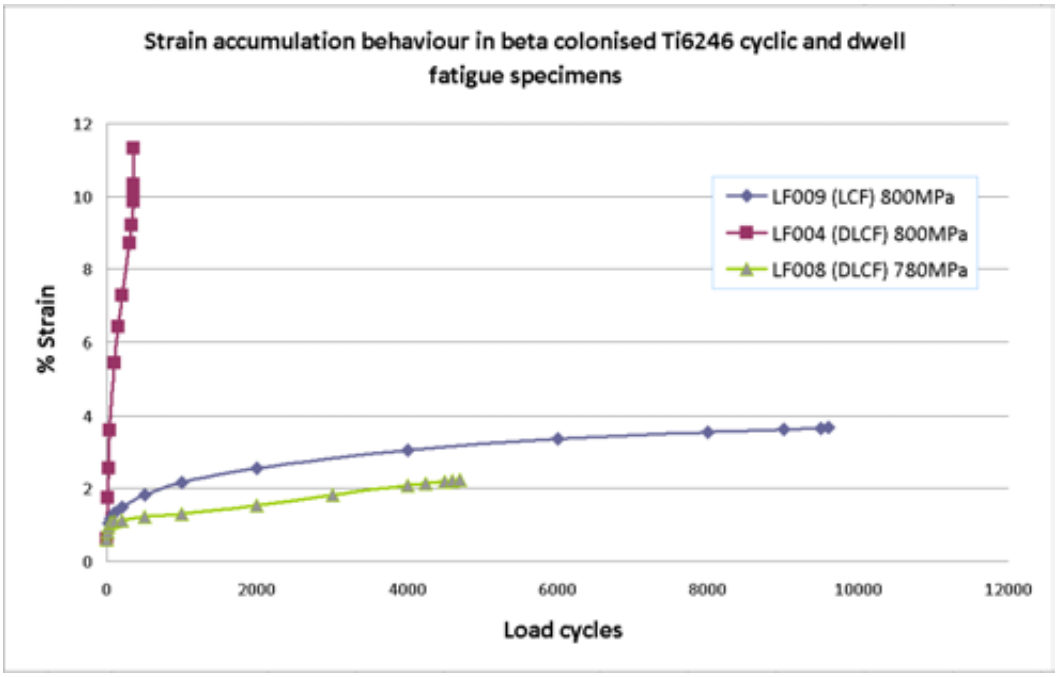

Figure 5-83 – Strain accumulation behaviour in fatigue tests of beta colonised Ti6246 material (Strain recorded at max load at the end of each load cycle)

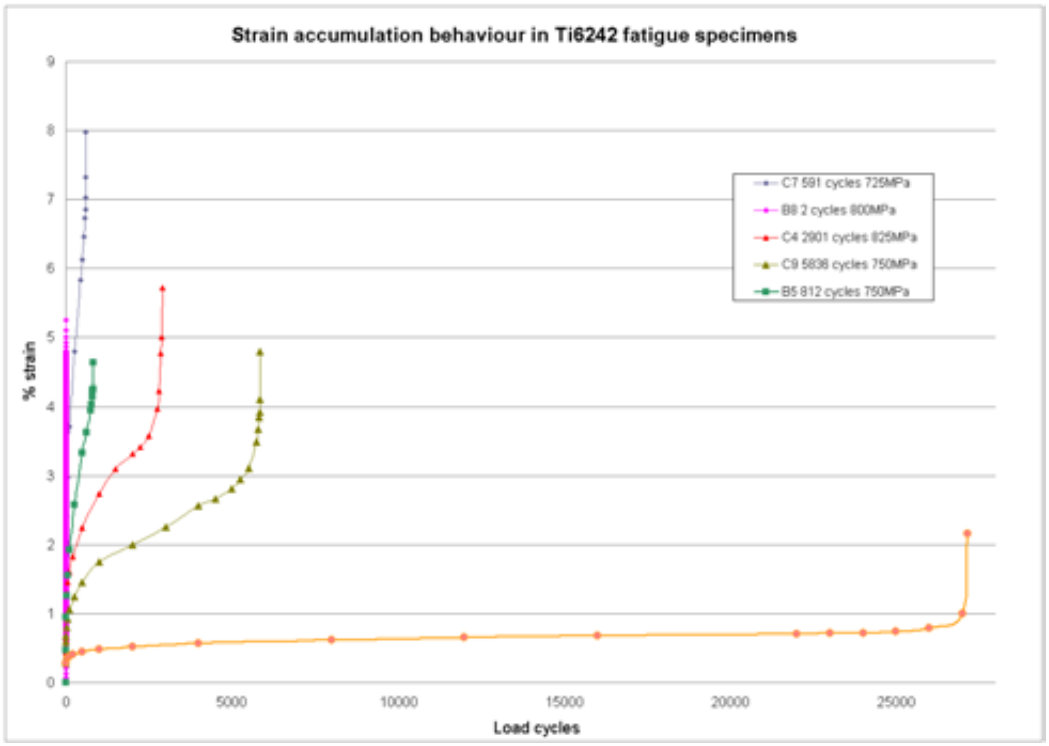

Figure 5-84 – Strain accumulation behaviour in fatigue tests of beta colonised Ti6242 material (Strain recorded at max load at the end of each load cycle)

5.8 TWI report on rotary friction welding of Ti64/Ti6242 Cylinders

The following five pages contain the report issued by The Welding Institute (TWI) on completion of the friction welding of Ti6/4 bar ends to Ti6242 gauge lengths.

6 Characterisation of macrozone and effective structural unit sizes in titanium alloys.... 6-2
6.1 Introduction.... 6-2
6.2 Experimental procedure.... 6-4
6.3 Results and discussion.... 6-5
6.3.1 Ti685 disc material.... 6-5
6.3.1.1 Ti685 cold dwell fatigue test specimens.... 6-11
6.3.2 Ti-6Al-4V fan disc material.... 6-14
6.3.2.1 Ti6/4 cold dwell fatigue test specimen.... 6-14
6.3.3 Ti834 disc material.... 6-20
6.3.4 Ti6242 material.... 6-23
6.3.4.1 Ti6242 billet.... 6-24
6.3.4.2 Ti6242 disc.... 6-27
6.3.5 Ti6246 disc material.... 6-30
6.3.5.1 Beta forged Ti6246 disc material.... 6-30
6.3.5.2 Alpha-beta solution heat treated Ti6246.... 6-37
6.3.5.3 Beta annealed Ti6246.... 6-39
6.3.6 Ti829 cold dwell fatigue test specimens.... 6-42
6.4 Conclusions.... 6-47

6B Volume B - Figures and tables.... 6-51
6.5 Introduction.... 6-51
6.6 Experimental procedure.... 6-52
6.7 Results.... 6-53
6.7.1 Ti685 disc material and test specimens.... 6-53
6.7.2 Ti-6Al-4V DLCF test specimen.... 6-63
6.7.3 Ti834 disc.... 6-70
6.7.4 Ti6242 billet.... 6-74
6.7.5 Ti6242 disc.... 6-81
6.7.6 Ti6246 disc material.... 6-84
6.7.7 Ti829 disc and test specimens.... 6-99
6.7.8 Conclusions.... 6-108

6 Characterisation of macrozone and effective structural unit sizes in titanium alloys

6.1 Introduction

Recent research has developed two terms relating to the crystallographic nature of titanium alloys; 'macrozone' and 'effective structural unit size'. A macrozone may be defined as a sharp local texture heterogeneity in a material, or more specifically in the case of a bimodal alloy as a region containing primary alpha grains orientated around a single texture component with ~20º spread [126]. This was particularly evident in the case of Ti834 billet material for which sectioning of a plane parallel to the compression axis revealed a banded structure of large regions of common alpha textures in an otherwise standard optical microstructure [126].

The term 'effective structural unit' (ESU) defines a length scale over which *"deformation processes do not recognise boundaries in the optical microstructure"* [131]. The most relevant examples are those of Ti834 and Ti6242 disc material with low levels of strain deformation. Under cold dwell fatigue (CDF) loading laboratory test specimens of these alloys can display a reduction in the number of cycles to failure and the presence of "quasi-cleavage" facets approximately normal to loading direction at the fracture surface initiation site [16]. Despite a relatively small optical grain size in these alloys (typically of the order of less than 50µm), CDF loading has been observed to lead to the formation of load normal facets of 500-1500µm in Ti834 and up to 2000µm in Ti6242 [118, 173]. In these materials, individual facets appear to form across favourably orientated single primary alpha grains and coalesce to form a large-scale facet extending across both primary alpha and transformed beta (secondary alpha) phases (illustrated in Figure 6-1) [61, 127]. The ESU size of these materials is therefore considered to be significantly greater than the optical unit size.

Because facet size appears to show some correlation to the size of regions of common crystallography in a microstructure it was considered important to characterise the texture variations in various titanium alloys.

In addition to Ti834 and Ti6242, the near alpha alloy Ti685 has also shown CDF sensitive behaviour. On this basis the crystallography and optical microstructure of these three alloys in various forms has been investigated to characterise the relationship between these features and relate both to previous studies of dwell fatigue behaviour in these alloys. Further work has also assessed the crystallography of sub-surface facet features in CDF tested Ti685, Ti829 and Ti6/4 specimens. This provides a comparison of facet fractographies in different alloys.

In addition to these "dwell sensitive" titanium alloys further EBSD analysis has been undertaken to study crystallographic micro-textures in Ti6246 and relate textures to optical microstructures and deformation length scales.

The relationship between macrozone/ESU size, optical microstructure and CDF facet size in common titanium aero-engine alloys is explored in this chapter.

6.2 Experimental procedure

EBSD maps have been taken to determine the length-scales over which common crystallographic orientations (i.e. potential ESUs) are present in the different alloys. Previous texture research and low cycle CDF behaviour (i.e. the size of facets observed) for the different alloys were taken as indicators of the length-scales of ESUs. Appropriate EBSD map sizes were selected accordingly. Sample axes have been selected to correspond to sample geometries as outlined in chapter three section 3.4. Further details of orientation are provided for individual EBSD maps and pole figures. Techniques and equipment for optical microscopy, SEM and EBSD are described in chapter three.

6.3 Results and discussion

Optical microstructures have been well characterised for the relevant alloys. Variations with processing changes and the limits of the acceptable range of microstructures have been studied and quantified. However, textures at different stages of processing from ingot to finished component are less well understood.

A full list of the material conditions studied in this assessment is given in Table 6-1. Details of the alloy, material form and microstructure are provided. The results and discussion provides details of each of the different alloys and material conditions examined and a comparison of optical microstructure and crystallography in each case.

6.3.1 Ti685 disc material

Previous research has indicated that the size of the facets associated with cold dwell failures in specimen tested Ti685 disc material is typically on the order of 0.50-0.75mm [71]. This has been shown to correspond to the size of regions of crystallographically aligned alpha platelet colonies present in disc material. These colony regions are also clearly observed in the optical microstructure.

The typical microstructure of Ti685 disc material is displayed in Figure 6-2 and Figure 6-3. Given that oil quenching is applied to forgings with irregular geometry there is considerable variation in the cooling rates. As the bore is the section of a compressor disc most susceptible to CDF effects (due to high stresses and low temperatures on take-off) this location was selected for examination. To assess the influence of the cooling rate on microstructure and crystallography, samples were taken from central and edge positions of a disc bore. The microstructure shown in Figure 6-2 is that of a sample obtained from the centre of a disc bore sectioned in the axial/radial plane.

From the microstructure it can be noted that the cooling rate in the centre of the disc bore was sufficiently slow to allow the formation and growth of optically aligned alpha colonies from the prior beta grain boundaries. Within the beta grains there is also some evidence of a basketweave platelet structure.

EBSD crystal orientation maps (COMs) approximately corresponding to the image displayed in Figure 6-2 are given in Figure 6-4. The mapped area is ~1200µm*1000µm. Map resolution was 256*192, giving a pixel size of ~23µm^2 and a step size of 4.79µm. Because of the heavy alpha stabilisation of the alloy there is only a small volume fraction of retained beta phase. At the selected magnification no significant information can be derived from the indexed beta phase due to the low number of indexed points.

COMs show that the slow cooling rate has led to the development of large alpha colonies in the microstructure. No strong alpha macro-texture is noted although this may be due to the relatively small map size in relation to the colony size. It is thought that the beta SHT leads to a near random beta macro-texture and consequently a randomised alpha macro-texture.

There is a clear correspondence between the optical microstructure and crystallography. Each optical colony (i.e. platelet growth direction) is observed to contain a single alpha crystal orientation. From these results a single crystallographic orientation in beta heat treated material can be related to a single optical colony.

Further COMs taken from the centre of a Ti685 disc bore are displayed in Figure 6-5 and Figure 6-6. These COMs again illustrate the presence of large crystallographic units in disc material. In addition they also show adjacent regions of colonies with different optical growth directions for which common basal and prismatic planes exist. As before, the retained beta content is too low to determine prior beta grain orientations, although these

closely related alpha colony orientations are thought to result from closely corresponding {110} beta poles and the preferential selection of alpha variants with basal planes parallel to this {110} plane. Examples are given in Figure 6-7 and Figure 6-8, with yellow boxes outlining the selected textures. These show comparisons of colonies growing from a common prior beta grain boundary into neighbouring beta grains. Figure 6-9 shows two colonies contained within a single prior beta grain. The pole figures show the presence of common basal plane orientations both in colonies in single beta grains and across neighbouring beta grains.

Previous work by Bhattacharyya et al. has demonstrated that optically different colonies of alpha platelets may contain common crystallographic features [115]. Analysis indicated that two colonies with a common basal plane orientation show different growth directions due to a rotation about the c-axis of the hexagonal crystal structure [115]. This occurs because of the Burgers orientation relationship between the alpha and beta phases and the alignment of different crystal directions in the two phases.

Similar observations have been noted in previous studies [117]. Work on colonised Ti-6Al-4V showed that two adjacent beta grains with a close {110} pole show precipitation of alpha at the grain boundary with the basal plane parallel to that pole in preference to the other five {110} poles. The critical angle between the {110} poles for this variant selection behaviour was given at ~10º. At beta misorientations greater than this angle there was no observation of variant selection on diffusional transformation to alpha phase [117].

Because common prismatic and basal planes are observed in adjacent colonies there is potential for common slip lengths to exist over distances in excess of the optical colony size. Where two colonies within a single grain show a common basal plane and a small rotation about the c-axis (as for Figure 6-8) there are two alpha/beta orientation relationships with

different mechanical responses. One orientation displays an a_1/b_1 relationship between the two phases with close alignment between $<111>_\beta$ and $<11\bar{2}0>_\alpha$ directions. Previous work has quoted a 0.7º misorientation between a_1 and b_1 directions in Ti6242S [114]. Due to the structure of the alpha and beta phases and the orientation relationship between them, the $<11\bar{2}0>$ slip direction in the second colony is misoriented by 10-11º from the <111> slip direction that displays the a_1/b_1 relationship in the first colony. This is the a_2/b_2 relationship. The misorientation between the alpha and beta slip directions in this colony results in greater resistance to deformation than for the a_1/b_1 interface relationship [114]. As a result, for planar slip transmission to occur across multiple colonies along a single {110}<111> slip direction it would be necessary for dislocations to transmit across interfaces with a ~10º misorientation between the easy <111> and $<11\bar{2}0>$ slip directions in the beta and alpha phases. The resistance that these interfaces provide is potentially reduced however, due to the high alpha stabilisation of the alloy and consequently the very fine and discontinuous nature of retained beta films [4, 81].

If the applied stresses were sufficiently high to allow a_1/b_1 type slip to continue through a_2/b_2 type colonies there would be implications in terms of mechanical behaviour and potentially in the CDF response of the alloy [131]. This is important in the case of beta solutioned Ti685 as the microstructure can be characterised by a large colony size and increased susceptibility to CDF behaviour results because of the potential accumulation of significant stresses at planar slip boundaries [16]. Furthermore the chemistry of the alloy is believed to give rise to high slip planarity (extremely planar slip behaviour occurs on basal and prismatic slip systems at >6wt% aluminium [114]) also promoting CDF susceptibility in the alloy.

Samples were sectioned from the bore of an ex-service compressor disc. No planar slip effects were observed in the microstructure. It is therefore probable that the engine operating conditions were insufficient for planar slip band formation.

To determine if planar slip bands form in Ti685 as dislocations traverse through colonies (under CDF loading) a test specimen with a high applied peak stress has been sectioned and examined. This work is discussed later in this section.

To estimate the length scale of macrozones and ESUs in this material, measurements of mean linear intercept (MLI) and colony size have been taken over a total of ~120 prior beta grains and ~400 alpha colonies from the centre of a disc bore. The average measured prior beta grain size was ~700µm whilst average colony size was ~210µm. Given the size of facets observed in Ti685 (on the order of 500-750µm across) when dwell fatigue loaded (relative to observed colony sizes) it can be concluded that large facets are likely to extend over two or more distinct alpha colonies. This could be related to the formation of planar slip bands across neighbouring colonies with a_1/b_1 and a_2/b_2 relationships between the phases.

The correspondence between the optical microstructure and crystallography is a result of the beta heat treatment that Ti685 receives. A sufficiently slow cool from above the beta transus allows the growth of aligned alpha platelets from prior beta grain boundaries [22]. If the cooling rate is increased the alpha platelets precipitate in basketweave morphologies. There is likely to be a reduced susceptibility to CDF in this microstructural form due to increased numbers of alpha variants and a reduction in planar slip length-scales. This can be observed at the edges of the disc bore (due to a higher post-SHT cooling rate). COMs were obtained for the microstructure displayed in Figure 6-10 and Figure 6-11.

As for the bore centre, COMs have been acquired over areas of ~1200µm*1000µm with similar acquisition settings. These COMs are displayed in Figure 6-12 and Figure 6-13. Qualitative comparison of the COMs shows a reduction in the macrozone size for material that experiences a higher cooling rate.

For Figure 6-12 three dominant basketweave alpha variants are noted in the centre of the grain. Analysis shows that the three distinct crystallographic orientations contain a common $\{11\bar{2}0\}$ plane, displayed in Figure 6-14. This common $\{11\bar{2}0\}$ plane does not contain any active slip systems and would not be expected to change the effective slip length in the material [28]. Common $\{10\bar{1}0\}$ or {0001} planes in basketweave platelets oriented for slip along a_1/b_1 and a_2/b_2 orientations may allow an effective slip length significantly greater than that expected based on optical microstructure assessments. This would depend on the presence of favourable slip directions in close proximity between the different variants and/or sufficiently high stresses for dislocations to transmit across interfaces. For the pole figures in Figure 6-14 it is noted that there are large orientation differences between the three variants and as such there would be significant differences in both a-type $<11\bar{2}0>$ and (c+a) type $<11\bar{2}3>$ slip directions. Planar slip across these different variants would not be expected to occur because of large angle differences between slip directions.

It is presumed that it is possible for basketweave alpha platelets to show common basal or prismatic crystal planes based on the nature of the Burgers orientation relationship and the limited number of alpha variants that can form from a single beta variant. A commonality of basal or prism planes may influence the effective slip length in the material (i.e. increase the ESU size above the length-scales of the optical microstructure).

6.3.1.1 Ti685 cold dwell fatigue test specimens

Examination of a Ti685 dwell fatigue test specimen subject to 120-second dwell periods at 772MPa at 80ºC and a stress ratio of zero (failure after 215 cycles) showed the presence of multiple faceted regions on the fracture surface. Facets often extended over distances greater than 1mm in length and had a reflective appearance. A plane was sectioned through the specimen to intersect two of the most prominent facets on the fracture surface. These facets were designated A and B. Both facets were approximately circular in shape and had diameters of ~2mm. On sectioning they were noted to be angled at ~10º and ~20º to the loading direction normal plane respectively.

Fractography at the plane of intersection was recorded using SEM imaging. The fractographies of facets A and B are displayed in Figure 6-15 and Figure 6-16 respectively. Each facet extends over a distance approximately indicated by the two arrows marking the facet boundaries. The plane of intersection is at the top edge of the image in each case.

In both cases there are distinct boundaries to the facet. The crack growth direction changes significantly at these boundaries. Facet A also shows noticeable variation in the fractography within the faceted region. Towards the left edge of the facet, crack progression lines can be observed. This supports the theory of facet formation through "quasi-cleavage" growth (although the facet plane is not load normal) [16]. A higher magnification image of the fracture surface shows this growth behaviour (Figure 6-17). The arrow highlights the apparent crack growth direction.

EBSD maps were taken of the microstructure of the cross-section of these two facets. Due to the size of the facets, in both cases two maps were obtained over the facet length (at increased magnifications) and combined afterwards. This helped retain high indexing levels

and provided more detailed information (i.e. resolved smaller colonies) in the COMs. Crystal orientations of facet A w.r.t. loading and load normal directions are displayed in Figure 6-18 and Figure 6-19 respectively.

These maps show that a change in the crystallographic orientation occurs at ~1/3 of the distance across the facet. This is in agreement with changes in the fracture surface (see Figure 6-17). The orientation change is clear although there is only a low misorientation angle between the two sections of the facet. In contrast, at the boundaries of the facet there are significant changes in crystal orientation.

It is presumed that the driving force for continuation of growth along the facet plane at the facet boundaries is lower than the resistance due to crystal orientation differences, leading to a change in the growth direction. The result does however, show that faceted growth can occur across more than one crystallographic colony.

BSE imaging shows that a grain boundary exists at the right hand edge of the facet, as shown in Figure 6-20. BSE imaging across the facet (not on exactly the same plane due to further sample preparation after imaging but before EBSD) shows the presence of a beta grain boundary in the centre of the facet, and another boundary at the left hand edge of the facet. The microstructure is displayed in Figure 6-21.

Facet A is not believed to be a true CDF facet both due to the angle to the loading direction (~80º) and more importantly, the significant difference of the crystal orientations from those of a conventional CDF facet where basal planes lie normal to the loading direction [16].

In comparison, facet B shows an approximately common crystallographic orientation across the cross-section. The facet also shows basal planes are orientated with the c-axis relatively

close to the loading direction. COMs are shown in Figure 6-22 and Figure 6-23. This correlates well with the model proposed in figure 2-40 [87].

The underlying pattern quality maps in these figures show the presence of several colonies across the facet. Although there is a significant change in crystallography at one end of the facet, leading to a change in crack growth direction, at the other end of the facet there is no evident change in crystal orientation that would contribute to the change in growth direction. The reason why facet growth does not continue beyond this point is unclear.

The facet microstructure is shown in Figure 6-24. Close examination shows that the facet extends across two beta grains, with a grain boundary present at the end of the facet where a marked change in crystal orientation occurs. There are distinctly different optical alpha platelet colonies in the microstructure although they show very similar crystallography, presumably relating to the two alpha variants that can form on a single {110} plane along the respective (111) directions [117].

Although this facet shows suitable crystallography for a CDF mechanism the ~20º misalignment from a load normal direction suggests that facet B is also not a true dwell fatigue failure [16]. Instead it may relate to slip band formation along a favourable plane under the application of a dwell period [87]. The presence of large colony structures (even in a relatively low volume such as a test specimen) may then allow such facets to form in relatively large numbers. By comparison, according to current theories, the criteria for CDF faceting requires a particular combination of neighbouring grains to develop local stress levels suitable to cause off-loading between grains [136]. The probability of this occurring frequently even in a material with a microstructure susceptible to this behaviour is relatively low (unless stresses are high enough, as tends to be the case for laboratory specimens).

Although the macrozone size and CDF facet size appears to be related to the optical microstructure in Ti685 the link between these features is less evident in (alpha + beta) processed alloys such as Ti6/4, Ti6242 and Ti834. These materials all show facet formation under dwell conditions over dimensions that greatly exceed the grain sizes observed in the optical microstructure. EBSD assessments have been undertaken as an initial characterisation of macrozone size in these bimodal alloys. This work is discussed in the following sections.

6.3.2 Ti-6Al-4V fan disc material

Based on the similar (alpha + beta) processing route to (CDF sensitive) Ti834 and Ti6242 disc alloys it was considered appropriate to characterise Ti6/4 disc. Because of the processing route there is a significant possibility that there are regions of primary alpha and transformed beta (secondary alpha) with common basal plane orientations extending over distances much larger than individual grain sizes [102, 126].

6.3.2.1 Ti6/4 cold dwell fatigue test specimen

Ti6/4 fan disc material was examined in the form of a CDF test specimen. The specimen was tested at 80°C using a two-minute dwell at peak stress of 772MPa and a stress ratio of zero. The specimen failed after 1408 cycles. By eye the fracture surface was noted to contain a large region of facet-like appearance. Under SEM the majority of the specimen shows ductile failure as illustrated in Figure 6-25. Although the fracture surface is relatively flat microstructural grain outlines can be resolved. There are regions of the fracture surface that show facet-like features (see Figure 6-26) [174]. In these regions of microstructure the fracture surface is approximately planar.

Examination at higher magnification shows progressive growth across individual grains. The growth directions appear to vary from grain to grain. No defects (such as porosity) were

noted at growth origins, which are usually located close to grain boundaries. Typical fractography in these faceted regions is displayed in Figure 6-27.

These observations support the theory of the accumulation of stress concentrations at the boundaries between weak and hard microstructural units, with the redistribution of stresses leading to quasi-cleavage crack growth across individual grains. For a region of microstructure with a preferential texture in either primary alpha grains, or both primary and secondary alpha, the growth of several cracks in a localised area on a similar plane may lead to coalescence and the formation of quasi-cleavage cracks significantly larger than the grain size [61, 132].

To establish the crystallographic nature of faceted and unfaceted regions of the microstructure, the specimen was sectioned along a plane to provide a comparison of three distinct regions. The first region was a reflective elliptical facet of dimensions approximately 1250µm in length by ~500-750µm in width. The second region was a more diffuse faceted region, which extended over dimensions of several millimetres in both length and width, although under binocular examination showed both dull and reflective regions. The third region was an unreflective unfaceted section of the specimen.

For EBSD analysis of the elliptical facet, four separate COMs were obtained over the length of the facet and combined into a single map. This allowed the accurate resolution of both primary alpha grains and secondary alpha phase, based on a corresponding BSE image.

The BSE image of the microstructure through the facet is shown in Figure 6-28. The approximate boundaries of the facet are indicated as positions X and Y. The corresponding COM showing crystal orientations parallel to the loading axis is shown in Figure 6-29. A

further COM showing crystal orientations from an arbitrary direction normal to the loading axis is given in Figure 6-30.

The EBSD maps show a concentration of both primary and secondary alpha grains close to the centre of the facet which display orientations with c-axes close to parallel to the loading axis. This suggests a CDF failure has occurred [16]. Whilst a large proportion of alpha grains show c-axis alignment parallel to the loading direction at the centre of the facet, there is no strong preferred rotation about the c-axis (as evidenced by variations in crystal orientations at the facet centre in Figure 6-30).

Manual separation of primary and secondary alpha textures gave the EBSD maps in Figure 6-31 and Figure 6-32 respectively. It is likely that initiation occurred from a region of the facet where multiple primary alpha grains shared a common crystal alignment. For CDF behaviour, some surrounding grains require a favourable weak orientation for stress redistribution to occur [136, 140]. If the remaining local microstructure consisted of similar crystal orientations to the primary alpha grains it would allow coalescence of individual facets to form a wider faceted zone [61, 127]. The growth path of the facet is noted to become less planar towards the edges of the facet as the alpha textures become less pronounced. The cross-section of the strong planar facet equates to the size of the region of strong basal texture which is ~600-700μm.

An EBSD map was taken over an area at the centre of the facet to determine the dimensions over which the strong basal texture exists. The map shows that the textured region (macrozone) has a shape that appears to be angled at ~45º with respect to the loading axis. The COM and potential macrozone shape is displayed in Figure 6-33. Because the other section of the specimen has not been examined the dimensions of this textured region

cannot be determined. However, the width is estimated at ~500µm. The length is at least 600-700µm (from COMs) but is thought to be between 1000µm and 1500µm (based on the assumption that the facet initiated close to the centre of the textured region). It is thought that the textured region corresponds to a prior beta grain, with grain flow angled with respect to the specimen loading axis [126].

The strong basal texture and the freedom of rotation about the c-axis for the macrozone in Figure 6-33 are shown in the corresponding pole figures (see Figure 6-34). It is likely that strong textures have been retained in the primary alpha grains through processing due to insufficient deformation during forging operations. This supposition is based on the microstructure throughout the specimen. Although in the local vicinity of the facet fracture there is no clearly anomalous microstructure other sections of the test specimen show microstructures indicative of low forging deformation [175, 176]. Figure 6-35 shows a microstructure where it appears that the colony structures present following an earlier beta heat treatment have not been fully broken down (i.e. globularised) following further processing. There are large 'strings' of semi-globularised primary alpha grains in this microstructure over a region thought to correspond to a prior beta grain. Further deformation would be expected to break these structures into separate equiaxed grains which may develop varied textures under further forging deformation [126, 175].

Further examination of the facet microstructure studied an area consisting of a 'diffuse' facet, similar to those examined by Germain and Bache in a Ti834 CDF specimen [132]. As for that work, the faceted region in the Ti6/4 specimen was observed to extend over a large area, containing numerous individual facets. EBSD analysis selected a random area within the intersected plane for mapping. The resulting COMs (see Figure 6-36) showed an unexpected result as no strong textures were observed in the mapped region.

Although under binocular examination the diffuse facet appeared relatively planar, sectioning showed the extent of non-planarity in this region of the specimen. There was no clear evidence of faceted growth, instead crack path appears to be influenced locally by the orientation of individual alpha grains. Pole figures for this section of the microstructure are displayed in Figure 6-37.

As the mapped areas are approximately the same, the pole figure textures in Figure 6-37 may be compared back to those in Figure 6-34. Although it is noted that the diffuse faceted region shows a concentration of basal textures at ~45º to the loading axis, the intensity of this basal texture is significantly lower than that observed for the strongly textured facet section. A possible explanation for the lack of strong texture is that the faceted region is relatively large (several millimetres length and width) and there may be a wide variation in texture throughout the facet.

Thirdly, a section of the specimen displaying no facet features has been examined using EBSD. This has again produced unexpected results as assessment showed the presence of a significant level of preferred alpha texture. As for 'strong' and 'diffuse' facet sections, an EBSD map has been obtained over a consistent area for texture comparison. The COMs are displayed in Figure 6-38. Associated pole figures are given in Figure 6-39.

Although there is a relatively strong texture (comparing Figure 6-39 with Figure 6-37 and Figure 6-34), which is similar to that for the 'diffuse' faceted region, it is noted that the texture is not favourable for initiation of CDF facets. Basal planes are offset at close to 90º from the strong orientation associated with conventional CDF facets.

This texture is not thought to be representative of the wider texture in unfaceted sections of the fracture surface. It is postulated that the specimen failure has occurred primarily

through the formation of a large CDF facet in a location with strong basal texture normal to loading axis. The 'diffuse' facet is believed to have consisted of a number of independent (i.e. unconnected) small faceted regions at the point when the 'strong' facet has started to propagate through the microstructure. Crack coalescence has then occurred throughout the diffusely faceted region as the applied stresses have increased [61]. Following facet formation, the growth of a relatively planar fracture surface may then have occurred due to the presence of large crystallographic units giving rise to favourable crack growth paths.

In summary, the specimen failure appears to have initiated in a region of sharp local texture favourable for CDF facet formation. This is thought to have arisen due to insufficient deformation during (alpha + beta) forging [118]. This has left retained textures in primary alpha grains from which variant selection appears to have occurred in neighbouring transformed beta [126]. Elsewhere in the specimen a 'diffuse' faceted region is present, although this is not believed to have been the life-determining factor in the specimen test. EBSD assessment of a localised section of this facet showed relatively weak textures, suggesting there is likely to be considerable variation in texture over such large facet features. In contrast, an unfaceted section of the microstructure showed a relatively strong alpha texture although the crystal orientations were unfavourable for CDF crack initiation. This implies that whilst strong alpha textures may exist throughout a specimen, CDF failure requires the appropriate crystal orientations with respect to the loading axis [16, 136].

As an alternative to EBSD assessment, macrozone size could be assessed using polarised light microscopy. This technique is based on the optical anisotropy of the crystal structure and would provide a quick and reliable indication of the degree of texture in the specimen [28]. The SRAS technique would also provide qualitative information on macrozone size [162, 170].

6.3.3 Ti834 disc material

As for Ti6/4, despite the small optical grain size there may still be large regions of common texture present in bimodal Ti834 alloy. Sackett et al. described continuous common basal plane orientations up to 400µm across (across primary alpha and transformed beta phases) in CDF tested Ti834 disc specimens [177]. Germain et al. also noted the presence of banded macrozones in Ti834 billet [126]. Because of the possible presence of large regions of common texture and the subsequent susceptibility to CDF the macrozone size of the alloy has been investigated in the current work.

The work of Bache and others has indicated that facet sizes in Ti834 relate to regions of common crystallography present at earlier stages of processing, i.e. ingot or billet material [16, 102]. Substantial characterisation work has been undertaken in the case of Ti834 billet [119, 126]. Large regions of common alpha texture observed in the billet material were previously thought to correspond to prior beta grains [127]. Other work suggests that common primary alpha grain orientations can be related to retention of textures throughout forging deformation and the globularisation of colonies of lamellar alpha platelets [126]. A third theory suggests rotation of alpha textures towards a stable deformation component with radially orientated c-axes and $\{11\bar{2}0\}$ poles in the compression direction [126].

In work characterising ESU size, Germain and Bache noted the presence of "diffusive and extensive" initiation zones in Ti834 CDF specimens. These initiation zones contained "numerous individual facets" [132]. The faceted regions displayed in the reference extend over distances in excess of 2mm. EBSD maps of a sub-surface region of microstructure showed an area greater than 1mm in length over which primary alpha grains possess a common basal plane orientation. This common crystallography in an otherwise normal

optical microstructure is thought to lead to the formation of these large facets under CDF loading conditions.

Because of the possibility of such behaviour in (alpha + beta) processed Ti834 material, an assessment has been made of the extent of common textures in compressor disc material. Two discs (identified as A and B) were selected due to the low levels of deformation in the disc bore on forging and the consequent increased likelihood of texture retention. Material was sectioned from bore locations due to its particular susceptibility to CDF effects.

Maps were obtained in regions displaying ordinary optical microstructures. COMs obtained from the microstructure are close to 100% alpha phase. To obtain information on the retained beta phase would require mapping at higher magnifications and/or the use of a higher map resolution.

Results for both discs show relatively varied/weak alpha textures and the restriction of macrozones to length scales no greater than several adjacent grains (both primary and secondary phases). COMs of alpha textures for the different discs are displayed in Figure 6-40 and Figure 6-41. Corresponding pole figures (Figure 6-42 and Figure 6-43) show a broad spread of orientations. Although there are specific orientations displaying increased texture intensities and there is evidence of deformation textures, it is clear that there is an acceptably random distribution of texture orientations.

Microstructures for each disc in the region of mapping are shown in Figure 6-44 and Figure 6-45. Both microstructures contain ~10-15% primary alpha grains that have been fully spherodised with processing. The remaining secondary alpha microstructure shows regular variation in the optical growth directions of alpha lamellae. No common optical growth directions are observed over length scales greater than ~50µm. The optical microstructure

and the alpha textures in the material suggest that any strong textures that may be present in the parent material are fully removed during (alpha + beta) processing.

Although stronger textures were detected in one of these discs the results only provide an indication of macrozone (and potentially ESU) size. To gain a more definitive assessment of the wider texture in the material would require assessment of an area large enough to include sufficient prior beta grain structures in order to be statistically representative. For the purposes of the current work large-scale texture analysis was not undertaken.

Higher magnification EBSD maps from similar locations in both discs A and B have confirmed the approximate macrozone size and texture distributions in these forgings. Further work has examined the textures present in the rim of a disc forging (disc C). COMs are displayed in Figure 6-46. As for bore locations, the alpha texture is relatively weak and the macrozone size is restricted to 2-3 neighbouring grains. The ESU length scale is presumed to vary between individual primary alpha grain size and macrozone size depending on the combination of crystal orientations and the applied loading conditions [131].

A higher magnification EBSD map was also obtained to identify and distinguish primary and secondary alpha textures, as shown in Figure 6-47. Primary alpha grains are outlined. Results show that relatively weak alpha textures in the disc rim. There is no evidence of preferential texture in the primary alpha grains or significant variation selection in secondary alpha.

For comparison, work by Germain using the automated separation of Ti834 primary and secondary alpha texture components has shown a greater number of texture components in secondary alpha phase than primary alpha grains [126]. The main secondary texture component observed had a higher intensity and a lower spread than the surrounding primary alpha phase, indicating a high degree of variant selection in the transformation from

beta phase. Germain suggested that the sharp local texture observed in macrozones is the combination of the single component of the primary alpha texture and the major component of the secondary alpha texture [126]. In the current work no strong textures have been observed in primary or secondary alpha phases. No strong variant selection has occurred in the phase transformation during thermomechanical processing of the selected discs.

From this work it is clear that the macrozone size in Ti834 disc material is often significantly smaller than in Ti685 disc material. Despite this difference in the crystallography of the two alloys a similar CDF response is observed [178]. This suggests that although stress redistribution effects are likely to occur on different length-scales in the two alloys, they are still capable of producing equally strong CDF effects.

As for Ti6/4, Ti834 crystallographic textures could also be quickly assessed using polarised light imaging or SRAS techniques to provide a preliminary indication of the extent of texture commonality [28, 170].

6.3.4 Ti6242 material

Previous assessment of bimodal Ti6242 has shown the presence of regions of common alpha texture over areas significantly larger than individual grain sizes. Woodfield et al. published work in 1995 showing the presence of large regions of equiaxed primary alpha grains with common basal orientations in Ti6242 forgings [118]. These primary alpha grains were thought to have spherodised from alpha lamellae during processing. It was suggested that the lamellae form during beta heat treatment in the billet conversion process. Insufficient subsequent (alpha + beta) deformation followed by annealing then resulted in lamellae spherodisation whilst retaining a common alpha orientation [118, 175]. Other work has related the common primary alpha grain orientations to the as-cast ingot microstructure,

correlating the macrozone size to the size of colonies in ingot material [126]. An alternative mechanism describes the limited slip systems in the alpha phase and the development of deformation textures in primary alpha grains [126].

Much of the research on the crystallography of Ti6242 has been undertaken by General Electric and Ohio State University [114, 133, 139]. The presence of zones of common alpha texture was attributed to the alloy processing history. This included billet conversion, forging and subsequent heat treatments. Failure investigation work identified an excessively large starting billet diameter with consequent insufficient forging deformation as the principal cause of CDF failures in Ti6242 compressor discs in General Electric engines [70, 118].

In the current work the variation in textures in Ti6242 billet material have been studied to assess both macrozone and ESU sizes. Similar work has assessed texture in a typical Ti6242 compressor disc forging. Further work studying Ti6242 textures was detailed in chapter five, discussing the characterisation of Ti6242 disc bore material used in a CDF test programme.

As for Ti6/4 and Ti834 macrozone size assessments, it is recognised that polarised light imaging or SRAS techniques could be used to provide a preliminary indication of the extent of texture commonality [28, 162].

6.3.4.1 Ti6242 billet

Six-inch diameter Ti6242 billet was sourced from Timet after conversion from 34" TVAR ingot. Material was sectioned from the centre and the edge of the billet as shown schematically in Figure 6-48.

The macrostructure in both the near centre and near edge locations shows elongated prior beta grains. At higher magnifications it is difficult to identify the prior beta grain boundaries. The optical microstructure in the centre of the billet typically consists of equiaxed primary

alpha grains with small amounts of retained beta phase. There was some evidence of elongated primary alpha grains in the microstructure (usually in localised regions). There was also evidence of differences in the level of retained beta in different regions of the microstructure. This variation of beta fraction and its effect on etching behaviour may be responsible for the contrast between prior beta grains at low magnification.

The optical microstructure at the centre of the billet is shown in Figure 6-49 to Figure 6-51. The optical microstructure at the edge of the billet is shown in Figure 6-52 and Figure 6-53. At the edge of the billet a lower primary alpha grain area fraction is observed, presumably due to higher cooling rates following deformation operations. Primary alpha grain morphologies also appear less equiaxed than in the billet centre. This may be due to inhomogeneous strain distributions throughout the billet.

Textures in the centre of the billet have been characterised by assembling three COMs taken from adjacent sections along the axial length of the billet. The total mapped area was ~1200µm in width and ~2700µm in length. Each map had a step size of ~4.7µm and indexed 75-80% alpha phase and ~5% beta phase.

The number of indexed beta points was too low to accurately assess beta texture. The three alpha COMs show the presence of elongated macrozones along the billet axis, as displayed in Figure 6-54. Although there is some rotation and distortion of maps in relation to one another this has not been accounted for in the assembly of the COMs.

The COMs show macrozones to be on the order of 750-1000µm along the length of the billet and 200-300µm in width. These macrozones may correspond to prior beta textures although the indexed beta fraction does not allow clear comparison of textures to assess phase transformation behaviour. Basal plane textures are most concentrated on the billet

axis normal plane, i.e. a radial distribution of c-axes perpendicular to the billet axis direction. There is no evidence of a preferred c-axis rotation aligning $\{10\bar{1}0\}$ planes with the billet axis.

Macrozones are more clearly identified if a nearest neighbour fit is applied to the alpha COMs. Unindexed and beta phase points are replaced by alpha textures selected according to the orientations of neighbouring alpha phase points. The enhanced alpha COMs are given in Figure 6-55.

To characterise texture in a radial edge section of the billet two adjacent EBSD maps have been obtained over a total area of ~600µm width and ~900µm length using a step size of ~2.4µm. Results gave an alpha fraction of ~85-90% and a retained beta fraction of ~10%. The microstructure in the area of interest is shown in Figure 6-56.

As before, there is insufficient information on beta phase to assess textures and macrozone sizes in this section of the billet. The alpha COMs in Figure 6-57 show macrozone features elongated along the billet axis, with lengths in excess of 900µm and widths of ~100-150µm. Alpha textures show significant preferential alignment of the basal plane close to a billet axis normal direction. The alpha textures for the respective COMs are displayed in Figure 6-58.

This is a $\{10\bar{1}0\}$ fibre deformation texture and is expected according to literature [179]. However, it is noted that the basal plane intensity is concentrated over a small range of angles, rather than a radial distribution as expected in billet or bar material. A freedom of rotation about the c-axis is noted leading to a distribution of $\{10\bar{1}0\}$ and $\{11\bar{2}0\}$ planes about a plane parallel to the billet axis. To determine if this texture is representative of the macro-texture at the billet edge would require assessment of a larger area.

The strong alpha texture observed in pole figures is presumed to be a deformation texture developed during (alpha + beta) working, rather than due to transformation variant selection. This strong texture can be related to the presence of relatively large macrozones in the material. Alpha macrozones appear to correspond in size and aspect ratio to the prior beta grain outlines observed in the optical microstructure at low magnifications. However, this optical-crystallographic relationship has not been confirmed. As was noted in other work on Ti6/4 macrozones, a ~90º misorientation between neighbouring macrozones can often be observed [180]. The reason for this macrozone orientation relationship is unclear.

Although macrozone size can be defined in terms of the length and width of observed zones of common textures the definition of ESU size is dependent on the orientation of macrozones in relation to an applied stress taking into account the deformation mode. In terms of CDF behaviour it is expected that the macrozone size may equate to the size of a 'diffuse' faceted region that may form under loading [132]. For an applied stress direction aligned with the macrozone flow, a CDF facet size may equate to ~100-150µm in accordance with the width of these macrozones. For an applied stress at 90º to the billet axis a planar facet may extend over distances exceeding 1000µm depending on the length of the macrozone. These features are likely to have a significant effect on CDF performance if stress redistribution events can occur on a local level between 'hard' and 'soft' grain orientations to initiate basal plane load normal facets from which 'diffuse' facets can then form through facet coalescence [61, 127, 131, 136].

6.3.4.2 Ti6242 disc

Ti6242 was examined in the form of compressor disc material in a bore location. As for work on Ti834, this assessment of crystallography was undertaken because of concerns

regarding macrozone and ESU sizes, particularly in material with optically acceptable microstructures. Woodfield et al. had previously demonstrated that large textured regions could exist in the alloy despite optical conformity [118]. Furthermore, the work in the previous section shows the presence of relatively large macrozone structures in Ti6242 billet, raising additional concerns about the potential for the retention of large macrozone structures through processing and into the final disc forging.

Sectioning of an axial-radial plane in the disc bore revealed a typical optical microstructure. No directionality was observed in primary alpha grain morphologies and secondary alpha lamellae grain sizes were ≤30µm with growth occurring in all directions. Typical optical microstructures are given in Figure 6-59. Primary alpha content is similar to that in Ti834 discs at 10-15% area fraction. The remaining microstructure consists of secondary alpha lamellae with ~1-2% area fraction of retained beta films.

To determine the macrozone size in the material an EBSD map was acquired over an area of ~1200µm by 1000µm. At this magnification, using a step size of ~4.8µm, relatively few beta phase points were indexed. Beta textures were therefore disregarded due to the potential inaccuracy of the data. Alpha phase pole figures show preferential orientations exist in the disc bore, although the observed texture intensities are low. These pole figures are displayed in Figure 6-60.

A tendency for basal poles to align with the disc axial direction is noted. There is also preferential alignment with the radial direction and in a radial distribution about the tangential axis. Different textures have been noted in other COMs, including alignment of basal poles with the tangential direction. These pole figures are therefore concluded not to be fully representative of the macro-texture of the disc bore.

Similar to Ti834 disc material, the macrozone size is observed to be only 2-3 neighbouring grains (or distances of less than 100µm). This is based on assessment of common texture length scales in several COMs. One example is the COMs displayed in Figure 6-61, corresponding to the pole figures in Figure 6-60. Another assessment has compiled COMs from six adjacent regions to give a map over an area of ~500µm width and ~600µm height. These COMs are shown in Figure 6-62.

In conclusion, the hot working and heat treatment operations involved in conversion of Ti6242 billet to the applicable disc geometry are sufficient to break down any large macrozones that may exist in the starting billet. This is the case in the bore section of the forging, which is likely to receive lower levels of deformation work on forging due to a lower reduction in axial height (according to finish forging geometry). Because there is an absence of substantial macrozones in the disc bore the macrozone size in diaphragm and rim regions should also be small (because of increased forging deformation levels).

As for textures in Ti834 disc, manual separation of primary and secondary alpha textures in Ti6242 disc has been undertaken for the COMs that form Figure 6-62. Example COMs showing the primary alpha textures and secondary alpha textures are displayed in Figure 6-63 and Figure 6-64 respectively. These results show a wide distribution of primary alpha textures and a similarly diverse range of secondary alpha textures. There is no evidence of the retention of macrozone textures from billet. These results and conclusions were consistent with those for the other acquired COMs.

Based on EBSD assessment both macrozone and ESU sizes of Ti6242 disc forgings appear to be less than 100µm (or several neighbouring grains). Although the inherent anisotropy of the HCP crystal structure may still allow stress redistribution to occur, the absence of large

macrozones or strong textures in the material are thought to mitigate the susceptibility of the disc alloy to pronounced CDF sensitivity in the (alpha + beta) processed condition.

6.3.5 Ti6246 disc material

Prior to the current studies, work investigating Ti6246 dwell fatigue behaviour in the alloy had concluded that no significant life debit exists under CDF loading [100, 164]. However, concerns were raised at a later date when large optical units were observed on etched rectilinear compressor disc forgings [155]. EBSD characterisation showed the potential presence of large units of crystallographic texture. These results led to an investigation covering variations in textures and CDF behaviour in production Ti6246 forgings. The work is covered in chapter four of this thesis. The work provided in this section of the thesis involves further characterisation of macrozone and ESU sizes in Ti6246 in different microstructural conditions.

6.3.5.1 Beta forged Ti6246 disc material

The microstructure of an axial-radial plane taken from the bore of a disc forging is displayed in Figure 6-65. The microstructure shows an alpha layer along a prior beta grain boundary with primary and secondary alpha platelets in the surrounding retained beta matrix.

An EBSD map of a neighbouring area of ~2800μm^2 was obtained with a map resolution of 256*192 pixels. Phase fractions were 80.0% alpha, 17.8% beta and 2.2% unindexed points. The COMs highlight the presence of the grain boundary and the influence of this boundary layer on platelet orientations near the boundary with variant selection on transformation. Beta phase COMs are displayed in Figure 6-66.

Based on other EBSD assessments (see chapter seven) the beta macrozone size can be in excess of 1mm across due to the presence of elongated prior beta grains with a preferred

deformation texture. However, other work (see chapters four and five) has indicated that common beta texture length-scales do not act as ESUs in terms of both cyclic fatigue and CDF loading behaviour. For Ti6246 in a beta forged, (alpha + beta) solution heat-treated and aged condition the ESU size is significantly lower (sub-100μm) and appears to be determined by the size of colonies of aligned primary alpha platelets. Other factors to consider in the ESU size behaviour include the dynamic recrystallisation fraction (varying with forging method) and the presence of a beta subgrain structure in some forgings.

Alpha COMs corresponding to the beta COMs in Figure 6-66 are displayed in Figure 6-67. These maps show 'clusters' of crystallographically aligned alpha platelets over localised areas (and hence volumes). Where these clusters are favourably orientated with respect to an applied stress their length-scales appear to determine the planar slip length (as shown in the following figures) and hence the ESU size. However, it also appears necessary to consider the extent of phase transformation on ageing, the nature of the secondary alpha platelet phase and their effects on the material behaviour.

Microstructural assessment has shown localised slip traces in ex-service Ti6246 material over several aligned primary alpha platelets [152, 181]. In laboratory test specimens slip bands have been observed running through platelet colonies growing from prior beta grain boundaries as in Figure 6-68. Slip bands are oriented at high angles to the optical platelet growth direction. This example shows slip bands intersecting primary alpha platelets, secondary alpha platelets and the retained beta matrix over a significant length scale.

Such slip features are relatively infrequently observed in the beta forged, (alpha + beta) SHT'd and aged Ti6246 microstructure. This suggests that either (a) engine operating conditions do not result in widespread plastic deformation over these length scales or (b)

plastic deformation is accommodated on a level not easily observed using SEM, e.g. as homogeneous deformation in the retained beta phase.

In the case of a CDF tested microstructure consisting primarily of equiaxed unrecrystallised beta grains with some smaller recrystallised (equiaxed) beta grains there is little evidence of plastic deformation in test specimens. No planar slip effects are noted in any feature of the microstructure. The ESU size is not clearly evident in this material and may be determined by the size of retained beta and/or secondary alpha platelet features. Typical microstructures in this material are shown in Figure 6-69 and Figure 6-70.

In other dwell fatigue test material, in this case with a large volume fraction of beta subgrain structures (recovery structures identified by optical boundaries with no grain boundary alpha precipitation), the ESU size appears to relate to the size of alpha colony structures. Figure 6-71 displays a typical microstructure from near the fracture surface of a CDF test specimen. No planar slip bands were observed near to the sample fracture surface. Instead plastic deformation was observed over volumes relating to primary alpha colonies, as in Figure 6-72. Closer examination of the secondary alpha platelet distribution showed no evidence of planar slip deformation on this length scale (see Figure 6-73).

Other Ti6246 material displaying beta grain sub-structures has been assessed following exposure to service conditions. As for test specimens there is an absence of planar slip deformation. In this case the behaviour may be related to both a low primary alpha platelet content (resulting in larger volumes of retained beta/secondary alpha platelets through which dislocation movement would have to occur) and potentially insufficient operating stresses for significant plastic deformation. This is despite the presence of a significant proportion of

aligned primary alpha colonies in the microstructure. A typical microstructure is displayed in Figure 6-74.

For standard Ti6246 material planar slip effects have been noted infrequently [69]. This is even the case for specimens subject to CDF tests at stresses in excess of 90% UTS. However, some specimens with premature failures under CDF loading have displayed planar slip deformation with significant shear offsets. Figure 6-75 shows parallel planar slip bands running across a primary alpha colony (N.B. this specimen was obtained from the same forging as the specimen showing large-scale planar slip in Figure 6-68). In both cases the slip traces exist in alpha platelet colonies growing from beta grain boundaries. On a macro-scale the beta grain structure was noted to be elongated with the grain flow angled at ~45º to the loading axis.

Close examination of the planar slip band shear offset in a different colony shows the optical boundary of the slip band occurs at a region where the primary alpha platelet spacing increases (see Figure 6-76). This indicates that the dislocation pile-up stresses that accumulate across the width of primary alpha platelets can have sufficient driving force to transmit across alpha/beta interfaces if the inter-platelet spacing is sufficiently low. However, as the alpha platelet spacing increases the slip activity is noted to cease. This can be related to the increased difficulty of planar slip behaviour across both the retained beta matrix and numerous secondary alpha platelet structures. Again planar slip bands do not appear to have formed at the secondary alpha platelet length scale, as shown in Figure 6-77 for a typical microstructure.

The premature failure of test specimens was attributed to sectioning with grain flow at ~45º to the specimen loading axis (refer to chapter four figure 4-31) [27, 60]. Examination of the

microstructure of test specimens again displayed infrequent evidence of planar slip deformation. A typical localised slip trace across a colony of closely spaced primary alpha platelets is shown in Figure 6-78. The microstructure is characterised by elongated prior beta grains with recrystallisation along the grain boundaries (Figure 6-79 and Figure 6-80).

Large planar slip bands are thought to form over primary alpha platelet colonies which have grown from prior beta grain boundaries where recrystallisation has not occurred. Whilst recrystallisation leads to the formation of equiaxed grains with platelet alignment the potential slip lengths are small due to the grain size. The planar slip lengths that can form in alpha colonies on prior beta grain boundaries are significantly larger. Where grain boundaries are angled to the loading axis premature failure is thought to result either due to grain boundary zone weaknesses or planar slip band separation [60].

In most Ti6246 microstructures containing primary alpha platelet colonies, colony optical growth directions are usually perpendicular to both prior beta grain flow and grain boundary direction. A typical example was given in Figure 6-68. In the case of recrystallised beta grains the alpha colony growth direction varies according to the orientation of the 'parent' grain boundary. However, in some Ti6246 forgings, unrecrystallised beta grains show the formation of alpha platelet colonies with their long axes parallel to the direction of grain flow. A typical example of the optical microstructure is given in Figure 6-81. Beta grains are elongated in the horizontal direction. In this microstructure it is possible to distinguish coarse primary alpha platelets and a finer primary alpha platelet phase. Both phases show common optical alignment of the platelets. At higher magnifications the secondary alpha platelet structure is observed to be Widmanstätten (see Figure 6-82).

EBSD analysis of these colony microstructures has been undertaken to establish their crystallography. In the first example, alpha phase COMs are given in Figure 6-83. These maps are taken from the area of the microstructure displayed in Figure 6-81. The prior beta grain displays a fibre texture with a (111) pole close to the compression axis. Analysis shows the coarse primary alpha platelet phase to have a single crystal orientation with the finer primary alpha platelet phase showing another orientation. The two major alpha variants that have been selected show a non-common basal plane, i.e. they have formed on different (110) planes. The reasons for the preferential selection of these two variants are unclear. The crystallography of the secondary alpha phase is unknown as it is unindexed at the magnification and step size selected for the map.

In a second example of a colony structure in a prior beta grain the beta texture consists of a {100} fibre approximately parallel to the compression axis. The COMs show that both the coarse and fine primary alpha platelet structures share a common crystallography. As for the first example, the c-axis of the platelets is close to the grain flow direction. The area of the microstructure that has been mapped is shown in Figure 6-84. The related alpha COMs are given in Figure 6-85. The map is still taken from an axial-radial plane although there is a 90º rotation such that the disc axial direction is horizontal.

Although these microstructures have not been assessed under CDF there is a possibility that these features will behave as the ESU under such loading conditions. Previous examples of planar slip deformation in Ti6246 material have been noted over primary alpha colonies where there are closely spaced alpha platelets, i.e. small retained beta/secondary alpha slip distances [69].

Due to the fact that easy slip occurs along the $<11\bar{2}0>$ direction of the HCP crystal structure and c-axes are near parallel to the direction of colony alignment, the ESU may be assumed to equate to the distance across a colony (i.e. the axial direction). Optically this has been observed to vary in length scale up to ~500µm. This may be a concern in compressor disc material as this would give some 'strong' alpha orientations with c-axes aligned with the direction of hoop stresses. However, for a CDF mechanism to operate (according to stress-redistribution theories) it would be necessary for surrounding weaker units to accumulate sufficient planar slip for an off-loading of stresses onto this strong unit with the resulting basal facet formation [136]. This is unlikely in unrecrystallised grains as a strong beta deformation texture will favour the selection of particular alpha variants leading to similar alpha colony orientations. Recrystallised grains may have beta orientations allowing the formation of alpha colonies at favourable misorientations for stress redistribution, although these grains are small in relation to unrecrystallised grains and the potential dislocation pile-up stresses are lower. It is therefore unlikely that there will be neighbouring combinations of 'weak' and 'strong' microstructural units leading to CDF susceptibility.

In summary it is likely that the ESU size of Ti6246 in a Widmanstätten primary alpha platelet, fine secondary alpha platelet and retained beta matrix microstructural condition is related to either the size of colonies of primary alpha platelets, the length-scales of secondary alpha platelets or the length-scales of retained beta matrix according to the applied stress and the presence of crystallographic structures with favourable orientations in relation to the applied stress. It is also noted from the investigations into CDF behaviour of the alloy (see chapters four and five) that the mechanism does not appear to occur. This is believed to be due to the homogeneous deformation behaviour of the retained beta phase and the resistance of the secondary alpha platelet structures to planar slip [152]. Where premature failures have

been observed under CDF loading they have been attributed to other causes such as grain flow effects.

6.3.5.2 Alpha-beta solution heat treated Ti6246

Standard Ti6246 material was obtained from a disc that displayed large optical structures on etch inspection. This disc was from the batch of forgings which showed large clusters resulting in the investigation into CDF behaviour of the alloy. CDF testing showed no significant life debit effect for this material. Further work was undertaken to heat treat the material to give different potentially more dwell susceptible microstructures.

One heat treatment involved solutioning the alloy in the (alpha + beta) phase field and water quenching, intended to remove secondary alpha platelets due to instability at higher temperatures. The secondary alpha platelet phase was observed to provide resistance to slip activity in Ti6246 in the standard microstructural condition (see the previous section). It was proposed that removing the secondary alpha phase may increase the effective slip length in the material. Primary alpha platelet structures remain in the microstructure at temperatures in the (alpha + beta) phase field. Water quenching ensures that only primary alpha platelets and retained beta matrix remain present in the microstructure at room temperature.

Because of the reduced planarity of beta phase slip deformation it was also necessary to reduce the retained beta content, to promote the planar slip deformation necessary for CDF behaviour [16, 136]. Beta content was reduced by cooling through the (alpha + beta) phase field to coarsen existing primary alpha platelets. Water quenching was from a temperature low enough to have allowed coarsening of the primary alpha platelets but high enough to have avoided secondary alpha platelet precipitation. The heat treatment was not observed to affect macro-texture and there was no beta recrystallisation.

The strength of the material was observed to drop substantially following the removal of secondary alpha precipitates. Consequently the test stresses were reduced to maintain fatigue data over a similar proportion of material UTS in comparison to standard Ti6246.

Examination of material following testing shows the presence of elongated prior beta grains with alpha platelet colony growth. The grain flow is parallel to the loading direction. Within prior beta grains typically there is a Widmanstätten distribution of primary alpha platelets although some regions of alpha platelet alignment are observed. Typical microstructures are displayed in Figure 6-86.

Despite the presence of aligned primary alpha colonies and the absence of secondary alpha platelets from the microstructure, planar slip traces are infrequently observed in sectioned test specimens. Slip lengths are limited to the length scales of closely spaced primary alpha platelets (as for Ti6246 in the standard microstructural condition). Planar slip behaviour is shown in Figure 6-87.

Although the planar slip band length was noted to be relatively low, the ESU length may increase for a loading axis angled at ~45º to grain flow, as was the case for the test specimen microstructure displayed in Figure 6-75. This is because the growth of alpha colonies approximately perpendicular to grain boundaries gives crystal orientations favourable for the activation of easy slip systems under loading. Whilst the applied stress was aligned with the prior beta grain flow, the ESU size was observed to be similar to that for most standard Ti6246 material. It may also be the case that the high retained beta content of the microstructure (relative to dwell sensitive alloys such as Ti685) prevents the formation of extensive planar slip band structures.

6.3.5.3 Beta annealed Ti6246

Standard Ti6246 disc material was held above beta transus for a significant time period to produce a large equiaxed beta grain microstructure with a randomised beta macro-texture. Slow cooling was applied to allow the growth of crystallographically aligned colonies from prior beta grain boundaries. The heat treatment was designed to produce large crystallographic units to determine the CDF sensitivity of the alloy [69, 84]. The heat treatment work is detailed in chapter four. In this section the crystallography and deformation behaviour of the material is assessed.

The typical microstructure after beta-annealing is displayed in Figure 6-88 and Figure 6-89. These images were obtained following CDF testing. They show both the large optical colony structures in the material and the presence of slip bands angled relative to the loading direction. Note that although material was obtained from a compressor disc forging, the hold at supra-transus temperature and consequent randomisation of the beta texture renders the loading direction insignificant in relation to the orientation of the disc axes.

EBSD maps corresponding to an area slightly larger than Figure 6-88 were obtained. The maps cover textures in four different prior beta grains. Beta COMs are given in Figure 6-90. Corresponding alpha phase maps are given in Figure 6-91. Large beta grains with a varied texture exist following the heat treatment. There are also large alpha colonies present, corresponding to the optical microstructures. This is the same as for beta processed Ti685 material which showed a correspondence of optical and crystallographic structures.

Closer examination of the crystallography of two optical colonies (within a prior beta grain) with significantly different growth directions shows two slightly misoriented alpha variants

exist. These colonies are highlighted in Figure 6-92. The corresponding pole figures show a common basal plane but a small rotation about the c-axis of the crystal structure.

Colony A and colony B represent two of the twelve potential Burgers orientation related alpha variants that could have transformed from the beta phase on cooling through the beta transus. They share a {0001} plane and therefore correspond to the two alpha variants that can form on a single {110} plane. The rotation of the c-axis between the two variants corresponds to the alignment of a $<11\bar{2}0>$ direction in the alpha phase with the two different <111> directions. This leads to a ~10º rotation of the alpha phase about the c-axis [139]. Neighbouring colonies with this crystallographic relationship were previously observed in beta SHT'd Ti685 material and are thought to potentially equate to the ESU size (i.e. planar slip length) in the material. This assessment was made based on the size of quasi-cleavage facet features in CDF loaded material.

Referring back to Figure 6-89 it is possible to observe parallel slip traces extending across colony A between optical colony boundaries. Analysis has indicated that this is prismatic slip deformation. At the boundary with colony B these slip traces are observed to end. The slip trace is believed to occur along the prism plane on an a_1/b_1 slip direction. In this direction $<11\bar{2}0>$ and <111> slip directions are aligned allowing slip transmission across the interfaces at lower stress levels [114]. The planar slip band does not continue into colony B. This is assumed to be because in colony B (according to the Burgers OR) there is a ~10-11º misorientation between the <111> slip direction and the easy $<11\bar{2}0>$ slip direction that is most closely orientated to this <111> direction. TEM work would be required to determine the nature of the slip system in colony A. An a_1/b_1 type relationship is expected as this requires the lowest CRSS for plastic deformation [114].

It is hypothesised that despite test stresses very close to UTS (>95%) the CRSS required for the transmission of dislocations across this misorientation in colony B is too high for continued planar slip. It is presumed that this leads to the pile-up of dislocations at the colony boundary. Potential explanations for the resistance to planar slip include the high retained beta content of the alloy and/or the effects of increased molybdenum concentrations around primary alpha platelets due to rejection from alpha phase precipitates on cooling [131].

It is unlikely that Ti6246 material in this microstructural condition will allow the transmission of dislocations across the boundaries of colonies along a_1 and a_2 type slip directions. Optical assessments have shown no evidence of planar slip transmission (i.e. shear offsets at alpha/beta interfaces) across colony boundaries. This provides an important indication that the ESU of this material is related to the optical colony size.

Other analyses of the COMs in Figure 6-90 and Figure 6-91 show two prior beta grains have a closely orientated {110} pole. As for previous work it is noted that the alpha colonies that grow from the boundary show variant selection to give {0001} planes in alignment with this shared {110} pole [117]. The prior beta grains labelled C and D on the COM have the shared {110} plane highlighted in pole figures in Figure 6-93. The alpha colonies E and F that form either side of the prior beta boundary show very similar crystal orientations as shown by pole figures (Figure 6-94) comparing the two colonies. As for earlier findings relating to Ti685 material, these observations again confirm the importance of {110} orientations in the selection of a particular variant for the grain boundary alpha layer, with the growth of alpha colonies with minimal orientation differences.

The common alpha colony crystallography across the grain boundary may have implications in terms of the ESU size of the material. However, for such behaviour to occur would require neighbouring colonies with favourable orientations (relative to the loading axis) for planar slip to traverse the colonies. No such behaviour has been observed in Ti6246 under CDF loading conditions.

6.3.6 Ti829 cold dwell fatigue test specimens

The optical microstructure of Ti829 is similar to that of Ti685. There are large equiaxed prior beta grains with a mixture of optical colonies and basketweave platelet structures. The typical optical microstructure is given in Figure 6-95. The alloy is heavily alpha stabilised resulting in a low retained beta fraction. Beta films in the microstructure are very fine and discontinuous (having broken down during ageing), as displayed in Figure 6-96.

With this microstructure there is a concern about the presence of large regions of crystallographic alignment as shown earlier (see section 6.3.1) for beta solutioned Ti685. CDF testing has confirmed the susceptibility of the alloy to sustained cyclic loads [182]. The low levels of retained beta phase may contribute to this behaviour. In the current work, large section LCF specimens involved in a CDF test programme were subject to fractographic and EBSD assessment. Cyclic fatigue specimen fracture surfaces showed no evidence of load normal facets. A typical LCF fracture surface is displayed in Figure 6-97.

Fractography shows the influence of the lamellar colony microstructure on the crack growth direction [90, 92]. Cracking in this test specimen appears to have initiated sub-surface (based on heavy gauge length plastic deformation) although the initiation site cannot be determined. Assuming sub-surface initiation has occurred, the absence of load normal facets can be attributed to the insufficient loading periods (one second) at peak stress. Without a dwell

period the build up and redistribution of stresses between neighbouring colonies is unable to occur [79, 136]. Facets are inclined with respect to the loading axis as a result of the influence of colony orientation [55, 165].

In comparison specimens subject to a two-minute dwell at peak stress showed multiple load normal facets on the fracture surface. The fracture surface of a specimen with ~10-15 facets up to ~1000μm in cross-section (with the facet plane within ~10º of loading direction normal) is shown in Figure 6-98.

A plane was sectioned from the fracture surface intersecting through three relatively large faceted regions of material. These facets were designated A, B and C (as labelled in Figure 6-98). The fracture surface in each of these locations is given in Figure 6-99 to Figure 6-101. In the lower magnification images the approximate direction of the plane of sectioning is displayed as a dashed line.

All three facets lie sub-surface. Each appears to have grown radially outwards from a central region. No defects such as porosity or inclusions could be observed at the initiation sites. Sectioning through the facets gave the fracture surface profile illustrated in Figure 6-102. All three facets are noted to lie at angles of ~85º to the loading axis. Also noted is sub-surface cracking (close to facet C) at a similar incline to the three surface facets. The microstructure of facet B is displayed in Figure 6-103 and Figure 6-104. This microstructure shows the presence of numerous optical colonies over the cross-section of the facet. EBSD mapping has confirmed that a number of crystallographic orientations exist through the facet. COMs for facet B are displayed in Figure 6-105. The variation in misorientations along the 2D plane through the facet is shown in the misorientation line scan in Figure 6-106. This shows that

the quasi-cleavage facet forms on a plane with significant orientation differences between neighbouring colonies.

The COMs in Figure 6-105 show significant variation in orientation through the facet. A central region of this section of the facet shows a colony with basal planes approximately normal to the loading direction. Based on the theory of Evans & Bache such a colony would act as a strongly orientated unit onto which weaker neighbouring units could off-load stresses [16, 136]. This would lead to the formation of a quasi-cleavage facet along a basal plane oriented at ~90º to the applied loading direction.

Up to this point it was recognised that the quasi-cleavage facet size would be determined by the extent of this 'hard unit' basal plane orientation. However, these EBSD maps suggest that for Ti829 alloy with a colony microstructure a quasi-cleavage facet may continue to grow through colonies with different crystal orientations, leading to facet sizes exceeding the crystallographic structural unit size (i.e. the macrozone size). This behaviour may be a function of the alloy chemistry (Ti829 is a relatively highly alpha stabilised, low beta stabilised composition with a low retained beta content) and the processing (SHT above beta transus) leading to an alloy with a propensity for planar slip and large macrozone and ESU sizes.

Because of the sectioning technique used the initiation site cannot be precisely determined from the COMs (due to limitations of mechanical polishing the cross-section plane is of an unknown position in relation to the facet origin). The approximate position of the line of sectioning is estimated to lie between the two dashed lines in Figure 6-107. This is based on the profile of the fracture surface in this image in relation to the cross-section profile (see Figure 6-102 and Figure 6-103). In particular there is a small 'lip' at the left edge of the facet that appears to correspond to the indicated region in Figure 6-107.

Referring back to Figure 6-100 the initiation site appears to be near to the centre of facet B (based on flow lines in the facet fracture surface). Given the cross-sectional size of the colony there is a substantial probability that the initiation site corresponds to this strong colony orientation. In this case the facet would then appear to have grown radially outwards from this position on a plane close to the load normal. Changes in crystal orientation do not appear to provide a sufficient obstacle to the formation of these quasi-cleavage facets over multiple colonies.

Facet C was also mapped to confirm the presence of multiple crystallographic orientations in a single facet. The facet microstructure is displayed in Figure 6-108. The COMs for facet C are displayed in Figure 6-109 (overlaid on pattern quality images). There is a distinct reduction in the indexed phase fraction of the map towards the left side of the images, due to microscope limitations in maintaining focus over the field of view. However, the crystallography of the length of the facet has been indexed satisfactorily.

As for facet B, multiple colonies with different crystallographies are present across the facet cross-section. Also, as for facet B, a colony with basal plane c-axes parallel to loading direction is present over a section of the facet. From the cross-section of the fracture surface it is not possible to deduce the position of the plane of sectioning relative to the facet. However, given the size of the facet and the size of the strong colony (over half the facet length) it is probable that this colony had some involvement in the initiation of the facet. It is believed this would occur through the stress-redistribution mechanism of Bache and Evans [16].

Although it is believed that the facets on the specimen fracture surface are the result of a stress redistribution mechanism there is no evidence of planar slip in 'weak' colonies in the

microstructure. The absence of planar slip bands in the microstructure is unexpected given the high alpha stabilisation of the alloy and the subsequent tendency for slip planarity [114]. Although beta films in the microstructure are often discontinuous it is still expected that planar slip would pass through beta films in some colonies. This would be observed in the form of shear offsets similar to those noted for Ti6246 planar slip bands. The absence of slip activity in the general microstructure may be explained by the relatively low test stress (~76% UTS) leading to the localisation of slip activity in the weakest colonies. The low stress may also offer an explanation for the presence of a large number of facets on the fracture surface [90].

Facet A was the largest facet observed on the specimen fracture surface. Given the varied crystallography in cross-sections of facets B and C and the reduced planarity of facet A (as viewed on cross-sectioning) it is considered probable that facet A contains a number of crystal orientations. This again suggests that the CDF facet size in Ti829 is not directly controlled by the size of the crystallographic unit as for the other titanium alloys assessed in this chapter.

The specimen of interest in this work showed a significant debit on fatigue life with the imposition of a two-minute dwell period. However, specimens tested at a higher peak stress (~84% UTS) showed both the formation of load normal facets and an increased debit on cyclic fatigue life. Further work should attempt to characterise the nature of the largest facets present on this test specimen (using serial sectioning) to determine the 3D facet crystallography (in particular examining for the presence of strong-weak colony orientation distributions near the facet initiation site).

6.4 Conclusions

The following conclusions can be taken from the work studying macrozone and effective structural unit size differences in the common titanium aerospace alloys:

- Ti685 shows significant variations in optical microstructure and macrozone size depending on the through-transus cooling rate. In slow-cooled large colony microstructures the macrozone size equates to the colony size and may be up to ~1000µm in cross-section. Macrozones are often equiaxed or low aspect ratio features. No strong beta deformation texture or alpha macro-texture are reported in the material.
- CDF facets in Ti685 are observed on non-load normal planes. Multiple facets are present on individual test specimens. Further work would be required to assess the ratio of load normal to non-load normal facets.
- Ti685 CDF facets that have been EBSD mapped show both conventional basal plane dwell fatigue facet crystal orientations and non-conventional prismatic facets close to the load normal direction.
- Multiple colonies and/or grains have been observed through the cross-section of two Ti685 CDF facets, highlighting the ability of facets to grow through optical boundaries provided there is not sufficient resistance due to crystal orientation mismatch. Sufficiently large misorientations (observed at facet boundaries) prevent further facet growth and lead to conventional crack propagation behaviour.
- Ti6/4 disc material has shown CDF behaviour under laboratory test conditions. EBSD analysis of the sub-surface texture of a test specimen has indicated failure due to the presence of a large region of commonly aligned basal texture with c-axes parallel to

the loading direction. This macrozone extended across both primary alpha grains and the transformed beta structure. The dimension of the macrozone across the specimen fracture surface was ~500-600µm whilst the facet extended over a distance of ~1250µm on the same plane. This indicates that facet growth may continue beyond the boundaries of the macrozone in Ti6/4 disc material.

- The macrozone size in Ti6/4 disc was found to be significantly greater than the optical microstructural unit size. This was attributed to the processing history of the disc and an inadequate level of forging strain to effectively remove textures present from earlier stages of disc processing. This conclusion was supported by the presence of regions of non-globularised primary alpha grains in other areas of the sub-surface microstructure.

- Ti834 disc material shows a varied alpha texture and macrozone dimensions of less than two or three neighbouring optical grain features (or ~100µm). These relatively randomised textures were observed in different discs and in different locations within discs. There is no evidence of the presence of strong textures or large macrozones retained from Ti834 billet material (characterised in other studies). Forging to typical finish geometries provides sufficient deformation to adequately break down billet textures.

- 6" diameter Ti6242 billet shows little change in alpha texture or macrozone size between billet centre and edge positions. The billet contains large macrozones elongated along the billet axis with typical aspect ratios of ~4:1. Macrozone dimensions of ~750-1000µm length and ~100-200µm width are observed.

- Ti6242 disc material shows small macrozones (<50μm) and relatively weak alpha textures. Observations are similar to those for Ti834 discs in terms of the breakdown of strong alpha textures and large macrozones on processing from billet to the finish forging geometry. In both cases the primary alpha grains showed random orientation distributions and there was limited evidence of variant selection in the transformed beta phase.

- (Alpha + beta) processed alloys Ti6/4, Ti834 and Ti6242 could be assessed using polarised light optical microscopy or SRAS techniques. This is based on the alpha phase anisotropy and the ability of each technique to detect an area of common texture greater in size than the optical microstructure, i.e. a macrozone.

- Conventional beta forged, (alpha + beta) solution heat-treated Ti6246 disc material shows localised colonies of aligned alpha platelets, which may be considered to represent the macrozone size. These colonies vary in size and shape according to the beta grain size and the post-forge cooling rate. Under CDF loading there are limited visible slip bands in the microstructure. Slip is observed over favourably oriented colonies (usually shear at angles ~45º to the loading direction), which have a low spacing between the primary alpha platelets and limited precipitation of secondary alpha platelets.

- The high retained beta content and the presence of a secondary alpha phase in Ti6246 disc material are believed to contribute to the reduction in the material ESU size. The reduced presence (or absence) of these features leads to an ESU size equivalent to the size of colonies of closely spaced alpha platelets. This is observed in both conventionally processed Ti6246 and in beta heat-treated large colony Ti6246.

- The ESU size in large colony Ti6246 material is thought to equate to the size of optical colonies. In the material studied these are large equiaxed colonies with dimensions typically >500µm. Despite the presence of neighbouring colonies (in a prior beta grain) with a shared basal plane there is no evidence of slip transmission across optical colony boundaries. This is unexpected given the very high applied test stresses, the length of slip bands and the resulting dislocation pile-up stresses at boundaries.
- Ti829 DLCF specimens show facet sizes (assumed ESU size) of ~500-1000µm. The microstructure consisted of smaller colonies than Ti685 disc. The macrozone size is estimated at <300µm from EBSD analysis. The presence of multiple colonies across the facet at significant misorientations with respect to one another leads to the conclusion that ESU size is 2-3x greater than macrozone size. From the analysis of two facets it is thought that a stress off-loading mechanism leads to the formation of a CDF facet through a strongly oriented colony. The alloy then allows the growth of the facet along a plane across colony boundaries despite the presence of significant crystal misorientations along this plane.

In summary the typical macrozone and facet sizes that have been observed in the titanium alloys are provided in Table 6-2. ESU sizes are inferred from facet sizes. From this table it appears that in most cases the facet size is equal to or greater than the macrozone size. This may be attributed to the continuation of the facet cracking plane beyond the boundaries of regions of common crystallographic texture.

6B Characterisation of macrozone and effective structural unit sizes in titanium alloys – Figures and tables

6.5 Introduction

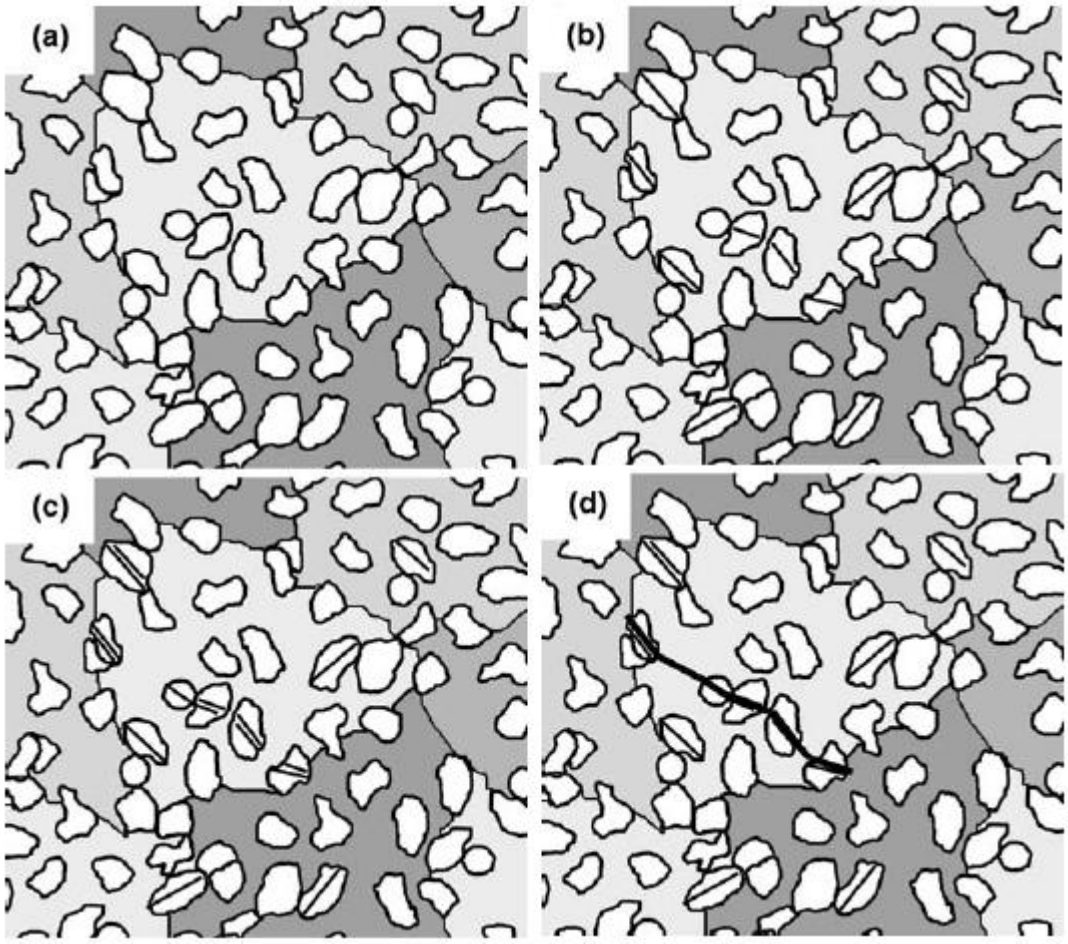

Figure 6-1 – Schematic of the crack initiation process in bimodal microstructures; (b) slip band formation in primary alpha grains, (c) primary alpha grain slip band intensification and crack formation, (d) crack coalescence across transformed beta matrix [61]

6.6 Experimental procedure

Table 6-1 – Material sources and processing history

Material	Source	Condition
Ti685 disc material	Compressor disc bore material	Standard Ti685 microstructure. Beta solution heat treated and aged
Ti685 DLCF specimens	Fan disc material	Standard Ti685 microstructure. Beta solution heat treated and aged
Ti6/4 DLCF specimens	Fan disc material	Standard Ti6/4 microstructure, (alpha + beta) solution heat treated and aged
Ti834 disc	Compressor disc bore and rim material (Forger 'A')	Standard Ti834 microstructure, (alpha + beta) solution heat treated, aged
Ti834 disc	Compressor disc bore material (Forger 'B')	Standard Ti834 microstructure, (alpha + beta) solution heat treated, aged
Ti6242 billet	Timet 6" billet	Standard Ti6242 billet microstructure
Beta forged Ti6246 disc	Compressor disc bore material	Standard Ti6246 microstructure. Beta forged, (alpha + beta) solution heat treated and aged
(Alpha + beta) solution heat treated Ti6246	Compressor disc bore material	Standard Ti6246 material, resolutioned in the (alpha + beta) phase field and water quenched
Beta annealed Ti6246	Compressor disc bore material	Standard Ti6246 material, resolutioned in the beta phase field and slow cooled (i.e. beta annealed)
Ti6242 disc	Compressor disc bore	Standard Ti6242 microstructure, (alpha + beta) solution heat treated, aged
Ti829 cold dwell fatigue specimens	Low pressure turbine disc material	Standard Ti829 microstructure, beta solution heat treated and aged

6.7 Results

6.7.1 Ti685 disc material and test specimens

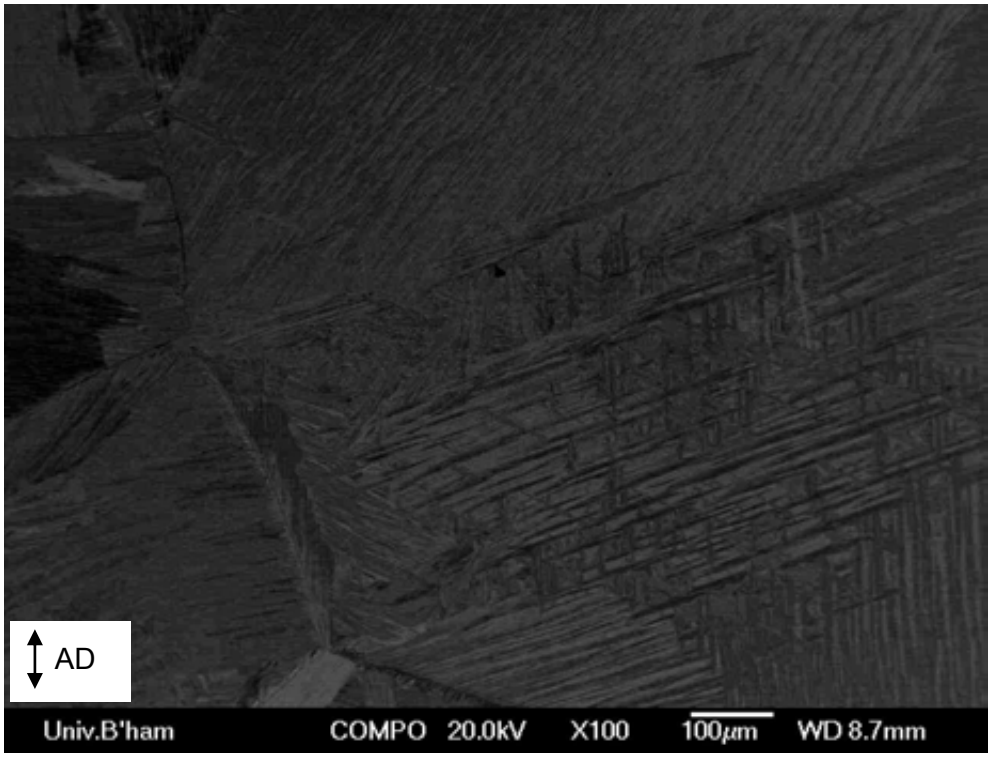

Figure 6-2 – BSE imaging microstructure of beta solution heat treated Ti685

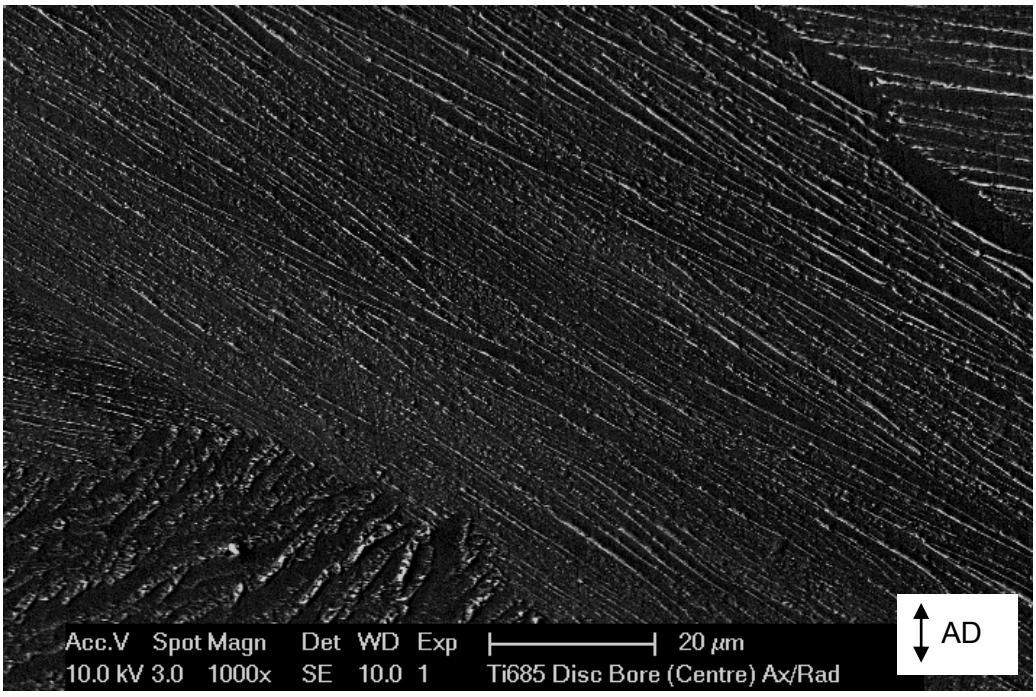

Figure 6-3 – SEI microstructure of beta solution heat treated Ti685

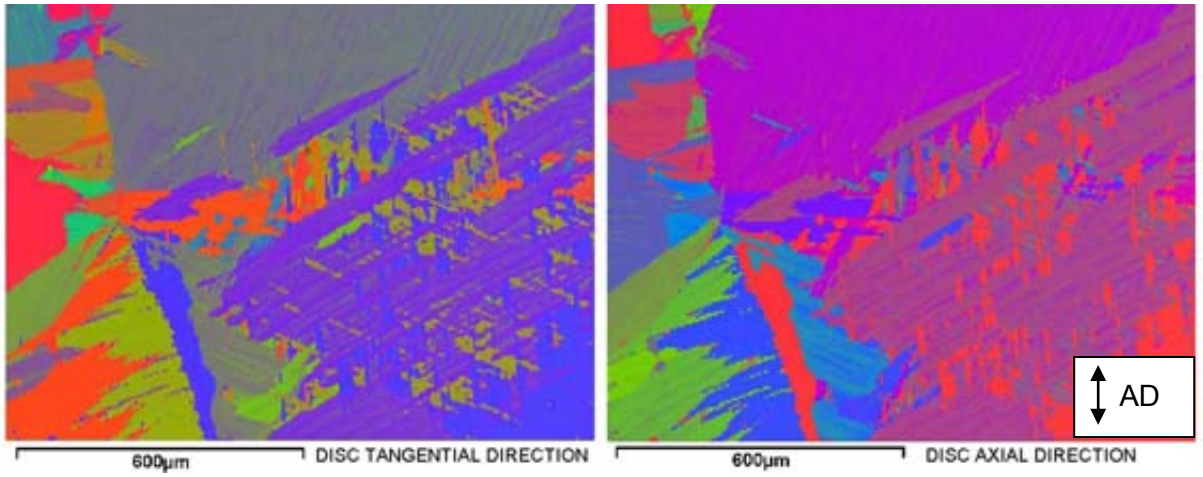

Figure 6-4 – Alpha crystal orientation maps (COMs) for Ti685 disc bore. Textures displayed w.r.t. tangential and axial disc directions

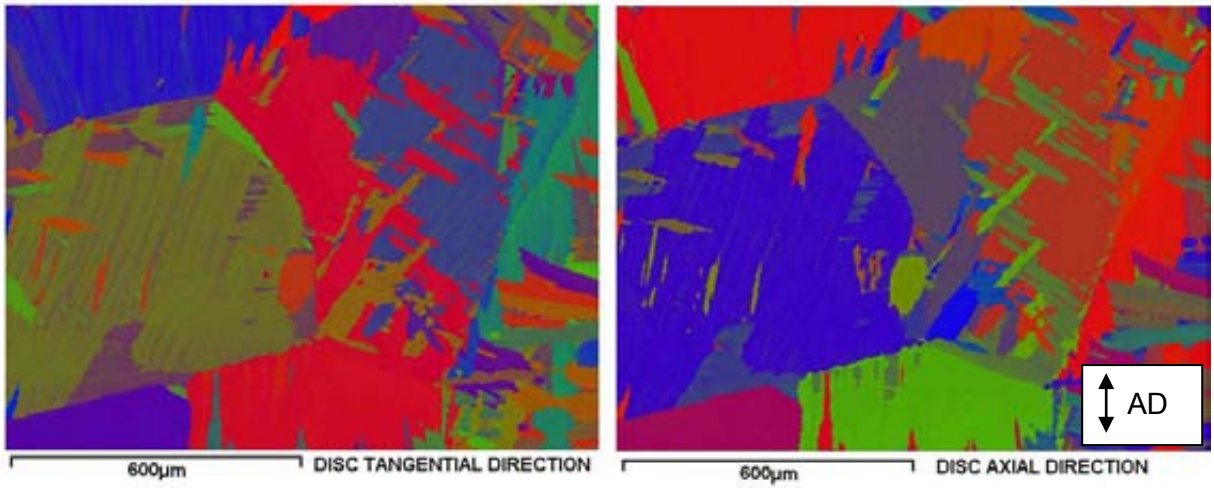

Figure 6-5 – Alpha COMs for Ti685 disc bore material

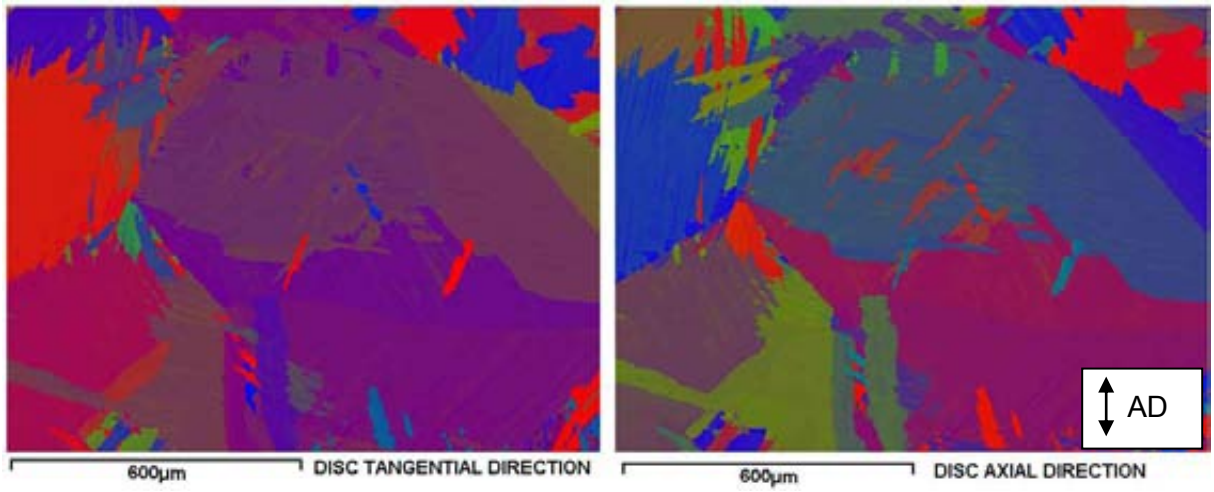

Figure 6-6 – Alpha COMs for Ti685 disc bore material

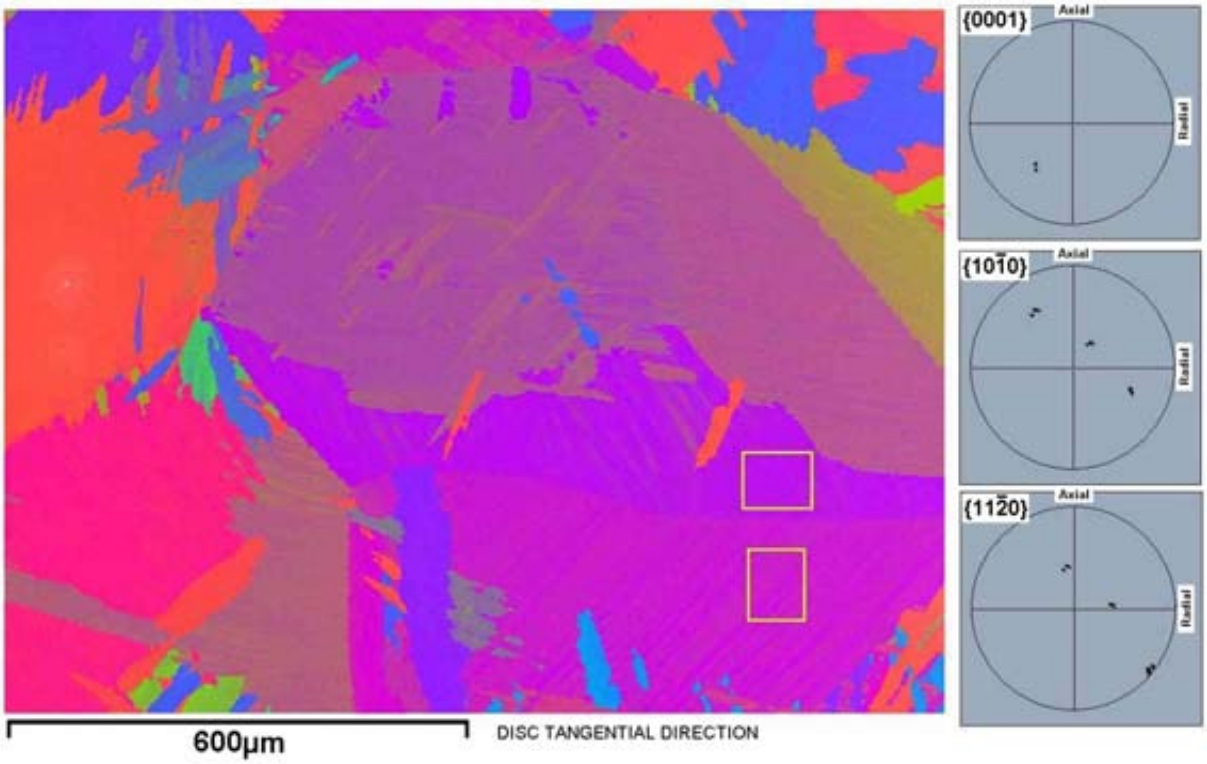

Figure 6-7 – Selected area alpha colonies and corresponding pole figures

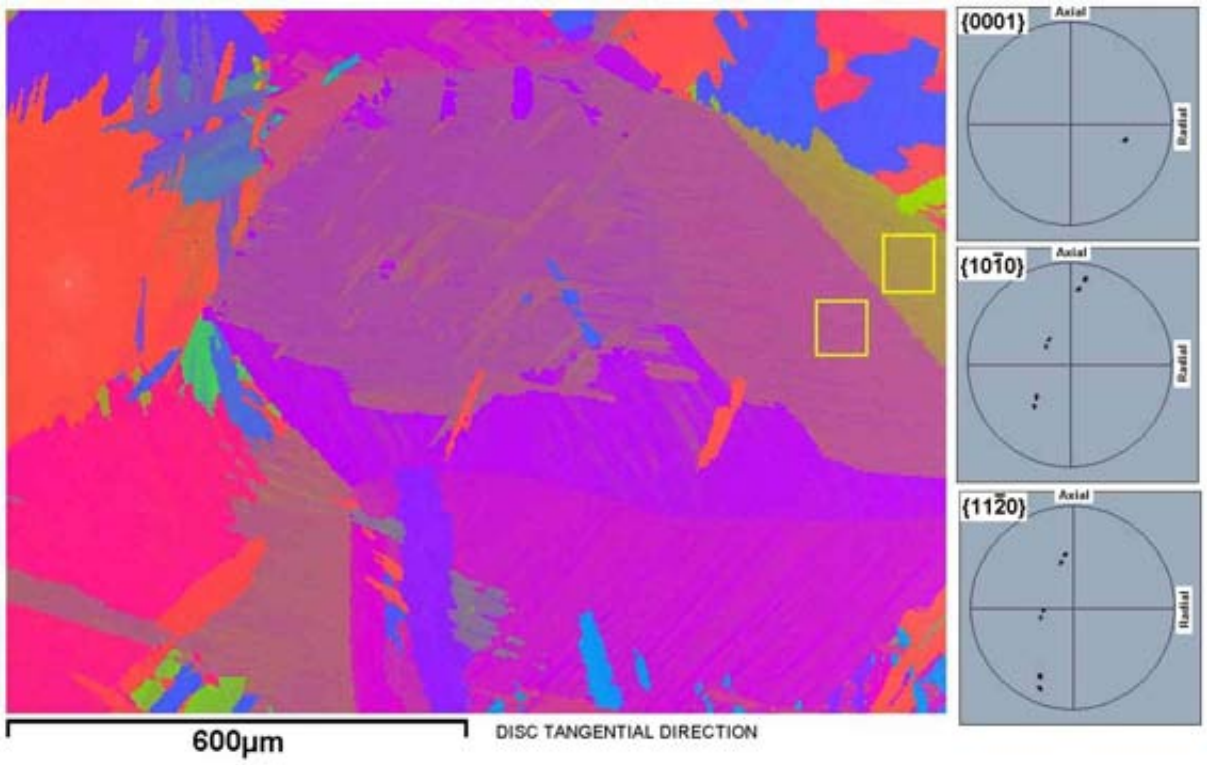

Figure 6-8 – Selected area alpha colonies and corresponding pole figures

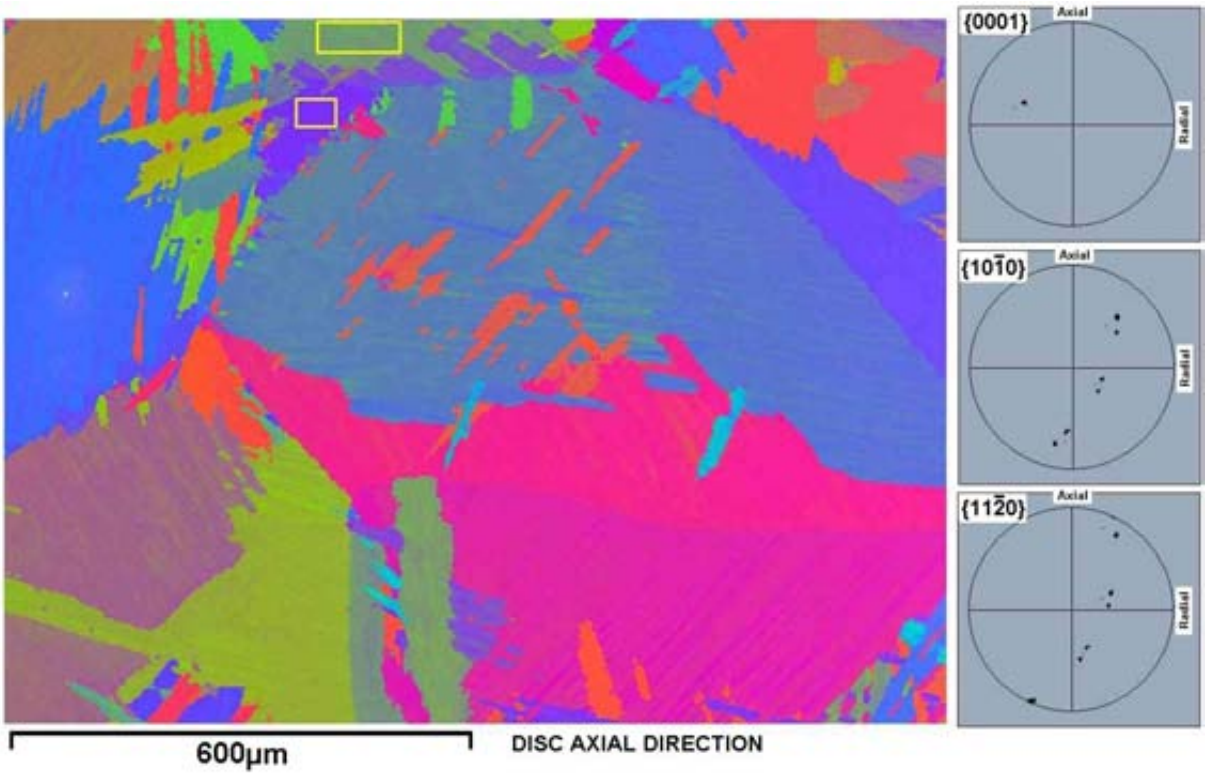

Figure 6-9 – Selected area alpha colonies and corresponding pole figures

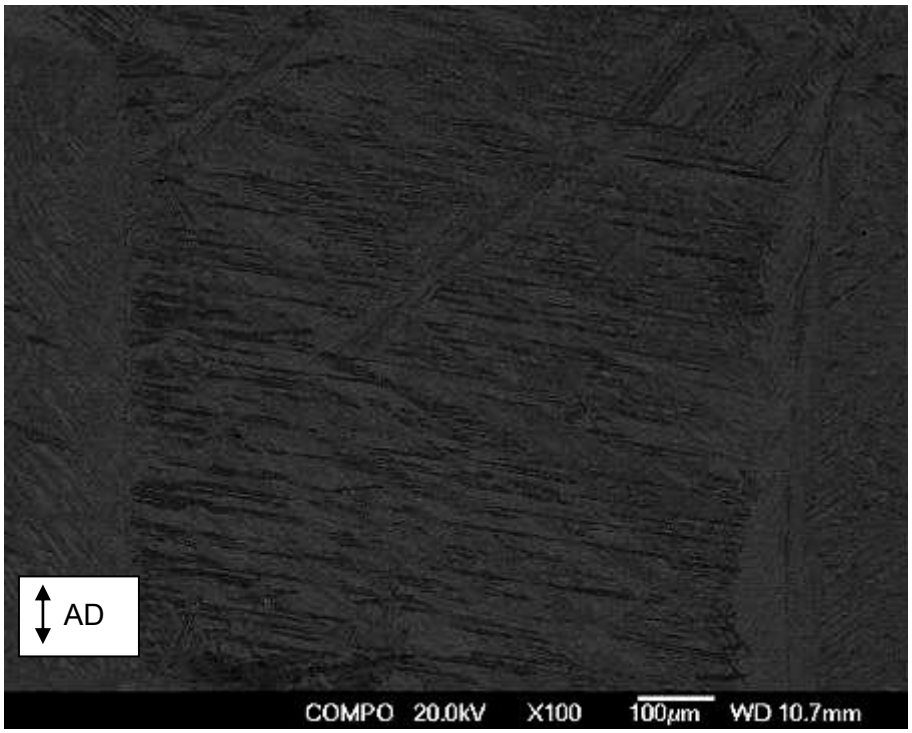

Figure 6-10 – BSE imaging microstructure of Ti685 disc bore edge

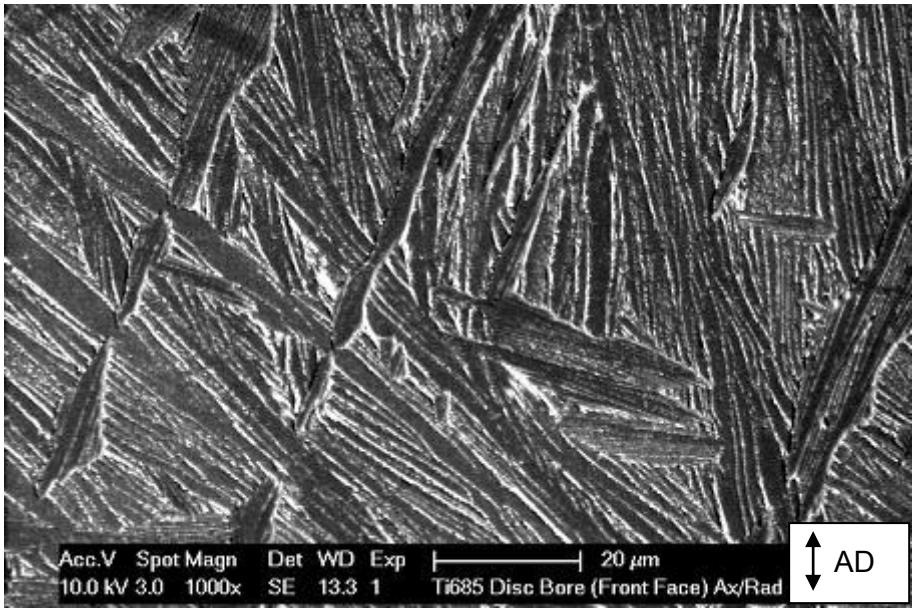

Figure 6-11 – SEI microstructure of Ti685 disc bore edge

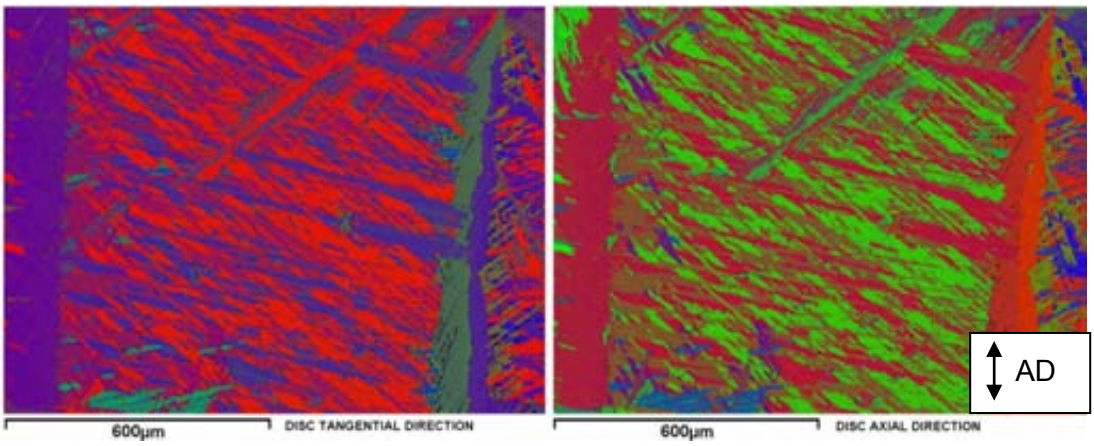

Figure 6-12 – Alpha phase COMs for Ti685 disc bore edge

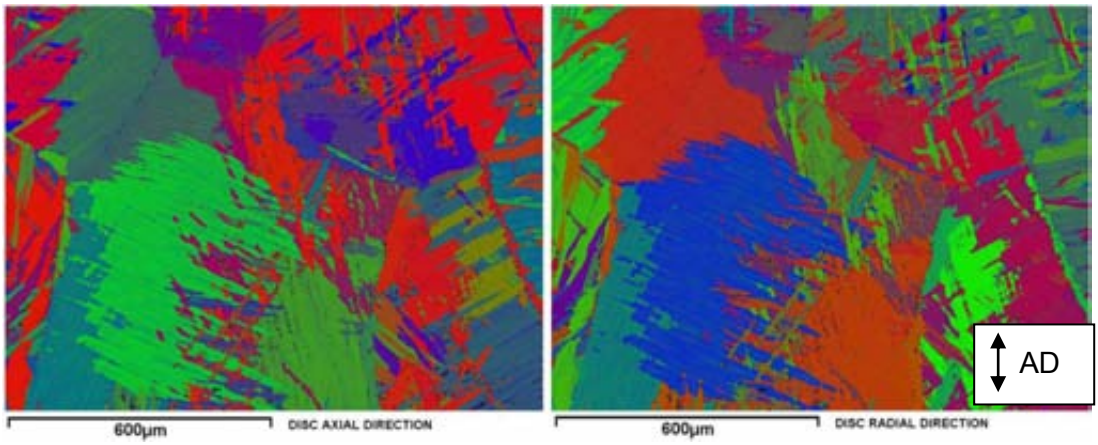

Figure 6-13 – Alpha phase COMs for Ti685 disc bore edge

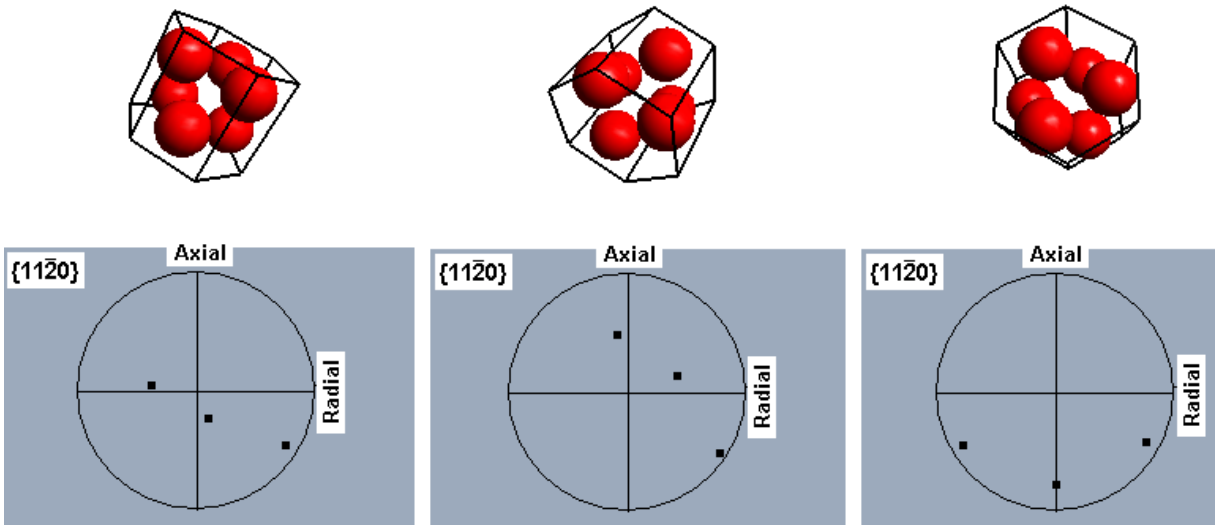

Figure 6-14 – Pole figure comparison of common {$11\bar{2}0$} plane for different basketweave alpha platelet variants

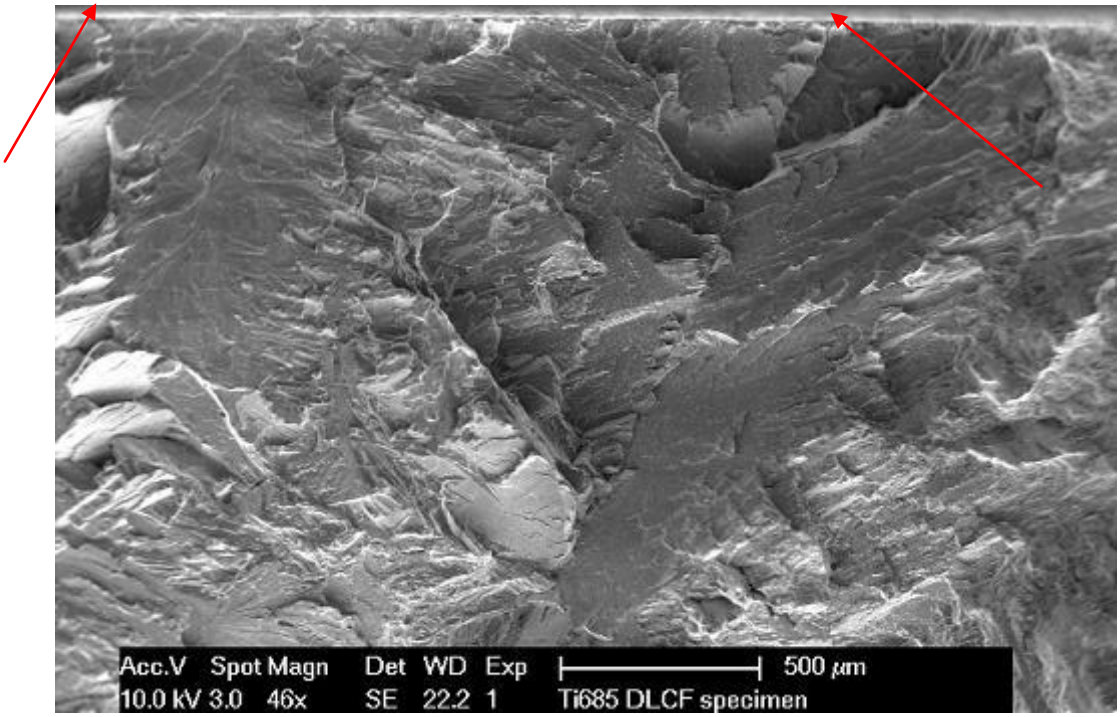

Figure 6-15 – Ti685 cold dwell fatigue specimen with multiple fracture surface facets. Facet A fractography at the sectioned surface (Loading axis is normal direction)

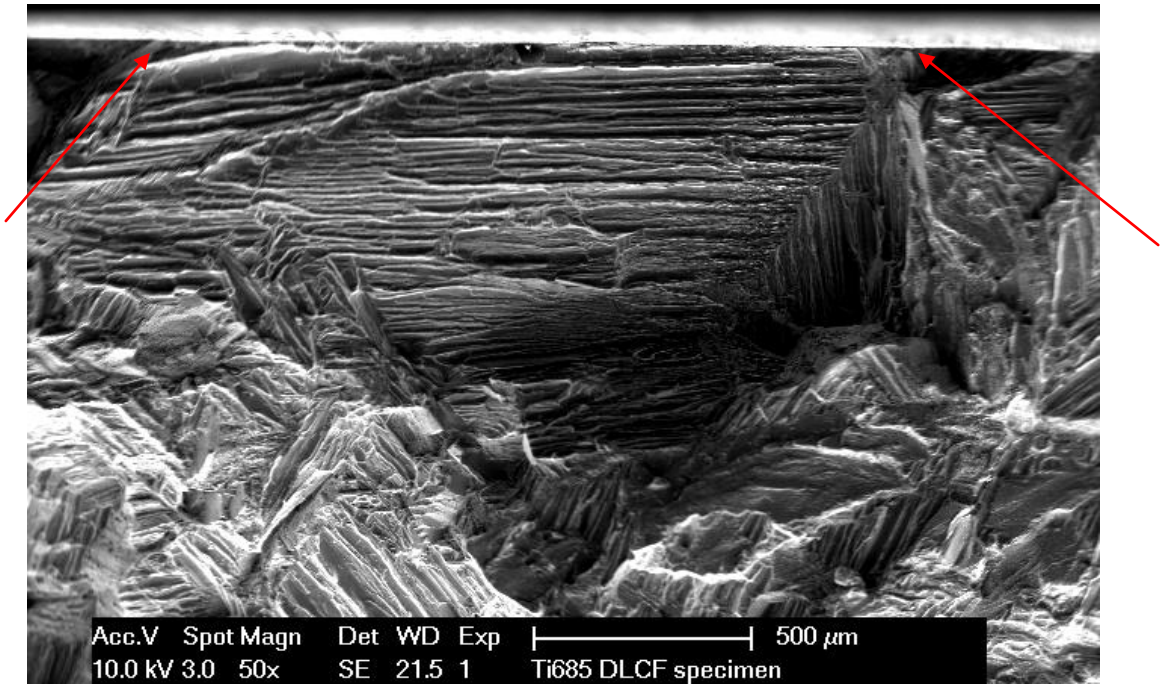

Figure 6-16 – Ti685 cold dwell fatigue specimen with multiple fracture surface facets. Facet B fractography at the section surface (Loading axis is the normal direction)

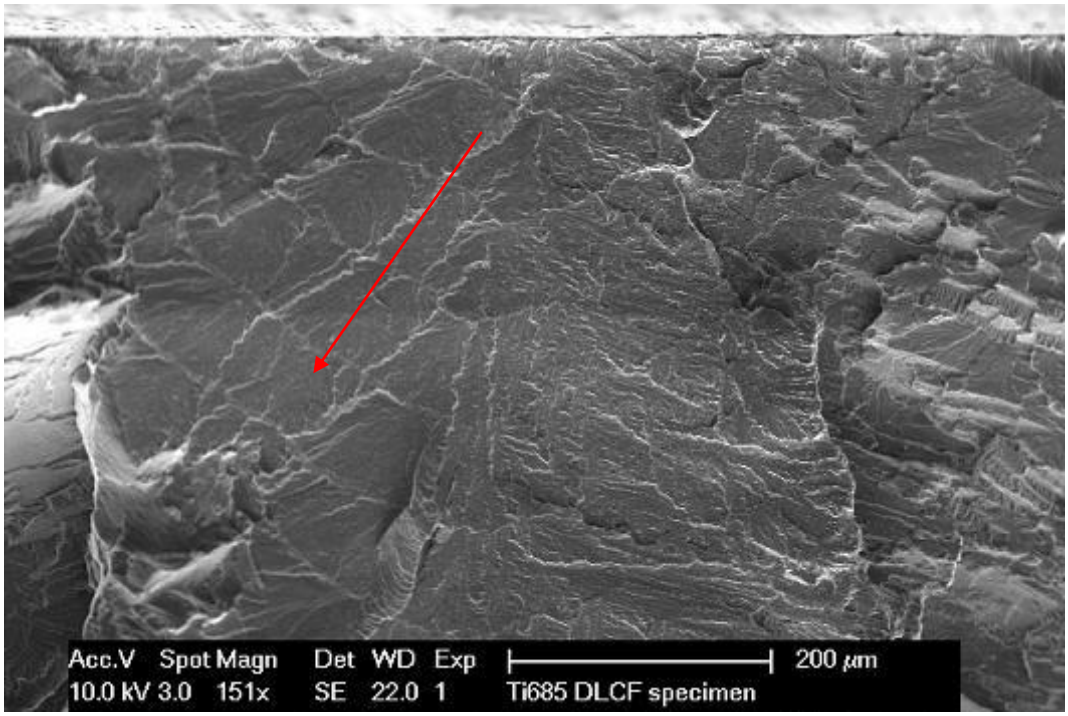

Figure 6-17 – Ti685 cold dwell fatigue specimen. Quasi-cleavage crack growth of facet A (Loading axis is the normal direction)

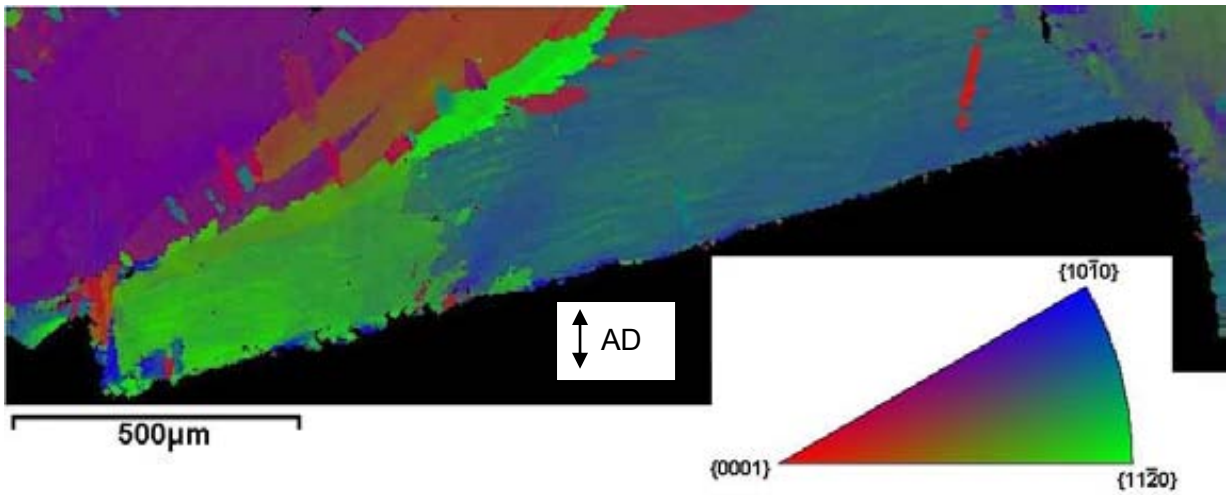

Figure 6-18 – Ti685 cold dwell fatigue specimen. Facet A crystallography (Orientations w.r.t. direction parallel to loading axis AD)

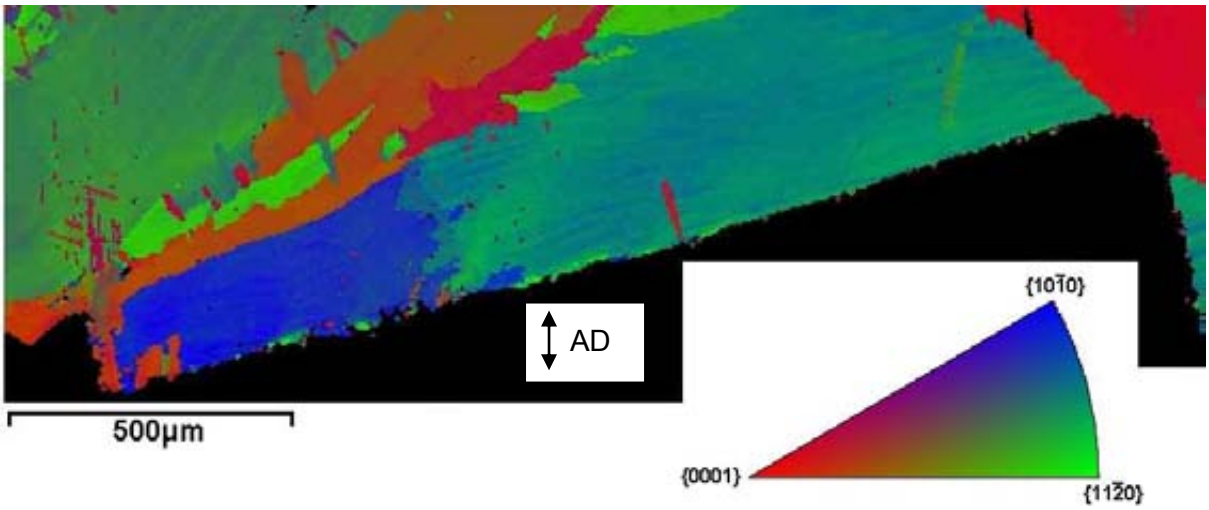

Figure 6-19 – Ti685 cold dwell fatigue specimen. Facet A crystallography (Orientations w.r.t. arbitrary direction normal to loading axis)

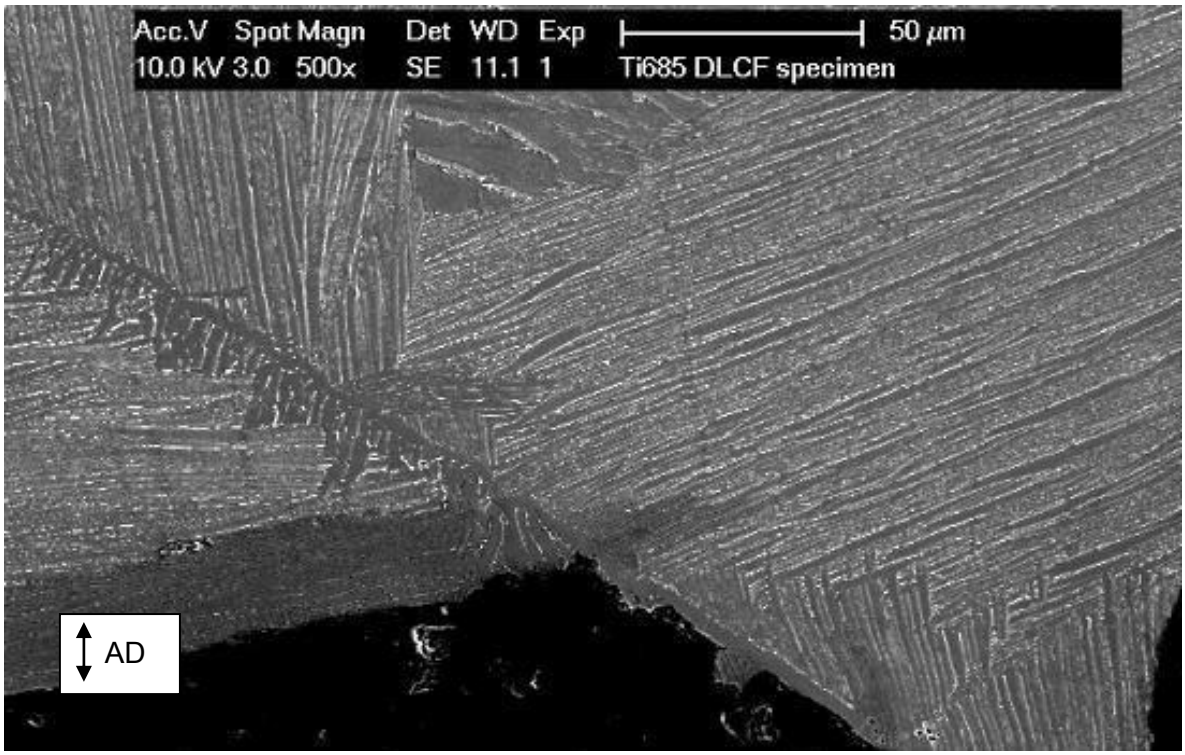

Figure 6-20 – Grain boundary at facet A edge location

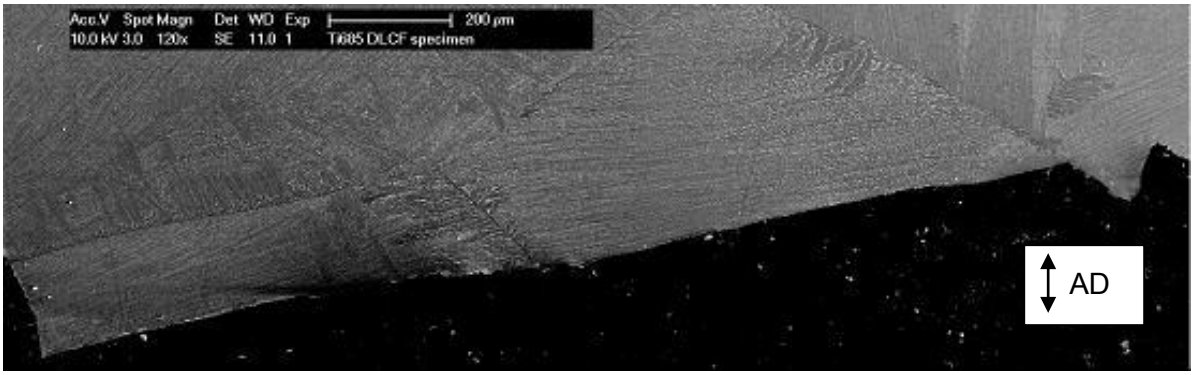

Figure 6-21 – Facet A microstructure

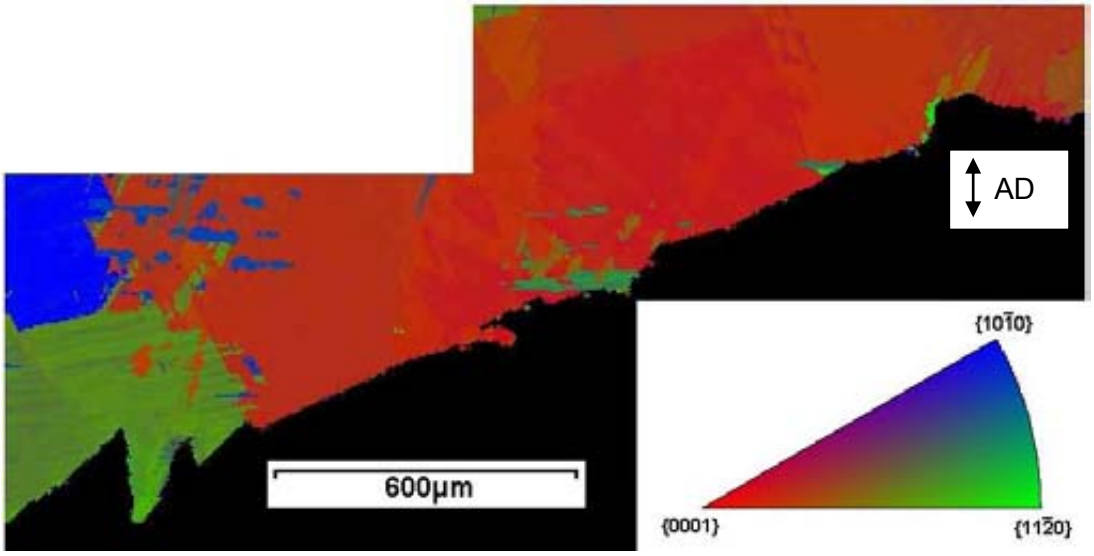

Figure 6-22 – Ti685 cold dwell fatigue specimen. Facet B crystallography (Orientations w.r.t. direction parallel to loading axis)

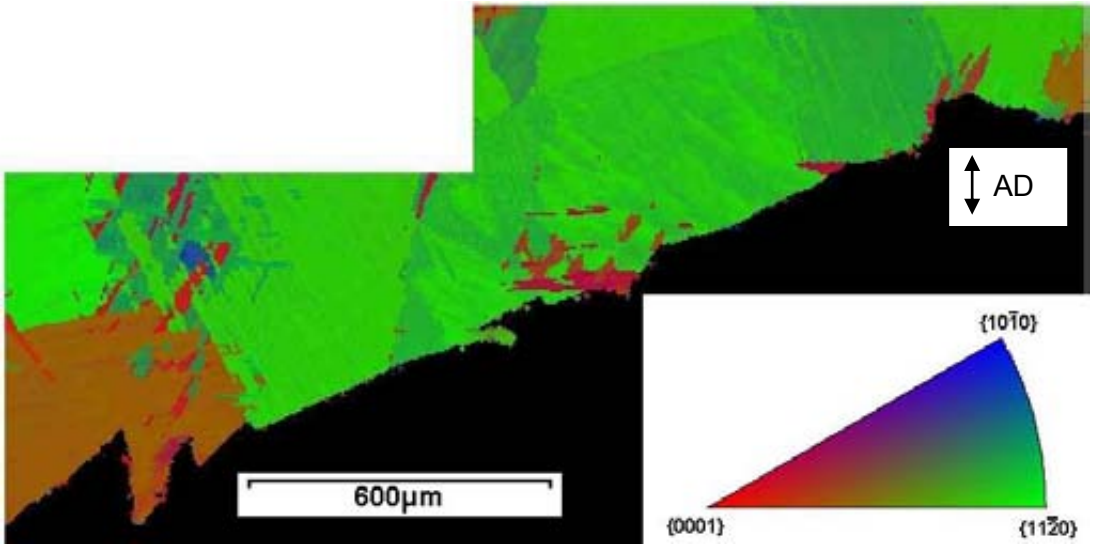

Figure 6-23 – Ti685 cold dwell fatigue specimen. Facet B crystallography (Orientations w.r.t. arbitrary direction normal to loading axis)

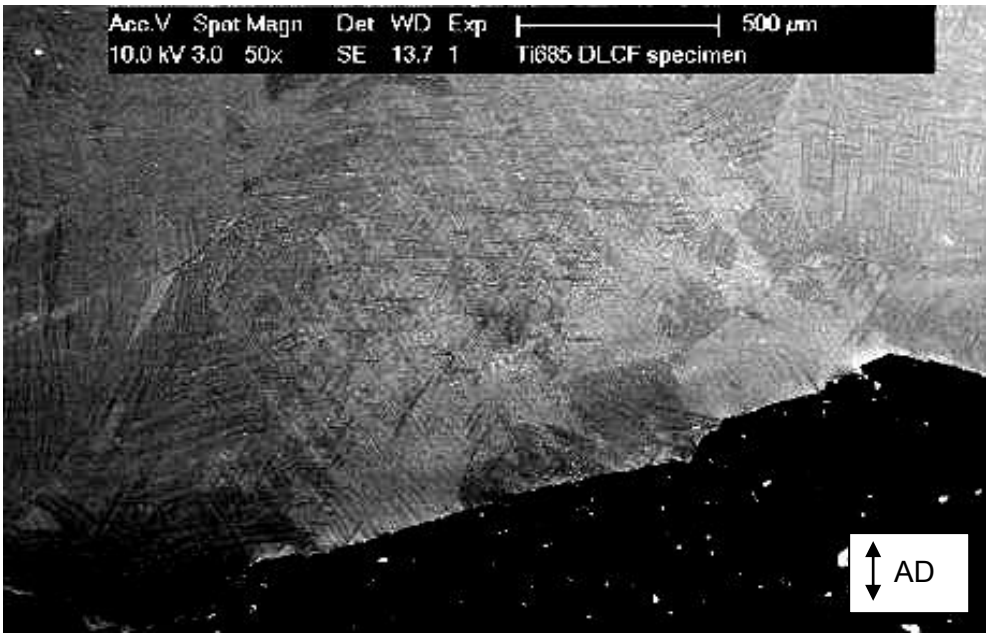

Figure 6-24 – Facet B microstructure

6.7.2 Ti-6Al-4V DLCF test specimen

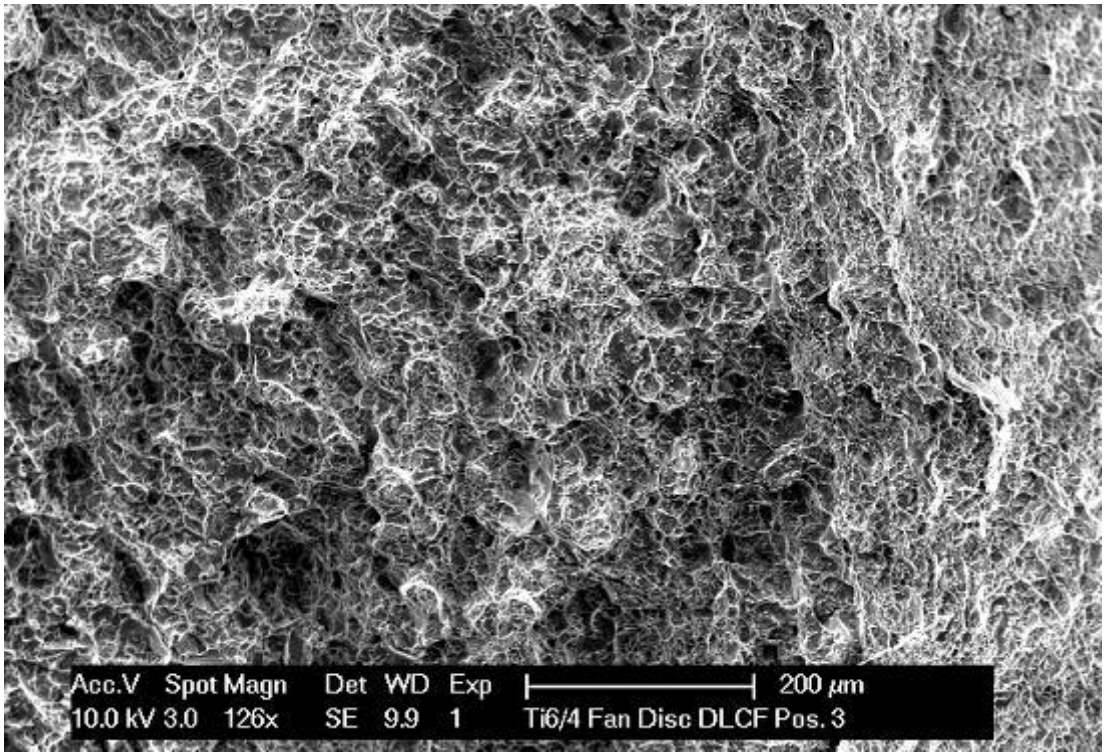

Figure 6-25 – Ductile failure region of Ti6/4 DLCF test specimen

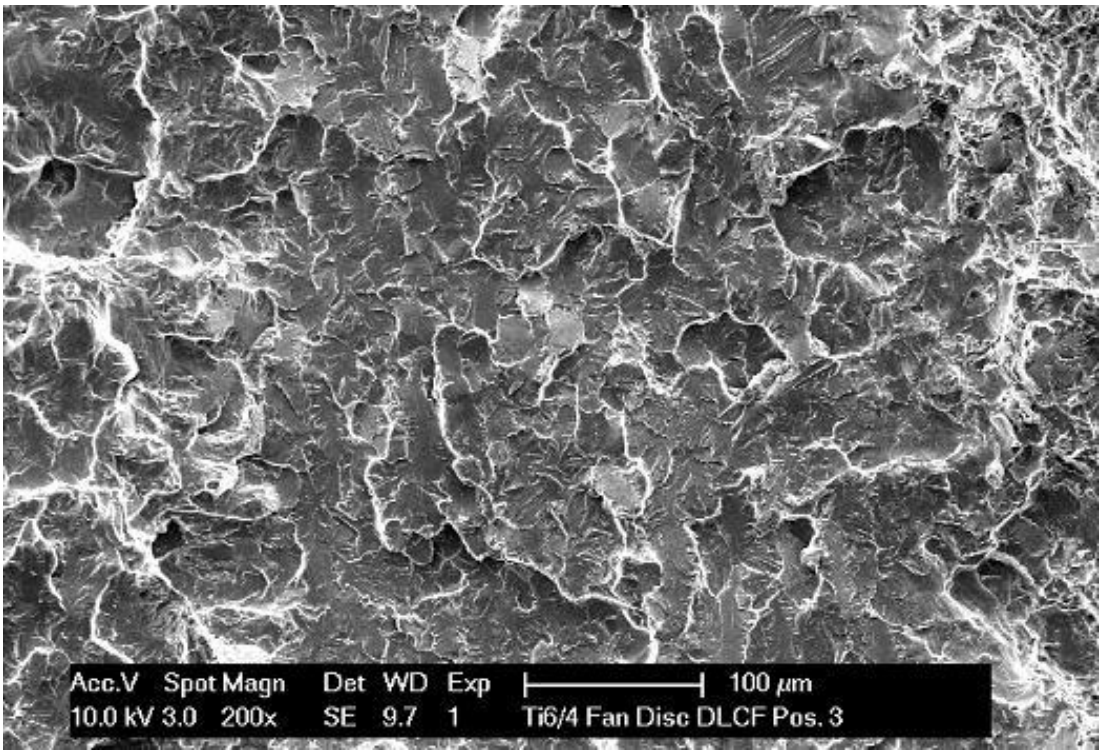

Figure 6-26 – Quasi-cleavage faceted region of Ti6/4 DLCF specimen

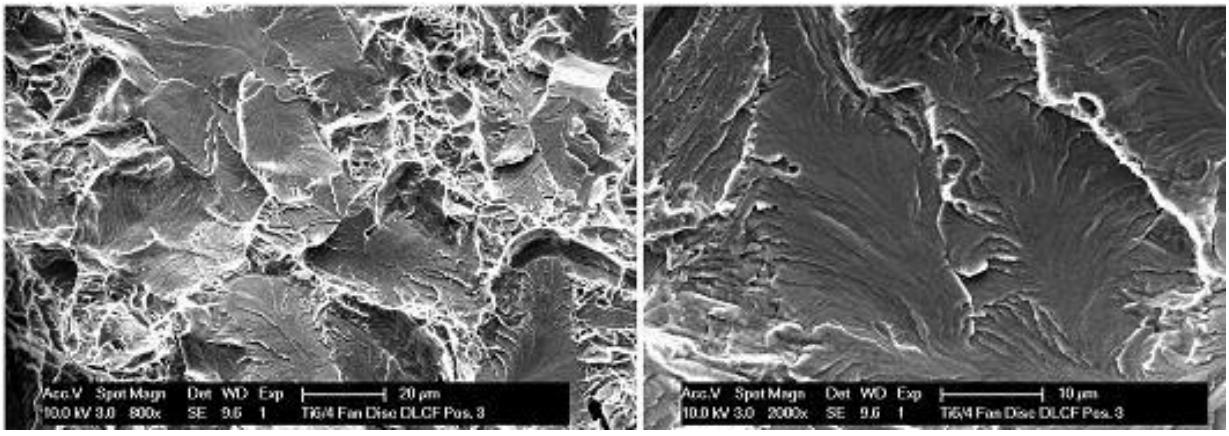

Figure 6-27 – Fractography of faceted region of Ti6/4 DLCF specimen

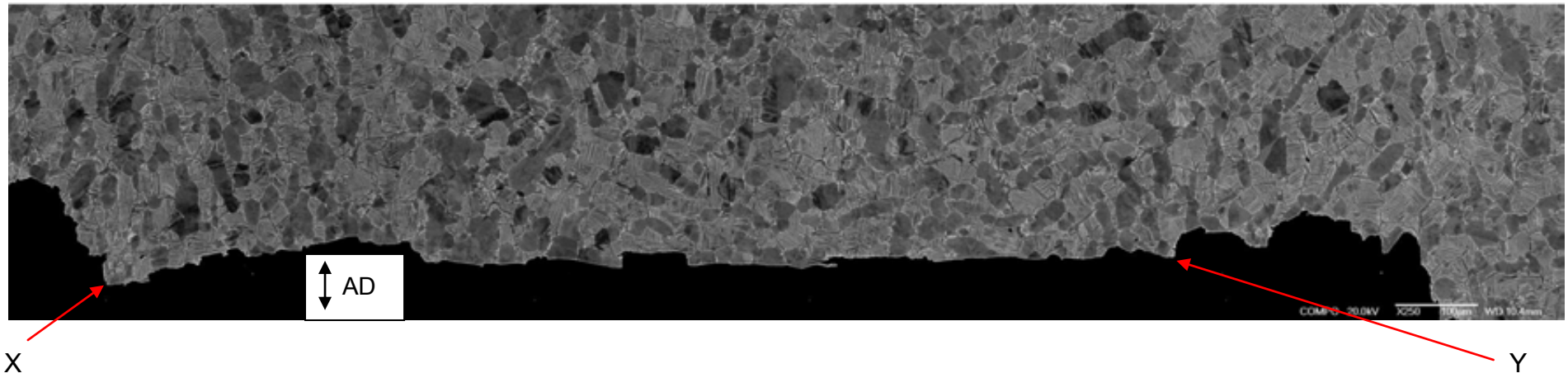

Figure 6-28 – BSE image of microstructure through the faceted region of the Ti6/4 DLCF specimen (AD direction is the loading axis)

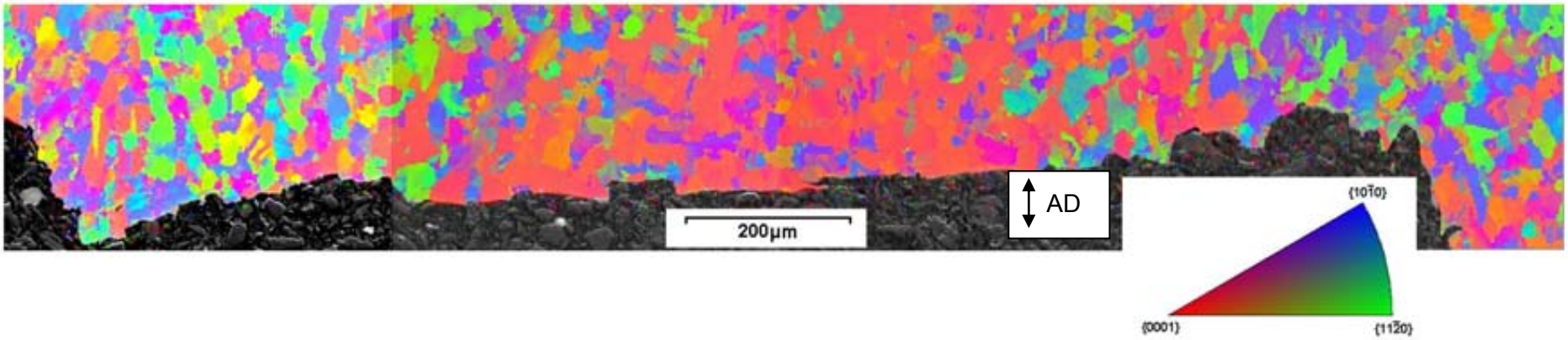

Figure 6-29 – Alpha phase COM of Ti6/4 facet cross-section. Textures are displayed w.r.t. axial loading direction (AD)

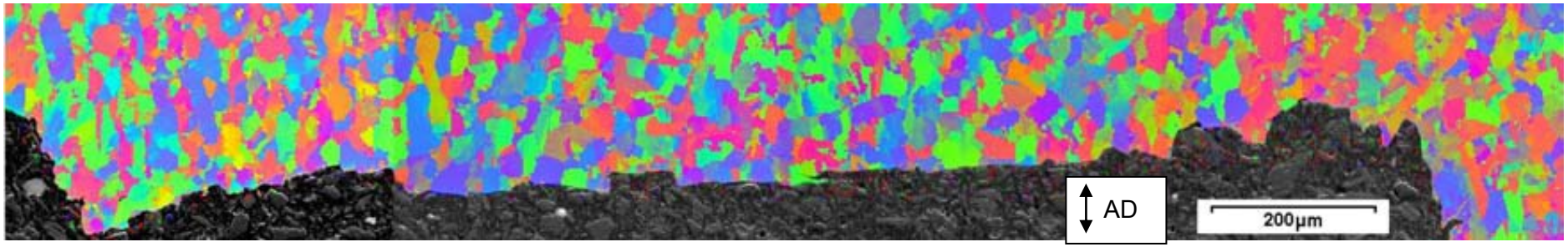

Figure 6-30 – Alpha COM of Ti6/4 facet cross-section. Textures are displayed w.r.t. direction normal to the loading axis

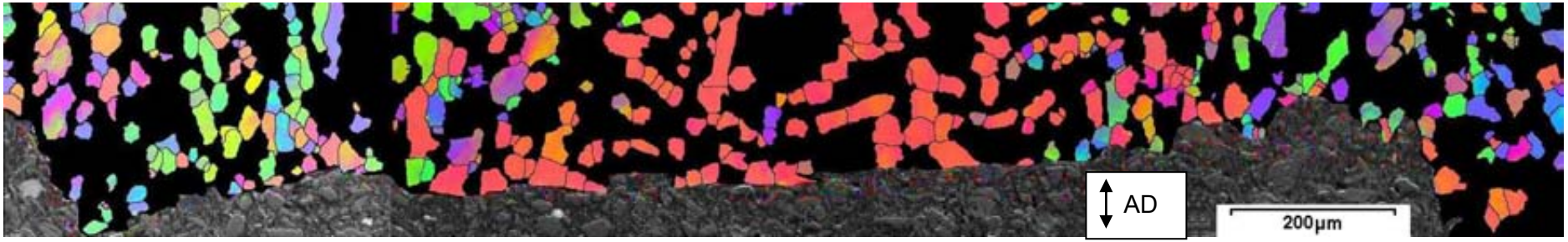

Figure 6-31 – COM of Ti6/4 primary alpha grain textures. Textures are displayed w.r.t. axial loading direction (Primary alpha grain textures manually separated based on BSE image contrast)

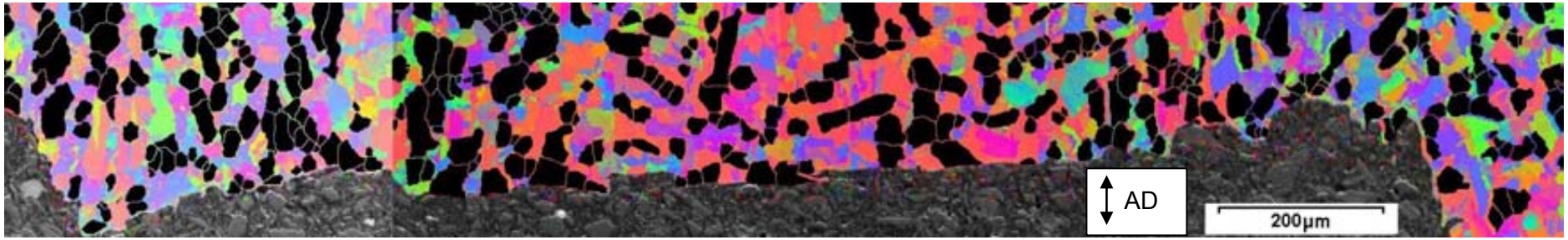

Figure 6-32 – COM of Ti6/4 secondary alpha grains textures. Textures are displayed w.r.t. axial loading direction (Secondary alpha textures manually separated based on BSE image contrast)

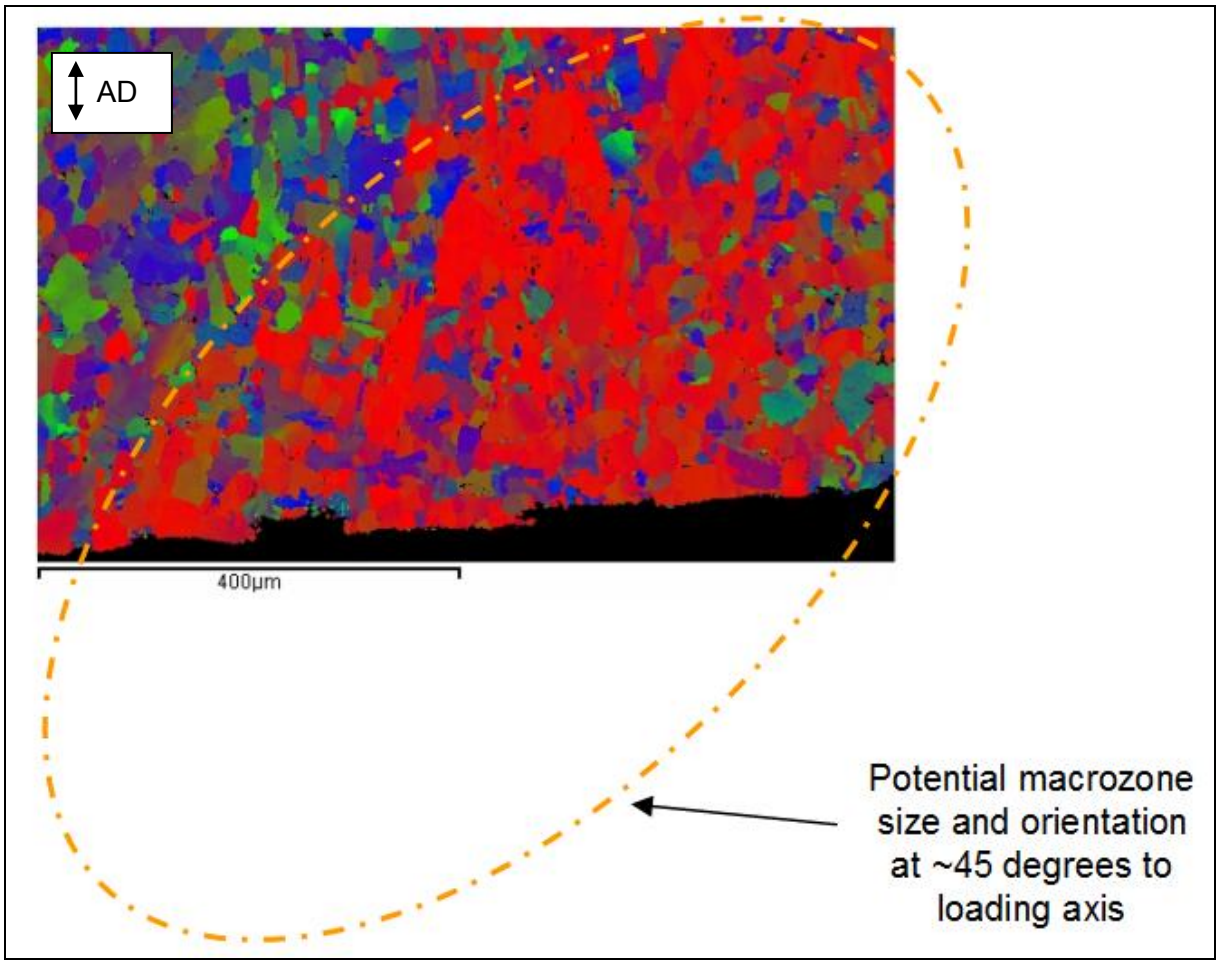

Figure 6-33 – Alpha phase COM displaying textures of Ti6/4 facet w.r.t. loading direction, with outline of potential macrozone shape and orientation

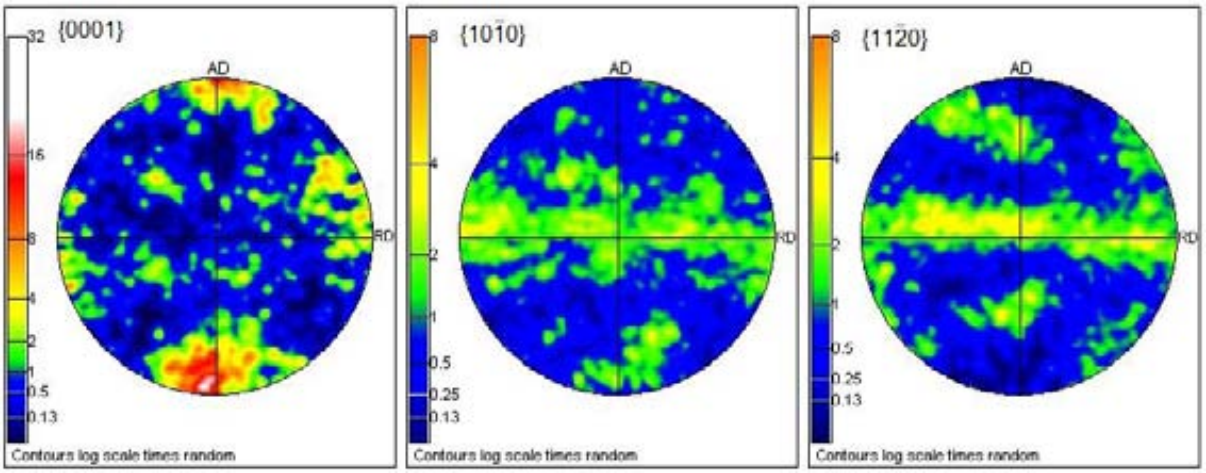

Figure 6-34 – Alpha phase pole figures for strongly faceted region of Ti6/4 DLCF specimen showing texture w.r.t. loading axis

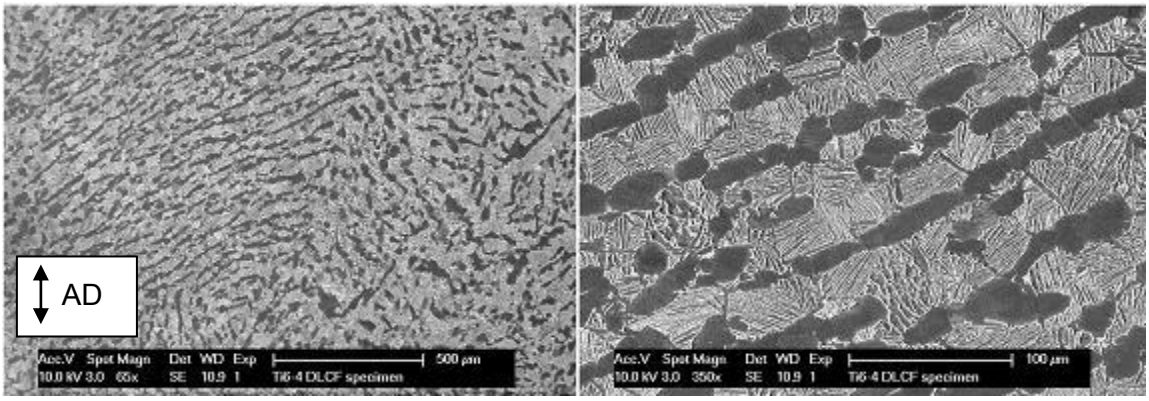

Figure 6-35 – Ti6/4 microstructure indicative of low forging deformation and incomplete breakdown of prior alpha textures

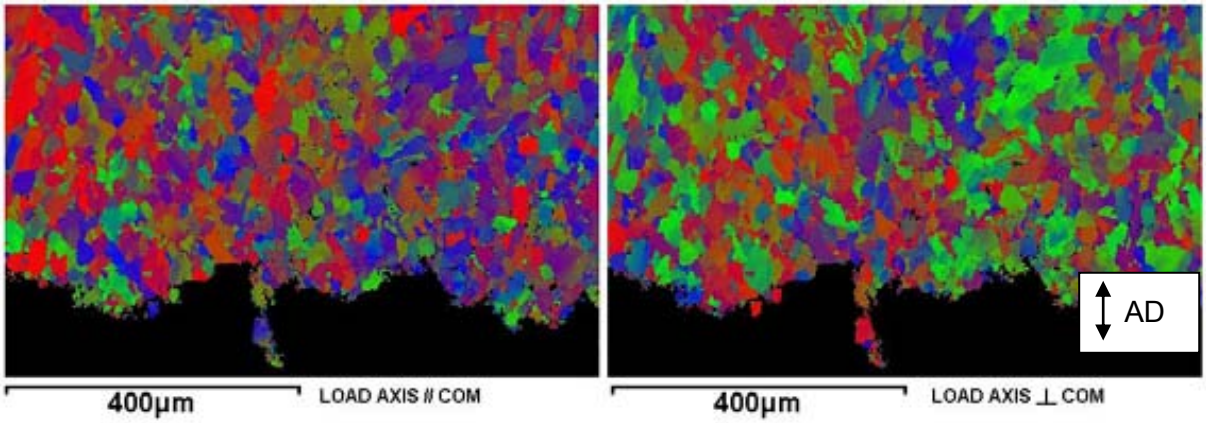

Figure 6-36 – Loading axis parallel and normal COMs of alpha textures in 'diffuse' faceted region of Ti6/4 DLCF specimen

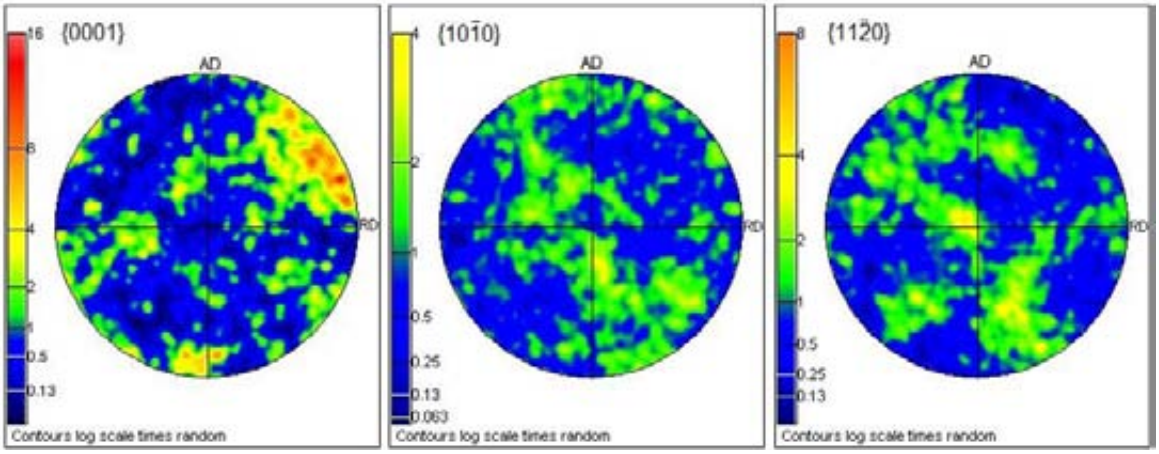

Figure 6-37 – Alpha phase pole figures for diffusely faceted region of Ti6/4 DLCF specimen

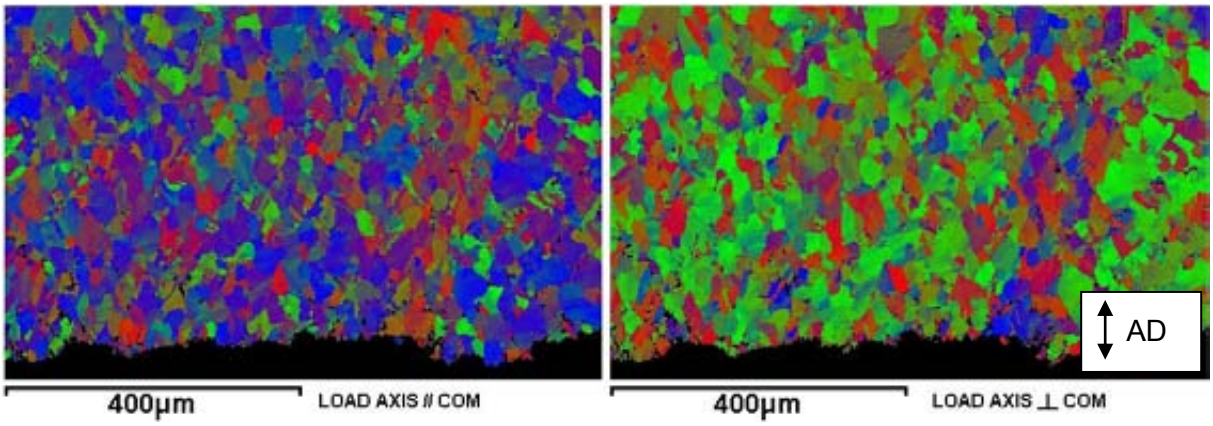

Figure 6-38 – Loading axis parallel and normal COMs of alpha textures in unfaceted region of Ti6/4 DLCF specimen

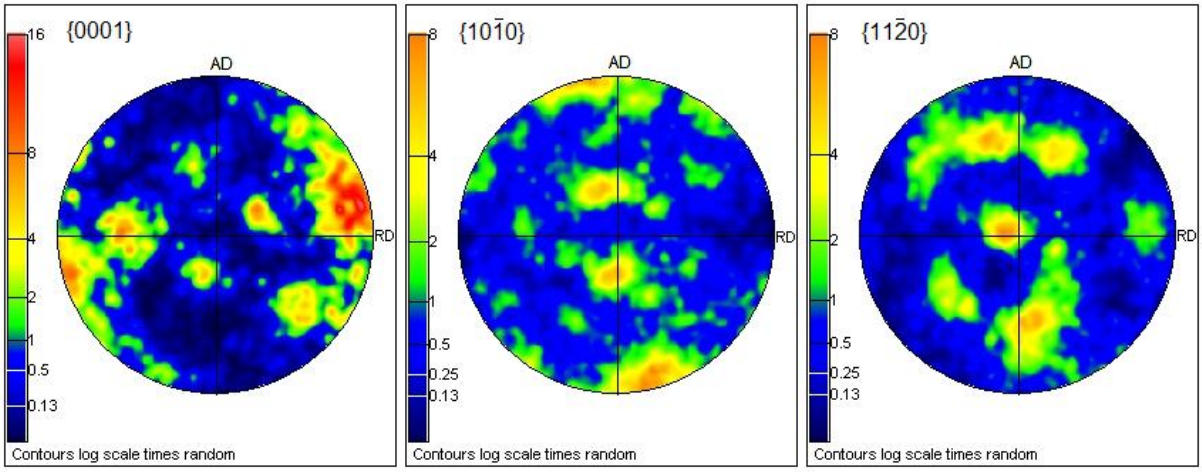

Figure 6-39 – Alpha phase pole figures for unfaceted region of Ti6/4 DLCF specimen

6.7.3 Ti834 disc

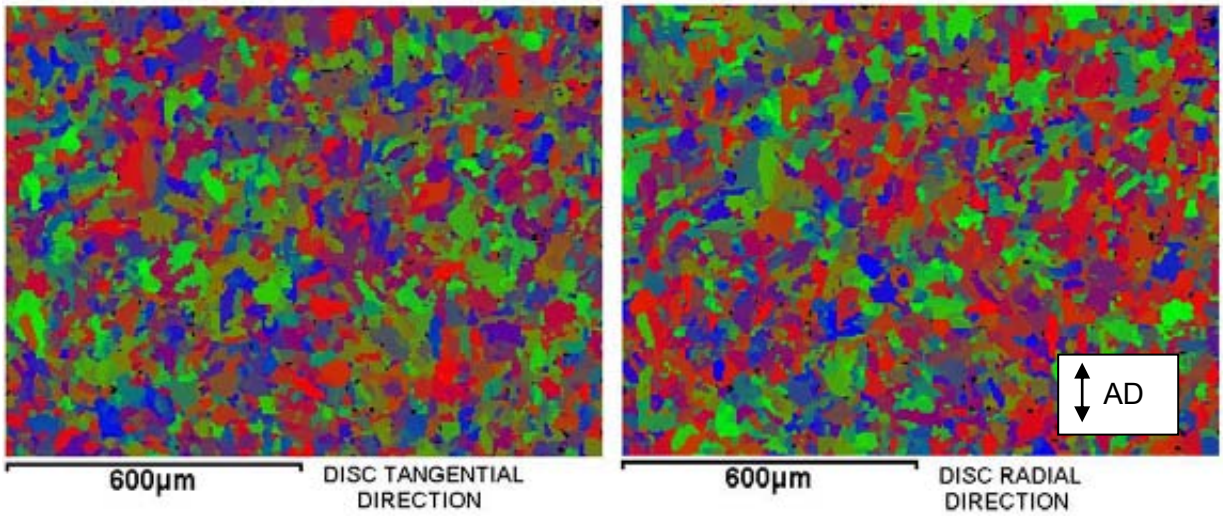

Figure 6-40 – Alpha phase COMs for Ti834 compressor disc A in bore location (Disc tangential and radial directions)

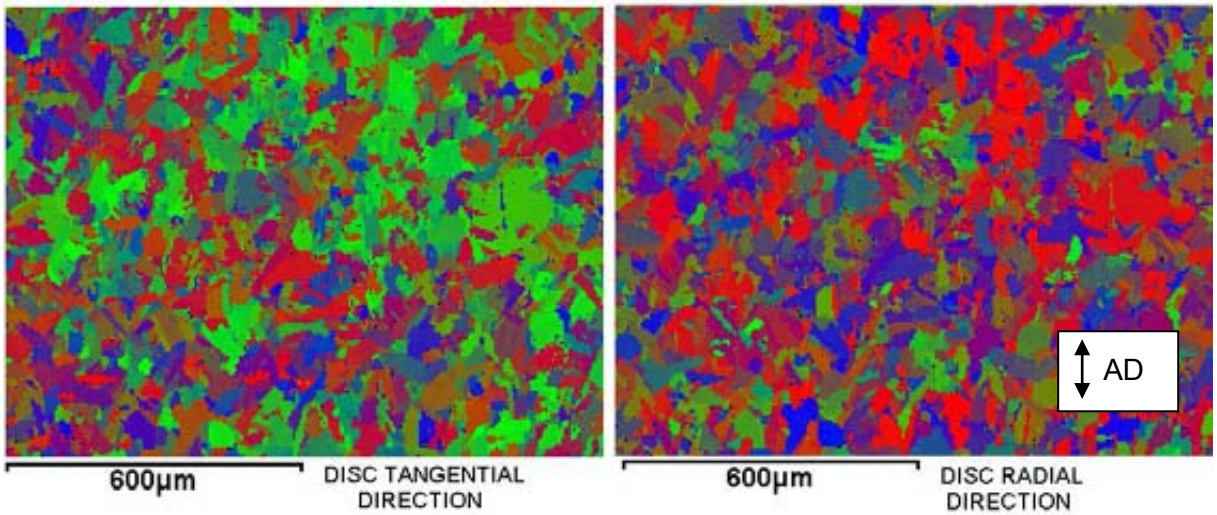

Figure 6-41 – Alpha phase COMs for Ti834 compressor disc B in bore location (Disc tangential and radial directions)

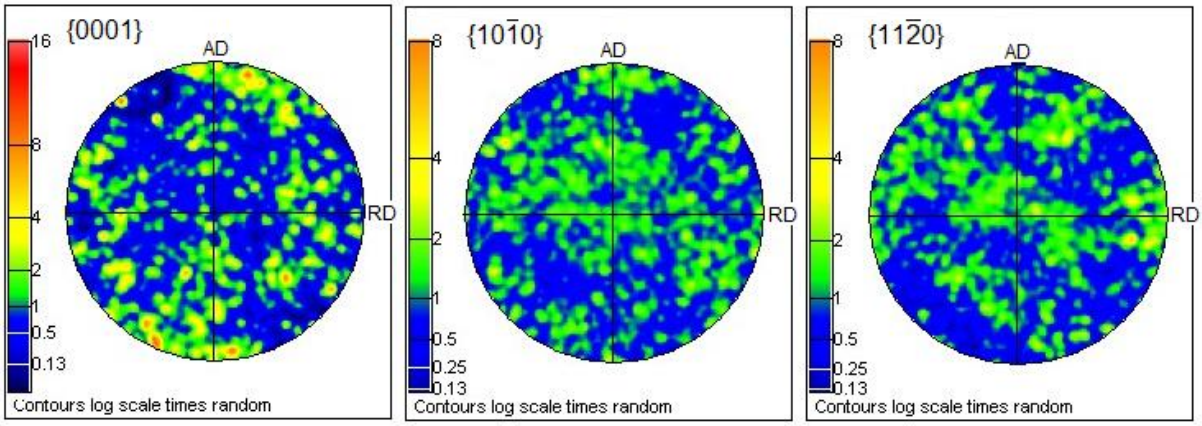

Figure 6-42 – Alpha phase pole figures displaying textures corresponding to COMs in Figure 6-40

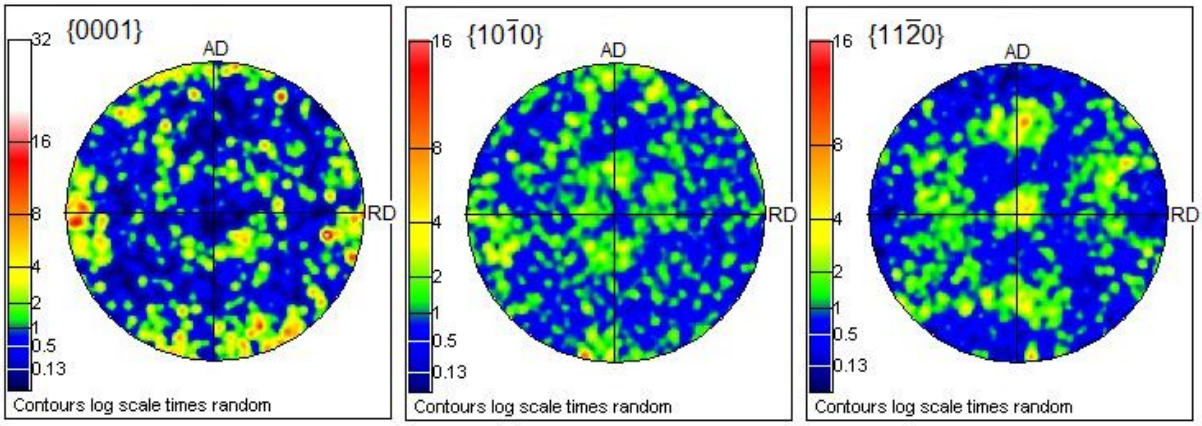

Figure 6-43 – Alpha phase pole figures displaying textures corresponding to COMs in Figure 6-41

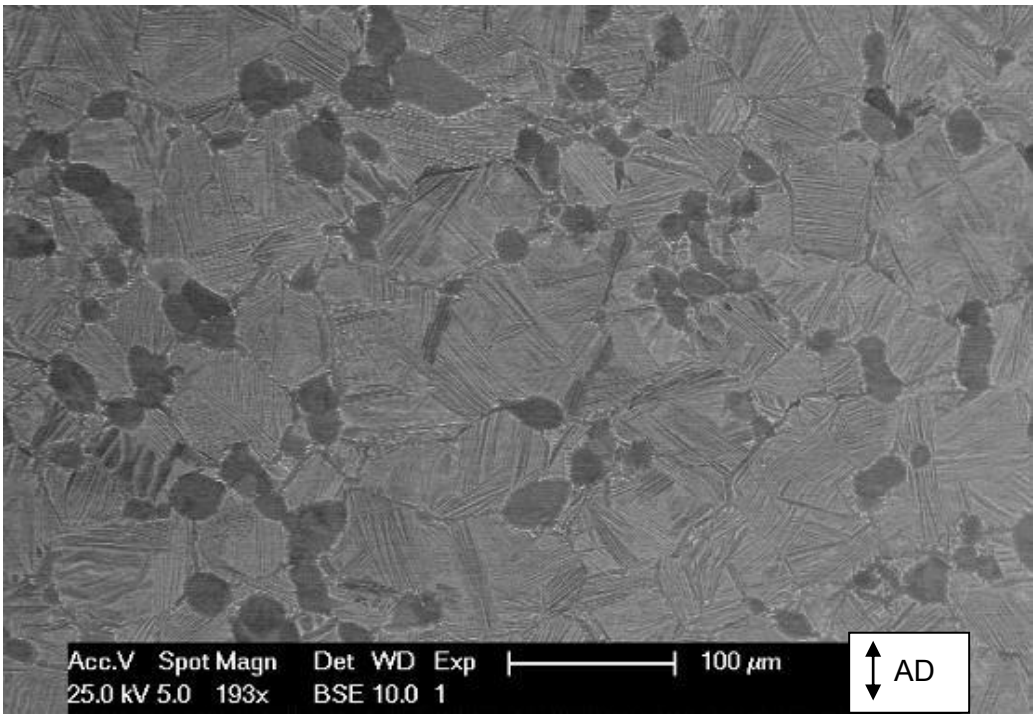

Figure 6-44 – Microstructure of compressor disc A in bore location (Back scatter electron imaging)

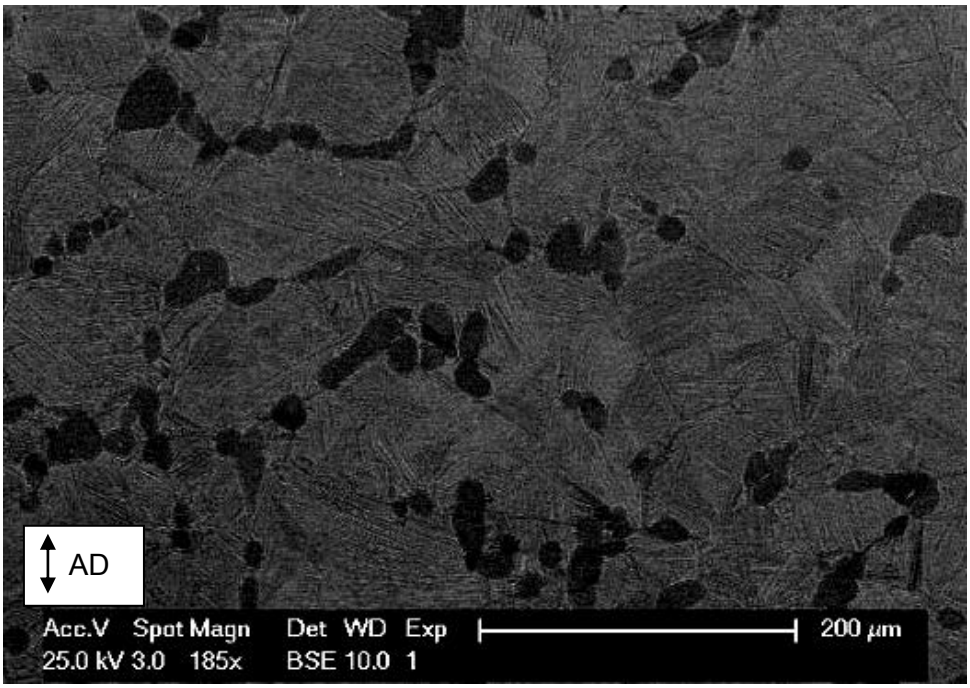

Figure 6-45 – Microstructure of compressor disc B in bore location (Back scatter electron imaging)

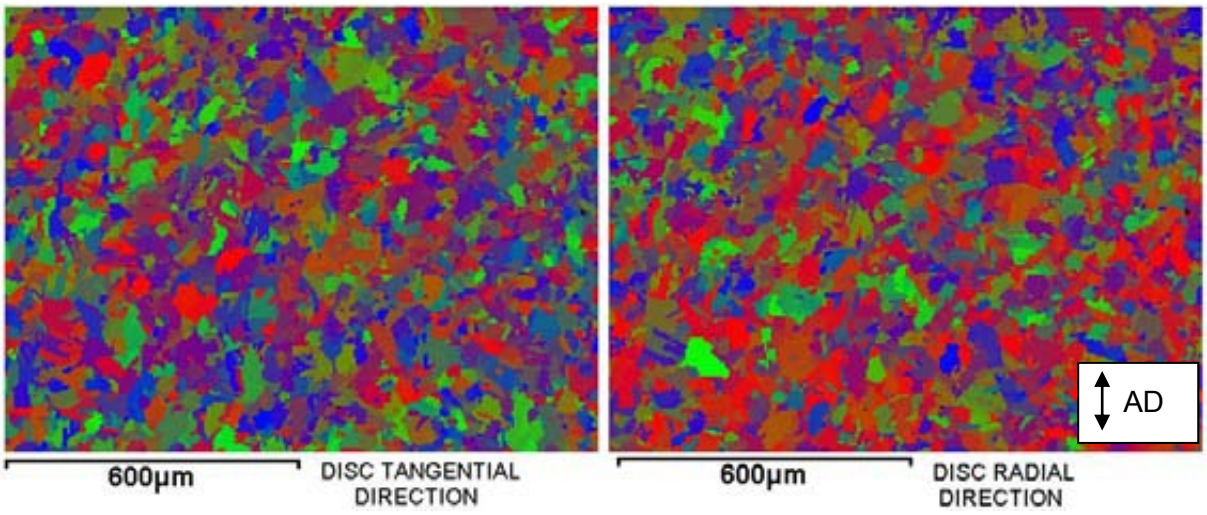

Figure 6-46 – Alpha phase COMs for Ti834 compressor disc C rim location (Disc tangential and radial directions)

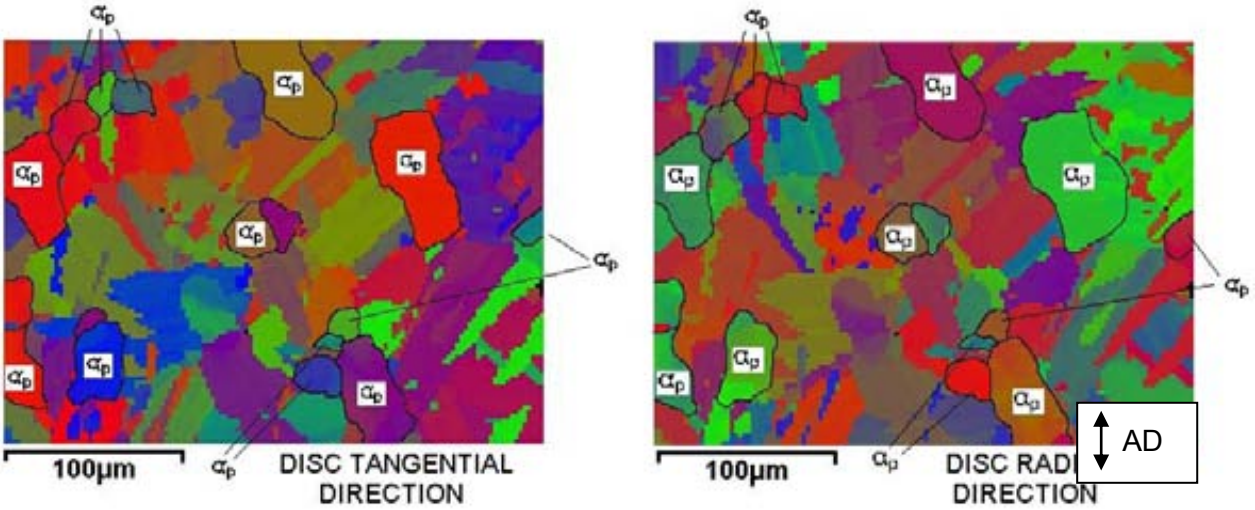

Figure 6-47 – Alpha phase COMs for Ti834 compressor disc C rim location (Disc tangential and radial directions)

6.7.4 Ti6242 billet

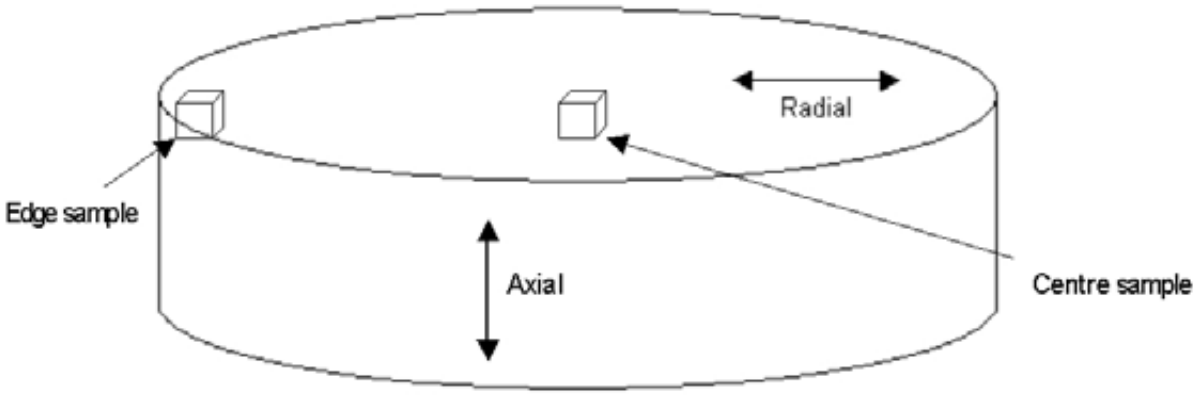

Figure 6-48 – Sectioning of sample from Ti6242 billet material

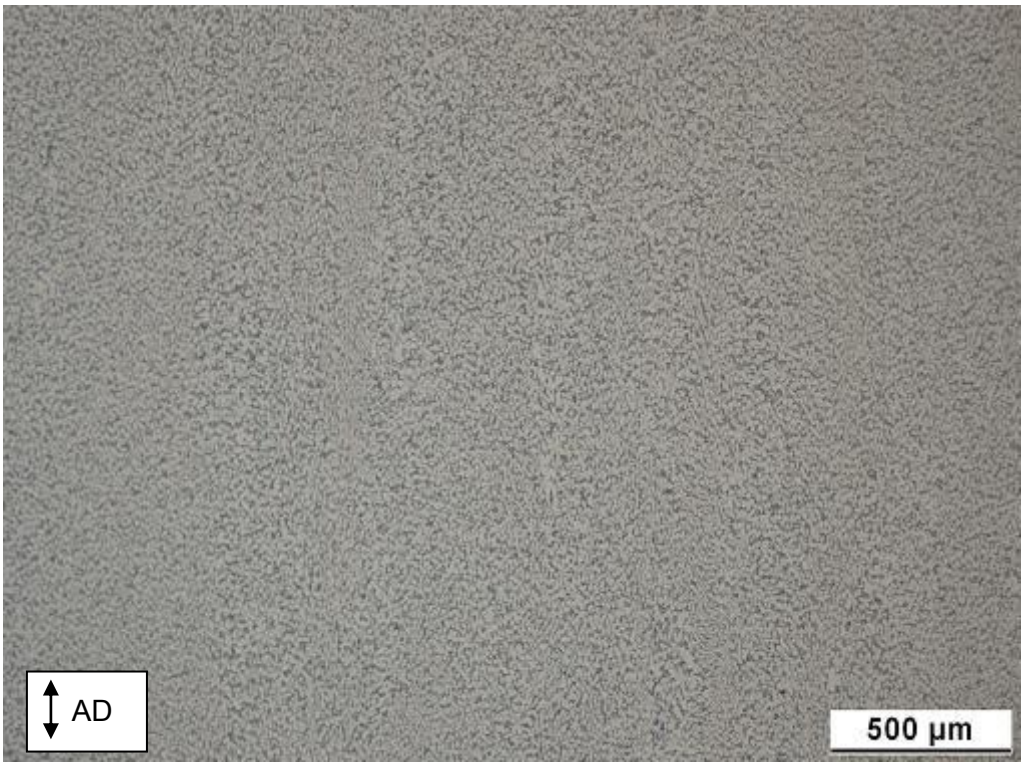

Figure 6-49 – Microstructure of Ti6242 billet at radial centre location

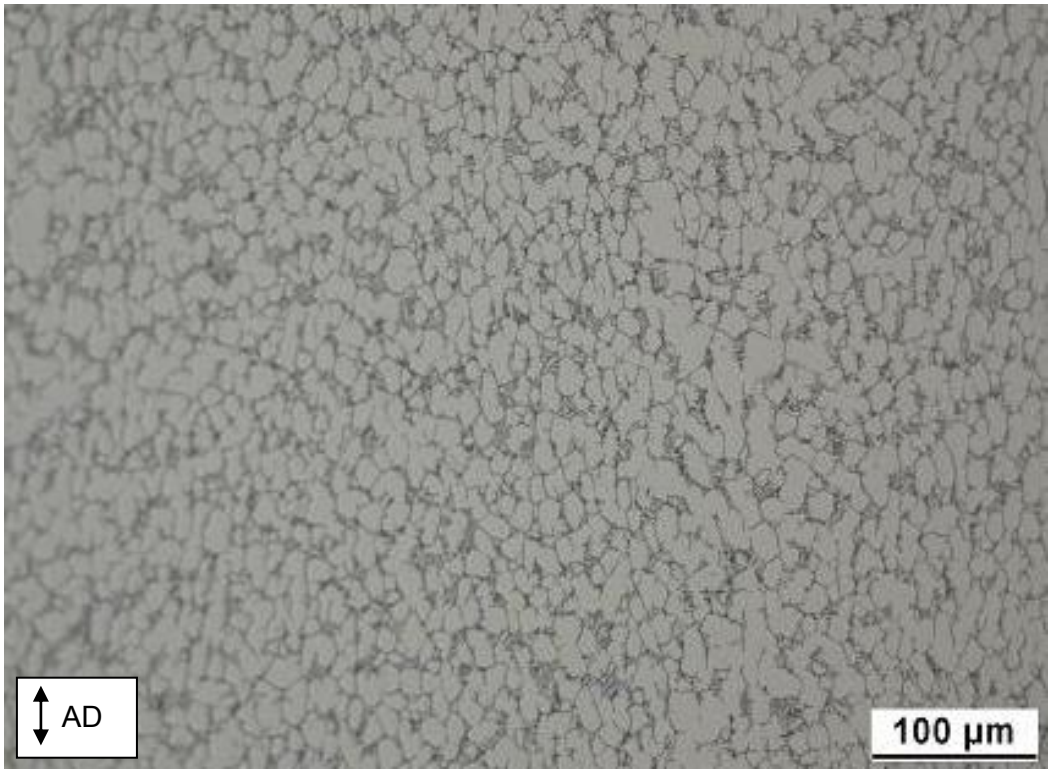

Figure 6-50 – Microstructure of Ti6242 billet at radial centre location

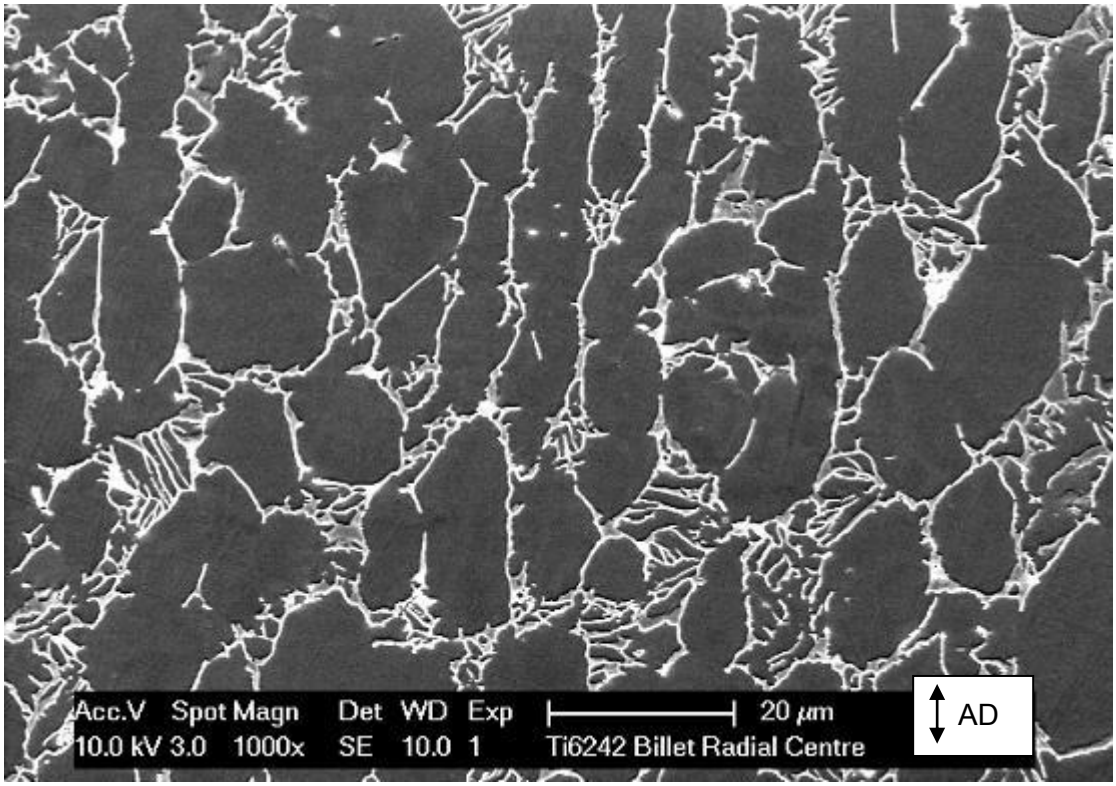

Figure 6-51 – Microstructure of Ti6242 billet at radial centre location

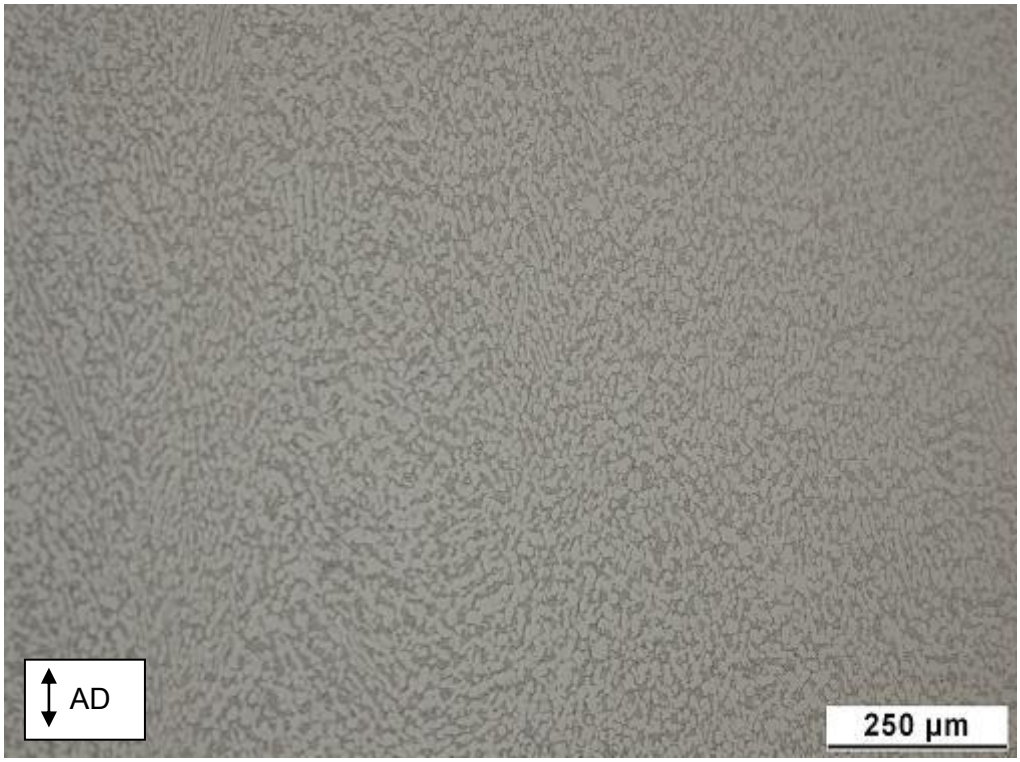

Figure 6-52 – Microstructure of Ti6242 billet at radial edge location

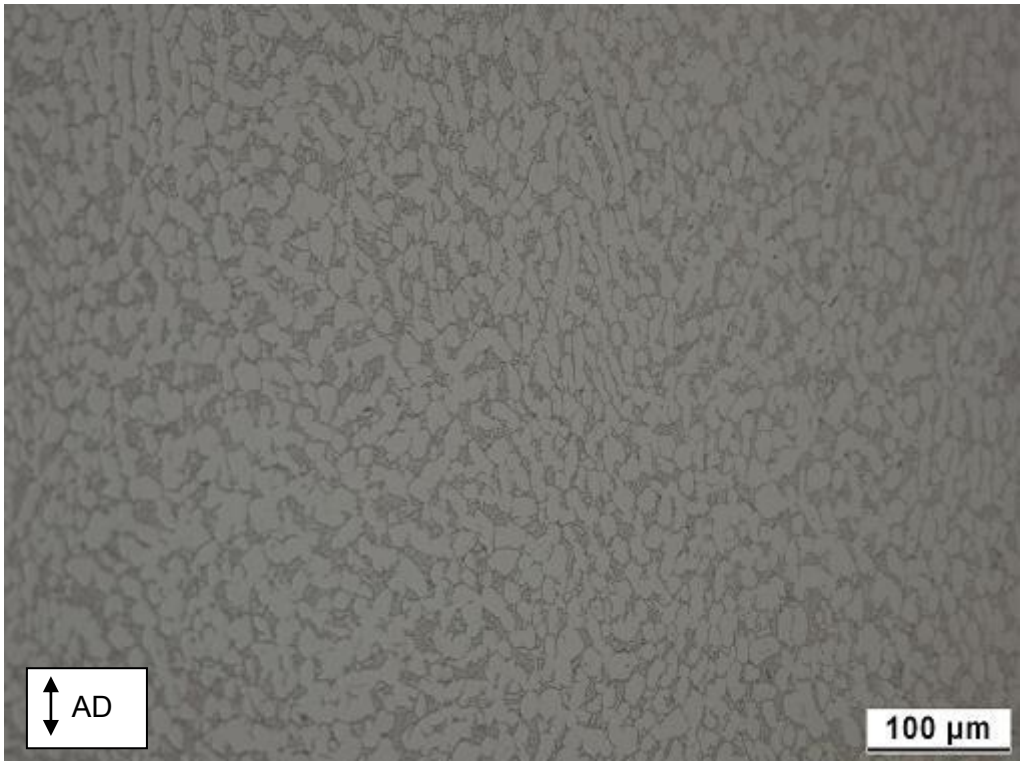

Figure 6-53 – Microstructure of Ti6242 billet at radial edge location

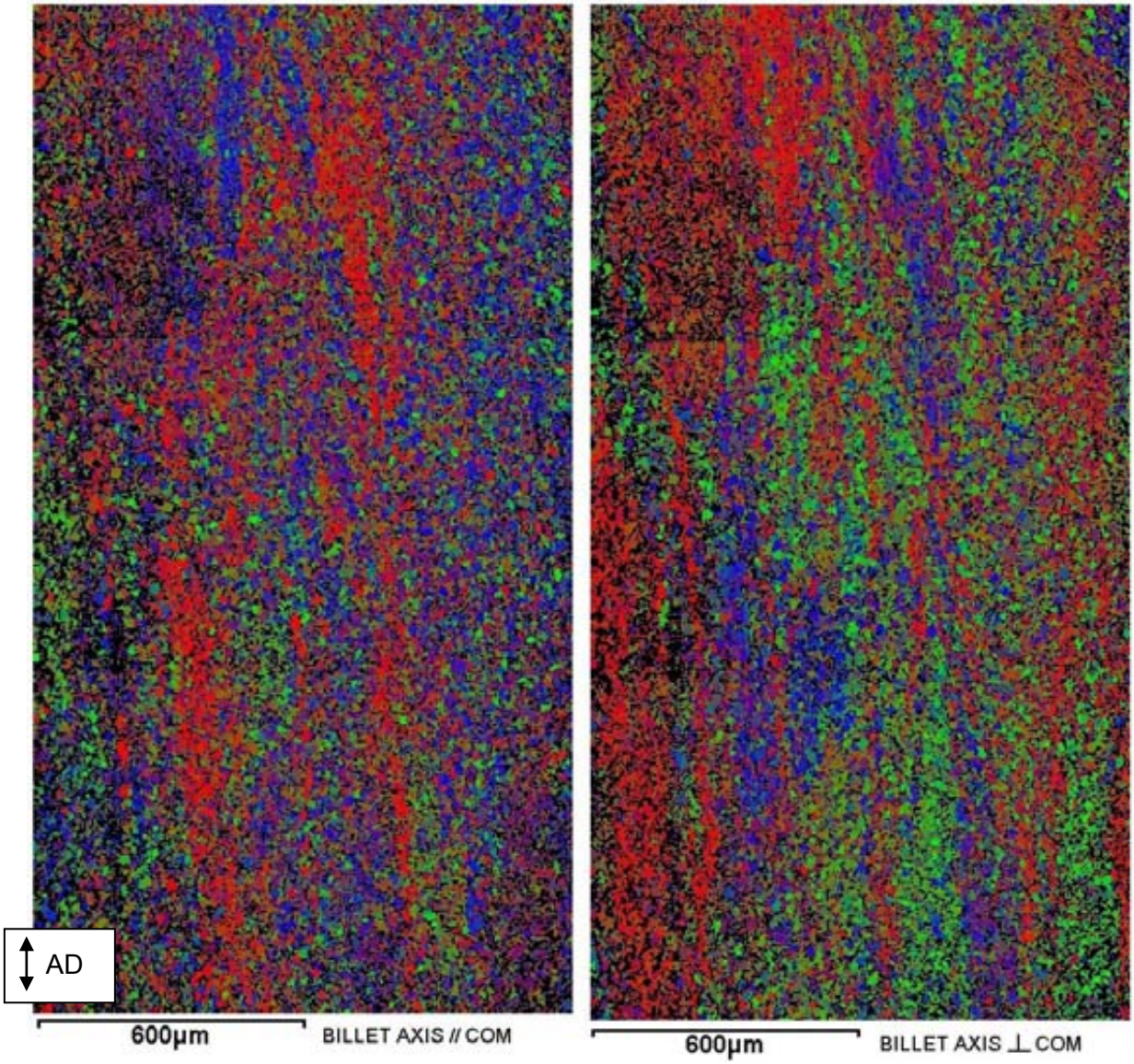

Figure 6-54 – Alpha phase COMs for Ti6242 billet centre section (Orientations w.r.t. billet axis and arbitrary billet axis normal directions)

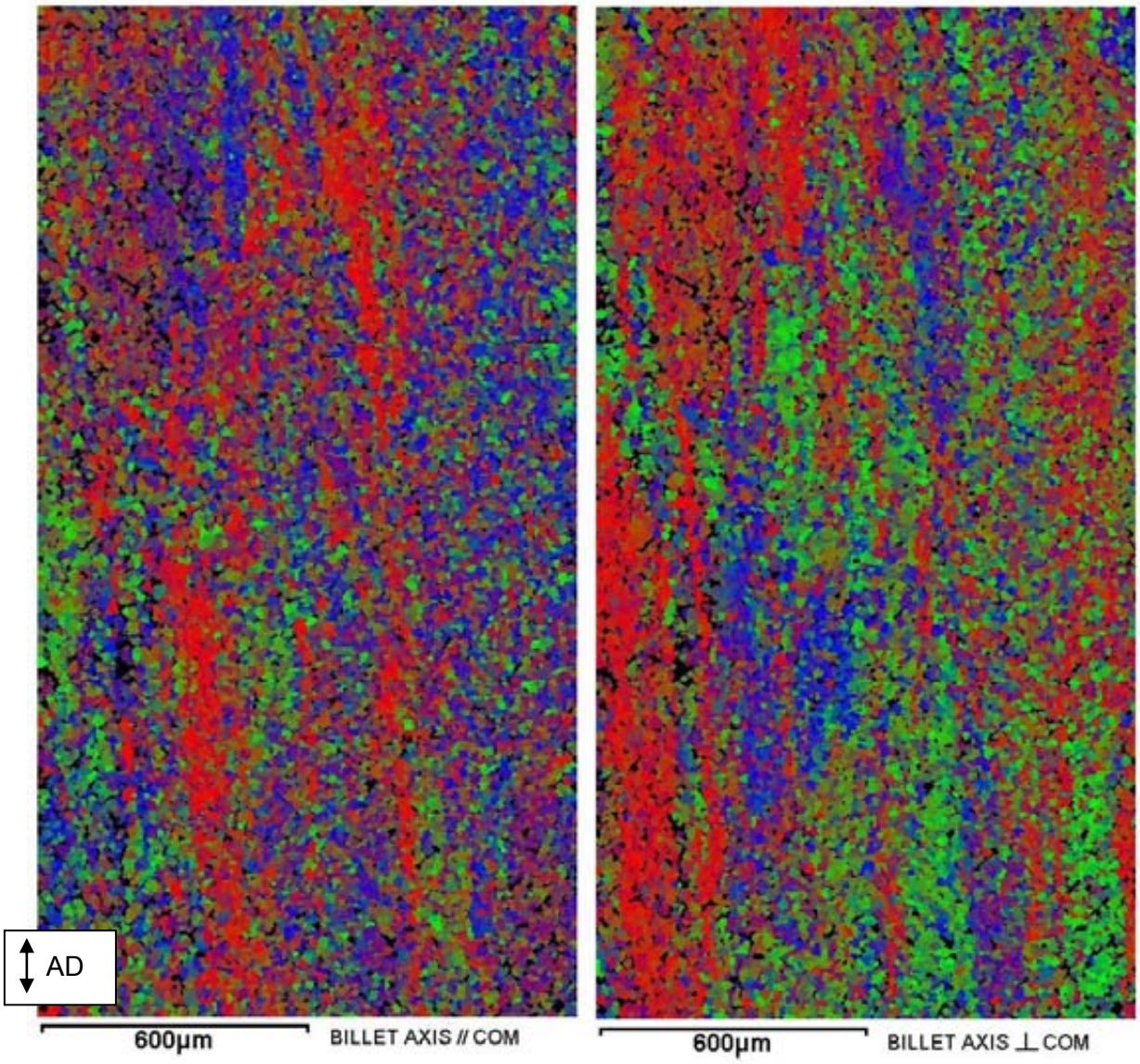

Figure 6-55 – Enhanced alpha phase COMs for Ti6242 billet centre (Billet axis and arbitrary billet axis normal directions respectively)

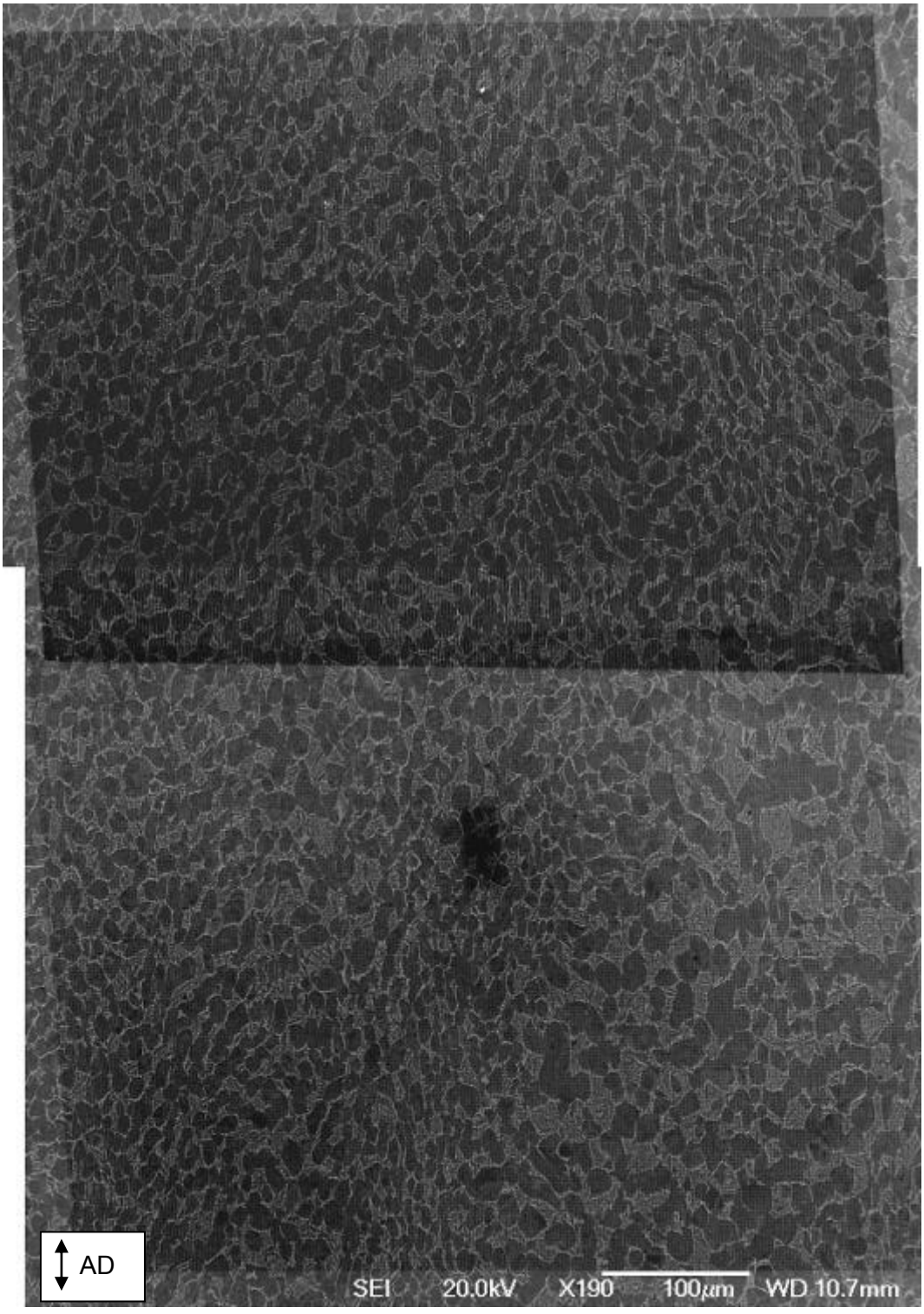

Figure 6-56 – Microstructure of Ti6242 billet edge in region of EBSD mapping

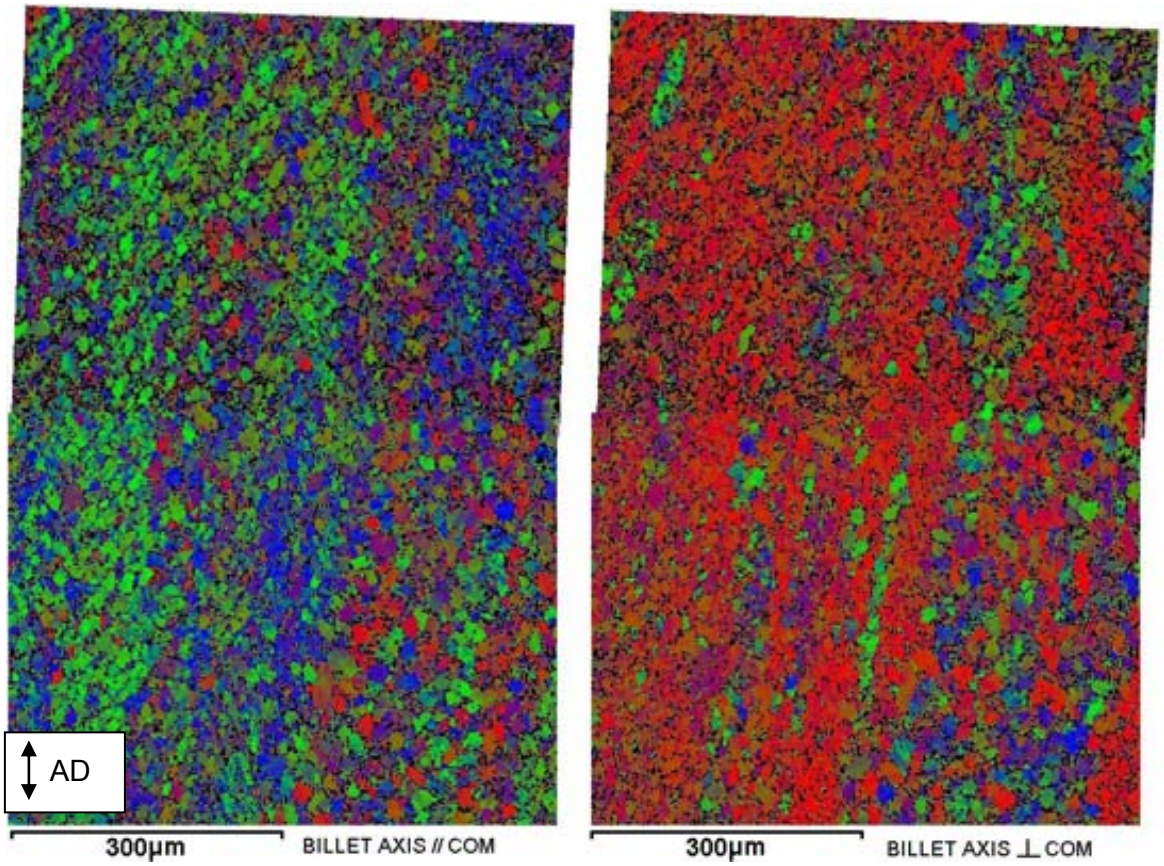

Figure 6-57 – Alpha phase COMs for Ti6242 billet edge material (Billet axis parallel and arbitrary billet axis normal direction COMs respectively)

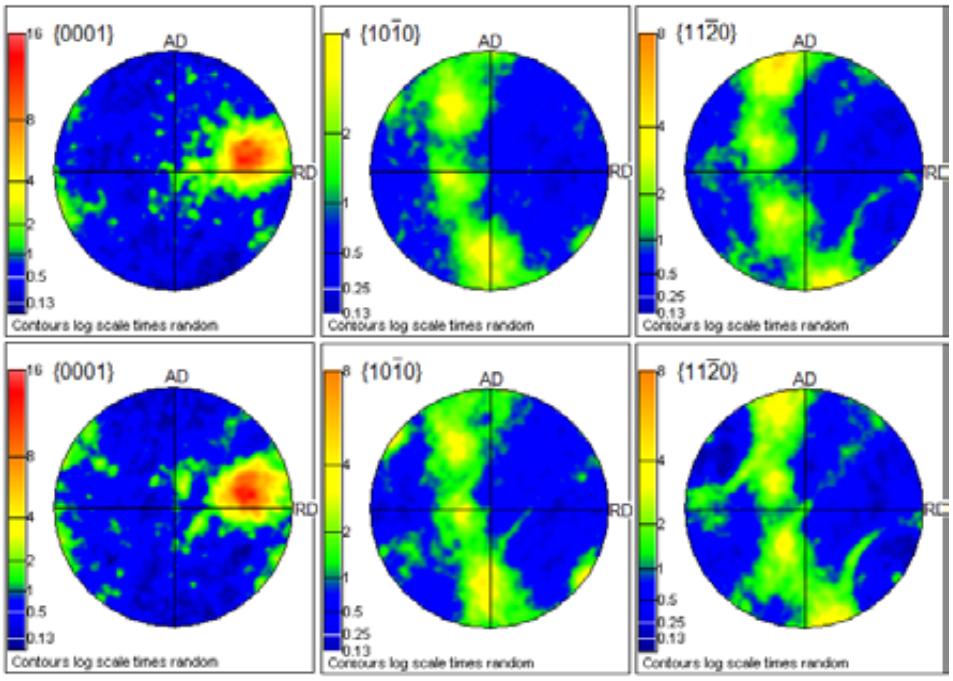

Figure 6-58 – Alpha pole figures for upper and lower sections of combined COM displayed in Figure 6-57

6.7.5 Ti6242 disc

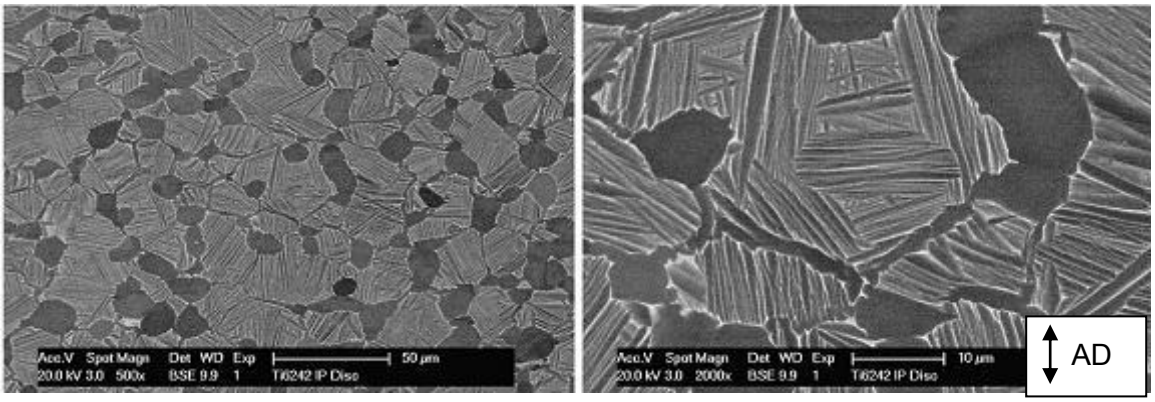

Figure 6-59 – Optical microstructure of Ti6242 disc bore

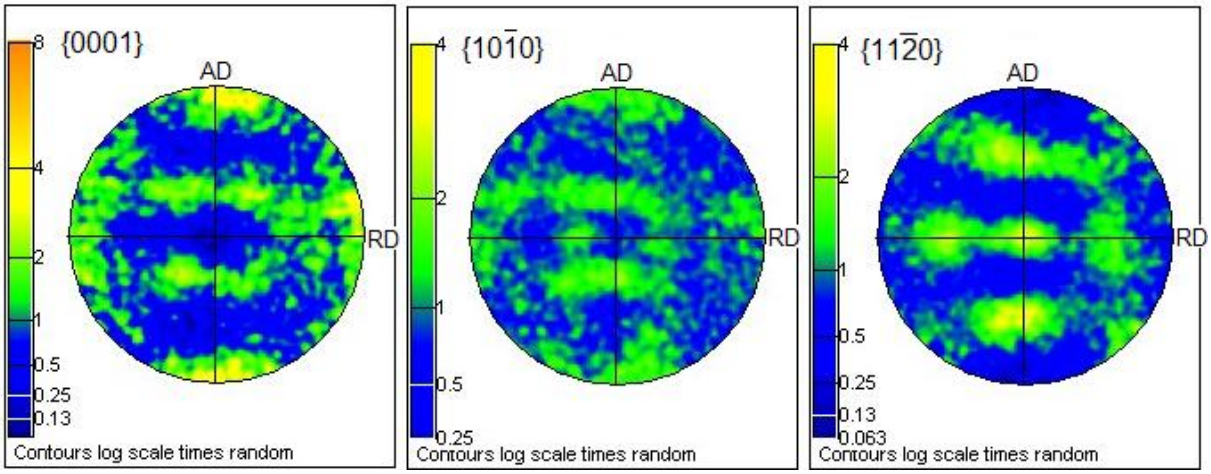

Figure 6-60 – Alpha phase pole figures for Ti6242 disc bore material

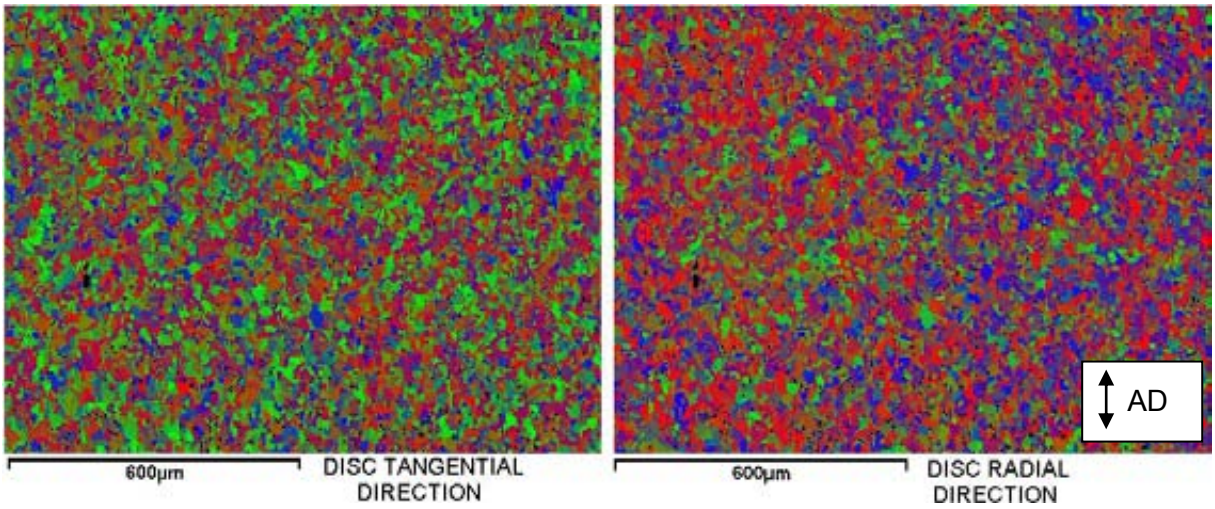

Figure 6-61 – Alpha phase COMs for Ti6242 disc bore material (Disc tangential and disc radial direction COMs respectively)

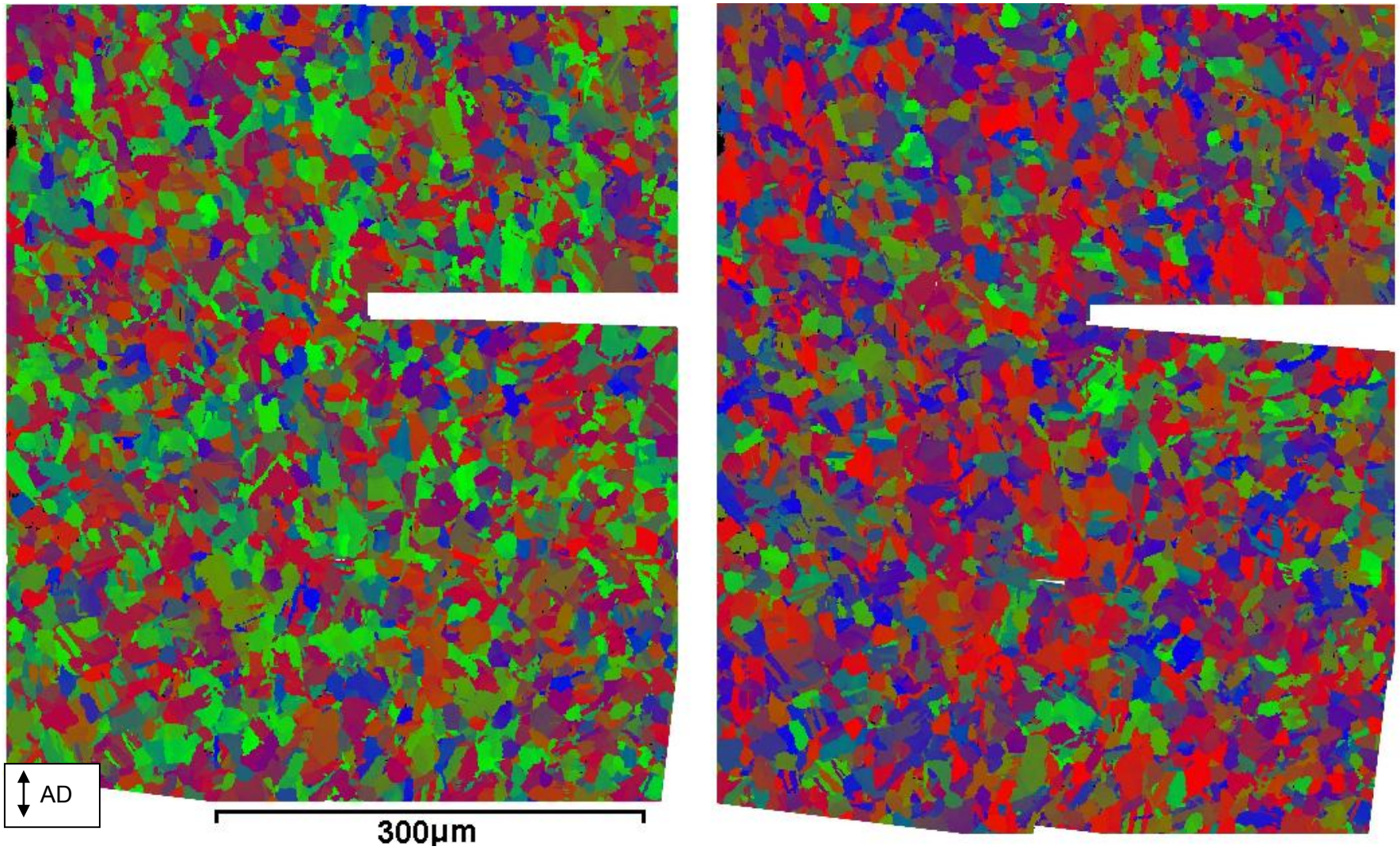

Figure 6-62 – Alpha phase COMs for Ti6242 disc bore material (Disc tangential and radial direction COMs respectively)

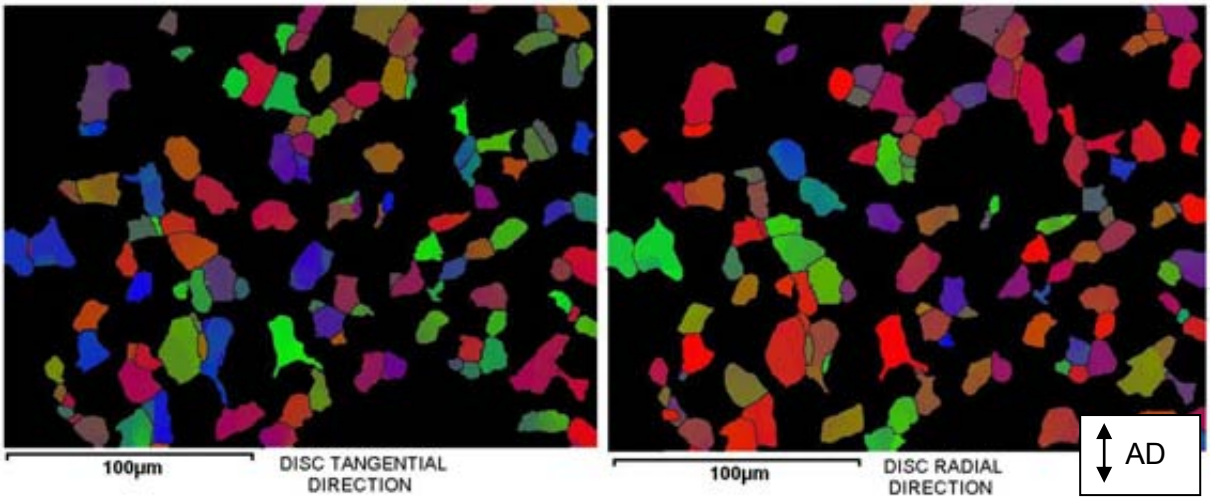

Figure 6-63 – Primary alpha textures in Ti6242 disc bore (Disc tangential and radial direction COMs respectively)

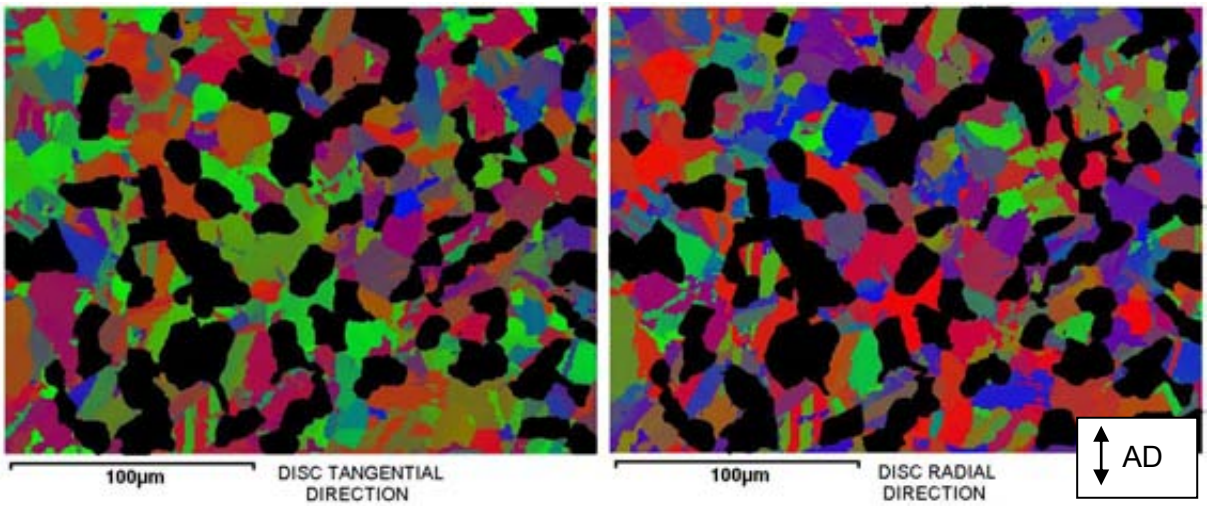

Figure 6-64 – Secondary alpha textures in Ti6242 disc bore (Disc tangential and radial direction COMs respectively)

6.7.6 Ti6246 disc material

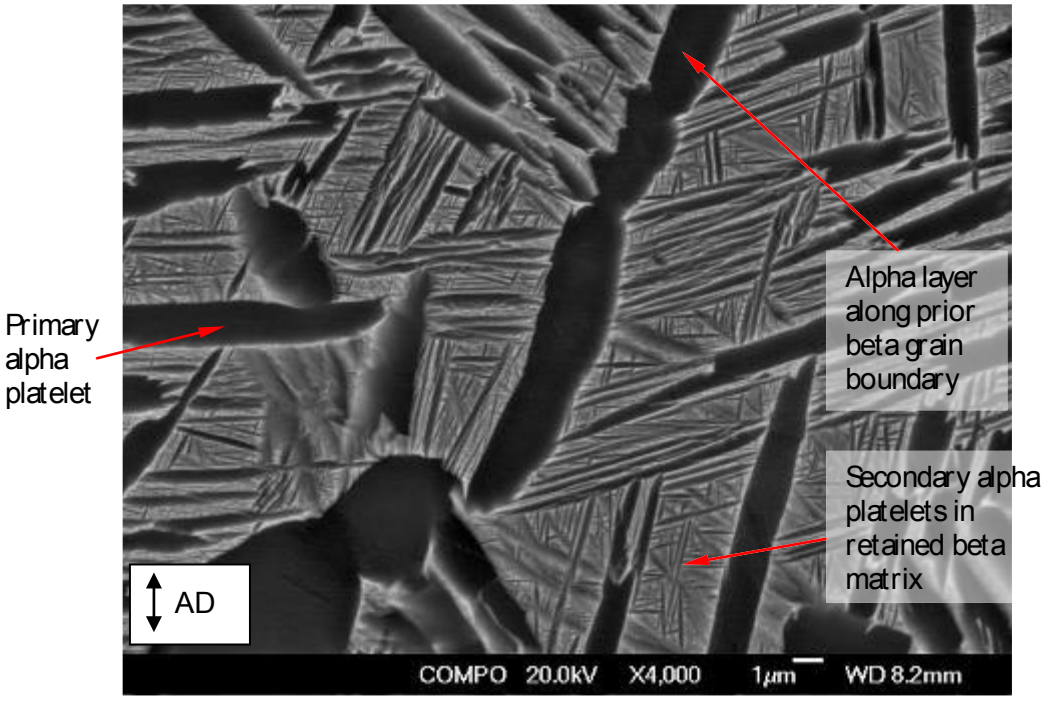

Figure 6-65 – Back scattered electron image of beta forged Ti6246 disc microstructure

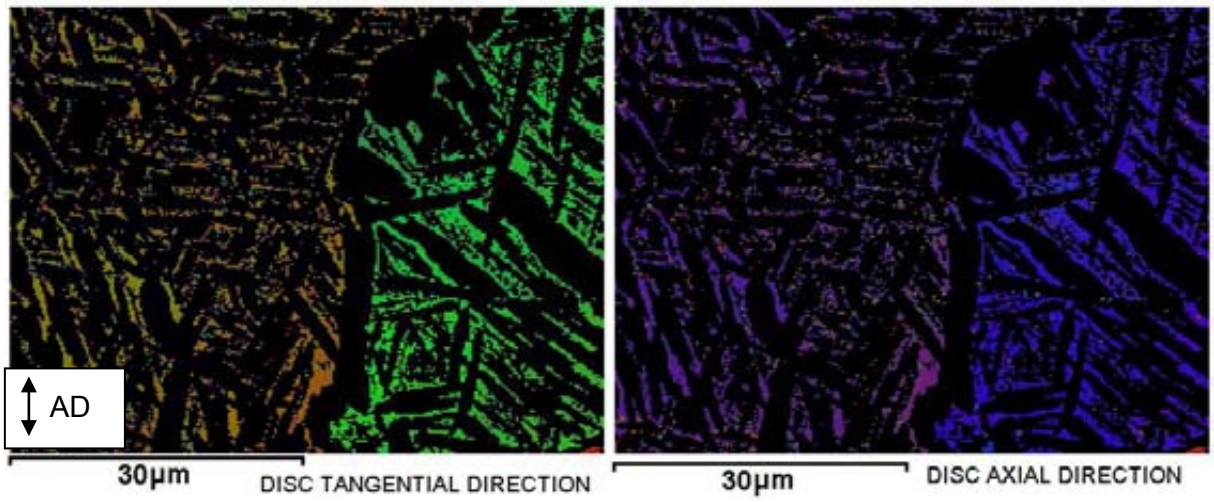

Figure 6-66 – Beta phase COMs for beta forged Ti6246 disc material (Crystal orientations displayed w.r.t. tangential and axial disc directions respectively)

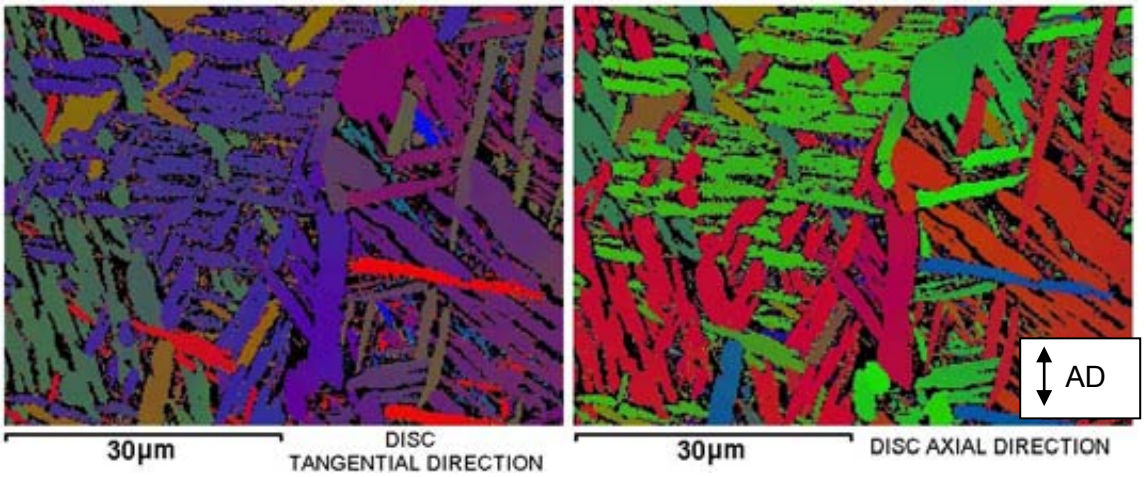

Figure 6-67 – Alpha COMs for beta forged Ti6246 disc material (Crystal orientations displayed w.r.t. tangential and axial disc directions respectively)

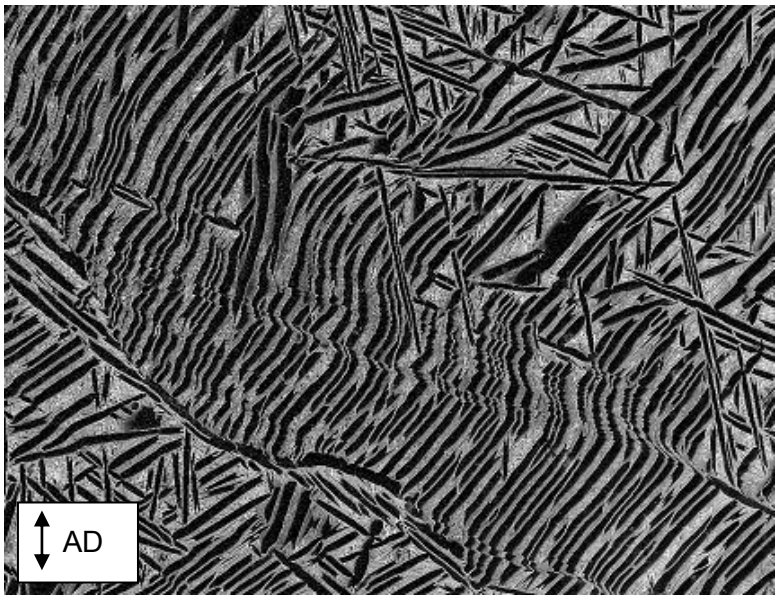

Figure 6-68 – Planar slip bands in beta forged Ti6246 disc material [181]

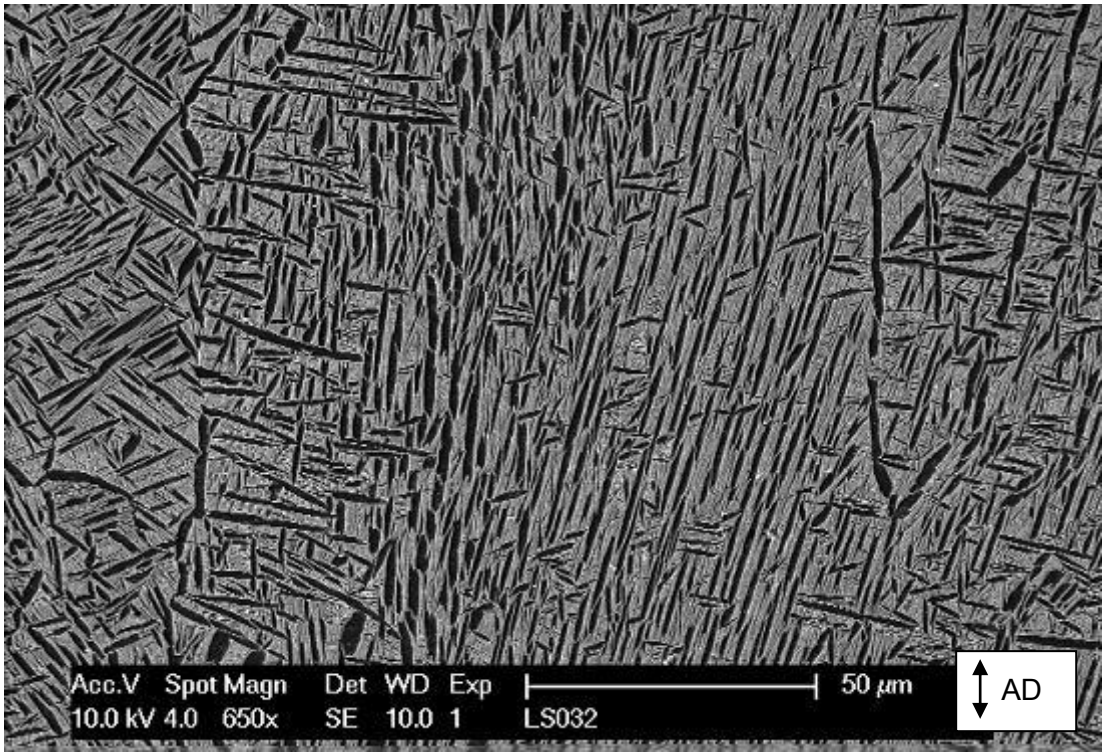

Figure 6-69 – Typical microstructures in Ti6246 material used for cold dwell fatigue testing

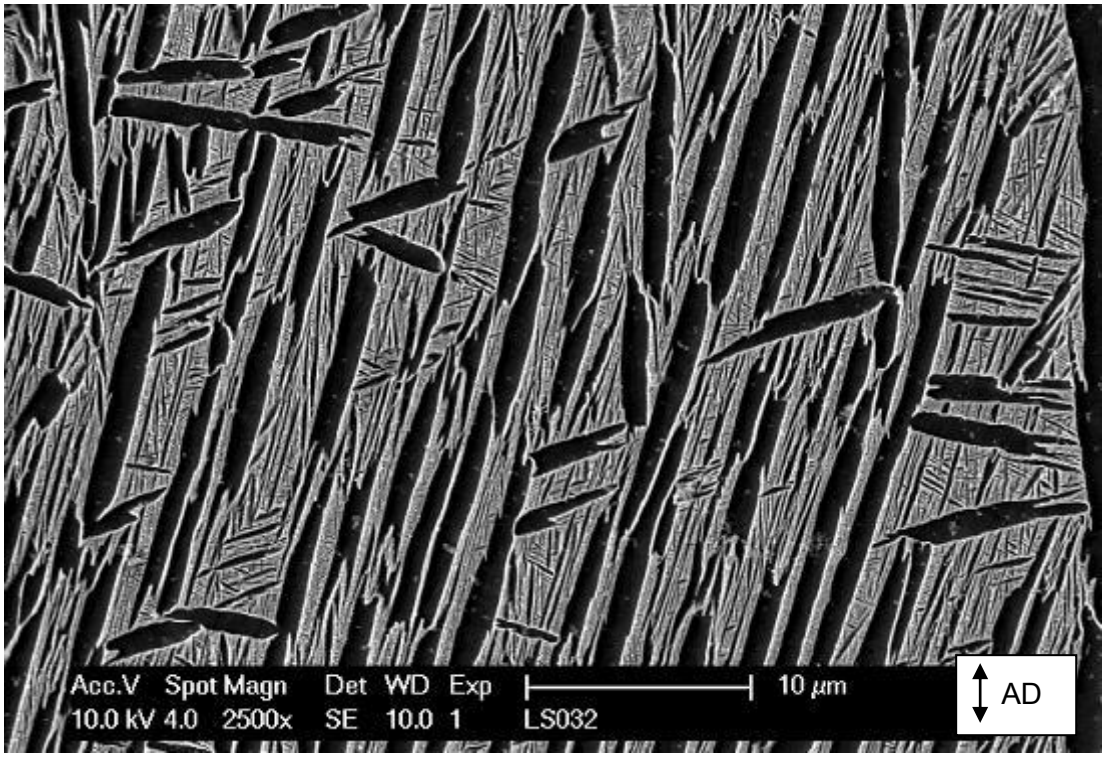

Figure 6-70 – Typical microstructures in Ti6246 material used for cold dwell fatigue testing

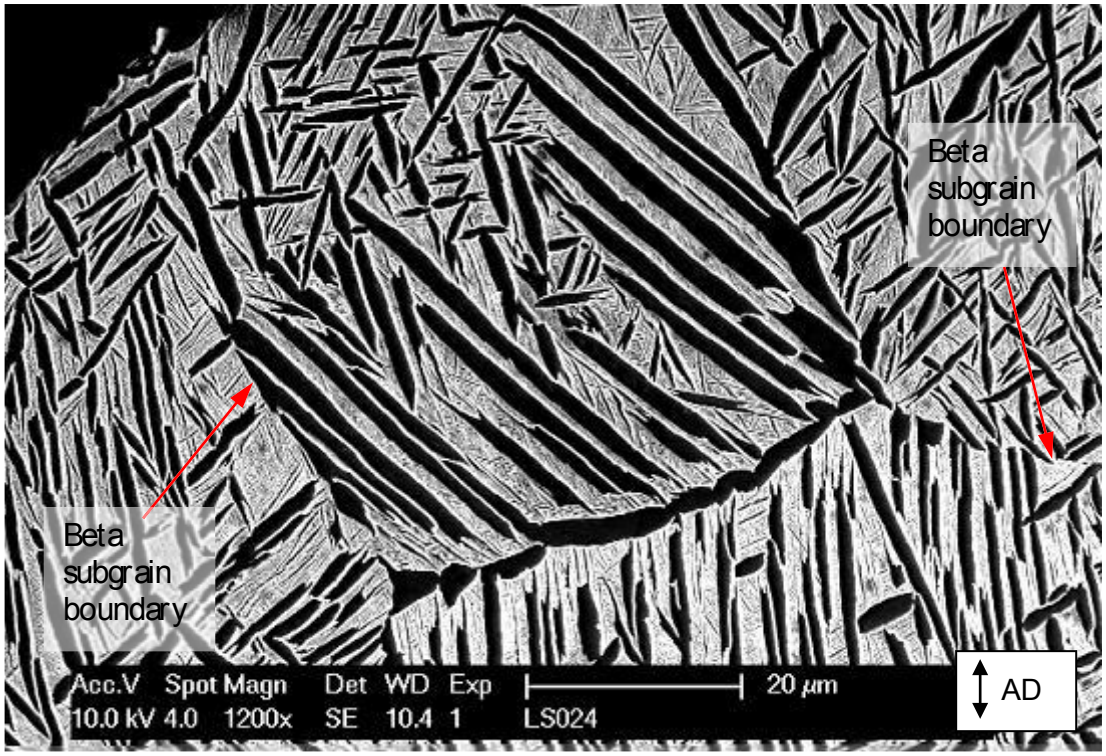

Figure 6-71 – Typical Ti6246 microstructure with 'beta subgrain' features

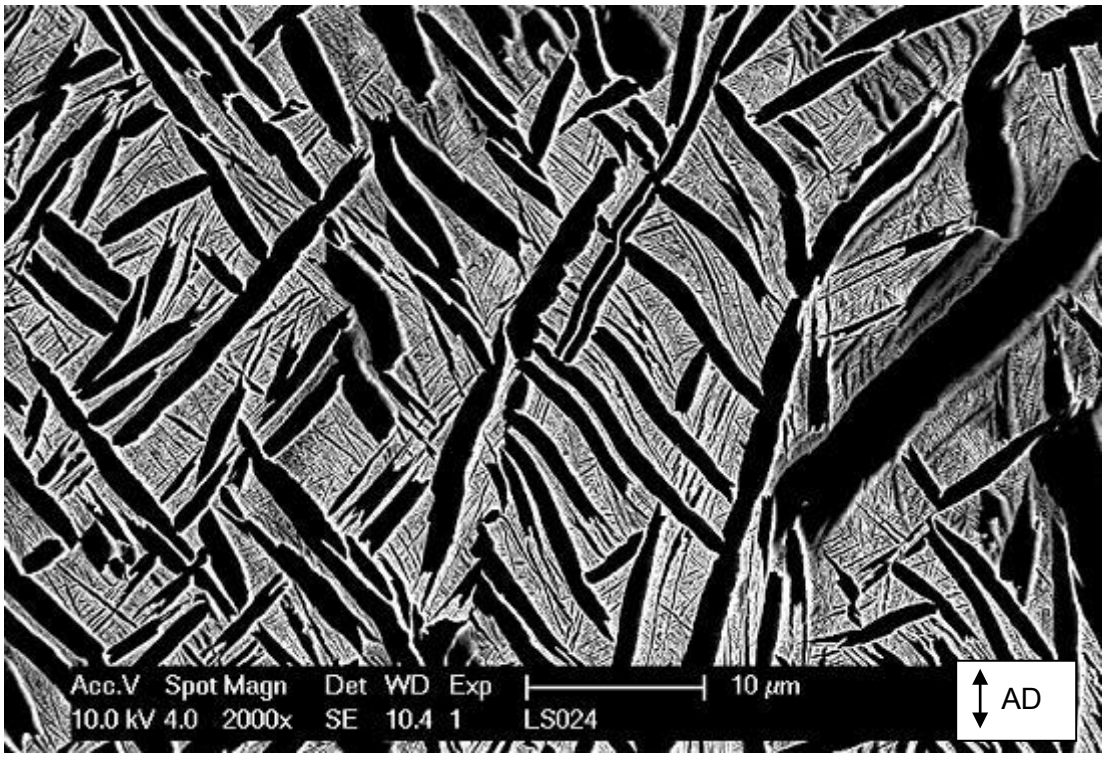

Figure 6-72 – Sub-surface plastic deformation in Ti6246 test specimen in close proximity to fracture surface

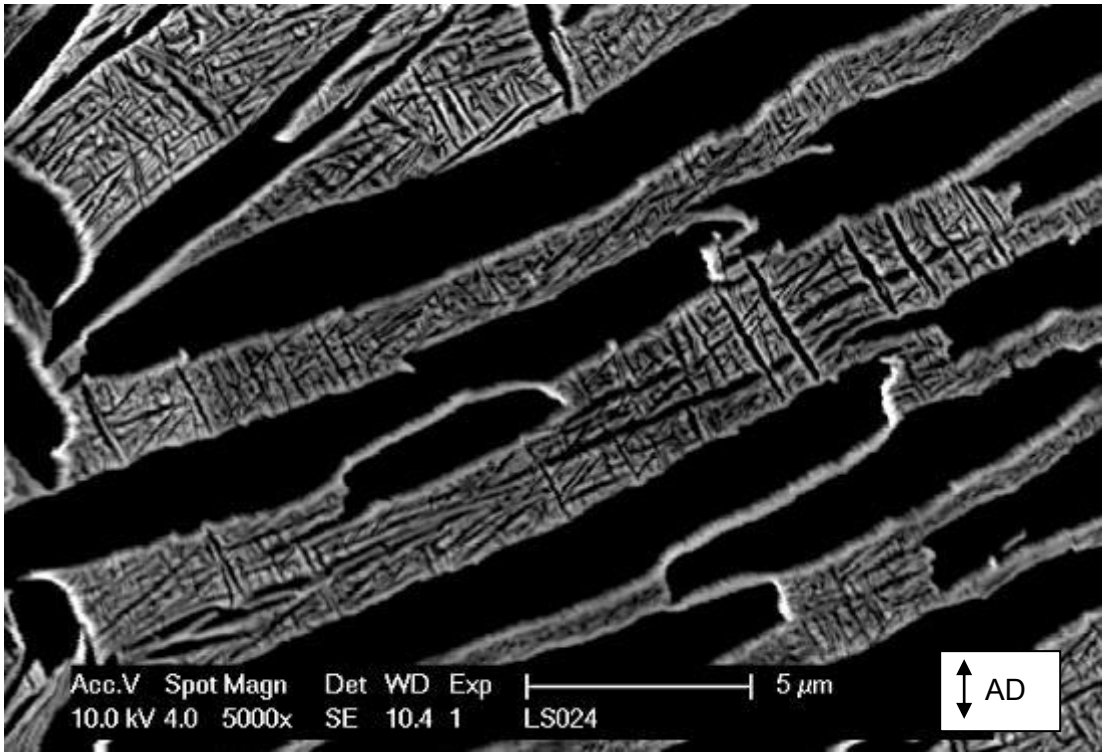

Figure 6-73 – Secondary alpha platelet/retained beta matrix in primary alpha platelet colony in Ti6246 material

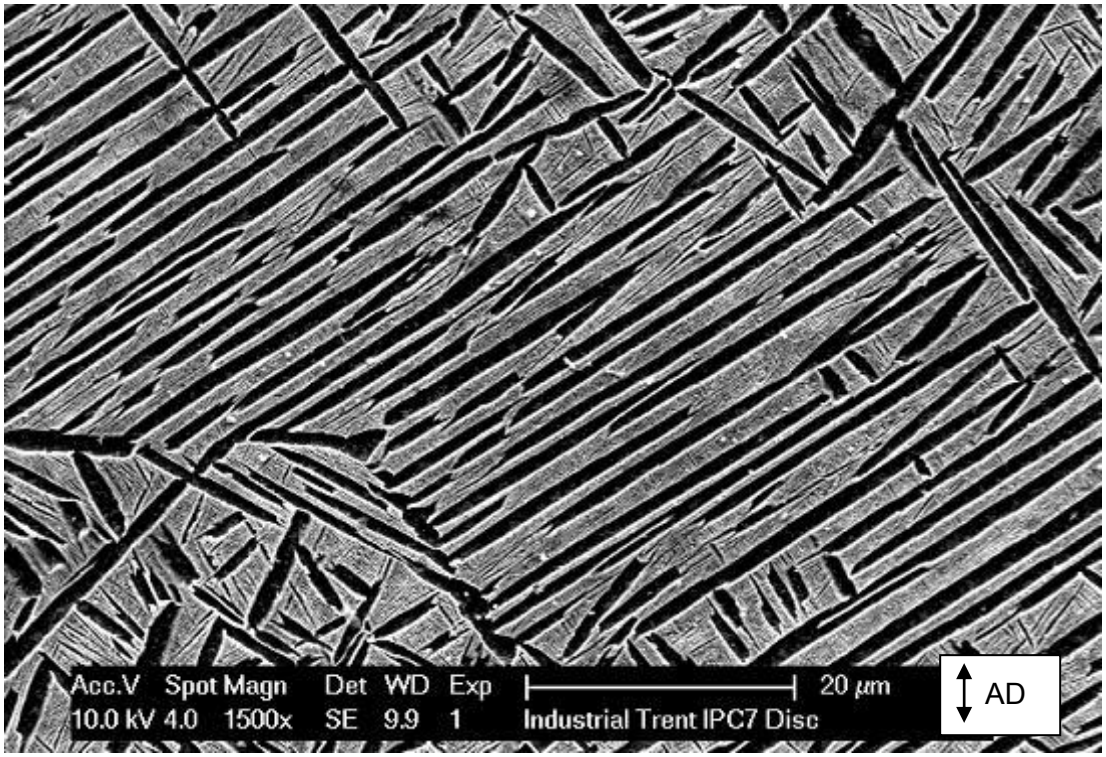

Figure 6-74 – Ex-service Ti6246 microstructure with beta sub-grain structure and low area fraction primary alpha platelet content

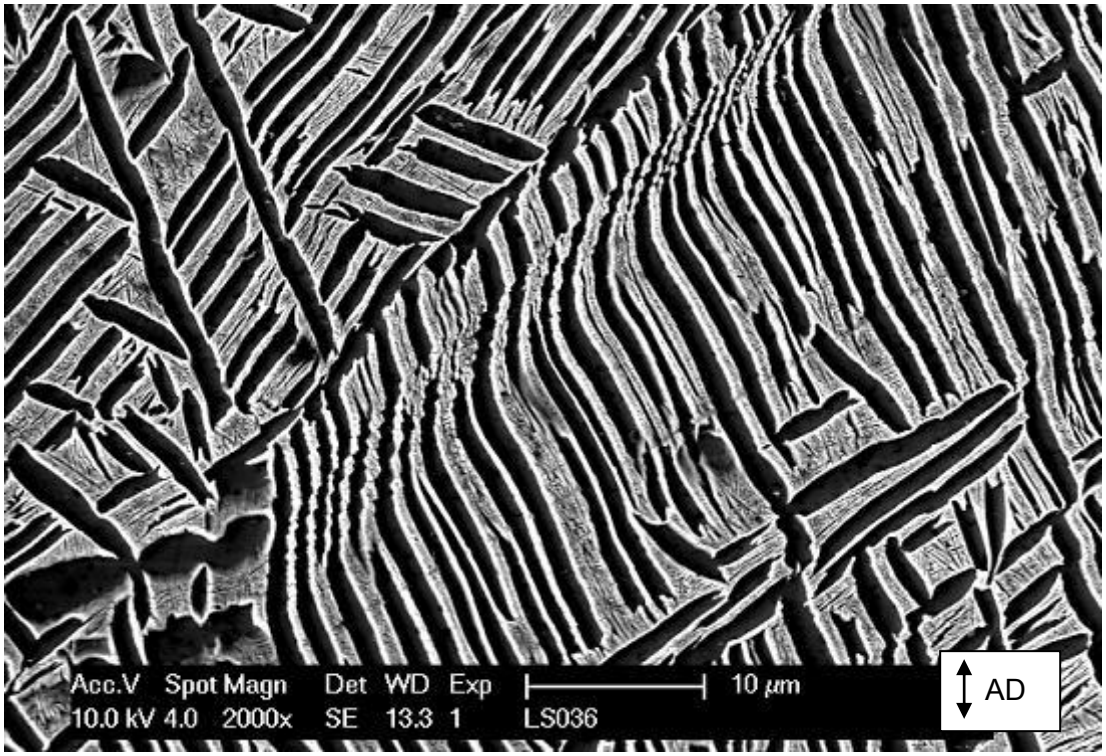

Figure 6-75 – Planar slip bands traversing a primary alpha colony in a Ti6246 cold dwell fatigue test specimen

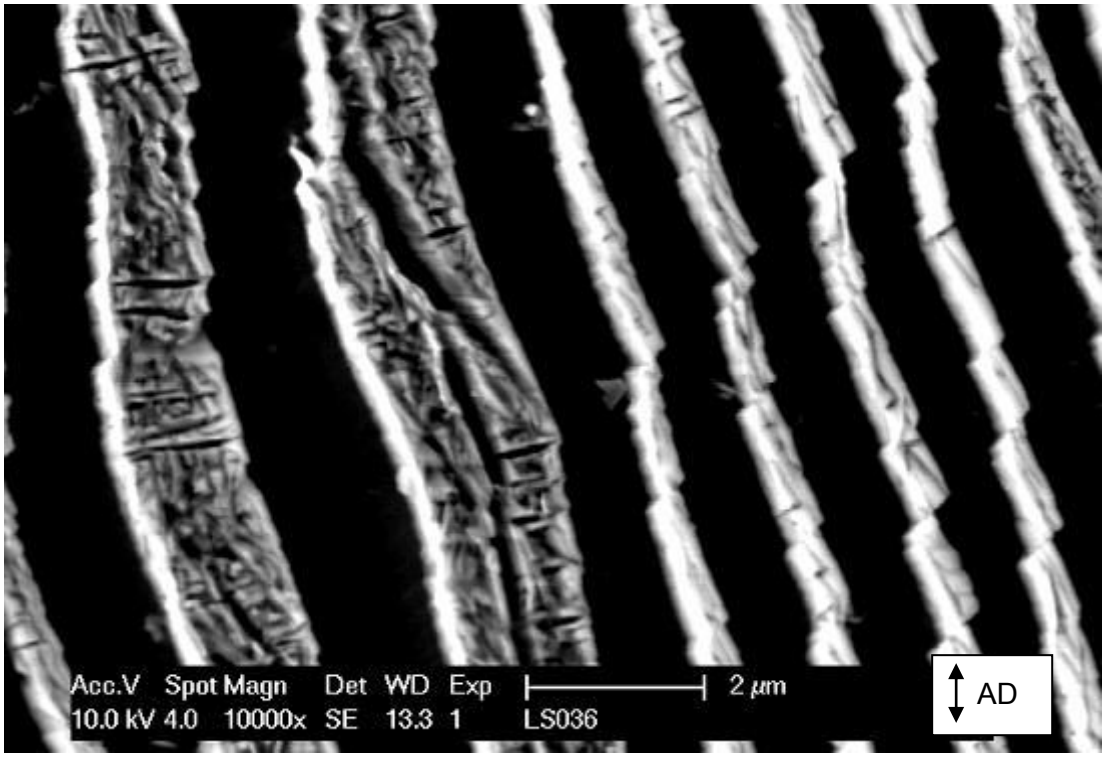

Figure 6-76 – Planar slip band boundary in Ti6246 cold dwell fatigue test specimen

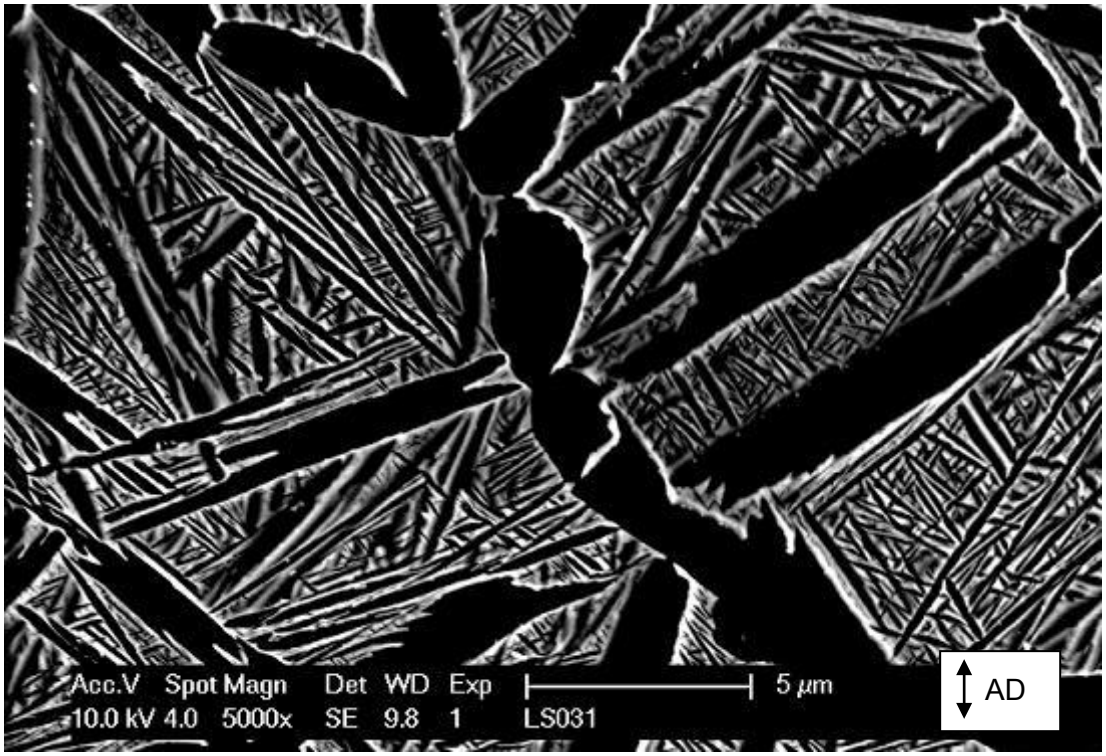

Figure 6-77 – Secondary alpha platelet structures in Ti6246 cold dwell fatigue test specimen

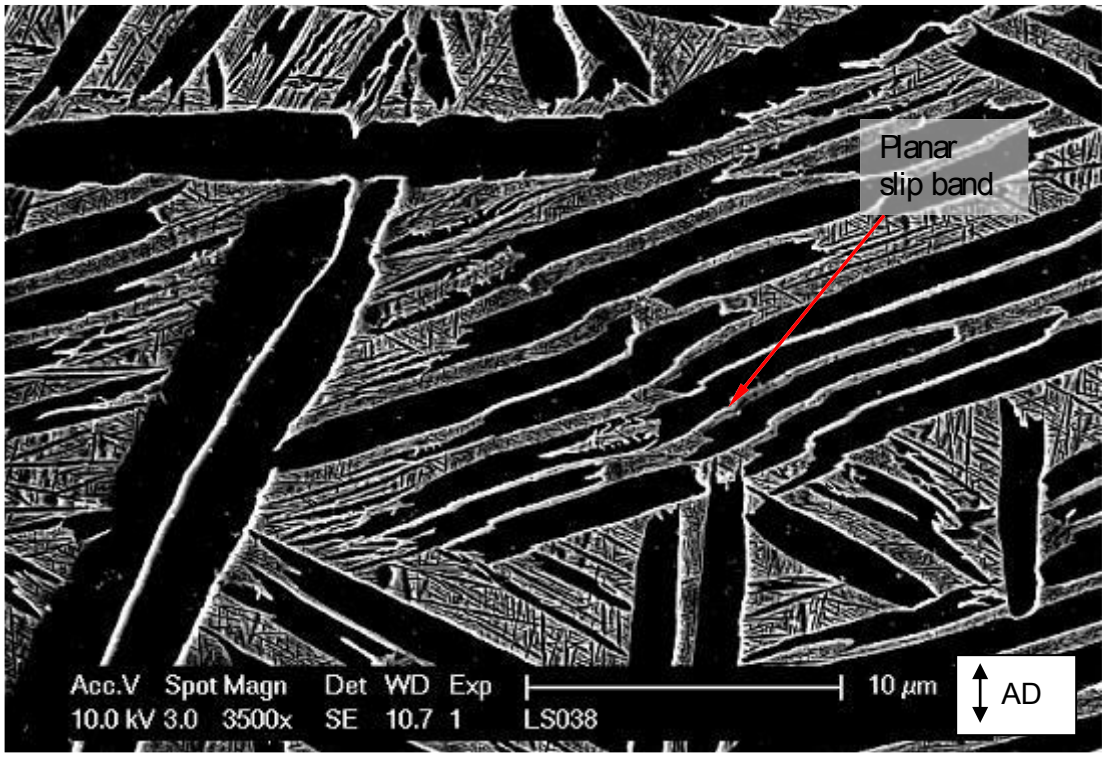

Figure 6-78 – Planar slip trace in Ti6246 DLCF test specimen

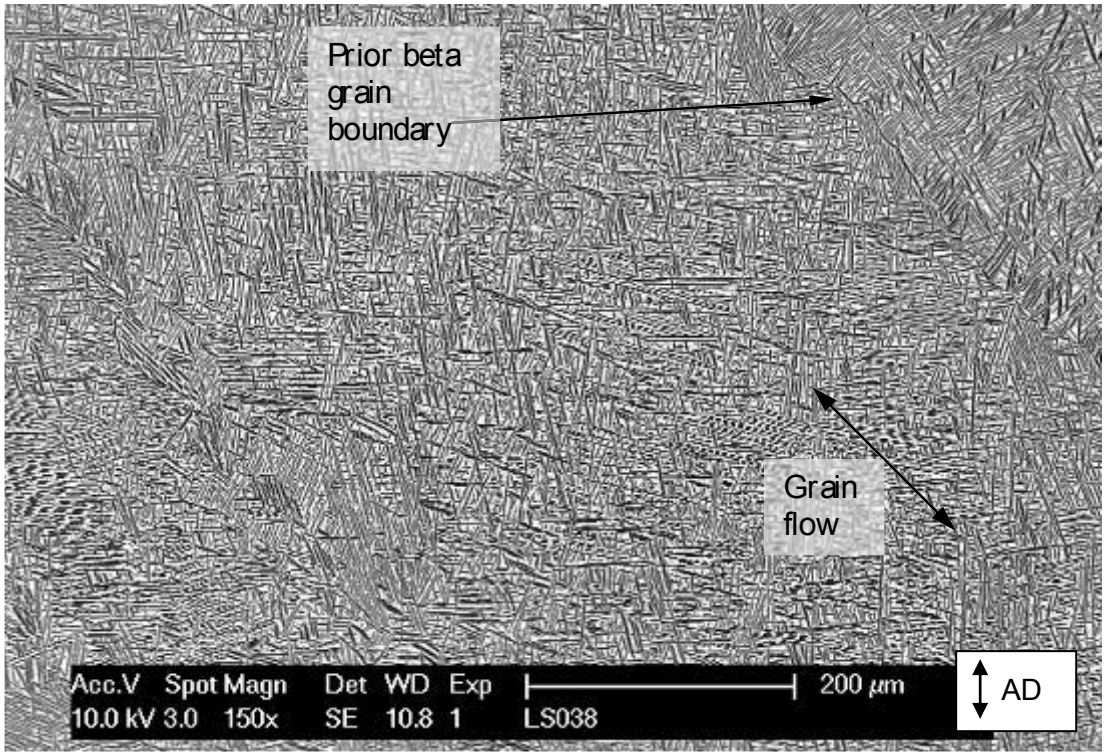

Figure 6-79 – Cold dwell fatigue tested Ti6246 specimen microstructure

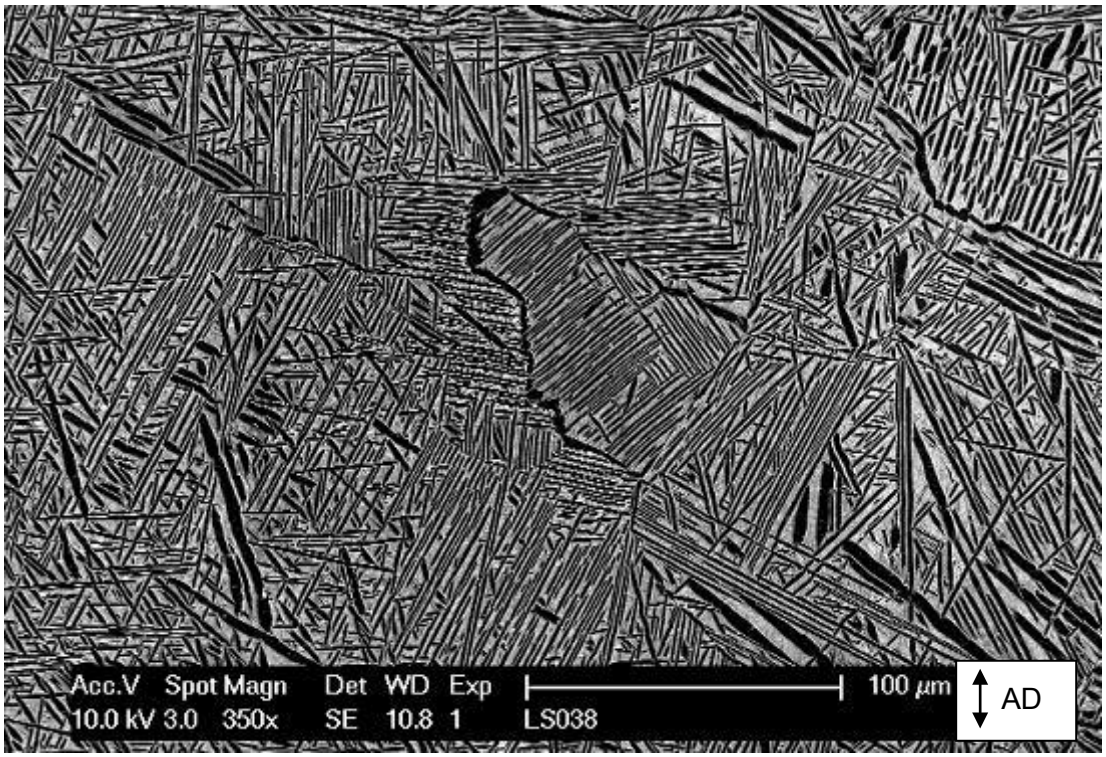

Figure 6-80 – Recrystallisation and alpha colony growth along a prior beta grain boundary in a Ti6246 DLCF test specimen

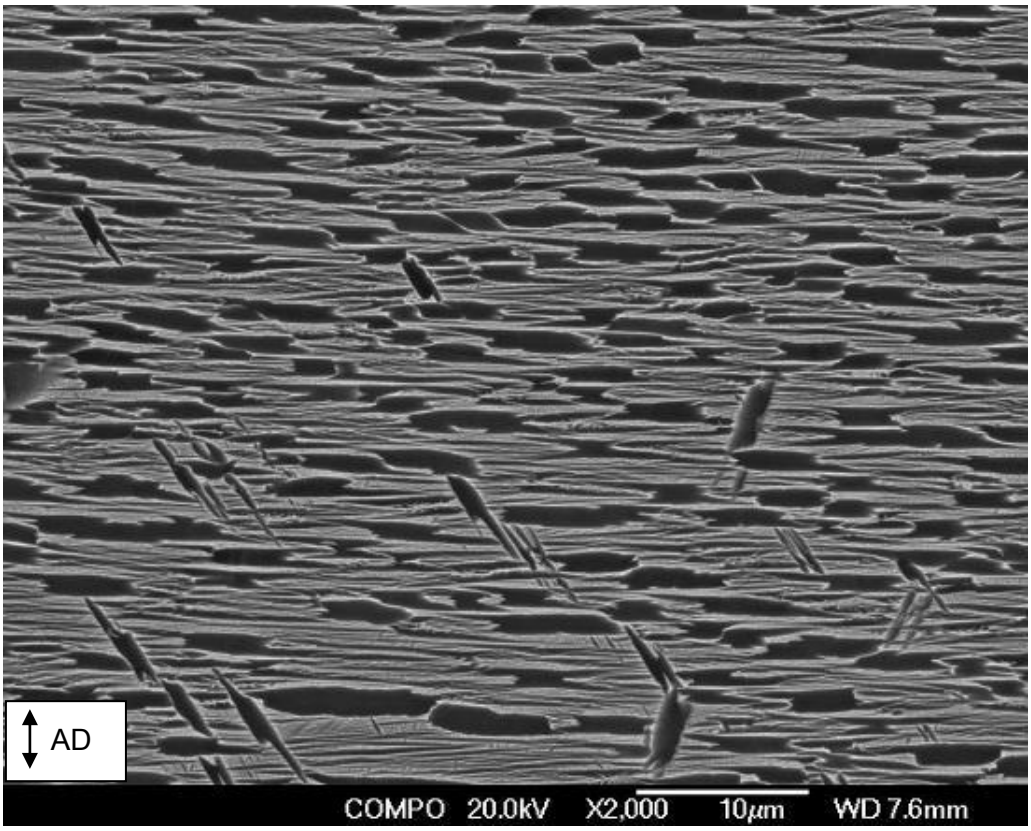

Figure 6-81 – Alignment of alpha platelet colonies with prior beta grain flow in Ti6246 disc material

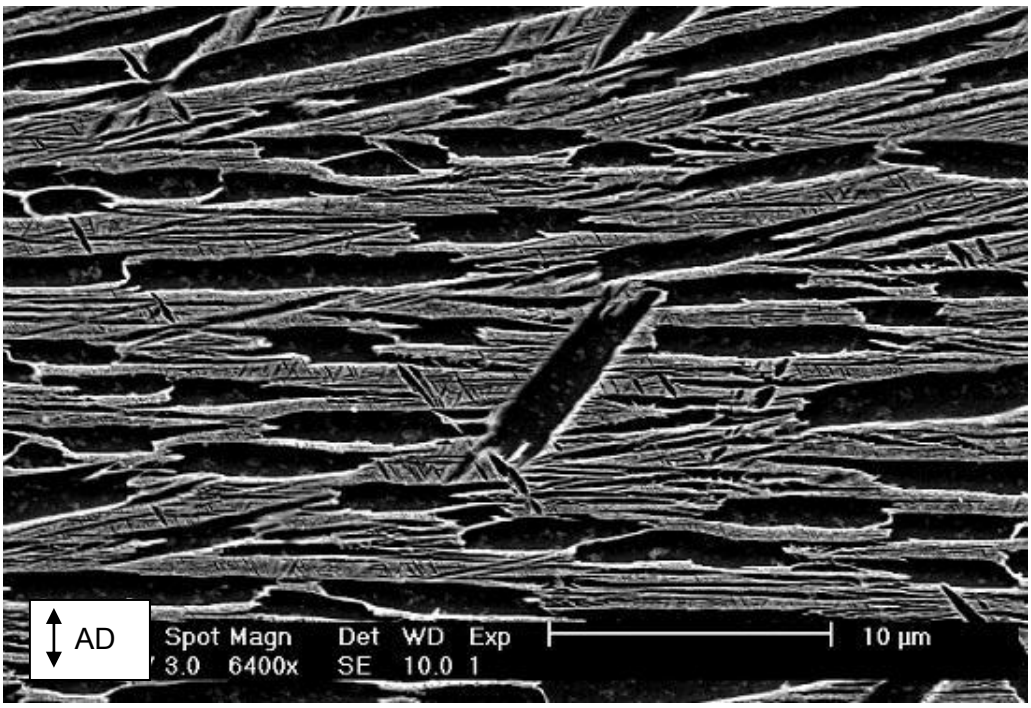

Figure 6-82 – W idmanstätten secondary alpha platelets between coarse and fine aligned primary alpha platelets in a retained beta matrix in Ti6246

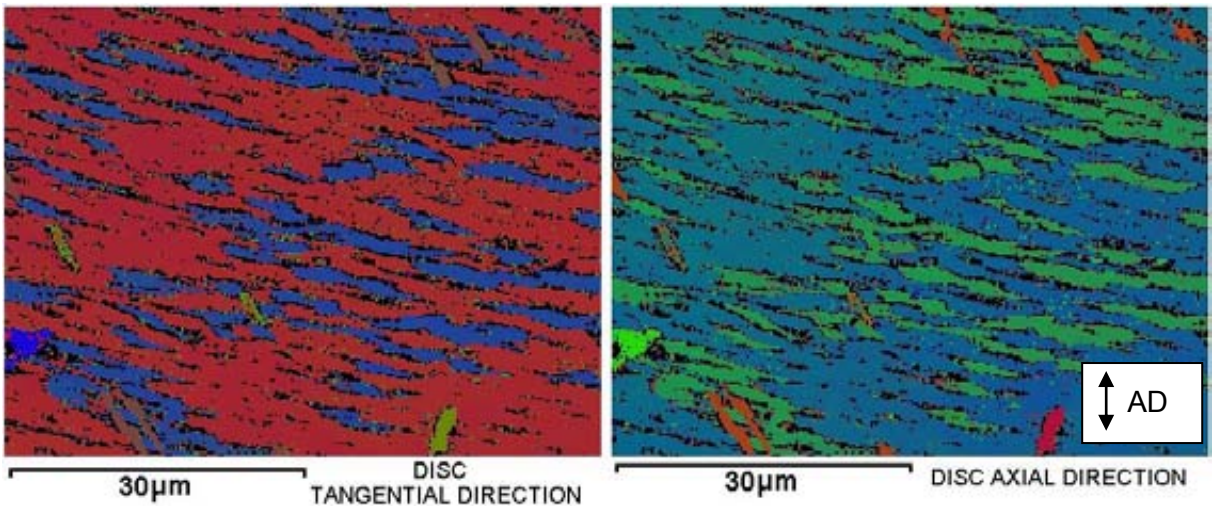

Figure 6-83 – Alpha COMs of aligned platelet colony structures (Crystal orientations displayed w.r.t. tangential and axial disc directions respectively)

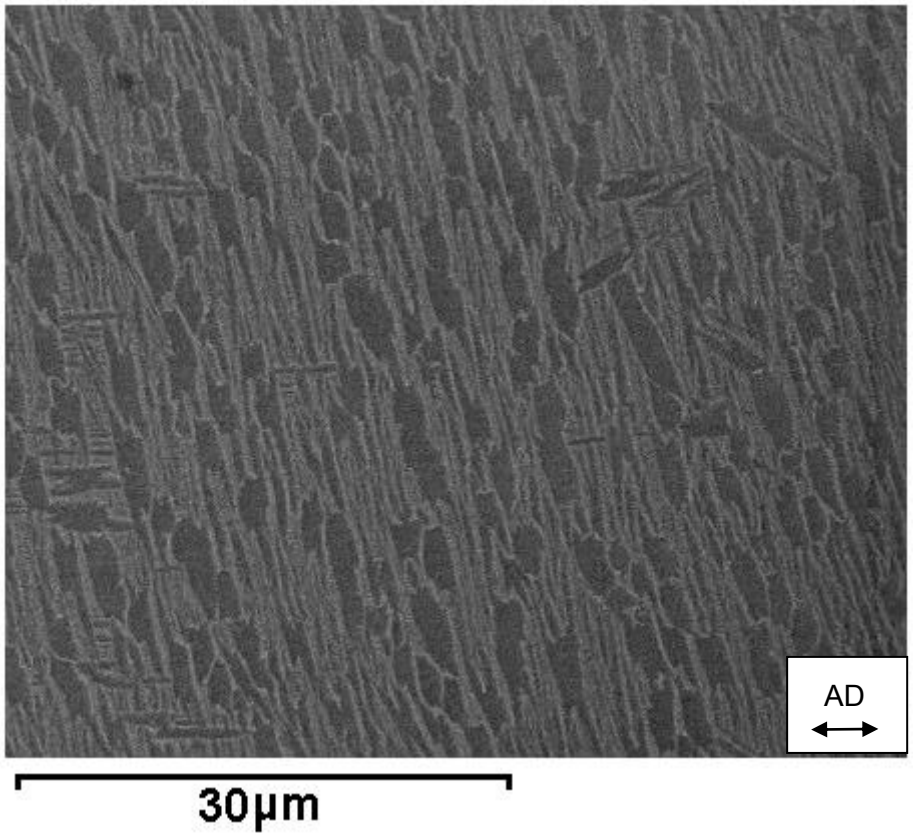

Figure 6-84 – Aligned alpha colony microstructure in Ti6246 disc material

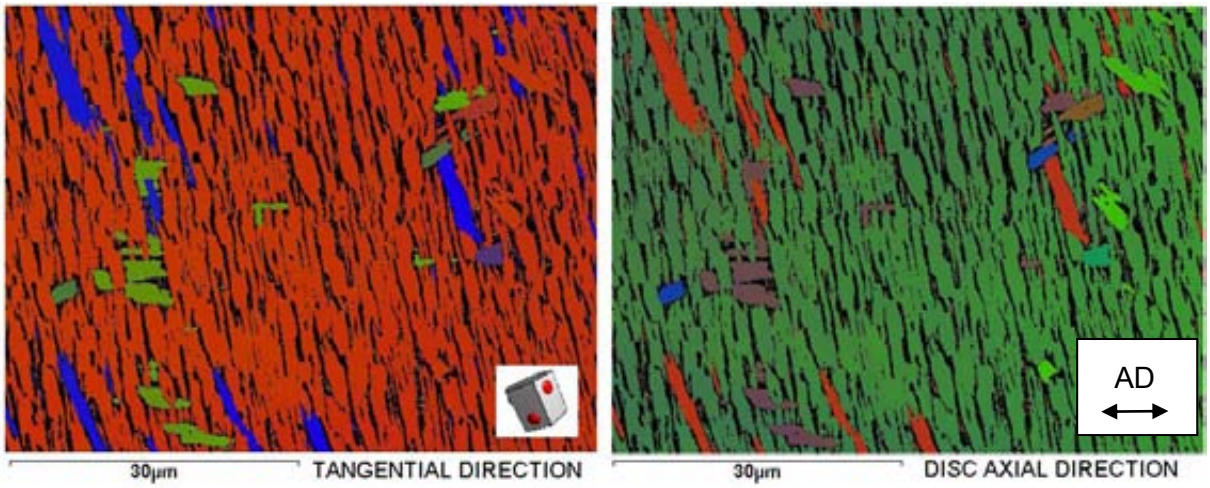

Figure 6-85 – COMs of aligned alpha platelet colony structure (Crystal orientations displayed w.r.t. tangential and axial disc directions respectively)

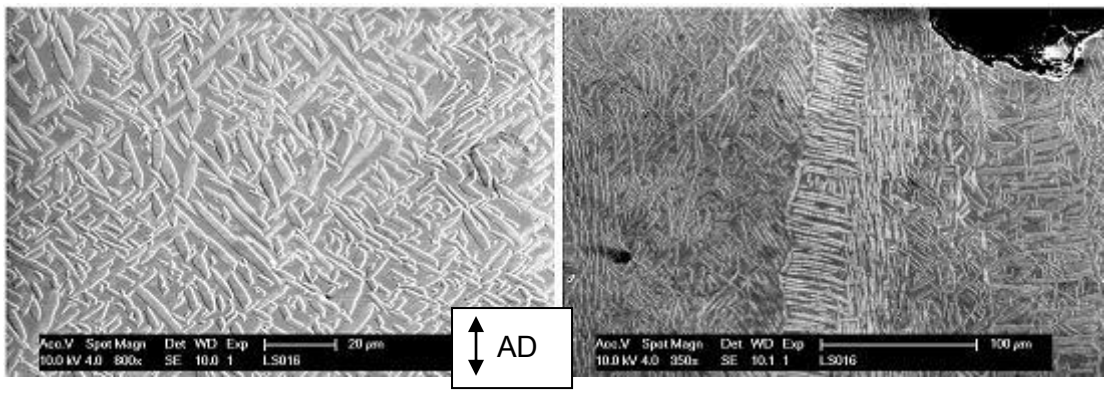

Figure 6-86 – Typical microstructure of (alpha + beta) solution heat treated Ti6246 test specimen (Vertical loading axis)

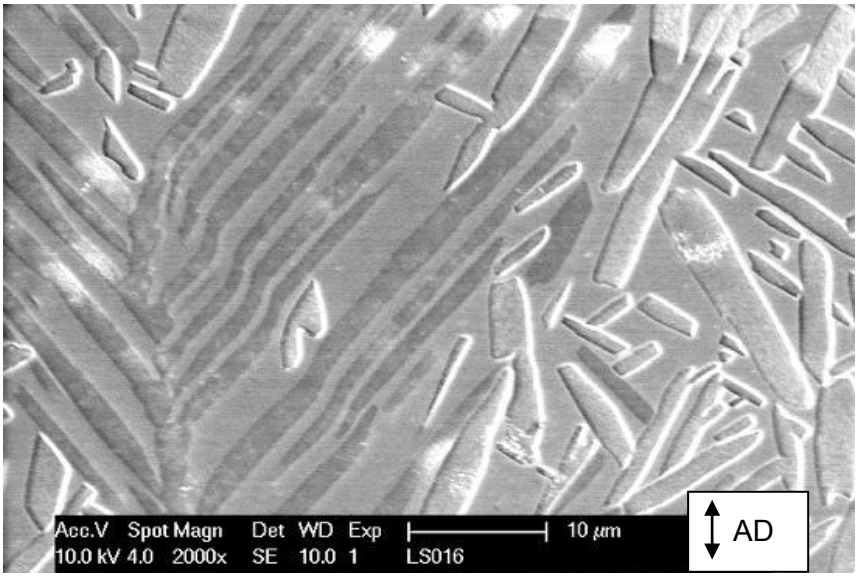

Figure 6-87 – Planar slip deformation in (alpha + beta) solutioned Ti6246

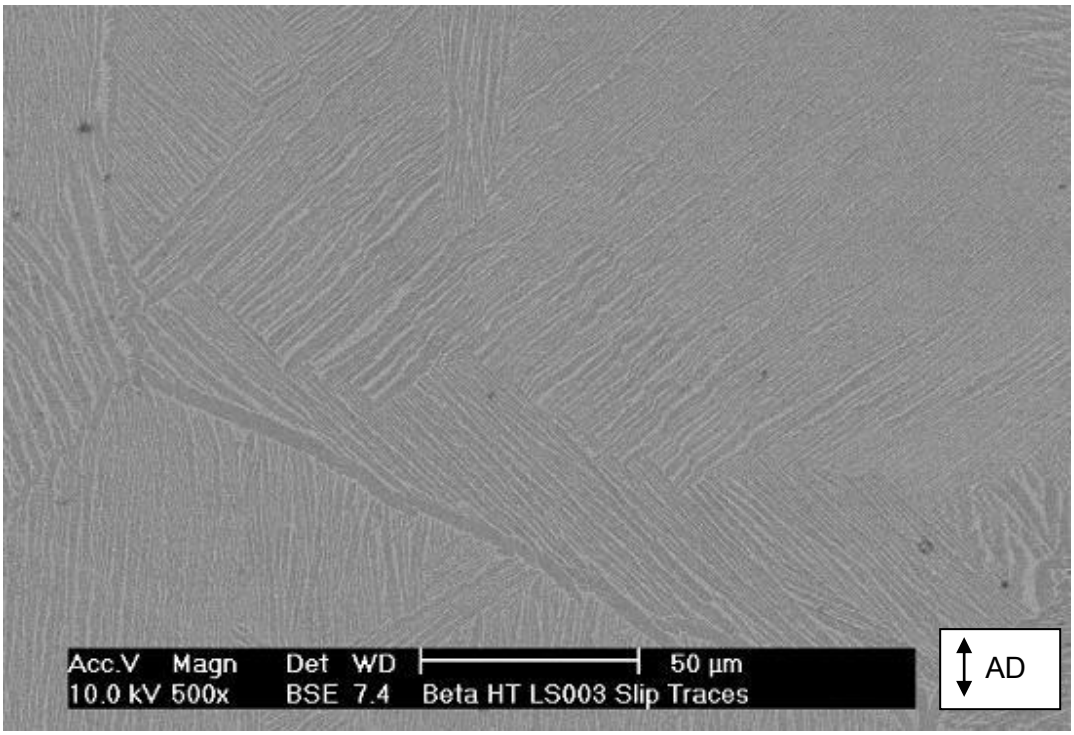

Figure 6-88 – BSE imaging microstructure of beta annealed Ti6246

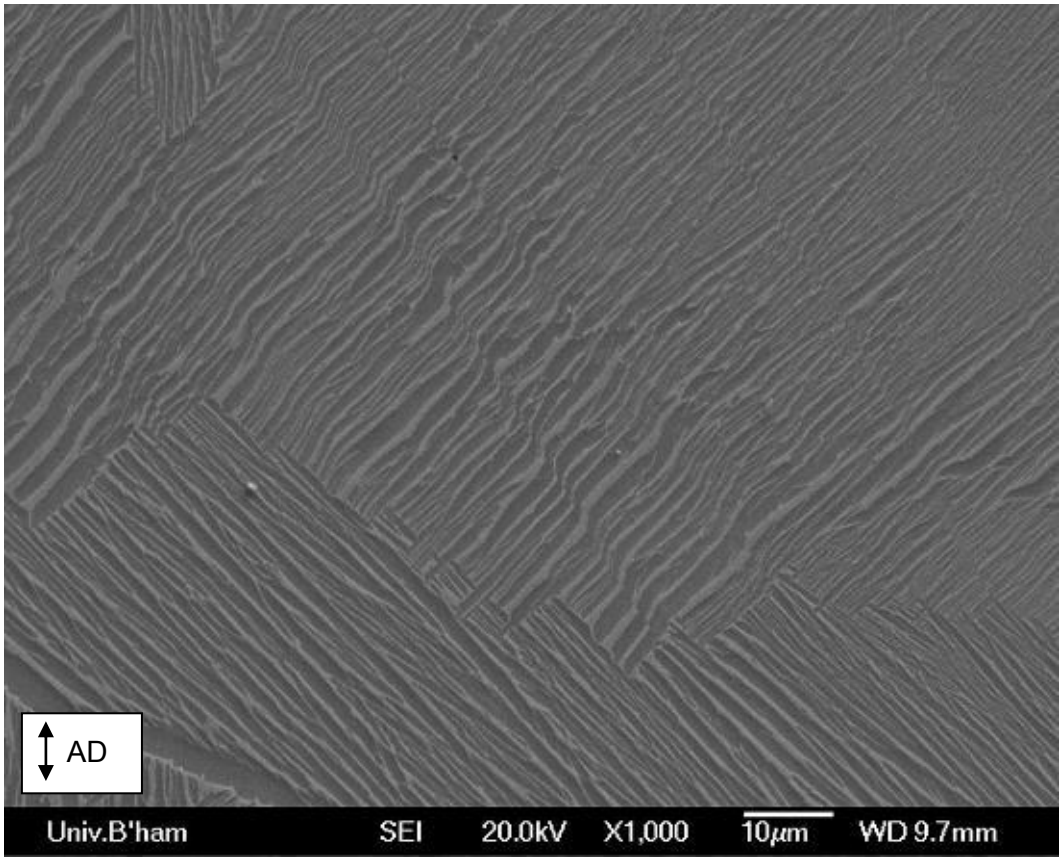

Figure 6-89 – Secondary electron imaging microstructure of beta annealed Ti6246

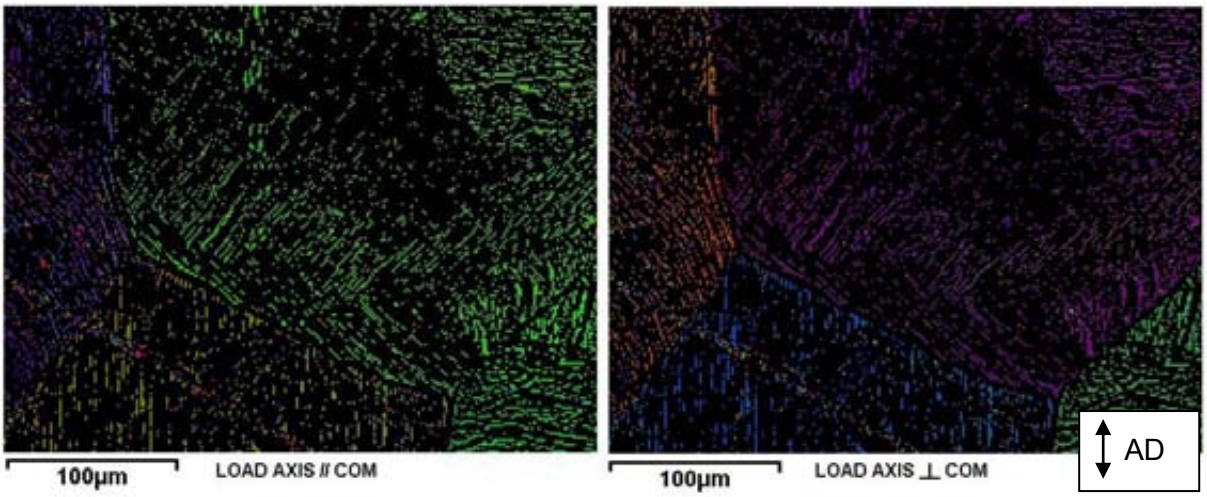

Figure 6-90 – Beta COMs for beta annealed Ti6246
(Crystal orientations displayed w.r.t. loading axis and load normal direction respectively)

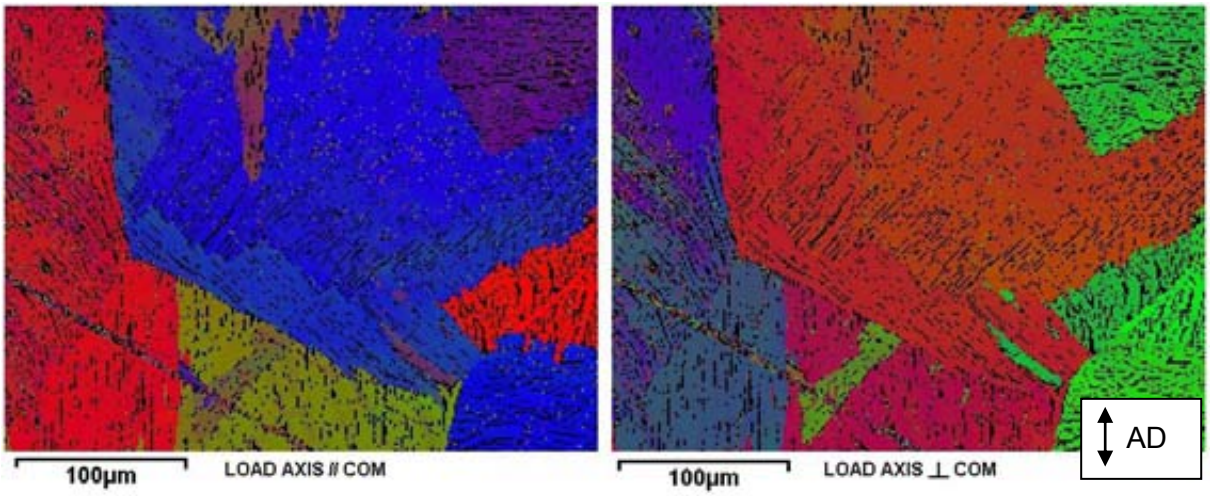

Figure 6-91 – Alpha COMs for beta annealed Ti6246
(Crystal orientations displayed w.r.t. loading axis and load normal direction respectively)

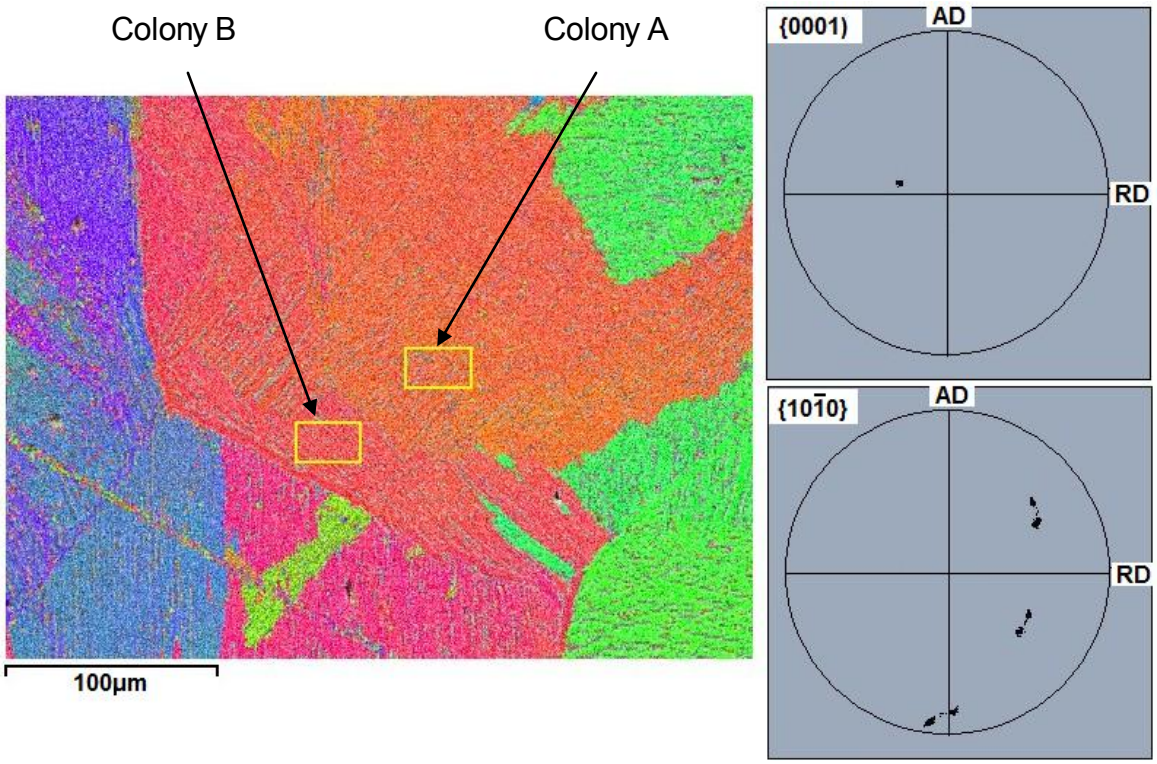

Figure 6-92 – Colonies A and B in beta annealed Ti6246 with corresponding basal and prism pole figures showing a shared {0001} plane

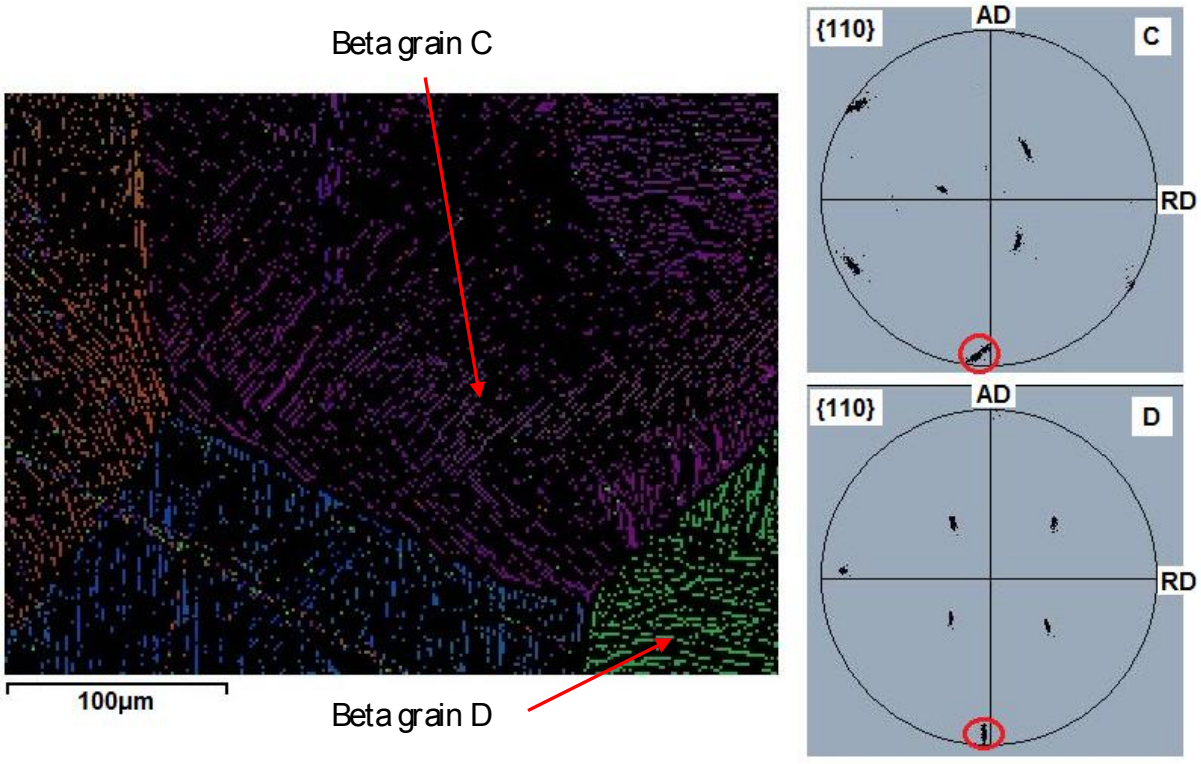

Figure 6-93 – Common {110} pole in neighbouring prior beta grains C and D in beta annealed Ti6246 circled in red

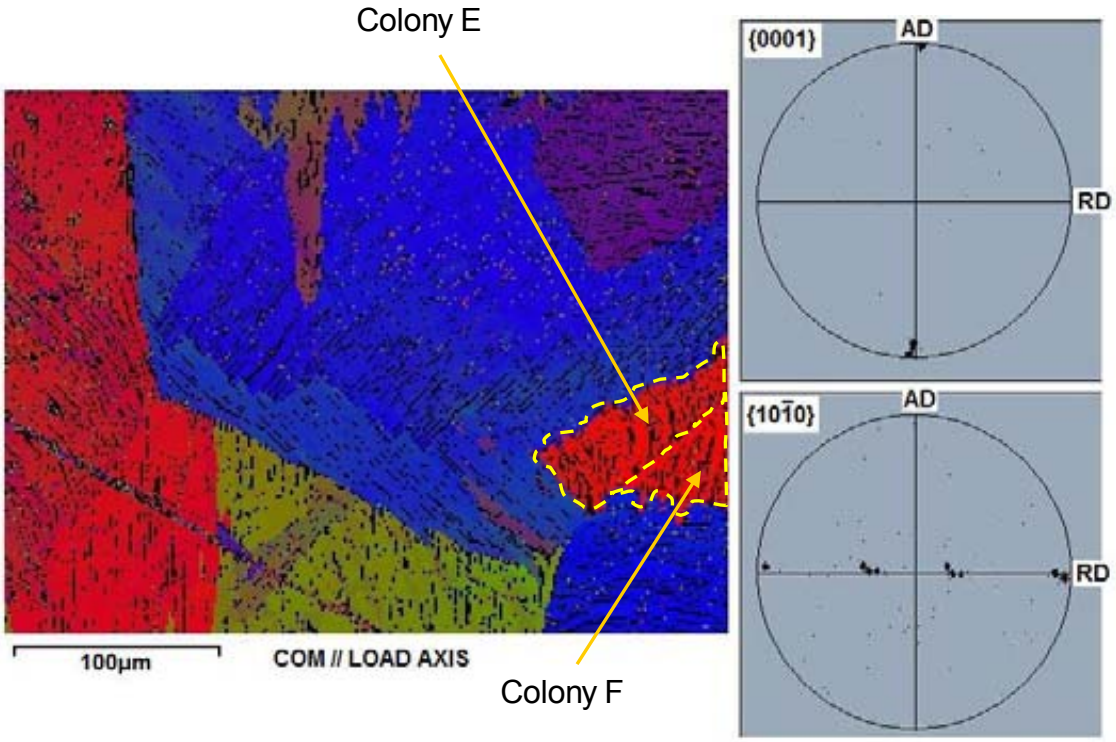

Figure 6-94 – Alpha colonies E and F and associated pole figures in beta annealed Ti6246

6.7.7 Ti829 disc and test specimens

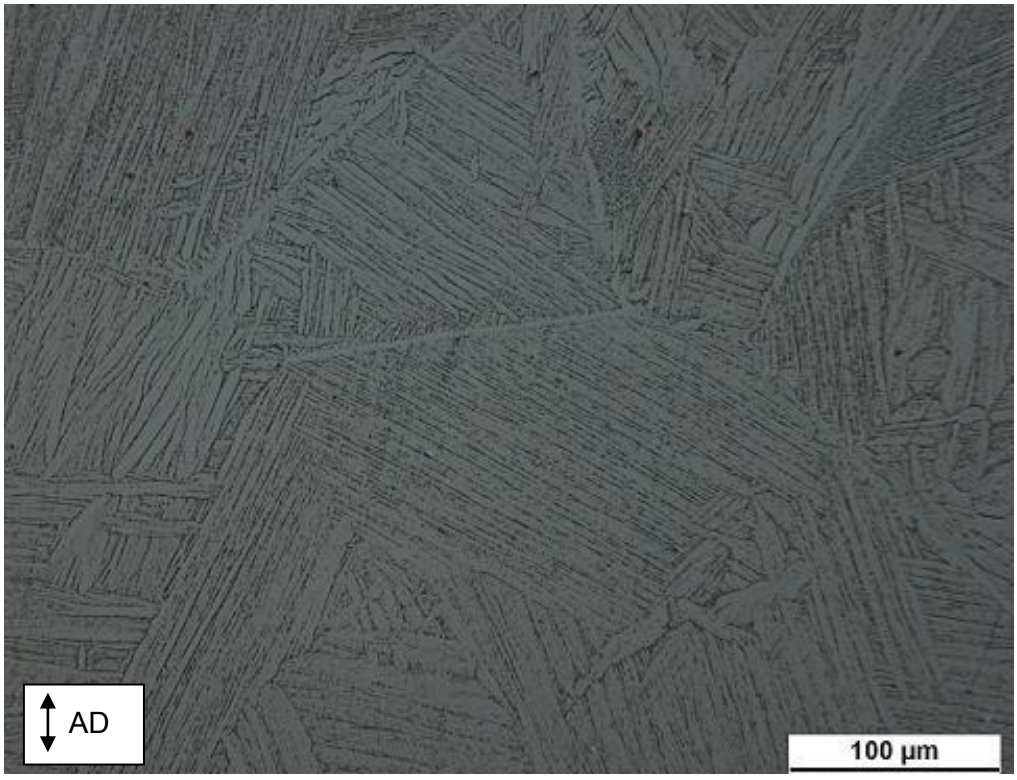

Figure 6-95 – Typical optical microstructure of Ti829 disc material

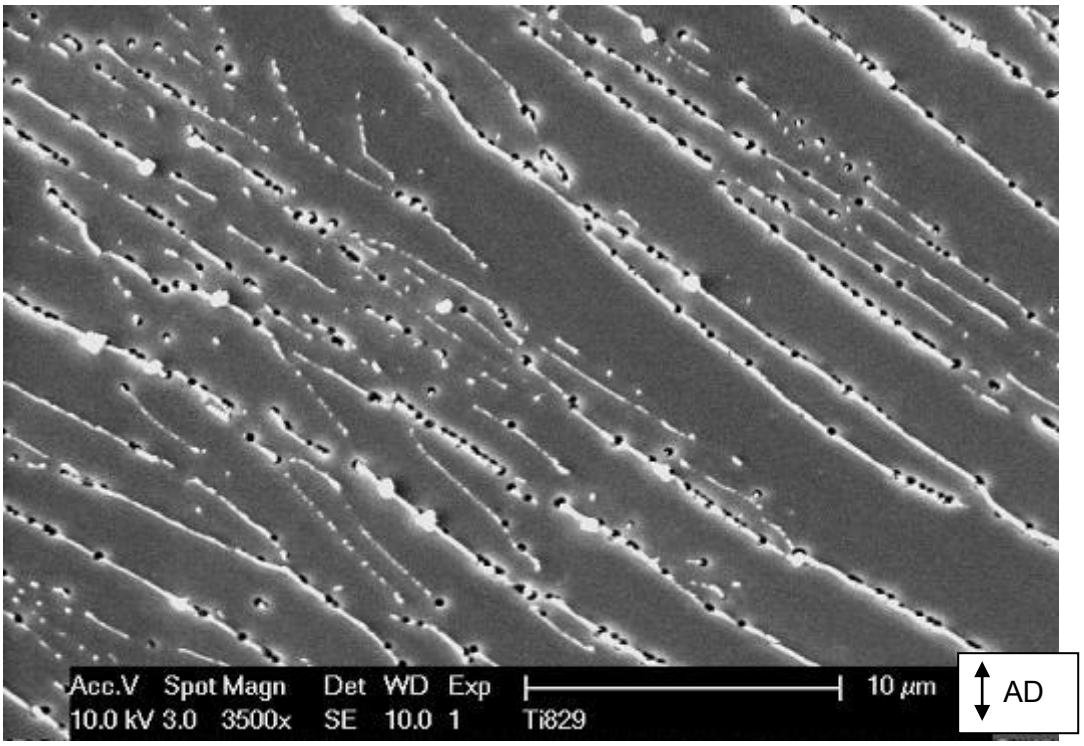

Figure 6-96 – Typical beta film structure in Ti829 disc material

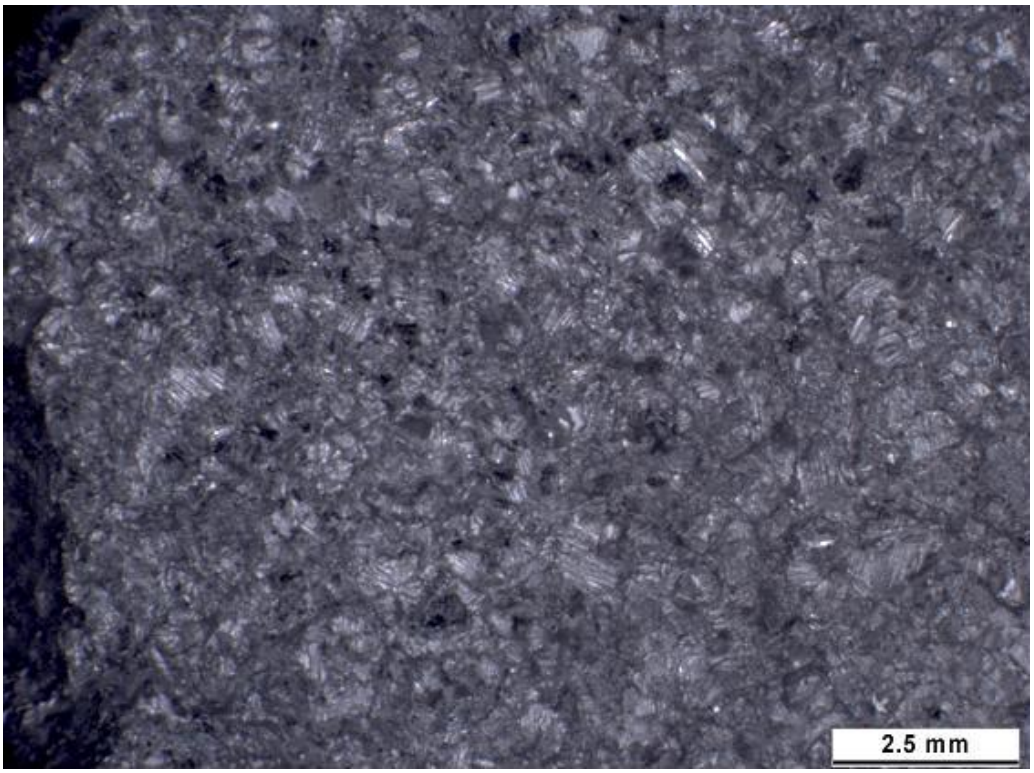

Figure 6-97 – Ti829 LCF test specimen fracture surface (σ_{max} ~91%UTS, R = 0, T = 20ºC, 15cpm)

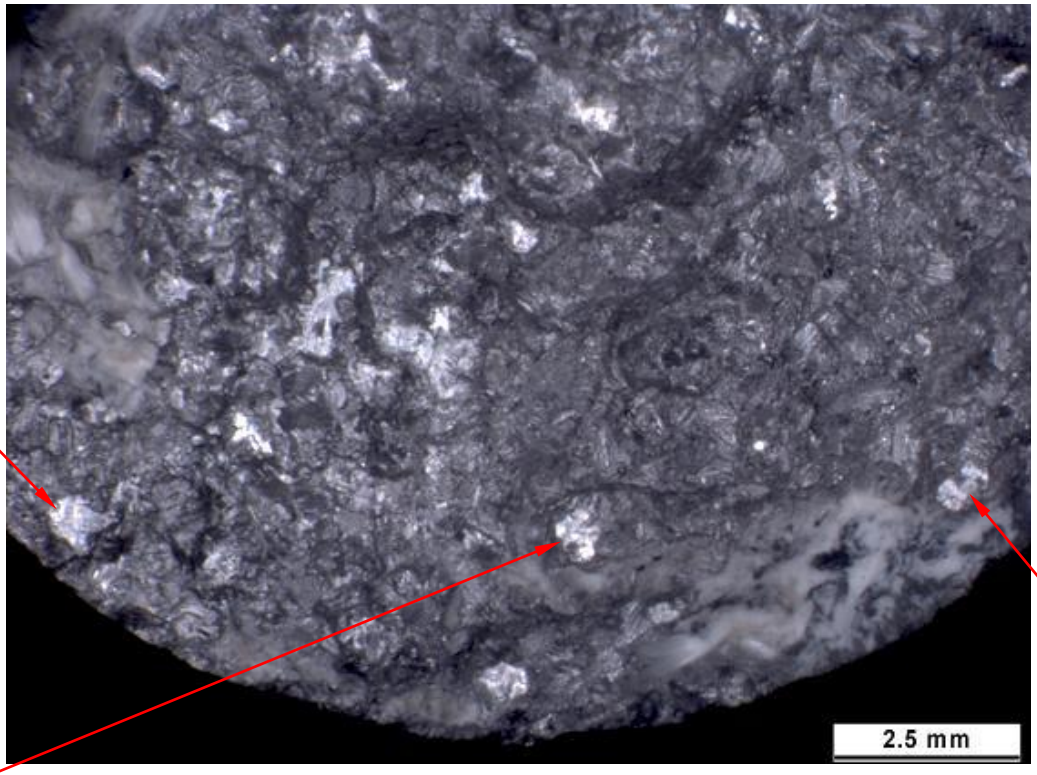

Figure 6-98 – Ti829 dwell LCF test specimen fracture surface (σ_{max} ~76%UTS, R = 0, T = 80ºC, 2 minute dwell)

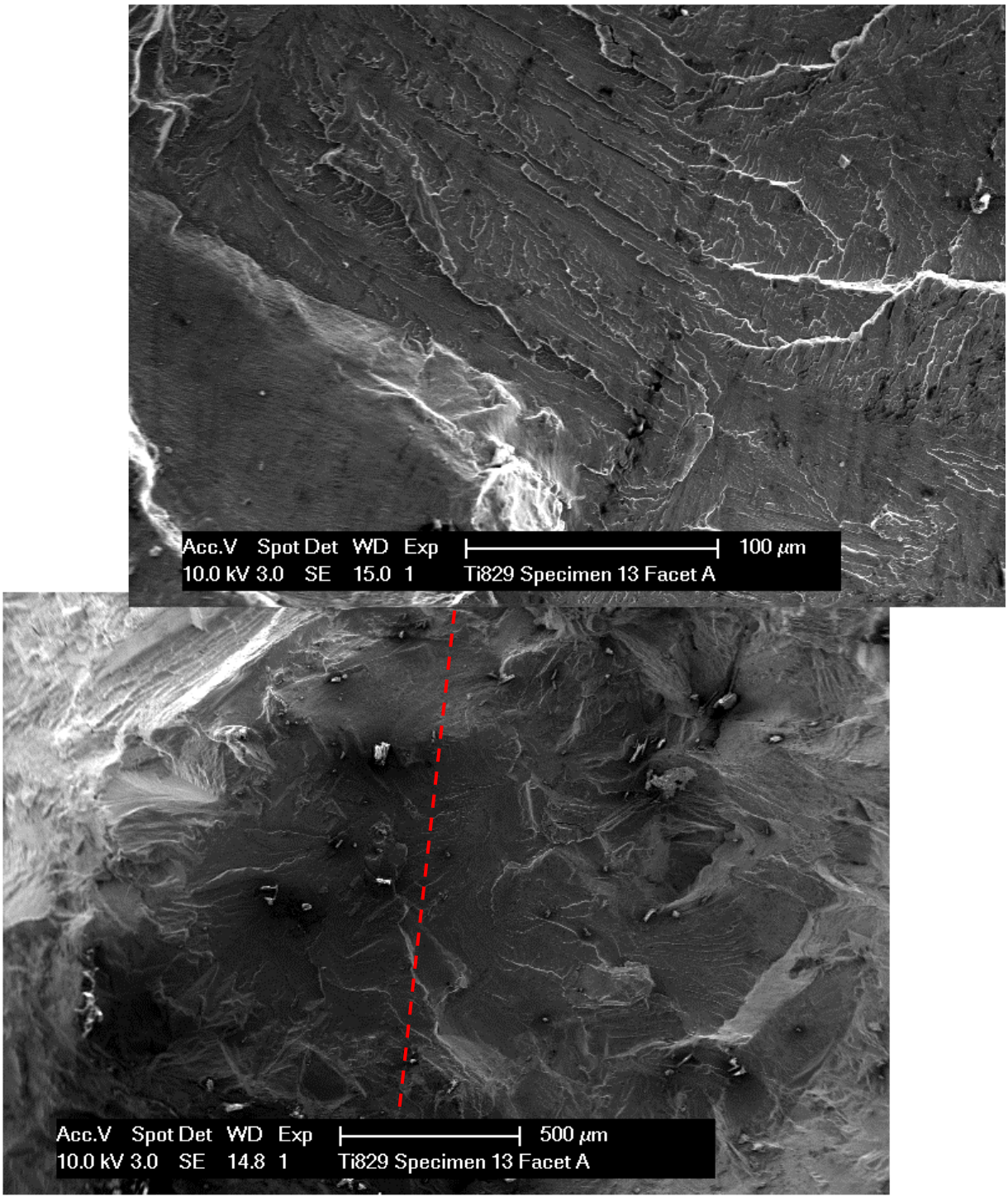

Figure 6-99 – Ti829 dwell LCF test specimen fracture surface – Facet A

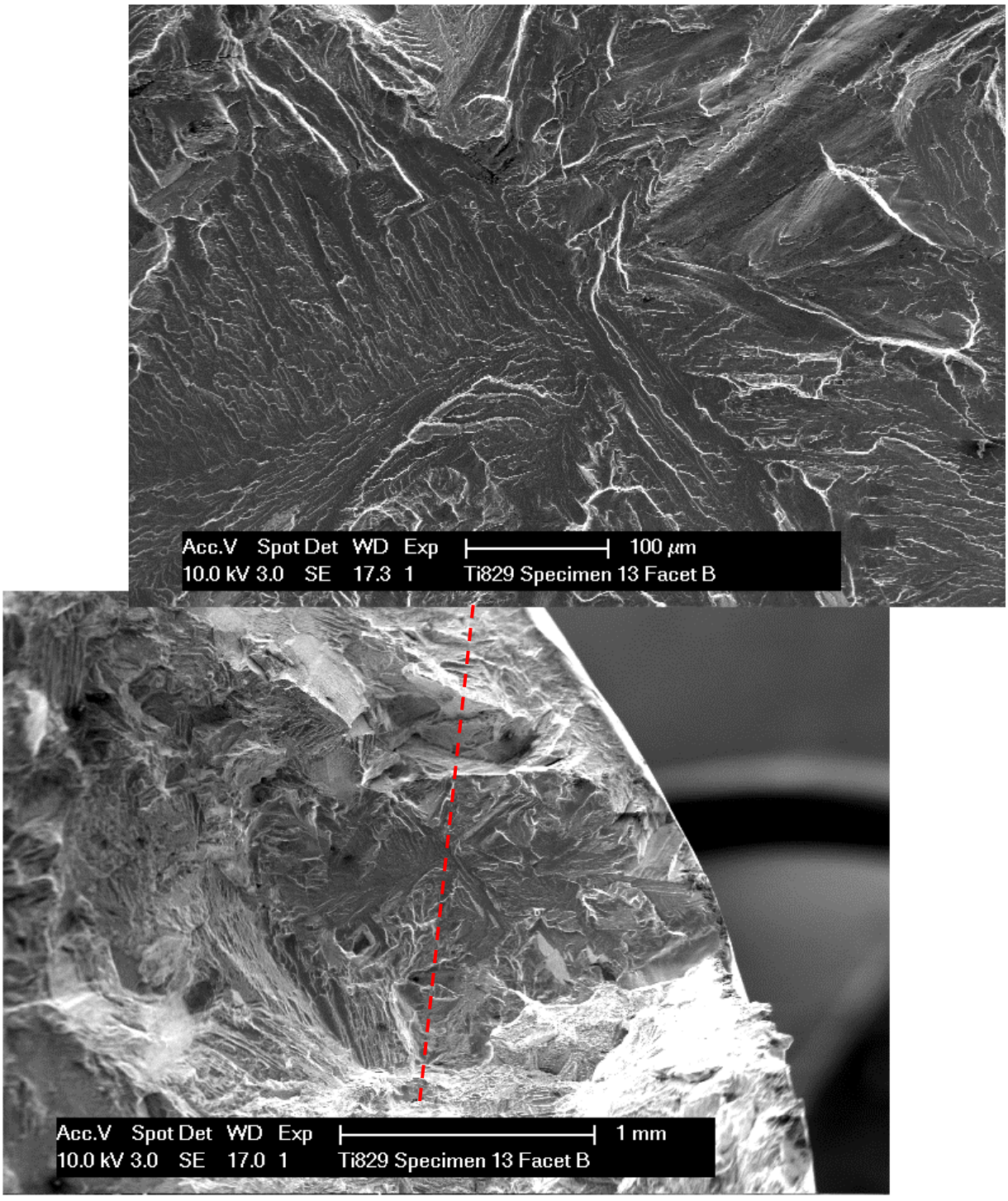

Figure 6-100 – Ti829 dwell LCF test specimen fracture surface – Facet B

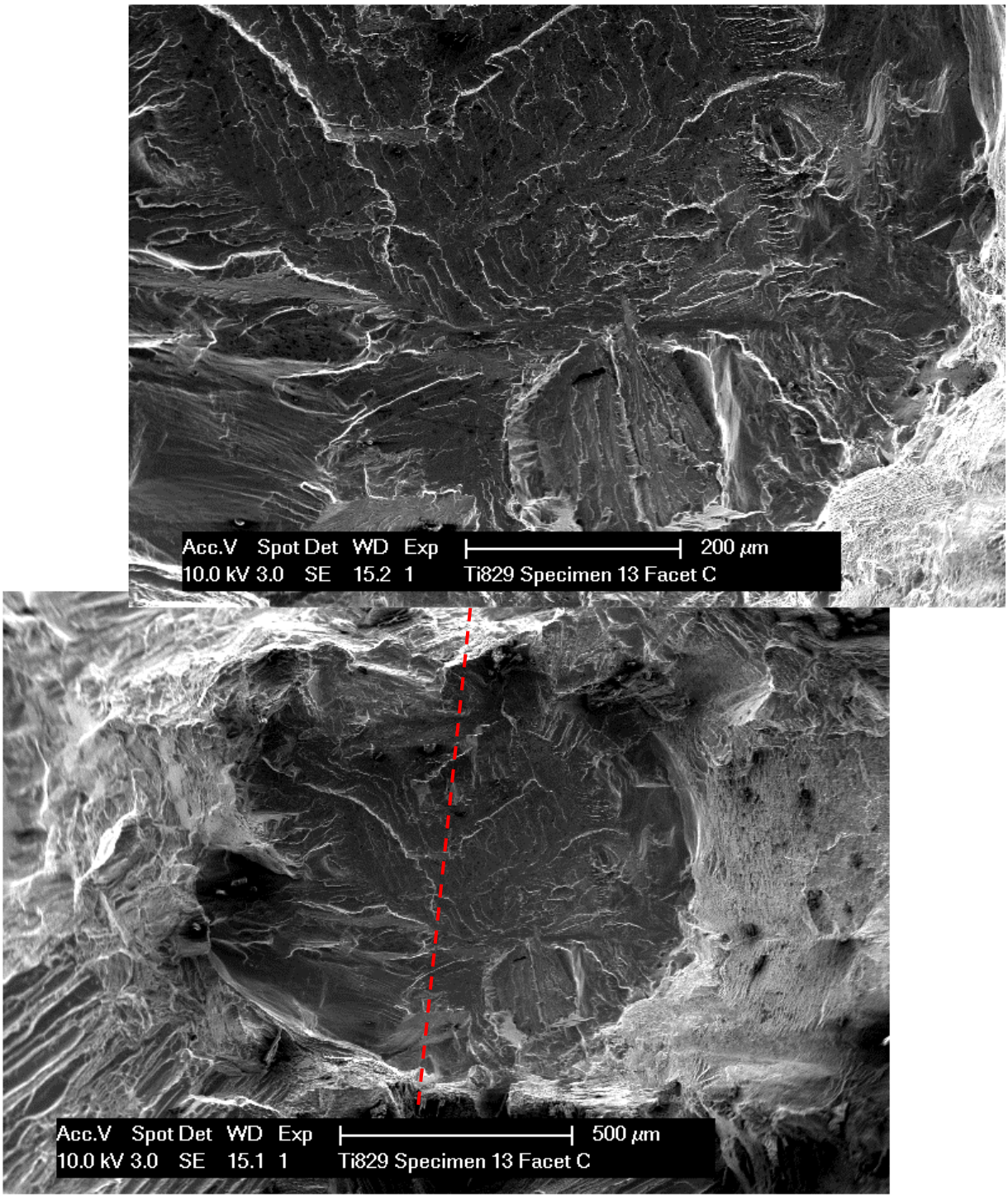

Figure 6-101 – Ti829 dwell LCF test specimen fracture surface – Facet C

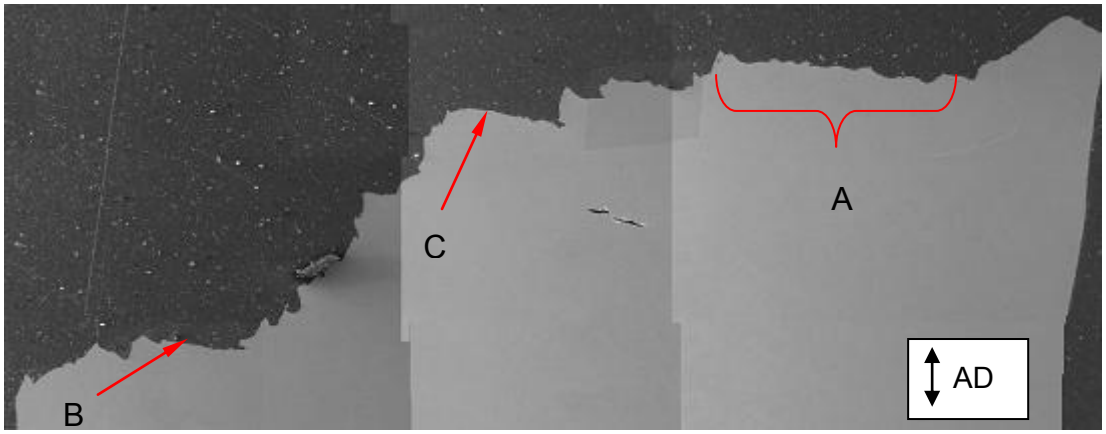

Figure 6-102 – Ti829 dwell LCF test specimen fracture surface cross-section

Figure 6-103 – Optical microstructure of Ti829 DLCF specimen facet B cross-section

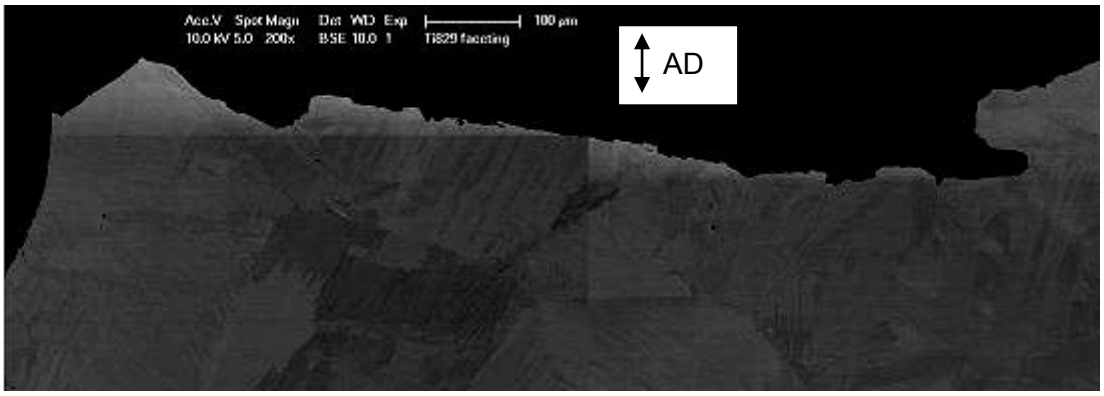

Figure 6-104 – Secondary electron imaging microstructure of facet B

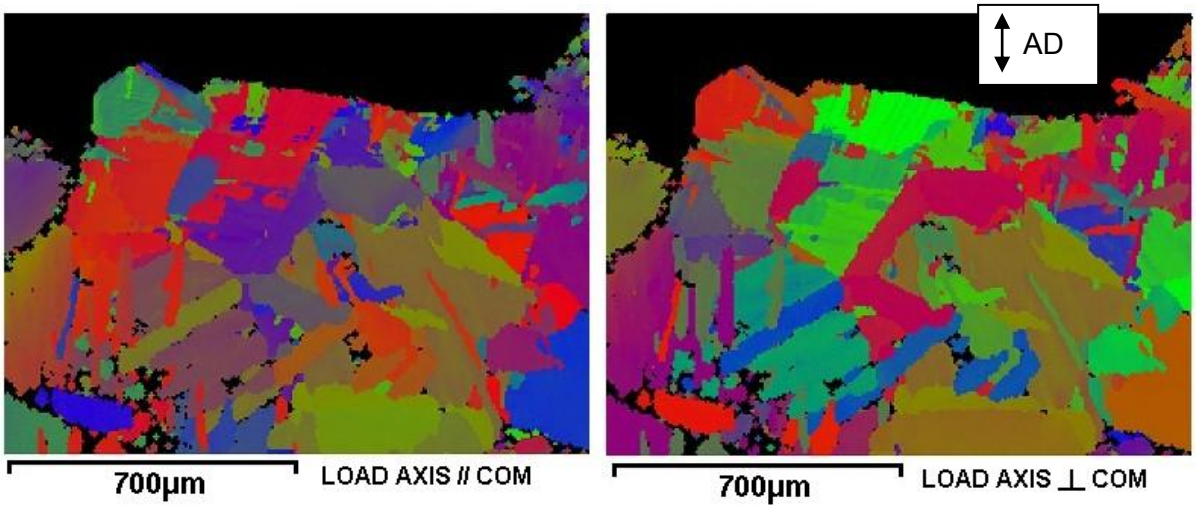

Figure 6-105 – Ti829 specimen facet B alpha COMs (Textures displayed w.r.t loading axis direction and loading axis normal direction)

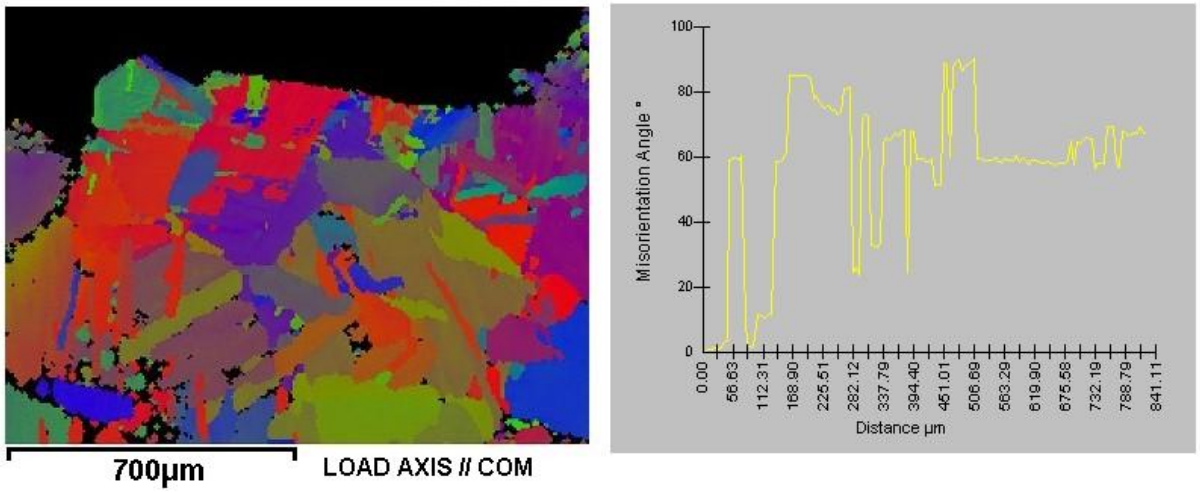

Figure 6-106 – Misorientations of alpha colonies along facet B

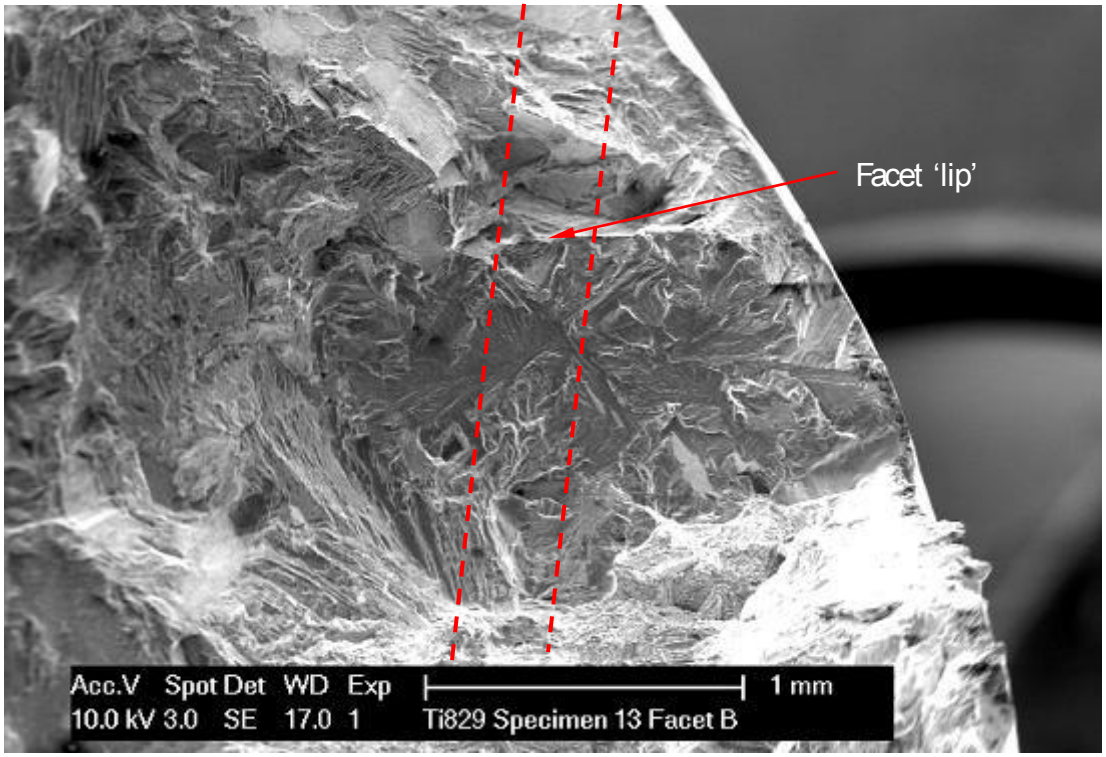

Figure 6-107 – Approximate position of sectioned plane through facet B in Ti829 DLCF test specimen

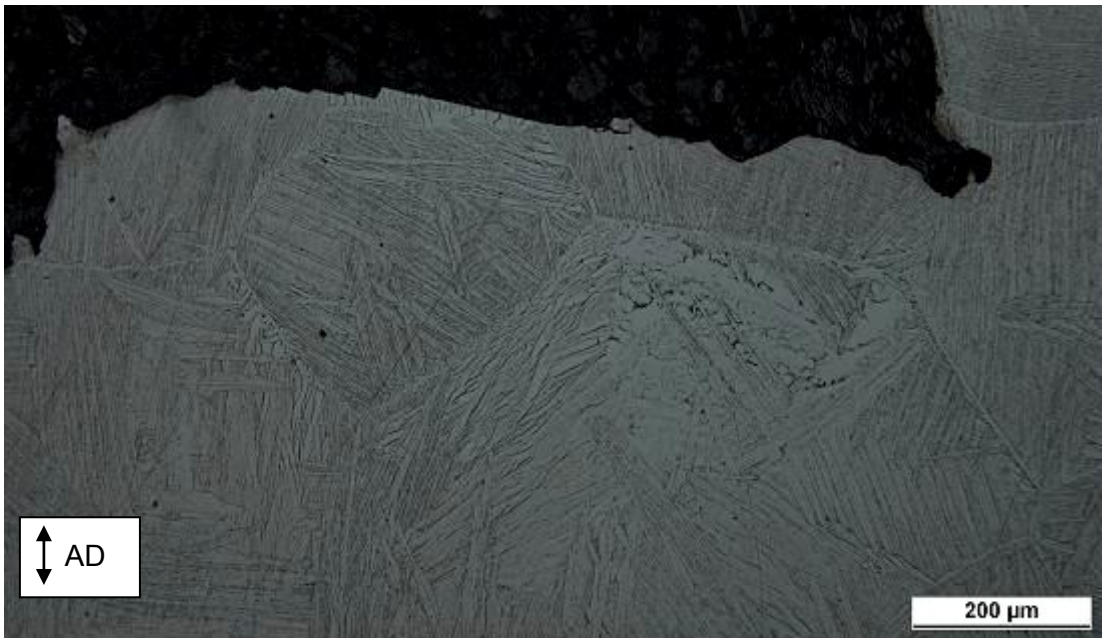

Figure 6-108 – Optical microstructure of Ti829 DLCF specimen facet C cross-section

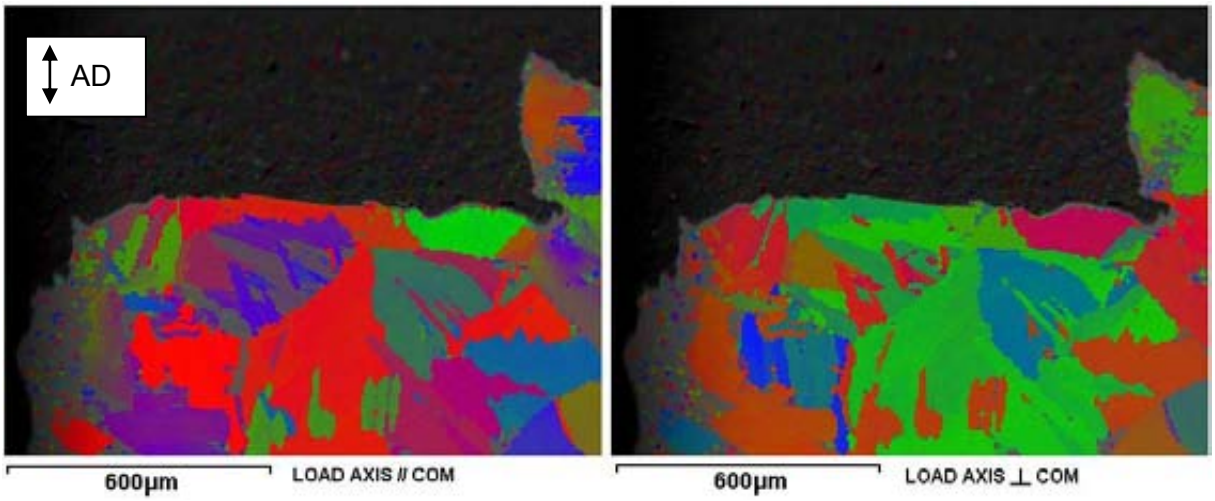

Figure 6-109 – Ti829 specimen facet C alpha COMs (Textures displayed w.r.t loading axis direction and loading axis normal direction)

6.7.8 Conclusions

Table 6-2 – Macrozone and facet sizes in titanium alloys

Alloy/Product form	Macrozone dimensions	Facet (ESU) size	Previous cold dwell fatigue behaviour?
Ti685 disc	<1000µm across, typically equiaxed morphologies	Up to ~2000µm	Yes [90, 178]
Ti6/4 fan disc	Up to ~750-1000µm	'Diffuse' facet size of 2000-3000µm across 'Sharp' facet ~1250µm in length	Yes [81, 178]
Ti834 disc	Up to ~100-200µm	'Diffuse' facet size of 3000-4000µm across [132]	Yes [102]
Ti6242 disc	Up to ~50-100µm	Up to ~2000µm [118]	YES [118]
Ti6242 billet	~750-1000µm length, 100-200µm width	Unknown	Unknown. Likely susceptibility based on behaviour of disc material [81, 118]
Ti6246 disc (Beta forged)	= Alpha colony size, varying depending on beta grain shape, size and post-forge processing	20-100µm depending on colony size & orientation	NO [164]
Beta HT Ti6246*	= Alpha colony size	Up to ~1000µm	NO [69]
Ti829 disc	Up to ~200-300µm	Up to ~1000µm	YES [81]

* Non-standard microstructural condition

7 Processing effects on texture in Ti6246 forgings....7-1
7.1 Introduction....7-1
7.2 Experimental method....7-2
7.3 Results....7-5
7.3.1 Grain flow....7-5
7.3.2 Microstructure and texture assessments....7-5
7.3.2.1 As-forged condition....7-5
7.3.2.1.1 Isothermal pancake forging....7-6
7.3.2.1.2 Hot die pancake forging....7-8
7.3.2.1.3 Hammer pancake forging....7-11
7.3.2.2 Solution heat treated condition....7-13
7.3.2.2.1 Isothermal pancake forging....7-13
7.3.2.2.2 Hot die pancake forging....7-16
7.3.2.2.3 Hammer pancake forging....7-19
7.3.2.3 Age heat treated condition....7-21
7.3.2.3.1 Isothermal pancake forging....7-22
7.3.2.3.2 Hot die pancake forging....7-23
7.3.2.3.3 Hammer pancake forging....7-23
7.3.2.4 Production disc forgings....7-23
7.4 Discussion....7-25
7.4.1 Effect of forging method on grain flow and optical microstructure....7-25
7.4.1.1 Isothermal forging....7-26
7.4.1.2 Hot die forging....7-30
7.4.1.3 Hammer forging....7-32
7.4.2 Effect of forging method on crystallographic texture....7-37
7.4.2.1 Isothermal forging....7-37
7.4.2.2 Hot die forging....7-41
7.4.2.3 Hammer forging....7-42
7.4.3 Cold dwell fatigue behaviour/Effective structural unit size effects....7-44
7.5 Conclusions....7-47
7.5.1 Isothermal forging....7-47
7.5.2 Hot die forging....7-48
7.5.3 Hammer forging....7-49

7B Volume B - Figures and tables....7-51
7.6 Experimental details....7-51
7.7 Results....7-53
7.7.1 Grain flow profiles....7-53
7.7.2 Microstructure and texture assessment....7-55
7.7.2.1 Isothermal pancake – As-forged condition....7-55
7.7.2.2 Hot die pancake – As-forged condition....7-64
7.7.2.3 Hammer pancake – As-forged condition....7-68
7.7.2.4 Isothermal pancake – Solution heat treated condition....7-75
7.7.2.5 Hot die pancake – Solution heat treated condition....7-83
7.7.2.6 Hammer pancake – Solution heat treated condition....7-93
7.7.2.7 Isothermal pancake – Age heat treated condition....7-100
7.7.2.8 Hot die pancake – Age heat treated condition....7-102
7.7.2.9 Hammer pancake – Age heat treated condition....7-103
7.7.2.10 Production disc forgings....7-105
7.8 Discussion....7-108

7 Processing effects on texture in Ti6246 forgings

7.1 Introduction

Pancake forgings were produced by Ladish (Cudahy, USA) with the intention of assessing texture development and the relationship to the processing route. The purpose of the task was to evaluate the effects of strain, strain rate and post forge cooling rate on the microstructure, specifically texture.

Three Ti6246 forgings were assessed. Forgings were studied in their as-forged, solution heat-treated, and aged conditions to establish processing effects on the evolution of microstructure and texture.

The work undertaken included an assessment of the variation of optical microstructures through an axial-radial plane cross-section. EBSD analysis of texture was also undertaken for the selected pancake forgings in specific locations.

A comparison of optical microstructures and texture is provided for hammer, hot die and isothermal forgings. A comparison is also made of the variation in these parameters between high strain/low cooling rate and low strain/high cooling rate sections of each pancake.

7.2 Experimental method

The experimental details of the forging methods for each of the forgings examined are listed in Table 7-1. All pancakes used Ti6246 billet with a normal starting grain size and microstructure. Forging was undertaken in the beta phase field to give a 70% reduction in height. Final pancake dimensions were ~220mm diameter and ~45mm axial height.

Pancake forgings were divided into two 'half-moon' sections; one left in an as-forged condition, the other solution heat-treated and aged as for following standard material (910˚C for 2hrs then fan air cool, 595˚C for 8hrs then air cool). These half pancakes were designated B and A respectively.

Slices of ~20mm thickness were taken from the inner face of both halves of the pancake forging. Each slice was divided into two parts at the centre. The schematic of the pancake cut-up is displayed in Figure 7-1. In this diagram (L) refers to Ladish, RR to Rolls-Royce. FGed refers to as-forged condition and HTed refers to the heat-treated condition.

Ladish used computer software to model the effective strain distribution through the pancake forging cross-section. The predicted strain profile for an axial-radial slice through the pancake (centre to edge) is displayed in Figure 7-2.

The slices taken from the fully heat-treated half of the pancake were examined for grain flow and microstructure. Standard metallographic procedures (described in chapter three) were used. Optical assessments were taken at two positions on each pancake forging, labelled A and F as shown in Figure 7-3. These positions provide a comparison of microstructures across the range of forging strains and cooling rates in each pancake (see Figure 7-2).

Each as-forged (AF) slice was divided into 4 sections along the radial direction, designated A to D (centre to edge). The cut-up of the as-forged slice is illustrated in Figure 7-4. These

slices were polished and etched (by Ladish) to show microstructure and grain flow. For the current work they were received in this condition.

For pancakes 1, 2 and 5 (isothermal, hot die and hammer forgings – see Table 7-1) the section of the slice designated A was sectioned into three smaller slices along the axial-radial plane as illustrated by the dashed red lines in Figure 7-4. These three slices were used in a study of the microstructural and texture evolution from the as-forged condition following solution heat treatment and then ageing operations. As the three slices were taken from a small volume of the pancake a similar strain distribution was assumed in each case (identified by the dashed red outline in Figure 7-2). On this basis a back-to-back comparison of the microstructure and texture was made in the as-forged, solution heat-treated and aged conditions for the three different forging types.

EBSD maps were taken from two sites for each pancake. These were approximately equivalent to location A (forging centre, high ε, low ΔT) and location F ('dead zone', low ε, high ΔT) as displayed in Figure 7-3. In selecting these positions the most extreme forging conditions were assessed to study the variability of texture in an individual pancake. For each EBSD assessment the corresponding optical microstructure was examined to correlate the texture and microstructure for the different forging types and stages of heat treatment.

Small samples (~5mm height * 5mm width * 5mm depth) were sectioned from pancake forging locations A and F using metallographic cut-up equipment for EBSD analysis. Low cutting speeds were used to prevent excessive heating or deformation. Standard metallographic preparation was undertaken.

Low magnification EBSD maps were acquired to study "macro-texture" over as large (i.e. representative) an area as possible. These maps were obtained over an area of ~1.2mm x

~0.9mm using a mapping resolution of 256 * 192 pixels. These settings give an individual pixel area of ~23μm^2 and a step size of ~4.8µm.

In addition to macro-texture analysis, more localised 'micro-texture' maps were obtained to study particular features of interest such as alpha platelet colonies or recrystallised grains. The area of the site of interest was selected accordingly. Map resolution was usually selected as 256*192 pixels. The step size varied with the mapping area.

In this work it is recognised that EBSD maps do not assess a sufficiently large area to accurately characterise macro-textures. The maps only provide an indication of the expected wider texture. The X-ray diffraction technique would be a suitable means to clearly identify both deformation and recrystallisation textures in the different forgings [158, 161].

7.3 Results

7.3.1 Grain flow

Grain flow profiles for pancake forgings in a fully heat treated condition are given in Figure 7-5 to Figure 7-7. The compression axis (axial direction) is vertical and the radial direction is horizontal.

Each pancake slice is ~40mm in axial depth and ~110mm in radial length. An approximate indication of size is provided by the scale bars in each figure. Scales are not fully accurate because equipment was set up to maximise the size of the pancake in the captured image.

Results show a similar grain flow pattern in the isothermal and hot die forgings. The hammer pancake forging shows significant differences in the mid to high strain regions of the cross-section. This is indicative of higher levels of beta grain recrystallisation in the hammer forging. This observation has been confirmed by the more detailed microstructural assessments that are discussed in the following sections.

7.3.2 Microstructure and texture assessments

This section of results discusses the variations in the texture and microstructure of the three pancake forgings in the two locations identified as A and F in Figure 7-3. Results are divided into sections covering the processing route of the material from an as-forged water quenched condition through solution and ageing heat treatments.

7.3.2.1 As-forged condition

Pancake forgings were produced by deformation at temperatures in the beta phase field. Following forging they were water quenched to room temperature. Analysis of the resulting microstructure and texture is given in the following three sub-sections.

7.3.2.1.1 Isothermal pancake forging

The optical microstructure of the as-forged pancake following water quenching shows low levels of alpha precipitation [22, 34]. This allows the beta grain structure to be clearly identified. In location A elongated prior beta grain structures exist. These grains contain a recovery substructure of cell wall boundaries [46, 183]. The cell boundaries are identified by blurred outlines. They are equiaxed in shape and on the order of 40-50μm in size.

The microstructure also contains recrystallised grains, formed at the boundaries of prior beta grains. They are distinguished from cell structures as alpha layers form on the boundaries of these recrystallised grains. The different features are identified in Figure 7-8 and Figure 7-9. The microstructural features are labelled in Figure 7-8.

In location A the microstructure is approximated to consist of ~20% area fraction recrystallised grains. The remaining microstructure consists of unrecrystallised beta grains with sub-structures.

With water quenching, the cooling rate at the centre of the forging remains high enough to force orthorhombic alpha double prime (α") transformation [22, 35]. These features are illustrated in the SEM image in Figure 7-9. These features are much finer than the alpha precipitates that are formed during conventional solution heat treatment. It is noted that there is no clear difference in the level of precipitation in recrystallised versus unrecrystallised beta grains, despite differences in the levels of stored energy in each type of grain.

As the effective strain decreases between locations A and F, the extent of recrystallisation and the prevalence of cell boundaries both decrease. This is shown by the optical microstructure at the mid-point between A and F (termed quarter depth) in Figure 7-10.

Recrystallisation still occurs preferentially at grain boundaries. α" precipitates form although they are only observed at very high magnifications.

At location F the recrystallisation fraction is 0%. Cell structures are no longer visible in the microstructure. The microstructure consists of large approximately equiaxed grains with alpha precipitation restricted to grain boundaries (see Figure 7-11). At high magnifications very fine α" platelets (resulting from the rapid cooling rate) are observed [22]. These features are also shown in Figure 7-11.

EBSD mapping of a localised region in location A showed the presence of {100}//AD or {111}//AD fibre textures in unrecrystallised beta grains[1]. The beta phase COM is displayed in Figure 7-12. The corresponding optical microstructure is outlined in Figure 7-13. A higher magnification image of the microstructure is given in Figure 7-14.

The mapped area was insufficient in size to allow an assessment of the fraction of each fibre texture. Figure 7-12 shows that orientation gradients are limited across the unrecrystallised beta grains. This was confirmed by analysis of crystal orientations over the length of beta grains. Cell boundaries in these grains were confirmed to be low angle boundaries (<5º).

A varied recrystallisation texture was observed over the sampled area. No clear trends could be determined from the area of the EBSD scan in Figure 7-12 although textures were noted to vary significantly from deformation textures. Beta and alpha textures for the assessed area are displayed in Figure 7-15.

From the optical microstructure the precipitation of coarse alpha features is restricted to grain boundaries. These 'colony' features are displayed in the COMs in Figure 7-16. Within grains the martensitic α" is a very fine structure existing in the retained beta phase. The size,

[1] Deformation fibre textures displaying alignment of either a {100} or a {111} pole with the compression axis of the forging.

morphology and crystal structure of the α" phase makes indexing of either α" or β by EBSD very difficult.

A COM was obtained at a higher magnification to confirm the presence of recrystallised grains and clearly index alpha features forming at beta grain boundaries. The site of interest is shown in the BSE image in Figure 7-17, with a higher magnification image showing alpha features in Figure 7-18. Corresponding phase maps showing distinct deformation textures, recrystallisation textures and alpha platelet growth from grain boundaries are shown in Figure 7-19 and Figure 7-20 respectively.

An EBSD map in location F of the isothermal forging (see Figure 7-21) was incapable of resolving beta textures within grains. The precipitation of very fine α" features (see Figure 7-22), with the resulting overlap of beta and orthorhombic alpha diffraction patterns making the resolution of textures difficult [36].

Larger alpha platelet features precipitating near beta grain boundaries can be indexed, with typical examples displayed in Figure 7-23 and Figure 7-24. Based on beta grain morphology and the grain-to-grain variation of alpha colony textures, the beta texture in this location of the forging is expected to be much weaker than for location A where strong deformation textures have developed.

7.3.2.1.2 Hot die pancake forging

The as-forged microstructure of the hot die pancake forging contains similar features to the isothermal forging. An unrecrystallised beta grain structure can be identified in the optical microstructure of the high strain section of the forging. As for the isothermal forging, unrecrystallised grains show {100}//AD and {111}//AD fibre textures and a network of cell boundaries.

Partial recrystallisation is observed at the boundaries of the prior beta grains. As for the isothermal microstructure, the recrystallised grains are distinguished from the cell/subgrain networks by the precipitation of alpha layers on their boundaries. Again it is not possible to identify preferred recrystallisation texture, although recrystallised textures are typically significantly different from those of neighbouring unrecrystallised grains.

Coarser alpha platelets are able to grow from beta grain boundary alpha layers given the slower cooling rate towards the centre of the forging. A fine distribution of martensitic alpha precipitates is observed within grains, with no notable differences in recrystallised and unrecrystallised precipitation levels. Typical microstructures in location A of the pancake forging are displayed in Figure 7-25.

A notable difference from the equivalent microstructure of the isothermal forging is the size of prior beta grains, recrystallised grains and cells/subgrains. The hot die pancake forging contains prior beta grains with a higher aspect ratio. Both the recrystallised grain size and the cell size are smaller than for the isothermal forging. Recrystallised grains are typically 10-20µm in cross-section in comparison to typical grain sizes of ~50µm in the isothermal forging. These features are indicative of a higher mean flow stress in the hot die pancake during the forging operation [159].

As for the isothermal forging, in the low strain 'dead zone' there is a large equiaxed beta grain microstructure. Optical assessment shows no evidence of recrystallisation at grain boundaries or the development of a recovery sub-structure within beta grains. The microstructure shows coarse alpha platelet formation at grain boundary locations, with finer martensitic alpha platelet structures forming in regions away from grain boundaries. These microstructures are illustrated in Figure 7-26.

In high strain regions it is noted that several recrystallised grains will often form in juxtaposition (from both optical and EBSD assessments). There are also lengths of adjacent beta grains with {100} and {111} textures over which no recrystallisation occurs. This may indicate that recrystallisation occurs preferentially at recrystallised/unrecrystallised grain boundaries rather than at the boundaries between unrecrystallised grains. Beta phase COMs displaying examples are given in Figure 7-27 and Figure 7-28. A pattern quality map and alpha COM corresponding to the mapped area in Figure 7-28 are displayed in Figure 7-29. Coarse alpha precipitation at/near grain boundaries is indexed in these maps. The prevalence of the {100} and {111} fibre textures is shown in the pole figures in Figure 7-30.

Analysis of alpha textures (from colony features at grain boundaries) shows a radial distribution of {0001} basal poles (see the pole figures in Figure 7-31). This can be related to the presence of a strong {100} fibre texture through variant selection according to the Burgers orientation relationship.

EBSD characterisation of the low strain microstructure of the hot die forging proved difficult (as for the isothermal forging). Again this was attributed to the precipitation of needle-like α" on cooling and the resulting difficulty in identifying distinct diffraction patterns. High magnification EBSD maps were able to index alpha colonies at beta grain boundaries although no information on the beta macro-texture was obtained. Results displayed in Figure 7-32 show the growth of alpha colonies from a prior beta grain boundary. The outlined areas of the phase map contain the textures displayed on the pole figures given in Figure 7-33. This result indicates the influence of the Burgers orientation relationship on the alpha precipitation behaviour – colonies either side of the grain boundary show a common basal plane and a small rotation about the c-axis, suggesting that the two neighbouring beta grains contain a common {110} pole [117].

7.3.2.1.3 Hammer pancake forging

At the axial centre of the hammer pancake forging a high level of dynamic recrystallisation has occurred. This is estimated at ~70-80% area fraction. Recrystallised grains are easily distinguished as equiaxed or low aspect ratio grains typically 50-100μm in cross-section. Unrecrystallised grains have higher aspect ratios and contain cell wall substructures [159]. Typical microstructures in this section of the hammer forging are displayed in Figure 7-34. A high contrast difference is observed between recrystallised and unrecrystallised grains. This may relate to differences in the level of stored work in each type of grain and the presence/absence of dislocation substructures and/or alpha precipitates.

As for the other pancakes following the forging operation, alpha precipitation at the centre of the pancake is largely limited to growth from grain boundaries. Finer α" platelet precipitation is observed in the centre of grains at high magnifications [22, 37].

At axial quarter depth the microstructure is similar to that at the centre of the forging. Because of the strain reduction there is a lower recrystallisation fraction and a small reduction in the aspect ratio of unrecrystallised beta grains. There is also a reduction in the level of alpha precipitation, attributed to a faster cooling rate closer to the surface of the forging.

At 1/8 axial depth the transition from the microstructure of unrecrystallised highly elongated grains and recrystallised grains to a low deformation microstructure of approximately equiaxed beta grains is most evident. Recrystallisation occurs preferentially around beta grain boundaries as was the case for the hot die and isothermal forgings at higher strains. The microstructure is shown in Figure 7-35. The SEM image clearly shows the difference in the

level of precipitation between recrystallised and unrecrystallised grains. Unrecrystallised grains show much higher levels of transformation due to higher levels of strain energy.

With the reduction in forging strain there is a noted reduction in the deformation observed along grain boundaries. Boundaries are observed to be more planar than for microstructures in higher strain locations and increasingly the alpha layers that form on these boundaries are continuous and undeformed. It is also no longer possible to detect a recovery sub-structure in unrecrystallised grains.

At the axial edge of the pancake equiaxed grains are present. These allow for the formation of clear layers of continuous grain boundary alpha phase. Very limited side-plate colony growth can be observed at boundaries (extending over distances <5μm) although no primary alpha precipitation is present near the surface of the pancake. Typical microstructures are shown in Figure 7-36. SEM images show α" precipitates present in the microstructure following water quenching [22, 37]. No recovery sub-structure could be observed in optical microstructures.

As for the isothermal and hot die forgings, heavily deformed grains in the microstructure show fibre textures of {100}//AD or {111}//AD. A tendency towards these fibre textures also exists in recrystallised grains. This may be due to the development of these textures as a result of continuing deformation following recrystallisation. There is no evidence of {110} textures aligned with the compression axis suggesting a preferred (i.e. non-random) recrystallisation texture exists. However, the recrystallisation texture cannot be determined from these results as the sampled area is not large enough to be representative of macro-texture. Macro-beta texture maps and the corresponding axial direction inverse pole figure

are displayed in Figure 7-37. Orthorhombic alpha phase has not indexed in EBSD mapping so the textures are unknown.

As for previous results, EBSD mapping indexes alpha platelet features growing from beta grain boundaries. In addition, alpha precipitates are also indexed on grain substructures in unrecrystallised grains. Preferential precipitation on subgrain features has been reported elsewhere [184]. These features are shown in the beta phase maps in Figure 7-38.

At the edge of the forging (low strain location F) it has been possible to index a representative area indicating the absence of a beta deformation texture in this location. This texture is shown in the COMs and the IPF contained in Figure 7-39. The optical microstructure is typically composed of large equiaxed beta grains with coarse alpha precipitation limited to grain boundaries. There are isolated examples of alpha transformation products extended across beta grains. EBSD mapping of a section of microstructure containing these features is shown in Figure 7-40.

7.3.2.2 Solution heat treated condition

Each as-forged pancake was subject to a two hour solution heat treatment in the (alpha + beta) phase field followed by a fast air cool to room temperature. Results are divided into the three sub-sections that follow.

7.3.2.2.1 Isothermal pancake forging

Following solution heat treatment it was possible to observe primary alpha precipitation throughout the microstructure. At the axial centre (location A) there was a distribution of Widmanstätten alpha platelets. Some grain boundary colony features could be observed, retained from the as-forged microstructure. Recrystallised grains can be identified by the grain boundary layer outlines that formed after forging and coarsened during SHT. However,

the recovery sub-structures noted in the as-forged microstructure are difficult to identify in the SHT'd microstructure. The typical microstructure is displayed in Figure 7-41.

The α" precipitates that were observed at high magnification in the as-forged microstructure appear to have been resolutioned during the SHT, followed by the precipitation of a distribution of stable primary alpha platelets [22, 32]. It is possible to resolve retained beta matrix between primary alpha platelets. There is no secondary alpha precipitation in this matrix.

There is no evidence of static recrystallisation following SHT. All recrystallisation appears to have occurred dynamically during the forging operation. There is no clear change in the recrystallisation area fraction following SHT. Beta textures are retained through the SHT, although because of the reduction in the beta phase fraction the pole figure intensities are reduced in comparison to the as-forged condition. The axial direction IPF in Figure 7-42 shows the retention of {100}//AD and {111}//AD fibre textures.

Low magnification COMs show the presence of large regions of common texture resulting from variant selection in the heavily deformed beta grains. At higher magnifications it is possible to resolve the primary alpha platelet features and their textures in orientation maps. Figure 7-43 displays a mapped area containing beta grains with {100}//AD and {111}//AD fibre textures. Figure 7-44 displays the corresponding alpha platelet crystallographies.

Higher magnification analysis of alpha textures in a {100}//AD textured beta grain shows the presence of eight alpha variants with six different basal plane orientations over a localised area of the microstructure. This is within a region of microstructure for which the axial direction COM only provides an indication of three alpha variants. A pattern quality map of the site of interest along with alpha COMs is displayed in Figure 7-45. Due to interference

from erroneous alpha texture indexing in the retained beta matrix a map enhancement has been used to remove these erroneous textures. Enhanced COMs and corresponding pole figures are given in Figure 7-46. There are six pole intensities corresponding to the alpha variants that form according to the Burgers orientation relationship.

At low strains the grain structure is similar to the as-forged condition as no static recrystallisation has occurred. Coarse alpha platelets are present near beta grain boundaries. Martensitic α" has been resolutioned and a fine distribution of primary alpha platelets has precipitated within grains. These platelets often show optical alignment. Typical microstructures are displayed in Figure 7-47.

EBSD results are given in Figure 7-48 and Figure 7-49. Following the precipitation of a stable primary alpha platelet distribution it is easier to index beta and alpha phases. This is due to the formation of coarser alpha platelets with diffraction patterns that can easily be differentiated from those of the beta matrix. There is no evidence of a preferential beta phase deformation macro-texture. This is expected as it is unlikely that a significant texture exists in the forging dead zone. Analysis of a greater area (sampling a statistically representative number of beta grains) would be required to determine if the beta macro-texture is fully randomised. Alpha COMs show the presence of large regions of aligned alpha colonies within individual grains. As for low magnification maps at the high strain location, there appears to be two or three dominant variants in a single beta grain. The typical microstructure of this region of the isothermal forging is displayed in Figure 7-50.

The higher magnification COMs in Figure 7-51 better illustrate the varied beta texture of location F. Corresponding alpha COMs (Figure 7-52) clearly display the influence of the textures of parent beta grains on the alpha variant that forms on the grain boundary.

Analysis show that the alpha variants that form on the grain boundaries appear to be favoured due to the presence of closely orientated {110} poles in the adjacent beta grains on which the {0001} plane can form [117]. In addition the dominance of one or two alpha variants in individual beta grains can be noted. A major difference from the high strain microstructure is that the growth of alpha platelets from a grain boundary alpha layer with common crystallography often occurs in the high strain microstructure. This behaviour is not readily observed at low strains (based on optical microstructures and texture maps).

High magnification pole figure analysis of the alpha platelets present in the equiaxed beta grain at the top centre of the maps in Figure 7-51 is able to distinguish two closely related variants. These variants share a common basal plane and are identified by a 10-11º rotation about the c-axis of the crystal structure, as shown in Figure 7-53. Although these platelets have a similar crystallography their morphological growth directions are significantly different. This is because they form to satisfy the Burgers orientation relationship such that a HCP $<11\bar{2}0>$ direction aligns with one of the two <111> directions of a single {110} plane [115].

7.3.2.2.2 Hot die pancake forging

As for the isothermal forging, following SHT a widespread distribution of primary alpha platelets has formed throughout the microstructure. {100}//AD and {111}//AD fibre textures are retained and no static recrystallisation has occurred. Observations are confirmed from the beta phase axial direction COM and IPF (see Figure 7-54). Large side-plate alpha colonies are observed to have formed (Figure 7-55). These features are characterised by a radial distribution of the basal plane, with the $\{11\bar{2}0\}$ plane aligned with the forging compression axis. These features were observed in the as-forged microstructure (consistent with the presence of side-plate alpha colony growth across highly elongated beta grains (see the

example in Figure 7-56)) although they are more clearly indexed following growth during SHT. The typical microstructure in region A of the hot die pancake following SHT is shown in Figure 7-57. The high magnification SEM image shows primary alpha platelets and the retained beta matrix. No partial ageing of the beta matrix (i.e. secondary alpha precipitates) can be identified.

EBSD maps obtained at higher magnifications have studied the influence of beta grain orientations on alpha side-plate colony growth and Widmanstätten alpha textures. The COMs in Figure 7-58 identify side-plate growth across a highly elongated prior beta grain structure. This growth occurs from the alpha layer on the grain boundary between {100}//AD and {111}//AD fibre texture grains. Analysis shows this is due to the selection of an alpha variant with a basal plane coherent with closely aligned {110} planes in the prior beta grains. Pole figures are given in Figure 7-59. Colony growth also occurs from the boundaries between other beta grains although these colonies are less clearly visible than the growth across grain C. This is presumably due to the growth direction with respect to the sectioned plane. Across grain C the long axis of platelets is aligned with the axial direction, making these colonies highly visible in the optical microstructure.

A similar example is provided in Figure 7-60, again showing alpha colonies growing perpendicular to a prior beta grain boundary, separating grains with {100}//AD and {111}//AD fibre textures. The colonies that form have basal planes coherent with shared {110} planes in the parent beta grains, resulting in c-axis distributions about the radial plane of the forging. Alpha COMs are given in Figure 7-61. Figure 7-62 displays textures from the top left region of the EBSD map in Figure 7-61. The accompanying pole figures show the two beta grains share a {110} beta plane, and the alpha layer that forms on and grows from the grain boundary aligns the basal plane to this {110} plane accordingly [117].

Analysis of Widmanstätten alpha platelet structures in a {100}//AD textured grain (over a highly localised area) shows the formation of variants on all six of the available {110} beta planes. The AD COM and IPF (Figure 7-63) and a distribution of the orientations of basal planes with respect to the axial direction (Figure 7-64) both appear to indicate the formation of a limited number of variants. However, the TD and RD COMs and pole figure analysis both show a greater number of alpha variants have precipitated. The {110} pole figure in Figure 7-65 shows the orientations of the six {110} planes for the beta grain. Beneath the {110} pole figure is the basal pole figure. This shows that alpha variants have formed on all six {110} poles [185].

Low strain microstructures show no static recrystallisation effects following SHT. The large equiaxed beta grain structure of the forging dead zone is retained. EBSD maps obtained at lower magnifications show polygonal beta grains with various textures. Examples are given in Figure 7-66. Typical microstructures are displayed in Figure 7-67. Large alpha colonies with high aspect ratio alpha platelets often grow from prior beta grain boundaries. In other cases finer low aspect ratio alpha platelets are present within grains. These often show optical alignment.

The large alpha colonies that grow from grain boundary alpha layers and interlocking Widmanstätten alpha platelets that typically constitute this microstructure are shown in alpha phase EBSD maps (see Figure 7-68 to Figure 7-70). Alpha precipitates form according to the Burgers orientation relationship. However, analysis has shown that the colony side-plates displayed in Figure 7-70 have different basal plane orientations despite growing into adjacent beta grains with some closely aligned {110} planes (see Figure 7-71). This result indicates that whilst the alpha variant that is selected is typically determined by the presence

of low misorientations of a particular {110} plane across the beta grain boundary it is not always the determining factor in variant selection [117].

Higher magnification SEM analysis has been unable to resolve any partial ageing of the retained beta matrix. This result is supported by evidence from EBSD analysis for which clear outlines of primary alpha platelets are separated by the beta matrix. An example of this is the phase map in Figure 7-72 corresponding to the COMs in Figure 7-71.

7.3.2.2.3 Hammer pancake forging

Following SHT there is no longer the high contrast between recrystallised and unrecrystallised grains (see Figure 7-34 for example) in higher strain regions of the hammer pancake forging although the two grain types are still distinguished by differences in aspect ratio. Typical microstructures are shown in Figure 7-73. Where grain flow aligned alpha precipitates were observed in unrecrystallised grains in the as-forged microstructure, in most cases Widmanstätten alpha platelets have now precipitated in the surrounding beta matrix. In some instances the primary alpha platelets in the surrounding beta matrix also show optically alignment with the grain flow. Recrystallised grains often show the growth of alpha colony features from grain boundaries. Because of the relatively small grain size (~50µm) these colonies often extend across the grain. Otherwise Widmanstätten alpha platelets are observed in recrystallised grains.

For low strain location F the polygonal beta grains of the as-forged condition are easily identified following SHT. Typical microstructures are displayed in Figure 7-74. Beta grains are usually delineated by semi-continuous grain boundary alpha layers which do not show the discontinuity associated with layers in higher strain microstructures. There is usually limited grain boundary alpha side-plate growth observed on the sectioned plane. This is in contrast

with the low strain microstructure of the hot die forging (and the isothermal forging to a lesser extent).

The majority of the low strain microstructure appears to be low aspect ratio primary alpha platelets in optical morphological alignment. Potentially, these 'colonies' may grow from grain boundaries not contained in the plane of sectioning if nucleation and growth is highly favourable on a particular grain boundary. An alternative explanation is nucleation and growth on recovery sub-structures if they are present at such low strains [186, 187]. Differences in the prevalence of recovery sub-structures at low strains for the different forging methods may therefore account for their microstructural differences.

The {100}//AD and {111}//AD textures present in the heavily strained as-forged material are retained in the SHT'd condition. This is shown in low magnification EBSD maps (see Figure 7-75). Corresponding alpha COMs show a variety of textures although the map area and step size make the resolution of features such as alpha colonies or lamellar boundaries difficult.

The EBSD map displayed in Figure 7-76 shows a higher magnification view of this microstructure. A pattern quality map is displayed alongside the AD beta phase COM. A number of recrystallisation textures are present along with an unrecrystallised beta grain with a {111}//AD texture. This grain contains alpha layers on recovery sub-structures as highlighted for the COMs in Figure 7-77. As has been noted previously for alpha colonies growing from beta grain boundaries, alpha precipitates on recovery sub-structures also show a radial distribution of basal plane intensities.

As for the other forging techniques, the presence of several alpha variants has been identified in the heavily strained microstructure, for both recrystallised and unrecrystallised

beta grains. Respective alpha phase COMs displaying texture variations in each are given in Figure 7-78 and Figure 7-79.

In low strain microstructures the optically aligned alpha platelets are confirmed to be crystallographic colonies. Large polygonal beta grains show no distinct texture. Low magnification EBSD maps show that a single alpha variant will often be present over the majority of a prior beta grain. This is illustrated in Figure 7-80 and Figure 7-81. Higher magnification maps (Figure 7-82 and Figure 7-83) illustrate the crystallography more clearly. The corresponding microstructure is displayed in Figure 7-84.

Although the alpha colonies do not show growth from the grain boundaries as clearly as in other microstructures (see Figure 7-58 for example), the alpha COMs in Figure 7-83 show that colony textures appear to be determined by the variant selected at the grain boundary (which itself is influenced by the orientations of {110} planes in adjacent grains).

Analysis of the crystallography at a prior beta grain boundary again highlights the importance of the Burgers orientation relationship and the presence of closely aligned {110} poles on the variant selection behaviour in grain boundary alpha layer formation [117]. Two common {110} poles are identified across a grain boundary, shown in Figure 7-85. The grain boundary alpha layer has a basal plane corresponding to one of these shared {110} poles (see Figure 7-86). Colony growth from this boundary into one of the grains corresponds to the other shared pole.

7.3.2.3 Age heat treated condition

Solution heat-treated pancakes were subject to an ageing heat treatment at ~600ºC for eight hours to precipitate a distribution of secondary alpha phase. Samples were air cooled to

room temperature. Results for the three different forging conditions are divided into the following sub-sections.

7.3.2.3.1 Isothermal pancake forging

The ageing heat treatment shows no effect on the microstructure at low magnifications. Primary alpha platelets are unsolutioned and there is no change in the prior beta grain structure. Differences are only noted at higher magnification where a partial ageing of the retained beta matrix is observed. The typical microstructure is displayed in Figure 7-87.

The primary alpha platelet distribution in the high strain section of the age heat-treated forging is shown in Figure 7-88. Beta textures are less easily indexed cf. the SHT'd condition due to the partial ageing of the beta matrix, although it is possible to detect the outlines of beta grains with {100}//AD and {111}//AD textures, supporting the assertion that no static recrystallisation occurs during ageing.

Attempts to index the crystallography of secondary alpha platelets were unable to resolve these features. This was attributed to the very fine nature of these platelets and the difficulty indexing them using typical microscope settings (i.e. excessive interaction volume). Attempts to improve the map indexing included varying the sample working distance, the accelerating voltage and the acquisition settings (e.g. map grid size). In each case, variations led to unsatisfactory indexing levels or acquisition times. Typical COMs indicating the textures of primary alpha platelets but unable to resolve the secondary precipitates are shown in Figure 7-89 and Figure 7-90. The presence of several Burgers variants (five unique basal plane orientations) is confirmed for both of these EBSD maps by the intensities on the corresponding {0001} pole figures (see Figure 7-91).

7.3.2.3.2 Hot die pancake forging

The results of the ageing heat treatment for the hot die pancake forging are as for the isothermal pancake. There is no effect on the primary alpha platelet microstructure but partial transformation of the retained beta matrix. Again it is not possible to resolve the crystallography of secondary platelets using the available EBSD facilities. Typical microstructures and textures of the aged pancake forging are given in Figure 7-92 and Figure 7-93.

7.3.2.3.3 Hammer pancake forging

Ageing heat treatment has a similar effect on the hammer pancake forging as for the isothermal and hot die forgings. Primary alpha textures are retained and partial transformation of the retained beta matrix occurs. Typical microstructures are shown in Figure 7-94. EBSD maps are able to resolve primary alpha platelets and (alpha denuded) regions of beta phase surrounding these platelets. Retained beta matrix/secondary alpha precipitate microstructures are not indexed. This is shown by a phase map and corresponding beta COM (see Figure 7-95). Alpha COMs are displayed in Figure 7-96.

7.3.2.4 Production disc forgings

Pancake forging heat treatment specimens have relatively small section sizes. Because of this the cooling rates following SHT and ageing will be significantly different from the cooling rates experienced in a large compressor disc forging. The variation in the cooling rates may affect the ageing behaviour in terms of the level of phase transformation and the fraction of retained beta phase [19]. For this reason the microstructures of typical hammer, hot die and isothermal forgings were examined. Typical fully heat-treated microstructures are displayed in Figure 7-97 to Figure 7-99.

In each case the secondary alpha platelets that have formed in the retained beta phase appear coarser than those present in the experimental pancake forgings. Although other factors may account for these differences, it suggests that cooling rate has a significant influence on the size distribution of secondary alpha platelets. It is probable in each of the following cases that a faster post-SHT cooling rate lead to a lower fraction of primary alpha platelets, consequently allowing the growth of coarser secondary alpha platelets during ageing.

As for the pancake forgings, it was not possible to index the crystallography of the secondary alpha phase. Although the acquired EBSD maps were unable to resolve secondary platelets, results are similar to those in the experimental pancake forgings, with multiple primary alpha variants occurring within a single beta grain. A typical example for an isothermal forging is given in Figure 7-100, Figure 7-101 and Figure 7-102.

7.4 Discussion

An attempt is made to correlate observations of optical microstructures and textures to the processing route and conditions. The discussion is divided into two sub-sections, the first examining the development of the optical microstructure and the second studying the variations in texture, each comparing results from the different forging routes.

7.4.1 Effect of forging method on grain flow and optical microstructure

There is a wide variation in the optical microstructure present in each pancake forging. This is a result of the effective strain distribution and the variation in the post-forge cooling rates throughout each pancake.

Isothermal and hot die forgings show similar optical grain flow profiles at low magnifications. The grain flow profile shows a coarse highly elongated region present at the axial centre of the pancakes that extends from the radial centre to approximately three quarters of the distance to the radial edge. Beyond this point a gradual transition to an equiaxed grain structure occurs. These observations correlate well with the modelling predictions of effective strain levels. Equiaxed grains are present towards the radial edge and also in the 'dead zone' of both forgings. Comparison of the aspect ratio and size of beta grains shows very similar size and shape distributions exist in both pancakes.

The hammer forging shows a very different grain flow profile. The high strain regions of the pancake show a much finer grain size and little evidence of grain flow. Towards the outer edges of the pancake (i.e. lower strains) there are large equiaxed grains of a similar size to those at the edges of the hot die and isothermal forgings.

Based on grain flow profiles alone, the fine and equiaxed grains in the high strain regions of the hammer forging suggest that extensive recrystallisation occurs during forging. High strain

regions of the hot die and isothermal forgings do not show the same evidence of dynamic recrystallisation based on grain flow observations. This indicates that for a given effective strain distribution, recrystallisation is more likely to occur when the hammer forging technique is used.

A comparison of prior beta grain flow in different heat treatment conditions shows that no clear change in grain flow patterns occurs during SHT and ageing processes. There is no evidence of static beta recrystallisation associated with these heat treatments.

7.4.1.1 Isothermal forging

Optical characterisation of the microstructure of the isothermal pancake shows a partial dynamically recrystallised 'necklace' microstructure at high strains (effective strain levels of E~≥0.5-1.0x). In an as-forged optical microstructure the recrystallised grains can be distinguished as equiaxed grains of ~40-50µm width. The presence of these grains in the as-forged condition indicates dynamic rather than static recrystallisation behaviour. Unrecrystallised grains are identified as high aspect ratio (typically >3:1) grains with recrystallised structures at their boundaries. Recrystallised grains can be identified (even in the as-forged condition) because of the precipitation of alpha layers on their boundaries. The relatively slow cooling rate close to the centre of the pancake forging, in combination with the presence of high angle grain boundary (HAGB) features, is sufficient to allow grain boundary alpha layer formation [22, 187].

At high strains it is possible to observe the presence of a 'subgrain/cell structure' in unrecrystallised grains. The cell structure consists of tangles of dislocations forming low misorientation angle (<2º) diffuse boundaries [159, 183]. From references a cell can be defined as a roughly equiaxed volume with a dislocation density well below the average, with

a rigid orientation rotation from neighbouring volumes. A ‘cell block’ structure consists of a contiguous group of cells with a shared set of operating dislocation glide systems [188].

The deformation strain of the forging has not reached the level at which the cell structure has evolved into a network of subgrains with sharp boundaries. Subgrains are defined as near dislocation free volumes surrounded by high angle boundaries [188]. This observation is supported by the absence of alpha precipitation on these cell walls in the as-forged condition. The observations indicate that dynamic recovery occurs during the isothermal forging process [189]. Although recrystallisation produces a necklace microstructure, the majority area fraction of this high strain microstructure consists of dynamic recovery cell structures. This observation is supported by the fact that the isothermal forging process uses die temperatures equal to the pancake temperature (therefore reducing temperature losses through die chill effects) and low strain rates. High forging temperatures and low deformation rates (low values of the Zener-Hollomon parameter) will favour recovery effects over recrystallisation behaviour [159].

Following SHT extensive phase transformation has occurred. Alpha layers present on recrystallised grain boundaries have coarsened providing a clear distinction between recrystallised and prior beta grains. The precipitation of a typically Widmanstätten optical distribution of primary alpha platelets in the beta matrix obscures the cell wall structures in the microstructure. However, these features can still be observed at high magnifications under close inspection. Although no alpha precipitation is present on these features following SHT it is possible to identify cell walls due to the obstacle that they provide to the growth of primary alpha platelets (see figure 2-19 and figure 6-71 for examples).

This observation conflicts with previous work which suggests that subgrain boundaries or other recovery substructures are crossed by alpha platelets during their growth [187]. Their work considered subgrain boundaries as nucleation sites for allotriomorphic alpha layers. However, this behaviour has not been observed for the cell wall boundaries present in the isothermal forging. Boundary alpha layers only formed on continuous dynamically recrystallised grains along prior beta grain boundaries. This transformation behaviour is attributed to the higher plastic strain energies at these high angle boundaries [184].

With SHT the growth of colonies from boundaries is favoured over Widmanstätten platelet nucleation mainly due to an increase in nucleation site density [186]. This observation in previous work is in agreement with the current work, however, the following differences are noted in the current work (based on assessment of optical microstructures):

- Allotriomorphic alpha layers do not form on cell wall structures. As a consequence there is no side-plate colony growth in these cells.
- Side-plate colonies grow from the boundaries of prior beta grains and recrystallised grains although they rarely show growth to length scales that traverse cell wall or subgrain boundary features.
- Widmanstätten alpha platelets precipitate within cells and grow to cell wall boundaries. No growth across these boundaries has been observed under SEM examination.

The experimental and modelling work of Da Costa Teixeira et al. indicated that a faster strain rate leads to a smaller subgrain size and a faster phase transformation rate (due to increased opportunities for nucleation and growth from subgrain boundaries) [187]. In the current work it appears unlikely that a reduction in cell size would result in increased

transformation kinetics. This conclusion is drawn as there is no evidence of the formation of alpha layers on cell boundaries in optical microstructures.

Following a typical ageing heat treatment there are no obvious changes to the existing beta grain structures or SHT alpha precipitates. As expected the age allows the transformation of a significant fraction of the retained beta matrix to secondary alpha platelets. However, the ageing temperature is not significantly high enough to affect stable alpha precipitates or cause any static recrystallisation effects.

Results show the transition from a heavily worked necklace microstructure to a low deformation unrecrystallised microstructure through an axial section of the pancake forging. Optical assessment of the as-forged condition appeared to indicate that recovery effects (i.e. visible cell wall network formation) are eliminated before recrystallisation effects (i.e. at higher strains and lower cooling rate levels). Despite the relatively low strains in the 'dead zone' of the forging the prior beta grain boundaries still show significant evidence of deformation [27]. Although water quenching, the post-forge cooling rate is sufficiently low towards the edges of the pancake to allow precipitation of fine alpha layers on grain boundaries [22]. Within grains there is a partial transformation to orthorhombic alpha double prime [22, 33]. No athermal omega precipitates are identified based on the fine cuboid morphology of this phase [190].

Although little primary alpha platelet precipitation occurs following forging, after SHT the low strain regions of the forging usually show large colonies of optically aligned low aspect ratio alpha platelets. This contrasts with high strain microstructures which usually show more optically random distributions of Widmanstätten alpha platelets [186].

These differences may potentially be explained by differences in dislocation densities in the respective microstructures. Whilst recovery and recrystallisation effects clearly occur in highly strained material and may result in relatively low dislocation densities, the low strain sections of the forging show no clear dynamic recovery or recrystallisation. Increased dislocation densities may result, which will affect phase transformation behaviour [186].

Despite the relatively fine scale of alpha platelets (potentially indicative of moderate to high dislocation densities), assessment of both the SHT'd and the fully aged microstructures of the isothermal forging in low strain locations showed no evidence of cell wall features as for the high strain microstructures. It is therefore apparent that the dislocation density levels in these lower strain sections of the forging do not reach the levels where visible recovery mechanisms come into effect [183].

7.4.1.2 Hot die forging

As for the isothermal forging the hot die pancake also shows necklace microstructures. The area fraction of unrecrystallised material is similar in both forgings, however, the typical recrystallised grain size is smaller in the hot die forged pancake (10-20μm cf. 40-50μm for isothermal forging location A). This may relate to the flow stress required on forging. Humphreys & Hatherly state that the mean subgrain diameter is usually observed to be inversely proportional to the high temperature flow stress of the material [159]. Because the heat losses associated with hot die forging will be greater than those for isothermal forging, the flow stress required to forge to a specified strain level will be greater for hot die forging. This decrease in forging temperature may account for a reduction in the recrystallised grain size.

Whilst the recrystallised grain size is smaller, a higher aspect ratio of prior beta grains in the hot die forging is also noted. Given the same starting material and forging schedule it is unclear why there are differences in the grain aspect ratio. However, the increase in aspect ratio of unrecrystallised grains is indicative of higher forging strains. This increased strain may also contribute to the reduction in recrystallised grain size.

Preferential recrystallisation is clearly evident at prior beta grain boundaries. As for the isothermal forging, the remaining microstructure in high strain locations consists of cell structures with diffuse boundaries. Considering the characteristics of hot die forging, dies are cooler and strain rates are higher than when isothermal forging. Both these conditions should raise the Zener-Hollomon parameter and favour dynamic recrystallisation as opposed to dynamic recovery. Despite this, no significant difference in the recrystallisation area fraction is observed in high strain sections of the two forgings. The influence of die chill effects on microstructure is largely discounted as they are not expected to significantly influence the temperature profile at the centre of the forging. However, the difference in strain rate between the two forging methods should be sufficiently large to potentially lead to variations in recrystallisation behaviour.

Widmanstätten alpha platelet structures typically form in the high strain microstructure. However, in some cases high aspect ratio unrecrystallised beta grains show the formation of side-plate colonies across their axial dimension (even in the as-forged condition). This suggests that favourable nucleation and growth from prior beta grain boundaries can occur in some cases [117].

The typical Widmanstätten alpha platelet precipitation towards the centre of the as-forged pancake is replaced by growth of ‘side-plate’ features from beta grain boundaries towards

the edges of the pancake. There is some growth of preferred alpha colony variants into grains, although the water quench after forging largely limits transformation, instead forcing partial transformation of beta phase to martensitic α" [34]. The lower stored energy at lower forging strains may be an additional factor influencing the extent of phase transformation.

Following SHT the high strain microstructure contains a mixture of Widmanstätten and colony primary alpha platelets. α" precipitates are resolutioned by the SHT [34]. Ageing only results in transformation of retained beta matrix to fine scale (sub-micron) alpha precipitates. No static recrystallisation events are observed following either heat treatment.

In low strain microstructures the coarse alpha side-plate features remain present following SHT. Thermally unstable α" precipitates are resolutioned, and a distribution of stable Widmanstätten alpha platelets forms from beta [34]. Ageing again only affects the retained beta matrix. No static recrystallisation effects are noted for either heat treatment.

7.4.1.3 Hammer forging

It is known that higher temperatures and lower strain rates (i.e. low Zener-Hollomon parameter) allow dynamic recovery effects to dominate whereas lower temperatures and higher strain rates favour dislocation generation behaviour, leading to increased dislocation densities and higher levels of dynamic recrystallisation. This change in deformation behaviour leads to significant differences in the resulting microstructures in isothermal, hot die and hammer forgings under equivalent processing conditions.

Characterisation of the optical microstructure of the hammer forging shows the formation of a predominantly recrystallised microstructure in high strain (typically $E \geq 1.5$ based on the predicted effective strain profile in Figure 7-2) regions of the hammer forging.

Recrystallisation occurs dynamically (i.e. during the forging operation) based on assessment of the as-forged microstructure.

Recrystallisation is known to occur as a result of the accumulation of dislocation defects (at grain boundaries) during plastic deformation. It involves the formation of high angle grain boundaries (HAGB's) that have adjacent grain misorientations of >10-15º [191]. Partial dynamic recrystallisation occurs when the dislocation density exceeds a critical level. In the hot die and isothermal forgings this leads to the formation of a 'necklace' microstructure at the centre of the forging, where equiaxed recrystallised grains are significantly smaller than the elongated prior beta grains. However, for the hammer forging the high strain microstructure largely consists of recrystallised grains rather than a 'necklace' microstructure. In this microstructure it appears that further recrystallisation events occur as nucleation sites form at the HAGB's of existing recrystallised grains [184].

The distinct differences in the microstructure of the hammer forged pancake can be related to the strain rates and temperatures that the forging experiences. The recrystallisation that occurs in the centre of the pancake is largely attributed to the high effective strain rates that apply during the impact blows of hammer forging. A high strain rate gives limited time for dislocation recovery effects (i.e. rearrangement to lower energy configurations such as low angle grain boundaries (LAGB's)) to occur and hence is likely to lead to rapid increases in dislocation densities under plastic deformation. Once the dislocation density exceeds a critical level it becomes favourable for recrystallisation to occur. Repeated exposure to high strain rate deformation is thought to lead to extensive recrystallisation, with new recrystallised grains forming on the HAGB's of previously nucleated recrystallised grains.

The high strain rate characteristic of the hammer forging process offers an explanation for the higher recrystallisation fractions observed by this process route. The lower die temperatures of hammer forging may also contribute by lowering temperatures in the forging due to heat transfer effects. A lower metal temperature should reduce dislocation mobility and also favour dynamic recrystallisation behaviour [159].

Despite this rationale, the effects of die chill on the temperature profile are unclear. At the edges of the pancake forging there are expected to be significant temperature loss effects due to the temperature mismatch between the pancake and the dies. However, at the centre of the pancake the temperature losses should be much less significant. In addition there are also the effects of adiabatic heating to take into consideration. Due to the nature of the hammer forging process there is potential for significant adiabatic heating at the centre of the forging where effective strains are high. However, because elevated temperatures would favour dynamic recovery rather than recrystallisation it may be concluded that even if significant adiabatic heating occurs during forging, the high strain rates clearly still provide sufficient driving force for recrystallisation over dynamic recovery.

Although recrystallisation events dominate the behaviour, it is noted that unrecrystallised highly worked grains contain alpha precipitates running parallel to grain flow. These precipitates have formed on grain sub-structures formed through dynamic recovery. According to recrystallisation theory LAGB's develop into HAGB's under continuing deformation [159]. LAGB's initially formed as dislocation tangles become ordered and create 'cell walls'. With further increases in dislocation density these cell walls develop into subgrain or cell structures. The stages of recovery are shown in Figure 7-103.

Optical microstructures of the hammer forging show limited alpha precipitation after water quenching. Orthorhombic alpha precipitates exist in recrystallised grains as a result of the high post-forge cooling rate rather than reduced strain energies [22]. In an etched condition unrecrystallised grains show darker contrast that is attributed to higher dislocation densities. Recovery sub-structures are present, and whilst the effects of dynamic recovery remove some of the driving force for alpha precipitation, the absence of primary alpha precipitation is again related to post forge water quenching [22].

After SHT, those alpha precipitates formed on recovery sub-structures in unrecrystallised grains in alignment with grain flow have coarsened. In most cases a distribution of Widmanstätten alpha platelets is noted to form around these precipitates. However, (as for the other forgings), no alpha precipitation can be identified on the surrounding cell boundaries.

Recrystallised grains contain no sub-structures and as a result, following SHT their microstructures consist of side-plate growth from their boundaries with Widmanstätten precipitation and growth within the centre of grains.

In comparison to the high strain microstructures of the hammer forging, isothermal and hot die forging conditions and the consequent recovery effects do not allow the development of recovery sub-structures allowing alpha phase nucleation and growth. This is evident from the as-forged optical microstructures, but also supported by the absence of any precipitate features aligning with the direction of beta grain flow in these forgings.

The low strain optical microstructure of the as-forged hammer pancake shows equiaxed grains with alpha precipitation limited to grain boundaries. The strain level does not appear to have been sufficient to allow dynamic recovery effects based on optical assessment.

Recovery sub-structures are not distinguished by optical microscopy or SEM. There are also no recrystallised structures present in the low strain material. High magnification images show the presence of orthorhombic alpha needles associated with water quenching of Ti6246 from above beta transus [22].

Following SHT the α" precipitates have been resolutioned, with coarse low aspect ratio alpha platelets having precipitated. These precipitates often exist in large optical colonies. In some cases there is no obvious optical relationship to grain boundary alpha layers, unlike for example, typical low strain microstructures in isothermal forgings. One possible explanation for this behaviour is the nucleation of alpha phase on existing features of the grain substructure rather than the more commonly observed epitaxial growth from grain boundary alpha layers [184, 187].

Other observations of the microstructure of low strain hammer forgings include the presence of relatively undeformed (i.e. linear) and continuous grain boundary alpha layers following the SHT. In some cases the grain boundaries are straight whilst in other instances a curvature (bulging) effect may be observed, indicative of grain boundary migration prior to the onset of recrystallisation [159].

The continuous alpha layers may be significant in terms of the mechanical behaviour of the alloy [27, 38, 60, 192]. This is because the continuous alpha layers have adjacent regions that are denuded of secondary alpha precipitates due to element partitioning effects on phase transformation. This results in preferential deformation in grain boundary locations, causing adverse effects on properties including ductility, fatigue performance and fracture toughness [60]. This may be of particular concern in a relatively high strength alloy such as Ti6246

because the negative influence of the grain boundary layers is increasingly significant as the strength difference between the matrix and boundary layers is increased [192].

The undeformed prior beta grain boundaries of the optical microstructures suggest that forging deformation occurs entirely above the beta transus. Through transus processing has been reported to lead to 'necklace' microstructures consisting of very fine round alpha precipitates on and close to grain boundaries [60]. As the hammer forging deformation appears to have occurred above the beta transus, it is also likely that the isothermal and hot die forging operations also occur entirely above transus temperature. This is based on the assumption that hammer forging will result in the greatest temperature losses through die chill effects.

As for the other forgings studied in this work, ageing was observed to have no recrystallisation or recovery effects on microstructure. Ageing behaviour is limited to the transformation of a fraction of the retained beta matrix to secondary alpha platelets.

7.4.2 Effect of forging method on crystallographic texture

As for the variation in optical microstructures, there are significant variations in the crystallographic textures in the pancake forgings according to the effective strains, cooling rates and strain rates that they experience. Again the results are divided into sub-sections for each forging method.

7.4.2.1 Isothermal forging

The beta phase COM for the pancake in the as-forged condition in a high effective strain location shows a predominantly {100} axial fibre texture. This texture and a {111} axial fibre texture are present in unrecrystallised grains. To make a statistically representative

evaluation of the deformation texture would require texture assessment of a larger area/volume of material e.g. using X-ray diffraction [161].

The misorientations across cell walls are small enough not to be clearly identifiable by EBSD. This confirms that these microstructural features are diffuse boundary cell structures (with low angle misorientations) rather than sharp boundary subgrains (with higher misorientation angles). No large orientation gradients are measured across unrecrystallised grains. This is consist with other findings, as post high-temperature deformation microstructures often consist of subgrains with a distribution of orientations about a mean value, with little overall orientation gradient [159].

Recrystallised grains are readily observed to form distinct textures on the boundaries of the prior beta grains. As for the deformation texture, the area sampled is insufficient to make a judgement on the recrystallisation texture. Whilst {100} and {111} axial fibre textures are identified in unrecrystallised grains, there is less evidence of a strong recrystallisation texture.

Orthorhombic alpha textures are not indexed by EBSD. Primary alpha side-plate formation is indexed at the boundaries of both recrystallised and unrecrystallised grains. The EBSD maps that have been acquired do not suggest the consistent selection of particular alpha variants in either type of grain.

The as-forged low strain section of the isothermal pancake was difficult to index. This was attributed to the partial transformation of beta to orthorhombic alpha [22]. Coarser alpha platelet precipitation can be identified at or near to grain boundaries. These features indicate the outline of large equiaxed grain shapes.

EBSD confirms the retention of the {100}//AD and {111}//AD fibre textures in unrecrystallised grains following SHT. It is also possible to identify the formation and growth of side-plates from grain boundaries and Widmanstätten alpha platelets within grains. EBSD confirms the growth of side-plates with crystallography determined by the grain boundary alpha variants. This is a well-documented phenomenon involving the selection of variants with the alpha basal poles corresponding to closely matched (where possible) {110} poles of the adjacent beta grains in order to minimise interfacial strain energies [117].

Higher magnification EBSD maps show the formation of multiple alpha variants in Widmanstätten distributions towards the centre of beta grains. Lower magnification maps often make the distinction of these variants more difficult and may only allow the resolution of two or three dominant variants.

Following SHT it is also possible to determine beta textures in low strain microstructures. This is attributed to resolutioning of α" and precipitation of primary alpha platelets [22, 31, 32]. The step size and microscope settings are sufficient to identify and resolve the SHT alpha precipitates and the retained beta matrix. The maps show the retention of large equiaxed beta grains with no strong deformation texture and no evidence of recrystallisation. Alpha COMs show large colonies often extending across >50% of the cross-sectioned area of individual beta grains.

Although large colonies of alpha platelets are observed in the microstructure, they often do not clearly show growth from grain boundary layers as for high strain microstructures. EBSD maps such as that of Figure 7-52 show distinct differences in the crystallography of grain boundary layers and adjacent alpha colonies. The alpha platelets are noted to be smaller and have shorter aspect ratios than is often the case in high strain microstructures. This may be

due to an increased dislocation density encouraging nucleation and growth of colonies in grains rather than from grain boundaries, however, this is unlikely as Widmanstätten microstructures would result from this behaviour [184]. Another possible explanation for the formation of alpha colonies with no apparent crystallographic relationship to grain boundary layer is precipitation on recovery sub-structures [184]. A third explanation is the highly preferential growth of colonies from particular grain boundaries, such that substantial growth of individual colonies can occur before colonies have begun to grow from other grain boundaries. However, this behaviour is considered unlikely, given that high strain microstructures of the as forged hot die pancake show the presence of side-plate colonies (Figure 7-56), and similar observations of colony growth would be expected in the as-forged material condition if such colony growth behaviour were to occur.

In the aged condition both low and high strain microstructures show no evidence of static recrystallisation or recovery. The SHT precipitates and the retained beta texture remain stable at the SHT temperature. Primary alpha platelets present after the SHT satisfy the Burgers orientation relationship. The fine secondary platelet precipitates are also expected to satisfy the relationship based on the slow diffusional phase transformation that ageing allows. However, it has not been possible to acquire crystallographic information for this phase and this relationship is unconfirmed. TEM work is required to confirm the crystallographic relationship between the retained beta matrix and the secondary alpha platelet phase.

A further observation from EBSD maps is the selection of alpha variants lying on unique {110} planes, i.e. Widmanstätten alpha platelets precipitate on different {110} planes rather than precipitating as a pair of variants on a single {110} plane. This observation is similar to that made by Cayron et al. [193]. Their work noted that in the absence of a common {110}

beta/beta interfacial plane the probability of alpha variants sharing a c-axis is very low. Calculations suggest that these 'twin sister variants' are energetically unfavourable based on elastic energy minimisation [194, 195]. In the current work, because of the localised area of the site of interest of EBSD maps, further investigation would be necessary to determine if such variant selection behaviour occurs on phase transformation.

7.4.2.2 Hot die forging

As for the isothermal forging, the beta textures detected after exposure to high effective strains in the hot die forging show the development of {100} and {111} axial fibres. Again, no orientation gradients are noted over the length of prior beta grains. Large scale COMs indicate the tendency towards particular alpha textures. A radial distribution of basal planes about the compression axis is observed for the side-plate colonies forming at heavily strained grain boundaries. This is a texture that has been widely reported for axial compression of titanium alloys [196]. These textures remain present following SHT, the only changes being some coarsening of alpha platelets and a small corresponding decrease in the retained beta fraction. COMs show a mixture of side-plate growth and Widmanstätten alpha platelet formation. Observations concerning the crystallographic nature of alpha platelets are very similar to the isothermal forging.

Insufficient data was acquired to make an assessment of the beta texture in low strain sections of the hot die forging. However, a varied beta macro-texture exists over large equiaxed prior beta grains (in the SHT'd condition). In the as-forged condition only primary alpha platelets growing from the beta grain boundaries could be indexed. These colonies show variant selection to minimise strain energies across boundaries. EBSD maps of the SHT'd microstructure show the retention of high aspect ratio grain boundary platelets

following the SHT. Orthorhombic alpha in the as-forged pancake has been resolutioned and replaced by a predominantly Widmanstätten distribution of high aspect ratio alpha platelets. This contrasts to the isothermal and hammer forgings, for which low strain regions of the forging often show small and low aspect ratio alpha platelets. The reasons for this difference in precipitation and growth behaviour are unclear although they may relate to the dislocation density within the material or the influence of recovery sub-structures. Optical assessment showed no recrystallisation in low strain microstructures. Beta texture maps confirm this observation.

As was the case for the isothermal forging, the hot die forging shows precipitation of a number of alpha variants. Analysis of high magnification COMs show that variants present within a localised area often show different basal plane orientations rather than pairs of variants with a common {0001}//(110) plane. Again this behaviour supports the theory of limited formation of 'twin sister variants' due to energetically unfavourable configurations [195].

Ageing does not affect the textures formed during forging or SHT. The Widmanstätten distribution of secondary alpha platelets formed in the retained beta matrix is expected to be Burgers orientation related to the beta matrix.

7.4.2.3 Hammer forging

The largely recrystallised microstructure observed by optical assessment of the high strain hammer forging is confirmed by EBSD assessment. Unrecrystallised grains show {100} or {111} axial fibre textures. The recrystallised beta texture is relatively randomised. Alpha COMs are unable to resolve significant precipitation at the centre of the forging despite a slower post forge cooling rate. Alpha precipitation on recovery sub-structures can be

identified and is noted to orientate with basal planes lying normal to the forging axis. There are some side-plate features growing from the boundaries of both recrystallised and unrecrystallised grains.

In some as-forged low strain microstructures EBSD maps show the precipitation and growth of singular alpha features across beta grains (e.g. Figure 7-40). These features are ~20µm width (in comparison to typical SHT'd alpha platelet widths of ~2-3µm) and may result from highly preferential growth from a grain boundary or by nucleation and growth on recovery sub-structures [184].

On SHT these coarse alpha precipitates remain present in both high and low strain microstructures. In unrecrystallised high aspect ratio grains the microstructures typically show the formation of Widmanstätten alpha platelets around the aligned alpha platelets observed after forging and water quenching. In some cases the SHT precipitates may also form in alignment with these features. This may be due to the influence of the existing alpha variants on the consequent selection of alpha variants on transformation [119].

In low strain microstructures the large colonies present in the optical microstructure following SHT are confirmed by EBSD. Colonies often extend over the majority of the cross-section of individual prior beta grains. These colonies consist of small and low aspect ratio alpha platelets (as for the isothermal forging).

As for the isothermal forging, there are large crystallographic colonies that show significant orientation differences from the corresponding grain boundary alpha layers. Again, this behaviour may be an effect resulting from the growth of colonies from boundary locations not contained within the plane of sectioning. Alternatively it may be due to the intra-granular nucleation and growth of platelets, for example on sub-structures within beta grains.

Ageing at low temperatures does not affect retained beta or primary alpha platelet textures. The fine secondary alpha platelets dispersed in the beta matrix cannot be resolved by EBSD, even using enhanced acquisition settings (reduced accelerating voltage) and reduced step sizes. These secondary platelets are likely to follow the Burgers orientation relationship based on previous results. Widmanstätten primary alpha platelets are again observed to form on distinct basal planes rather than as pairs of 'twin sister variants' in order to minimise strain energies [193].

7.4.3 Cold dwell fatigue behaviour/Effective structural unit size effects

Following on from the characterisation of isothermal, hot die and hammer forged pancake microstructures, an attempt has been made to relate the differences in microstructural evolution to potential differences in material behaviour.

Other work undertaken in this thesis has led to the conclusion that Ti6246 is insensitive to cold dwell fatigue (CDF). This judgement is made based on higher beta stabilisation levels (cf. other disc alloys) leading to an increased beta content, resulting in the inability for dislocation pile-up stresses to accumulate through the alpha phase and allow stress redistribution events.

Whilst under some forging and heat treatment conditions it is possible to observe the formation of large colonies of alpha platelets these have been shown not to act as the effective structural units in the material when loaded under cold dwell fatigue [152]. The planar slip length in cold dwell fatigue tested beta-forged, (alpha + beta) SHT'd and aged Ti6246 has been observed as the length-scale across closely spaced optically (and crystallographically) aligned alpha platelets (see chapter six section 6.3.5.3). Although large

alpha colonies exist, the presence of large amounts of retained beta and Widmanstätten secondary alpha platelets make planar trans-colony slip extremely unlikely to occur.

In the isothermal forging the dynamic recovery cell structures developed on forging to high effective strains may offer some barrier to dislocation movement. However, these features are unlikely to have a significant effect on mechanical behaviour in the fully aged condition. This is based on the property changes that occur through low temperature ageing and the precipitation of a fine distribution of alpha platelets.

Because there is generally a Widmanstätten or small colony microstructure for the high strain isothermal forging it is unlikely that planar slip deformation will occur. It is also unlikely that neighbouring microstructural regions with suitable crystallographic relationships for stress redistribution will be present, given the widespread development of {100} and {111} axial fibres and the radial distribution of {0001} planes resulting following phase transformation.

Low strain microstructures generally show large primary alpha colony structures with approximately equiaxed prior beta grains. Such microstructures may offer favourable combinations of colony misorientations allowing any significant dislocation pile-up stresses to redistribute onto strong colony orientations. However, this behaviour is extremely unlikely based on the typical spacings of primary alpha platelets and the levels of both retained beta matrix and secondary alpha platelets in the material.

In the hot die pancake forging the recrystallisation area fraction is very similar to the isothermal forging for the same forging conditions. However, both the recrystallised grain size and the size of cells in the cell structure network are both smaller in the hot die forging. The work in the previous chapters concluded that the beta grain size (i.e. the beta texture

length-scale) is not the feature of concern in CDF behaviour. Common alpha texture length-scale is the facet size controlling feature, provided that the alloy chemistry allows the transformation to sufficiently high alpha phase fractions. Therefore the differences in recrystallisation behaviour are considered highly unlikely to affect CDF loading response. Given previous observations, the effects of a high retained beta fraction and a fine dispersion of secondary Widmanstätten alpha platelets are considered to have a significantly greater influence on the material behaviour.

The observations regarding the effect of recrystallisation in hot die and isothermal forgings also apply to the hammer forging. The increased recrystallisation fraction will lead to an increased concentration of grain boundaries although the growth of side-plate features will be limited by the grain size. Whilst there may be a greater probability of neighbouring colonies with suitable misorientation for stress redistribution, the colony size is relatively small and any dislocation pile-up stresses would be limited. In microstructures containing large colonies of alpha platelets (i.e. low strains) the effect of the retained beta matrix, the secondary alpha platelet phase and the primary alpha platelet spacing is assumed to be stronger in preventing CDF than the effect of the alpha colony size in promoting it.

7.5 Conclusions

Combined metallographic assessments and EBSD texture analysis has allowed the following major conclusions to be drawn for the respective forging techniques:

7.5.1 Isothermal forging

- Partial dynamic recrystallisation occurs during beta forging at moderate to high effective strains ($E \geq \sim 1$). Recrystallised grains are observed on prior beta grain boundaries and are typically 40-50µm in cross-section.
- Recovery sub-structures (cell wall boundaries) form in unrecrystallised grains at medium to high strains. Allotriomorphic alpha layers form on the boundaries of prior beta grains and recrystallised grains, but not on cell wall boundaries.
- Pronounced {100} and {111} beta axial fibre textures are present following beta forging at medium to high strains. These are typical deformation textures for body centred cubic structures. Recrystallised grains show different textures although these have not been identified. The 'dead zone' of the pancake forging shows no beta deformation texture.
- (Alpha + beta) phase solution heat treatment allows side-plate colonies to coarsen/grow from boundary layers although they do not appear to traverse cell wall boundaries. Widmanstätten alpha platelets forming during SHT also do not grow across cell wall boundaries. SHT leads to the formation of a predominantly Widmanstätten distribution of alpha platelets in medium to high strain regions of the isothermal forging.
- SHT allows nucleation and growth of large colonies of alpha platelets in low strain microstructures. Some colonies show no crystallographic relationship to adjacent

grain boundary alpha layers. This may be a sectioning effect, with colony growth nucleating at a different location not contained within the plane of sectioning. Alternatively it may indicate an intra-granular mechanism of nucleation and growth of colonies rather than the planar diffusion controlled growth from grain boundaries.

- Limited alpha variants (i.e. < 12) form for each beta texture, with 'twin sister variants' (with common basal planes) infrequently observed in Widmanstätten platelet distributions. No evidence of non-Burgers oriented alpha platelets has been noted in SHT'd and aged microstructures.
- Fine (secondary) alpha platelets form in Widmanstätten optical distributions during low temperature ageing. Their crystallographic textures are unknown.

7.5.2 Hot die forging

- Partial dynamic recrystallisation is observed for the hot die forging at moderate to high effective strains ($E \geq \sim 1$) as for the isothermal forging. However, the recrystallised grain size is smaller (typically 20-30μm cross-section) and the area fraction is lower in comparison. The size of cells in the network is also smaller than for the isothermal forging. The reasons for these differences in behaviour are unclear but presumed to relate to differences in strain rate between the two forging methods.
- As-forged material shows limited alpha platelet precipitation and similar recovery/recrystallisation effects to the isothermal forging. In some cases high aspect ratio unrecrystallised grains show the growth of large side-plate colonies across the grain. This is more evident than for side-plate growth in the isothermal forging and may be related to the level of stored energy in these beta grains.

- {100} and {111} beta deformation axial fibre textures are observed in the forging (for medium to high strains). Recrystallisation textures are different but have not been identified from the acquired EBSD maps.
- Lower strains (the forging 'dead zone') show no clear beta deformation textures.
- After SHT high strain microstructures usually consist of Widmanstätten alpha platelets. Low strain microstructures often contain large high aspect ratio alpha platelets. As for the isothermal forging, these often show both optical and crystallographic alignment but appear to nucleate and grow internally within beta grains. Again this may be attributed to a sectioning effect.
- As for the isothermal forging, Widmanstätten alpha platelets tend to show unique basal plane orientations. Variants with shared basal planes are infrequently observed.

7.5.3 Hammer forging

- High strain sections of the pancake forging show a predominantly dynamically recrystallised microstructure. This is attributed to the high strain rates that are characteristic of hammer forging. Recrystallised grains are characterised by equiaxed morphologies of ~50-100μm, with recrystallisation occurring initially at the boundaries of prior beta grains.
- A varied texture is observed in recrystallised beta grains, whilst unrecrystallised heavily worked grains show {100} or {111} axial fibre textures. A significant proportion of recrystallised grains also show textures close to the {100} or {111} axial fibre, suggesting that the onset of recrystallisation occurred early enough in the forging schedule to allow further deformation leading to the development of these textures.

- Unrecrystallised grains in high strain microstructures show sub-structures. Alpha precipitation occurs on some sub-structures to give platelet features aligned parallel to grain flow.
- Intermediate to low strain microstructures occasionally show the presence of trans-granular alpha colony features. These are presumed to be the result of growth of preferred alpha variants from grain boundaries. Recovery sub-structures acting as nucleation sites for the formation of these features is another explanation.
- Beta textures at lower effective strain levels are relatively weak, with no deformation texture observed in the forging dead zone. Despite weak beta textures, SHT often leads to the formation of large colonies of relatively fine alpha platelets. This may be due to the growth of platelets from grain boundary layers or due to the nucleation and growth of colonies within beta grains.
- Widmanstätten alpha platelet distributions within the hammer forging typically consist of variants with unique basal plane orientations. Variants with shared basal planes are infrequently observed.
- In broad conclusion, EBSD analysis has provided an indication of the textures and the phase transformation processes occurring during forging, solution heat treatment and ageing of Ti6246. The textures reported in this chapter require further characterisation to ensure statistical accuracy. X-ray diffraction would be a suitable method for the determination of recrystallisation and deformation textures in the three pancake forgings in various locations.

7B Processing effects on texture in Ti6246 forgings – Figures and tables

7.6 Experimental details

Table 7-1 – Ladish pancake forgings experimental data

Pancake	Forging Temperature /˚C	Forging Method	Post Forge ReX Anneal	Post Forge Cooling Rate
1	970	Isothermal	No	Water Quench
2	970	Hot Die	No	Water Quench
5	970	Hammer	No	Water Quench

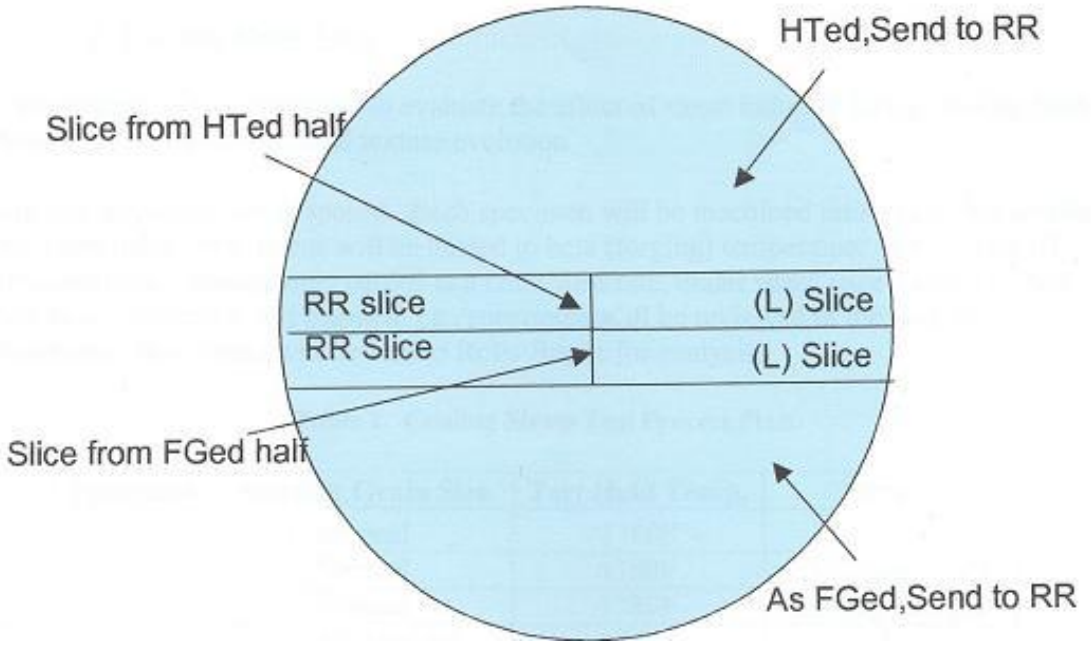

Figure 7-1 – Schematic of sectioning of pancake forgings (Viewed from the direction of the compression axis)

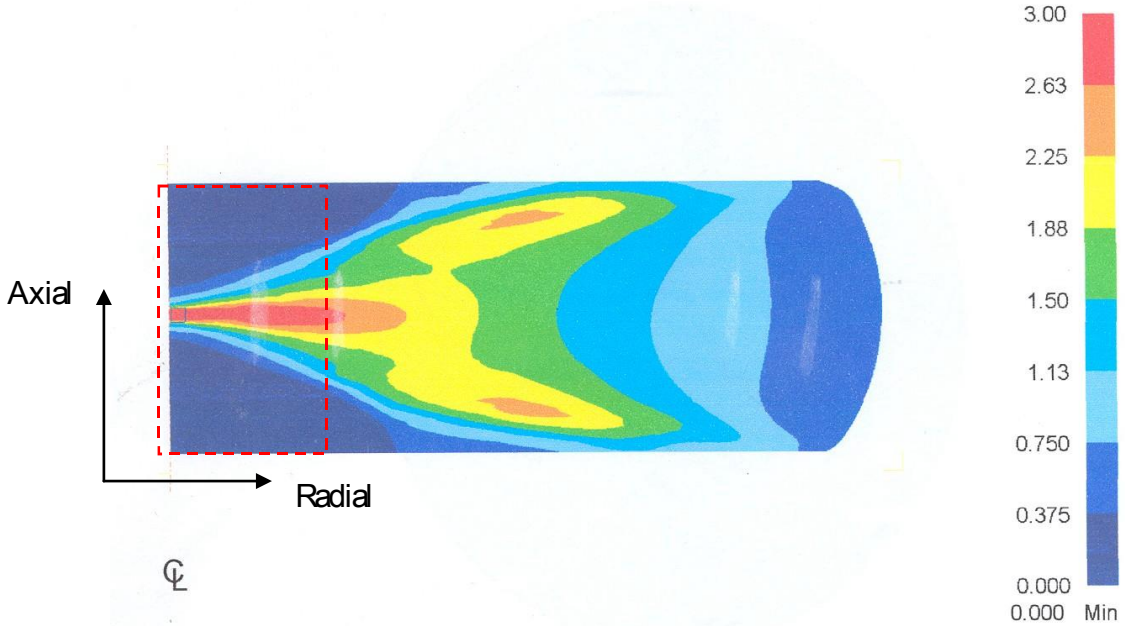

Figure 7-2 – Effective strain distribution in pancake forgings (Cross-section through the axial-radial plane) [197]

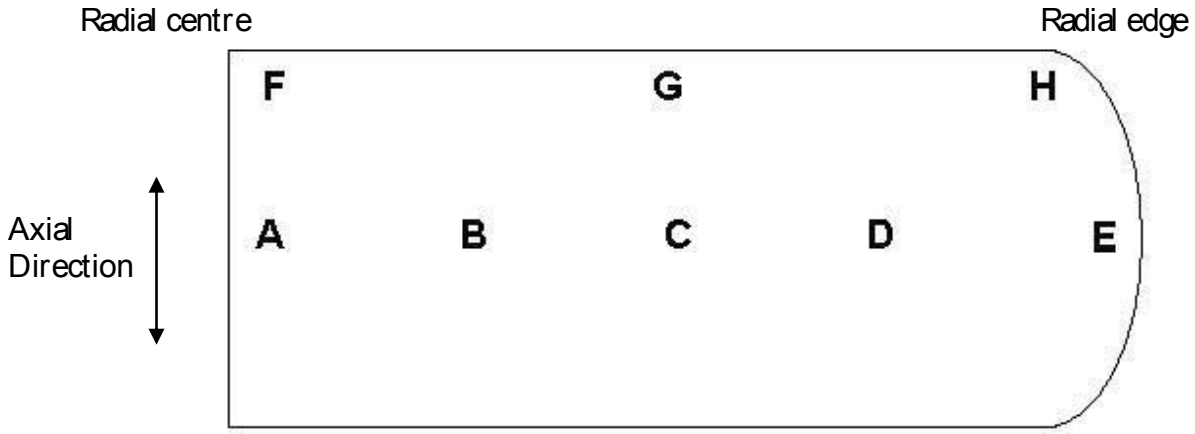

Figure 7-3 – Locations A and F for analysis of optical microstructures

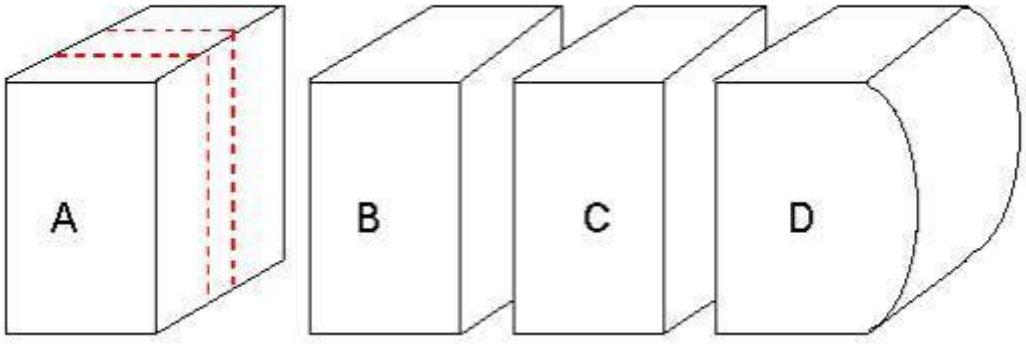

Figure 7-4 – Cut up of as-forged Ladish pancake slice

7.7 Results

7.7.1 Grain flow profiles

Figure 7-5 – Grain flow cross-section of isothermal pancake forging 1A

Figure 7-6 – Grain flow cross-section of hot die pancake forging 2A

Figure 7-7 – Grain flow cross-section of hammer pancake forging 5A

7.7.2 Microstructure and texture assessment

7.7.2.1 Isothermal pancake – As-forged condition

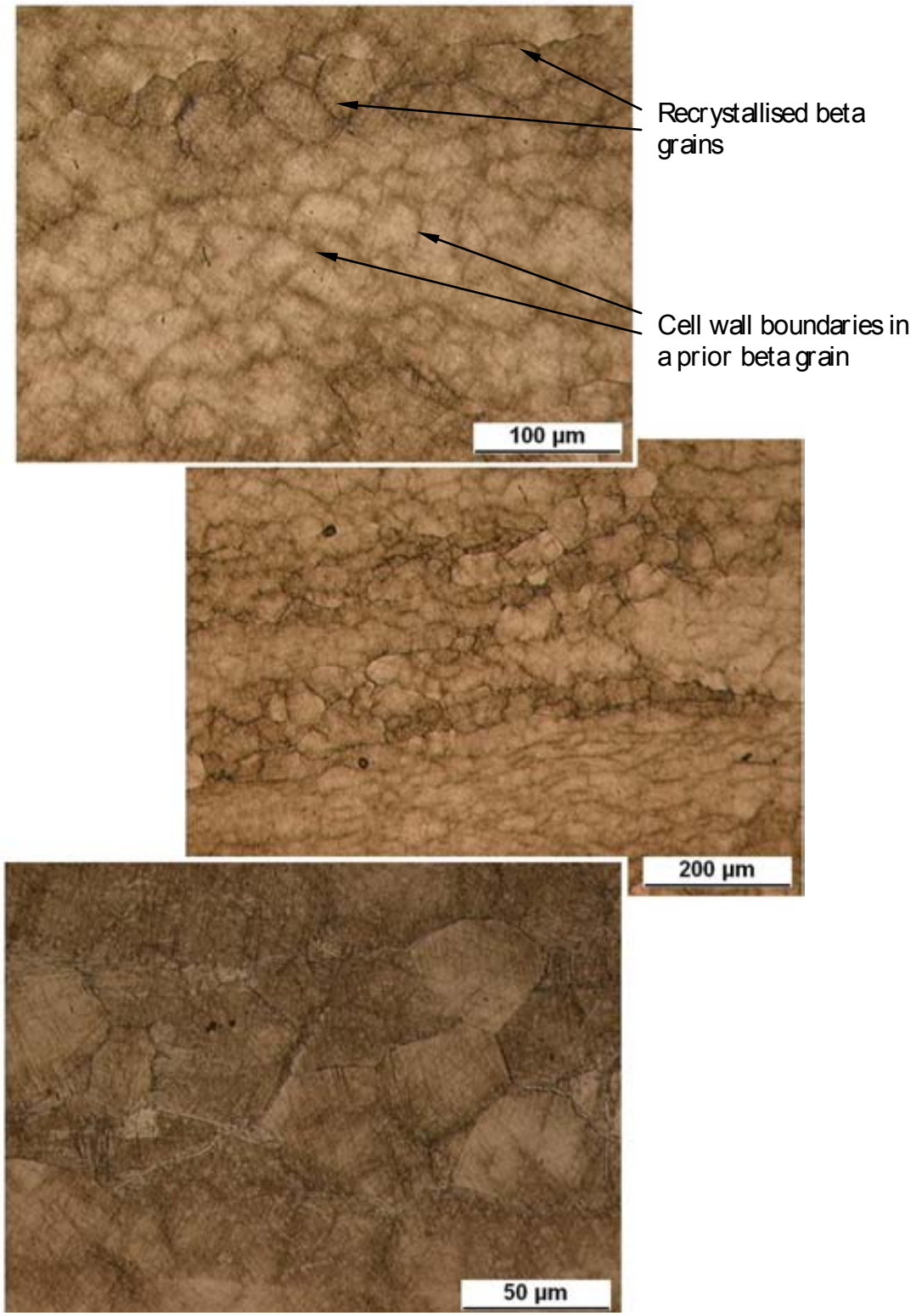

Figure 7-8 – Optical microstructure of isothermal pancake 1B (Location A)

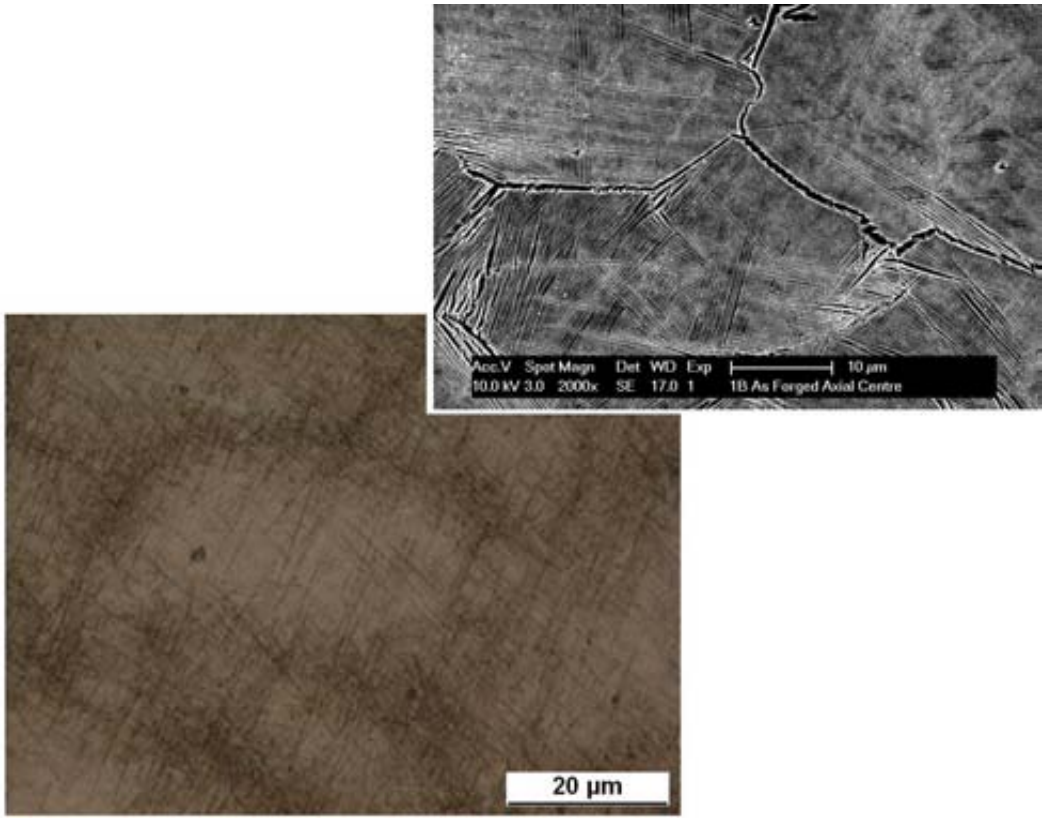

Figure 7-9 – Microstructure of isothermal pancake 1B (Location A)

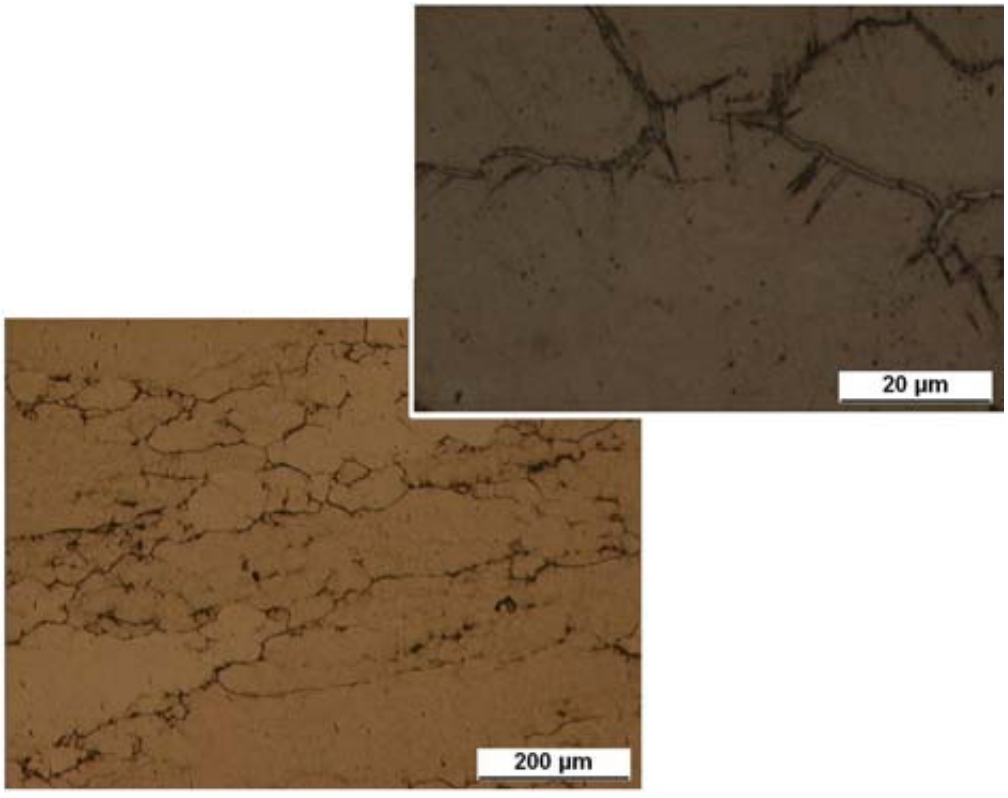

Figure 7-10 – Optical microstructure of isothermal pancake 1B (¼ axial depth)

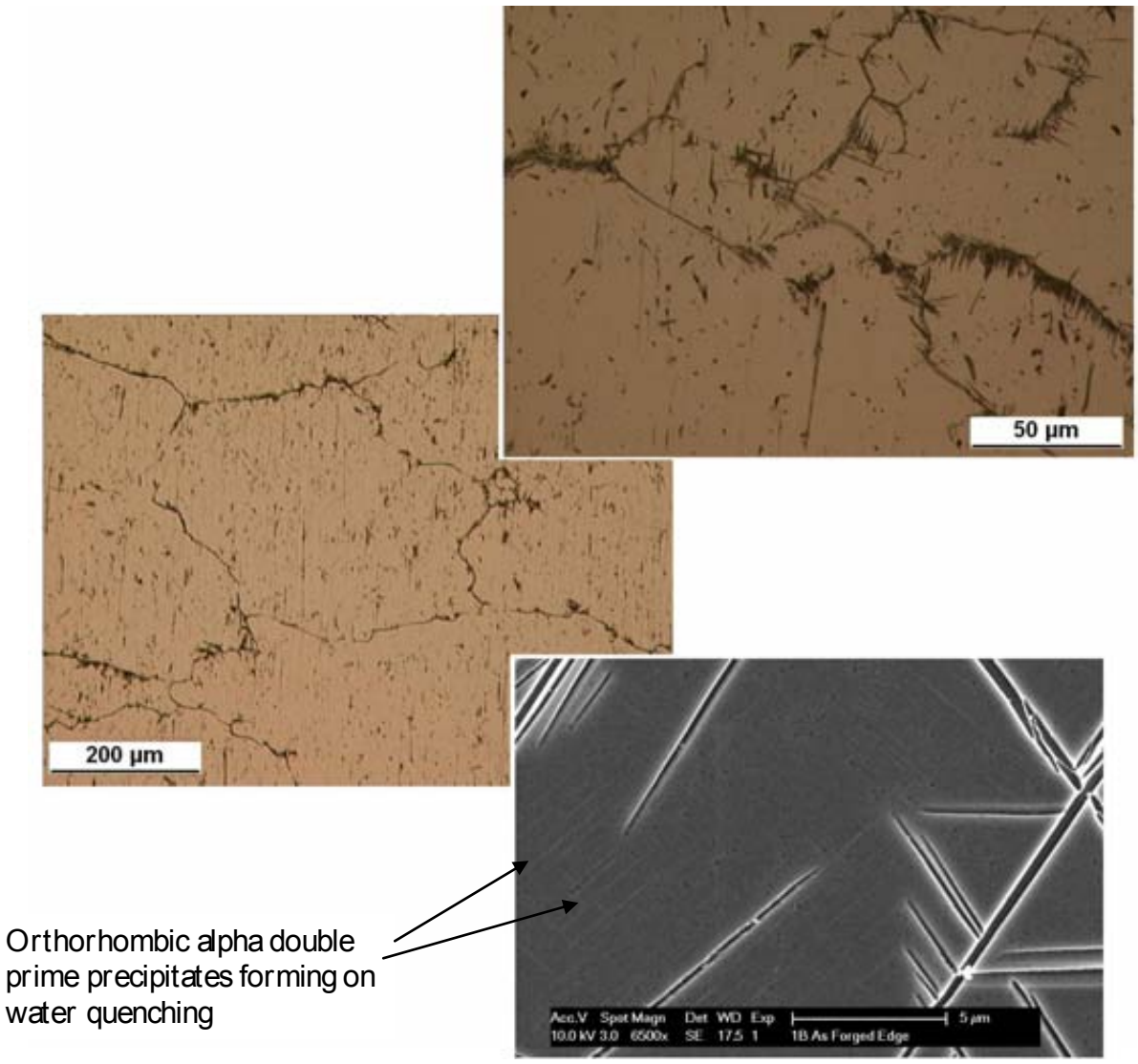

Figure 7-11 – Microstructure of as-forged isothermal pancake (Location F)

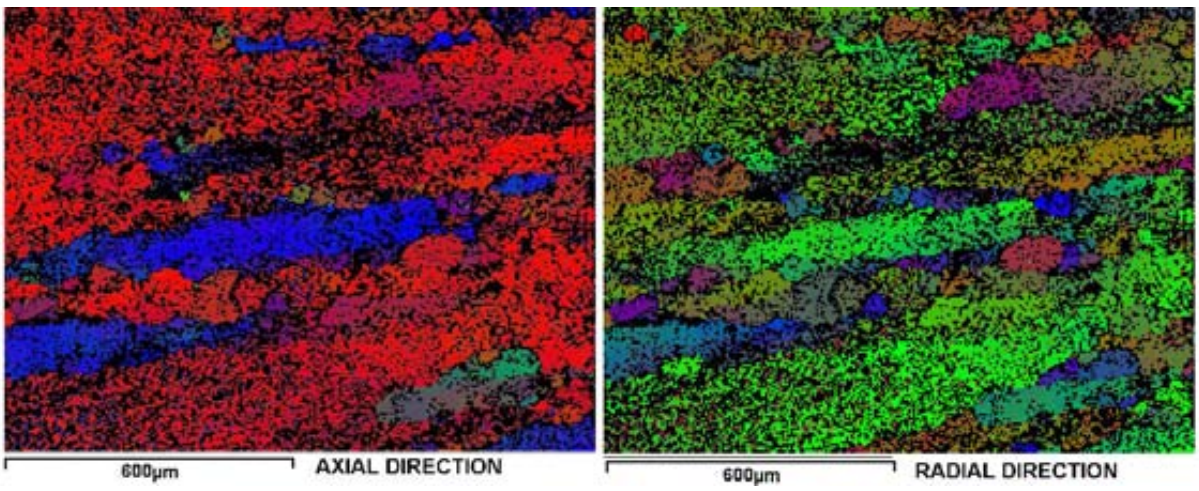

Figure 7-12 – As forged isothermal pancake location A – Beta COMs for axial and radial directions (I.e. directions parallel and normal to compression axis)

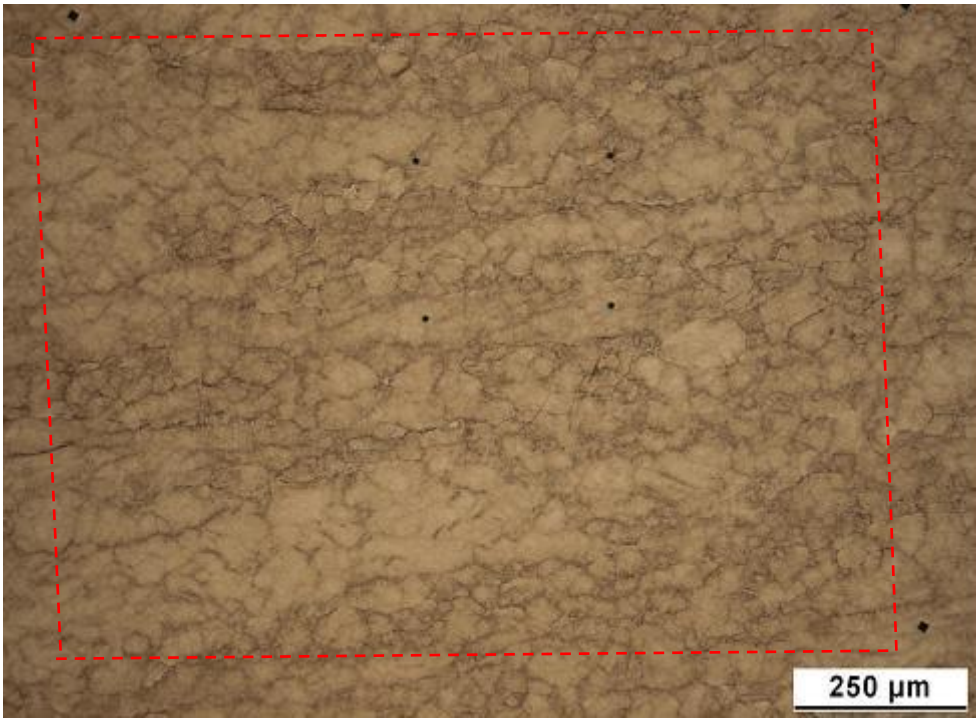

Figure 7-13 – Optical microstructure of site of interest of as-forged isothermal pancake location A

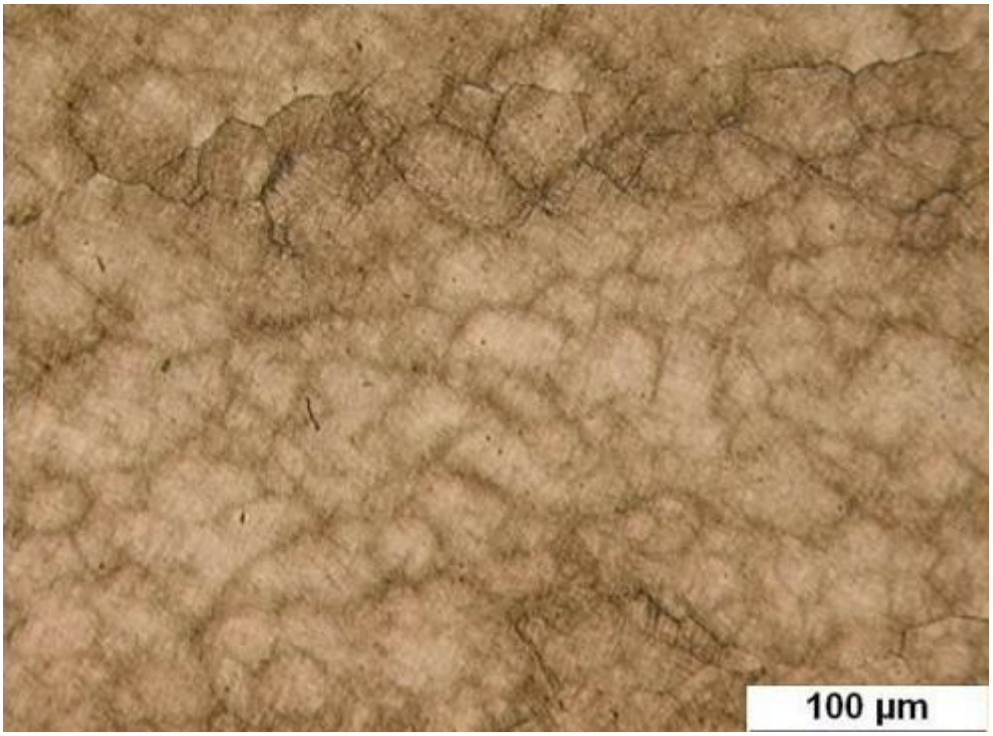

Figure 7-14 – Optical microstructure of as-forged isothermal pancake location A

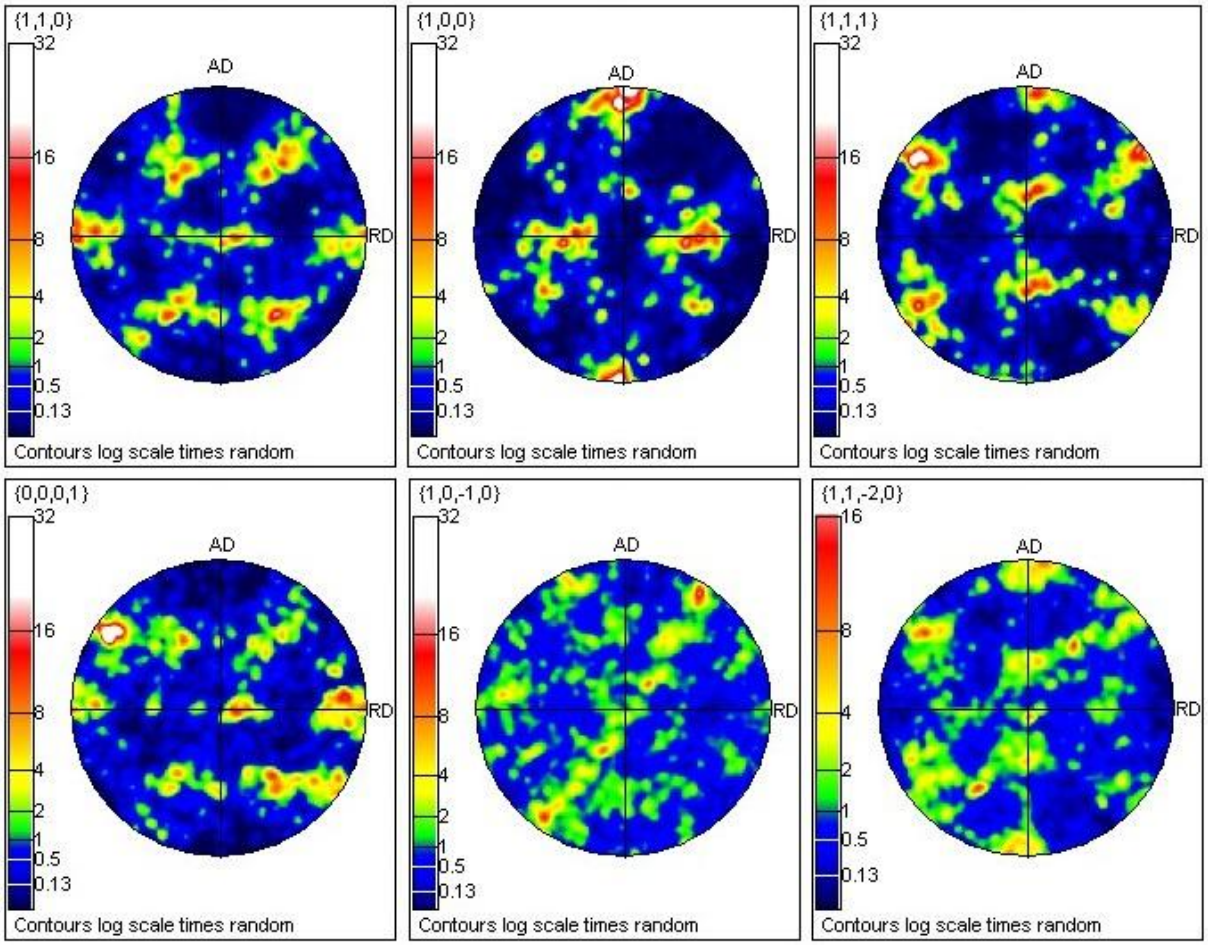

Figure 7-15 – Pole figures showing beta and alpha textures for as-forged isothermal pancake location A (see COM in Figure 7-12). AD represents axial direction (compression axis), RD represents radial direction

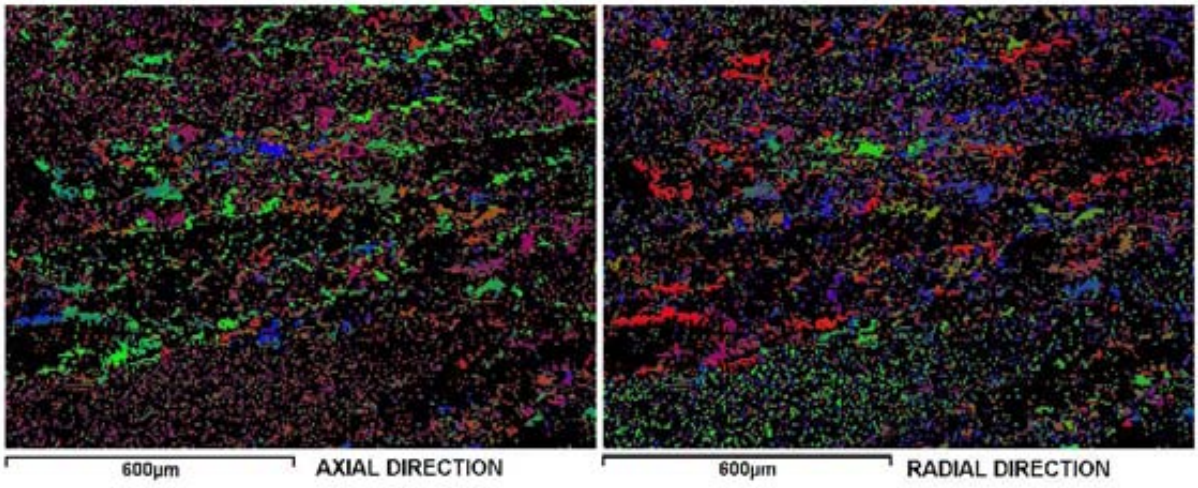

Figure 7-16 – As-forged isothermal pancake Location A. Alpha COMs displaying textures w.r.t. axial and radial directions

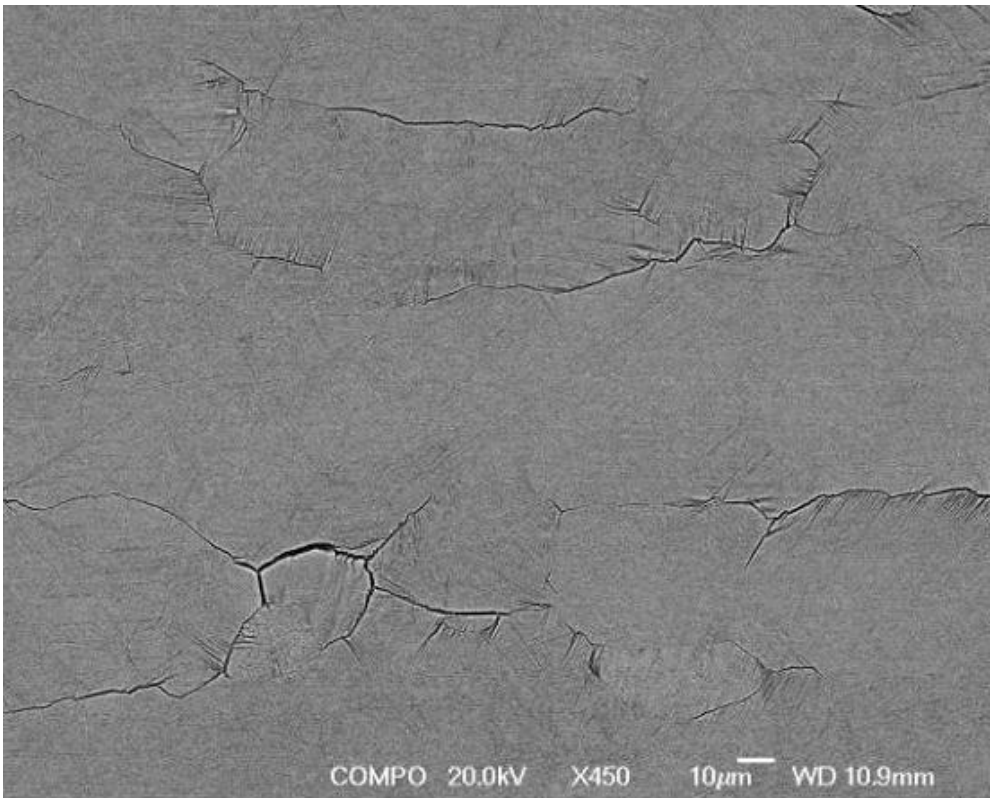

Figure 7-17 – Microstructure of as forged isothermal pancake location A site of interest

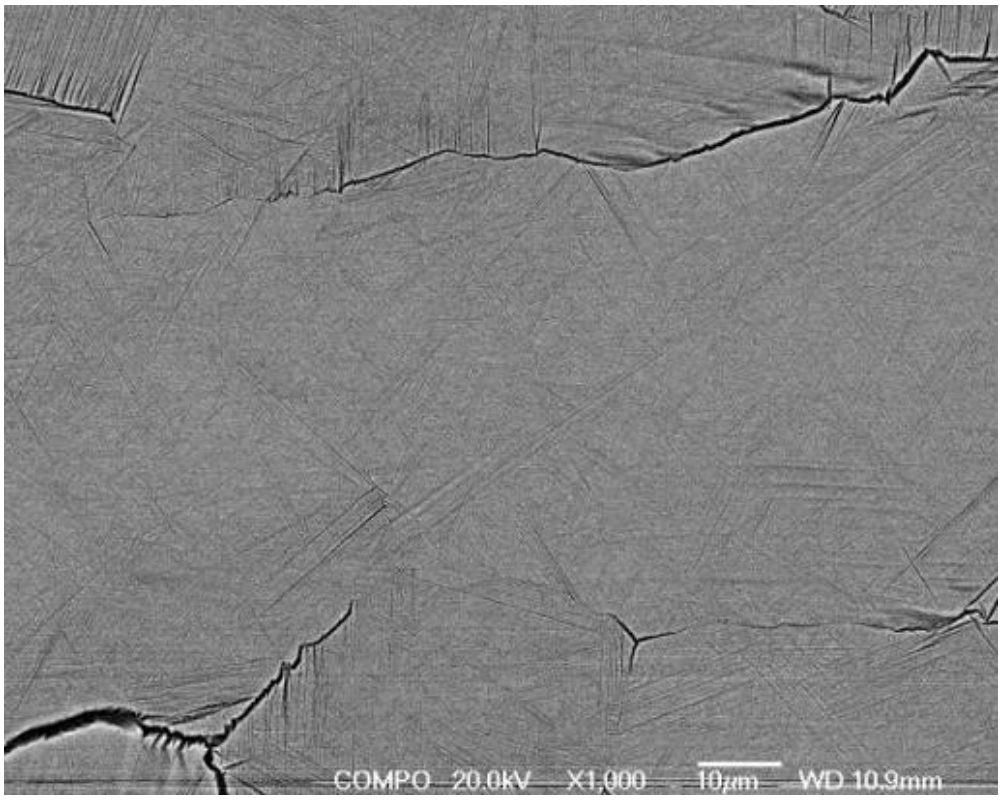

Figure 7-18 – Microstructure of as forged isothermal pancake location A

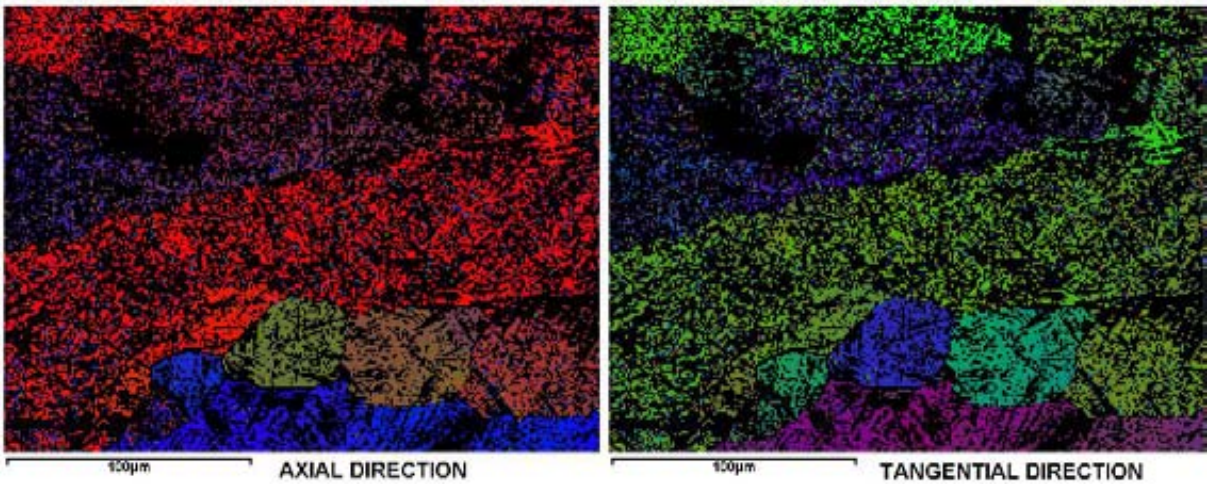

Figure 7-19 – As forged isothermal pancake location A. Beta COMs displaying textures w.r.t. axial and tangential directions

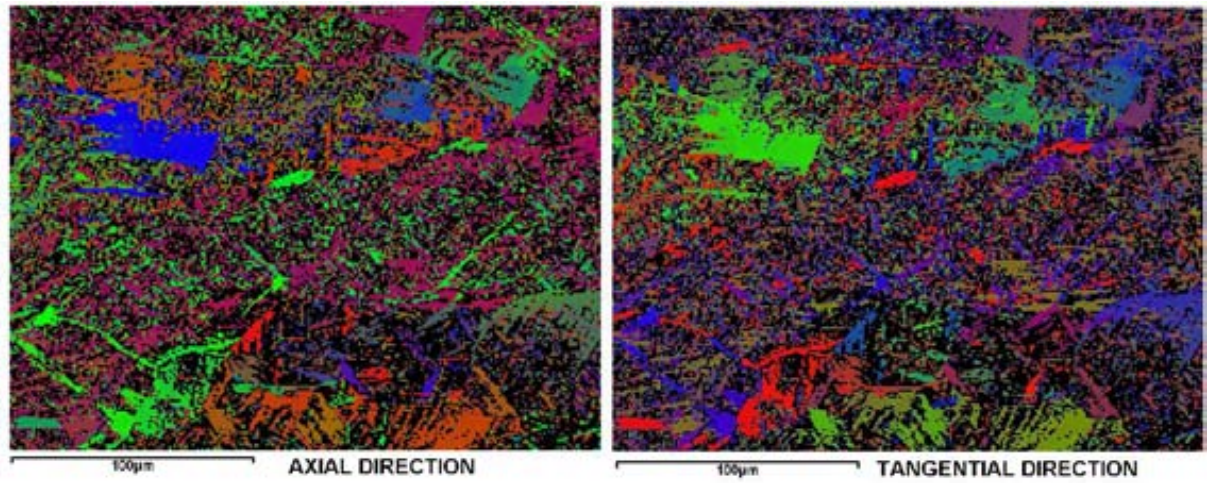

Figure 7-20 – As forged isothermal pancake location A. Alpha COMs displaying textures w.r.t. axial and tangential directions

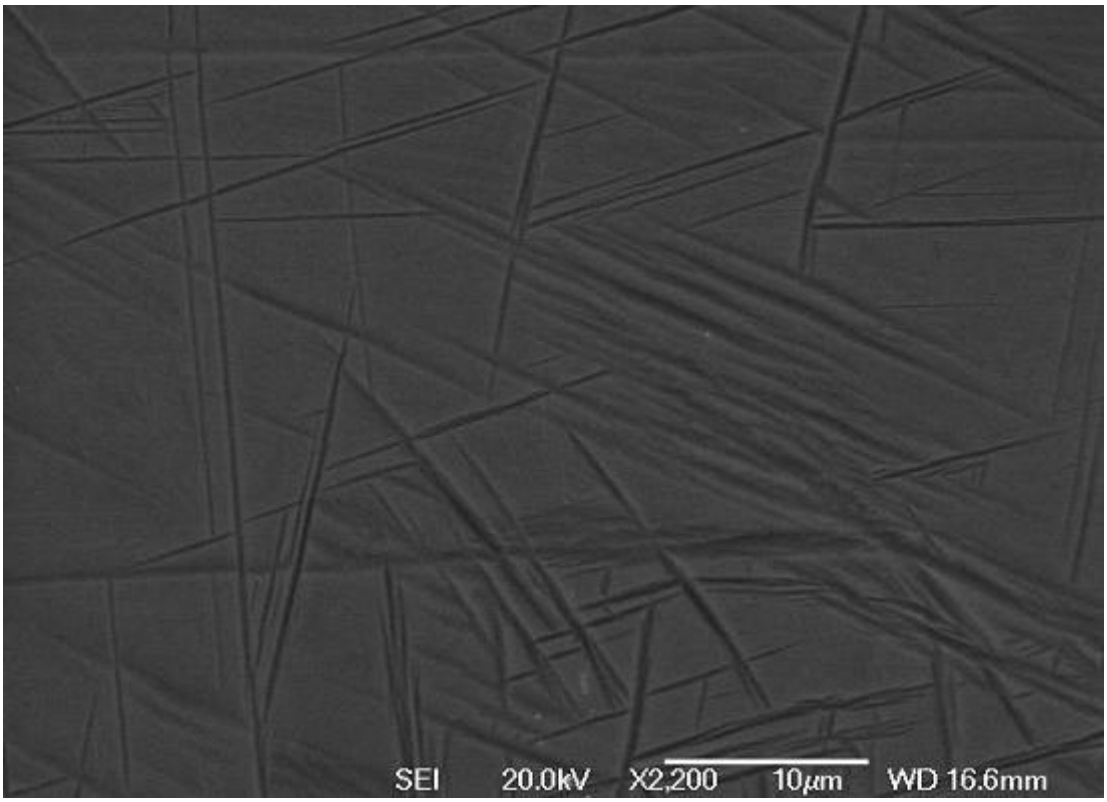

Figure 7-21 – Back-scatter electron image of typical microstructure of as-forged isothermal pancake location F

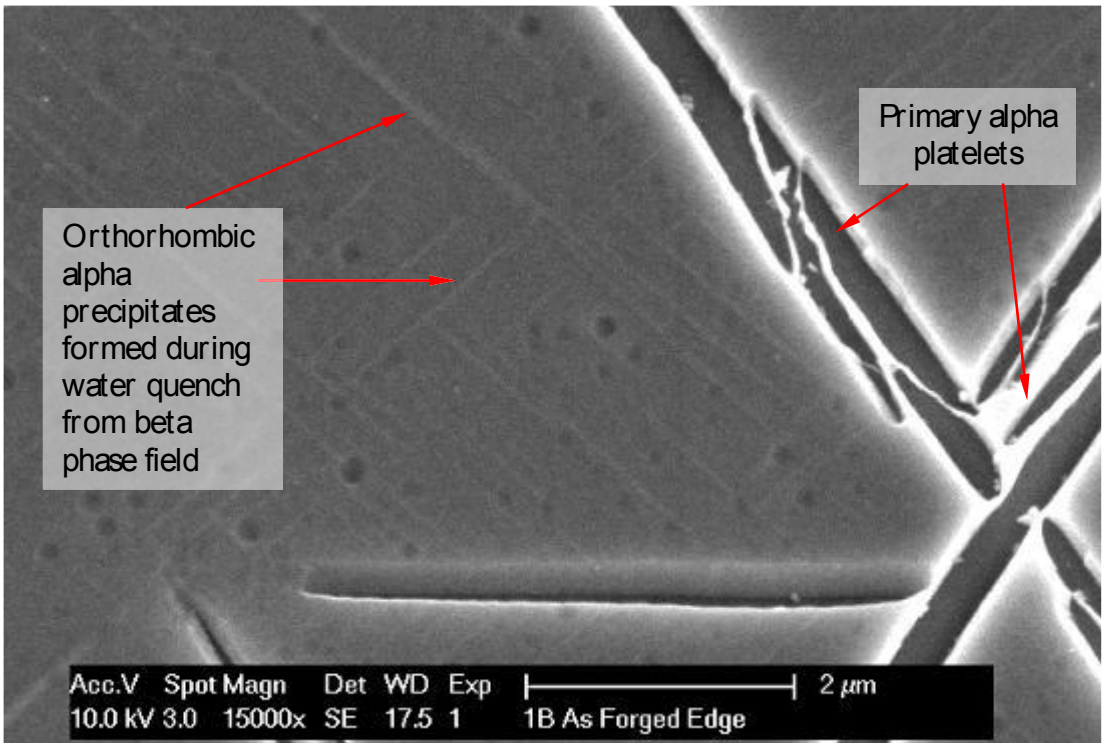

Figure 7-22 – Coarse and fine alpha platelet precipitates in as-forged isothermal pancake location F

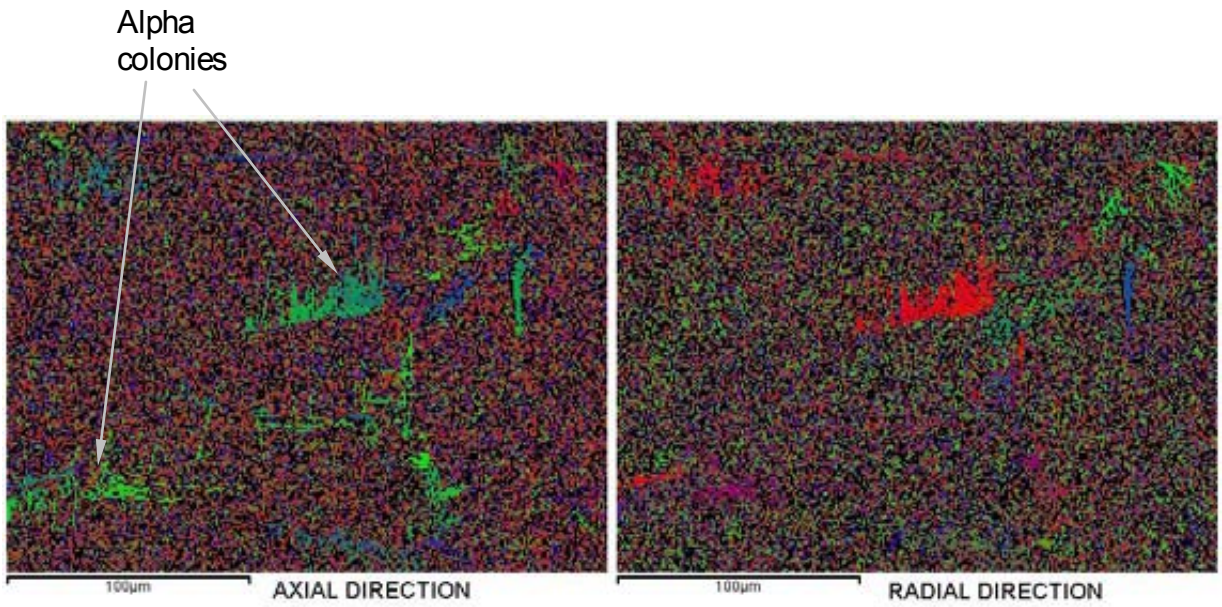

Figure 7-23 – As forged isothermal pancake location F. Alpha COMs displaying textures w.r.t. axial and radial directions

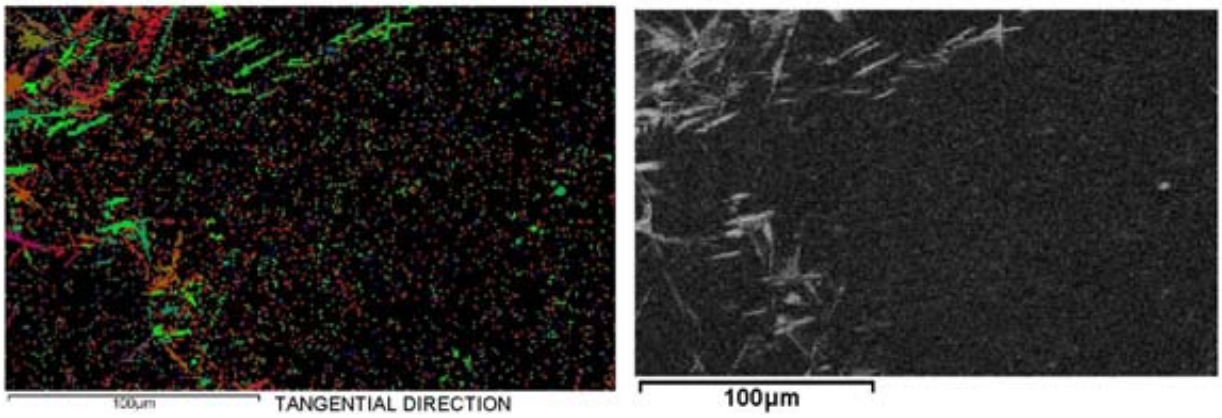

Figure 7-24 – As forged isothermal pancake location F. Alpha COM displaying texture w.r.t. tangential direction and corresponding pattern quality map

7.7.2.2 Hot die pancake – As-forged condition

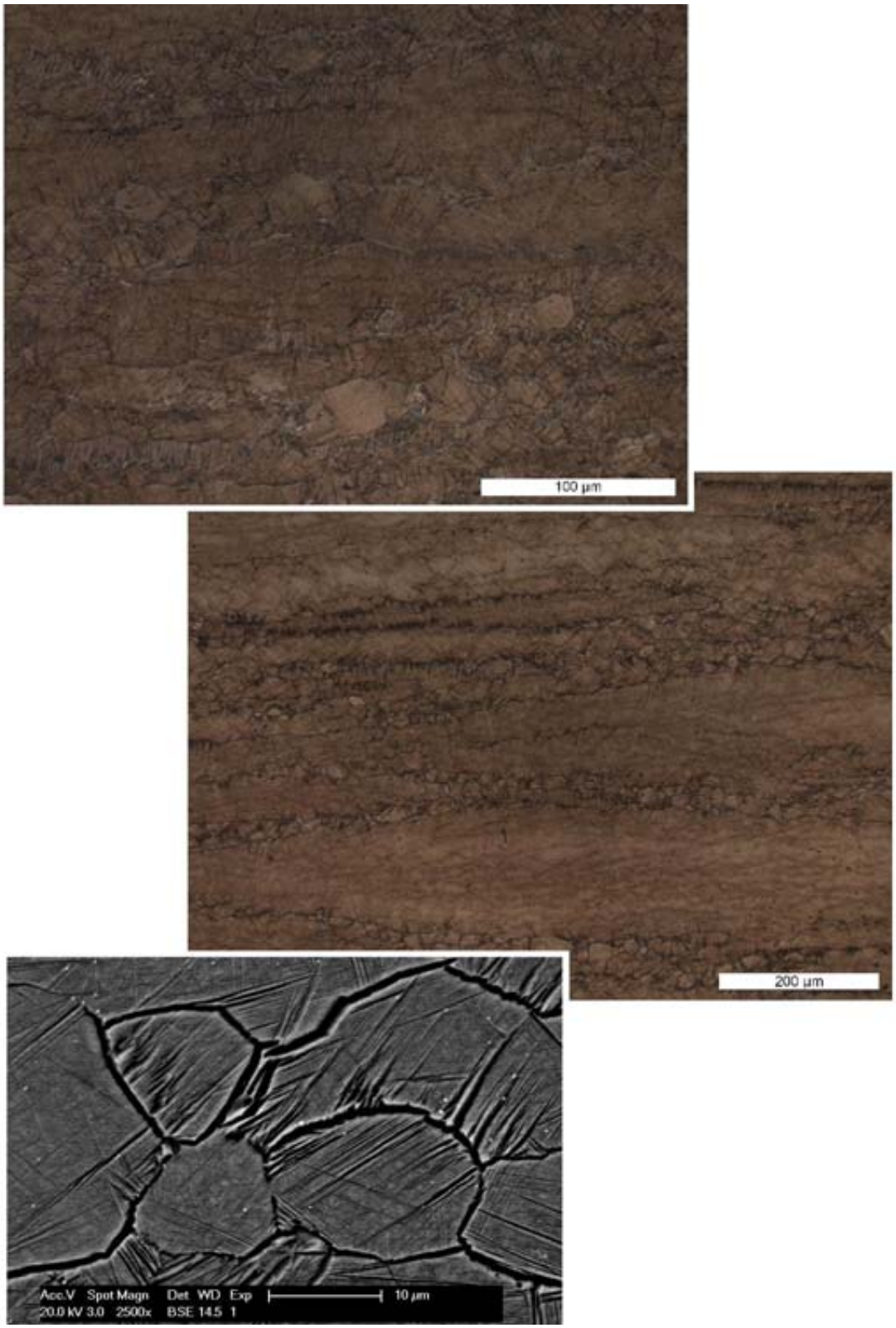

Figure 7-25 – Microstructure of as-forged hot die pancake forging in high strain location A

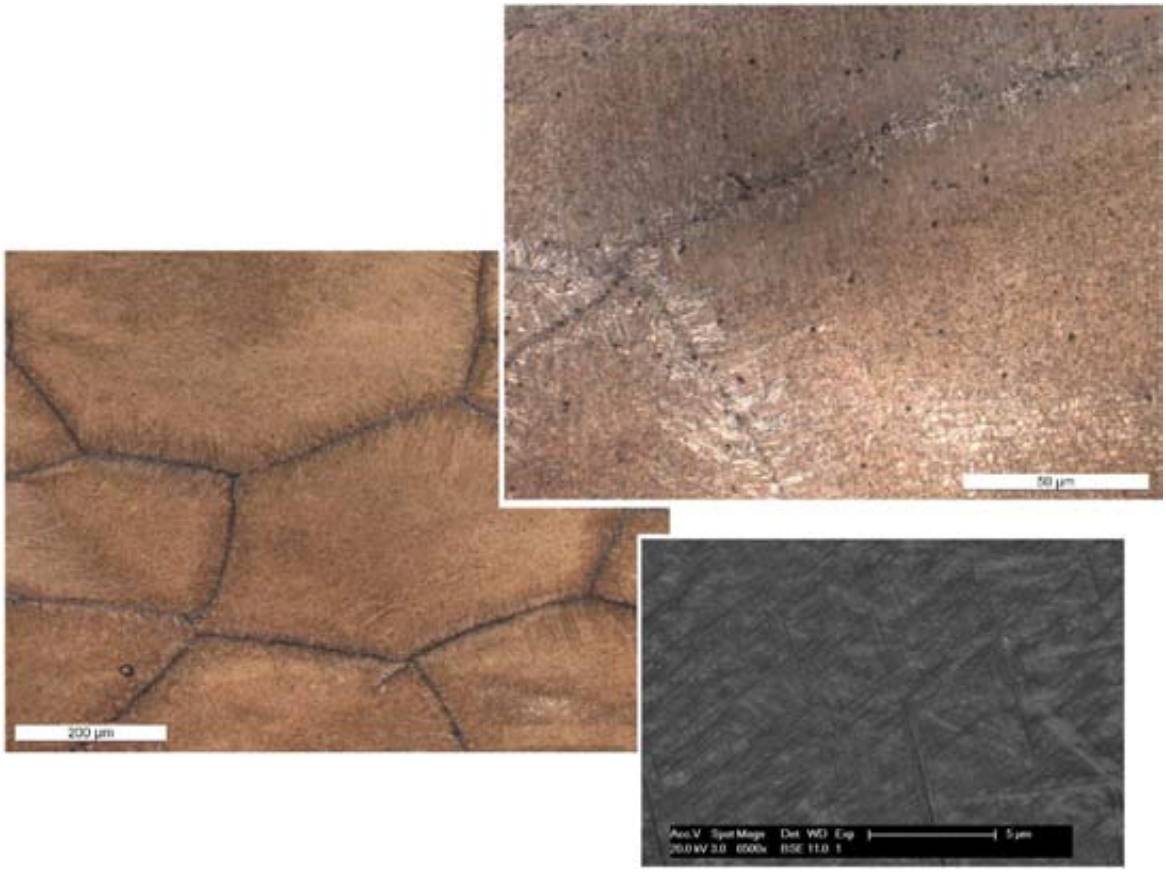

Figure 7-26 – Microstructure of as-forged hot die pancake forging in low strain location F

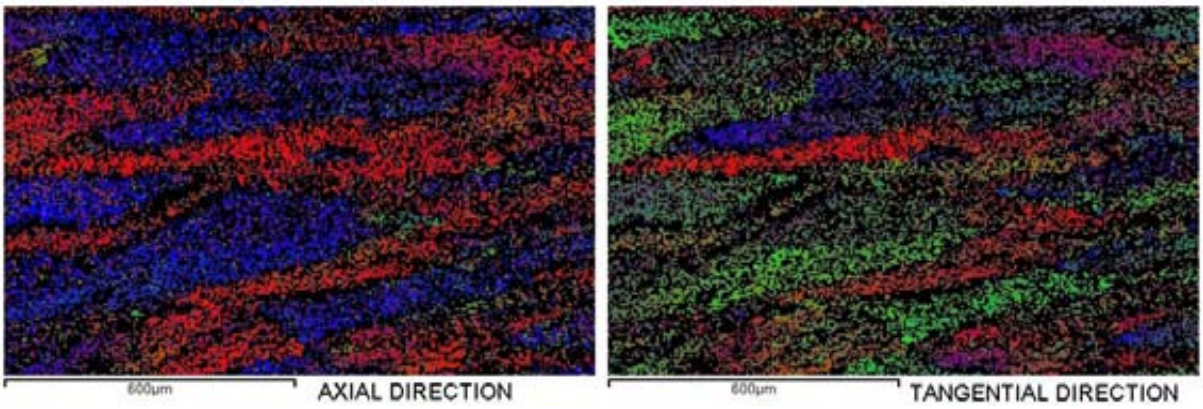

Figure 7-27 – As forged hot die pancake location A. Beta COMs displaying textures w.r.t. axial and tangential directions

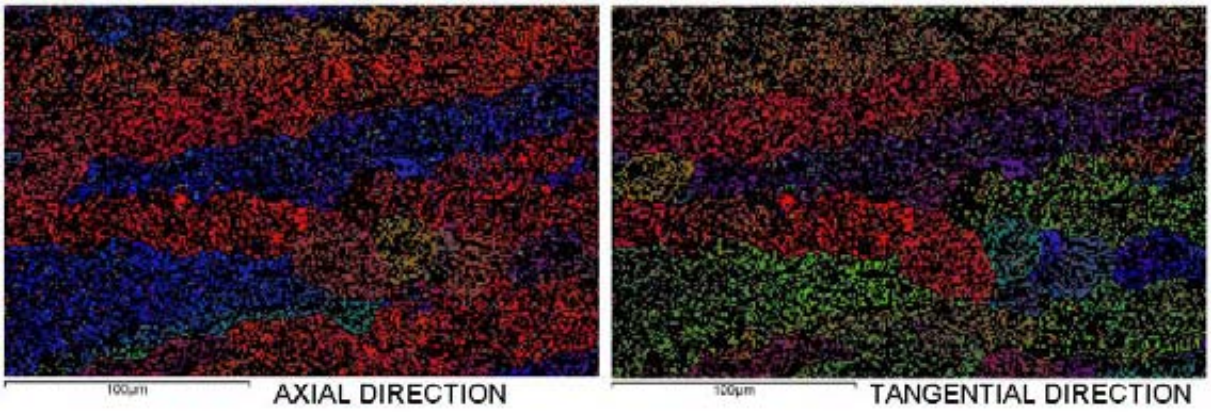

Figure 7-28 – As forged hot die pancake location A. Beta COMs displaying textures w.r.t. axial and tangential directions

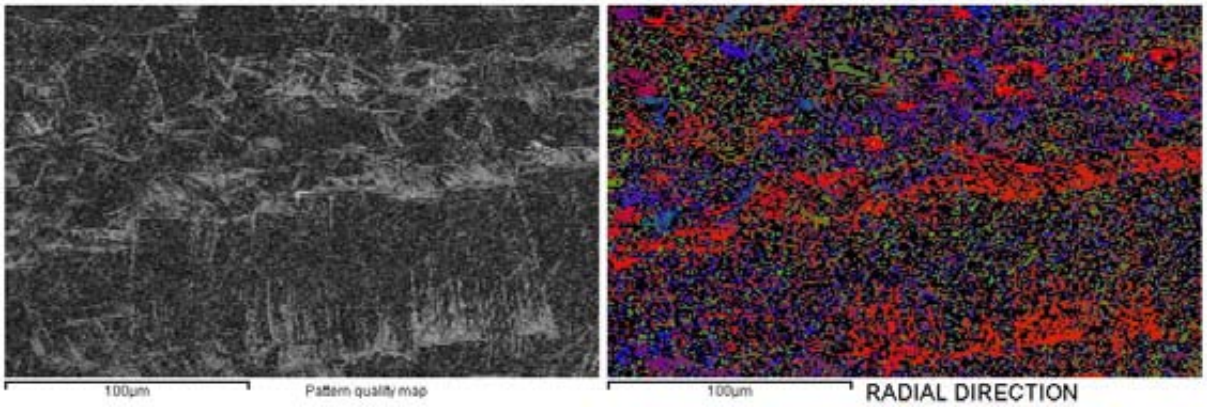

Figure 7-29 – As forged hot die pancake location A. Pattern quality map and alpha phase COM displaying textures w.r.t. radial direction

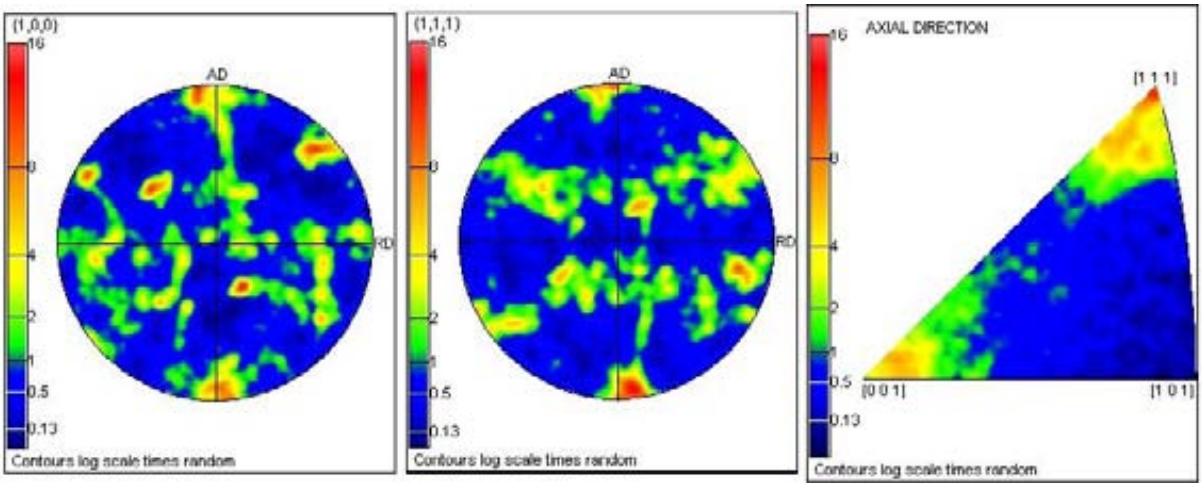

Figure 7-30 – As forged hot die pancake location A. {100} and {111} pole figures and axial direction inverse pole figure (For the EBSD map area in Figure 7-27)

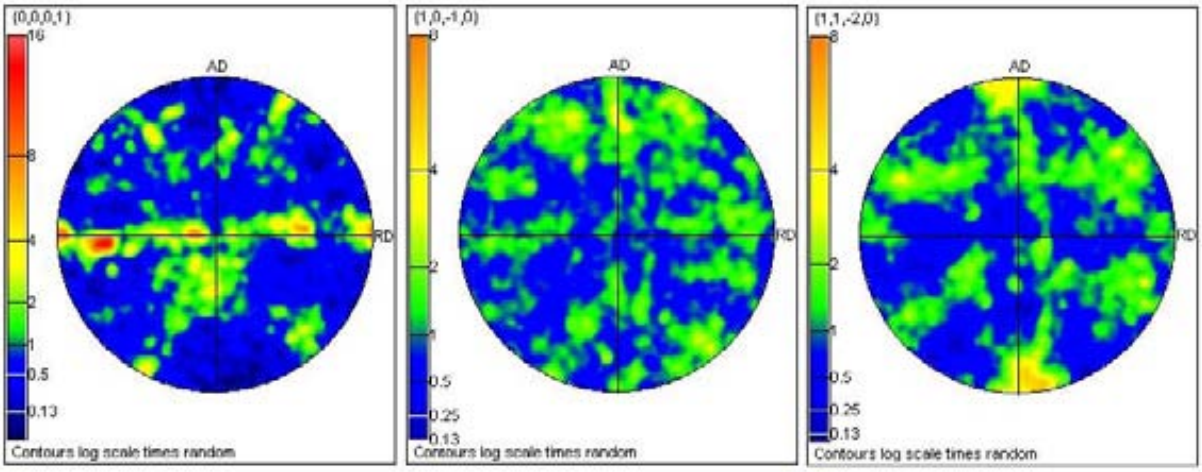

Figure 7-31 – As forged hot die pancake location A. Alpha phase pole figures (For the EBSD map area in Figure 7-27) showing radial distribution of basal plane intensities

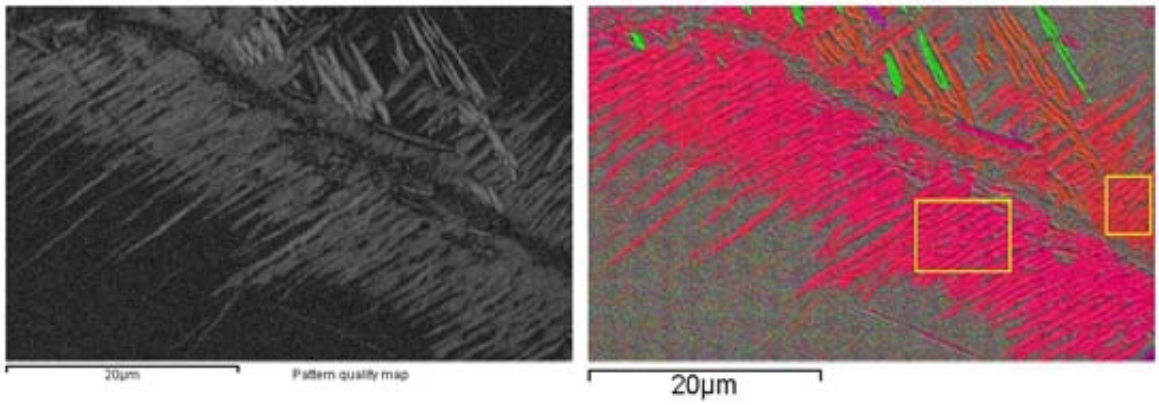

Figure 7-32 – As forged hot die pancake location F. Pattern quality map and alpha phase COM displaying textures w.r.t. radial direction

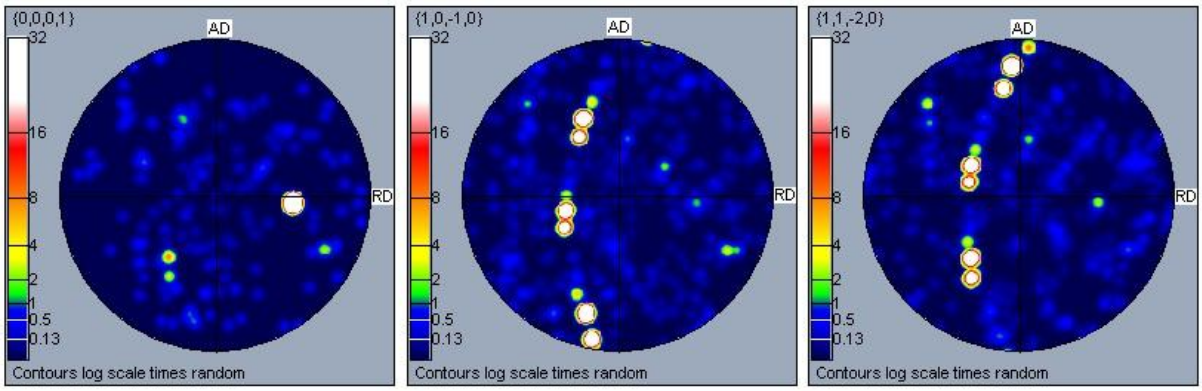

Figure 7-33 – Alpha phase pole figures displaying textures containing in areas outlined in alpha phase map in Figure 7-32

7.7.2.3 Hammer pancake – As-forged condition

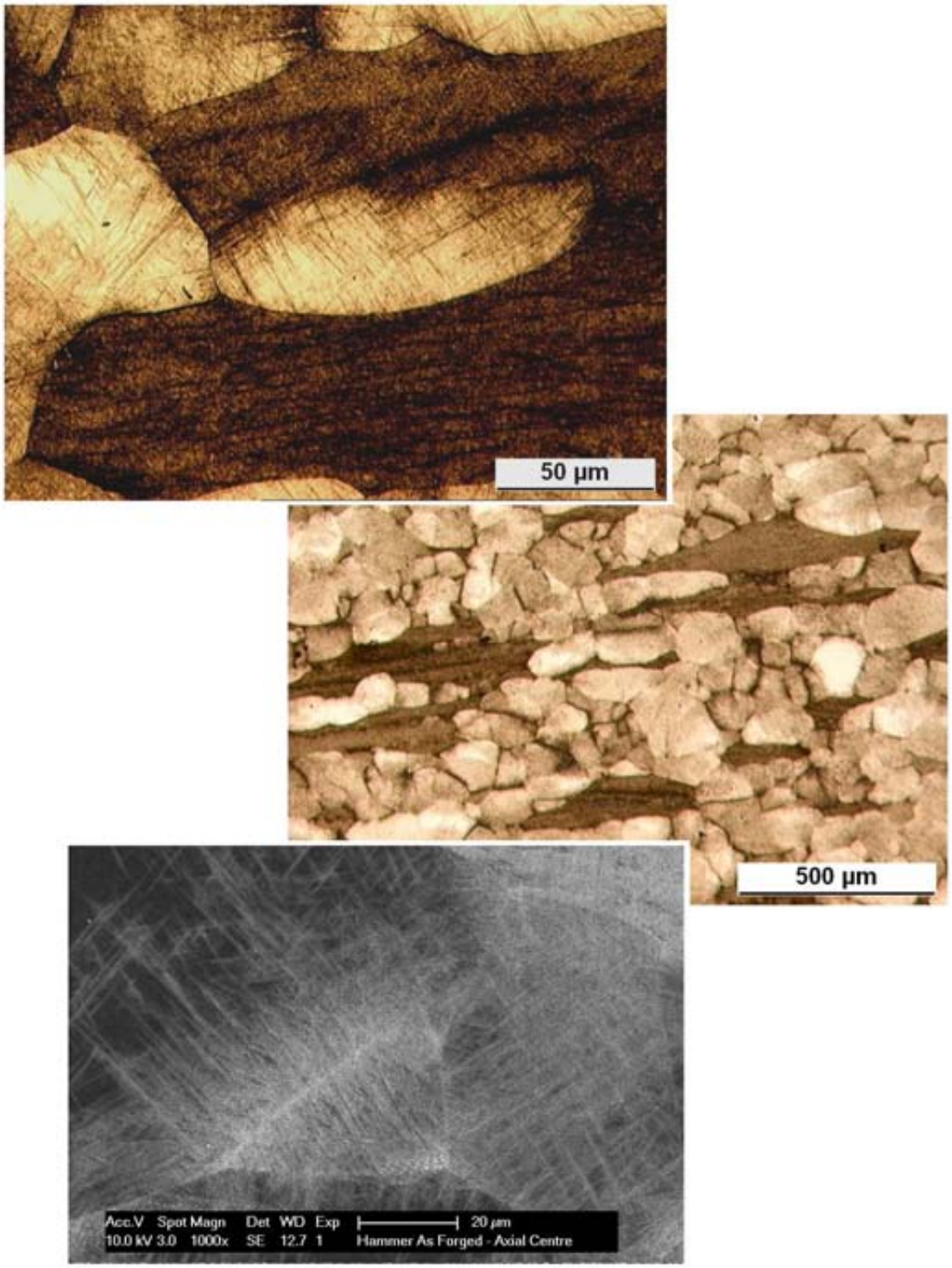

Figure 7-34 – Microstructure of as-forged hammer pancake forging in high strain location A

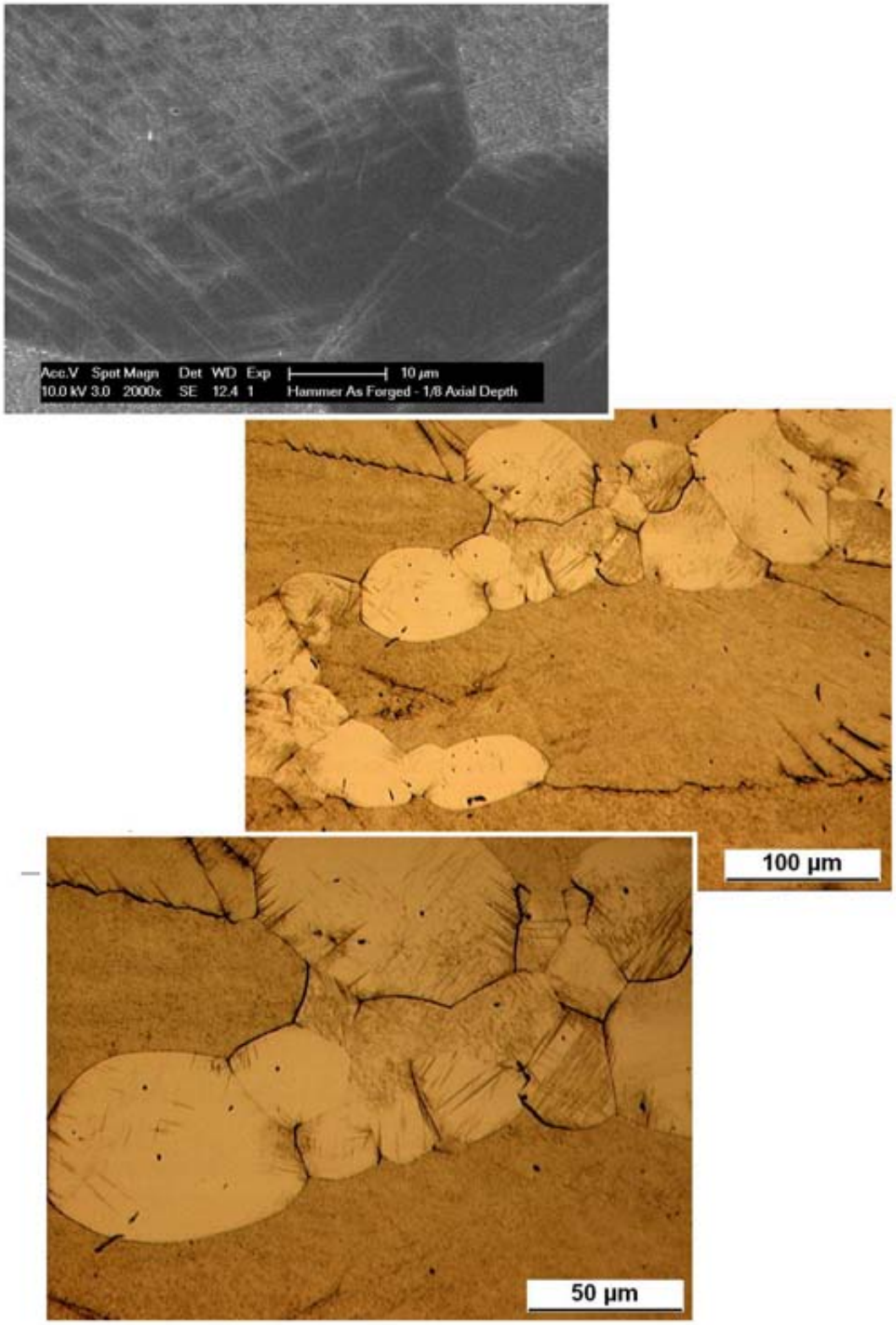

Figure 7-35 – Microstructure of as-forged hammer pancake forging at 1/8 axial depth (Between location F at edge and A at 1/2 axial depth)

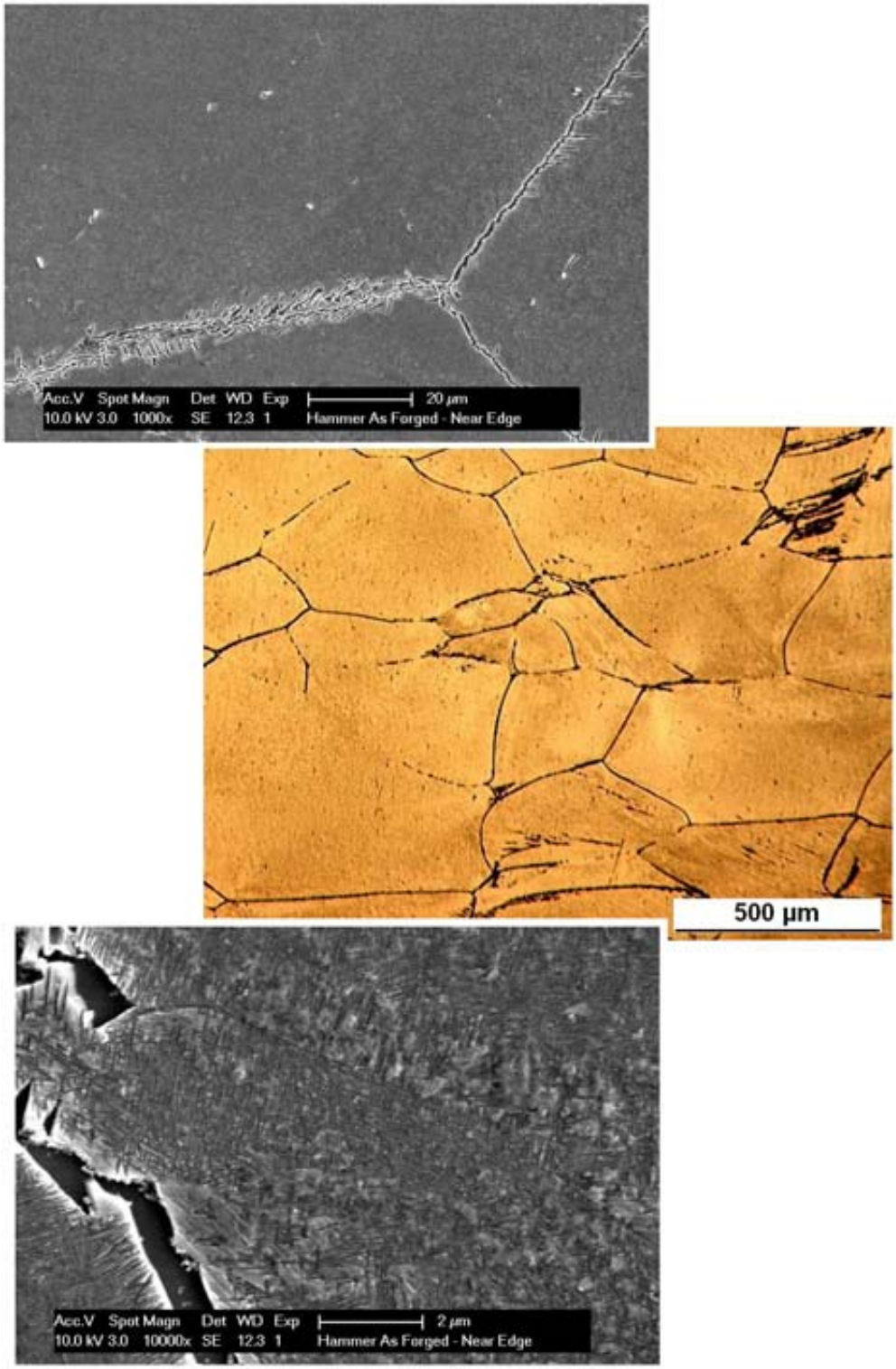

Figure 7-36 – Microstructure of as-forged hammer pancake forging in low strain location F

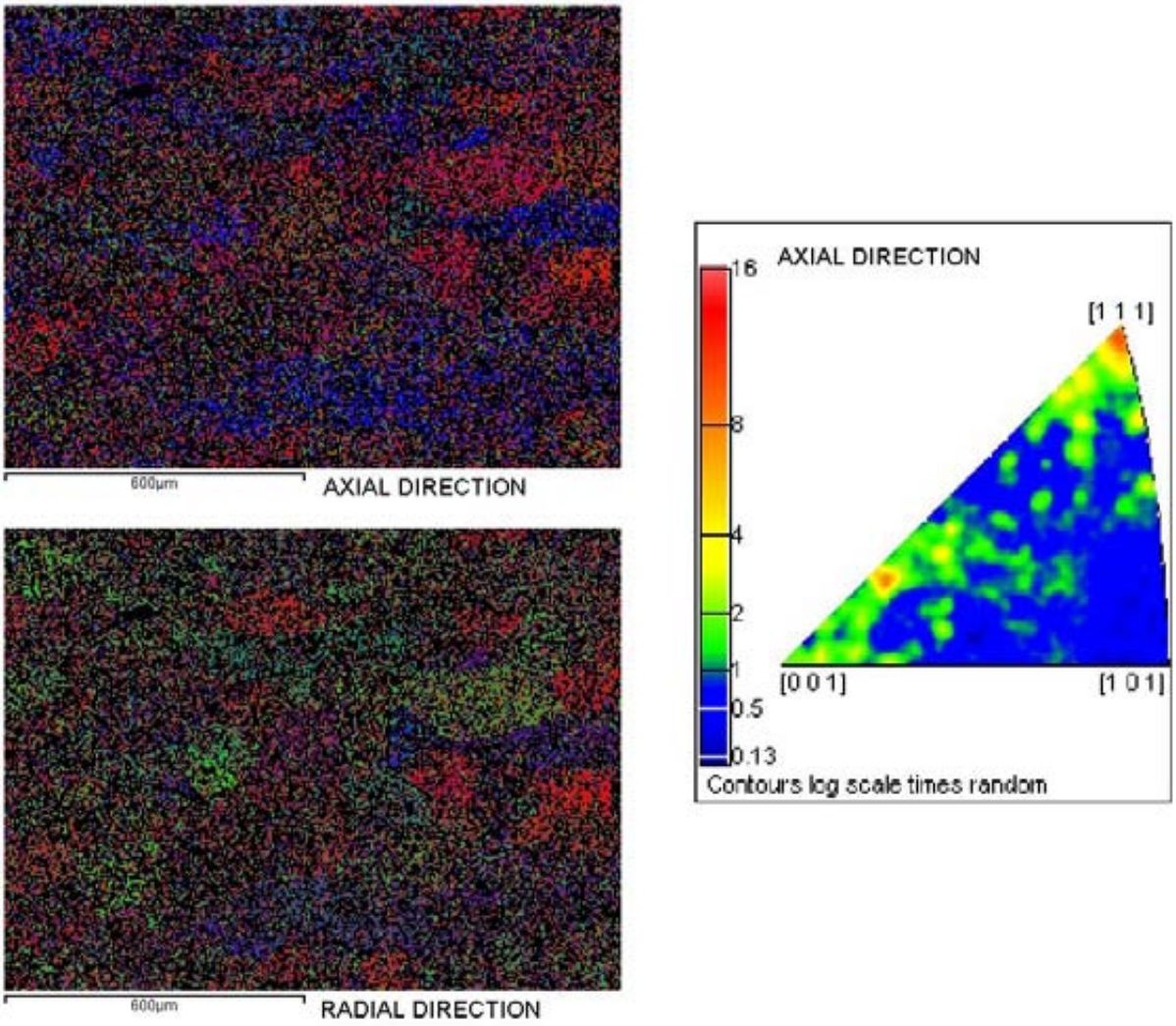

Figure 7-37 – As forged hammer pancake location A. Beta COMs displaying textures w.r.t. axial and radial directions and corresponding axial direction inverse pole figure

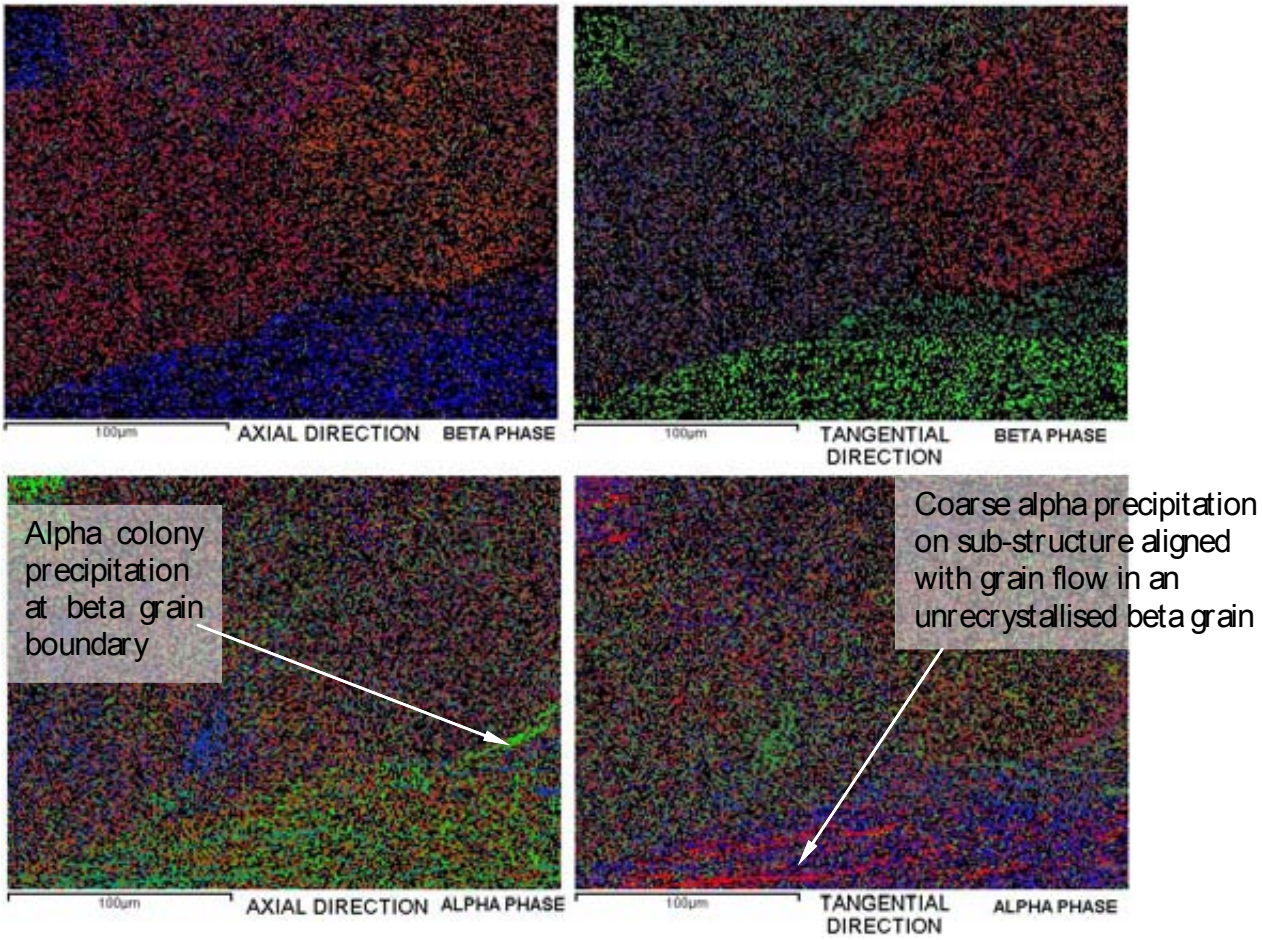

Figure 7-38 – As forged hammer pancake location A. Beta COMs displaying textures w.r.t. axial and tangential directions. Corresponding alpha COMs showing alpha precipitation at grain boundaries and within unrecrystallised prior beta grains

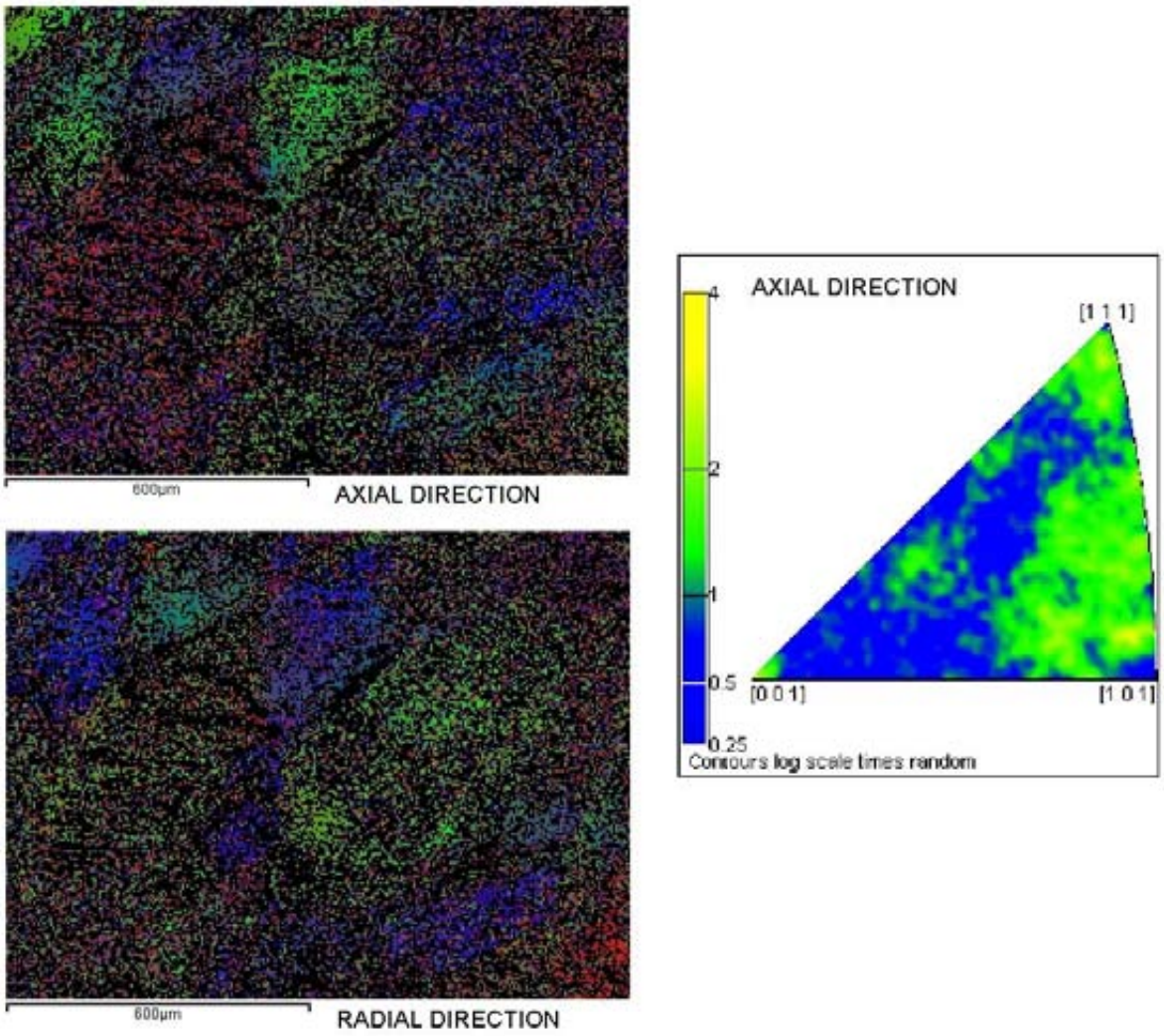

Figure 7-39 – As forged hammer pancake location F. Beta COMs displaying textures w.r.t. axial and radial directions and axial direction inverse pole figure

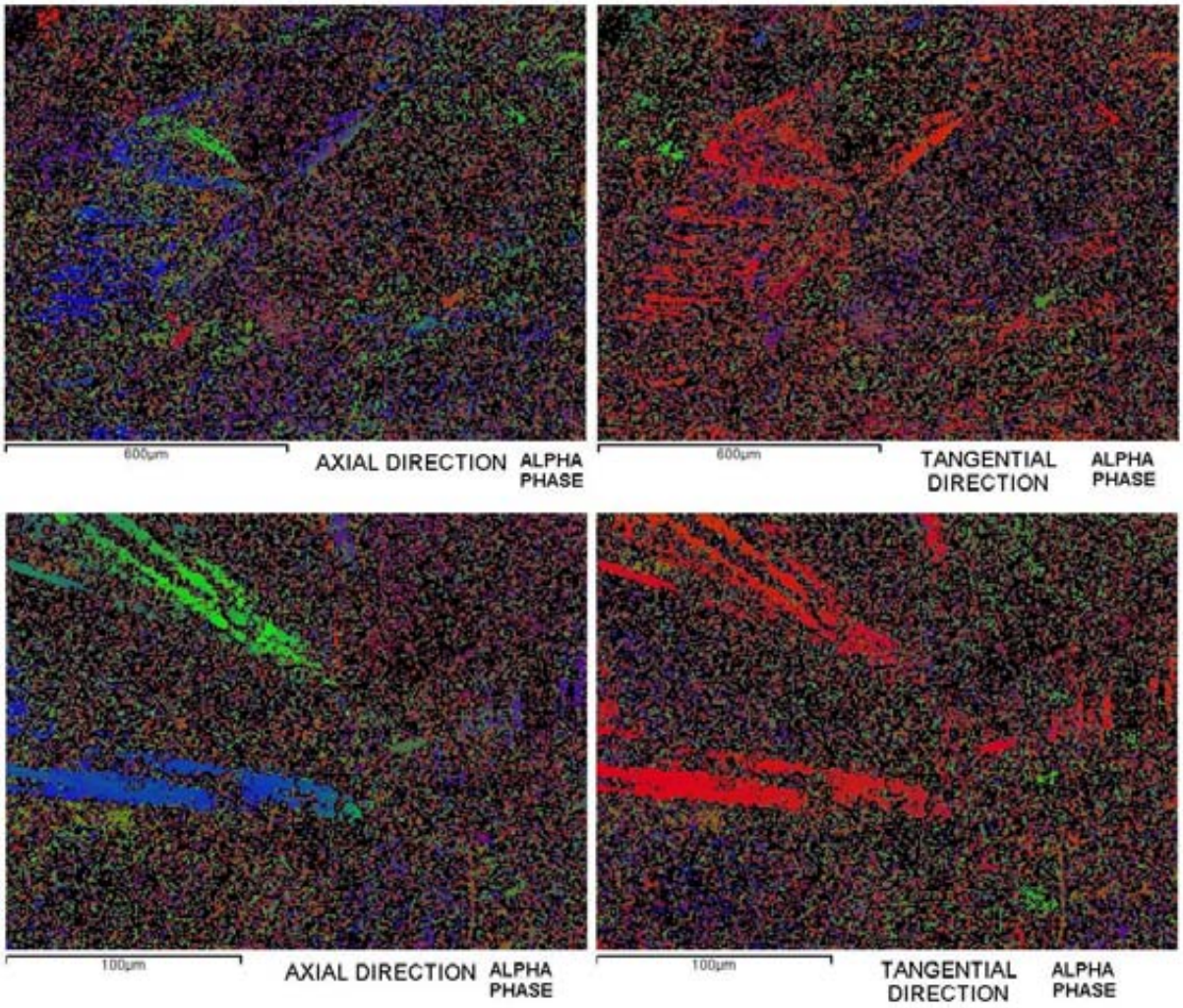

Figure 7-40 – As forged hammer pancake location F. Alpha COMs displaying alpha precipitation across beta grains in low strain microstructures

7.7.2.4 Isothermal pancake – Solution heat treated condition

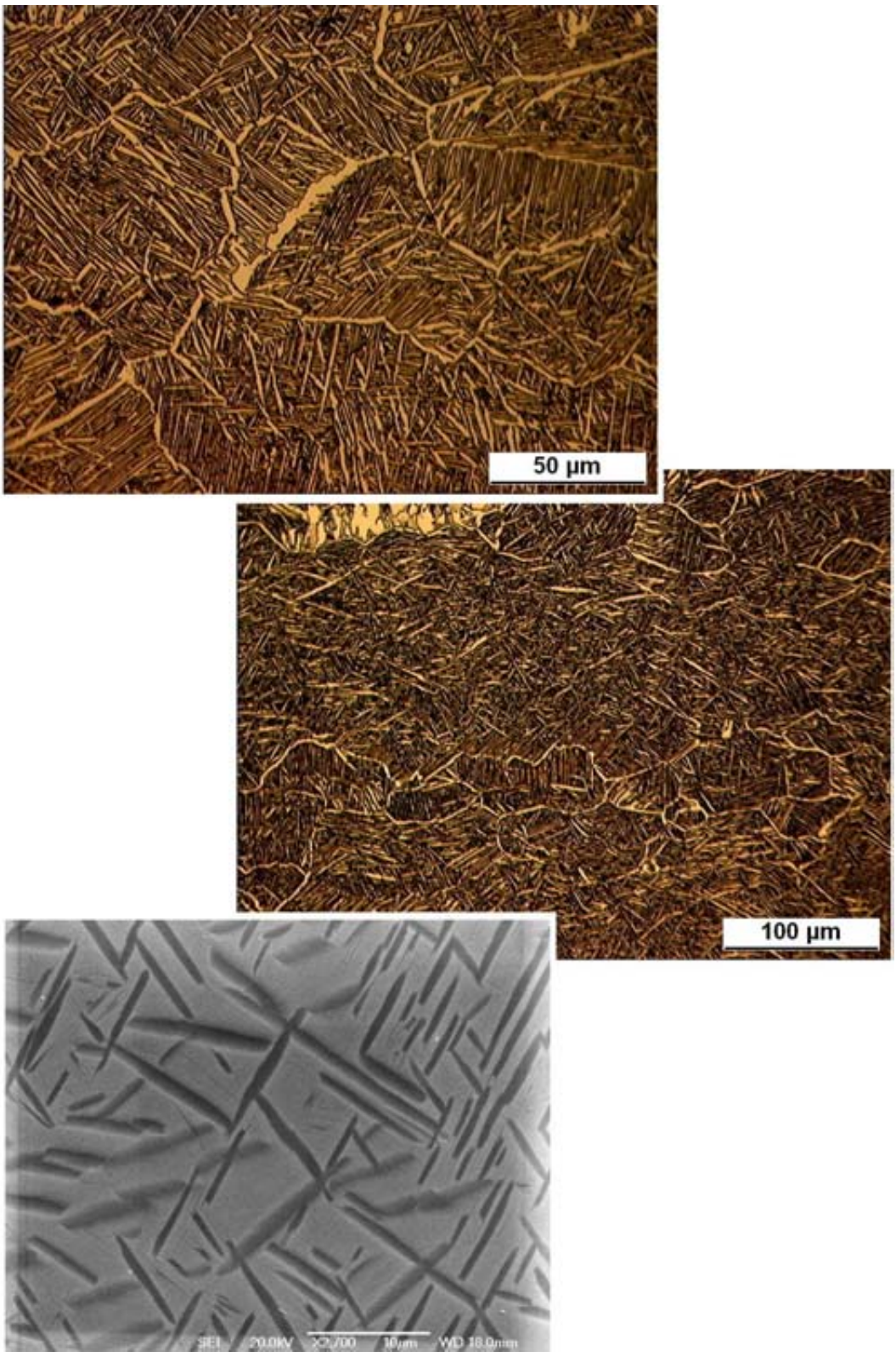

Figure 7-41 – Microstructure of solution heat treated isothermal pancake forging in high strain location A

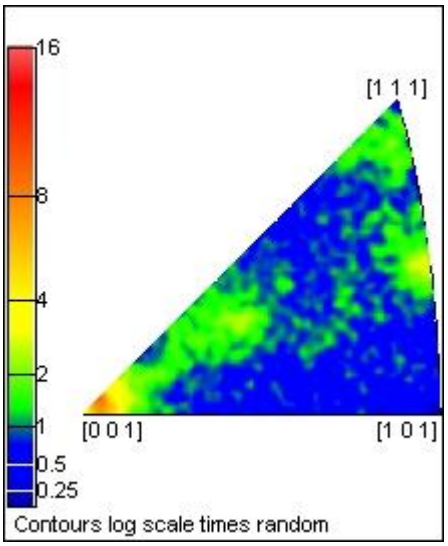

Figure 7-42 – Axial direction beta phase inverse pole figure for SHT'd isothermal pancake in location A

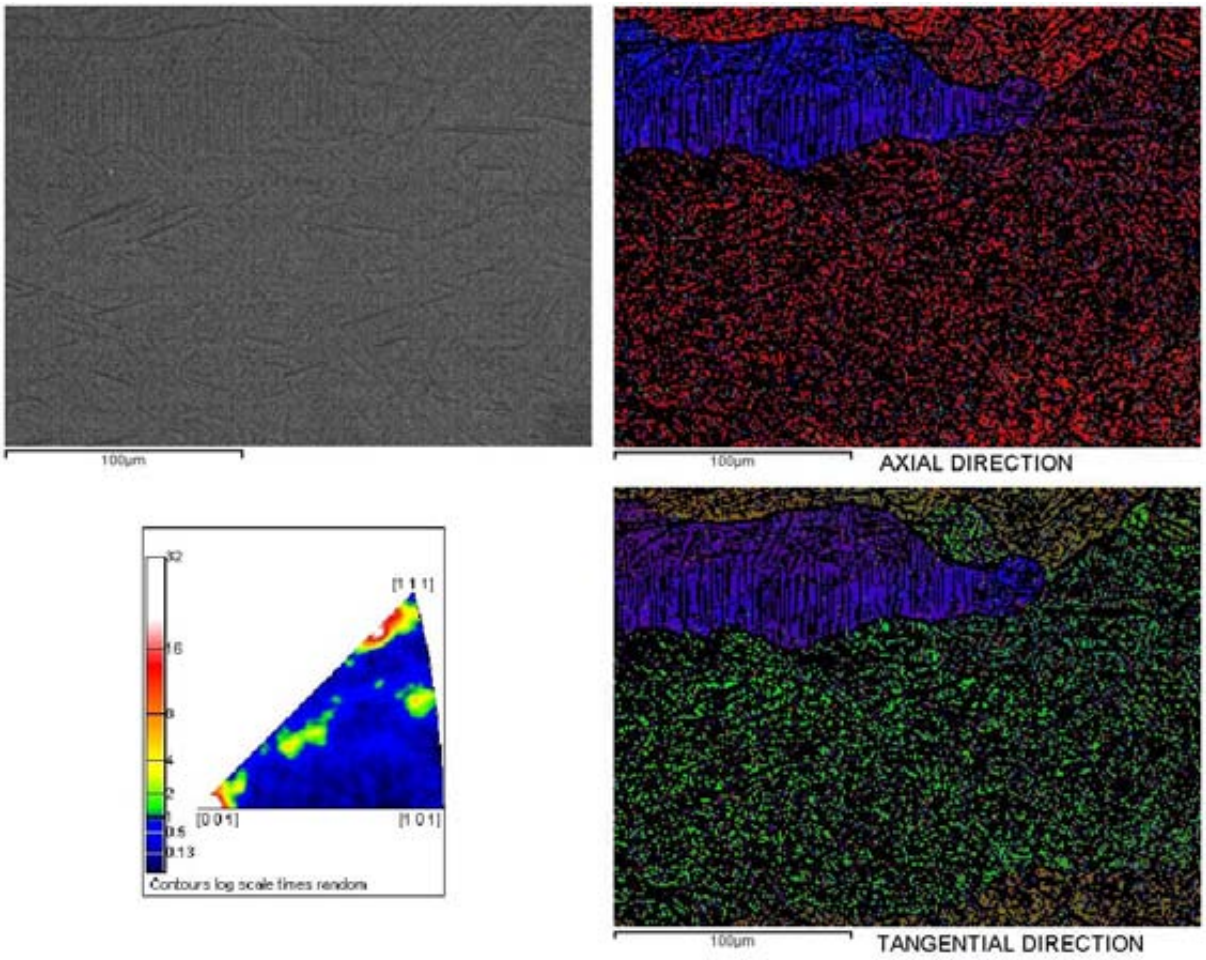

Figure 7-43 – SHT'd isothermal pancake location A. Map area containing {100}//AD and {111}//AD beta fibre textures. Beta COMs displaying textures w.r.t axial and tangential directions and axial direction beta phase IPF

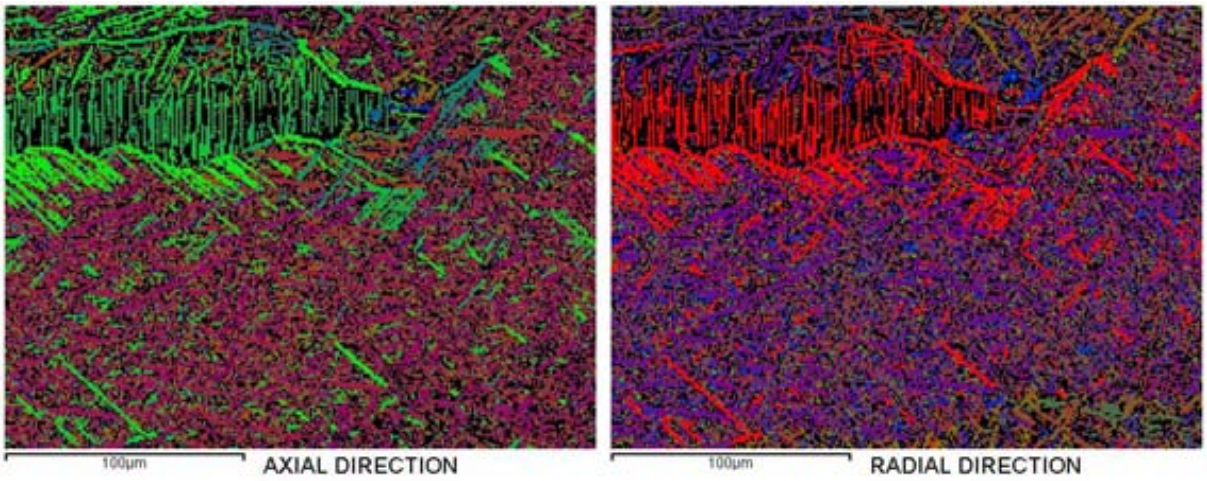

Figure 7-44 – SHT'd isothermal pancake location A. Alpha COMs displaying textures w.r.t. axial and radial directions

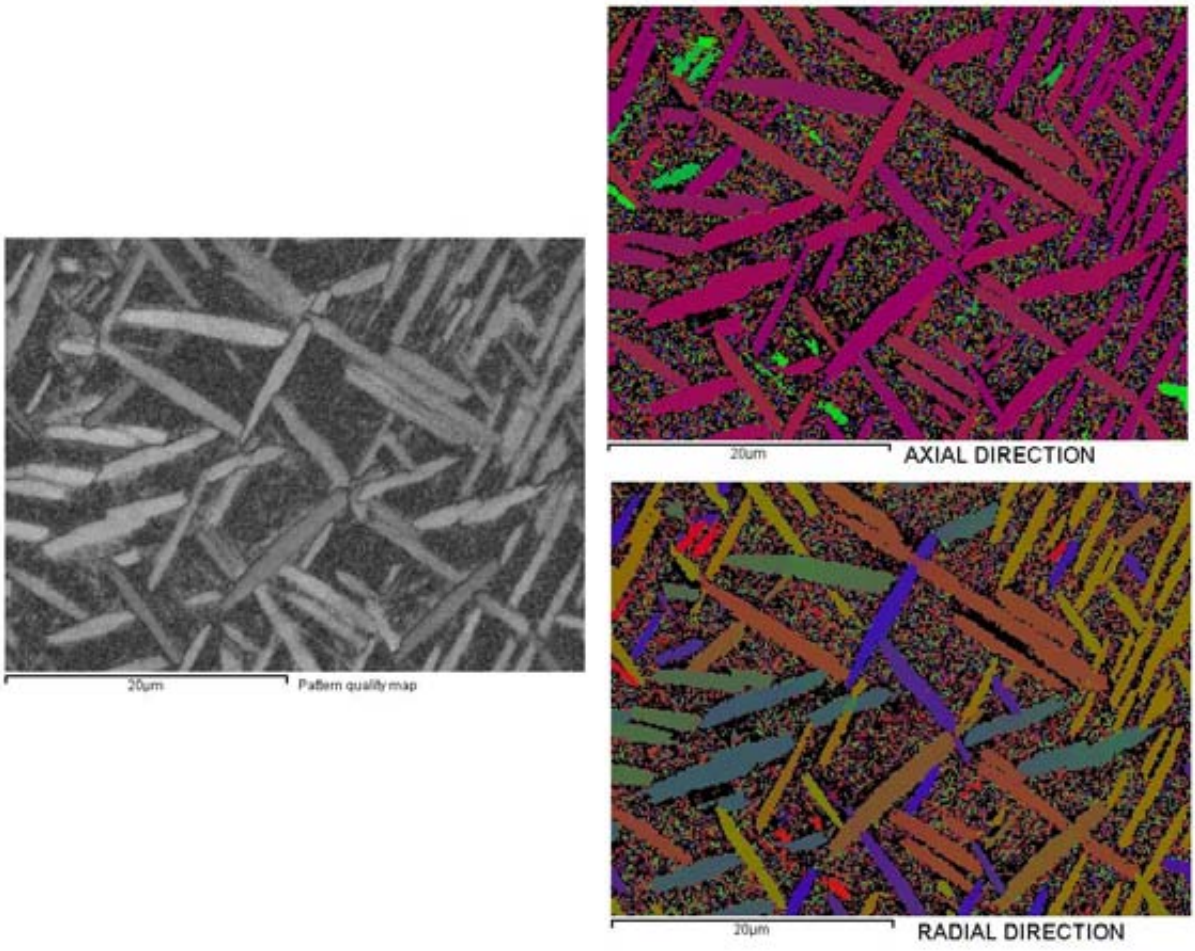

Figure 7-45 – SHT'd isothermal pancake location A. Alpha textures within beta grain with a {100}//AD fibre texture. Pattern quality map and alpha COMs displaying textures w.r.t. axial and radial directions

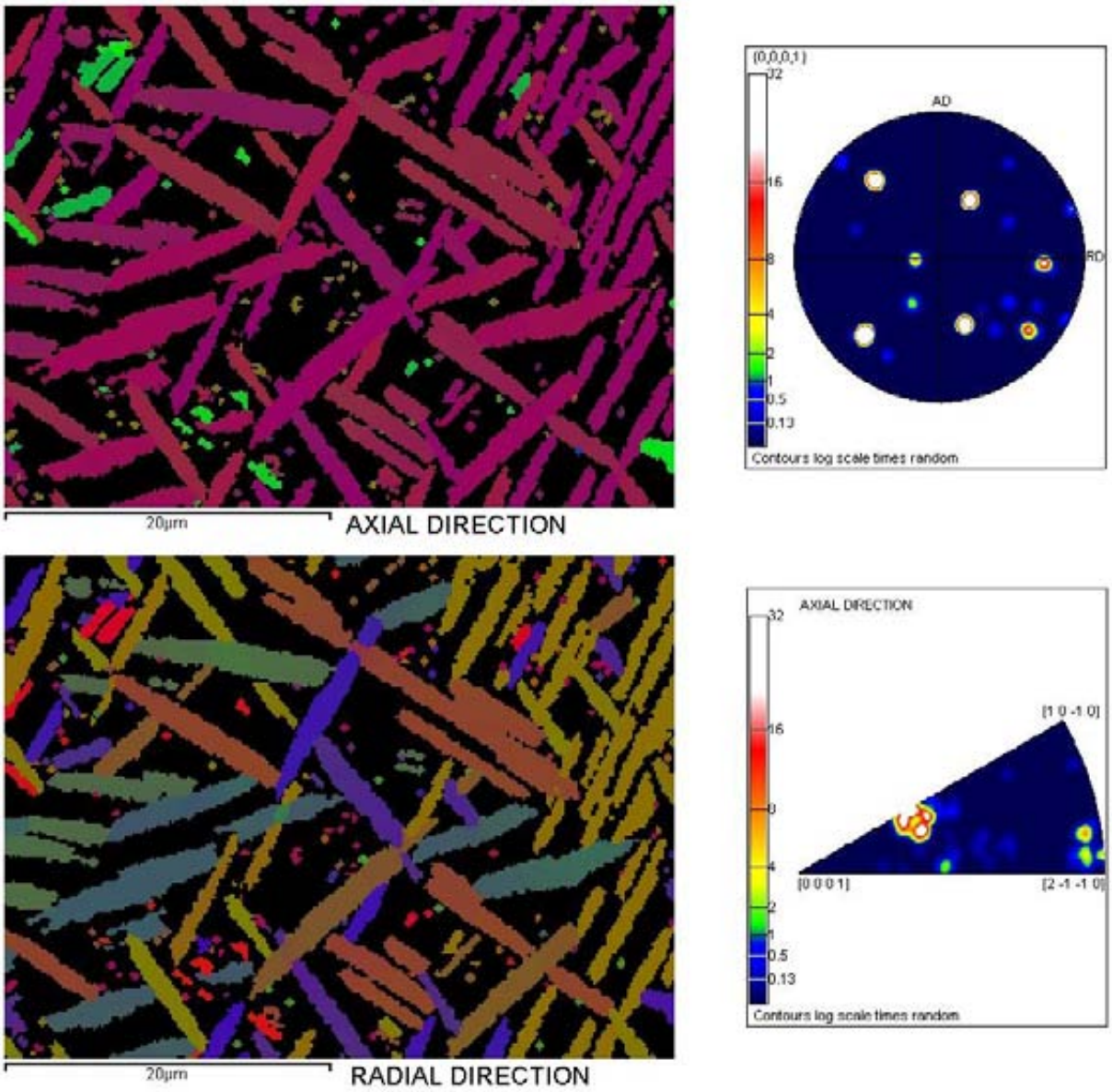

Figure 7-46 – SHT'd isothermal pancake location A. Enhanced COMs of alpha textures with corresponding basal plane pole figure and axial direction IPF

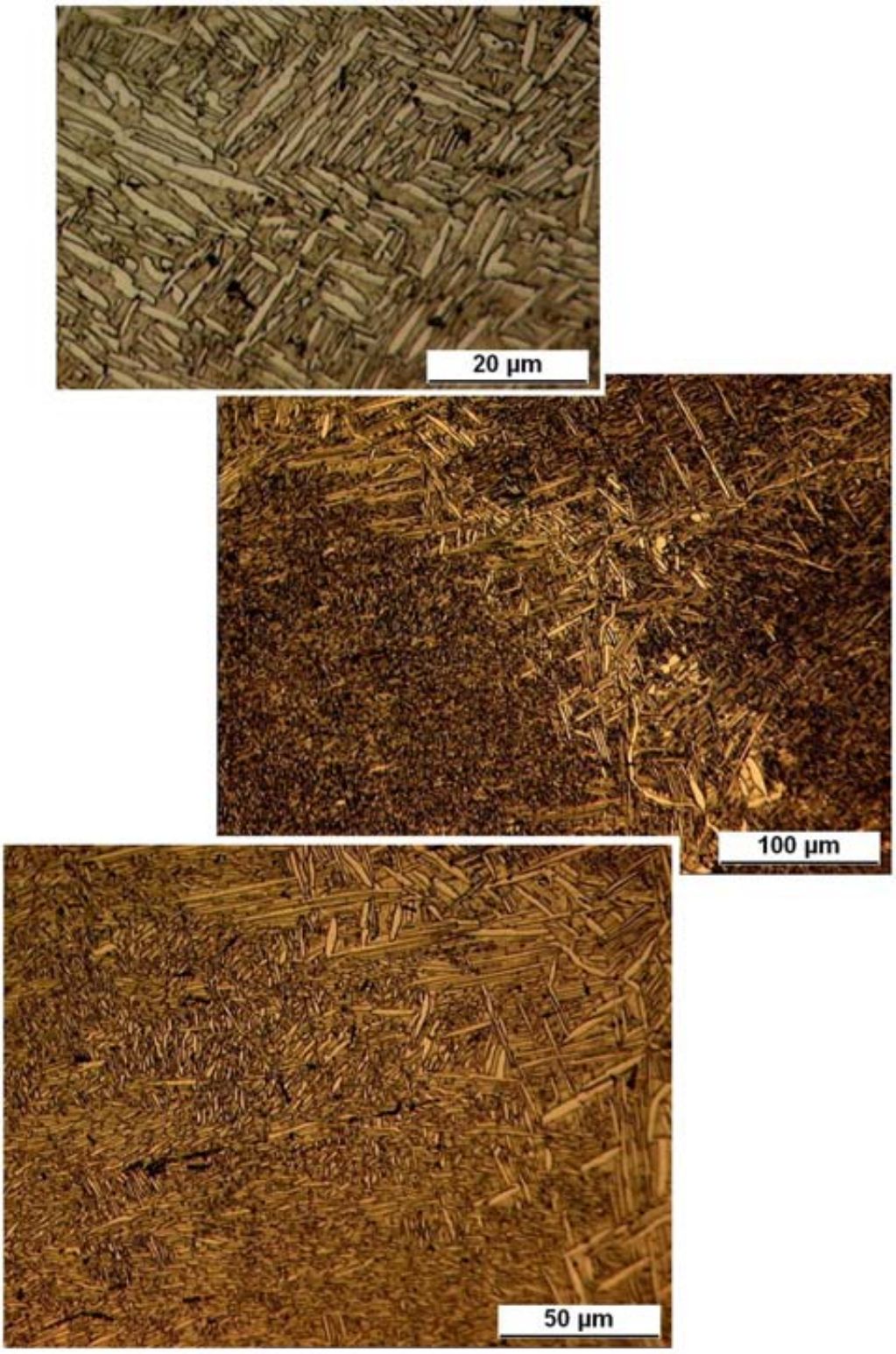

Figure 7-47 – Microstructure of solution heat treated isothermal pancake forging in low strain location F

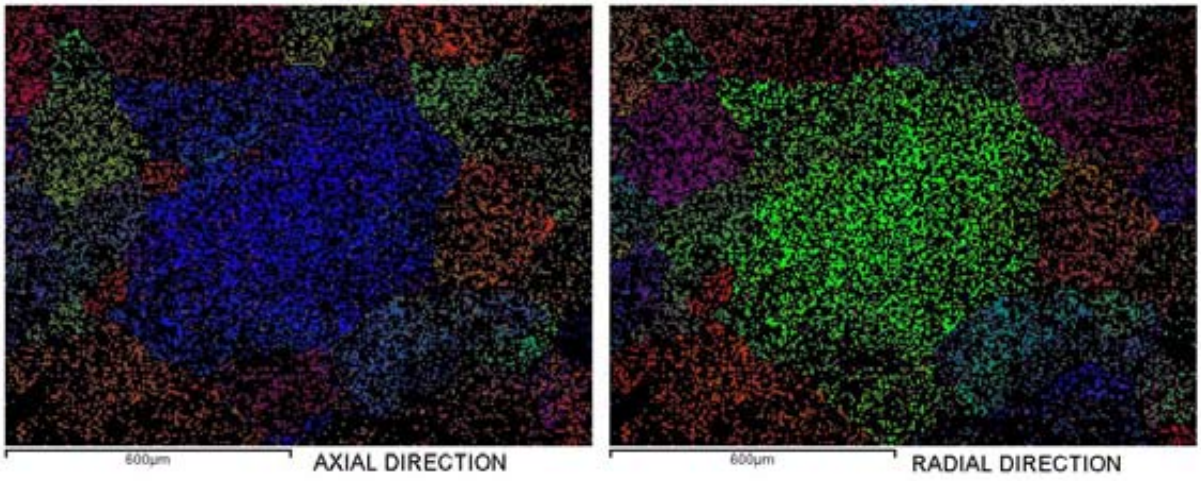

Figure 7-48 – SHT'd isothermal pancake location F. Beta COMs displaying textures w.r.t. axial and radial directions

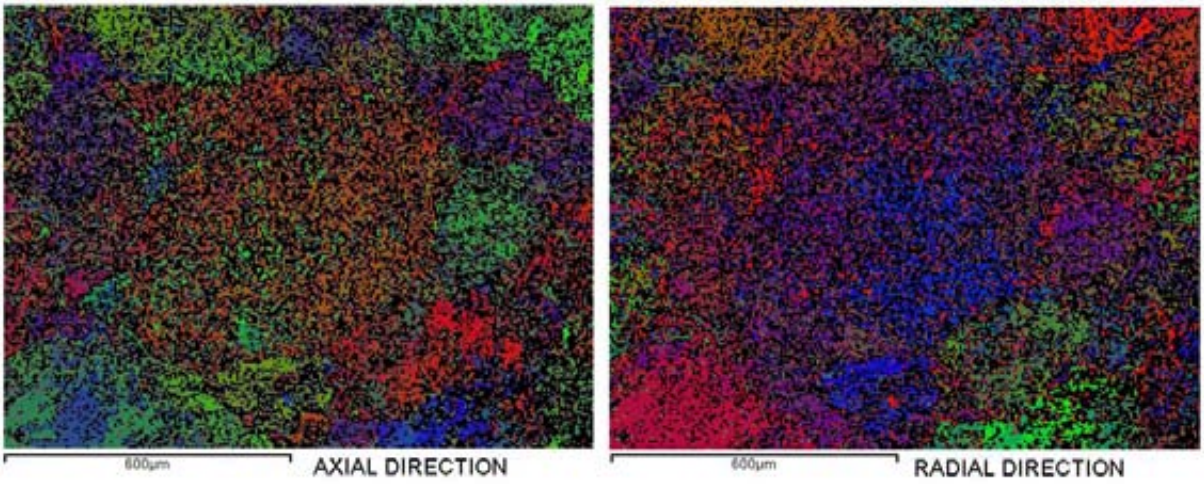

Figure 7-49 – SHT'd isothermal pancake location F. Alpha COMs displaying textures w.r.t. axial and radial directions

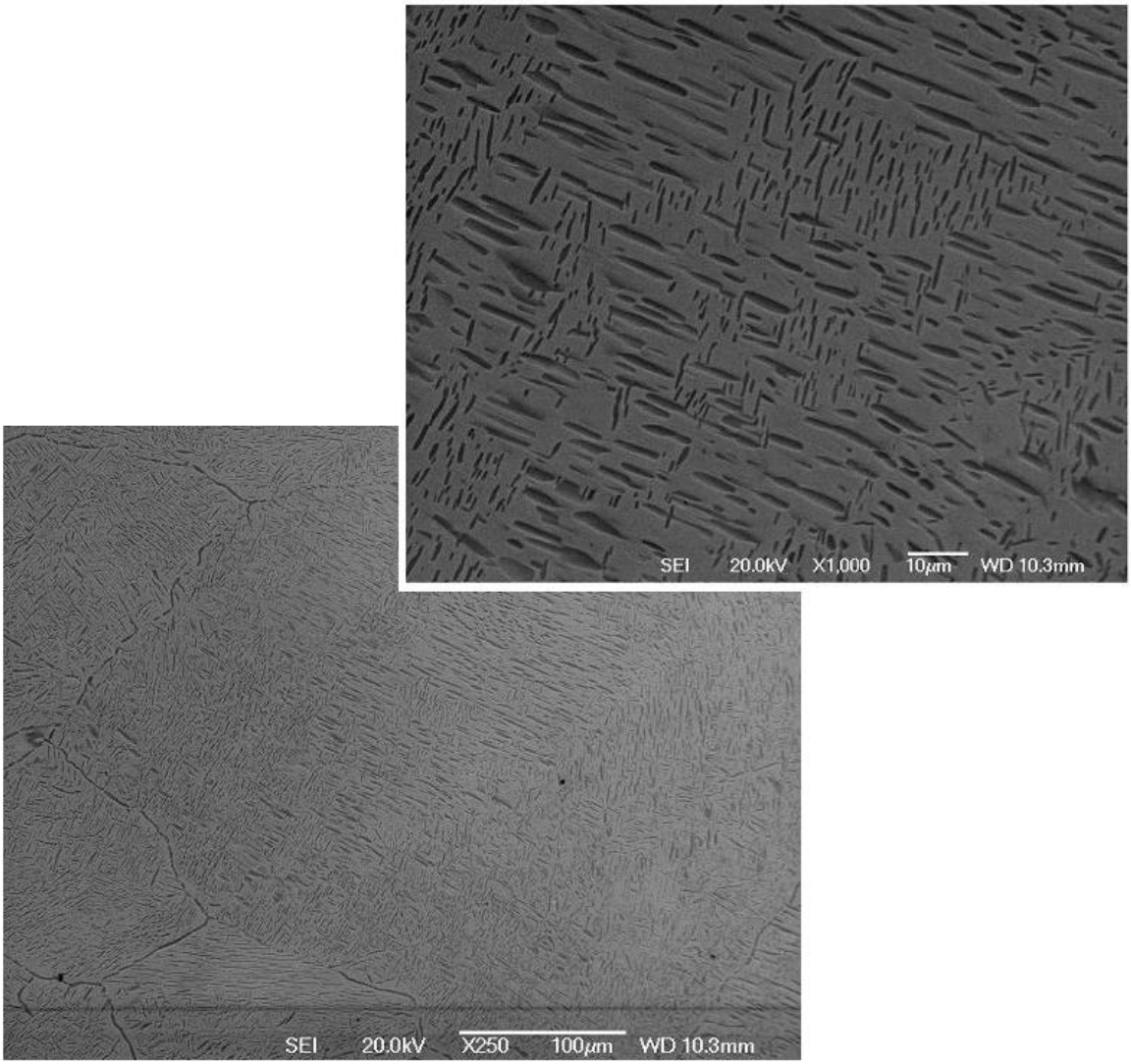

Figure 7-50 – Typical microstructure of SHT isothermal pancake location F

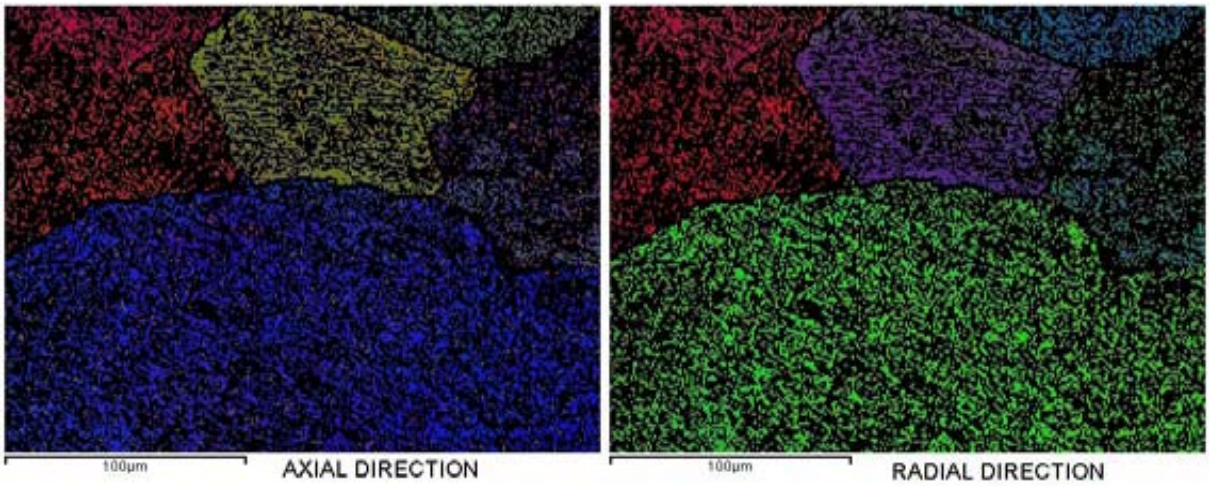

Figure 7-51 – SHT isothermal pancake location F. Beta COMs displaying textures w.r.t. axial and radial directions

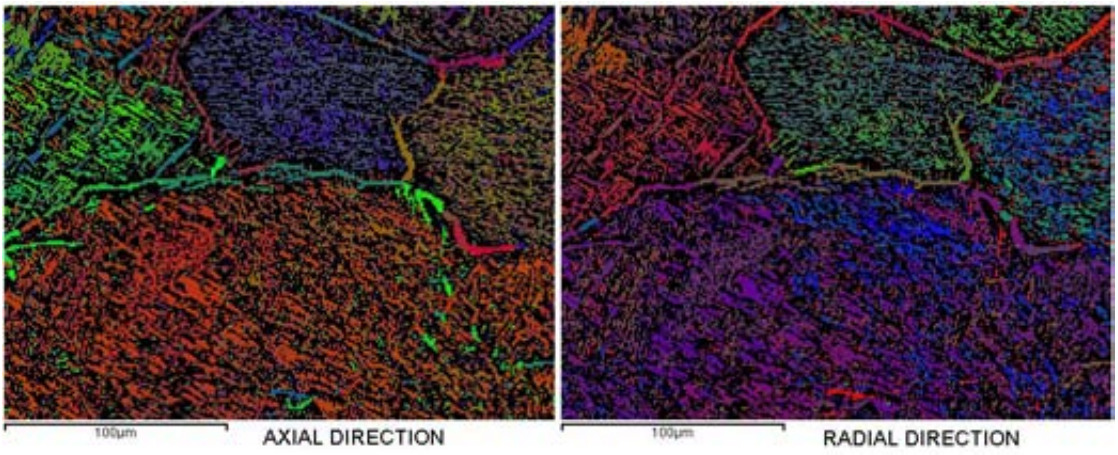

Figure 7-52 – SHT isothermal pancake location F. Alpha COMs displaying textures w.r.t. axial and radial directions

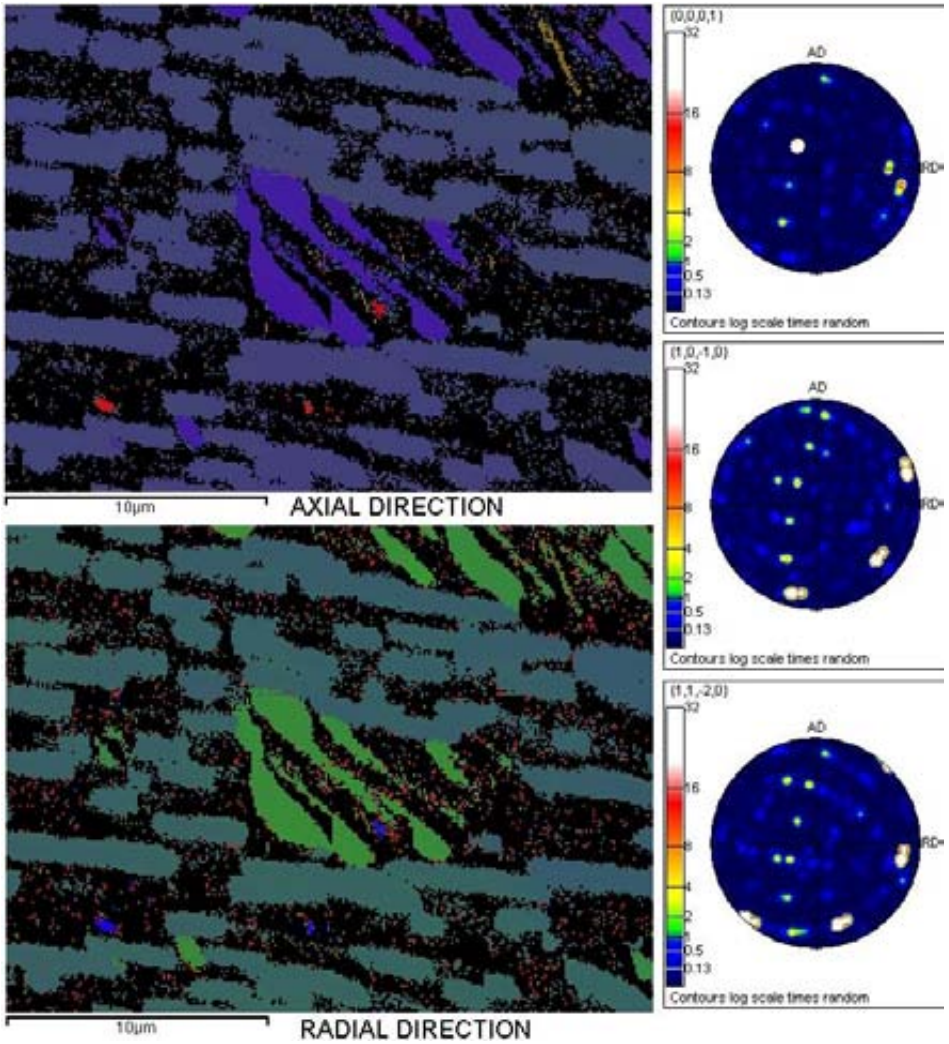

Figure 7-53 – SHT isothermal pancake location F. Alpha COMs displaying textures w.r.t. axial and radial disc directions. Corresponding pole figures showing crystallography of the two alpha platelet variants

7.7.2.5 Hot die pancake – Solution heat treated condition

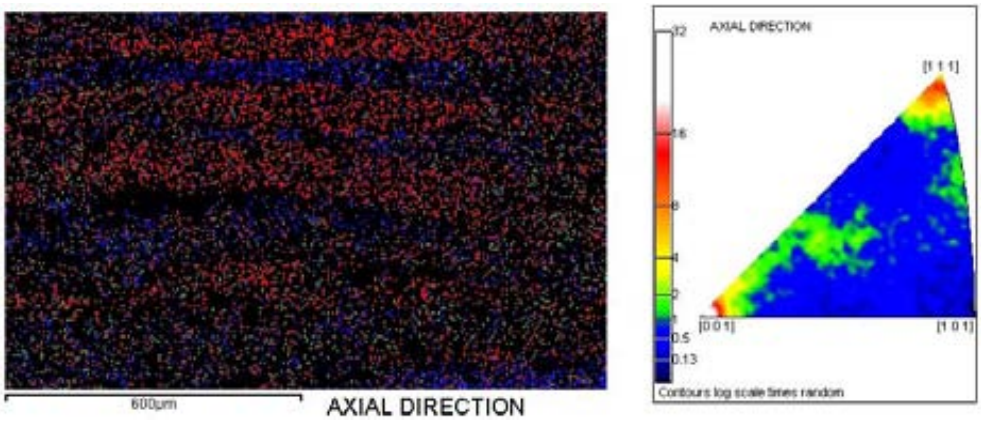

Figure 7-54 – SHT hot die forging location A. Beta phase COM displaying textures w.r.t. axial direction and corresponding IPF showing {100}//AD and {111}//AD fibre textures

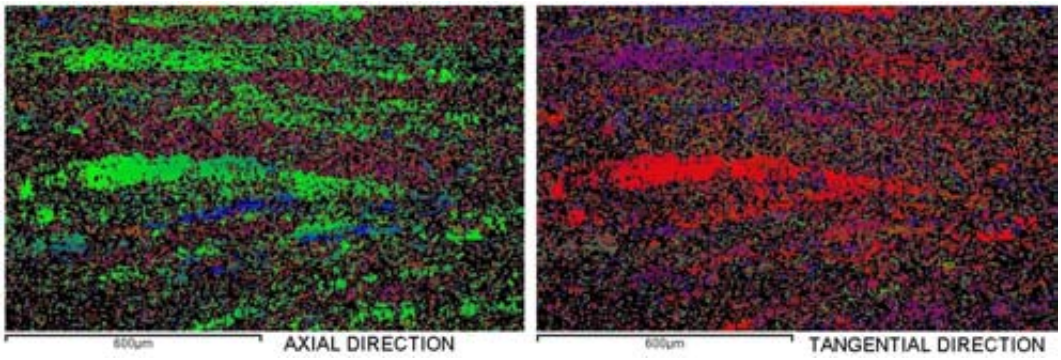

Figure 7-55 – SHT hot die forging location A. Alpha phase COMs displaying textures w.r.t. axial and tangential directions

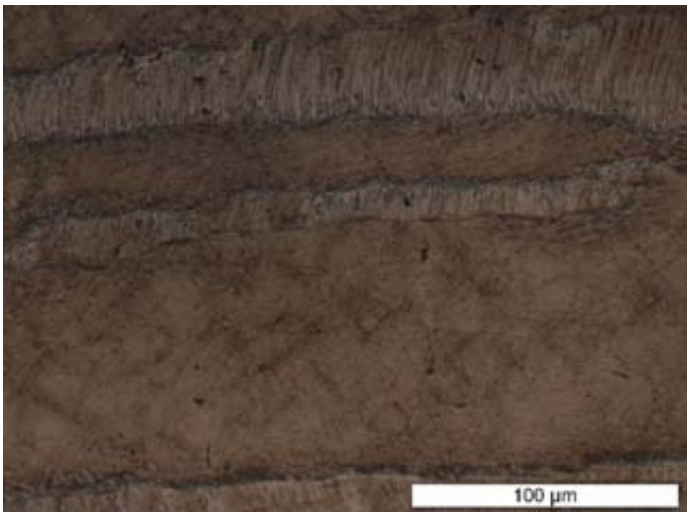

Figure 7-56 – Alpha side-plate colony growth in as-forged hot die pancake location A

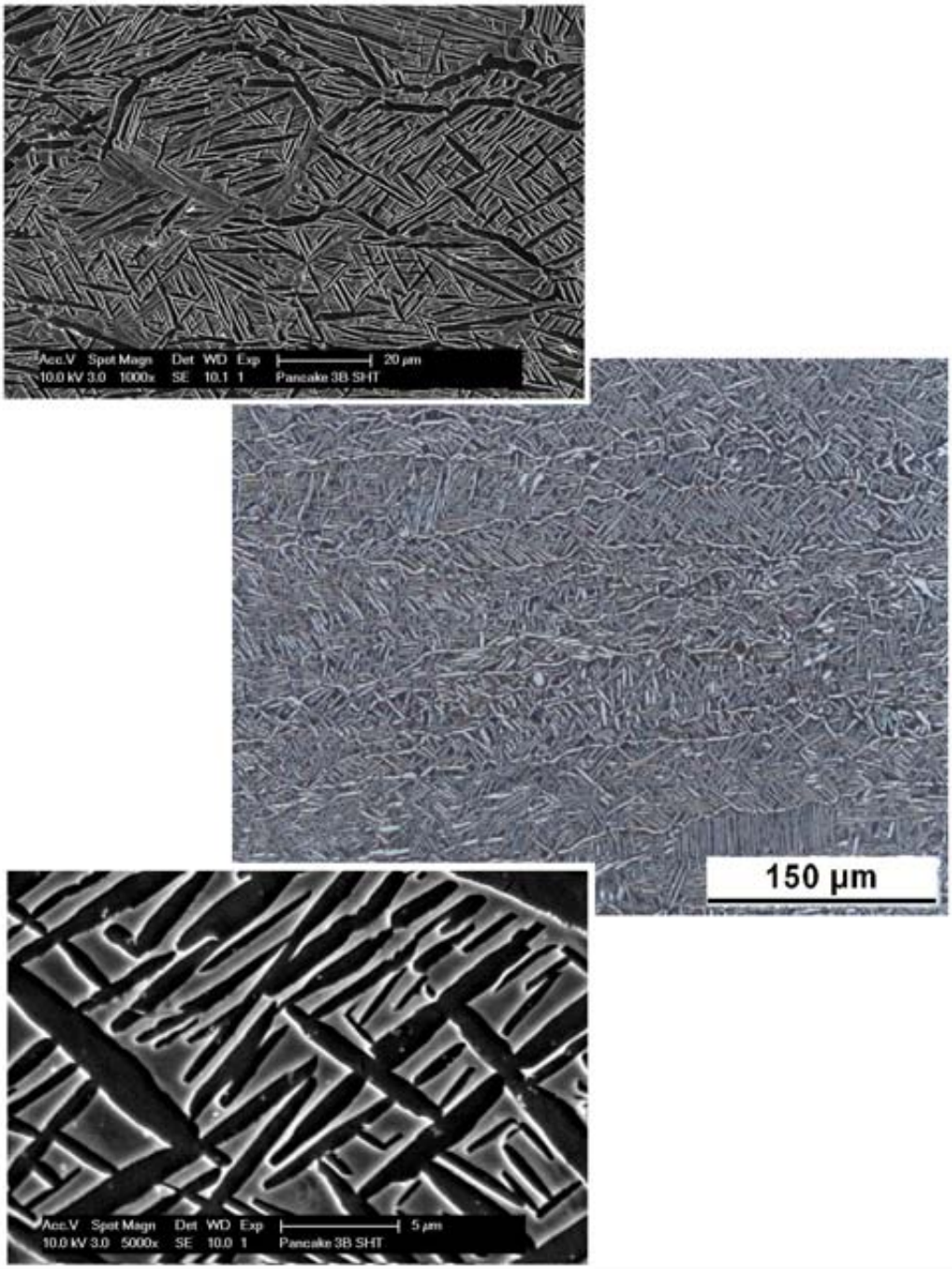

Figure 7-57 – SHT hot die forging location A. Typical microstructures

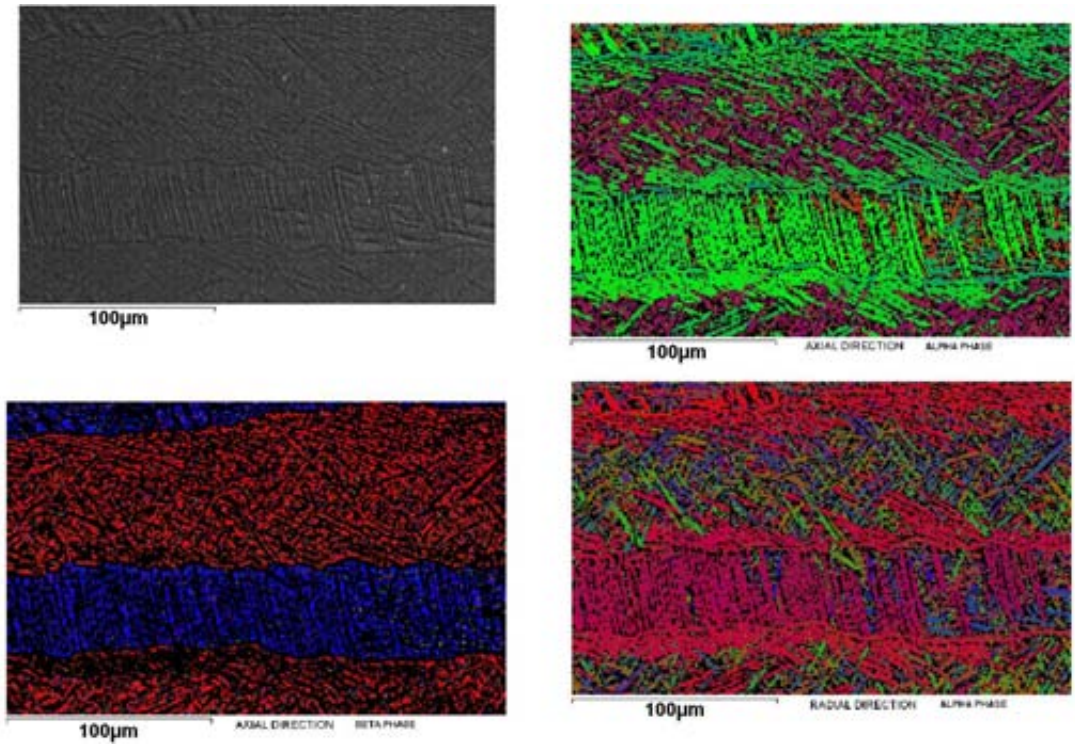

Figure 7-58 – SHT hot die forging location A. Alpha side plate colony growth from prior beta grain boundaries. Beta COM displaying textures w.r.t. axial direction. Alpha COMs displaying textures w.r.t. axial and radial directions

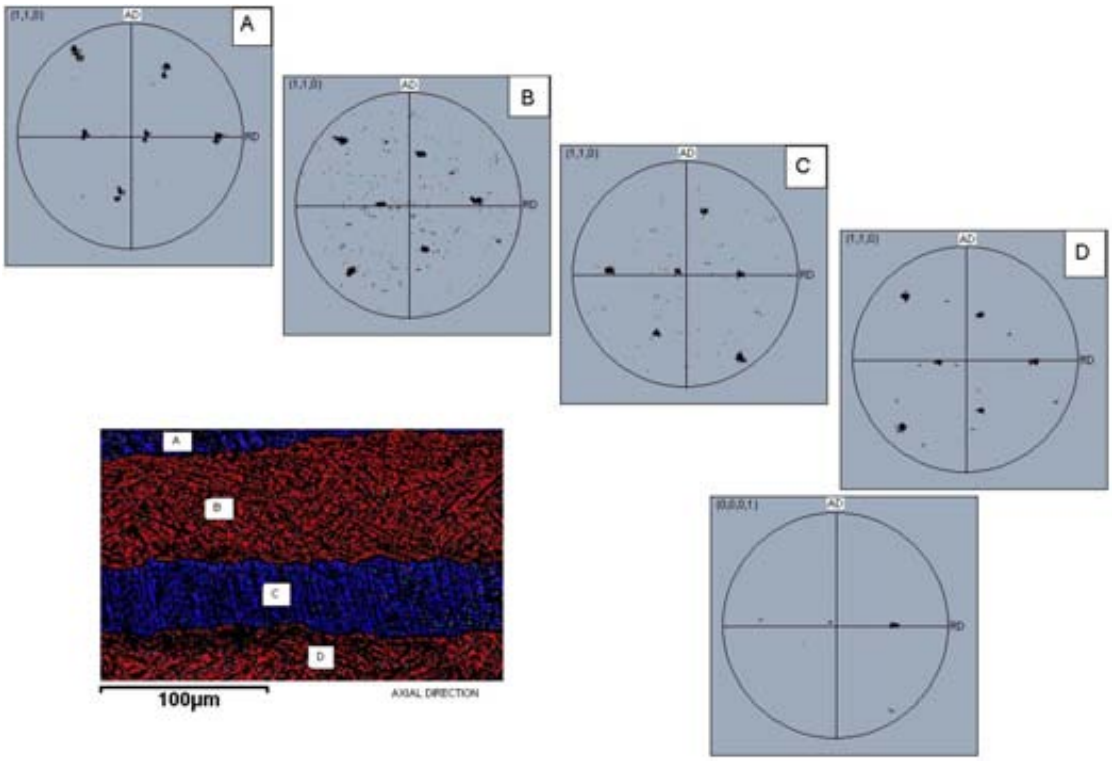

Figure 7-59 – Prior beta textures in adjacent beta grains A to D and texture of alpha side-plate colonies in beta grain C

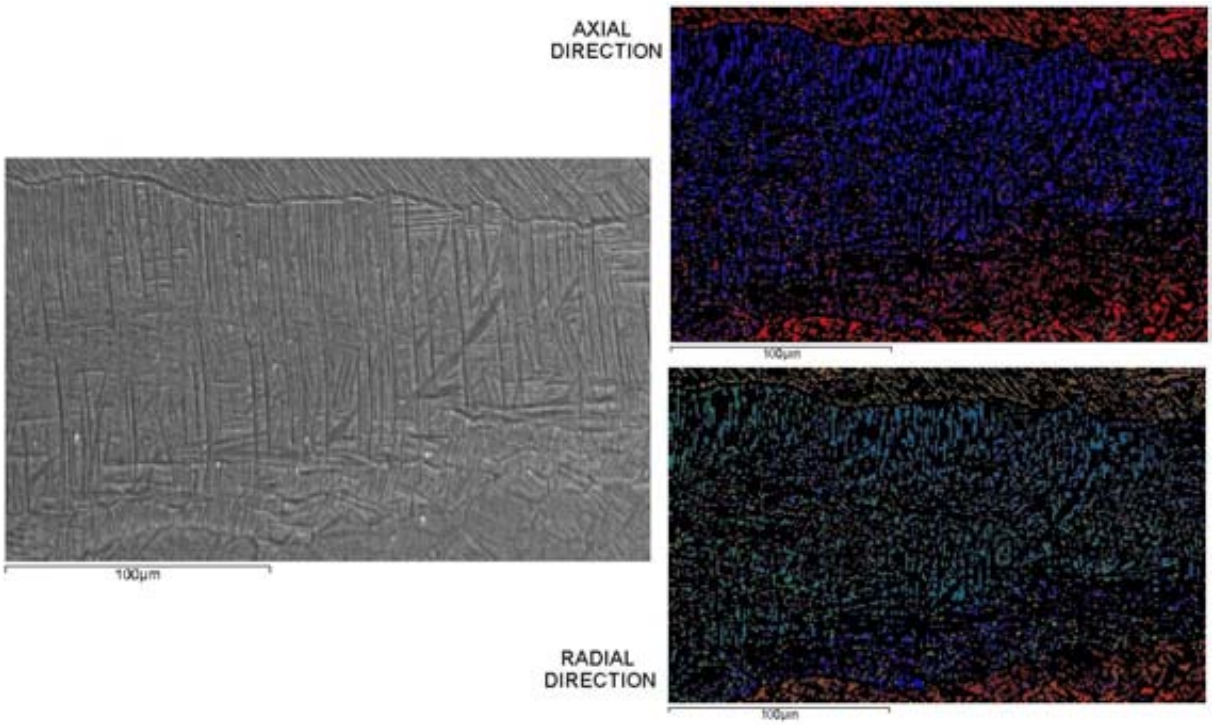

Figure 7-60 – SHT hot die forging location A. Site of interest image and corresponding beta COMs displaying textures w.r.t. axial and radial directions

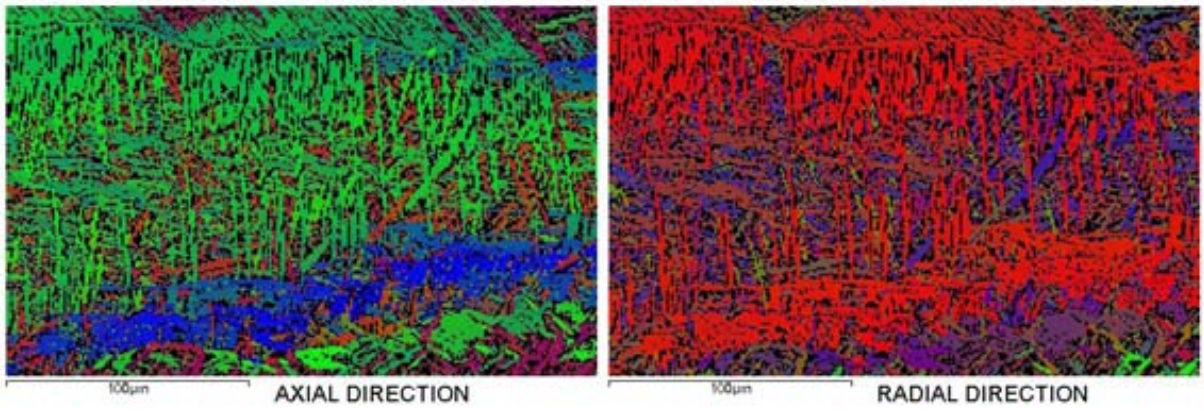

Figure 7-61 – SHT hot die forging location A. Alpha COMs displaying textures w.r.t. axial and radial directions

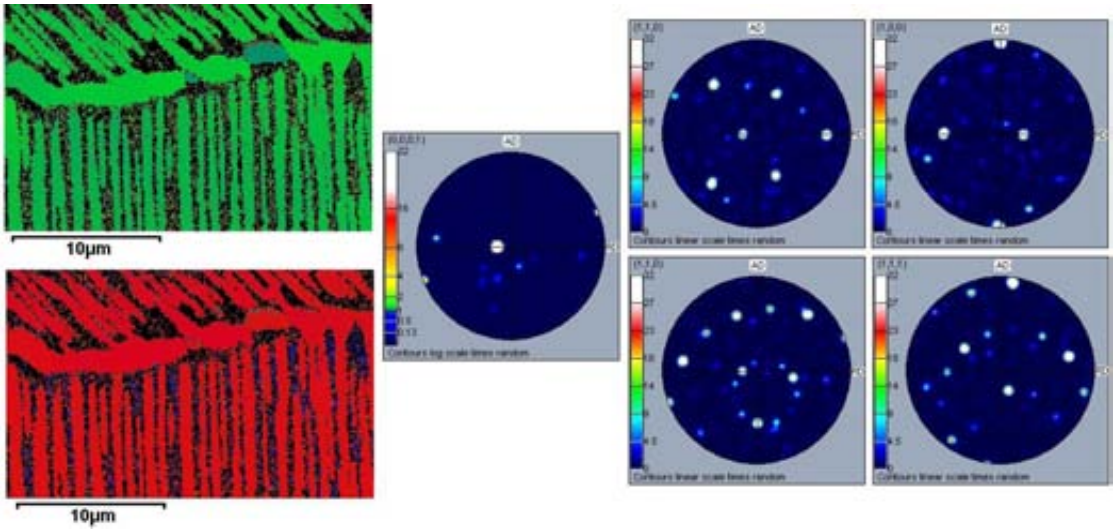

Figure 7-62 – High magnification alpha COMs with accompanying pole figures displaying grain boundary alpha variant selection on a shared {110} beta plane

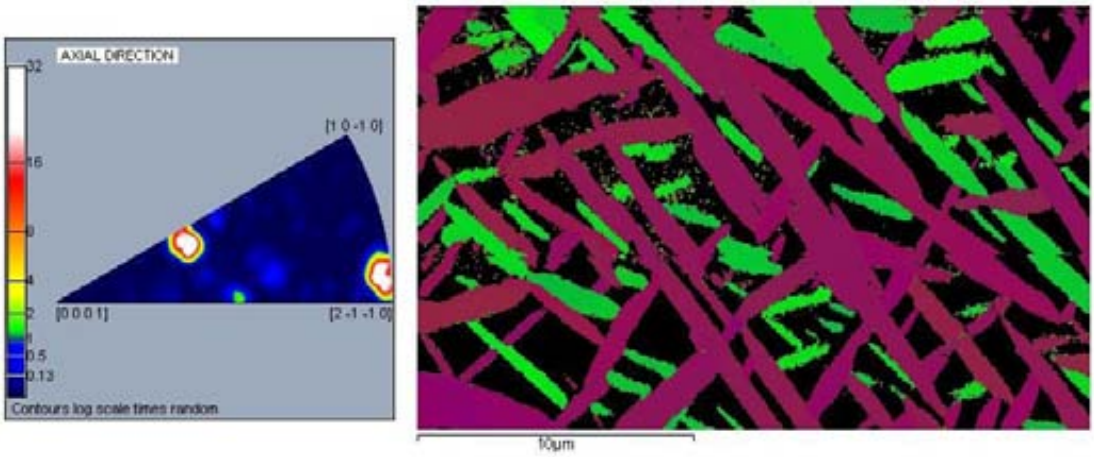

Figure 7-63 – SHT hot die forging location A. Axial direction IPF and alpha COM displaying Widmanstätten alpha platelet microstructure

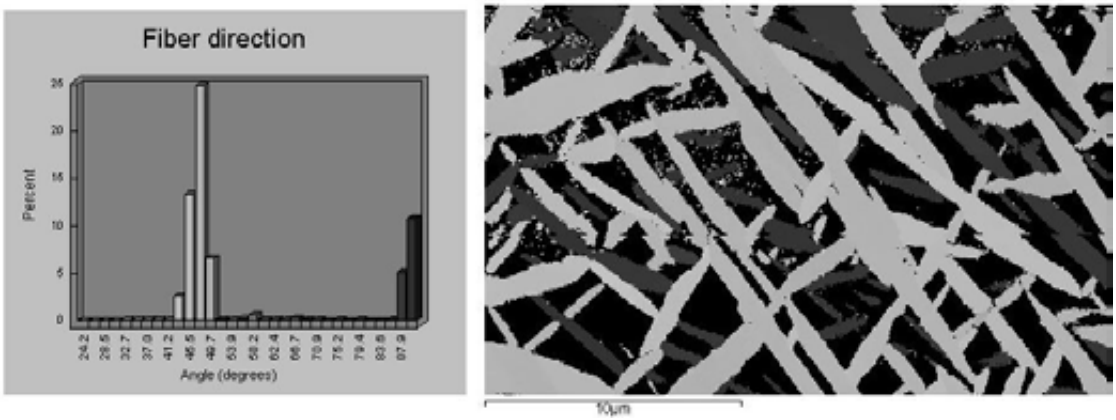

Figure 7-64 – SHT hot die forging location A. Distribution of basal planes with respect to axial direction and corresponding greyscale COM

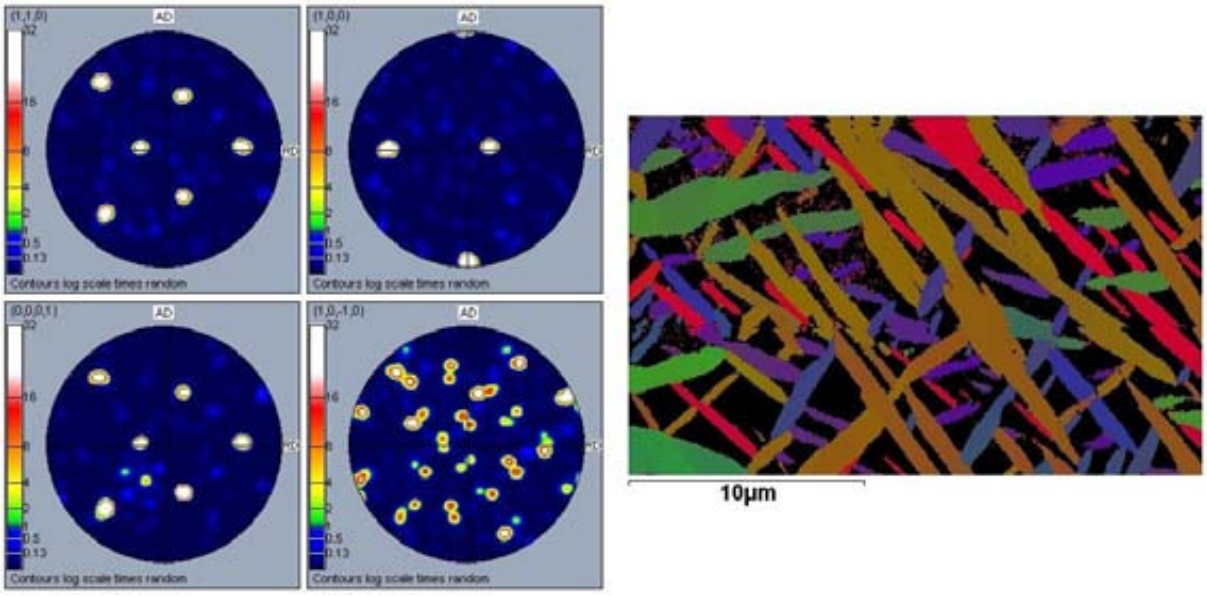

Figure 7-65 – SHT hot die forging location A. Beta and alpha pole figures and alpha COM displaying textures w.r.t. tangential direction

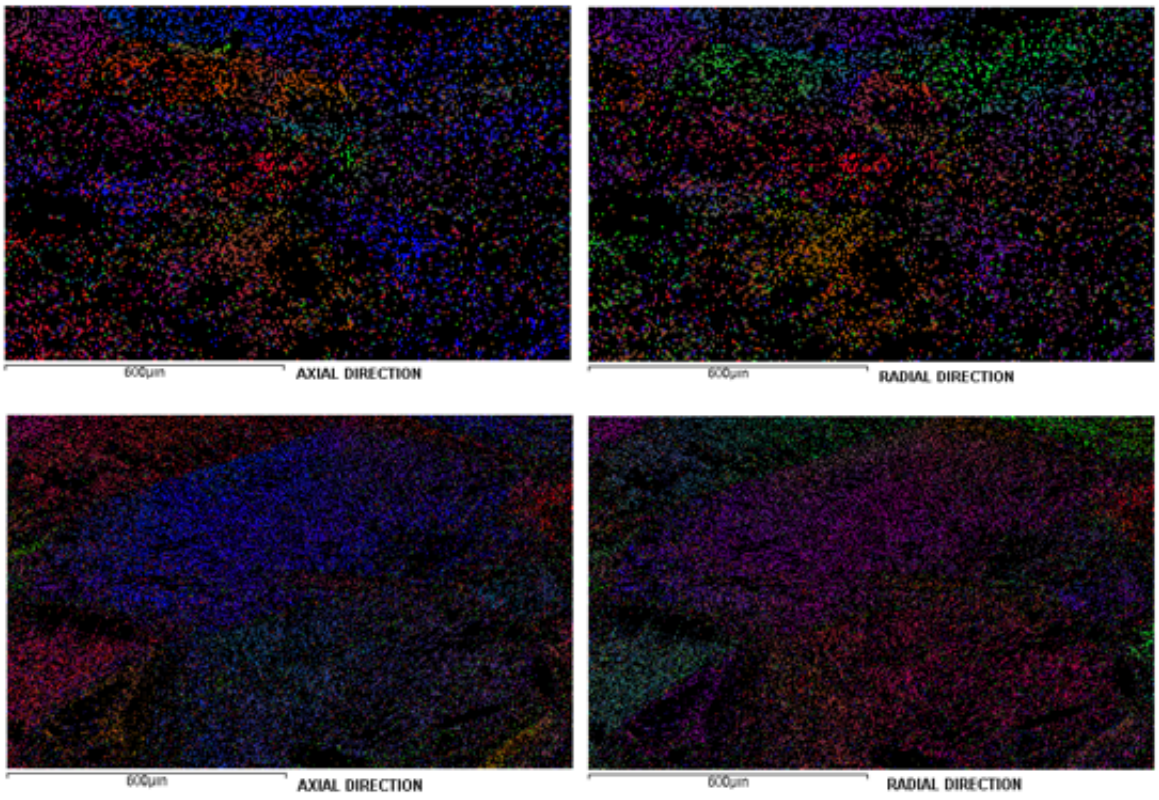

Figure 7-66 – SHT hot die forging location F. Beta phase COMs from two different locations displaying textures w.r.t. axial and radial directions

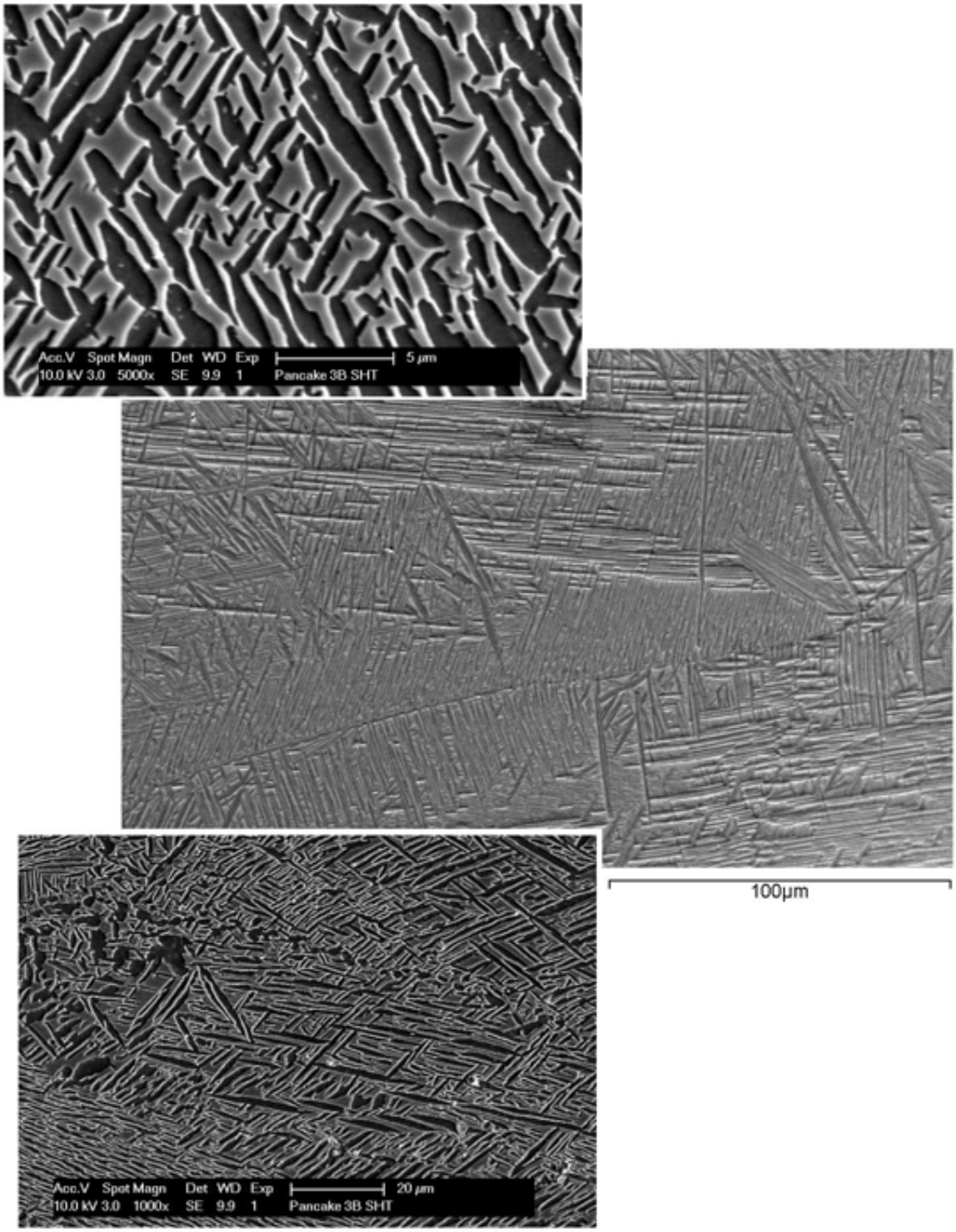

Figure 7-67 – SHT hot die forging location F. Typical microstructures

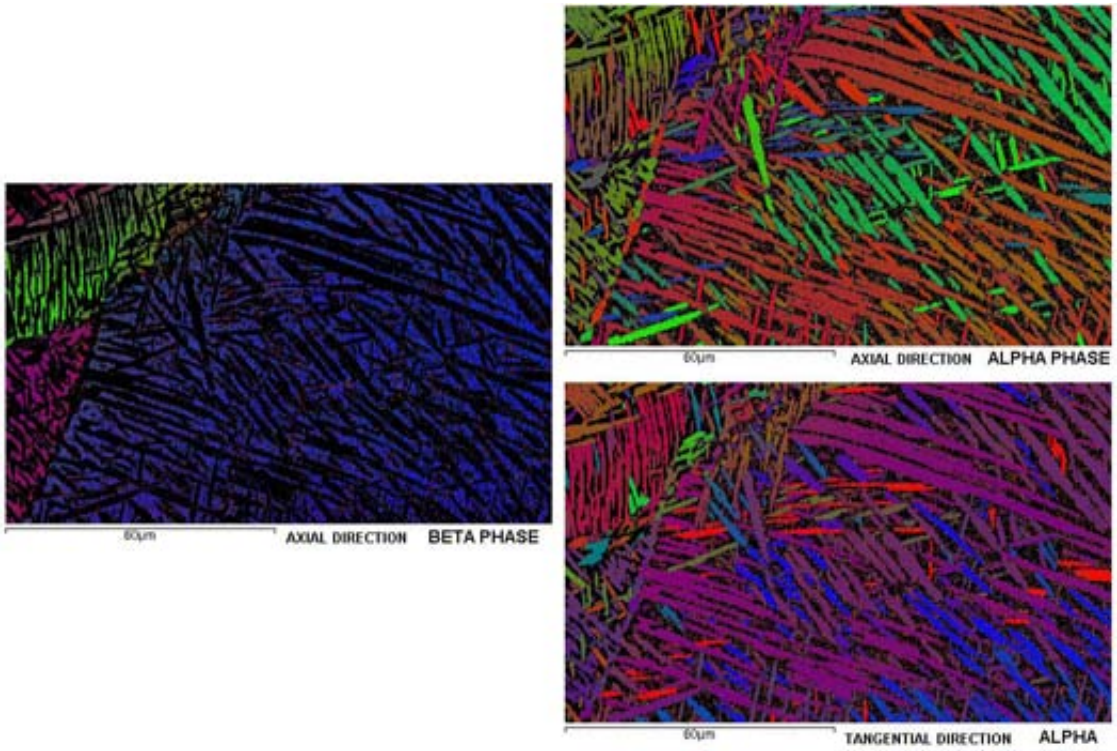

Figure 7-68 – SHT hot die forging location F. Beta COM displaying textures w.r.t. axial direction. Alpha COMs displaying textures w.r.t. axial and radial directions

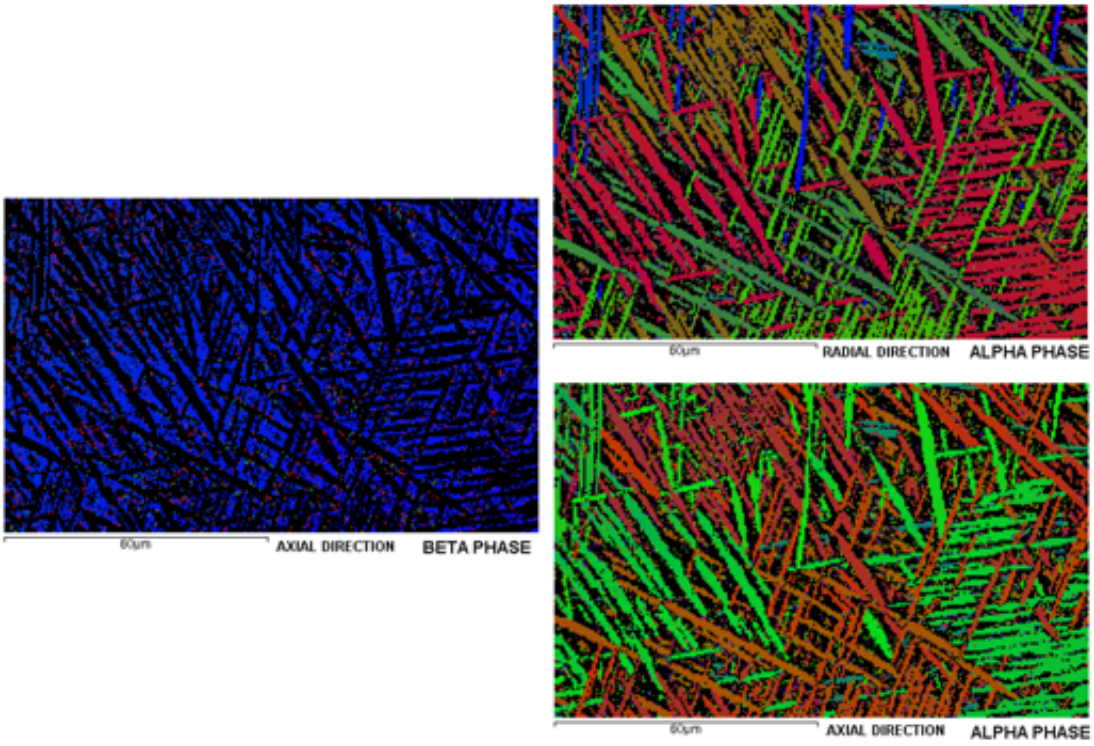

Figure 7-69 – SHT hot die forging location F. Beta and alpha phase COMs displaying textures w.r.t. axial and radial directions

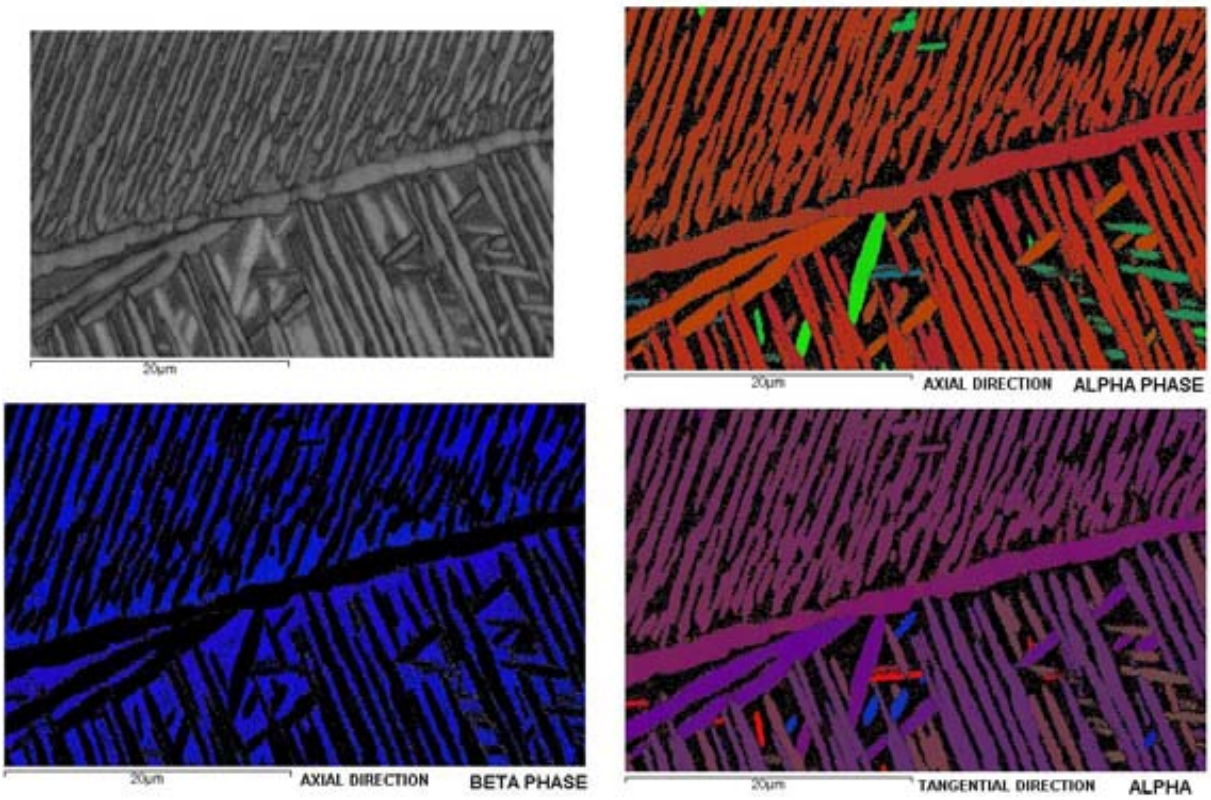

Figure 7-70 – SHT hot die forging location F. Beta and alpha phase COMs displaying textures w.r.t. axial and radial directions

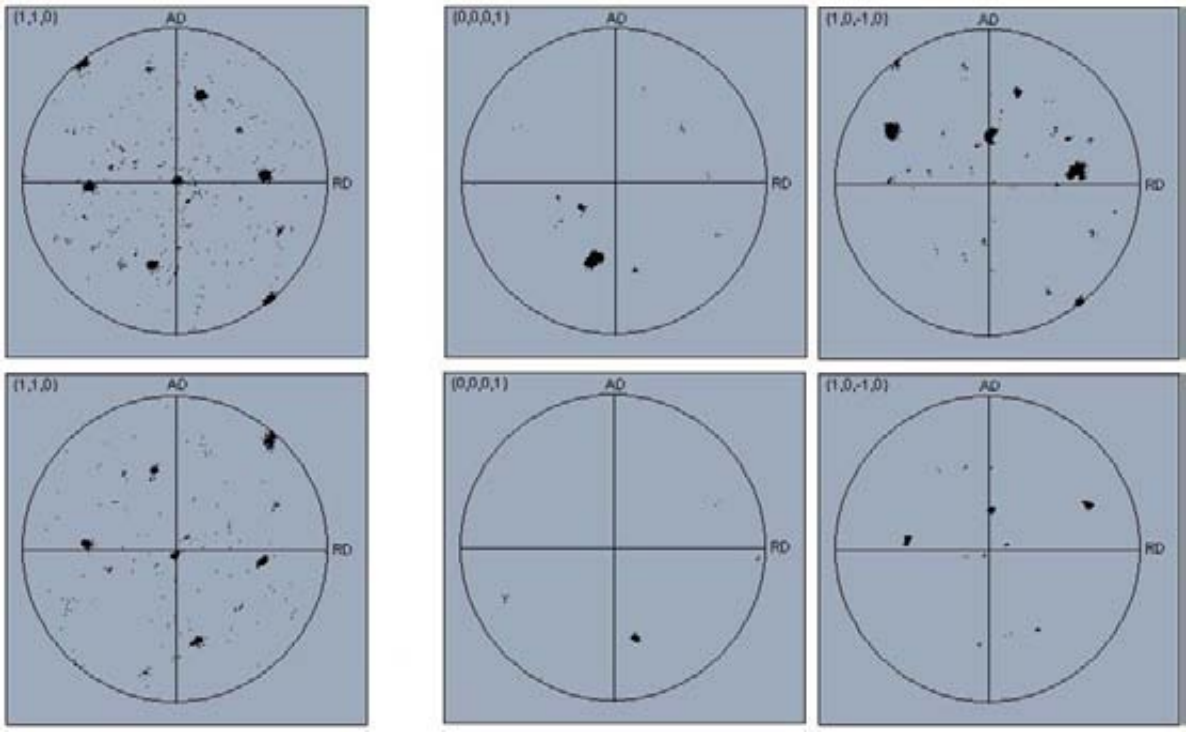

Figure 7-71 – SHT hot die forging location F. Beta {110} and alpha {0001} and $\{10\bar{1}0\}$ pole figures for textures in EBSD maps given in Figure 7-70

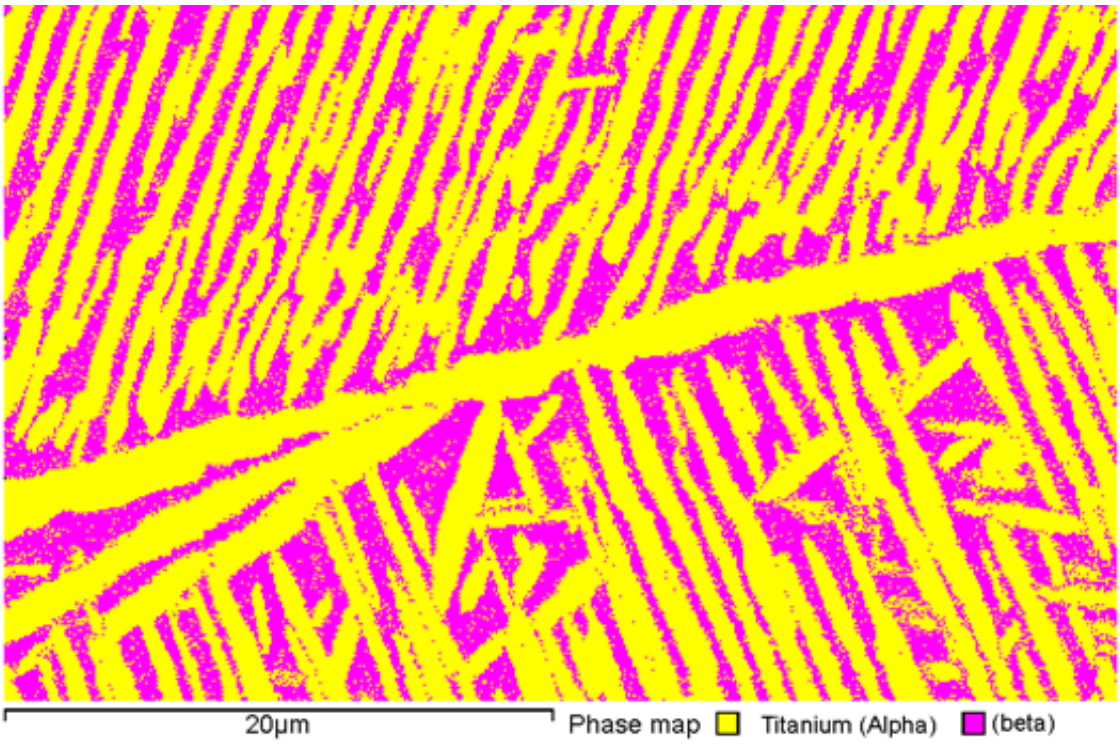

Figure 7-72 – Phase map displaying primary alpha platelets and retained beta matrix in SHT hot die forging location F

7.7.2.6 Hammer pancake – Solution heat treated condition

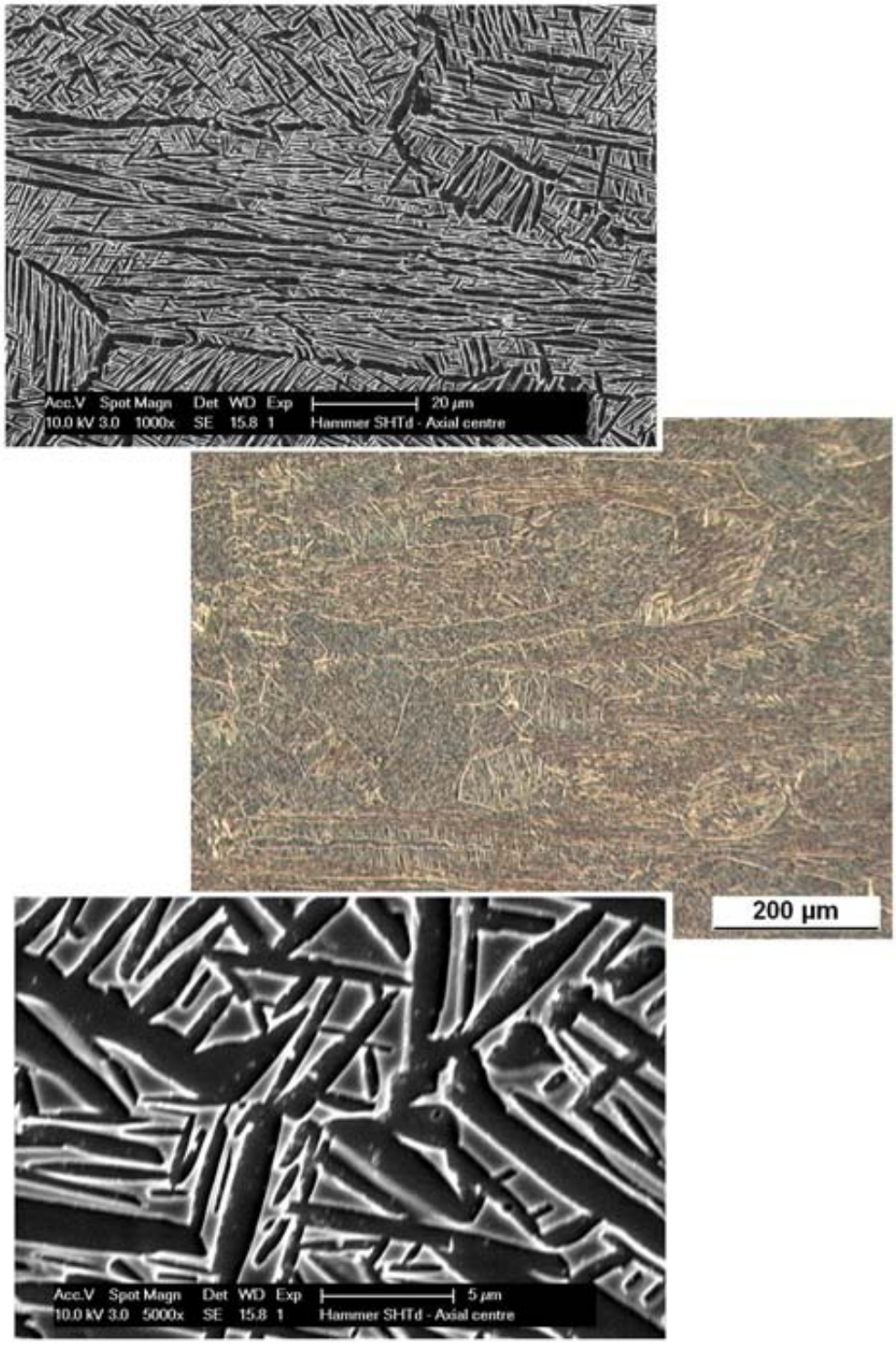

Figure 7-73 – SHT hammer forging location A. Typical microstructures

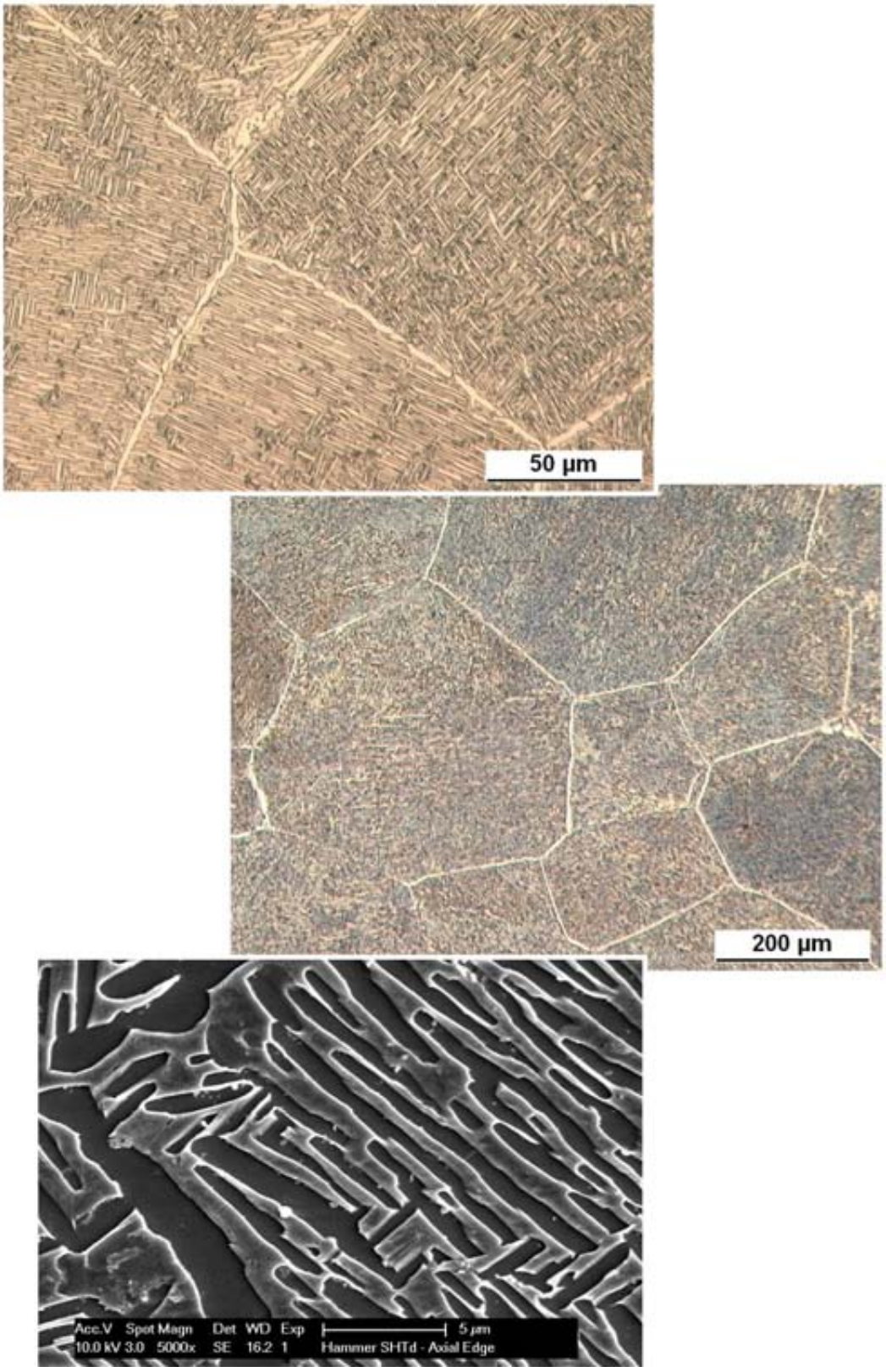

Figure 7-74 – SHT hammer forging location F. Typical microstructures

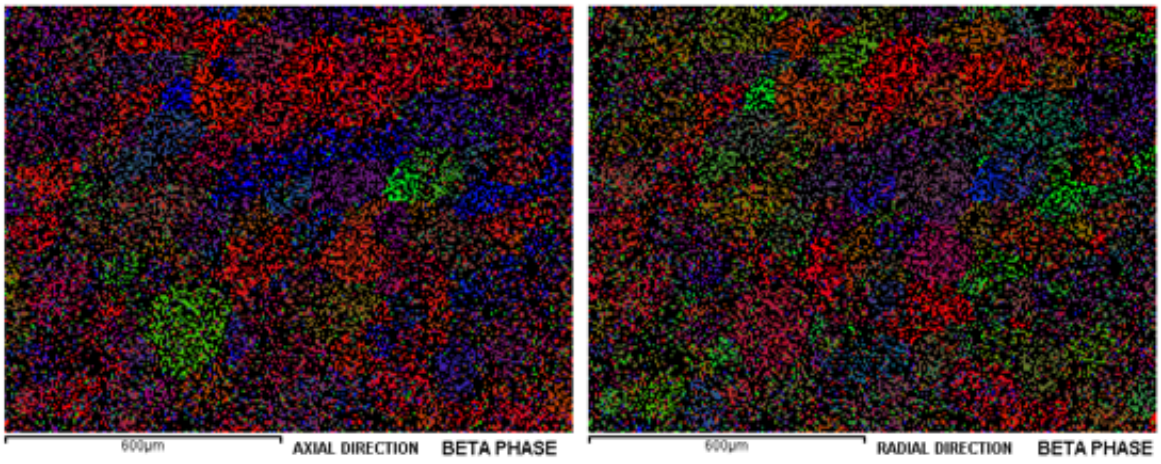

Figure 7-75 – SHT hammer forging location A. Axial and radial beta phase COMs

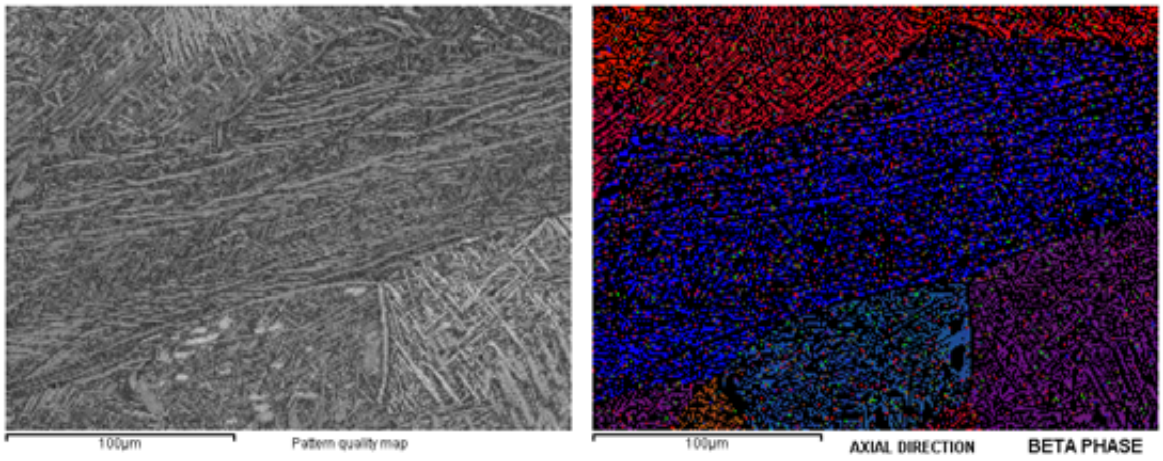

Figure 7-76 – SHT hammer forging location A. Pattern quality map and corresponding axial direction beta phase COM

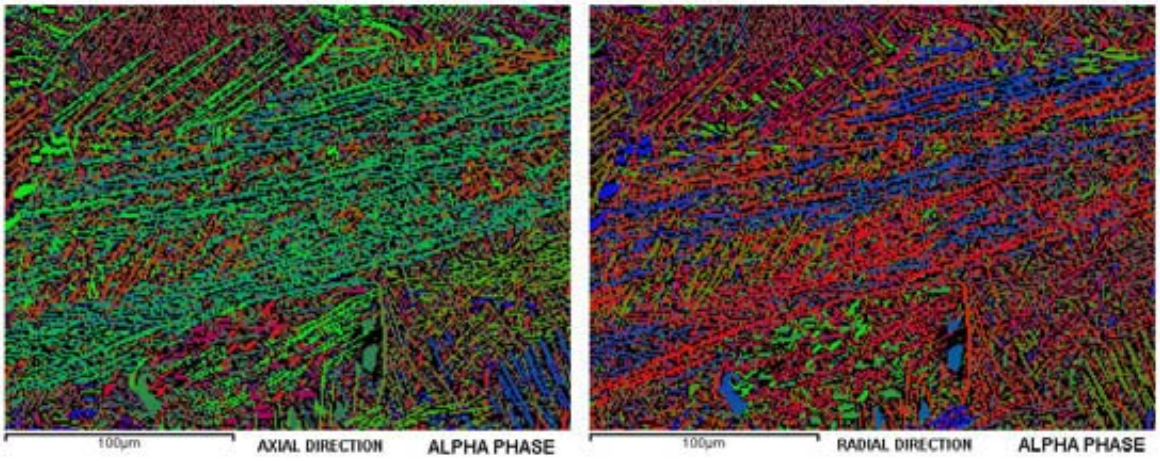

Figure 7-77 – SHT hammer forging location A. Alpha phase COMs displaying textures w.r.t. axial and radial directions

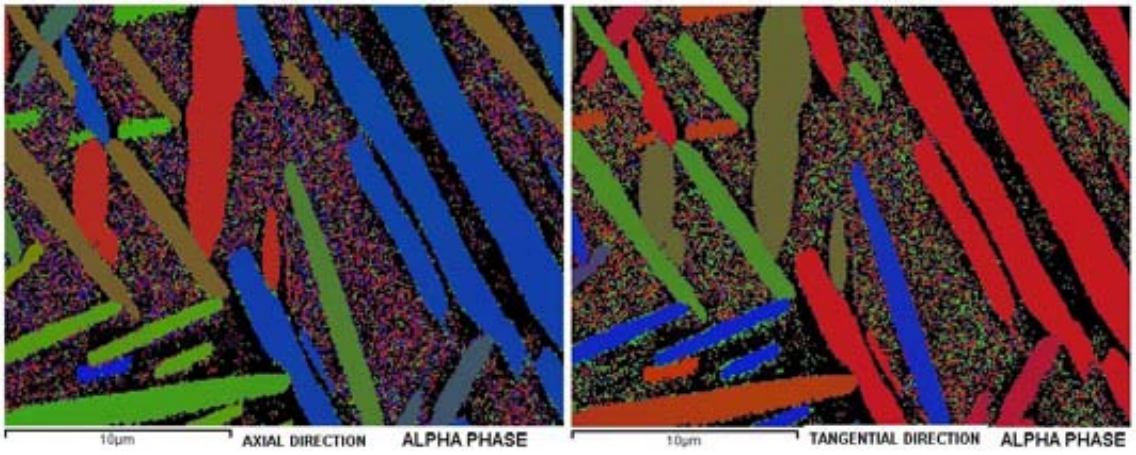

Figure 7-78 – Alpha COMs for hammer forging location A (Recrystallised grain) in SHT'd condition. Textures displayed w.r.t. axial and tangential directions

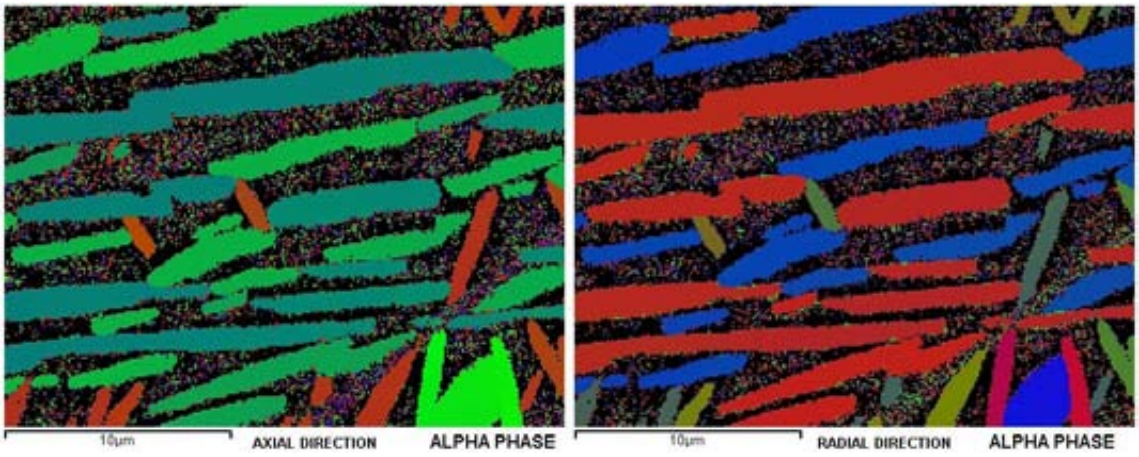

Figure 7-79 – Hammer forging location A (Unrecrystallised grain with {111}//AD fibre texture) in SHT'd condition. Alpha COMs displaying textures w.r.t. axial and radial directions

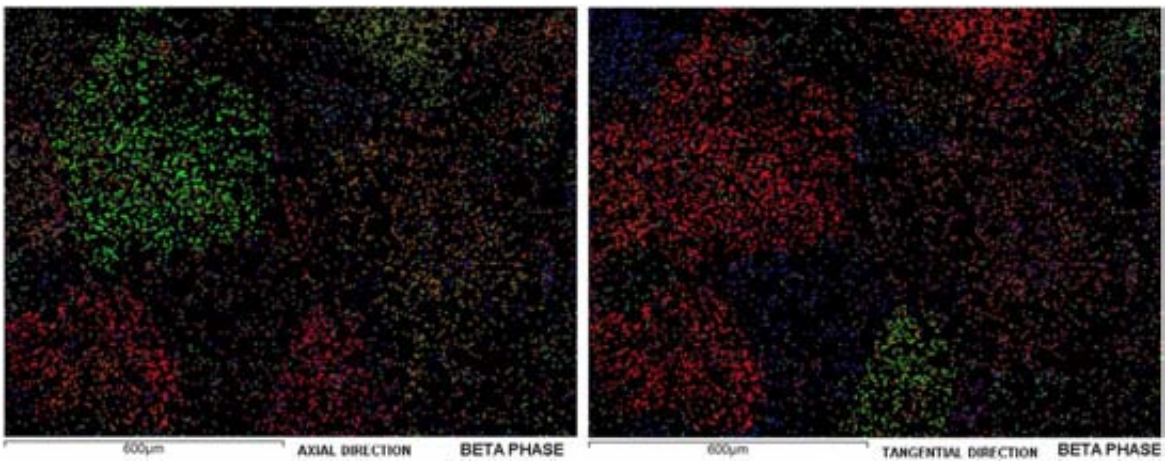

Figure 7-80 – SHT hammer forging location F. Beta phase COMs displaying textures w.r.t. axial and tangential directions

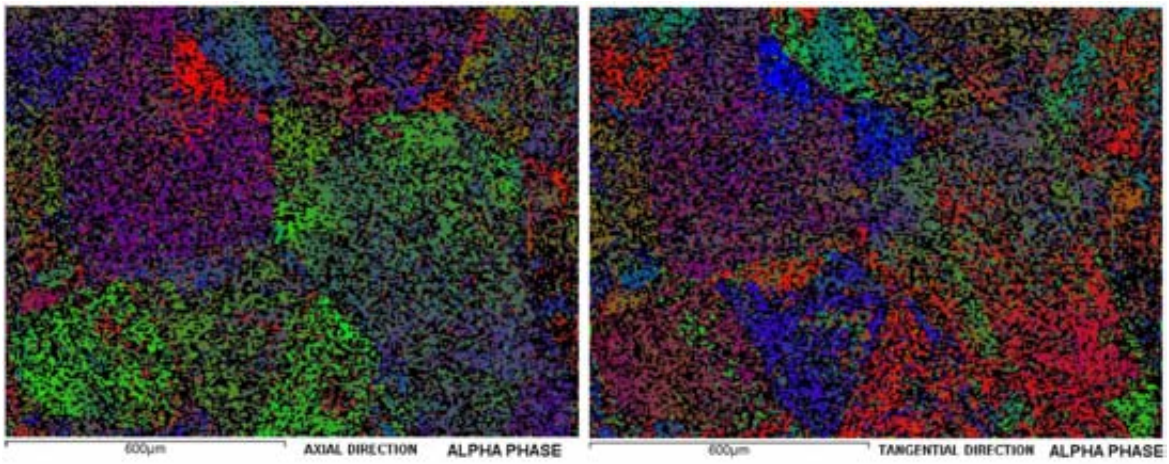

Figure 7-81 – SHT hammer forging location F. Alpha phase COMs displaying textures w.r.t. axial and tangential directions

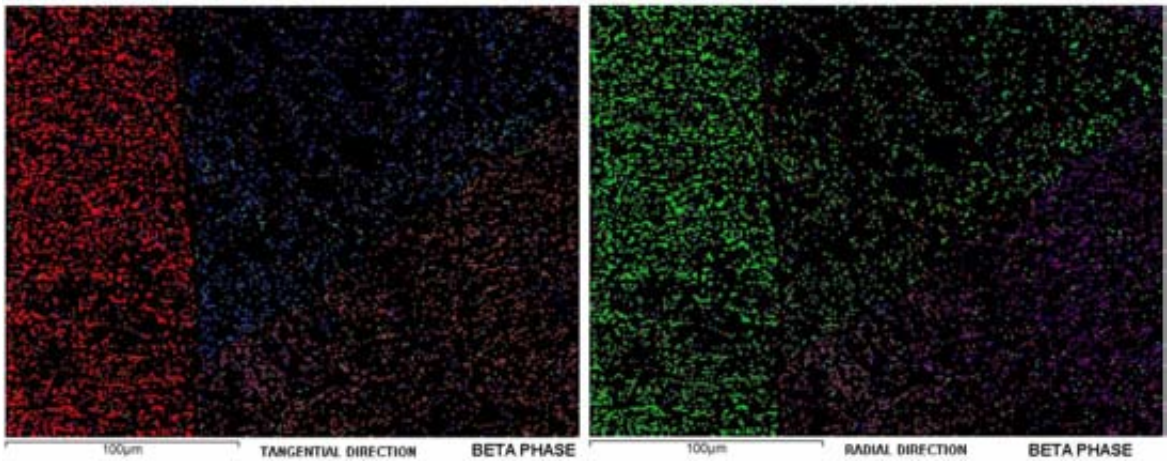

Figure 7-82 – SHT hammer forging location F. Beta phase COMs displaying textures w.r.t. tangential and axial directions

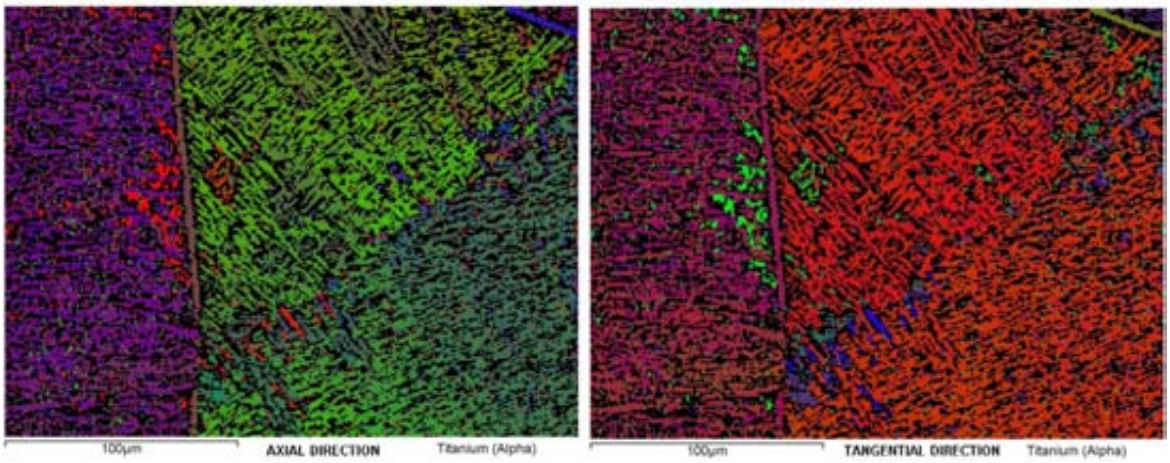

Figure 7-83 – SHT hammer forging location F. Alpha phase COMs displaying textures w.r.t. axial and tangential directions

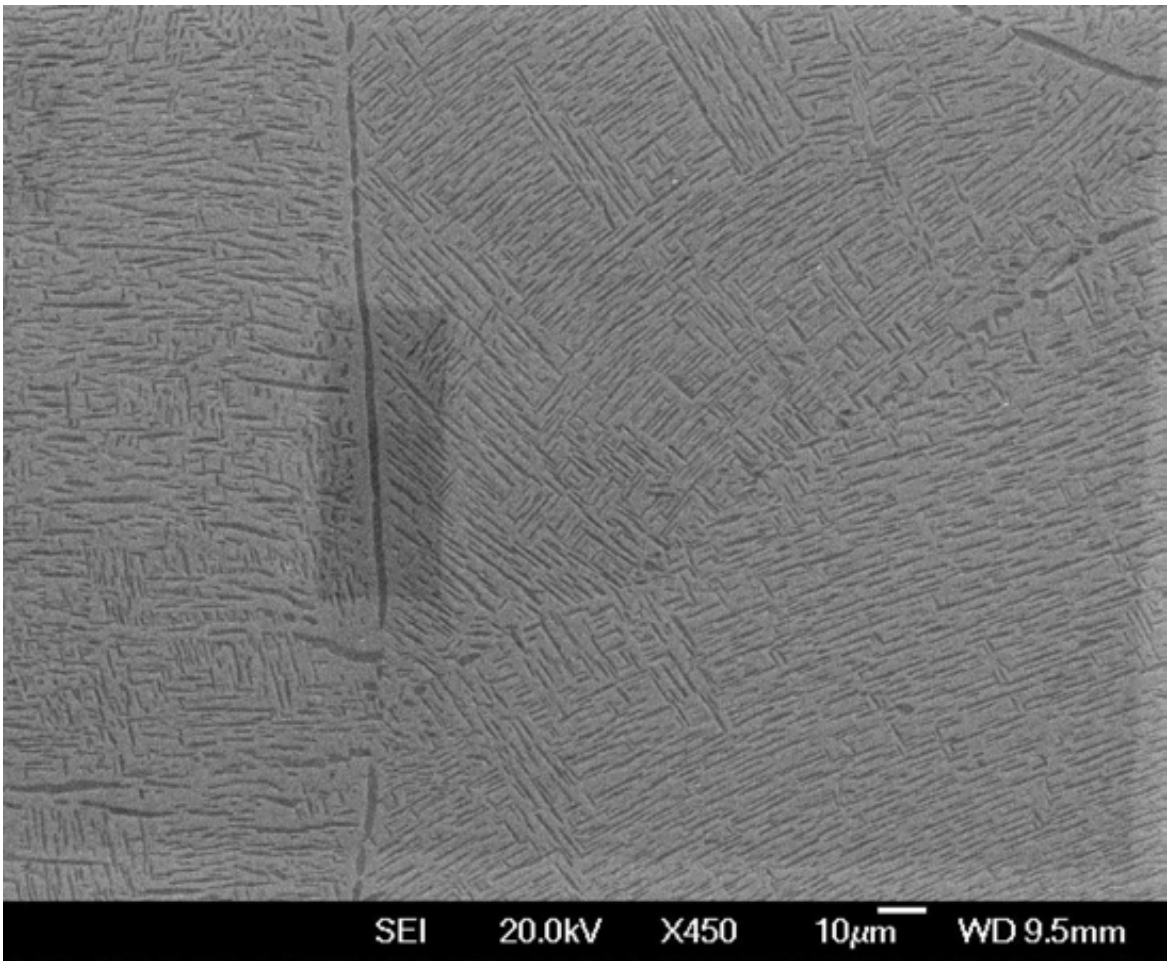

Figure 7-84 – SHT hammer forging location F. Secondary electron image of EBSD site of interest

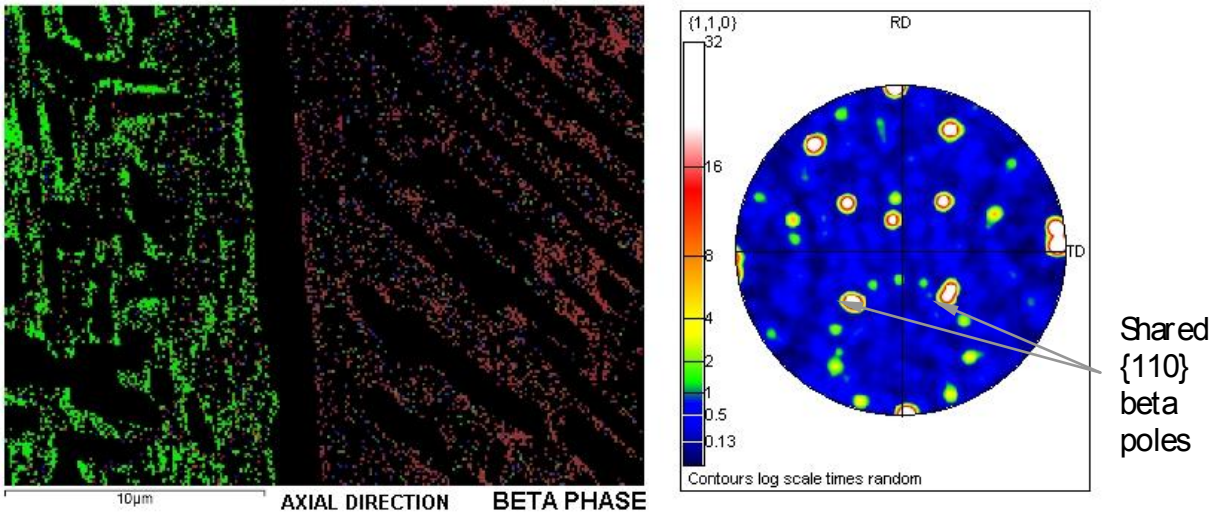

Figure 7-85 – SHT hammer forging location F. Beta COM displaying beta grain boundary. Corresponding {110} pole figure showing shared {110} poles across a beta grain boundary

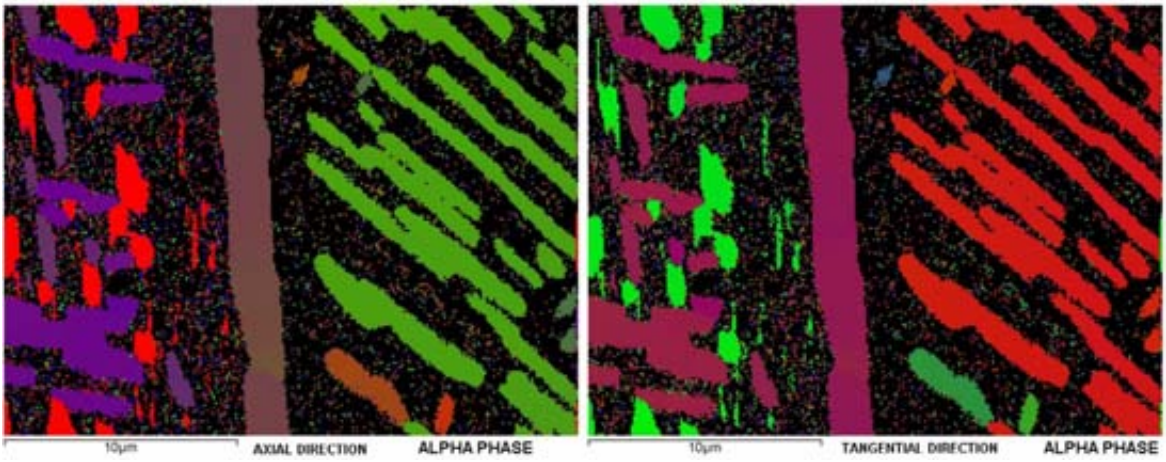

Figure 7-86 – SHT hammer forging location F. Alpha textures at a beta grain boundary. Alpha COMs displaying textures w.r.t. axial and tangential directions

7.7.2.7 Isothermal pancake – Age heat treated condition

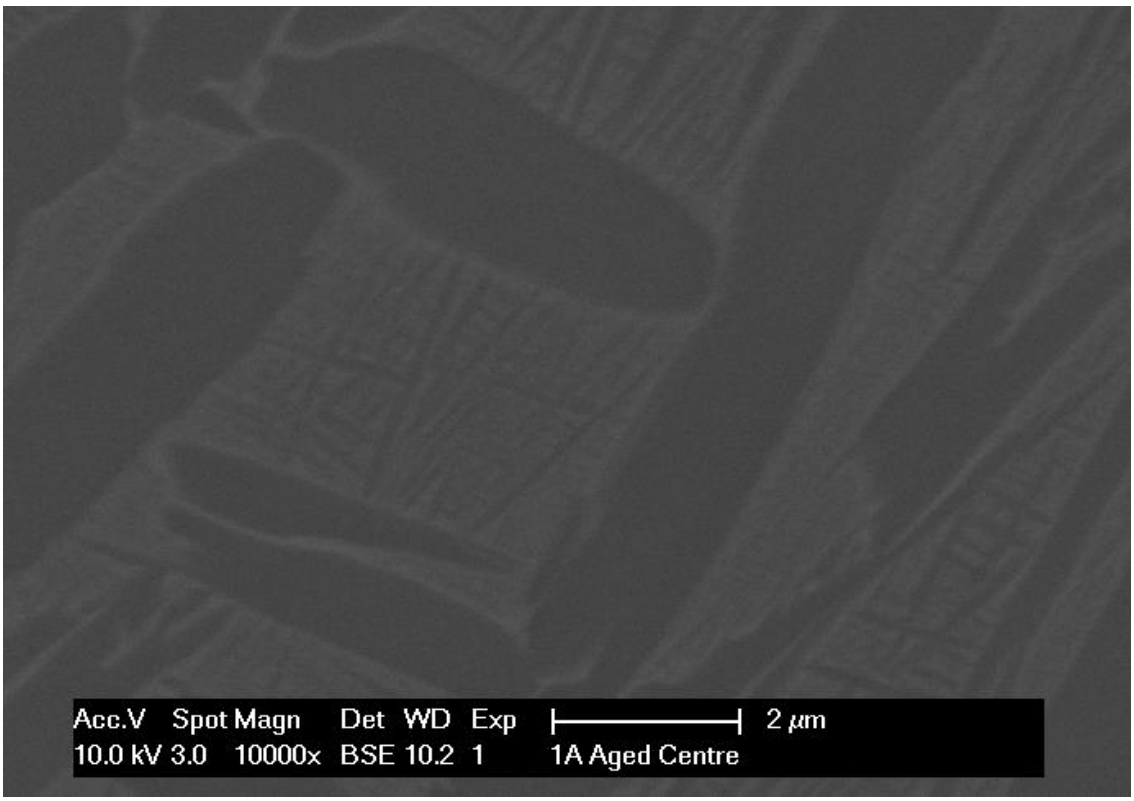

Figure 7-87 – Age HT'd isothermal forging location A. Typical microstructure

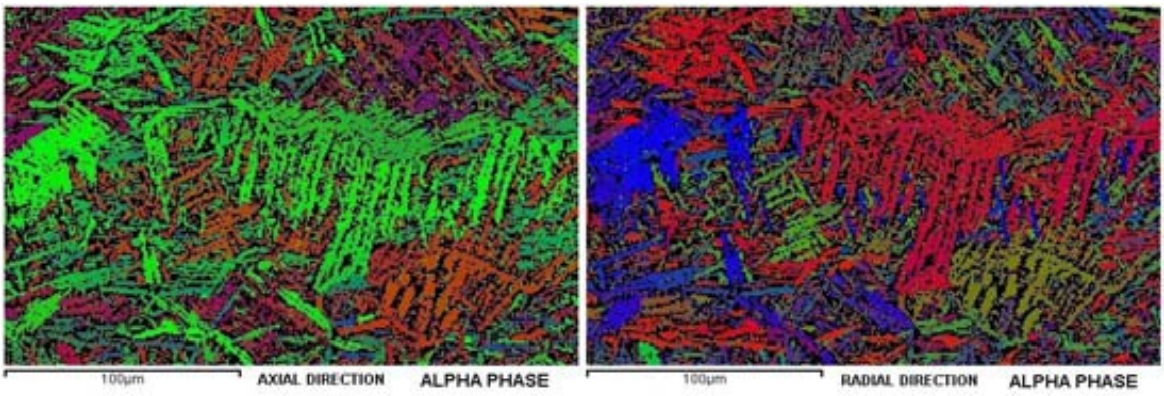

Figure 7-88 – Age HT'd isothermal forging location A. Primary alpha platelet structures. Alpha COMs displaying textures w.r.t. axial and radial directions

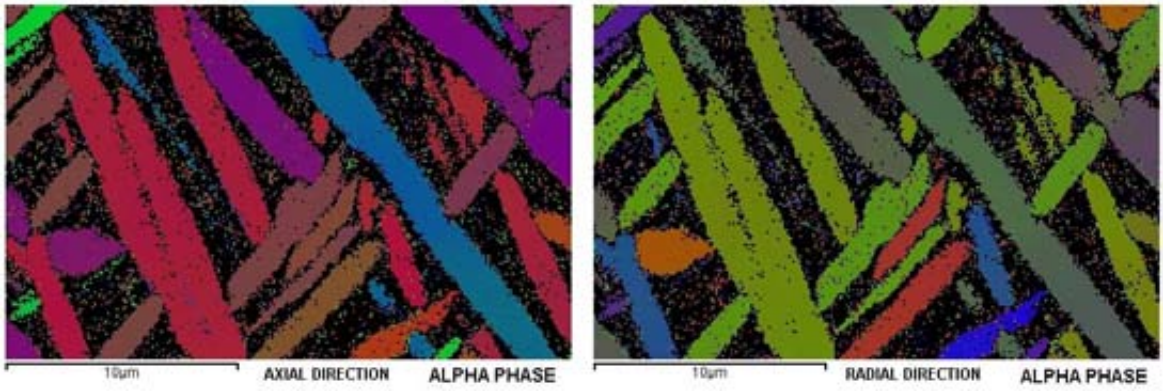

Figure 7-89 – Age HT'd isothermal forging location A. Map area within a beta grain with a {100}//AD fibre texture, displaying primary alpha platelet structures. No secondary alpha structures resolved by EBSD

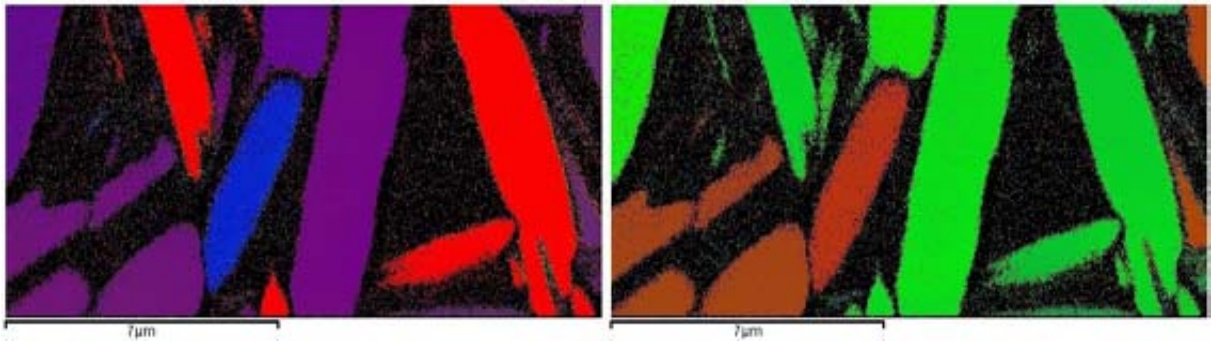

Figure 7-90 – Age HT'd isothermal forging location A. Map area within a beta grain with a {111}//AD fibre texture, displaying primary alpha platelet structures. No secondary alpha structures resolved by EBSD

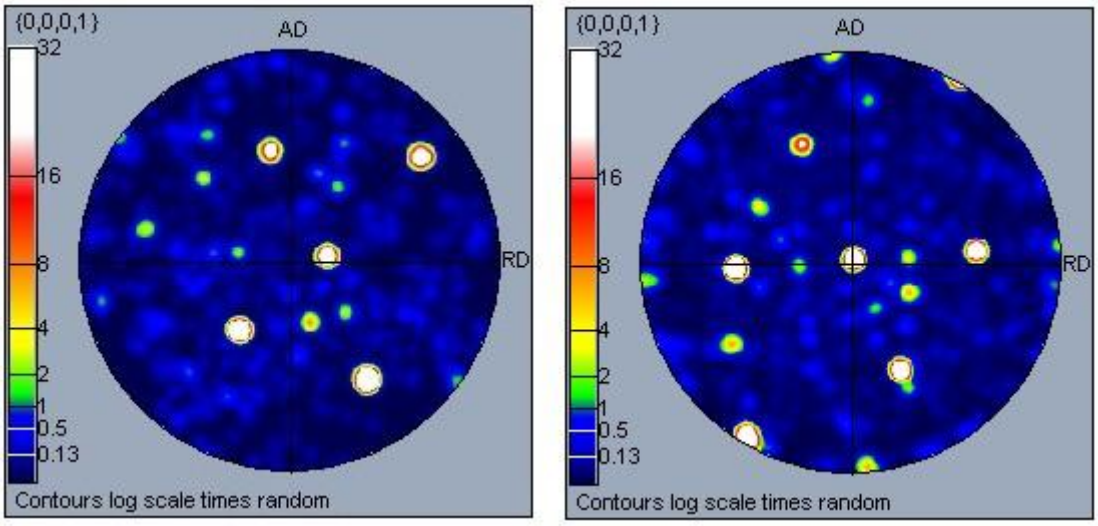

Figure 7-91 – Basal plane pole figures for Figure 7-89 and Figure 7-90 showing selection of several alpha variants on phase transformation

7.7.2.8 Hot die pancake – Age heat treated condition

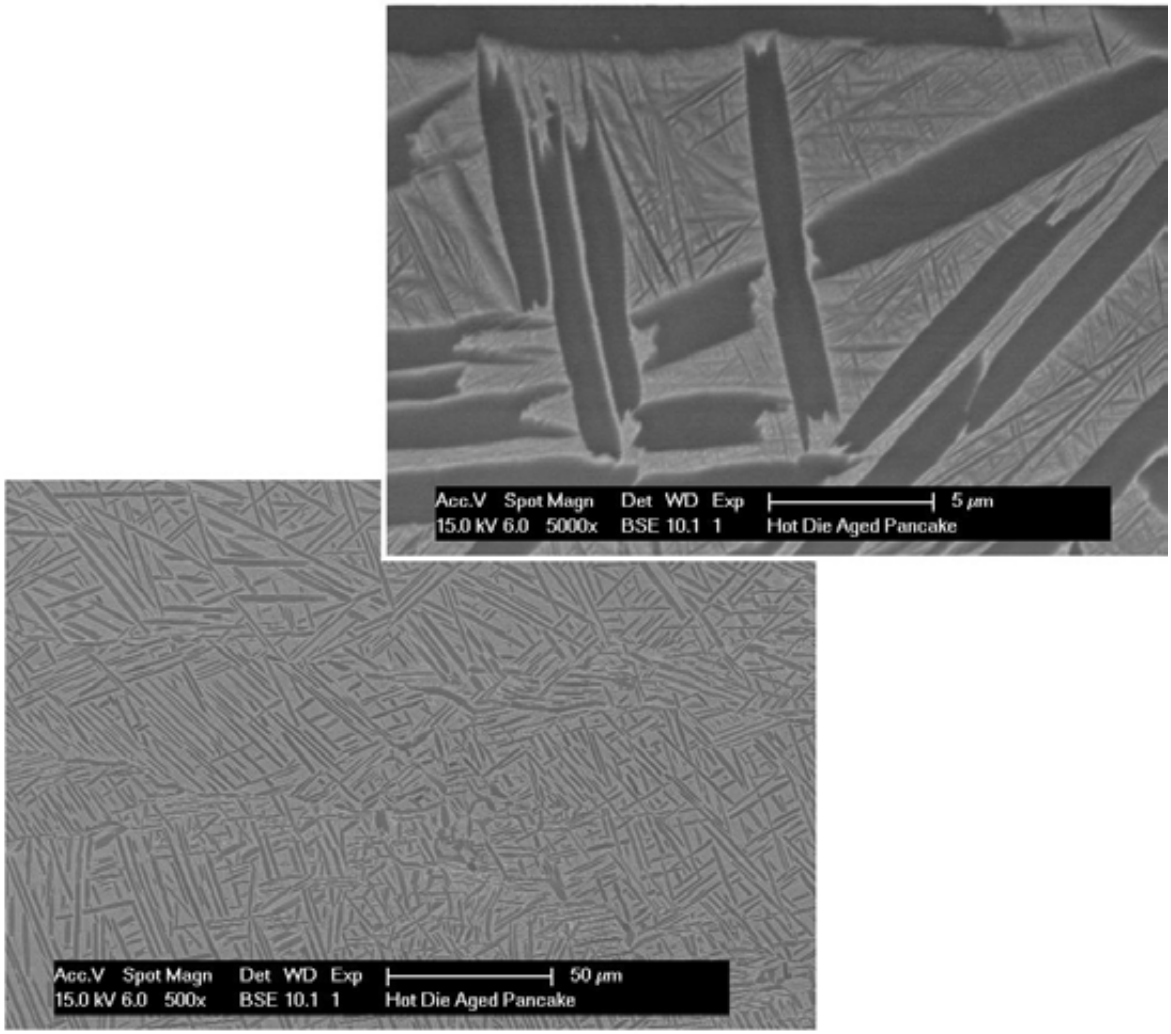

Figure 7-92 – Age HT'd hot die forging location A. Typical microstructures

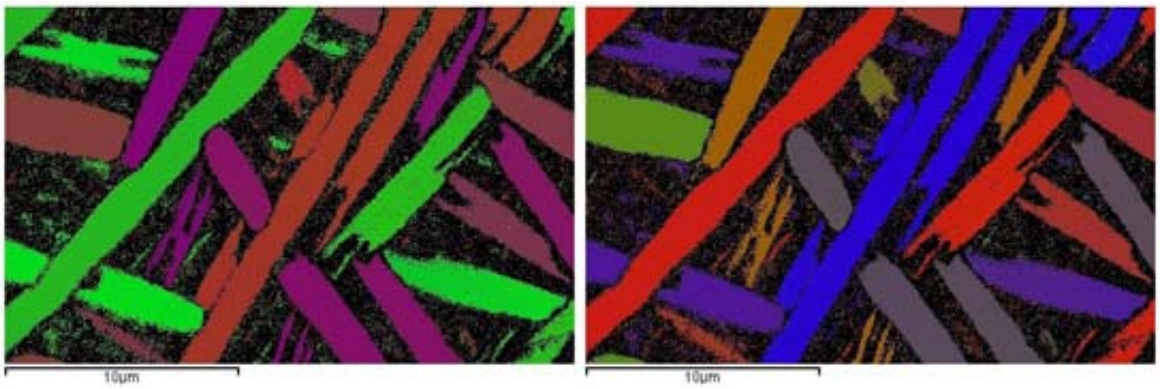

Figure 7-93 – Age HT'd hot die forging location A. Alpha COMs displaying primary alpha platelet structures. No secondary alpha structures resolved by EBSD

7.7.2.9 Hammer pancake – Age heat treated condition

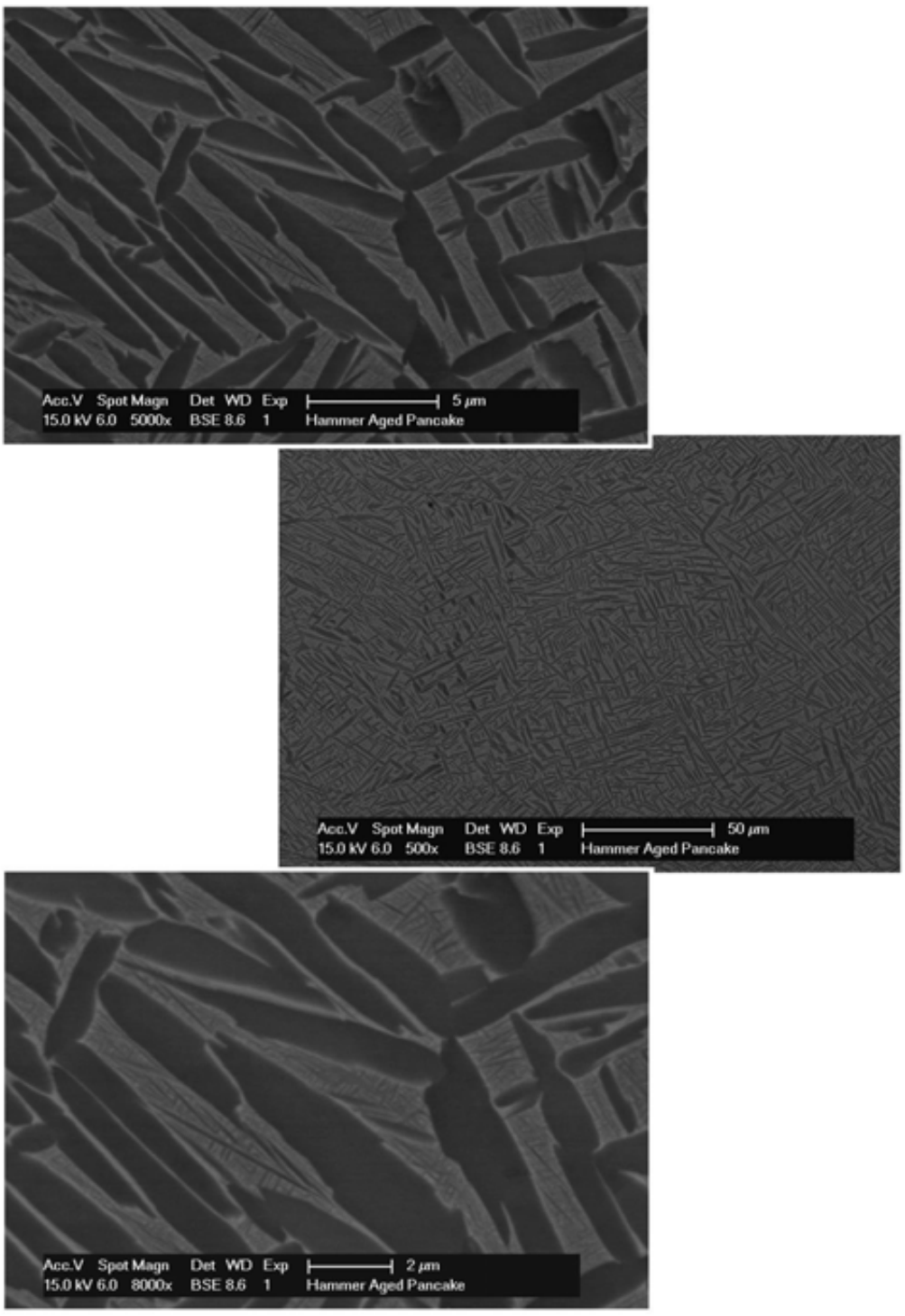

Figure 7-94 – Age HT'd hammer forging location A. Typical microstructures

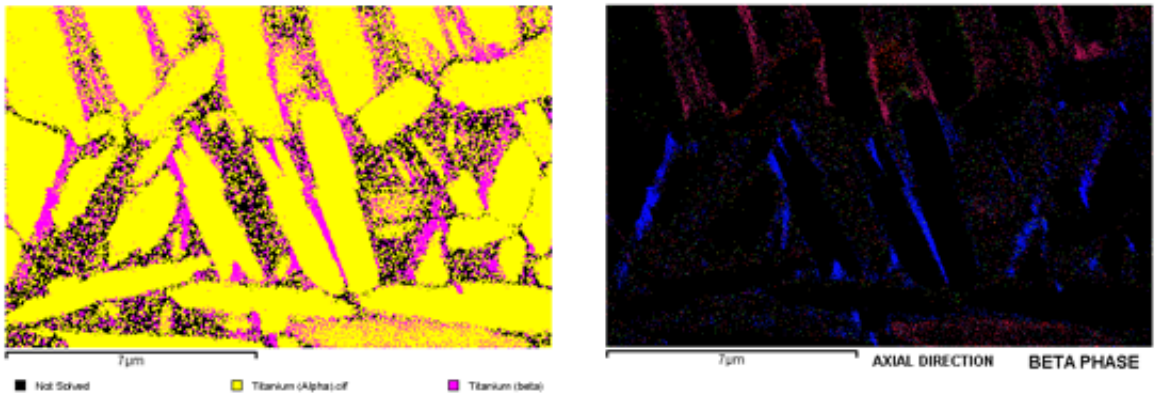

Figure 7-95 – Age HT'd hammer forging location A. EBSD phase map and beta phase COM displaying textures w.r.t. axial direction

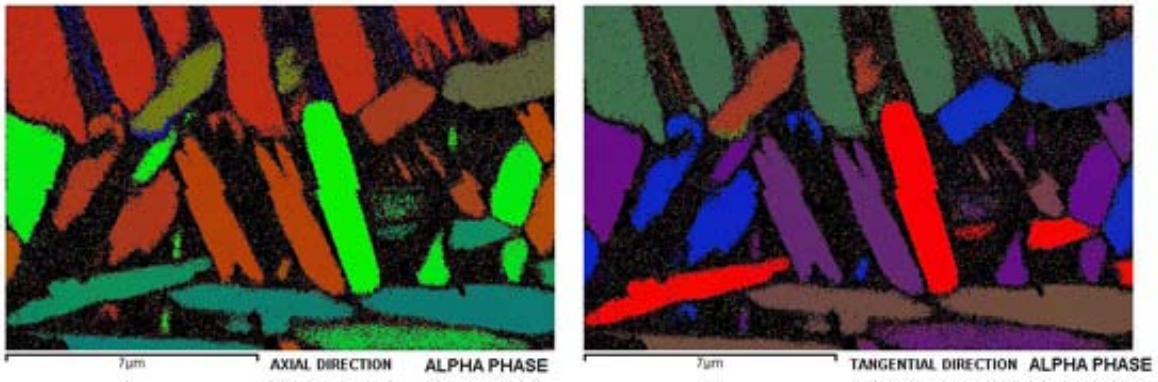

Figure 7-96 – Hammer forging location A in aged condition. Alpha COMs displaying textures w.r.t. axial and tangential directions respectively

7.7.2.10 Production disc forgings

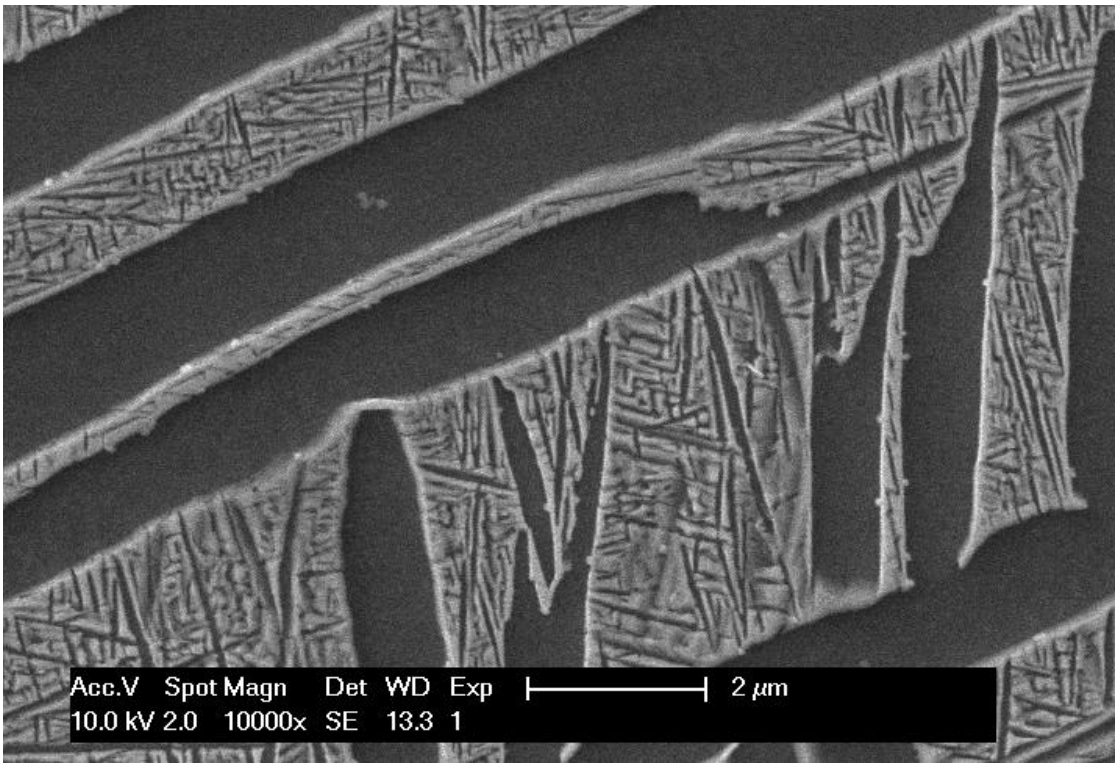

Figure 7-97 – Typical microstructure of isothermal disc forging

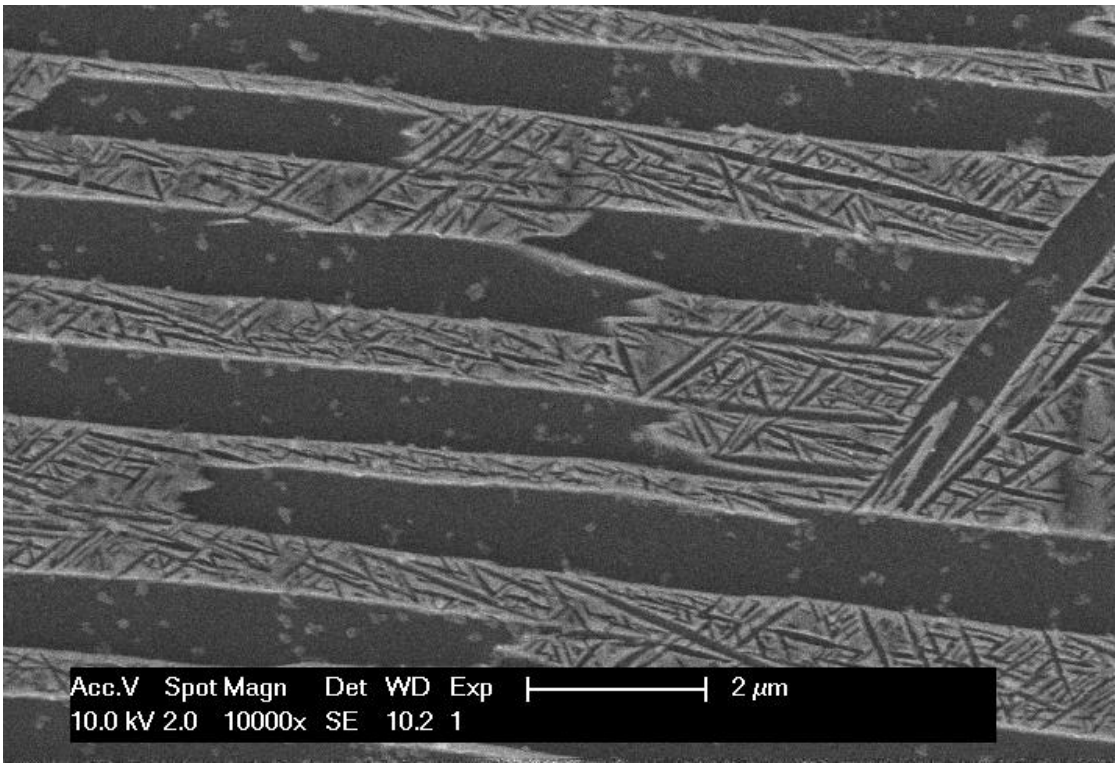

Figure 7-98 – Typical microstructure of hot die disc forging

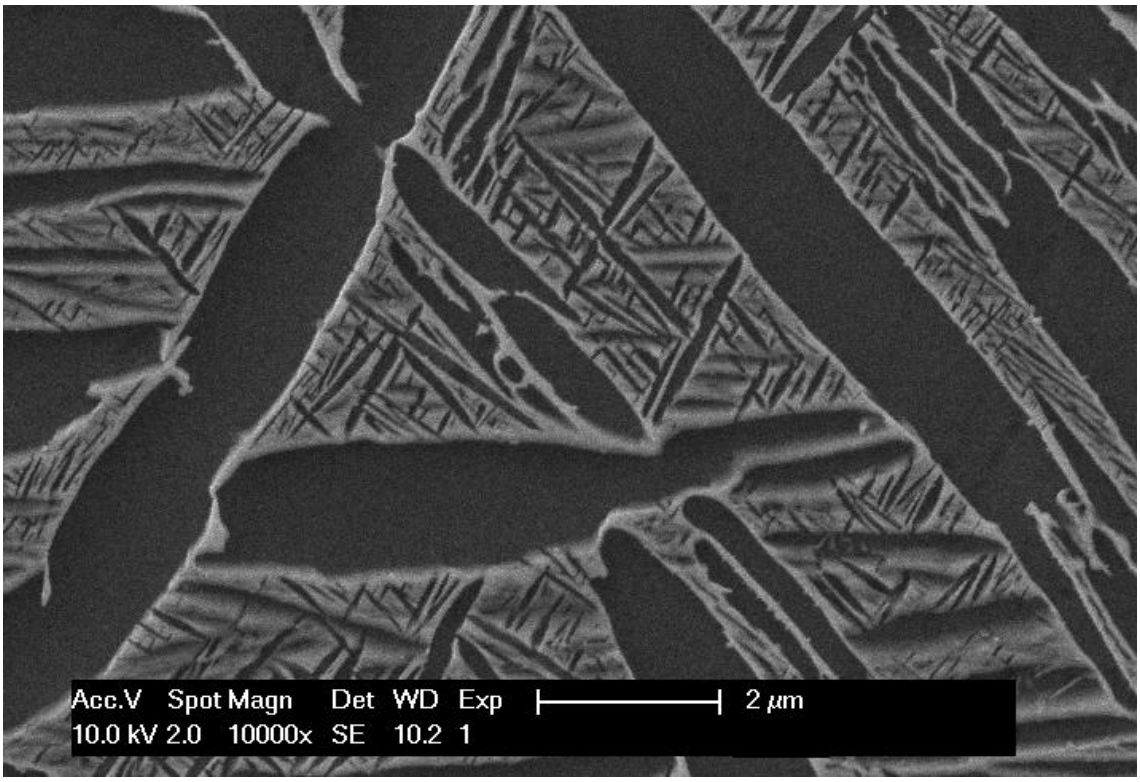

Figure 7-99 – Typical microstructure of hammer disc forging

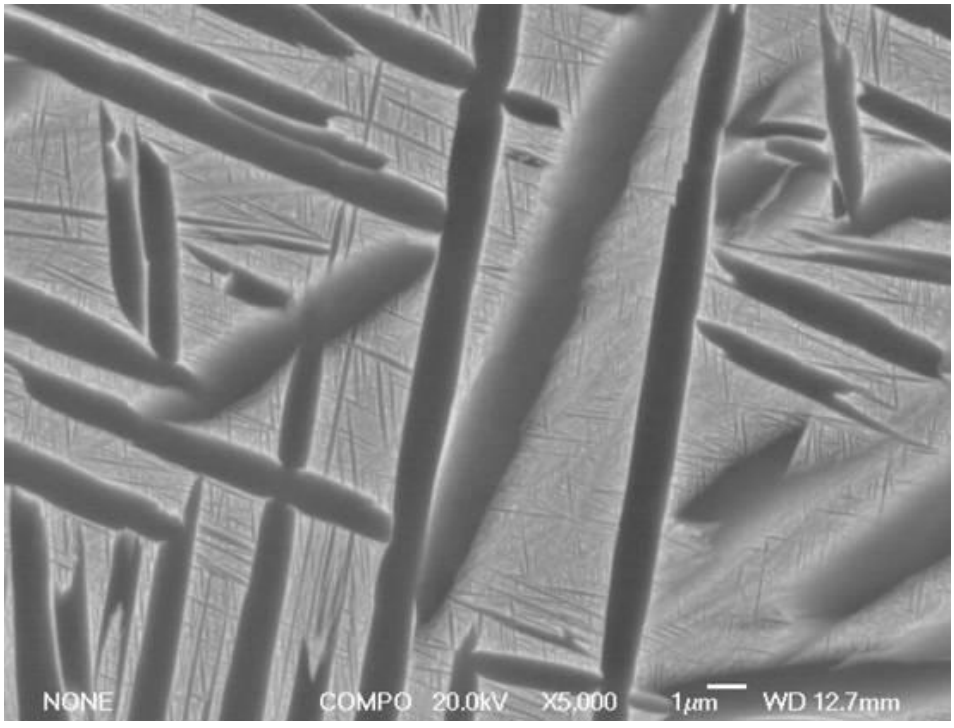

Figure 7-100 – Back-scatter electron image of EBSD site of interest for typical isothermal disc forging

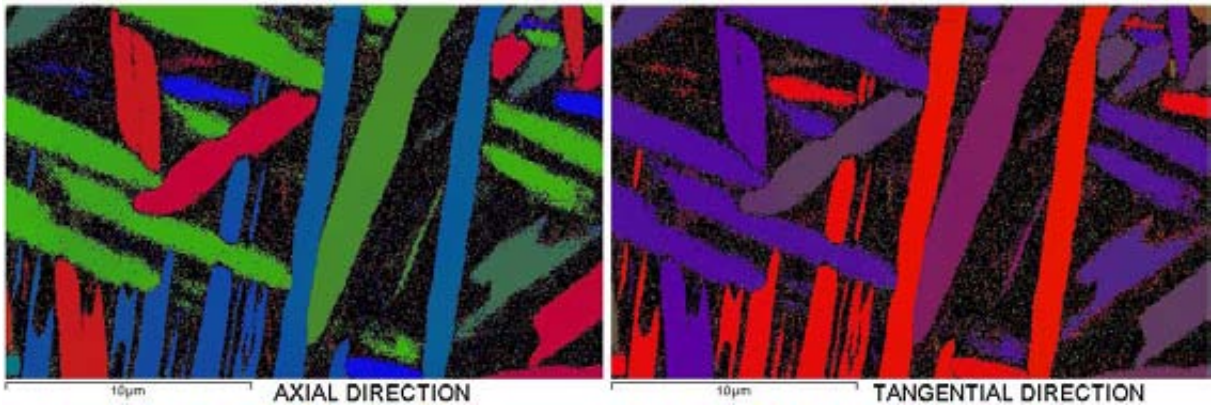

Figure 7-101 – Alpha phase COMs displaying textures w.r.t. disc axial and tangential directions respectively for an isothermal disc forging

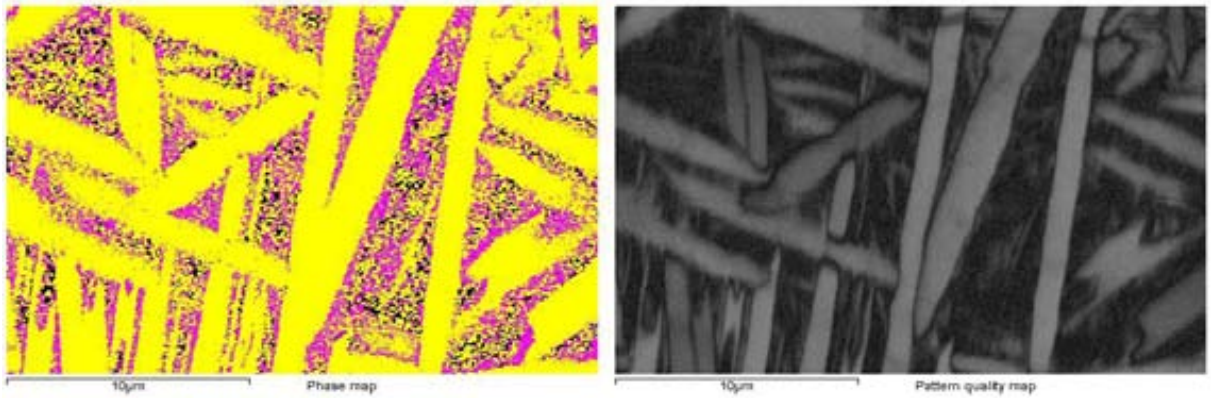

Figure 7-102 – Phase map and pattern quality map corresponding to EBSD maps in Figure 7-101

7.8 Discussion

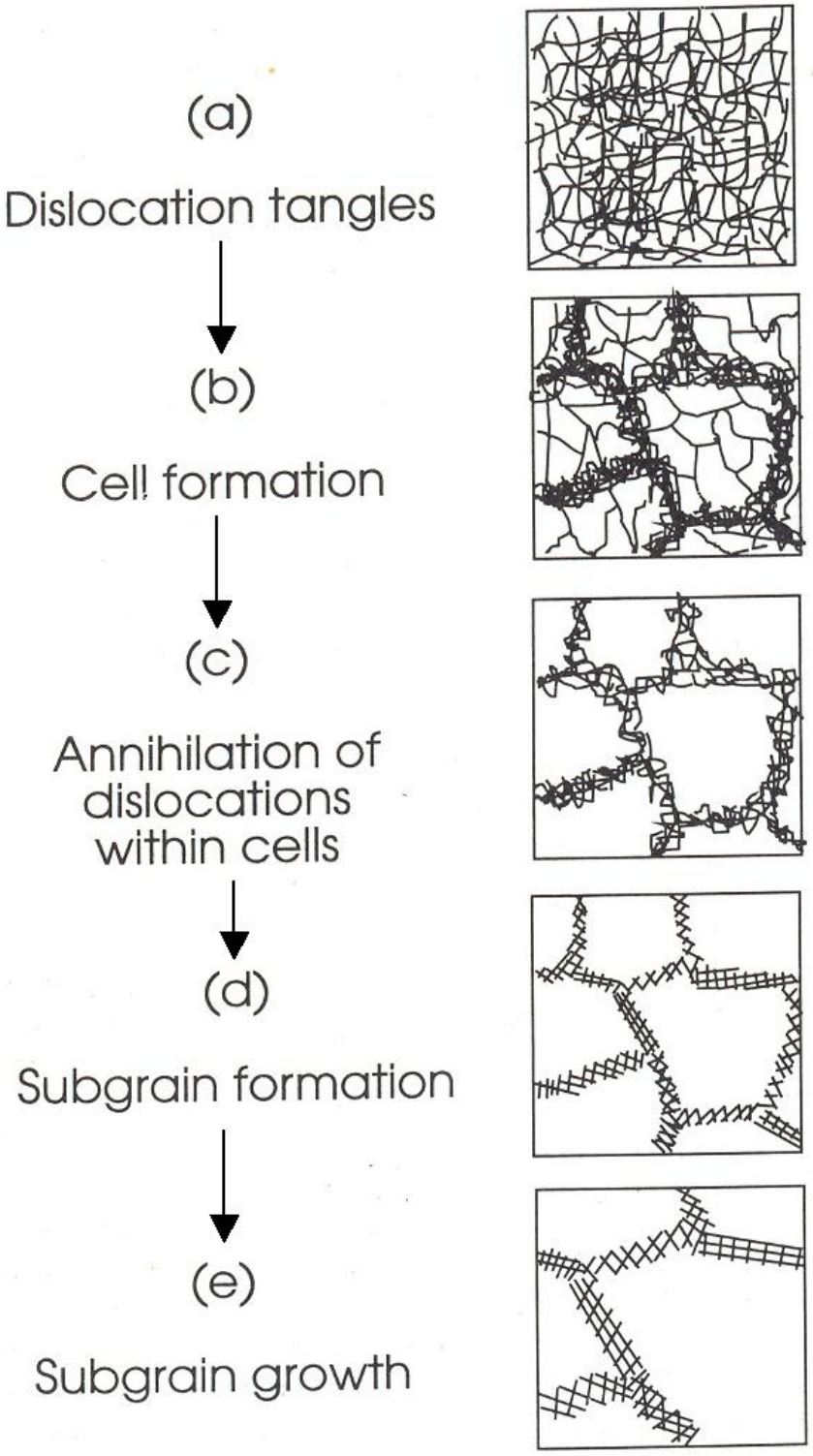

Figure 7-103 – Stages of recovery of a plastically deformed material [159]

8 Conclusions and Further Work 8-2
8.1 Summary of conclusions 8-2
8.2 Further work 8-5

9 References 9-1

8 Conclusions and Further Work

8.1 Summary of conclusions

Chapter two reviewed the literature available relating to cold dwell fatigue behaviour. This review highlights a gradual development of understanding from early theories of hydrogen induced embrittlement and sustained load cracking to the current model of a stress redistribution mechanism leading to sub-surface load normal quasi-cleavage facet features.

Chapter four studied variability in Ti6246 microstructures and textures. Significant variability in different production forgings was noted and related to process route. Stronger beta and alpha textures were observed in isothermal forgings (as a general trend, not accounting for differences in forging strain or other factors). Hammer forgings showed the smallest average grain sizes and the most equiaxed morphologies, indicative of a higher recrystallisation fraction.

CDF testing of Ti6246 in a standard microstructural condition showed low life debit levels and no load normal facet features. Similar testing of modified microstructures at equivalent proportions of UTS also showed limited cold dwell fatigue effects and no facet formation. Ti6246 was concluded not to be a cold dwell sensitive alloy. This behaviour was attributed primarily to an increased volume fraction of beta phase relative to other disc alloys. Other mitigating factors include the presence of secondary alpha platelets resulting in small effective slip lengths in the typical Ti6246 disc microstructure.

Chapter five compared the apparently dwell insensitive Ti6246 to an alloy with a lower level of beta stabilisation and previous experience of cold dwell fatigue susceptibility (Ti6242). Beta annealing heat treatments were used to create large

equiaxed grain colonised microstructures. The very slow cooling rate required to create a large colony microstructure in Ti6246 led to a coarsening of both alpha and beta phases. In test specimens a reduction in planar slip deformation was noted in comparison to the beta annealed specimens tested in chapter four. This was attributed to the coarsening of beta layers and the greater number of operative slip systems in this phase. In the absence of planar slip deformation there was no dislocation build-up at colony boundaries to allow stress redistribution as required for CDF. As such there was no load normal facet formation and only small debits on cyclic life were recorded.

Because of the reduced beta stabilisation of Ti6242 faster cooling rates could be used to achieve suitably sized colony microstructures. The microstructure was similar to that of beta annealed Ti6246 tested in chapter four. CDF testing produced planar slip trace deformation, however, only small debits on cyclic life were observed. No load normal facet formation was observed on fracture surfaces. The absence of dwell fatigue effects was unexpected and was attributed to one or more causes, including specimen volume effects and/or a potential reduction of fatigue performance due to microstructural effects.

Chapter six evaluated the variation in macrozone and effective structural unit sizes for different titanium alloys. Optical microstructure was found to be an unreliable indicator of the macrozone size. Macrozone size was also found to differ from the ESU size. Beta processed alloys show macrozone sizes equivalent to the size of optical colonies. Shared crystallographic planes may extend over larger length scales of two or more grains according to the orientation of prior beta grains and the selection of particular alpha variants. ESU size were generally found to correspond to

the optical colony size suggesting that even where common slip planes exist there are barriers to dislocation transmission across colony boundaries.

Bimodal alloys showed significant macrozone size refinement from billet to disc microstructures. Disc microstructures typically contain macrozones of less than two to three neighbouring alpha grains (approximately 100-200μm in length). However in some cases macrozones exist over much larger volumes, ostensibly as a result of insufficient forging strain to break down retained textures. In these cases CDF behaviour becomes an issue.

Chapter seven evaluated variations in optical microstructures and textures in Ti6246 pancake forgings. Both were observed to vary significantly with changes in effective forging strain and post forge cooling rate. Heavily strained microstructures showed elongated unrecrystallised prior beta grains containing a distribution of six or more alpha variants for each parent beta orientation. Unrecrystallised grains show alignment of {100} or {111} poles with the compression axis. Heavily strained microstructures show partial dynamic recrystallisation on prior beta grain boundaries. Isothermal and hot die forgings show similar recrystallisation area fractions for consistent forging conditions. The hammer forging technique leads to a higher recrystallisation fraction. This is attributed to the high strain rate characteristic of the technique. No strong recrystallisation texture was identified. Alpha textures often show a radial distribution of basal planes due to the nature of the Burgers orientation relationship and the post-forge beta textures.

Low strain microstructures show equiaxed beta grains and low levels of recrystallisation. Forging dead zones show no recrystallisation. Large (optical and crystallographic) colonies of alpha platelets were observed in typical microstructures. Alpha macro-texture is varied due to the absence of a strong beta macro-texture.

8.2 Further work

The following further work is recommended:

- Study of textures throughout Ti6246 pancake forgings to determine macro-textures for specific forging strain and cooling rate conditions.
- TEM study of the crystallographic nature of secondary platelets in the retained beta matrix in Ti6246 to determine the nature of the interface, i.e. does a Burgers orientation relationship exist?
- Development of a software code for the INCA EBSD software package allowing the back-calculation of parent beta textures from alpha phase data as for other EBSD software (e.g. HKL). This would allow the accurate assessment of prior beta grain sizes in bimodal alloys such as Ti834, Ti6/4 and Ti6242 (all characterised in disc conditions for which previous experience of cold dwell sensitive fatigue exists).
- TEM studies of the beta colonised Ti6246 test specimens subject to cyclic and dwell fatigue testing in chapter four of the thesis. Characterisation of planar slip bands to determine if dislocation pile-ups occur at colony boundaries or if trans-colony dislocation movement occurs under either type of loading.
- Characterisation of planar slip bands to determine the operational slip systems at high proportions of UTS and the Schmid factors associated with each type of slip behaviour.
- The undertaking of a statistically significant survey of macrozone sizes in titanium alloys using EBSD or spatially resolved acoustic scanning (SRAS) techniques.

9 References

[1] Welsch G, Boyer R, Collings EW. *Materials Properties Handbook: Titanium Alloys*. 1994. Ohio: ASM International.

[2] *Timetal® 6246 data-sheet*. 2000. Cited 22/02/2008; Available from: http://www.timet.com/6-2-4-6frame.html.

[3] *Timetal® 834 data-sheet*. 1999. Cited 22/02/2008; Available from: http://www.timet.com/834frame.html.

[4] *Timetal® 685 data-sheet*. 1999. Cited 22/02/2008; Available from: http://www.timet.com/685frame.html.

[5] *Timetal® 829 data-sheet*. 1999. Cited 22/02/2008; Available from: http://www.timet.com/829frame.html.

[6] *Timetal® 6/4 data-sheet*. 2000. Cited 22/02/2008; Available from: http://www.timet.com/6-4frame.html.

[7] *Timetal® 6242 data-sheet*. 2000. Cited 22/02/2008; Available from: http://www.timet.com/6-2-4-2frame.html.

[8] Cumpsty, N., *Jet Propulsion*. 2nd ed. 2003: Cambridge University Press.

[9] *The Jet Engine*. 2005. Rolls-Royce plc.

[10] Corran, R.S.J. and S.J. Williams, *Lifing methods and safety criteria in aero gas turbines.* Engineering Failure Analysis, 2007. **14**(3): p. 518-528.

[11] Powell, B.E., *Fatigue Crack Growth Behaviour of Two Contrasting Titanium Alloys.* International Journal of Fatigue, 1995. **170**(3): p. 221-227

[12] Polmear, I.J., *Light Alloys*. 2nd ed. 1989: Edward Arnold.

[13] Unknown Author, *Critical Parts Lifing and Integrity webpage*. Rolls-Royce Intranet – Private Data. Cited 13/12/2007.

[14] Howland, C. and M.J. Hill, *Behaviour of Beta Processed Titanium Alloys and their Application in Gas Turbine Engines.* The Institute of Metals, 1986: p. 183-190.

[15] Bache, M.R. and W.J. Evans, *Dwell sensitive fatigue response of titanium alloys for power plant applications.* Journal of Engineering for Gas Turbines and Power-Transactions of the ASME, 2003. **125**(1): p. 241-245.

[16] Bache, M.R., *A review of dwell sensitive fatigue in titanium alloys: the role of microstructure, texture and operating conditions.* International Journal of Fatigue, 2003. **25**(9-11): p. 1079-1087.

[17] Crystal Structures. Cited 10/06/2011; Available from: http://engineeronadisk.com/notes_material/materiala3.html.

[18] Bhadeshia, H. *Titanium and its alloys*. Cited 13/12/2007; Available from: http://www.msm.cam.ac.uk/phase-trans/2004/titanium/titanium.html.

[19] Lütjering, G., *Influence of processing on microstructure and mechanical properties of (alpha+beta) titanium alloys.* Materials Science and Engineering A, 1998. **243**(1-2): p. 32-45.

[20] Lütjering, G., *Property optimization through microstructural control in titanium and aluminum alloys.* Materials Science and Engineering A, 1999. **263**(2): p. 117-126.

[21] Guo, Z., A. P. Miodownik, N. Saunders and J-Ph. Schille, *Influence of stacking-fault energy on high temperature creep of alpha titanium alloys*. Scripta Materialia, 2006. **54**: p.2175-2178

[22] Bein, S. and J. Bechet. *Phase Transformation Kinetics and Mechanisms in Titanium Alloys Ti-6.2.4.6, Beta-CEZ and Ti-10.2.3.* Journal de Physique IV, 1996. **6**(C1): p. 99-108

[23] The Kroll Process. Cited 13/12/2007; Available from: http://en.wikipedia.org/wiki/Kroll_process.

[24] ALD Vacuum Technologies AG. Vacuum Arc Remelting Processes and Furnaces. Cited 17/07/2007; Available from: www.ald-vt.de.

[25] Dixon, M., Private Communication. *Rolls-Royce Materials - Processing of Ti6246*. 06/04/2006.

[26] Unknown Author, *Ti6246 Supplementary Information*. Rolls-Royce Intranet – Private Data. Cited 13/07/2007.

[27] G. Terlinde, T.W., G. Fischer. *Ti6246 Forgings for Compressor Discs*. In *Titanium 2003 - Science and Technology*. 2003. Hamburg.

[28] Lütjering, G., J. C. Williams., *Titanium*. 2nd ed. 2007: Springer.

[29] Chakrabarti, A.K., M. Burn, D. Fournier and G. W. Kuhlman, *Microstructure and Mechanical Property Optimization through Thermomechanical Processing in Ti6-4 and Ti-6-2-4-6 Alloys*. In *Sixth World Conference on Titanium*. 1988. France.

[30] Chakrabarti, A.K., R. Pishko, and G.W. Kuhlman. *Microstructure - Fracture Toughness - Fatigue Crack Growth Rate Optimization of Ti-6Al-2Sn-4Zr-6Mo Alloy Forgings*. In *TMS-AIME Annual Symposium*. 1987. Denver, Colorado: Metallurgical Society Inc

[31] Williams, J. C. And B. S. Hickman. *Tempering Behavior of Orthorhombic Martensite in Titanium Alloys.* Metallurgical Transactions, 1970. **1**: p. 2648-2650.

[32] Young, M., E. Levine, H. Margolin. *Age Hardening of Alpha/Beta Ti-6Al-2Sn-4Zr-6Mo.* Metallurgical Transactions A, 1974. **10**: p. 359-362.

[33] Mantani, Y., Y. Takemoto, M. Hida, A. Sakakibara and M. Tajima. *Phase Transformation of Alpha Double Prime Martensite Structure by Aging in Ti-8 mass% Mo Alloy.* Materials Transactions, 2004. **45**(5): p. 1629-1634.

[34] Tarin, P., I. Alonso, A. G. Simon, J. M. Badia and N. M. Piris. *Characterization of the alpha - beta transformations in a Ti-6Al-2Sn-4Zr-6Mo (wt.%) alloy.* Materials Science and Engineering A, 2008. **481-482**: p. 559-561.

[35] Sugimoto, T., K. Kamei, S. Komatsu, K. Sugimoto, H. Matsumoto and M. Ikeda. *Aging Behavior of Alpha Double Prime Martensite Formed in a Quenched Ti-6Al-2Sn-4Zr-6Mo Alloy.* Deutsche Geselleschaft fur Metallkunde, 1984. **3**: p. 1583-1590.

[36] Ito, Y., Y. Moriguchi and T. Nishimura. *The Effect of Microstructures on Mechanical Properties of the Beta Rich Alpha-Beta Titanium Alloy Ti-6Al-2Sn-4Zr-6Mo. Journal of the Iron and Steel Institute of Japan*, 1986. **72**: p. 625-632.

[37] Mendiratta, M. G. And J. A. Roberson. *Tensile Properties to 550°C and Microstructures in Quenched and Aged Ti-6Al-2Sn-4Zr-6Mo Alloy.* Metallurgical Transactions A, 1975. **6**: p. 940-943.

[38] Sauer, C. and G. Lütjering, *Thermo-mechanical processing of high strength beta-titanium alloys and effects on microstructure and properties.* Journal of Materials Processing Technology, 2001. **117**(3): p. 311-317.

[39] Meadows, D., *Quantifying the Ageing Response of Martensite in the Ti-6Al-2Sn-4Zr-6Mo Alloy*, School of *Metallurgy and Materials*. 1996, University of Birmingham.

[40] Unknown Author, *Ti6246 Material Specification (MSRR8684)*. Rolls-Royce Intranet – Private Data. Cited 13/12/2007.

[41] Liu, Y. and T.N. Baker, *Deformation characteristics of IMI685 titanium alloy under beta isothermal forging conditions.* Materials Science and Engineering, 1995. **A197**: p. 125-131.

[42] Guo, Z.X. and T.N. Baker, *On the microstructure and thermomechanical processing of titanium alloy IMI685.* Materials Science and Engineering, 1992. **A156**: p. 63-76.

[43] Unknown Author, *Supplementary Information Sheet – Titanium 6/4*. Rolls-Royce Intranet – Private Data. Cited 17/07/2007.

[44] Plumbridge, W.J., *Damage production during high temperature-low cycle fatigue of a titanium alloy (IMI829).* Fatigue and Fracture of Engineering Materials and Structures, 1987. **10**(5): p. 385-398.

[45] Ma, F., W. Lu, J. Qin and D. Zhang, *Microstructure evolution of near alpha titanium alloys during thermomechanical processing.* Materials Science and Engineering, 2006. **A416**: p. 59-65.

[46] Weiss, I., *Thermomechanical processing of beta titanium alloys - an overview.* Materials Science and Engineering, 1998. **A243**: p. 46-65.

[47] Weiss, I., *Thermomechanical processing of alpha titanium alloys - an overview.* Materials Science and Engineering, 1999. **A263**: p. 243-256.

[48] EBSD Explained. Cited 13/12/2007; Available from: www.ebsd.com\ebsdexplained.htm.

[49] Evolution of EBSD Patterns during Sample Preparation. Cited 15/09/2010. Available from: http://www.oxford-instruments.com/products/x-ray-microanalysis/ebsd/ebsd-applications/Pages/Evolution%20of%20EBSD%20Patterns%20during%20Sample%20Preparation.pdf

[50] U. Kocks, C.T., H. Wenk, *Texture and Anisotropy*. 1998, Cambridge: Cambridge University Press.

[51] University of Cambridge - DoITPoMS. Cited 13/12/2007; Available from: http://www.doitpoms.ac.uk/index.html.

[52] Dungey, C., *The Influence of Process History and Defect Type on the Fatigue Behaviour of Ti-6Al-4V Under Complex Aero-Engine Load Regimes*, in *Metallurgy and Materials*. 2006, University of Birmingham.

[53] Ince, R., *Rolls-Royce Guidelines - Fatigue Principles*. Rolls-Royce Private Document, Cited 13/12/2007.

[54] Suresh, S., *Fatigue of Materials*. 2nd ed. 2003: Cambridge University Press.

[55] Hall, J. A., *Fatigue crack initiation in alpha-beta titanium alloys.* International Journal of Fatigue, 1997. **1**: p. 23-27.

[56] Suresh, B. and Ritchie, R. O., International Reviews, 1984, **29**, p. 445.

[57] Birosca, S., J. Y. Buffiere, F. A. Garcia-Pastor, M. Karadge, L. Babout and M. Preuss, *Three-dimensional characterization of fatigue cracks in Ti-6246 using X-ray tomography and electron backscatter diffraction.* Acta Materialia, 2009. **57 (19)**: p. 5834-5847.

[58] Birosca, S., J. Y. Buffiere, M. Karadge and M. Preuss, *3-D observations of short fatigue crack interaction with lamellar and duplex microstructures in a two-phase titanium alloy.* Acta Materialia, 2009. **59 (4)**: p. 1510-1522.

[59] Demulsant, X. and J. Mendez, *Influence of environment on low cycle fatigue damage in Ti-6Al-4V and Ti6246 titanium alloys.* Materials Science and Engineering A, 1996. **219**: p. 202-211.

[60] Sauer, C. and G. Lütjering, *Influence of alpha layers at beta grain boundaries on mechanical properties of Ti-alloys.* Materials Science and Engineering A, 2001. **319-321**: p. 393-397.

[61] Szczepanski, C. J., S. K. Jha, J. M. Larsen and J. W. Jones, *Microstructural influences on very high cycle fatigue crack initiation in Ti-6246.* Metallurgical and Materials Transactions A, 2008. **39A**: p. 2841-2851.

[62] Mendez, J., S. Mailly and P. Villechaise, *Temperature and environmental effects on low cycle fatigue resistance of titanium alloys.* European Structural Integrity Society, 2002. **29**: p. 95-102.

[63] Mendez, J., *On the effects of temperature and environment on fatigue damage processes in Ti alloys and in stainless steel.* Materials Science and Engineering A, 1999. **A263**: p. 187-192.

[64] Benedetti, M., V. Fontanari, G. Luetjering and J. Albrecht, *The effect of notch plasticity on the behaviour of fatigue cracks emanating from edge-notches in high strength beta-titanium alloys.* Engineering Fracture Mechanics, 2008. **75** (2): p. 169-187.

[65] Evans, W.J. and M.R. Bache, *Dwell-sensitive fatigue under biaxial loads in the near-alpha titanium alloy IMI685.* International Journal of Fatigue, 1994. **16**(7): p. 443

[66] Evans, W.J., *Dwell Sensitive Fatigue in a Near Alpha Titanium Alloy.* Journal of Materials Science Letters, 1987. **6**: p. 571-574.

[67] Evans, W.J. and M.R. Bache, *Hydrogen and fatigue behaviour in a near alpha titanium alloy.* Scripta Metallurgica et Materialia, 1995. **32**(7): p. 1019-1024.

[68] Stubbington, C.A. and S. Pearson, *Effect of Dwell on the Growth of Fatigue Cracks in Ti-6Al-4V Alloy Bar.* Engineering Fracture Mechanics, 1978. **10**: p. 723-756.

[69] Bache, M. R., L. Germain, T. Jackson and A. R. M. Walker. *Mechanical and Texture Evaluations of Ti 6246 as a Dwell Fatigue Tolerant Alloy*. In *11th World Conference on Titanium*. 2007. Japan.

[70] Hall, J. Safety Recommendation A-95-84-85. Cited 18/10/2007; Available from: www.ntsb.gov/recs/letters/1995/A95_84_85.pdf.

[71] Walker, A., Private Communication. *Rolls Royce Materials - Titanium Disc Cold Dwell Overview Jan 2006*, 15/05/2009.

[72] McBagonluri, F., E. Akpan, C. Mercer, W. Shen and W. O. Soboyejo, *An investigation of the effects of microstructure on dwell fatigue crack growth in Ti-6242.* Materials Science and Engineering: A, 2005. **405**(1-2): p. 111-134.

[73] Shen, W., A.B.O. Soboyejo, and W.O. Soboyejo, *Microstructural effects on Fatigue and Dwell Fatigue Crack Growth in Alpha/Beta Ti6Al-2Sn-4Zr-2Mo-0.1Si.* Metallurgical and Materials Transactions A, 2004. **35A**: p. 163-187.

[74] Zeng, W.D. and Y.G. Zhou, *The influence of microstructure on dwell sensitive fatigue in Ti-6.5Al-3.5Mo-1.5Zr-0.3Si alloy.* Materials Science and Engineering A, 2000. **290**(1-2): p. 33.

[75] Williams, D.N., *Sub-Critical Crack Growth Under Sustained Load.* Metallurgical Transactions, 1974. **5**: p. 2351-2358.

[76] Simpson, C.J. and C.E. Ells, *Delayed Hydrogen Embrittlement in Zr-2.5wt%Nb.* Journal of Nuclear Materials, 1974. **52**: p. 289-295.

[77] Meyn, D.A., *Effect of Hydrogen on Fracture and Inert Environment Sustained Load Cracking Resistance of Alpha/Beta Titanium Alloys.* Metallurgical Transactions, 1974. **5**: p. 2405-2414.

[78] Beachem, C.D., *A New Model for Hydrogen Assisted Cracking (Hydrogen "Embrittlement").* Metallurgical Transactions, 1972. **3**: p. 437-451.

[79] Eylon, D. and J.A. Hall, *Fatigue Behaviour of Beta Processed Titanium Alloy IMI685.* Metallurgical Transactions A, 1977. **8A**: p. 981-990.

[80] Shih, D.S., I.M. Robertson, and H.K. Birnbaum, *Hydrogen embrittlement of [alpha] titanium: In situ tem studies.* Acta Metallurgica, 1988. **36**(1): p. 111-124.

[81] Neal, D.F. *Creep Fatigue Interactions in Titanium Alloys*. In *Sixth World Conference on Titanium*. 1988. France.

[82] Evans, W.J. and M.R. Bache. *The Role of Hydrogen in Cyclic and Dwell Sensitive Fatigue of a Near Alpha Titanium Alloy*. In *Ti'92 Science and Technology*. 1992.

[83] Pao, P.S. and J.E. O'Neal, *Hydrogen-enhanced fatigue crack growth in Ti-6242S.* Journal of Nuclear Materials, 1984. **123**(1-3): p. 1587-1591.

[84] Evans, W.J., *The influence of microstructure on dwell sensitive fatigue in a near alpha titanium alloy.* Scripta Metallurgica, 1987. **21**(4): p. 469-474.

[85] Wanhill, R.J.H., *A Consideration of Cleavage in Alpha Titanium.* Acta Metallurgica, 1973. **21**: p. 1253-1258

[86] Cotterill, P., *A Review of Hydrogen Embrittlement.* Progress in Materials Science, 1961. **9**: p. 205-297.

[87] Neal, D.F. and P.A. Blenkinsop, *Internal Fatigue Origins in Alpha-Beta Titanium Alloys.* Acta Metallurgica, 1976. **24**: p. 59-63

[88] Eylon, D., J. A. Hall, C. M. Pierce and D. L. Ruckle, *Microstructure and Mechanical Properties Relationships in the Ti-11 Alloy at Room and Elevated Temperatures.* Metallurgical Transactions A, 1976. **7A**: p. 1817-1826.

[89] Hammond, C. in *TMS-AIME Fall Meeting Abstract Book*. 1976.

[90] Evans, W.J. and C.R. Gostelow, *The Effect of Hold Time on the Fatigue Properties of a Beta-Processed Titanium Alloy.* Metallurgical Transactions A, 1979. **10A**: p. 1837-1846.

[91] Davidson, D.L. and D. Eylon, *Titanium Alloy Fatigue Fracture Facet Investigation by Selected Area Electron Channeling.* Metallurgical Transactions A, 1980. **11A**: p. 837-843

[92] Bania, P.J. and D. Eylon, *Fatigue Crack Propagation of Titanium Alloys Under Dwell-Time Conditions.* Metallurgical Transactions A, 1978. **9A**: p. 847-855.

[93] Hack, J.E. and G.R. Leverant, *The Influence of Microstructural on the Susceptibility of Titanium Alloys to Internal Hydrogen Embrittlement.* Metallurgical Transactions A, 1982. **13A**: p. 1729-1738.

[94] Hack, J.E. and G.R. Leverant, *A model for hydrogen-assisted crack initiation on planar shear bands in near-alpha titanium alloys.* Scripta Metallurgica, 1980. **14**(4): p. 437-441.

[95] Lankford, J., D.L. Davidson, and G.R. Leverant, *Study of Fatigue Mechanisms in Aerospace Structural Materials*, Feb 1982. Annual Scientific Report, South West Research Institute, USA/

[96] Thomsen, M.L. and D.W. Hoeppner, *The effect of dwell loading on the strain accumulation behavior of titanium alloys.* International Journal of Fatigue, 1998. **20**(4): p. 309-317.

[97] Clarke, J.M., *A model for uniaxial creep based on internal-stress redistribution.* The Journal of Strain Analysis for Engineering Design, 1969. **4**(2): p. 95.

[98] Evans, W.J., *Creep-Fatigue Interactions in Ti-6Al-4V at Ambient Temperatures.* Creep and Fracture of Engineering Materials and Structures, 1987: p. 603-613.

[99] Evans, W.J., *Stress relaxation and notch fatigue in Ti-6Al-4V.* Scripta Metallurgica, 1987. **21**(9): p. 1223-1227.

[100] Cope, M.T., *A Detailed Evaluation and Associated Numerical Study of the Factors of Cold Dwell in Titanium Alloys*, Rolls-Royce Private Report, DNS14880, 29/09/1994

[101] Bache, M.R., W.J. Evans, and H.M. Davies, *Electron back scattered diffraction (EBSD) analysis of quasi-cleavage and hydrogen induced fractures under cyclic and dwell loading in titanium alloys.* Journal of Materials Science, 1997. **32**: p. 3435-3442.

[102] Bache, M.R., M. Cope, H.M. Davies, W.J. Evans and G. Harrison, *Dwell sensitive fatigue in a near alpha titanium alloy at ambient temperature.* International Journal of Fatigue, 1997. **1**: p. 83-88.

[103] Wojcik, C.C., K.S. Chan, and D.A. Koss, *Stage I fatigue crack propagation in a titanium alloy.* Acta Metallurgica, 1988. **36**(5): p. 1261-1270.

[104] Bache, M.R., W. J. Evans, V. Randle and R. J. Wilson, *Characterization of mechanical anisotropy in titanium alloys.* Materials Science and Engineering A, 1998. **257**(1): p. 139-144.

[105] Suri, S., G. B. Viswanathan, T. Neeraj, D. -H. Hou and M. J. Mills, *Room temperature deformation and mechanisms of slip transmission in oriented single-colony crystals of an [alpha]/[beta] titanium alloy.* Acta Materialia, 1999. **47**(3): p. 1019-1034.

[106] Viswanathan, G.B., S. Karthikeyan, R. W. Hayes and M. J. Mills, *Creep behaviour of Ti-6Al-2Sn-4Zr-2Mo: II. Mechanisms of deformation.* Acta Materialia, 2002. **50**(20): p. 4965-4980.

[107] Hasija, V., S. Ghosh, M. J. Mills and D. S. Joseph, *Deformation and creep modeling in polycrystalline Ti-6Al alloys.* Acta Materialia, 2003. **51**(15): p. 4533-4549.

[108] Brandes, M. and M. Mills, *Static recovery in titanium alloys at lower temperatures.* Materials Science and Engineering A, 2004. **387-389**: p. 570-575.

[109] Kassner, M.E., Y. Kosaka, and J.A. Hall, *Low Cycle Dwell Time Fatigue in Ti-6242.* Metallurgical and Materials Transactions A, 1999. **30A**: p. 2383-2389.

[110] Bache, M.R., *Processing titanium alloys for optimum fatigue performance.* International Journal of Fatigue, 1999. **21**(1): p. 105-111.

[111] Sinha, V., M. Mills, and J. Williams, *Understanding the contributions of normal-fatigue and static loading to the dwell fatigue in a near-alpha titanium alloy.* Metallurgical and Materials Transactions A, 2004. **35**(10): p. 3141-3148.

[112] Bridier, F., P. Villechaise, and J. Mendez, *Analysis of the different slip systems activated by tension in a alpha/beta titanium alloy in relation with local crystallographic orientation.* Acta Materialia, 2005. **53**(3): p. 555-567.

[113] Bridier, F., P. Villechaise, and J. Mendez, *Slip and fatigue crack formation processes in an alpha/beta titanium alloy in relation to crystallographic orientation on different scales.* Acta Materialia, 2008. **56**(15): p. 3951-3962.

[114] Savage, M.F., J. Tatalovich, M. Zupan, K. J. Hemker and M. Mills, *Deformation mechanisms and microtensile behaviour of single colony Ti-6242Si.* Materials Science and Engineering A, 2001. **319-321**: p. 398-403.

[115] Bhattacharyya, D., G. B. Viswanathan, R. Denkenberger, D. Furrer and H. L. Fraser, *The role of crystallographic and geometrical relationships between alpha and beta phases in an alpha/beta titanium alloy.* Acta Materialia, 2003. **51**(16): p. 4679-4691.

[116] Bhattacharyya, D., G.B. Viswanathan, and H.L. Fraser, *Crystallographic and morphological relationships between beta phase and the Widmanstätten and allotriomorphic alpha phase at special beta grain boundaries in an alpha/beta titanium alloy.* Acta Materialia, 2007. **55**(20): p. 6765-6778.

[117] Stanford, N. and P. Bate, *Crystallographic variant selection in Ti-6Al-4V.* Acta Materialia, 2004. **52**(17): p. 5215-5224.

[118] Woodfield, A., M. D. Gorman, R. R. Cordemann, J. A. Sutliff and B. Yamrom, *Effect of microstructure on dwell fatigue behaviour of Ti-6242*. In *Titanium '95: Science and Technology*. 1995.

[119] Humbert, M., L. Germain, N. Gey, P. Bocher and M. Jahazi, *Study of the variant selection in sharp textured regions of bimodal IMI 834 billet.* Materials Science and Engineering: A, 2006. **430**(1-2): p. 157-164.

[120] Moustahfid, H., M. Humbert, and M.J. Philippe, *Modeling of the texture transformation in a Ti-64 sheet after hot compression.* Acta Materialia, 1997. **45**(9): p. 3785-3790.

[121] Germain, L., N. Gey and M. Humbert, *Reliability of reconstructed beta-orientation maps in titanium alloys.* Ultramicroscopy, 2007. **107**: p. 1129-1135.

[122] Glavicic, M.G., P. A. Kobryn, T. R. Bieler and S. L. Semiatin, *A method to determine the orientation of the high-temperature beta phase from measured EBSD data for the low-temperature alpha phase in Ti-6Al-4V.* Materials Science and Engineering A, 2003. **346**(1-2): p. 50-59

[123] Glavicic, M.G., P.A. Kobryn, and S.L. Semiatin, *Validation of an automated EBSD method to deduce the [beta]-phase texture in Ti-6Al-4V with a colony-[alpha] microstructure.* Materials Science and Engineering A, 2004. **385**(1-2): p. 372-376

[124] Germain, L., N. Gey, M. Humbert, A. Hazotte, P. Bocher and M. Jahazi., *An automated method to analyze separately the microtextures of primary alpha grains and the secondary alpha inherited colonies in bimodal titanium alloys.* Materials Characterization, 2005. **54**(3): p. 216-222.

[125] Thomas, M.J., B.P. Wynne, and W.M. Rainforth, *An alternative method to separate and analyse the microtextures and microstructures of primary alpha grains and transformed beta grains in near-alpha titanium alloy Timetal 834.* Materials Characterization, 2005. **55**(4-5): p. 388-394.

[126] Germain, L., N. Gey, M. Humbert, P. Bocher and M. Jahazi, *Analysis of sharp microtexture heterogeneities in a bimodal IMI 834 billet.* Acta Materialia, 2005. **53**(13): p. 3535-3543.

[127] Biavant, K.L., S. Pommier, and C. Prioul, *Local texture and fatigue crack initiation in a Ti-6Al-4V titanium alloy.* Fatigue & Fracture of Engineering Materials & Structures, 2002. **25**(6): p. 527-545

[128] Glavicic, M.G., J.D. Miller, and S.L. Semiatin, *A method to measure the texture of secondary alpha in bimodal titanium-alloy microstructures.* Scripta Materialia, 2006. **54**(2): p. 281-286.

[129] Germain, L., N. Gey, M. Humbert, P.Vo, M. Jahazi and P. Bocher, *Texture heterogeneities induced by subtransus processing of near alpha titanium alloys.* Acta Materialia, 2008. **56**(16): p. 4298-4308

[130] Wynne, B.P. *EBSD Users Conference*. 2009. University of Wales, Swansea: RMS

[131] Rugg, D., M. Dixon, and F. Dunne, *Effective structural unit size in titanium alloys.* Journal of Strain Analysis for Engineering Design, 2007. **42**(4): p. 269-279.

[132] Germain, L. and M.R. Bache, *Crystallographic texture and the definition of effective structural unit size in titanium products*. 2007, University of Wales Swansea.

[133] Sinha, V., M. Mills, and J. Williams, *Determination of crystallographic orientation of dwell-fatigue fracture facets in Ti-6242 alloy.* Journal of Materials Science, 2007. **42**(19): p. 8334-8341

[134] Sinha, V., M. Mills, and J. Williams, *Crystallography of fracture facets in a near-alpha titanium alloy.* Metallurgical and Materials Transactions A, 2006. **37**(6): p. 2015-2026.

[135] Sinha, V., M. Mills, J. C. Williams and J. E. Spowart, *Observations on the faceted initiation site in the dwell-fatigue tested ti-6242 alloy: Crystallographic orientation and size effects.* Metallurgical and Materials Transactions A, 2006. **37**(5): p. 1507-1518.

[136] Dunne, F.P.E. and D. Rugg, *On the mechanisms of fatigue facet nucleation in titanium alloys..* Fatigue and Fracture of Engineering Materials & Structures, 2008. **31**: p. 949-958.

[137] Dunne, F.P.E., A. Walker, and D. Rugg, *A systematic study of hcp crystal orientation and morphology effects in polycrystal deformation and fatigue.* Proceedings of the Royal Society A: Mathematical, Physical and Engineering Science, 2007. **463**(2082): p. 1467-1489.

[138] Dunne, F.P.E., D. Rugg, and A. Walker, *Lengthscale-dependent, elastically anisotropic, physically-based hcp crystal plasticity: Application to cold-dwell fatigue in Ti alloys.* International Journal of Plasticity, 2007. **23**(6): p. 1061-1083

[139] Venkatramani, G., S. Ghosh, and M. Mills, *A size-dependent crystal plasticity finite-element model for creep and load shedding in polycrystalline titanium alloys.* Acta Materialia, 2007. **55**(11): p. 3971-3986.

[140] Kirane, K. And S. Ghosh, *A cold dwell fatigue crack nucleation criterion for polcrystalline Ti-6242 using grain-level crystal plasticity FE model.* International Journal of Fatigue, 2008. **30**: p. 2127-2139.

[141] Venkataramani, G., K. Kirane, and S. Ghosh, *Microstructural parameters affecting creep induced load shedding in Ti-6242 by a size dependent crystal plasticity FE model.* International Journal of Plasticity, 2008. **24**(3): p. 428-454.

[142] Turbofan. Cited 13/12/2007; Available from: http://en.wikipedia.org/wiki/Turbofan

[143] Cervenka, M. The Rolls-Royce Trent Engine. Cited 13/12/2007; Available from: http://www.msm.cam.ac.uk/phase-trans/mphil/Trent1.

[144] Bache, M.R. and W.J. Evans, *Impact of texture on mechanical properties in an advanced titanium alloy.* Materials Science and Engineering A, 2001. **319-321**: p. 409.

[145] aluMATTER - Representing Texture. Cited 13/12/2007; Available from: http://aluminium.matter.org.uk/content/html/eng/default.asp?catid=100&pageid=1039432491.

[146] *INCA - The Microanalysis Suite*. 2003, Oxford Instruments Analytical Ltd.

[147] Engineering Stress-Strain Curve. Cited 13/12/2007; Available from: http://www.key-to-steel.com/default.aspx?ID=CheckArticle&NM=43.

[148] Dislocation. Cited 18/07/2007; Available from: http://en.wikipedia.org/wiki/Dislocation.

[149] Behaviour and Manufacturing Properties of Materials. Cited 13/12/2007; Available from: http://www.engr.ku.edu/~rhale/ae510/lecture2/index.htm.

[150] Crystalline Structure Subject Guide: ASM International. Cited 20/05/2010; Available from: http://www.asminternational.org/portal/site/www/SubjectGuideItem/?vgnextoid=ad7cdc8cc359d210VgnVCM1000000621e010aRCRD.

[151] Engrasp, I. Stress-Life Fatigue Analysis. Cited 13/12/2007; Available from: www.engrasp.com/doc/etb/mod/fm1/stresslife/stresslife_help.html.

[152] Jackson, T., *Dwell LCF and LCF testing of macro colonised and "random texture" Ti6246 (TJK) material at R=0.3 and room temperature. In support of RT/TRE/000050*, Rolls-Royce Private Report, DHC226770, 23/06/2006.

[153] Unknown Author, *Test Laboratories webpage*. Rolls-Royce Intranet – Private Data. Cited 15/09/2007.

[154] Roberts, N., *The Influence of Surface Processing and Residual Stress on Fatigue in Titanium Disc Alloys*. Academic Report. University of Wales, Swansea. 26/10/2000.

[155] Robbie, W., *Summary of Cold Dwell Testing to Support H/1/TRE000050*, Rolls-Royce Private Report, DNS90941, 14/12/2006.

[156] Fox, K., *Cold Dwell Behaviour of Ti6246 - Analysis of Pole Figures and Orientation Distribution Functions measured by Manchester University*, Rolls-Royce Private Report, DNS129671, 15/05/2007.

[157] Jackson, T. and R. Whittaker, *Heat treatment of Ti6246 (TJK) alloy to produce microstructures suitable for cold dwell specimen testing*, Rolls-Royce Private Report, DNS129178, 23/03/2007.

[158] Attallah, M. M., S. Zabeen, R. J. Cernik and M. Preuss, *Comparative determination of the alpha/beta phase fraction in alpha + beta titanium alloys using X-ray diffraction and electron microscopy.* Materials Characteriation, 2009. **60**: p. 1248-1256.

[159] Humphreys, F.J. and M. Hatherly, *Recrystallisation and Related Annealing Phenomena*. 3rd ed. 1995.

[160] Bozzolo, N., N. Dewobroto, T. Grosdidier and F. Wagner, *Texture evolution during grain growth in recrystallized commercially pure titanium.* Materials Science and Engineering A. 2005. **397**: p. 346-355.

[161] Karthikeyan, T., A. Dasgupta, R. Khatirkar, S. Saroja, I. Samajdar and M. Vijayalakshmi, *Effect of cooling rate on transformation texture and variant selection during beta to alpha transformation in Ti-5Ta-1.8Nb alloy.* Materials Science and Engineering A. 2010. **528**: p. 549-558.

[162] Sharples, S., M. Clark and M. G. Somekh. *Fast non-contact imaging of material microstructure using local surface acoustic wave velocity mapping*. In *IEEE Ultrasonics Symposium*. 2005. p. 886-889

[163] Jackson, T., *Dwell LCF and LCF testing of beta heat-treated, alpha -beta heat-treated and production standard Ti6246. In Support of Red Top TRE/000050*, Rolls-Royce Private Report, DHC260077, 17/01/2007

[164] Evans, W.J., *Optimising mechanical properties in alpha+beta titanium alloys.* Materials Science and Engineering A, 1998. **243**(1-2): p. 89.

[165] Lefranc, P., V. Doquet, M. Gerland and C. Sarrazin-Baudoux, *Nucleation of cracks from shear-induced cavities in an alpha/beta titanium alloy in fatigue, room-temperature creep and dwell-fatigue.* Acta Materialia, 2008. **56**: p. 4450-4457.

[166] Jackson, T., *Analysis of Strain Induced Porosity (SIP) Size and Rate in Ti6246 Disc*. Rolls-Royce Private Report, DKC254934,07/06/2006

[167] Gil, F. J. and J. A. Planell, *Grain Growth Kinetic of the Near Alpha Titanium Alloys.* Journal of Materials Science Letters, 2000. **19**: p. 2023-2024.

[168] Brandes, M. C., M. J. Mills and J. C. Williams. *The effect of primary and secondary alpha morphology on the cold creep response of beta-processed Ti-6-2-4-2*. In *11th World Conference on Titanium*. 2007. Japan.

[169] Saal, S., L. Wagner, G. Luetjering, H. Pillhofer and M. A. Daeubler. *Effect of cooling rate on creep and low cycle fatigue resistance in Ti-6242.* Deutsche Geselleschaft fur Metallkunde, 1990. Bd.81 H**8**: p. 535-539.

[170] Sharples, S. D., M. Clark and M. G. Somekh, *Spatially Resolved Acoustic Spectroscopy for Fast Noncontact Imaging of Material Microstructure.* Optics Express, 2006. **14**: p. 10435-10440.

[171] Neeraj, T., D. -H. Hou, G. S. Daehn and M. J. Mills, *Phenomenological and microstructural analysis of room temperature creep in titanium alloys.* Acta Materialia, 2000. **48**(6): p. 1225

[172] Gerland, M., P. Lefranc, V. Doquet and C. Sarrazin-Baudoux, *Deformation and damage mechanisms in an alpha/beta 6242 Ti alloy in fatigue, dwell fatigue and creep at room temperature. Influence of internal hydrogen.* Materials Science and Engineering A, 2009. **507**: p. 132-143.

[173] Davies, H. M., *Low temperature dwell sensitive fatigue in near alpha alloys*. Academic Report. University of Wales, Swansea. 1998.

[174] Wanhill, R. J. H., R. Galatolo and C. E. W. Looije, *Fractographic and microstructural analysis of fatigue crack growth in a Ti-6Al-4V fan disc forging.* International Journal of Fatigue, 1989. **11**: p.407-416.

[175] Weiss, I., F. H. Froes, D. Eylon and G. E. Welsch, *Modification of alpha morphology in Ti-6Al-4V by thermomechanical processing.* Metallurgical Transactions, 1986. **17A**: p. 1935-1947.

[176] Seshacharyulu, T., S. C. Medeiros, W. G. Frazier and Y. V. R. K. Prased, *Microstructural mechanisms during hot working of commercial grade Ti-6Al-4V with lamellar starting structure.* Materials Science and Engineering, 2002. **A325**: p. 112-125.

[177] Sackett, E.E., L. Germain, and M.R. Bache, *Crystal plasticity, fatigue crack initiation and fatigue performance of advanced titanium alloys.* International Journal of Fatigue, 2007. **29**(9-11): p. 2015-2021.

[178] Fox, K. M., *Cold dwell behaviour of IMI829, IMI685/65s and IMI834 - Analysis of cold dwell rig test and engine service experience*, Rolls-Royce Private Report. DHC110272, 17/07/2005

[179] Wang, Y.N. and J.C. Huang, *Texture analysis in hexagonal materials.* Materials Chemistry and Physics, 2003. **81**(1): p. 11-26.

[180] Bantounas, I., T. Lindley, D. Rugg and D. Dye, *Effect of microtexture on fatigue cracking in Ti-6Al-4V.* Acta Materialia, 2007. **55**(16): p. 5655-5665.

[181] Germain, L., Private communication. *"Planar slip in Ti6246"*. 25/05/2007.

[182] Pearson, C.F., *RB211-535 Engines Examination of Burst LP2 Turbine Slab Disc in Ti5331s Material Cold Cyclic Dwell Test*, Rolls-Royce Private Report, CML37842. 21/07/1983.

[183] Kassner, M. E., *Role of small-angle (subgrain boundary) and large-angle (grain boundary) interfaces on 5- and 3-power law creep*. Materials Science and Engineering A, 1993. **A166**: p. 81-88.

[184] Furuhara, T. and T. Maki., *Variant selection in heterogeneous nucleation on defects in diffusional phase transformation and precipitation*. Materials Science and Engineering, 2001. **A312**: p. 145-154.

[185] Cayron, C., *Importance of the alpha --> beta transformation in the variant selection mechanisms of thermomechanically processed titanium alloys*. Scripta Materialia, 2008. **59**(5): p. 570.

[186] Da Costa Teixeira, J., B. Appolaire, E. Aeby-Gautier, S. Denis and L. Hericher, *Modeling of the phase transformations in near-beta titanium alloys during the cooling after forging*. Computational Materials Science, 2008. **42**(2): p. 266.

[187] Da Costa Teixeira, J., B. Appolaire, E. Aeby-Gautier, S. Denis and F. Bruneseaux, *Modeling of the effect of the beta phase deformation on the alpha phase precipitation in near-beta titanium alloys*. Acta Materialia, 2006. **54**(16): p. 4261.

[188] ASM Handbook Volume 9: Metallography and Microstructures. 2004.

[189] Wang, K, S. La, M. W. Fu, X. Li and X. Dong, *Optimisation of beta/near-beta forging process parameters of Ti-6.5Al-3.5Mo-1.5Zr-0.3Si.* Materials Characterization, 2009. **60**: p. 492-498.

[190] Ankem, S. and C.A. Greene, *Recent developments in microstructure/property relationships of beta titanium alloys.* Materials Science and Engineering A, 1999. **263**(2): p. 127.

[191] Doherty, R.D., D. A. Hughes, F. J. Humphreys, J. J. Jonas, D. J. Jensen, M. E. Kassner, W. E. King, T. R. McNelley, H. J. McQueen and A. D. Rollett, *Current issues in recrystallization: a review.* Materials Science and Engineering A, 1997. **238**(2): p. 219.

[192] Lütjering, G., J. Albrecht, C. Sauer and T. Krull, *The influence of soft, precipitate-free zones at grain boundaries in Ti and Al alloys on their fatigue and fracture behavior*. Materials Science and Engineering: A, 2007. **468-470**: p. 201.

[193] Cayron, C., *Importance of the alpha --> beta transformation in the variant selection mechanisms of thermomechanically processed titanium alloys*. Scripta Materialia, 2008. **59**(5): p. 570.

[194] Chauvy, C., P. Barberis, and F. Montheillet, *Microstructure transformation during warm working of beta-treated lamellar Zircaloy-4 within the upper alpha-range*. Materials Science and Engineering: A, 2006. **431**(1-2): p. 59.

[195] Barberis, P., F. Montheillet, and C. Chauvy, *Variant Selection in Zr Alloys: How Many Variants Generated from One Beta Grain?* Solid State Phenomena, 2005. **105**: p. 133-138.

[196] Wang, Y.N. and J.C. Huang, *Texture analysis in hexagonal materials.* Materials Chemistry and Physics, 2003. **81**(1): p. 11.

[197] Dixon, M., Private communication*. "Ladish pancake forgings information"*. 13/03/2007.